Title
EARTH SCIENCES DIVISION, ANNUAL FEPOPT 1984

Permalink
https://escholarship.org/uc/item/0ht1t9f5

Author
Lawrence Berkeley National Laboratory

Publication Date
1985-06-01

LBL-18496
UC-13 c1

Annual Report 1984

Earth Sciences Division

JUNE 1985

LAWRENCE BERKELEY LABORATORY
UNIVERSITY OF CALIFORNIA
BERKELEY, CALIFORNIA 94720

Prepared for the U.S. Department of Energy under Contract No. DE-AC03-76SF00098

EARTH SCIENCES DIVISION ANNUAL REPORT 1984

Lawrence Berkeley Laboratory
University of California
Berkeley, California 94720

June 1985

Prepared for the U.S Department of Energy under Contract No. DE-AC03-76SF00098

ACKNOWLEDGMENTS

This work was supported through U.S. Department of Energy Contract No. DE-AC03-76SF00098 by (1) the Assistant Secretary for Energy Research, Office of Basic Energy Sciences, Division of Engineering and Geosciences; (2) the Assistant Secretary for Conservation and Renewable Energy, Office of Renewable Technology, Division of Geothermal and Hydropower Technologies; (3) the Assistant Secretary for Conservation and Renewable Energy, Office of Advanced Conservation Technology, Division of Thermal and Mechanical Storage Systems; (4) the Assistant Secretary for Fossil Energy, Office of Oil, Gas, and Shale Technology, Division of Oil; (5) the Assistant Secretary for Nuclear Energy, Office of Nuclear Waste Management, Division of Nuclear Waste Isolation; (6) the Assistant Secretary for Nuclear Energy, Office of Nuclear Waste Management, Division of Remedial Action Programs; (7) the Waste Management Research Branch, Division of Health, Siting and Waste Management, Office of Nuclear Regulatory Research, U.S. Nuclear Regulatory Commission, through Interagency Agreements DOE-60-84-033 and DOE-60-84-146; (8) the Center for Seismic Studies, through Order No. 4306 from the Division of Geophysical Studies of the Department of Defense Advanced Research Projects Agency; (9) the Groundwater Research Branch of the Robert S. Kerr Environmental Laboratory, U.S. Environmental Protection Agency, through Interagency Agreements DW-89930198-01-0 and DW-89930722-01-0; (10) the U.S. Geological Survey, Western Region Office, through Interagency Agreement 40369; (11) the Electric Power Research Institute, through DOE/EPRI Agreement S-302-5; (12) the Gas Research Institute, through Contract No. 5081-212-0552; and (13) the Amoco and Shell Oil Companies, through Consortium Agreement WN-19.

CONTENTS

GEOMECHANICS 49

RESERVOIR ENGINEERING AND HYDROGEOLOGY 83

INTRODUCTION

Scientists and engineers of the Earth Sciences Division conduct research on a wide variety of topics relevant to the nation's energy development programs. This report summarizes the activities for 1984, illustrating the breadth and relevance of scientific investigations appropriate to the mission of a multipurpose National Laboratory. The Earth Sciences Division has developed unique expertise in several of the research areas reported upon here—expertise due in part to the special resources and facilities available to researchers at the Lawrence Berkeley Laboratory and to the Laboratory's commitment to technical and managerial competence. In addition to the permanent Laboratory staff, University faculty members, graduate students, and visiting scientists participate in many investigations. Interlaboratory cooperation and collaboration with other research institutions provide unmatched intellectual and technological resources for the study of complex problems.

Much of the Division's research deals with the physical-chemical properties and processes in the earth's crust, from the partially saturated, low-temperature, near-surface environment to the high-temperature environments characteristic of regions where magmatic-hydrothermal processes are active. Strengths in laboratory instrumentation, numerical modeling, and field measurement allow study of the transport of mass and thermal energy through geologic media—studies that now include the appropriate chemical reactions and the hydraulic-mechanical complexities of fractured rock systems. Related and parallel laboratory and field investigations are concerned with the effects of temperature, pressure, stresses, pore fluids, and fractures on the elastic and electrical properties of rock masses. These studies are concerned with rock behavior in the brittle and ductile crustal regimens, and they drive the development of improved geomechanical and geophysical tools and techniques for mapping and characterizing subsurface fractures.

This annual report presents summaries of research activities grouped according to the principal disciplines of the Earth Sciences Division: Geochemistry, Geomechanics, Reservoir Engineering and Hydrogeology, and Geophysics. We are proud to be able to bring you this report, which we hope will convey not only a description of the Division's scientific activities but also a sense of the enthusiasm and excitement present today in the earth sciences.

GEOCHEMISTRY

The geochemical research summarized here emphasizes in large part the interaction between subsurface aqueous fluids and rock at high temperatures and pressures. In these rock-water interactions, fluids are capable of dissolving and transporting considerable quantities of material. Such transport and deposition is a principal concern of radioactive waste disposal, and the security of the waste—both chemically and physically—has led to extensive modeling of the repository environment and to the analysis of ion migration and chemical interactions of fluids and rocks. In addition, analogs of repository conditions are studied in laboratory experiments, as are the surface chemistry of minerals likely to be used in repository barriers and the thermodynamics of radionuclide species. Rock-water interactions are also important components of other areas of investigation: the geochemistry of hydrothermal systems associated with young calderas, the occurrence of abiogenic methane, and the generation and migration of petroleum compounds in the earth's crust.

Work continues on the distribution and abundance of naturally occurring radioelements in the earth's crust. Because these elements produce a substantial proportion of the heat that drives hydrothermal systems, they form the natural "baseline" upon which the radiological effects of nuclear waste will be superimposed.

Experimental results obtained at low temperatures allow the prediction of properties of solids in regions that are presently experimentally inaccessible. Thus we continue to investigate the thermodynamic properties of high-temperature brines that occur in geothermal systems and that emanate from mid-ocean ridges and of silicate liquids that might occur in the earth's lower crust and upper mantle.

Thermodynamic Properties of Silicate Materials

I.S.E. Carmichael, R. Lange, J.F. Stebbins, D. Stein, and Q. Williams

Our program has continued this year as a set of interrelated but diverse projects, several of which are described here. The overall purpose is twofold: to produce thermodynamic data that are useful for calculations about natural petrologic processes and to interpret those results on the basis of an improved understanding of underlying molecular structure. For example, new density measurements will eventually be used to help predict the properties of lavas more accurately; these measurements are being made in systems that are compositionally simple enough to allow their interpretation on the basis of structure.

Results from various projects relate closely to one another. Liquid heat capacity data, which will be greatly refined by our new drop calorimeter, are (inversely) correlated with thermal expansions and compressibilities and give information about underlying molecular processes. The details of the thermodynamics of the phase transitions in a series of tectosilicate minerals have been quantified for the first time by our calorimetry and can be interpreted in light of data on Al/Si ordering from our NMR study of these materials (Murdoch et al., 1985).

DENSITIES OF MOLTEN SILICATES

The density of a magma strongly influences many igneous processes, including the initial separation of a melt from its source rocks and the sinking or floating of minerals as they crystallize. Recent calculations have shown that convection in a basaltic magma chamber can be driven by density differences as small as a few tenths of a percent. The importance of silicate liquid densities to answering geologic questions and to understanding the underlying details of the structure of the melts has led us to measure the effects of composition and temperature on melt density (Nelson and Carmichael, 1979; Mo et al., 1982). By making ultrasound velocity measurements, the influence of pressure can also be determined; when combined with results for heat capacity, density, and thermal expansion, these data yield values for the isothermal compressibility.

Recent interpretation and analysis of silicate liquid density data have been controversial (Bottinga et al., 1982; Ghiorso and Carmichael, 1984). To eliminate the problems caused by systematic, interlaboratory errors, we have begun a program in which the most precise techniques available will be used to redetermine densities and compressibilities in simple, three-component systems. We have relied upon Archimedes' method for density determinations, which involves the careful weighing of a platinum bob, first in air and then in the liquid of interest. We used two or three bobs to correct for surface tension effects. Overall accuracy was confirmed by measuring the density of molten NaCl at 900°C. Our value is within 0.7% of that recommended by the National Bureau of Standards. For ultrasound velocity measurements, we have used a highly precise interferometric technique (Rivers and Carmichael, 1982a,b).

The first results of this new program are for eight compositions in the Na_2O–Al_2O_3–SiO_2 ternary at temperatures from 1100 to 1550°C (Stein et al., 1984). A linear regression of molar volume with temperature and composition has a standard error of less than 0.2%, showing that there is no significant departure from linearity within the range of the data. This is illustrated by the two binaries within the system (Fig. 1). On the other hand, extrapolation in composition and temperature to the Al_2O_3–SiO_2 binary gives volumes much greater than those reported by Aksay et al., 1979. If the latter data are accurate, substantial variations from constant partial molar volumes and/or thermal expansions are indicated.

Our new data confirm also our earlier estimate of the density of $NaAlSi_3O_8$ liquid, which we used to suggest that this material undergoes an unusual, inelastic volume change at pressures above atmospheric but below 10 kbar (Navrotsky et al., 1982).

We have also measured ultrasound velocities in the same series of liquids over similar temperature ranges and at frequencies from 2 to 10 MHz. Results agree well with those of previous work and are being used to refine models of compressibility in multicomponent systems.

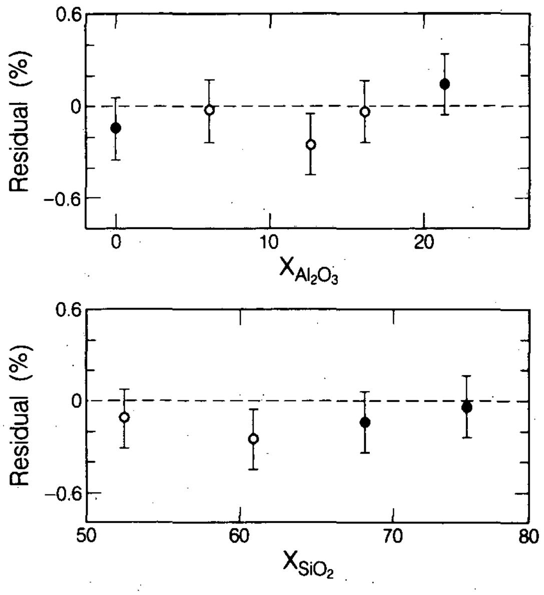

Figure 1. Residuals at 1673 K to a linear regression of molar volume with temperature and composition in the system Na_2O–Al_2O_3–SiO_2. Shown are values of 100 × ($V_{measured} - V_{calculated}$)/$V_{calculated}$ along a parabinary with constant mole fraction (X) of SiO_2 of 60% (**top**) and along a pseudobinary with constant $X_{Na}/X_{Al} = 2.0$ (**bottom**). Open circles are data collected at 1673 K; solid points represent results that were extrapolated to 1673 K from measurements at higher or lower temperatures. Note that the line of zero residuals is the best fit for *all* data, not just those shown here. Error bars are estimated from the general reproducibility of the measurements. [XBL 8410-9975]

PHASE TRANSITIONS IN TECTOSILICATE MINERALS

Many tectosilicate minerals important to petrologic studies, such as alkali feldspars ((K,Na)$AlSi_3O_8$), leucite ($KAlSi_2O_6$), and kaliophilite ($KAlSiO_4$), have high-order phase changes that are affected by composition, ordering state, and crystal structure. To understand transition mechanisms and to calculate high-temperature phase equilibria, we must know the energetics of these transitions. We have therefore measured the heat capacities of natural and synthetic leucite and $KAlSiO_4$ and their iron analogs ($KFe^{3+}Si_2O_6$ and $KFe^{3+}SiO_4$) from 400 to 1000 K, using a differential scanning calorimeter (DSC) (Lange et al., 1984).

Leucite is a characteristic mineral of potassium-rich, silica-poor lavas. At high temperatures it is cubic, but during cooling it reversibly changes to tetragonal symmetry. The transition is accompanied by a collapse of the (Si,Al)–O framework about the potassium cations and by complex, repeated twinning on the [110] crystallographic plane. Previous studies indicate that the transition temperature varies between 878 K and 963 K (Faust, 1963; Peacor, 1968; Taylor and Henderson, 1968; Hirao et al., 1976). Typically, the phase change occurs over a broad temperature interval and produces two exothermic peaks on a differential thermal analysis (DTA) curve. Iron leucite, on the other hand, has a single, sharp DTA peak at a lower temperature. Similarly, the triclinic-monoclinic phase transition in the iron analog of potassium feldspar ($KFeSi_3O_8$) is much sharper and more rapid than that in the aluminous phase (Wones and Appleman, 1963).

Our heat capacity data are plotted in Fig. 2 for five leucite samples: (a) synthetic iron leucite; (b) synthetic aluminum leucite; (c) a natural sample from Mt. Cimini in the Roman Volcanic Province, Italy; (d) heat treated Mt. Cimini leucite (1 week at 1673 K); and (e) a sample from a wyomingite lava from Leucite Hills, Wyoming. The last material contains excess silica in solid solution and is optically isotropic despite x-ray diffraction evidence for tetragonal symmetry. As expected, the abrupt phase change in the iron leucite contrasts sharply with the broad, double-peaked transitions of the aluminous samples. The transition in the iron phase has an enthalpy change about 15% less than that of the syn-

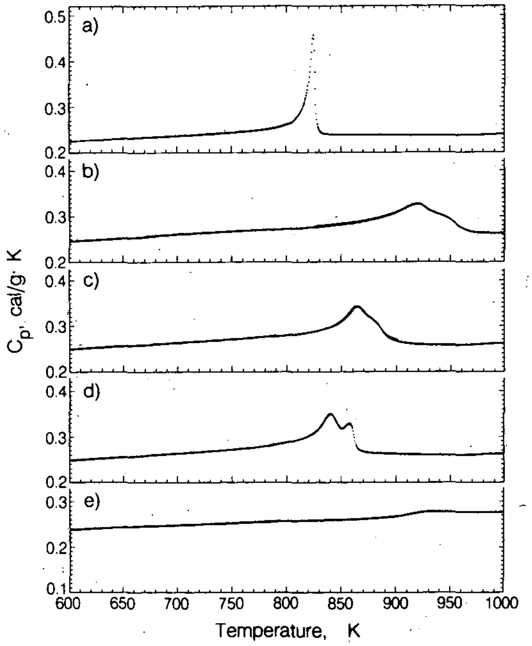

Figure 2. Heat capacity measurements, showing phase transitions in five leucite samples: **(a)** synthetic $KFeSi_2O_6$; **(b)** synthetic $KAlSi_2O_6$; **(c)** leucite from Mt. Cimini, Italy; **(d)** heat-treated Mt. Cimini leucite; **(e)** leucite from a wyomingite lava. [XBL 8410-9973]

thetic aluminum leucite, which in turn is 12% less than the Mt. Cimini sample. The double-peaked nature of the transition is accentuated in the heat-treated Mt. Cimini sample, for which the transition temperature is reduced by 10 K and the enthalpy change lowered by 4%. The wyomingite leucite begins to transform at 940 K, but continues above the limit of the DSC of 1000 K.

Several different polymorphs of $KAlSiO_4$ also occur in silica-poor volcanic rocks. The highest-temperature phase probably has hexagonal symmetry and rapidly inverts to a metastable orthorhombic form $o-KAlSiO_4$ at about 810 K (Pankratz, 1968; Abbot, 1984). Again, to study the effects of cation size and ordering on the phase transitions, we synthesized $o-KAlSiO_4$ and $o-KFeSiO_4$. Heat capacity data for these phases are shown in Fig. 3. The curves show that, in contrast with the results for leucite and potassium feldspar, the effect of Fe^{3+} substitution in $KAlSiO_4$ is to make the transition broader rather than narrower.

HIGH-TEMPERATURE DROP CALORIMETER

A major effort over the past 2 years has been the design and construction of a new drop calorimeter that will extend our measurements of heats of fusion and liquid heat capacities to 2400°C. This will enable us to study the very refractory materials, such as forsterite-rich olivine, that make up most of the earth's mantle and which constitute the source rocks of most or all of basaltic volcanism. The instrument is nearly complete, with all major components fabricated and assembly underway.

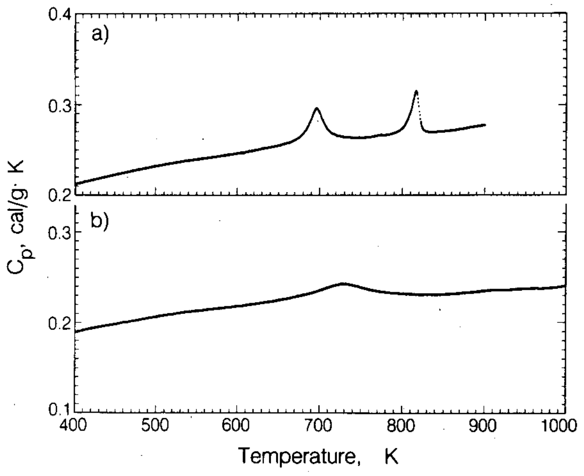

Figure 3. Heat capacity data showing phase transitions in **(a)** $o-KAlSiO_4$ and **(b)** $o-KFeSiO_4$. Units are as in Fig. 2. The first peak in (a) is caused by the presence of a second phase. [XBL 8410-9974]

REFERENCES

Abbott, R.N., Jr., 1984. $KAlSiO_4$ stuffed derivatives of tridymite: Phase relationships. Am. Mineral., v. 69, p. 449–457.

Aksay, I.A., Pask, J.A., and Davis, R.F., 1979. Density of SiO_2–Al_2O_3 melts. J. Am. Ceram. Soc., v. 62, p. 332–336.

Bottinga, Y., Weill, D.F., and Richet, P., 1982. Density calculations for silcate liquids. I. Revised method for alumino-silicate compositions. Geochim. Cosmochim. Acta, v. 46, p. 909–919.

Faust, G.T., 1963. Phase transition in synthetic and natural leucite. Schweitz. Mineral. Petrog. Mitt., v. 43, p. 165–195.

Ghiorso, M.S., and Carmichael, I.S.E., 1984. Comment on: "Density calculations for silicate liquids. I. Revised method for alumino-silicate compositions," by Bottinga, Weill, and Richet. Geochim. Cosmochim. Acta, v. 48, p. 401–408.

Hirao, K., Soga, N., and Kunugi, M., 1976. Thermal expansion and structure of leucite-type compounds. J. Phys. Chem., v. 80, p. 1612–1616.

Lange, R., Stebbins, J.F., and Carmichael, I.S.E, 1984. Phase transitions in leucites and kalsilites. Geol. Soc. Am., Abstr. Progr., v. 16, p. 568.

Mo, X., Carmichael, I.S.E., Rivers, M., and Stebbins, J., 1982. The partial molar volume of Fe_2O_3 in multicomponent silicate liquids and the pressure dependence of oxygen fugacity in magmas. Min. Mag., v. 45, p. 237–245.

Murdoch, J.B., Stebbins, J.F., and Carmichael, I.S.E., 1985. High-resolution nuclear magnetic resonance spectroscopy of aluminosilicate crystals, glasses, and liquids. *In* this Annual Report.

Navrotsky, A., Capobianco, C., and Stebbins, J.F., 1982. Some thermodynamic and experimental constraints on the melting of albite at atmospheric and high pressure. J. Geol., v. 90, p. 679–698.

Nelson, S.A., and Carmichael, I.S.E., 1979. Partial molar volumes of oxide components in silicate liquids. Contrib. Mineral. Petrol., v. 71, p. 117–124.

Pankratz, L.B., 1968. High-temperature heat contents and entropies of dehydrated analcite, kaliophilite, and leucite. U.S. Bur. Mines Rept. Inv. 7073, 8 p.

Peacor, D., 1968. A high-temperature single crystal diffractometer study of leucite, $(K,Na)AlSi_2O_6$. Z. Kristall., v. 127, p. 213–224.

Rivers, M., and Carmichael, I.S.E., 1982a. Ultrasonic velocity and attenuation of liquids in the system $NaAlSi_3O_8$–$CaAl_2Si_2O_8$–$CaMgSi_2O_6$. Trans. Am. Geophys. Union, v. 63, p. 1136.

Rivers, M., and Carmichael, I.S.E., 1982b. The ultrasonic velocity and attenuation of silicate melts. Geol. Soc. Am., Abstr. Progr., v. 14, p. 600.

Stein D., Stebbins, J.F., and Carmichael, I.S.E., 1984. New measurements of liquid densities in the system Na_2O–Al_2O_3–SiO_2. Trans. Am. Geophys. Union, v. 65, p. 1140.

Taylor, D., and Henderson, C.M.B., 1968. The thermal expansion of the leucite group of minerals. Am. Mineral., v. 53, p. 1476–1489.

Wones, D.R., and Appleman, D.E., 1963. Properties of synthetic triclinic $KFeSi_3O_8$, iron microcline, with some observations on the iron-microcline iron-sanidine transition. J. Petrol., v. 4, p. 131–137.

High-Resolution Nuclear Magnetic Resonance Spectroscopy of Aluminosilicate Crystals, Glasses, and Liquids

J.B. Murdoch, J.F. Stebbins, and I.S.E. Carmichael

Many aspects of the molecular structure of materials influence their bulk physical and chemical properties. Entropies, for example, are affected by the state of ordering of ionic and molecular species, and enthalpies are controlled by bond lengths and angles. Information about the details at the microscopic level, while of course interesting for their own sake, can thus also help to explain and predict macroscopic properties. Nuclear magnetic resonance spectroscopy is sensitive to many such structural parameters. In collaboration with Professor Alex Pines and Erika Schneider of the Materials and Molecular Research Division at this Laboratory, we have used nuclear magnetic resonance (NMR) to probe the structure of a variety of aluminosilicate materials important in the earth and materials sciences.

One aspect of this work has focused on the ordering of aluminum and silicon cations in crystals and glasses. Because the chemical shift of ^{29}Si is strongly affected by the number of next-nearest-neighbor aluminum atoms, information on this ordering can be obtained. We have collected ^{29}Si magic-angle spinning spectra of a series of glasses that contain K, Na, and Ca and have various Al/Si ratios. As previously observed for nonaluminous systems (Murdoch et al., 1985), the field strength of the cation systematically changes the variety of the anionic species that are present. Thus, for a given stoichiometry, NMR line width increases from K to Na to Ca. In addition, though, we have found that the pattern of variation of NMR line width with Al/Si is consistent with a statistical model in which Al and Si are randomly distributed on tetrahedral sites and in which Al–O–Al bonds are excluded (Fig. 1) (Stebbins et al., 1984a). The data are inconsistent with either of the simple alternatives of Al/Si ordering or complete disorder. This represents one of the first relatively direct views of ordering in these amorphous phases.

As an extension of previous work on the crystalline phase albite ($NaAlSi_3O_8$), we have studied the effect of heat treatment on Al/Si ordering in a

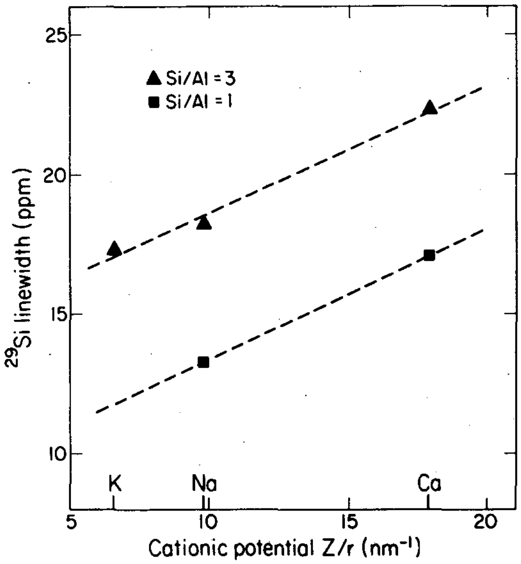

Figure 1. Integrated line widths (full width at half maximum, divided by peak height) of tectosilicate glasses (formula $M^{n+}_{x/n}Al_xSi_{1-x}O_2$, M = Ca, Na, K) as a function of silicon to aluminum ratio. [XBL 842-9644]

variety of other aluminosilicate minerals, including nepheline ($NaAlSiO_4$), analcite ($NaAlSi_2O_6 \cdot H_2O$), kalsilite ($KAlSiO_4$), and leucite ($KAlSi_2O_6$). The ^{29}Si NMR spectra for all of these show clear separation of silicon crystallographic sites, which reflect both local bond configuration and aluminum next-nearest-neighbor population. For example, the spectra of both a natural leucite and one synthesized at 1400°C (Fig. 2) contain eight distinct peaks superimposed on a much broader absorption band. The sharp features can be assigned to Si atoms in all three tetrahedral sites in the crystals, each having from zero to three aluminate neighbors. Unlike that for albite, however, the spectrum does not change appreciably on long-term heating near the melting point, suggesting that the natural phase is initially disordered (Murdoch et al., 1984a). The high-temperature origin of the natural mineral is probably the cause of this disorder. Our NMR work has also provided structural information that will be useful in interpreting the results of a companion study of the thermodynamics of phase transitions in these minerals (Carmichael et al., 1985).

Thermodynamic studies of silicate liquids have shown the energetic importance of the differences between glasses and liquids. Large values of heat capacity and entropy in silicate liquids (relative to glasses and crystals) suggest that nonvibrational variations in liquid structure increase with temperature (Stebbins et al., 1984b). The nature of these configurational changes is not well known, but they must be tied to the details of molecular motion in the liquid state. To study these dynamics, we have designed and built a novel, high-resolution, high-temperature NMR apparatus. The first experiments on actual molten silicates, at temperatures to 1300°C, were even more successful than expected. We obtained spectra for ^{27}Al, ^{29}Si, and ^{23}Na in six different liquids over a range of temperature wide enough to observe the high-frequency liquid-glass transition (Stebbins et al., 1985). Results show that local structure, as reflected in the influence of bulk composition on chemical shift (δ), is similar in glasses and corresponding liquids. For example, $\delta(^{29}Si)$ becomes more negative in more polymerized liquids because of an increase in the chemical shielding of the Si sites. Similarly, $\delta(^{23}Na)$ decreases systematically as the ratio O/Na increases, as is expected if Na occupies large, open sites surrounded entirely by oxygens.

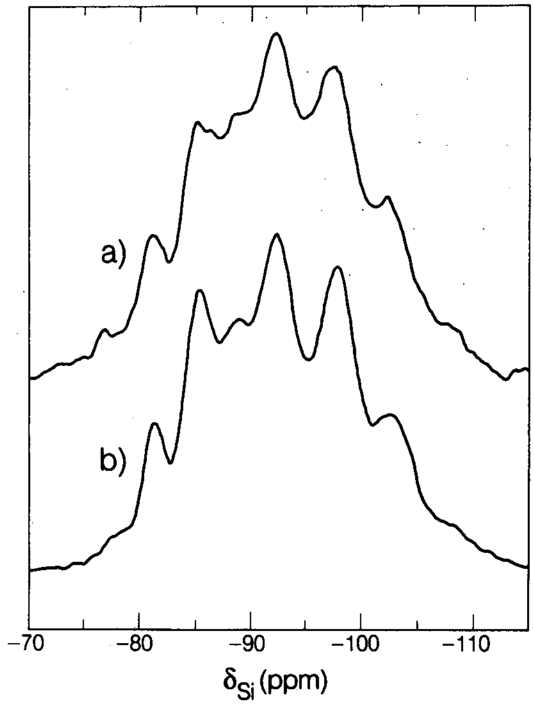

Figure 2. ^{29}Si magic-angle spinning NMR spectrum for leucites. **(a)** Synthetic leucite. **(b)** Natural sample from Mt. Cimini, Roman Volcanic Province, Italy. δ is the chemical shift, in ppm, relative to TMS. [XBL 841-9986]

NMR results on molten silicates also provide the first direct information on the dynamics of molecular motion, which is the ultimate cause of the energetic differences between liquids and glasses. Apparently, the polymerized, anionic structural "backbone" of the liquid is in rapid motion at high temperatures, with bonds constantly breaking and reforming. In the liquid region, ^{29}Si spectra consist of single lines as narrow as 100 Hz or 3 ppm at a field strength of 4.2 Tesla (Fig. 3) (Murdoch et al., 1984b; Schneider et al., 1984). This implies that the silicate species are moving faster than the total frequency range of the chemical shift anisotropy (about 3.5 kHz). In addition, if it is assumed that the liquid contains a range of silicate anion types comparable to that of the glass, then the species must be chemically exchanging more rapidly than the typical separation in resonant frequency between the species, or 300–500 Hz. If Q^n refers to an SiO_4 tetrahedral structural unit bound to n other $(Si,Al)O_4$ units, then reactions such as $2Q^3 = Q^2 + Q^4$ must be taking place. A time-averaged view of the structure results. Broad shoulders in some spectra suggest that the exchange frequencies may drop below this limit of a few hundred hertz at the lowest temperatures studied.

^{27}Al spectra are very broad (about 20 kHz) at all temperatures. Since Al and Si occupy similar sites in the melts and Si lines are narrow, this broadening must be due to rapid quadrupole relaxation of the

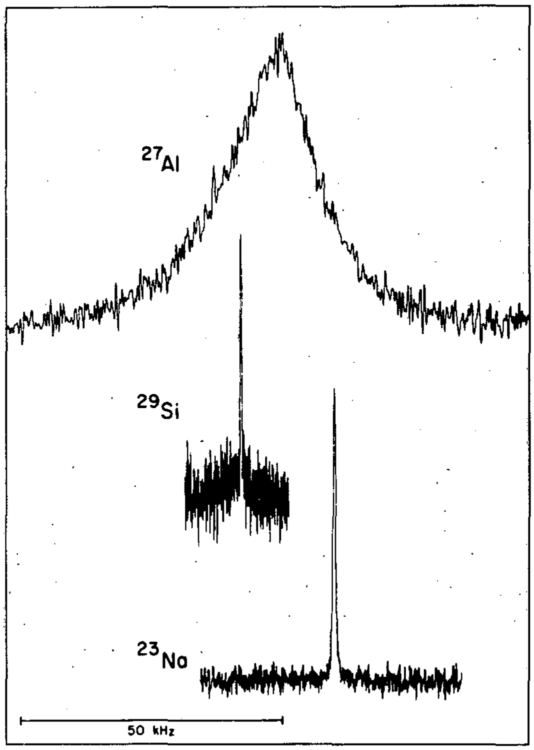

Figure 3. Typical NMR spectra for molten silicates. Data are for $NaAlSi_2O_6$ at about 1300°C. Relative locations of spectra are arbitrary, but all have the same frequency scale, as shown at bottom. [XBL 849-9926]

aluminum nuclei. As for ^{29}Si, ^{23}Na spectra show narrow, liquid-like lines at high temperature, again as expected from the relatively high freedom of motion of interstitial cations.

REFERENCES

Carmichael, I.S.E., Lange, R., Stebbins, J.F., Stein, D., and Williams, Q., 1985. Thermodynamic properties of silicate materials. *In* this Annual Report.

Murdoch, J.B., Stebbins, J.F., and Carmichael, I.S.E., 1984a. Silicon-29 MAS nuclear magnetic resonance study of the structure of feldspathoid minerals. Geol. Soc. Am., Abstr. Progr., v. 16, p. 604.

Murdoch, J.B., Stebbins, J.F., Schneider, E., and Carmichael, I.S.E., 1984b. NMR spectroscopy of Si-29, Na-23, and Al-27 in molten silicates to 1300°C: Approach and spectra. Trans. Am. Geophys. Union, v. 65, p. 1141.

Murdoch, J.B., Stebbins, J.F., and Carmichael, I.S.E., 1985. High-resolution ^{29}Si NMR study of silicate and aluminosilicate glasses. The effect of network-modifying cations. Am. Mineral., in press.

Schneider, E., Stebbins, J.F., Murdoch, J.B., and Carmichael, I.S.E., 1984. NMR spectroscopy of Si-29, Na-23, and Al-27 in molten silicates to 1300°C: Technique and analysis. Trans. Am. Geophys. Union, v. 65, p. 1141.

Stebbins, J.F., Murdoch, J.B., and Carmichael, I.S.E., 1984a. Structure of aluminosilicate glasses: A silicon-29 nuclear magnetic resonance study. Trans. Am. Geophys. Union, v. 65, p. 1141.

Stebbins, J.F., Carmichael, I.S.E., and Moret, L.K., 1984b. Heat capacities and entropies of silicate liquids and glasses. Contrib. Mineral. Petrol., v. 86, p. 131–148.

Stebbins, J.F., Murdoch, J.B., Schneider, E., Carmichael, I.S.E., and Pines, A., 1985. A high temperature nuclear magnetic resonance study of ^{23}Na, ^{27}Al, and ^{29}Si in molten silicates. Nature, in press.

Thermodynamics of High-Temperature Brines

K.S. Pitzer and R.C. Phutela

Current interest in a variety of geochemical phenomena, including geothermal and geopressurized brines, has focused attention on the importance of a model of aqueous solution properties at high temperatures and pressures. The usefulness of a model for aqueous solutions is not limited to geothermal or other natural brines. Research and engineering design in the fields of desalination, industrial waste treatment, hydrometallurgy, materials corrosion, solution mining, and hydrothermal ore deposition all depend on a knowledge of brine chemistry.

The number of different brines encountered is large, so that making detailed measurements on each of them is impractical. A model that can predict the properties of complex brines, yet is based on a minimum amount of experimental data on a few key systems, has been developed (Pitzer and Kim, 1974; Pitzer, 1979) and has been remarkably successful in a wide variety of cases at room temperature (Harvie and Weare, 1980; Harvie, et al., 1982 ,1984). As the data base has expanded, successful calculations have been made for mixed electrolytes at higher temperatures (de Lima and Pitzer, 1983a,b).

With the completion of a very comprehensive treatment for the thermodynamics of aqueous NaCl (Pitzer and Li, 1983, 1984; Pitzer, 1984; Pitzer et al., 1984), it seems desirable to review the status of the data base at high temperatures for other important brine components.

The basic equation for the excess Gibbs energy may be written

$$
\begin{aligned}
G^{EX}/n_w RT &= f(I) \\
&+ 2\sum_c \sum_a m_c m_a[B_{ca}(I) + (\Sigma mz)C_{ca}] \\
&+ \sum_c \sum_{c'} m_c m_{c'}[\Theta_{cc'}(I) + \sum_a m_a \psi_{cc'a}] \\
&+ \sum_a \sum_{a'} m_a m_{a'}[\Theta_{aa'}(I) + \sum_c m_c \psi_{caa'}] \,,
\end{aligned}
$$

where n_w is the number of kilograms of water and $f(I)$ is a general function of the ionic strength, I, which represents the electrostatic effects and includes the Debye-Hückel limiting law. The exact definitions and explanations of all of the other terms have been given elsewhere (Pitzer, 1979) and would overburden this brief summary. The sums for the ion-interaction terms run over all cations, c, and anions, a. Terms for neutral solute species can be added. Where dependency on ionic strength is indicated, it is given by a general function with one additional parameter for the given pair of ions.

By far the most important terms at high temperatures are the electrostatic or Debye-Hückel term, $f(I)$, which is completely determined by the properties of water, and the terms that express the binary interactions for unlike charged ions. Each binary interaction term comprises one component that is independent of ionic strength $\beta_{ca}^{(0)}$ and less important components that are dependent on ionic strength. The triple ion interactions and the binary interactions of ions of the same sign are much less important but are necessary for accuracy approaching that of the best experiments.

Other thermodynamic properties are obtained from derivatives of the Gibbs energy. For example, the enthalpy and entropy depend on the temperature derivative and the volume, the pressure derivative. Activity and osmotic coefficients are obtained from composition derivatives and require only the parent parameters, including $\beta_{ca}^{(0)}$.

DATA BASE

As an indication of the present status of the full array of parameters for this model, Table 1 gives the value of $\beta_{ca}^{(0)}$ for various brine components at a series of temperatures and the saturation pressure of water. Where both the first and second temperature derivatives are known to a particular temperature, the parent function is integrated to the next-higher temperature entry of the table.

The value of $\beta_{ca}^{(0)}$ suggests how those ions behave in water. A negative value indicates a tendency toward ion pairing, whereas a large positive value indicates very strong ion hydration.

Where an entry is given in Table 1 for $\beta_{ca}^{(0)}$, information on the other ion-interaction parameters is available. The pressure dependency is determined from volumetric information, which is usually, but not always, available over the same temperature range. The pressure effect is relatively small except at very high pressures or quite near the critical point of water. The range of composition for the model

Table 1. The ion-interaction parameter $\beta_{ca}^{(0)}$ for various brine components at a series of temperatures.

	$\beta_{ca}^{(0)}$ at T(K)			
	298	373	473	573
NaCl	0.0754	0.1002	0.0938	0.0768
LiCl	0.1485	0.1369	0.1214	0.1060
KCl	0.0481	0.0695	0.0707	0.0618
CsCl	0.0335	0.0576	0.0624	0.0615
HCl	0.1775	0.1572	0.5187	
NaI	0.1195	0.1558	0.1778	
CsI	0.0244	0.0581	0.0455	
CsF	0.1306	0.1213	0.0804	
Na_2SO_4	0.0186	0.1057	0.1415	0.1656
$MgCl_2$	0.3511	0.3111	0.2682	
$CaCl_2$	0.3053	0.3032	0.2693	
$SrCl_2$	0.2858	0.3165	0.3850	

extends usually to an ionic strength of at least 5 mole/kg and often to saturation with the solid, although in a few cases it is less. But the greatest interest is in cases where only one component, usually NaCl, is at very high concentration. In these cases the parameters that are available will yield accurate results for the effects of the other components.

The information in Table 1, and that for the other parameters, has been expressed by equations giving the dependency on temperature and pressure. These equations are given in the original publications (Rogers and Pitzer, 1981; de Lima and Pitzer, 1983b; Holmes and Mesmer, 1983; Phutela, and Pitzer, 1983; Saluja, Phutela, and Pitzer, in preparation).

BRINES AT HIGH TEMPERATURE

As test calculations for brines at high temperatures, the activity coefficient was calculated for several systems, each at saturation pressure and in equilibrium with one solid component (de Lima and Pitzer, 1983a,b). The activity coefficient can be calculated separately from the model for the brine and from the thermodynamics of the solid phase. The first example concerns solutions of NaCl and $MgCl_2$ in equilibrium with solid NaCl. The composition is given as the ionic strength fraction, y ($MgCl_2$). The curves in Fig. 1 represent the predictions of the brine model; the points are calculated from solubility measurements. The agreement is excellent even for the remarkably rapid change in $\gamma_\pm$ at 200°C at large y ($MgCl_2$).

A second example is the solubility of Na_2SO_4 in NaCl at high temperature. Here the activity coefficient of Na_2SO_4 is compared; the results are in Table 2. Among the examples chosen from the very long list of results, some have a very high molality of NaCl, and others are mostly Na_2SO_4. While the agreement is less than perfect, the results indicate that the model would yield very useful solubility predictions even to 300°C, which is well above the range of the measurements on which the model parameters for Na_2SO_4 were determined. Similar calculations were made for $NaCl–Na_2SO_4–H_2O$ in equilibrium with solid NaCl and with both NaCl and Na_2SO_4, as well as for various alkali chloride mixtures in equilibrium with one or more solid alkali chlorides. The agreement is generally good. The few substantial discrepancies are attributed to solubility measurements from old or doubtful sources.

These calculations for brines at very high ionic strength constitute a severe test of the equations and parameters. At more moderate concentration the model should yield higher accuracy. It should also be noted that these solubility data were not used in evaluating any of the parameters of the model. Thus the comparisons are true tests of the capacity of the model to make predictions.

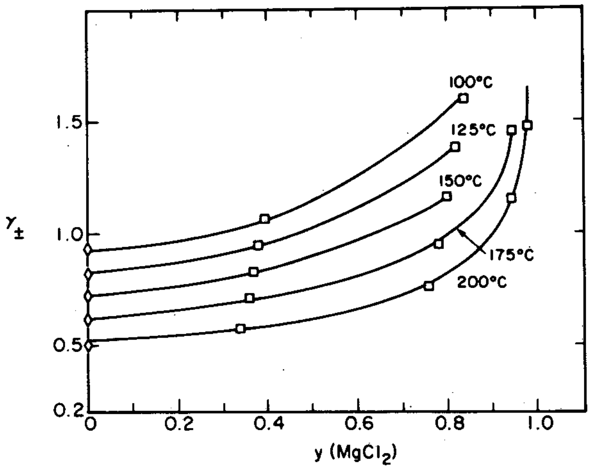

Figure 1. The activity coefficient of NaCl in aqueous mixtures of $MgCl_2$ with NaCl in equilibrium with solid NaCl. Curves are calculated from the brine model; points, from solubility measurements. [XBL 8411-4820]

Table 2. Activity coefficients of Na_2SO_4 in a saturated aqueous mixture of NaCl + Na_2SO_4.

			$\gamma_\pm(Na_2SO_4)$ from	
t(°C)	m(NaCl)	m(Na_2SO_4)	Brine model	Solubility data
100	1.78_0	1.77_6	0.157	0.153
100	4.32_2	0.846	0.199	0.181
150	0.821	2.36_6	0.0937	0.0917
150	6.98_1	0.507	0.136	0.120
200	0.856	2.53_4	0.0524	0.0511
200	5.57_8	0.894	0.0698	0.0625
250	0.907	2.40_1	0.0272	0.0270
250	5.25_3	1.62_2	0.0308	0.0285
300	1.02_7	1.35_9	0.0205	0.0176
300	5.73_2	1.24_6	0.0123	0.0107

REFERENCES

de Lima, M.C.P., and Pitzer, K.S., 1983a. Thermodynamics of saturated aqueous solutions including mixtures of NaCl, KCl, and CsCl. J. Solution Chem., v. 12, p. 171–185.

de Lima, M.C.P., and Pitzer, K.S. 1983b. Thermodynamics of saturated electrolyte mixtures of NaCl with Na_2SO_4 and with $MgCl_2$. J. Solution Chem., v. 12, p. 187–199.

Harvie, C.E., Eugster, H.P., and Weare, J.H., 1982. Mineral equilibria in the six-component seawater system, Na–K–Mg–Ca–SO_4–Cl–H_2O at 25°C. II: Compositions of the saturated solutions. Geochim. Cosmochim. Acta, v. 46, p. 1603–1613.

Harvie, C.E., Moller, N., and Weare, J.H., 1984. The prediction of mineral solubilities in natural waters: The Na–K–Mg–Ca–H–Cl–SO_4–OH–HCO_3–CO_3–H_2O system to high ionic strengths at 25°C. Geochim. Cosmochim. Acta, v. 48, p. 723–751.

Harvie, C.E., and Weare, J.H., 1980. The prediction of mineral solubilities in natural waters: The Na–K–Mg–Ca–Cl–SO_4–H_2O system from zero to high concentration at 25°C. Geochim. Cosmochim. Acta, v. 44, p. 981–997.

Holmes, H.F., and Mesmer, R.E., 1983. Thermodynamic properties of aqueous solutions of the alkali metal chlorides to 250°C. J. Phys. Chem., v. 87, p. 1242–1255.

Phutela, R.C., and Pitzer, K.S., 1983. Thermodynamics of aqueous calcium chloride. J. Solution Chem., v. 12, p. 201–207.

Pitzer, K.S. 1979. Theory: Ion interaction approach. *In* R.M. Pytkowicz (ed.), Activity Coefficients in Electrolyte Solutions (Vol. 1). Boca Raton, Florida, CRC Press, p. 157–208.

Pitzer, K.S., 1984. Thermodynamic properties of aqueous NaCl from 273 to 823 K with estimates for higher temperatures. Lawrence Berkeley Laboratory Report LBL-18183. (To be published in the Proceedings of the Tenth International Conference on the Properties of Steam, Moscow, September 1984).

Pitzer, K.S., and Kim, J.J., 1974. Thermodynamics of electrolytes. IV. Activity and osmotic coefficients for mixed electrolytes. J. Am. Chem. Soc., v. 96, p. 5701–5707.

Pitzer, K.S., and Li, Y.-g., 1983. Thermodynamics of aqueous sodium chloride to 823 K and 1 kbar. Proc. Nat. Acad. Sci. U.S.A., v. 80, p. 7689–7693.

Pitzer, K.S., and Li, Y.-g., 1984. Critical phenomena and thermodynamics of dilute aqueous sodium chloride. Proc. Nat. Acad. Sci. U.S.A., v. 81, p. 1268-1271.

Pitzer, K.S., Peiper, J.C., and Busey, R.H., 1984. Thermodynamic properties of aqueous sodium chloride solutions. Phys. Chem. Ref. Data, v. 13, p. 1–102.

Rogers, P.S.Z., and Pitzer, K.S., 1981. High-temperature thermodynamic properties of aqueous sodium sulfate solutions. J. Phys. Chem., v. 85, p. 2886–2895; see also v. 86, p. 2110.

Methane Formation During Hydrolysis by Mafic Rock

J.A. Apps

During the past few years, the possible abiogenic formation of methane in the mantle and its subsequent migration into the crust has excited considerable interest. Some scientists (Gold, 1978; 1979a,b, 1980; Gold and Soter, 1980; Giardini and Melton, 1981; Giardini et al., 1982) believe that the significant quantity of carbon that was trapped in the earth during planetary accretion and differentiation some 4.5 × 10^9 years ago is migrating from the mantle and contributing to the formation of many of the world's oil and gas reserves.

Gold and his supporters hold that methane should be chemically stable in the upper mantle and that some mechanism exists by which it is transported to the crust. I argue instead that methane of abiogenic origin is most probably generated in the crust at relatively shallow depths, at intermediate temperatures (100–500°C), and under the strongly reducing conditions resulting from hydrolysis by mafic and ultramafic rocks. The source of the carbon may lie either in the mantle or in the crust.

CARBON REDUCTION DURING ULTRAMAFIC ROCK HYDROLYSIS

Ferromagnesian silicates, such as olivine or enstatite, are dominant mineral components of ultramafic rocks. Reducing conditions may arise wherever these minerals are serpentinized in shallow crustal regions. Favorable environments for carbon reduction would be (1) obducting oceanic crust where it collides with continental crust, (2) ultramafic horizons in layered mafic intrusions, and (3) regions of oceanic crust undergoing hydrothermal alteration due to convection of heated sea water at spreading centers. Hydrolysis by continental basalts and gabbros may also produce favorable conditions.

Ferromagnesian silicate hydrolysis leads to oxidation of part of the ferrous iron to the ferric state, with concomitant reduction of water and other components in the system. Graphite, methane, hydrogen, and even iron and nickel-iron alloys may form under these conditions. Graphite has been observed in several ultramafic rocks (Cady et al., 1963; Krishnarao, 1964; Shteynberg and Lagutina, 1978; Elliott et al., 1982). Shteynberg and Lagutina, in particular, have correlated the graphite and cohenite (Fe_3C) contents of Russian ultramafic rocks with the degree of serpentinization. Significant carbon concentrations are also found throughout 500 m of the Middle and Upper Critical Zones of the Bushveld Complex in South Africa. Elliott et al. (1982) note the occurrence of graphite aggregates in the Merensky Reef that are up to meters in size. Occurrences of iron and nickel-iron alloys are less common but widely distributed (Apps and Cook, 1981).

Field observations confirm that methane is generated by hydrothermal alteration of mafic and ultramafic rocks. Thayer (1966) reports two analyses of gas seeps containing 41.4 and 45.6 mole% hydrogen and 52.6 and 53.8 mole% methane from peridotite in the Zambales ultramafic complex near Mt. Lanat, Philippines. Methane, together with small amounts of hydrogen, ethane, and propane, is observed to emerge from rocks of the Moncheyorsk ultramafic pluton of the Kola Peninsula, USSR (Petersil'ye et al., 1970). Hahn-Weinheimer and Rost (1961) have found reducing gases in serpentinites. In the Bushveld Complex, CH_4, H_2S, and H_2 occur at high pressures in cavities associated with the platinum group metals zone (Elliott et al., 1982). A somewhat similar environment favorable for methane production is described by Bezrodnov (1979) from the Pechenga synclinorium of the Kola Peninsula. The synclinorium is filled with a sedimentary volcanogenic sequence consisting of basalts, diabases, pillow lavas, and gabbro-diabasic and peridotite intrusions. All rocks have been metamorphosed to greenschist grade. Wells in the synclinorium intersect fissures containing alkaline water in which the dissolved gases consist mostly of methane (up to 81.5%) and hydrogen (up to 24.8%). Finally, Johan and LeBel (1980) note that fluid inclusions in secondary chromite from altered ophiolites contain methane.

Hydrogen and methane are present in submarine thermal springs on the East Pacific Rise (Whelan and Craig, 1979; Gerlach and Wells, 1980; Lupton and Craig, 1981; Revelle, 1981), suggesting that the hydrothermal alteration of basalts and underlying ultramafic rocks by sea water at sea-floor spreading centers (Wolery and Sleep, 1976; Cathles, 1981) may also produce methane. Using the ratios of hydrogen and methane to excess helium measured at thermal springs of the East Pacific Rise, Revelle calculates that the current hydrogen and methane fluxes from plate margins are 1.3×10^9 and 1.6×10^8 m^3/year, respectively. He estimates the methane flux to be approximately 0.1% of the present annual world consumption of natural gas. Alternatively, the amount of methane produced from this source since the beginning of the Cambrian (5.7×10^{13} tons) is approximately 10 times the estimated world tonnage of fossil fuel resources.

One can argue from a different perspective, assuming that the production of hydrogen and methane is based on the reaction

$$15FeO_{(fo,en)} + 3H_2O + CO_2 = 5Fe_3O_4 + H_2 + CH_4$$

This reaction, proceeding in 100 km^3 of oceanic crust containing 8 wt% FeO, would reduce 0.45 wt% carbonate carbon and produce 20×10^{12} scf methane and a corresponding quantity of hydrogen, comparable to the amount in a typical gas-producing field. If we assume that approximately 25 km^3 of oceanic crust is created each year, then only 1.1% of this mass need be altered to produce Revelle's estimate of the annual production of methane.

Mathematical Simulation of Methane Formation During Ultramafic Rock Hydrolysis

I have tested the thermodynamic plausibility of abiogenic methane production by ultramafic rock hydrolysis at 25°C and 1 atmosphere using a reaction progress computer code (FASTPATH) similar to that developed by Helgeson and his coworkers (Helgeson et al., 1970). The simulation involves the progressive chemical reaction (expressed as a function of the reaction progress variable) of an infinite supply of Tinaquillo peridotite from Venezuela (Green, 1963) with 1 kg of water in a closed system. All carbon is initially present as calcium carbonate, with total carbon set at 0.5 wt%, a concentration exceeding that of primary carbon expected in mantle rock.

Results (Figs. 1–3) show that the alteration sequence is similar to serpentinization reactions in ultramafic bodies and that methane synthesis is thermodynamically plausible. Noteworthy are the approximately equivalent molar concentrations of hydrogen and methane generated during alteration.

The thermodynamic simulation given here correlates reasonably well with field observations of ultramafic rock alteration by fresh water. However, the chemical evolution of the system also is probably qualitatively similar when sea water is the reactant.

Although methane formation during hydrolysis by ultramafic rocks is plausible, we know little about the mechanism involved. There is surprising evidence that methanogenic bacteria may mediate the production of "abiogenic" methane and hydrogen in "black smoker" vents of the East Pacific Rise (Baross et al., 1982; Baross and Deming, 1983), possibly with aqueous ferrous ion acting as the electron donor. Another possible mechanism of methane production is the catalytic conversion of graphite to methane and carbon dioxide, as is shown to occur in the presence of alkali and water vapor at 200–400°C (Cabrera et al., 1981a,b). Although the conditions cited by Cabrera and his coworkers differ considerably from those expected during serpentinization, some similarities warrant serious consideration of this mechanism.

Clearly, many questions regarding methane formation under the specified conditions remain to be answered. Yet there is plenty of evidence that this process could be a major pathway through which carbon is stripped from oceanic crust. Its role in contributing to gas and petroleum reserves, however, is much more tenuous. If some connection between ultramafic rock hydrolysis and gas field occurrences can be established, then theories regarding the formation of natural gas may need reappraisal.

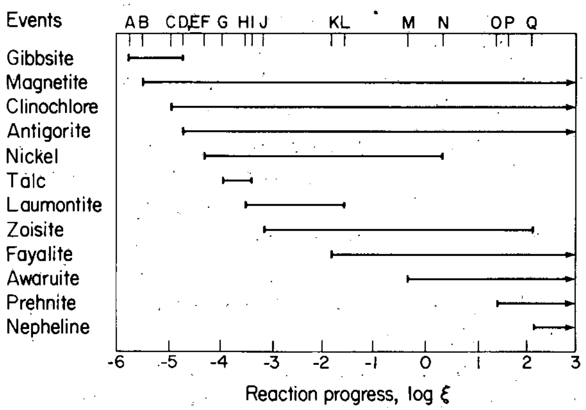

Figure 1. A plot of the quantity of minerals produced as a function of reaction progress, ξ, when peridotite reacts with water. [XBL 833-1307]

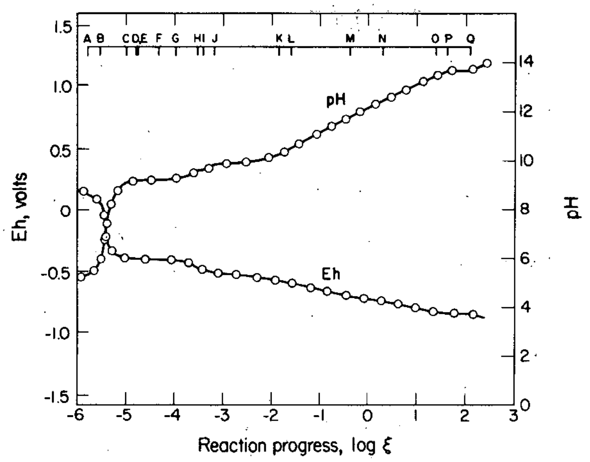

Figure 2. The functional relationship between pH, Eh, and log ξ. Noteworthy is the sharp rise in pH due to the precipitation of magnetite followed by a steady shift to progressively higher pH as serpentinization proceeds. [XBL 833-1305]

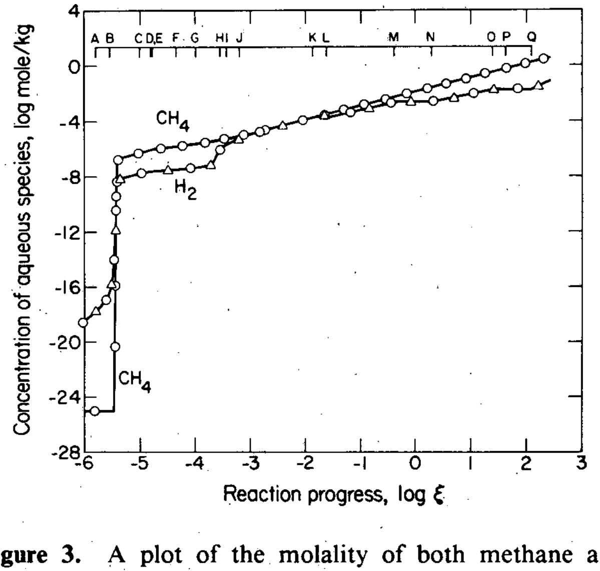

Figure 3. A plot of the molality of both methane and hydrogen in solution as a function of log ξ. The sudden appearance of these two gases is determined by magnetite precipitation. [XBL 833-1308]

REFERENCES

Apps, J.A., and Cook, N.G.W., 1981. Backfill barriers: The use of engineered barriers based on geologic materials to assure isolation of radioactive wastes in a repository. *In* J.G. Moore (ed.), Scientific Basis for Nuclear Waste Managment III, Proceedings, Materials Research Society Symposia. New York, Plenum Press, p. 291–298.

Baross, J.A., and Deming, J.W., 1983. Growth of "black smoker" bacteria at temperatures of at least 250°C. Nature, v. 303, p. 423–426.

Baross, J.A., Lilley, M.D., and Gordon, L.I., 1982. Is the CH, H and CO venting from submarine hydrothermal systems produced by thermophilic bacteria? Nature, v. 298, p. 366-368.

Bezrodnov, V.D., 1979. Subsurface chloride waters of the Kola Peninsula. Internat. Geol. Rev., v. 24, no. 5, p. 533–540.

Cabrera, A.L., Heinemann, H., and Somorjai, G.A., 1981a. Potassium catalyzed methane production from graphite at low temperatures (473–673 K). Lawrence Berkeley Laboratory Report LBL-12665, 11 p.

Cabrera, A.L., Heinemann, H., and Somorjai, G.A., 1981b. Methane production from the catalyzed reaction of graphite and water vapor at low temperatures (500–600 K). Lawrence Berkeley Laboratory Report LBL-12812, 42 p.

Cady, W.M., Albee, A.L., and Chidester, A.H., 1963. Bedrock geology and asbestos deposits of the upper Mississquoi Valley and vicinity, Vermont. U.S. Geol. Survey Bull. 1122-B, p. B1–B78.

Cathles, L.M., 1981. Fluid flow and the genesis of hydrothermal ore deposits. Economic Geology; Seventy-fifth anniversary volume; 1905–1980 (B.J. Skinner, ed.), p. 424–457.

Elliott, W.C., Grandstaff, D.E., Ulmer, G.C., Buntin, T., and Gold, D.P., 1982. An intrinsic oxygen fugacity study of platinum-carbon associations in layered intrusions. Econ. Geol., v. 77, p. 1493–1510.

Gerlach, T., and Wells, J., 1980. CH_4 in hydrothermal discharges on the sea floor. Alternative Gas Workshop, Final Report. Los Alamos Scientific Laboratory Report LA-8155c, 30 p.

Giardini, A.A., and Melton, C.E., 1981. Experimentally based arguments supporting large crustal accumulations of non-biogenic petroleum. Petrol. Geol., v. 4, p. 187–190.

Giardini, A.A., Melton, C.E., and Mitchell, R.S., 1982. The nature of the upper 400 km of the earth and its potential as the source for non-biogenic petroleum. J. Petrol. Geol., v. 5, p. 173–190.

Gold, T., 1978. Terrestrial sources of carbon and earthquake outgassing. Presented at International Scientific Forum on an Acceptable World Energy Future, Univ. Miami, Florida, Nov. 27–Dec. 1.

Gold, T., 1979a. Terrestrial sources of carbon and earthquake outgassing. J. Petrol. Geol., v. 2, p. 3–19.

Gold. T., 1979b. The earthquake evidence for earth gas. Presented at Conference on Energy for Survival, Sydney, Australia, Aug. 27–Sept. 7, Pergamon press, p. 65–78.

Gold, T. 1980. Outgassing and the power source for plate tectonics. Presented at the NATO Advanced Study Institute on the Mechanism of Continental Drift and Plate Tectonics, Newcastle on Tyne, United Kingdom, March 27–April 10, 1979, p. 343–344.

Gold, T., and Soter, S., 1980. The deep-earth-gas hypothesis. Sci. Am., v. 243, p. 154–170.

Green, D.H., 1963. Alumina content of enstatite in a Venezuelan high-temperature peridotite. Bull. Geol. Soc. Am., v. 74, p. 1397–1402.

Hahn-Weinheimer, P., and Rost, F., 1961. Akzessorische mineralen and elemente in serpentinit von Leopoldgrun (Munchberger Greissmasse), ein beitrag zur geochimie ultabasischer gesteine. Geochim. Cosmochim. Acta, v. 21, p. 165–181.

Helgeson, H.C., Brown, T.H., Nigrini, A., and Jones, T.A., 1970. Calculations of mass transfer in geochemical processes involving aqueous solutions. Geochim. Cosmochim. Acta, v. 34, p. 569–592.

Johan, Z., and LeBel, L., 1980. Genese des couches et podes de chromite dans les complexes ophiolitiques. Congr. Geol. Int. Resumé, v. III, p. 950.

Lupton, J.E., and Craig, H., 1981. A major helium-3 source at 15°S on the East Pacific Rise. Science, v. 214, no. 4516, p. 13–18.

Petersil'ye, I.A., Kozlov, Y.K., Belyayev, K.D., Sholokhnev, V.V., and Dokuchayeva, V.S., 1970. Nitrogen and hydrocarbon gases in ultramafic rocks of the Sopcha stock of the Monchegorsk pluton, Kola Peninsula. Doklady Akad. Nauk SSSR, v. 194 (English trans.), p. 200–203.

Revelle, R., 1981. Introduction. *In* C. Emiliani (ed.), The Oceanic Lithosphere (Vol. 7 of The Sea: Ideas and Observation on Progress in the Study of the Seas). New York, Wiley, p. 1–17.

Shteynberg, D.S., and Lagutina, M.V., 1978. Carbon balance in serpentinization of ultramafic rocks. Doklady Akad. Nauk SSSR, v. 243 (English trans.), p. 200–203.

Thayer, T.P., 1966. Serpentinization considered as a constant volume metasomatic process. Am. Mineral., v. 51, p. 685–710.
Whelan, J.A., and Craig, H., 1979. Methane and hydrogen in East Pacific Rise hydrothermal fluids. Geophys. Res. Lett., v. 6, p. 829–831.
Wolery, T.J., and Sleep, N.J., 1976. Hydrothermal circulation and geochemical flux at mid-ocean ridges. J. Geol., v. 84, p. 249–275.

The Aqueous Solubilities of Radioelements in the Presence of Hydrothermally Altering Basalt

J.A. Apps, F. Asaro, L. Tsao, and A. Yee

Hydrothermal processes will modify radionuclide transport through the backfill and near-field host rocks of a basalt waste repository. The magnitude and importance of such processes are presently unknown. However, it is expected that significant changes will occur in the solubility and complexation of migrating radionuclides and in the mineral composition of the basalt.

Presented here are the preliminary findings of an experiment to assess the maximum concentrations of radioelements expected in the near field of a basalt repository. The goal of the experiment is to identify the thermodynamic controls affecting the source concentrations of radionuclides and the relationship of those controls to the hydrothermal processes that will affect radionuclide transport.

The approach taken was to agitate −65 + 150 mesh Cohassett basalt particles in an autoclave containing a synthetic groundwater similar in composition to that found in the Grande Ronde basalts of the Pasco Basin, Washington. Particles were agitated for approximately 3000 hours at 250°C. Aqueous solution samples were taken at periodic intervals and analyzed for all major rock-forming elements and for the major cations and anions present in Hanford groundwater. The pH and Eh were determined immediately upon quenching the sample solution. Solution volume was maintained with additions of fresh synthetic Hanford groundwater. The purpose of this phase of the experiment was to achieve approximate chemical equilibrium between the rock and the aqueous phase.

After 3000 hours, a solution containing small concentrations of radionuclide surrogate elements was injected into the autoclave. Table 1 shows the elements injected, the detection limits possible with the analytical methods employed, and the salts used to make the solution. The concentrations of the injected elements were such that dilution by the solution in the autoclave would result in an initial concentration equivalent to ~1000 ppb for all elements except Sm, Th, and U, which were set at 100 ppb.

Solution samples were taken at periodic intervals for 22 days after injection. These samples were analyzed for the radioelement concentrations by furnace atomic absorption, atomic absorption spectroscopy, and neutron activation analysis (NAA).

RESULTS

Nickel. This element found its way into solution from the autoclave alloy, Hastelloy C-276, which consists of about 65% Ni. The equilibrium background concentration was between 150 and 500 ppb.

Selenium. The background concentration of selenium in the synthetic Hanford groundwater under the conditions of the experiment was less than 4 ppb. Injection of 1000 ppb resulted in precipitation of all but 12 ppb, which diminished to less than 4 ppb within 8 days.

Molybdenum. Dissolution of the autoclave alloy, Hastelloy C-276, which contains 15–17% Mo, resulted in a background concentration of 11–30 ppm. Indications are that this element equilibrated with powellite ($CaMoO_4$), but further study of analyses of the elements of the rock-forming minerals in the aqueous phase will be required to confirm this.

Palladium. The palladium concentration in solution, both before and after injection of 1000 ppb, remained below the limits of detection by furnace atomic absorption (<5 ppb) and by NAA (<0.8 ppm).

Tin. The tin concentration in solution, both before and after injection of 1000 ppb, remained below the limits of detection by furnace atomic absorption (<5 ppb) and by NAA (<30 ppb).

Table 1. Spiking salts and analytical methods of radionuclide surrogate elements and detection limits in 5-ml aliquots of solution.

Element	Spiking salt	Initial concentration (ppb)	Detection limits (ppb)	
			Furnace AA	NAA
Se	H_2SeO_3	1000	0.05	1.2
Mo	$(NH_4)_6Mo_7O_{24}$	1000	0.00003	138
Pd	$PdCl_2$	1000	5	800
Sn	$SnCl_2$	1000	2	30
I	KI	1000	—	200
Cs	CsCl	1000	—	0.09
La	$LaCl_3$	1000	0.5	3.5
Sm	$SmCl_3$	100	—	0.04
Th	$Th(NO_3)_4$	100	—	0.046
U	$UO_2(NO_3)_2$	100	—	0.8

Antimony. The background concentration of antimony varied between 2 and 3 ppb. After injection of the other radionuclide surrogate elements, the antimony concentration fell below the detection limit of approximately 1 ppb.

Iodine. Upon addition of iodine, the aqueous concentration rose to 1300 ppb from a background level of <200 ppb but fell to about 300 ppb in 9 days. Part of this decline was due to sample removal and dilution by make-up solution, but weak iodine sorption appears to have taken place.

Cesium. The background cesium concentration was about 10 ppb. Upon injection of 1000 ppb, the concentration rose to about 180 ppb. This concentration decreased somewhat near the end of the experiment 21 days later, but the trend is probably not significant. Cesium equilibration appears to have been rapid, probably because of ion exchange on clay minerals.

Lanthanum. This element and samarium (see below) were selected as surrogates for trivalent actinides. Lanthanum was not detected in solution either before or after injection of 1000 ppb. The detection limit by NAA is 15 ppb.

Samarium. Samarium was chosen because of its ease of detection by NAA (0.1 ppb). Samarium was found to be at or below the limits of detection both before and after injection of 100 ppb.

Thorium. After injection of 100 ppb of thorium, the concentration ranged between 1 and 2 ppb. The background concentration was somewhat higher than this. Further study is required to elucidate the cause of this behavior.

Uranium. The background concentration of uranium was about 1.3 ppb. After injection of 100 ppb, the concentration fluctuated somewhat more than previously but generally remained constant at about the limit of detection, 0.8 ppb.

DISCUSSION

Two significant conclusions can be drawn from the results that bear on the containment capability of the basalt host rock. First, it is clear that all elements, even Cs, I, and Se, can sorb or precipitate from a 1-ppm solution at elevated temperatures in a basalt host rock environment and that this behavior should be taken into account in evaluating a repository in basalt.

Second, the results are in reasonable record with estimates of some of the radionuclide element solubilities at about 25°C compiled by Krauskopf for a recent report of the National Research Council (1983). Krauskopf's estimates are compared with those of the present work in Table 2.

Table 2. Comparison of estimated element saturation in aqueous solution concentrations at 25°C with observed saturation concentrations at 250°C in a simulated basalt host rock environment

Isotope	Half-life (years)	Estimated element saturation at ≈ 25°C[a] (ppb)	Measured element saturation at 250°C (ppb)
^{59}Ni	$\sim 10^5$	—	360
^{78}Se	$\sim 6.5 \times 10^4$	1	4
^{93}Mo	$\sim 1 \times 10^2$	—	20,000
^{107}Pd	$\sim 7 \times 10^6$	—	<5
^{126}Sn	$\sim 10^5$	1	<2
^{126}Sb	3.4×10^{-2}	1	≅3
^{129}I	1.7×10^7	high	300
^{135}Cs	3.0×10^6	high	160
^{151}Sm	9.3×10^{-1}	—	0.2
^{230}Th	8.0×10^{-4}	1	1
^{234}U	2.47×10^5	1	1
^{237}Np	2.14×10^6	1	[1][b]
^{239}Pu	2.439×10^4	1	[1][b]
^{240}Pu	6.58×10^3		
^{241}Am	4.334×10^2	0.1 (?)	[0.2][b]

[a] Estimate by Krauskopf; from National Research Council (1983).

[b] Estimate based on 1 ppb concentration of Th or 0.2 ppb of Sm.

In a basalt repository environment, many other factors will decrease concentrations of radionuclides to less than saturation levels before they reach the accessible environment: for example, controlled leaching of the waste form, diffusive release from the waste-package/backfill assemblage, dilution by groundwater, hydraulic dispersion, dilution by naturally occurring stable isotopes, and radioactive decay.

Some of these factors have been taken into account by the Waste Isolation Systems Panel (WISP) of the Board of Radioactive Waste Management (National Research Council, 1983) in calculating the expected dose rate of various radionuclides to individuals from a repository containing unreprocessed waste at Hanford, Washington. Their calculations suggest that control of the source concentration, either by thermodynamic solubility or by leaching, would be sufficient to keep all radionuclide concentrations within safe levels in surface waters. However, toxic concentrations of ^{14}C, ^{129}I, and ^{237}Np would still remain in groundwater 10,000 years after burial of unreprocessed fuel.

The results of the present study and the findings of WISP suggest that further study is warranted of the aqueous solubility of neptunium in saturated rocks at elevated temperatures.

REFERENCE

National Research Council, 1983. A study of the isolation system for geologic disposal of radioactive wastes. Washington, D.C., National Academy Press, 345 p.

The Interaction of Copper(II) Ions with Galena: An Important Reaction in the Processing of Lead

D.L. Perry and L. Tsao

The reaction of aqueous copper(II) ions with galena is one of the most important reactions in the processing of that lead ore. Several other workers (Bushell et al., 1961; Shimoiizaka, 1976) have studied this reaction in the hope of better understanding its mechanism.

Our research on this reaction has focused upon the effects of changing certain experimental parameters, such as copper(II) concentration, temperature, counterion associated with the copper(II) salt, and reaction time. The galena surface was monitored using scanning electron microscopy, scanning Auger microscopy, and x-ray photoelectron spectroscopy.

RESULTS AND DISCUSSION

A galena surface that has been reacted with copper(II) shows several features that are always the same, regardless of the reaction conditions. For example, Figure 1 shows the surface of both oxidized and unoxidized galena after reaction with copper(II) sulfate pentahydrate (100 ppm concentration) for 15 min at 25°C. In addition to the solid particles that are observed on the surface, a thin film of a mixture of different lead reaction products (Taylor and Perry, 1984) also covers the entire surface. The particles were shown by Auger electron spectroscopy to be enriched in copper(I) sulfide (Perry et al., 1984a). These particles are always more nucleated when oxidized galena is used. The effects of changing specific parameters are described below.

Reaction Time. When the reaction time (duration of exposure) of the minerals is increased beyond the normal 15-min period, more copper is adsorbed as a function of time. The nucleation of the copper sulfide surface particles, presumably occurring at surface defect sites, becomes more complex as a function of both time and temperature. When *unoxidized* galena is exposed for reaction times of less than a minute at 25°C, a thin film consisting probably of a couple of monolayers of copper sulfide forms along with a few dispersed islands. Increasing the reaction time increases the number of particles that form on the surface. These same trends are observed for *oxidized* galena, but the formation of the copper sulfide particles is more rapid and extensive.

Temperature. Studies of temperature dependence were conducted at 25°C and 100°C. While x-ray photoelectron and Auger spectra for the reacted galena remain invariant as a function of reaction temperature, the morphology of the reacted surfaces (and the species observed on the surfaces) does *not*. Varying the temperature of the reaction also dramatically changes the amount of copper observed on the reacted surface. For example, the maximum Cu:Pb ratio was found to be ~ 1.5 (using x-ray photoelectron spectroscopy) for the reaction of copper(II) and galena at 25°C, whereas the ratio increased to a maximum of ~ 9.0 for the same reaction at 100°C.

Counterion Effects. Experiments were conducted using the nitrate, sulfate, and chloride salts of copper(II). No equivocal major differences in the surface chemistry of the copper-reacted galena can be attributed to counterion effects when sulfate and nitrate are used. Differences are observed, however, when $CuCl_2^-$ is used; in this case, significant amounts of sulfur (many times being equal to the amount of sulfide) are observed in the spectrum. This observation may be due to differences in nucleation processes on the surface and in the bulk observed for other metal reaction systems involving the chloride ion (Brittain et al., 1984).

Nature of the Copper Sulfide Overlayer. We have extensively studied the copper sulfide species that formed on the surface of the reacted galena. While previous research has suggested that this principal surface product might be covellite, our work does not corroborate that finding. Instead, after comparing the surface data with well-documented standards, the data strongly suggest (but do not unequivocally prove) that *the copper sulfide is chalcocite*, or Cu_2S. The binding energies and other spectral data for copper and sulfur for the galena reaction system agree with those for chalcocite. Additionally, the difference in binding energies for the Cu $2p_{3/2}$ and S $2p_{3/2}$ photoelectron lines obtained from the reacted surfaces are also in excellent agreement with that of chalcocite. The Auger parameter (α^*) observed for copper for the reacted surface of galena is also identical to the value for chalcocite. The atomic ratio of Cu:S was found to be almost exactly 2:1, or Cu_2S. Finally, the larger dipyramidal particles that formed at 100°C in the galena/Cu(II) reaction are compatible

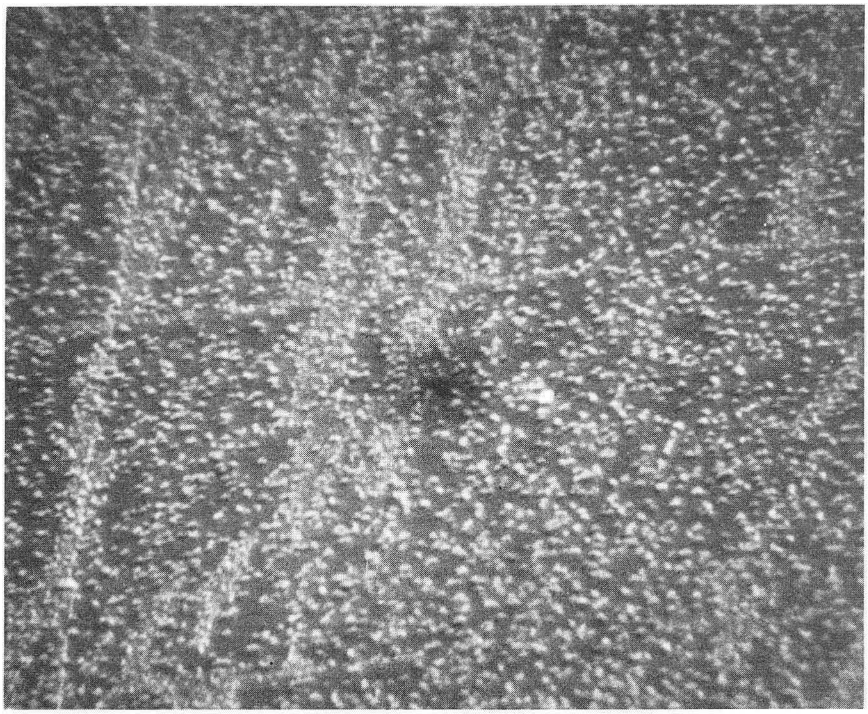

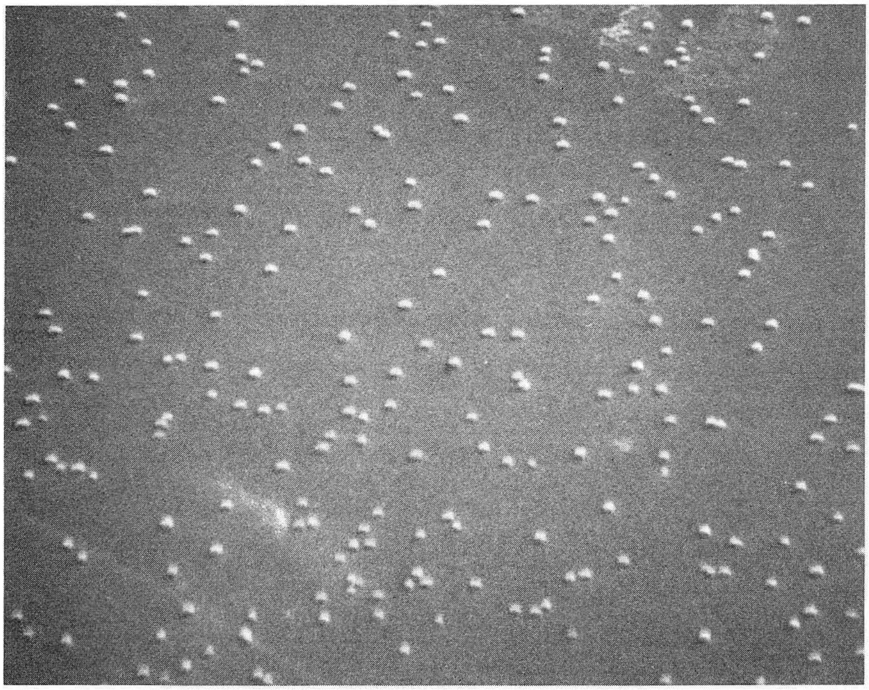

Figure 1. Scanning electron microscope pictures of *oxidized* galena (**top**) and *unoxidized* galena (**bottom**) that have undergone reaction with copper(II) sulfate pentahydrate at 25°C. The magnification is 5000×. [XBB 845-3270A]

with chalcocite. While all these data are in strong agreement with chalcocite, one should not accept them as unequivocal proof. This is especially true in light of the extreme complexity of the copper-sulfur mineral systems.

Concentration of Copper Ion. While the original concentration of the copper(II) ion does affect the amount of copper complexed to the galena surfaces, it does not affect the *chemistry.* There is no change in spectral features (other than quantitative ones) as a function of concentration, an observation that agrees with data reported by Perry et al. (1984b) on x-ray photoelectron studies of the interaction of aqueous dichromate with galena.

Variation of pH. In general, less copper is retained on the galena reacted at higher pH values (10–12) than at lower pH values ($<$ pH = 4), all other reaction parameters being held constant. This is not surprising, since the copper(II) ion exists as a nonhydrolyzed ion at low pH and is thus a rather simple ionic system. At high pH values, however, the copper(II) exists as polymeric hydroxide complexes; any interaction of these copper(II) polymers with galena, therefore, would involve a decidedly different reactant than one involving a simple copper ion found at low pH. Moreover, these polymerization reactions result in precipitation of much of the copper(II), effectively changing the solution concentration of copper available to react with the galena. When the reactions are conducted at high pH values at 100°C, however, considerably more copper is found on the surface than is found for 25°C reactions. Two possible explanations for this observation are the probably increased solubility of the copper(II) polymers and, *more* probably, the increased kinetics of the copper(II)-mineral reactions at the elevated temperatures.

REFERENCES

Brittain, H.G., Perry, D.L., and Tsao, L., 1984. Photophysical studies of uranyl complexes. 4. X-ray photoelectron and luminescence studies of hydrolyzed uranyl salts. Inorg. Chem., v. 23, p. 1232–1237.

Bushell, C.H.G., Kraus, C.J., and Brown, G., 1961. Some reasons for selectivity in copper activation of minerals. Can. Min. Metall. Bull., v. 54, p. 244–251.

Perry, D.L., Tsao, L., and Taylor, J.A., 1984a. Surface studies of the interaction of copper ions with metal sulfide minerals. *In* Proceedings, Symposium on the Electrochemistry in Mineral and Metal Processing, 165th National Meeting of the Electrochemical Society, Cincinnati, Ohio, May 6–11, 1984, p. 169–184.

Perry, D.L., Tsao, L., and Taylor, J.A., 1984b. The galena-dichromate solution interaction and the nature of the resulting chromium(III) species. Inorg. Chim. Acta, v. 85, p. L57–L59.

Shimoiizaka, J., Yamamoto, Y., Sahara, T., Kanazawa, T., and Miura, H., 1976. Activation of galena with copper ions and floatability of copper-activated galena in the presence of sulfite. Nippon Kogyo Kaishi, v. 92, p. 803–808.

Taylor, J.A., and Perry, D.L., 1984. An x-ray photoelectron and electron energy loss study of the oxidation of lead. J. Vac. Sci. Technol. A, v. 2, p. 771–774.

Aqueous Oxidation-Reduction Kinetics Associated with Coupled Electron-Cation Transfer from Iron Silicates at 25°C

A.F. White and A.W. Yee

Because oxygen fugacities in magma are low, ferrous iron is dominant in primary silicates. This reduced iron is inherently unstable in oxygenated environments at the earth's surface. Potential oxidation-reduction reactions between these iron-containing silicates and groundwater include reduction of coexisting aqueous species, consumption of dissolved oxygen, and precipitation of ferric hydroxide and oxyhydroxide phases. Although these redox-controlled reactions are critical in determining aqueous transport in problems of toxic and radioactive waste disposal, acid mine drainage, and leaching of rocks by acid rain, the pathway of electron transfer between reduced silicate phases and the oxidizing aqueous environment is not well understood. The purpose of this study and previous work on basalt (White et al., 1985) has been to define more clearly the mechanisms and kinetics associated with electron transfer from silicates over a wide range of experimental conditions.

The surface chemistry and oxidation state of both weathered and unweathered augite, biotite, and hornblende were characterized by x-ray photoelectron spectroscopy (XPS). As shown in Fig. 1, the intensities of the $2p_{1/2}$ and $2p_{3/2}$ electron peaks for hornblende and biotite indicate the relative immobility of surface iron under both oxic and anoxic conditions in solutions of basic to neutral pH. This discounts the proposed formation of a thick, kinetically inhibiting iron hydroxide layer as proposed by Siever and Woodford (1979). The position of the XPS peaks can be used to characterize the oxidation states of surface iron (Furstenau and Chandler, 1982). Corrected binding energies for the Fe $2p_{1/2}$ peak of -709.9 to -710.8 eV closely correspond to the value determined for ferric oxides, indicating that surface iron on both the unweathered and weathered surfaces is oxidized. Bulk chemical analysis of the iron silicates indicates that ferrous iron dominates beneath the mineral surfaces, as is typical for igneous rocks.

Release rates of major aqueous chemical species from augite, biotite, and hornblende, including Si, Na, K, Ca, and Mg, were found to be generally linear with time, as reported for other silicates by Schott and Berner (1983). However, the changes in both Fe^{2+} and Fe^{3+} concentrations exhibit a much more complex behavior, with ferrous iron increasing rapidly at first and then remaining constant or decreasing in solutions above pH 3.5. Small concentrations of Fe^{3+} are released initially and then decrease below detection limits in oxic and anoxic solutions, even at low pH.

Direct dissolution of Fe^{2+} from oxidized iron silicate surfaces is difficult to explain. The fate of Fe^{3+} in solution was investigated by reacting iron silicate mineral phases at pH 3.0 in 3.5×10^{-4}M $FeCl_3$ solutions. The initial concentrations of Fe^{3+} were only slightly reduced in the presence of muscovite (Fig. 2). The addition of biotite to the $FeCl_3$ solutions resulted in rapid decreases in Fe^{3+} and

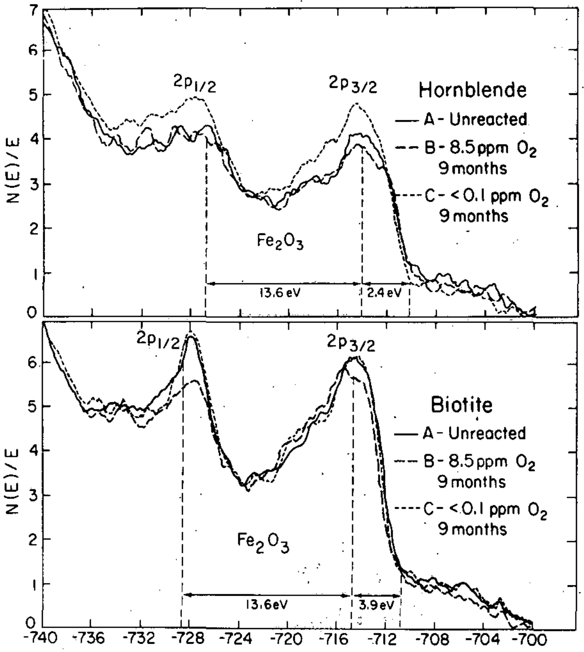

Figure 1. XPS spectra for $2p_{1/2}$ and $2p_{3/2}$ ion bonding on the surfaces of unreacted and reacted hornblende and biotite. The respective 2.4- and 3.9-eV shifts are the result of surface charging. The vertical broken lines are peak positions for ferric oxide. [XBL 8210-2539A]

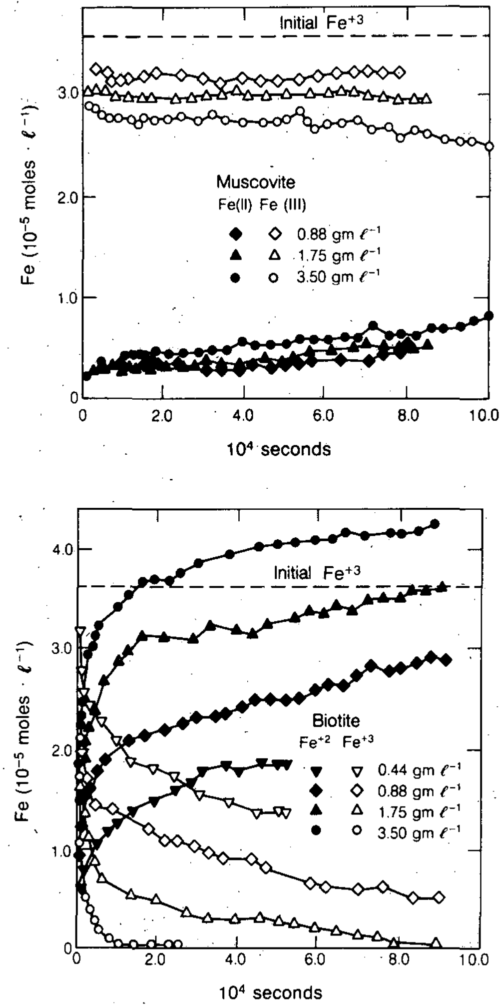

Figure 2. Changes in aqueous Fe^{2+} and Fe^{3+} concentrations with time in the presence of muscovite and biotite. Horizontal broken lines are initial concentrations of $FeCl_3$. [Top, XBL 8410-4518; Bottom, XBL 844-9758]

increases in Fe^{2+}. For relatively small amounts of biotite, a direct correlation exists between the rates of Fe^{2+} increase and Fe^{3+} decrease, with the total iron in solution remaining constant.

Three potential mechanisms can explain the observed Fe^{3+} decrease and Fe^{2+} increase in solution in the presence of iron silicate surfaces: (1) Fe^{3+} in solution is reduced in response to the release of an oxidizable species during silicate dissolution; (2) Fe^{3+} undergoes stoichiometric exchange with Fe^{2+} on the surface of the iron silicates; and (3) Fe^{3+} is reduced in solution by electron transfer during the in situ oxidization of surface iron.

The first mechanism requires an oxidizable species in solution at concentrations comparable to that of Fe^{3+}. Although small concentrations of reduced forms of Mn and S may be present in the iron silicates, as indicated by bulk chemical analysis and electron probe studies, corresponding oxidized species in aqueous solution could not be detected even at low pH.

The potential for the exchange of Fe^{2+} and Fe^{3+} between the solution and the iron silicate surface was investigated by tagging the initial ferric chloride solutions with $^{59}Fe^{3+}$. Although experiments exhibited an initial small decrease relative to the activity of the blank solution, activities during the remaining time were essentially constant. The initial $^{59}Fe^{3+}$ remained in solution after reduction to $^{59}Fe^{2+}$ and was not exchanged for Fe^{2+} on the silicate surface.

The elimination of aqueous oxidation-reduction and ferrous-ferric surface exchange mechanisms suggests that observed changes in aqueous iron speciation result from a coupled surface-solution oxidation-reduction mechanism. Such a redox couple can be written in the form

$$[Fe^{2+},1/zM^{2+}]_{silicate} + Fe^{3+} \quad [Fe^{3+}]_{silicate} + Fe^{2+} + 1/zM^{2+} \qquad (1)$$

where M is a cation of charge $+z$.

Equation (1) is self-consistent relative to charge balance. However, the reaction occurs between heterogeneous phases and requires an additional coupled reaction to maintain charge balances internally in the silicate mineral and solution. The net electron transfer from the solid to the solution can be coupled with a simultaneous transfer of a cation; i.e.,

$$[Fe^{2+},1/zM^{2+}]_{silicate} + Fe^{3+}[Fe^{3+}]_{silicate} + Fe^{2+} + 1/zM^{2+} \qquad (2)$$

The total net mass transfer is then

$$[e,1/zM^{2+}]_{silicate} \; e^{-} + 1/zM \qquad (3)$$

which maintains internal charge balances. Equation (3) is entirely consistent with experimental results. XPS data indicate that the dominantly ferrous iron in the bulk silicate phases is oxidized to ferric iron on the surface. Simultaneously, Fe^{3+}, either contained initially in solution or dissolved from the oxidized surface, is reduced to Fe^{2+}. The process occurs in conjunction with measurable cation release to solution from the mineral surface.

A calculated standard half-cell potential of +0.88 to +1.01 for the surface iron oxidation is bracketed by the ability of the reaction to reduce Fe^{3+} in solution spontaneously but not to reduce Fe^{3+} from precipitated $Fe(OH)_3$. The potential range makes surface Fe^{2+} oxidation a slightly better reducing agent than aqueous Fe^{2+}. The major significance of coupled electron-cation transfer during surface oxidation of iron silicates in natural systems is to increase kinetically the extent and rates by which such reduction can occur in solution by acting as a major electron donor. This would be particularly important in poorly poised redox systems at neutral to basic pH, in which concentrations of reducible aqueous species such as iron are extremely low because of solubility controls by iron hydroxides and oxyhydroxides.

REFERENCES

Furstenau, D.W., and Chandler, S., 1982. Surface characterization in mineral processing. *In* L.A. Casper and C.J. Powel (eds.), Industrial Applications of Surface Analysis. American Chemical Society Symp. Series 199, 438 p.

Schott, J., and Berner, R.A., 1983. X-ray photoelectron studies of the mechanism of iron silicate dissolution during weathering. Geochim. Cosmochim. Acta, v. 47, p. 2233–2240.

Siever, R., and Woodford, N., 1979. Dissolution kinetics and weathering of mafic minerals. Geochim. Cosmochim Acta, v. 43, p. 717–724.

White, A.F., Yee, A., and Flexser, S., 1985. Surface oxidation-reduction kinetics associated with experimental basalt/water reaction at 25°C. Chem. Geol., in press.

Temperature Dependence of Actinide Solubilities and Speciation

R.J. Silva

Computer calculations show that the actinides, U through Am, are the major contributors to the radioactivity of nuclear waste after storage times of 1000 years or longer (Little, 1977; NRC, 1983a). If released from the waste package into the groundwater system, the actinides will react with various components of the system to form insoluble compounds and solution complexes that can control migration rates. Thus information on the solubilities of these actinides is needed to predict the amounts and rates of their release from proposed underground repositories.

Most of the available thermodynamic data on the nature and solubilities of compounds, as well as solution species, of the actinides come from measurements made at or near 25°C. Elevated temperatures are, however, expected in a nuclear waste repository (Press, 1983). Since oxidation state distributions, solubility product constants, and formation constants for solution complexes are in general a function of temperature, one would expect the solubilities, and perhaps even the nature of stable compounds and solution species, of the actinides to change with increasing temperature in a complex way. Unfortunately, not nearly enough thermodynamic data are available for temperatures above 25°C to allow accurate prediction of solubilities as a function of temperature. However, using available data for 25°C and estimates of the temperature dependence of reaction constants, one can perform equilibrium calculations that may provide information on the trends in solubilities and speciation and delineate the important parameters. This was done for U, Np, Pu, and Am.

CALCULATIONS

Of the many inorganic components in groundwaters, hydroxide and carbonate anions are expected to play a dominant role in the formation of insoluble compounds and solution complexes of the actinides in groundwaters of low salt content (Allard, 1982; Moody, 1982). Therefore, to reduce the magnitude of the task, only oxide, hydroxide, and carbonate compounds and only hydrolysis and carbonate complexation of U, Np, Pu, and Am were considered in the calculations. Reactions involving the tri-, tetra-, penta-, and hexavalent oxidation states of all four actinides were considered.

Equilibrium constants relating the four oxidation states of each actinide for 25°C were calculated from reported free energy data (Fuger and Oetting, 1976). Solubility product, hydrolysis, and carbonate complexation constants for 25°C were obtained from a number of compilations (Baes and Mesmer, 1976; Lemire and Tremaine, 1980; Phillips, 1982; NRC, 1983b; Silva and Nitsche, 1983). In cases where a value had not been reported for a reaction constant for one of the actinides, an estimate was obtained from correlations in the reported value or values for one or more of the other three actinides in the same oxidation state (Baes and Mesmer, 1976, 1981).

For only a few reactions—primarily involving uranium—have experimental data been reported on the variation of equilibrium constants with temperature (Lemire and Tremaine, 1980). However, the equilibrium constant for a reaction at a given temperature, T, can be approximated if the entropy change for the reaction at 25°C and the average value of the heat capacity change for the reaction between T and 25°C are known or can be estimated (Criss and Cobble, 1964a; Helgeson, 1969). Since few entropies or heat capacities are known for the compounds and solution species of interest, several standard methods were used to estimate the required values (Lewis and Randall, 1923; Latimer, 1953; Criss and Cobble, 1964a,b; Baes and Mesmer, 1976, 1981).

Data bases were generated that contain the various solubility product, hydrolysis, carbonate complexation, and redox constants for the four actinides for 25, 60, 100, and 150°C. These data bases were used in the computer code MINEQL (Westall et al., 1976) to calculate the stable solid phases and solution species formed by U, Np, Pu, and Am as a function of pH (6–9) and Eh (−0.22, 0.0, +0.22 V) for an ionic strength of 0.01 M and a total fixed carbonate (all species) concentration of 120 ppm.

RESULTS

The results of the calculations for U, Np, Pu, and Am for an Eh of 0.0 V are shown in Fig. 1. The curves represent the sum of the concentrations of all solution species, i.e., the solubility lines. The curves are labeled with the controlling solid phases. Similar plots, not shown, were obtained for the other two Eh values. The following trends were observed in the results of the calculations:

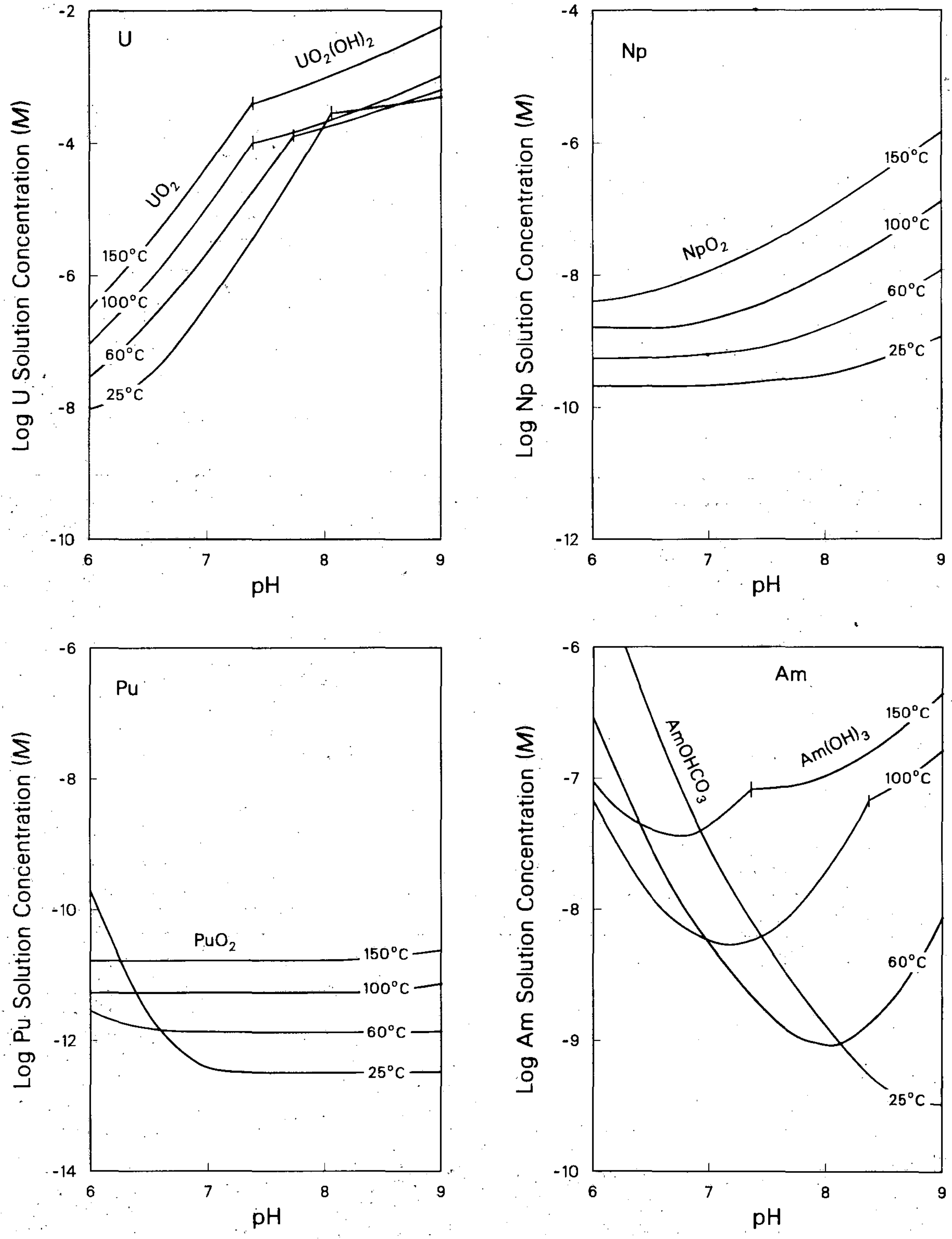

Figure 1. Sums of the calculated concentrations of all solution species (curves are labeled with controlling solid phases) for 0.01 M ionic strength, Eh = 0.0 V, and total fixed carbonate (all species) concentration of 120 ppm as a function of pH and temperature. Short vertical lines on curves indicate where the nature of the controlling solid phase changes. [XCG 8411-13480]

1. Increasing *T* tends to favor the formation of the higher oxidation states.

2. Solubility product constants for all compounds decrease with increasing *T*.

3. Hydrolysis constants and most carbonate complexation constants increase with increasing *T*. The hydrolysis constants tend to increase relatively more rapidly with *T* than the carbonate complexation constants.

4. Although solubility product constants decrease with *T*, the increasing hydrolysis and carbonate complexation constants tend to dominate, and the solubilities of U, Np, Pu, and Am tend to increase with increasing *T* (factors of 10–1000, depending on the element and solution conditions). This trend is reversed for Am and Pu at the lower pH values. The increase is due primarily to the rapid increase in the formation constants of the higher and more complex hydrolysis products.

5. The solubilities of U and Np increase dramatically with increasing Eh as the 5+ and 6+ oxidation states become dominant.

REFERENCES

Allard, B., 1982. Solubilities of actinides in neutral or basic solutions. *In* N. Edelstein (ed.), Actinides in Perspective. New York, Pergamon Press, p. 533–580.

Baes, C.F., Jr., and Mesmer, R.E., 1976. The Hydrolysis of Cations. New York, Wiley.

Baes, C.F., Jr., and Mesmer, R.F., 1981. The thermodynamics of cation hydrolysis. Am. J. Sci., v. 281, p. 935–962.

Criss, C.M., and Cobble, J.W., 1964a. The thermodynamics of high temperature aqueous solutions. V. The calculation of ionic heat capacities up to 200°C. Entropies and heat capacities above 200°C. J. Am. Chem. Soc., v. 86, p. 5390–5393.

Criss, C.M., and Cobble, J.W., 1964b. The thermodynamic properties of high temperature aqueous solutions. IV. Entropies of ions up to 200°C and the correspondence principle. J. Am. Chem. Soc., v. 86, p. 5385–5390.

Fuger, J., and Oetting, F.L., 1976. The chemical thermodynamics of actinide elements and compounds. Part 2. The actinide aqueous ions. Vienna, International Atomic Energy Agency.

Helgeson, H.C., 1969. Thermodynamics of hydrothermal systems at elevated temperatures and pressures. Am. J. Sci., v. 267, p. 729–804.

Latimer, W.M., 1952. Oxidation Potentials. Englewood Cliffs, N.J., Prentice-Hall, p. 359–369.

Lemire, R.J., and Tremaine, P.R., 1980. Uranium and plutonium equilibria in aqueous solutions to 200°C. J. Engin. Data, v. 25, p. 361–370.

Lewis, G.N., and Randall, M., 1923. Thermodynamics and the free energy of chemical substances. New York, McGraw-Hill, p. 71–82.

Little, A.D., 1977. Mechanical support standards for high-level radioactive waste management. Washington, D.C., U.S. Environmental Protection Agency Report EPA-520/4-79-007A.

Moody, J.B., 1982. Radionuclide migration retardation. Columbus, Ohio, Office of Nuclear Waste Isolation Report ONWI-321, p. 6.

NRC, 1983a. Staff analysis of public comments on proposed rule 10CFR Part 60, disposal of high-level radioactive wastes in geologic repositories. Washington, D.C., U.S. Nuclear Regulatory Commission Report NUREG-0804, p. 467.

NRC, 1983b. Draft site characterization analysis of the site characterization report for the basalt waste isolation project. Washington, D.C., U.S. Nuclear Regulatory Commission Report NUREG-0960, p. U-16–U-21.

Phillips, S.L., 1982. Hydrolysis and formation constants at 25°C. Lawrence Berkeley Laboratory Report LBL-14313.

Press, F. (Chairman), 1983. A study of the isolation system for geologic disposal of radioactive wastes. Washington, D.C., National Research Council, National Academy Press, p. 122–138.

Silva, R.J., and Nitsche, H., 1983. Thermodynamic properties of chemical species of waste radionuclides. (Topical Report for the U.S. Nuclear Commission.) Lawrence Berkeley Laboratory Report LBL-16696.

Westall, J.C., Zachary, J.C., and Morel, F.N.M., 1976. MINEQL, A computer program for the calculation of chemical equilibrium composition of aqueous systems. (Department of Civil Engineering Mechanical Report.) Cambridge, Massachusetts Institute of Technology Technical Note 18.

Simulation of Coupled Mass Transport Processes in a Saturated Clay

C.L. Carnahan and J.S. Remer

Saturated clays are expected to be present in nuclear waste repositories either as components of engineered barriers or as naturally occurring fillings and linings of fractures in surrounding rocks. These materials are known to exhibit the properties of semipermeable membranes (Marine and Fritz, 1981). In the presence of gradients of temperature, pressure, and fluid composition, thermodynamically coupled transport processes (thermal osmosis, chemical osmosis, ultrafiltration, and thermal diffusion) can occur in saturated clays simultaneously with the direct transport processes (advection and mass diffusion) expressed by Darcy's law and Fick's law.

On the basis of methods of the thermodynamics of irreversible processes, we are developing a numerical simulator of coupled transport processes driven by gradients of temperature, pressure, and composition. The present version of the simulator assumes specified constant gradients of temperature and pressure and solves the nonlinear equation of transport of a single ideal solute either with or without coupling to transport of heat and volume.

BASES OF SIMULATIONS

Although data relevant to thermal conductivity, permeability, and mass diffusivity of proposed engineered barrier materials are abundant in the literature, data relevant to the coupled processes are scarce. Published data, from which values of direct and coupling coefficients can be calculated, are available on chemical osmosis, advection, and mass diffusion in bentonite (Letey and Kemper, 1969), on thermal osmosis and advection in kaolinite (Srivastava and Avasthi, 1975), and on thermal diffusion in alumina (Thornton and Seyfried, 1983). We adopted directly the data for bentonite and assumed that the thermal diffusion coefficient for alumina would apply also to bentonite. We then assumed that the ratio of coefficients of thermal osmosis and advection in bentonite would be identical to that in kaolinite, allowing us to estimate a coefficient for thermal osmosis in bentonite. This procedure provides a complete set of direct and coupling coefficients for a single material that, in the strict sense, should not be regarded as bentonite but rather as a hypothetical clay-like material whose transport properties are composites of those of bentonite, kaolinite, and alumina.

One-dimensional transport through a 1-m column of clay material was simulated. The clay was assumed to have a porosity of 0.30 and to be saturated by the fluid phase. Initially, the solute concentration throughout the column was 0.4 kg/m^3, the temperature gradient -2 K/m, and the pressure gradient -10 Pa/m. At the inner boundary the temperature was 325 K and the pressure 1×10^7 Pa; these conditions were maintained throughout each simulation. The temperature gradient used here is based on calculations reported for a hypothetical repository in basalt (Hodges, 1980); the pressure gradient is equivalent to a groundwater hydraulic gradient of 10^{-3}, the order of magnitude commonly assumed in calculations of solute transport (Wang et al., 1983). The initial solute concentration is characteristic of dissolved solids contents of basaltic groundwaters.

RESULTS OF SIMULATIONS

Figures 1–3 show results of numerical simulations of coupled and uncoupled transport processes with a constant solute concentration of 1.0 kg/m^3 at the inner boundary ($x = 0$) at 10^9 s. In Figs. 2 and 3, arrows indicate the directions of the flux vectors in either the positive or negative x direction.

Figure 1 shows solute concentration profiles with no coupling and with full coupling between transport processes. It is seen that full coupling produces significant retardation of solute migration relative to the case without coupling and produces a very steep gradient of concentration near the inner boundary, where the concentration is held constant.

Figure 2 shows the three components of the volume flux (broken lines) and their resultant (solid line) for the case of full coupling. The contribution from advection equals that in the uncoupled case, but now the total volume flux is dominated by the coupled processes, thermal osmosis and chemical osmosis, which are oppositely directed. Near the inner boundary, chemical osmosis, driven by the steep concentration gradient, produces a net volume flux that is negatively directed. As distance from this boundary increases, the magnitude of the chemical-osmotic flux decreases until it equals the sum of the positively directed thermal-osmotic and

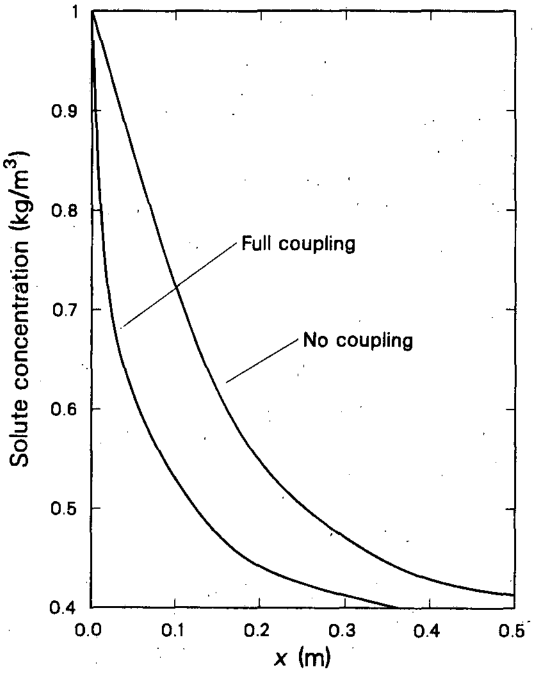

Figure 1. Solute concentrations. [XCG 8412-13481]

advective fluxes, resulting in a point of stagnation near 0.25 m. As distance increases past this point, the total volume flux, now positive, approaches the magnitude of the thermal-osmotic flux. The latter remains constant at a value approximately three orders of magnitude larger than the advective flux. In these simulations the contribution to the volume flux from thermal osmosis is constant because the gradient of temperature is constant.

Figure 3 displays the six components of the solute flux (broken lines) and their resultant (solid line). The flux of solute carried by advection is about equal to that without coupling. However, in the fully coupled case, the total flux of solute is dominated by diffusion and two coupled processes, chemical osmosis and thermal osmosis. Near the inner boundary, the diffusive and chemical-osmotic fluxes are each about one order of magnitude larger than the diffusive flux in the uncoupled case because of the larger concentration gradient there. However, the diffusive flux is largely canceled by the negatively directed chemical-osmotic flux, and the resultant of these two fluxes plus the positively directed thermal-osmotic flux is slightly smaller in magnitude than the diffusive flux in the uncoupled case. As distance from the inner boundary increases, the total solute flux does not decrease monotonically, as in the uncoupled case, but approaches the magnitude of

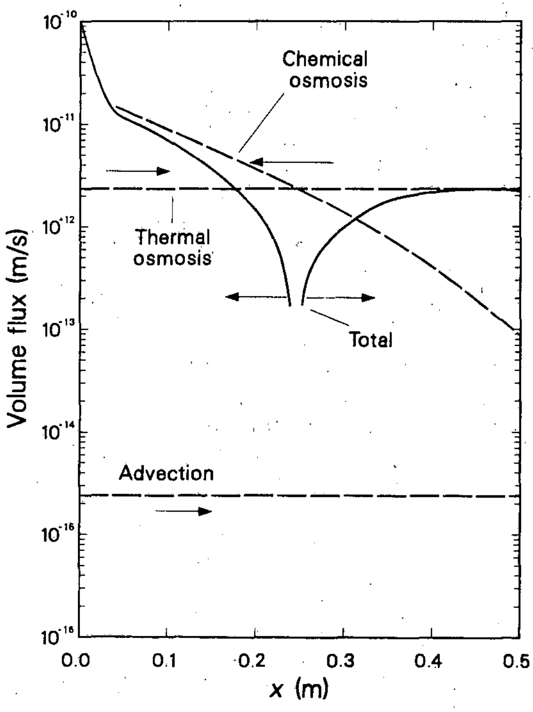

Figure 2. Volume fluxes, full coupling. [XCG 8412-13482]

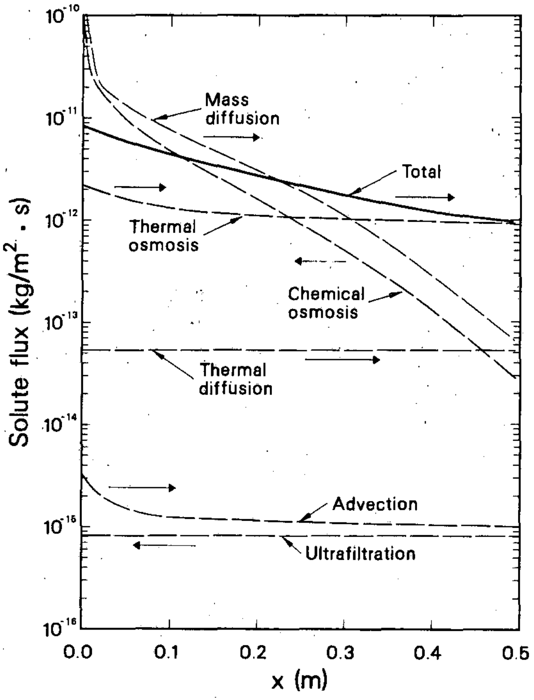

Figure 3. Solute fluxes, full coupling. [XCG 8412-13483]

the thermal-osmotic flux and thenceforth remains approximately constant at a value about three orders of magnitude larger than the flux of solute carried by advection.

Simulations with the constant-flux condition at the inner boundary produce results that are similar to those obtained with the constant-concentration boundary condition. The principal difference between the two sets of simulations results from smaller gradients of solute concentration near the inner boundary in the constant-flux case. When full coupling is considered, the profiles of solute concentrations indicate slight retardation of solute migration relative to the case without coupling. Moreover, the retardation is less than in the fully coupled case with a constant-concentration condition at the inner boundary.

Results of simulations at large elapsed times show that the point of stagnation in the volume flux with full coupling moves away from the inner boundary as elapsed time increases and as the system approaches a steady state. The rate of movement is larger in the case of the constant-concentration boundary condition. At the largest simulated elapsed time, 10^{12} s, the point of stagnation has vanished in both cases, and the total volume flux is negative throughout the spatial domain included in the simulations.

DISCUSSION

In the systems simulated in this work, full coupling of processes affecting mass transport leads to retardation of solute movement and significant enhancement of volume fluxes relative to results predicted without coupling. Retardation of solute movement is greater in the case of a constant-concentration condition at the inner boundary, where gradients of solute concentration can be very large, producing correspondingly large negative contributions to solute fluxes as a result of chemical osmosis. Thermal osmosis alone can, in the presence of a rather mild gradient of temperature, produce a volume flux several orders of magnitude larger than the advective flux. The addition of chemical osmosis can produce a large negative contribution to the volume flux, resulting in a point of stagnation that migrates away from the inner boundary with increasing time. These effects would not be predicted by application of Fick's law and Darcy's law without inclusion of coupling.

The results of numerical simulations presented here have indicated the possible significance of thermodynamically coupled transport processes in saturated clay materials and the magnitudes of errors that could result by omission of coupled processes from transport calculations in such materials. However, application of these methods to predictive analyses of the performance of clay-containing engineered barriers at nuclear waste repositories will require further development.

REFERENCES

Hodges, F.N., 1980. Repository conditions. *In* M.J. Smith (principal author), Engineered Barrier Development for a Nuclear Waste Repository in Basalt: An Integration of Current Knowledge. Richland, Washington, Rockwell Hanford Operations Report RHO-BWI-ST-7, p. 2–105 to 2–133.

Letey, J., and Kemper, W.D., 1969. Movement of water and salt through a clay-water system: Experimental verification of Onsager reciprocal relation. Soil Sci. Soc. Am. Proc., v. 33, p. 25–29.

Marine, I.W., and Fritz, S.J., 1981. Osmotic model to explain anomalous hydraulic heads. Water Resour. Res., v. 17, p. 73–82.

Srivastava, R.C., and Avasthi, P.K., 1975. Non-equilibrium thermodynamics of thermo-osmosis of water through kaolinite. J. Hydrol., v. 24, p. 111–120.

Thornton, E.C., and Seyfried, W.E., 1983. Thermodiffusional transport in pelagic clay: Implications for nuclear waste disposal in geological media. Science, v. 220, p. 1156–1158.

Wang, J.S.Y., Mangold, D.C., and Tsang, C.F., 1983. Long-term thermomechanical and thermohydrological factors controlling the optimal design of a nuclear waste repository. Mat. Res. Soc. Symp. Proc., v. 15, p. 531–538.

Effective Retardation Factors for Nonequilibrium Mass Transfer

J.S. Remer and C.L. Carnahan

The computer code NONEQ (Remer and Carnahan, 1982) has been used to model mass transport by dispersion and advection through an infinite, isotropic, homogeneous porous medium; interphase mass transfer is governed by either a first-order or second-order rate law. This report discusses the interpretation of our simulations with NONEQ in the context of two conventional measures of the ability of a solute to migrate: the effective retardation factor and the ratio of the solid-phase to fluid-phase concentration.

EFFECTIVE RETARDATION FACTOR FOR NONEQUILIBRIUM SORPTION

In the case of equilibrium sorption, the retardation factor can be derived analytically from the transport equation. If the sorption reaction can be described by a first-order, reversible rate law, the retardation factor is constant. If the reaction is described by a second-order rate law, the retardation factor is not constant but is a function of the sorptive capacity of the solid phase and of the fluid-phase concentration.

In the case of nonequilibrium sorption, an analytical expression for the retardation factor cannot be derived from the transport equation. In practice, the retardation factor is defined as the ratio of the pore fluid velocity to the solute velocity. The solute velocity is the ratio of the location of the solute peak to the time required for the solute peak to move from the point of solute release to that location.

We calculated solute velocities and effective retardation factors for two sets of parameters for both the first- and second-order rate laws. The two sets of parameters differed only in the value of the backward rate constant, which differed by four orders of magnitude. The results of these calculations are listed in Table 1. Interesting comparisons can be made between the concentrations for the first-order rate laws for the two data sets, between the concentrations for the second-order rate laws for the two data sets, and between the concentrations for the first- and second-order rate laws for each data set.

When the first-order rate law is used to govern mass transfer between the phases, the distance between the point of release and the location of the solute peak increases with time for the data set with the smaller value of the backward rate constant and decreases with time for the other data set. For both data sets, the value of the retardation factor increases with time (the solute velocity decreases with time), but the actual values differ by an order of magnitude or more.

When the second-order rate law is used, the movement of the solute peaks and values of the solute velocities and retardation factors are comparable for the two data sets. The distance between the origin and the solute peak increases with time, and the effective retardation increases with time (the solute velocity decreases with time). The larger backward rate constant produces a higher fluid-phase concentration near the origin, where the solid-phase concentration is the largest. Therefore, the solute velocity is less than that calculated using the smaller rate constant.

The calculations discussed above show that the first-order rate law magnifies the effect of varying the backward rate constant. When the second-order rate law is used, the location of the solute peak, the solute velocity, and the retardation factor are comparable for the two data sets. When the first-order rate law is used, the movement of the solute peak differs in both direction and magnitude, and the solute velocity and retardation factor differ by one to three orders of magnitude for the two data sets.

The movement of the solute peaks and the values of the solute velocities and retardation factors differ significantly for the two rate laws used for both data sets. For the data set with the larger value of the backward rate constant, the distance between the origin and the solute peak decreases with time for the first-order rate law and increases with time for the second-order rate law. The retardation factor increases with time for both rate laws but increases much faster for the first-order rate law.

For comparison, we can calculate the retardation factor for the case of equilibrium sorption using the rate constants for the two data sets used in the numerical simulations described above. For the smaller backward rate constant, the retardation factor for the corresponding (in parameter values) case of equilibrium sorption is 40,001; for the larger backward rate constant, the value is 5.

Table 1. Solute peak location (z_m), solute velocity (v_s), and effective retardation factor (B) calculated as functions of time for an instantaneous release of 0.1 mole.

	First-order rate law used to govern mass transfer			Second-order rate law used to govern mass transfer		
t (years)	z_m (m)	v_s (m/year)	B	z_m (m)	v_s (m/year)	B
9.851×10^{-2}	9.852×10^{-2}	1.000	1.000	9.527×10^{-2}	0.967	1.034
1.968×10^{-1}	1.967×10^{-1}	0.999	1.001	1.784×10^{-1}	0.907	1.103
3.934×10^{-1}	3.932×10^{-1}	0.999	1.001	3.024×10^{-1}	0.769	1.301
5.245×10^{-1}	5.239×10^{-1}	0.999	1.001	3.626×10^{-1}	0.691	1.446
7.866×10^{-1}	7.838×10^{-1}	0.996	1.004	4.580×10^{-1}	0.582	1.717
1.049	1.039	0.990	1.010	4.918×10^{-1}	0.469	2.133

Note: Backward rate constant (for both rate laws) = 10^{-4}/year.

	First-order rate law used to govern mass transfer			Second-order rate law used to govern mass transfer		
t (years)	z_m (m)	v_s (m/year)	B	z_m (m)	v_s (m/year)	B
9.851×10^{-2}	6.346×10^{-2}	6.443×10^{-1}	1.552	9.517×10^{-2}	0.966	1.035
1.968×10^{-1}	1.267×10^{-2}	6.437×10^{-2}	1.554×10^{1}	1.770×10^{-1}	0.899	1.112
3.934×10^{-1}	6.715×10^{-3}	1.707×10^{-2}	5.859×10^{1}	2.845×10^{-1}	0.723	1.383
5.245×10^{-1}	6.155×10^{-3}	1.174×10^{-2}	8.522×10^{1}	3.222×10^{-1}	0.614	1.628
7.866×10^{-1}	6.245×10^{-3}	7.938×10^{-3}	1.260×10^{2}	3.517×10^{-1}	0.447	2.237
1.049	6.678×10^{-3}	6.367×10^{-3}	1.571×10^{2}	3.642×10^{-1}	0.347	2.880

Note: Backward rate constant (for both rate laws) = 1/year.

Parameter values: Forward rate constant (first-order rate law) = 1/year; forward rate constant (second-order rate law) = 10 m^3/mole·year; sorptive capacity = 0.1 mole/m; longitudinal dispersion coefficient = 0.7 m^2/year; transverse dispersion coefficient = 0.2 m^2/year; fluid velocity = 1 m/year; porosity = 0.2.

VARIATION OF Q/C WITH TIME AND SPATIAL COORDINATES

The distribution of a sorbable solute between the solid and fluid phases can be measured by the ratio Q/C, where C is the fluid-phase concentration of the solute and Q is the solid-phase concentration. The distribution coefficient, K_d, is related to the equilibrium value of Q/C by

$$K_d = \frac{1}{\rho_s} \left(\frac{Q}{C} \right)_{eq} ,$$

where ρ_s is the bulk density of the solid phase. The value of K_d is used as a measure of the extent to which the motion of a solute is retarded relative to the advective velocity of the fluid phase. In the case of a first-order, reversible rate law for the sorption reaction, Q/C is equal to the (constant) ratio of the forward rate constant to the backward rate constant, hence K_d is constant.

K_d is not defined in systems that are not in chemical equilibrium, but because of the widespread use of the K_d concept in analytical and numerical models of solute transport, it is of interest to calculate the ratio Q/C for nonequilibrium systems and to study its variations in time and space and with different values of the rate constants for the sorption reactions. Calculations of Q/C were made for concentrations along the z axis (in the direction of the flow field) for several sets of parameters at a single time and for two parameter sets at three different times; the parameter sets used in the calculations differ by the value of the backward rate constant used. These results are shown in Fig. 1. The first-order rate law was used to calculate the concentrations in Fig. 1a. The second-order rate law was used for those in Fig. 1b.

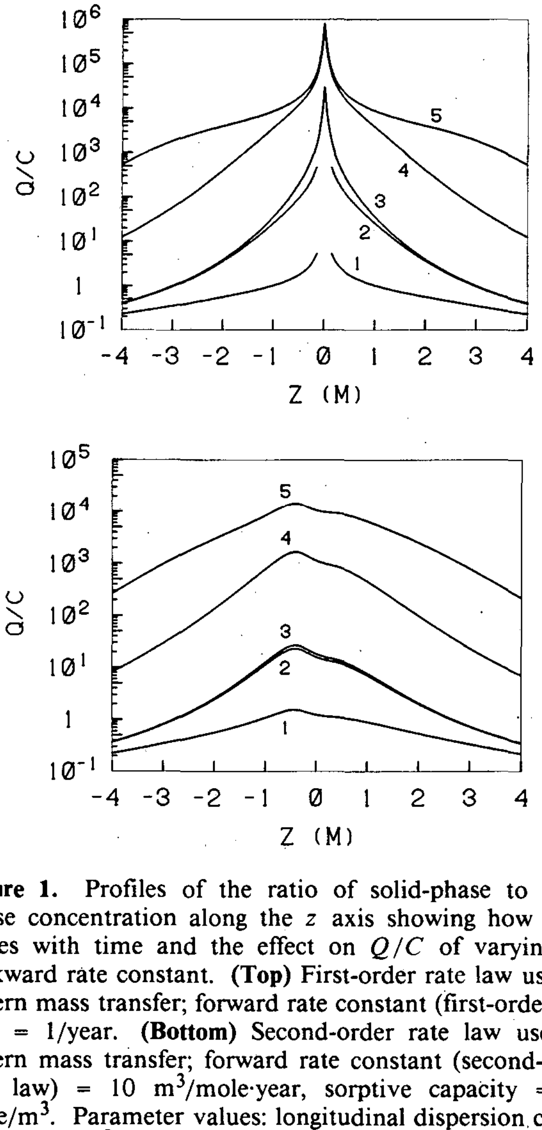

Figure 1. Profiles of the ratio of solid-phase to fluid-phase concentration along the z axis showing how Q/C varies with time and the effect on Q/C of varying the backward rate constant. **(Top)** First-order rate law used to govern mass transfer; forward rate constant (first-order rate law) = 1/year. **(Bottom)** Second-order rate law used to govern mass transfer; forward rate constant (second-order rate law) = 10 m^3/mole·year, sorptive capacity = 0.1 mole/m^3. Parameter values: longitudinal dispersion coefficient = 0.7 m^2/year, transverse dispersion coefficient = 0.2 m^2/year, fluid velocity = 1 m/year, porosity = 0.2, instantaneous release of 0.1 mole at time $t = 0$. Curve 1 — t = 1 year, k_2 (backward rate constant) = 1/year; curve 2 — t = 1 year, $k_2 = 10^{-2}$/year; curve 3 — t = 1 year, $k_2 = 10^{-4}$/year; curve 4 — t = 2 years, $k_2 = 10^{-4}$/year; curve 5 — t = 3 years, $k_2 = 10^{-4}$/year. [Top, XBL 846-2510; Bottom, XBL 846-2511]

The most important point is that the ratio Q/C varies with distance and with time for both rate laws; it is not approximately constant for any of the cases for which it was calculated. Not surprisingly, it decreases with distance from the origin. Both the fluid- and the solid-phase concentrations decrease with distance, but Q decreases at a faster rate. The region in which the curves of Q/C for the two rate laws differ the most is near the origin, as expected from the behavior of the solid-phase concentrations. The maximum of Q/C for the first-order rate law occurs at the origin (Fig. 1a) because the solid-phase concentration is infinite there (Carnahan and Remer, 1984). For the parameter sets used in the simulations, the maximum of Q/C for the second-order rate law occurs not at the origin but at a distance upstream from the origin (Fig. 1b).

Another interesting way in which the profiles for the two rate laws differ is that the ratio of Q to C is symmetric with respect to z when the first-order rate law is used (Fig. 1a) but not when the second-order rate law is used (Fig. 1b). The symmetry of Q/C in the former case can be verifed by examining the analytical solutions for Q and C (Eqs. 32 and 33, Carnahan and Remer, 1984).

SUMMARY

We have used the computer code NONEQ to calculate effective retardation factors for nonequilibrium sorption for two parameter sets with different values of the backward rate constant. The tabulated results show that the first-order rate law magnifies the effect of varying the backward rate constant. In addition, they suggest that tracking the solute peak may not be a good indicator of solute movement.

Because many treatments of chemical transport in advective systems assume chemical equilibrium, we have included calculations of Q/C from our simulations with NONEQ to show how the ratio varies with time and distance when the system is not in chemical equilibrium. Our results clearly show the inapplicability of using the K_d approach to describe or even approximate nonequilibrium systems. Solute movement must be tracked numerically for each set of physical and chemical parameters using computer codes such as NONEQ.

REFERENCES

Carnahan, C.L., and Remer, J.S., 1984. Nonequilibrium and equilibrium sorption with a linear isotherm during mass transport through an infinite, porous medium: Some analytical solutions. J. Hydrol., v. 73, p. 227–258.

Remer, J.S., and Carnahan, C.L., 1982. Advective/dispersive solute transport through an infinite porous medium with a second-order rate of interphase mass transfer. Presented at the 1982 Fall Meeting of the American Geophysical Union, San Francisco, California, December 7–15, 1982.

Organic Chemistry of Petroleum Generation

*O. Weres and A.S. Newton**

The objective of this project is to simulate the production of natural petroleum in the laboratory. The ultimate purpose is to improve understanding of the chemical reactions that produce petroleum in nature. This knowledge may lead to improved methods of finding and recovering oil and gas.

Organic compounds and polymers are reacted with clay and brine in an autoclave at 315°C for several days. The reaction products are extracted and identified using gas chromatography, coupled gas chromatography/mass spectrometry, and mass spectrometry. The elevated temperature allows reactions that require millions of years in nature to take place in days. Indeed, there are some very deep gas wells along the Gulf Coast in which the temperature approaches 300°C (Price et al., 1979, 1981; Price, 1982). Our results are directly applicable to these gas reservoirs without extrapolating over temperature.

Starting materials belonging to three classes have been studied:

1. Kerogen and related natural materials. To date, experiments have been performed using Green River Oil Shale (type I kerogen) and humic acid.
2. Artificial polymeric materials that resemble natural lipids but have well-defined chemical composition and molecular structure. To date, polymerized tung oil and two commercially available polyterpene resins have been studied.
3. Representative compounds from chemical classes that are known or believed to play a role in natural petroleum genesis. Thus far, low-molecular-weight carboxylic acids, fatty acids, diacids, alcohols, phenols, cycloketones, ethers, and esters have been studied.

RESULTS

Work with oil shale quickly established that oil and gas similar to natural petroleum from high-temperature reservoirs may be produced in the laboratory. Substantial amounts of water-soluble by-products were also produced: acetate and other low-molecular-weight organic acid anions, phenols, and cycloketones. Reacting humic acid produced methane, low-molecular-weight organic anions, and smaller amounts of phenols, cycloketones, and aromatic hydrocarbons.

Work with the polymerized tung oil indicated the source of the organic anions: side chains that terminate with a carboxylic acid group tend to break off from the polymer. Chain breakage at the beta carbon is particularly favored, giving abundant acetate. Chain breakage at the point of attachment to the polymer is also favored, in this case also giving a large yield of organic anions C-6 to C-8. Alkyl side groups also break off, producing alkane gases methane through butane.

Work with polyterpene resins has demonstrated that a single bond linking a secondary carbon with a quaternary carbon is particularly likely to break. Loss of alkyl side groups to produce hydrocarbon gases was also confirmed.

An experiment with myristic (tetradecanoic) acid showed that about 40% of the molecules that decompose yield acetate ion and a C-12 alkene, the remainder yielding carbon dioxide plus a C-13 alkane or alkene. This result confirms that decomposition of larger organic acids is the source of acetate in many of the experiments. In no case was carboxylation of hydrocarbon materials by carbon dioxide observed.

Formic acid decomposes rapidly, mostly to carbon dioxide and hydrogen, with a subordinate amount of carbon monoxide also produced. The carboxylic acids C-2 to C-6 decarboxylate slowly to give the gaseous *n*-alkanes C-1 to C-5; among these small acids, acetic acid is the most reactive.

---

*Applied Science Division, Lawrence Berkeley Laboratory.

The cycloketones commonly observed among our reaction products may be formed from dicarboxylic acids. In fact, we found that the C-6 to C-8 diacids do give abundant cycloketones. Oxalic acid decomposes rapidly. Malonic and succinic acids decarboxylate to acetic and propionic acids, respectively.

Alcohols and ethers dehydrate rapidly to alkenes, which then polymerize slowly. Esters hydrolyze to acids and alcohols, which react further as described above. Cycloketones and phenols are relatively stable. They polymerize slowly with loss of water.

The use of propyl esters for the analysis of mixed carboxylic acids has been systematized, and a collection of propyl ester mass spectra will be published.

DISCUSSION

Polymeric materials, artificial as well as natural, are highly reactive under the conditions employed, with analyzable product yields corresponding to 10–50% of the starting material. Specific compounds range from highly reactive to relatively stable. This agrees with our expectation that polymeric lipids decompose to smaller, more stable molecules, including petroleum hydrocarbons. Frequently, a tarry residue is also produced, similar to natural asphalt.

This work has established that a substantial fraction of the carboxylic acid groups in the kerogen will break off as acetate and propionate. Decarboxylation of acetate in the laboratory suggests the fate of the low-molecular-weight carboxylic acid anions in nature: they ultimately decarboxylate to give natural gas hydrocarbons. These anions, which are abundant in many oil and gas field waters, are evidently important intermediates in the formation of natural gas hydrocarbons (Carothers and Kharaka, 1978; Kharaka et al., 1983).

The observation that 40% of myristic acid molecules will decompose to give acetate is also important in connection with interpreting the characteristic "carbon preference index" of the *n*-alkanes in natural oils; even-numbered *n*-alkanes may, in fact, be produced directly from even-numbered carboxylic acids.

Results of this project have found application in two disparate areas. We have applied our analytical methods to a gas field brine and explained why this brine was causing a serious water pollution problem (Weres and Newton, 1985). The observation that humic acid yields a large amount of acetate at 315°C helped explain why acetate and other organic anions are the major anions in the condensate of several nuclear power plants (Weres and Tsao, 1984).

REFERENCES

Carothers, W.W., and Kharaka, Y.K., 1978. Aliphatic acid anions in oil-field waters—Implications for origins of natural gas. Am. Assoc. Petrol. Geol. Bull., v. 62, p. 2441–2453.

Kharaka, Y.K., Carothers, W.W., and Rosenbauer, R.J., 1983. Thermal decarboxylation of acetic acid: Implications for origin of natural gas. Geochim. Cosmochim. Acta, v. 47, p. 397–402.

Price, L.C., Clayton, J.L., and Rumen, L.L., 1979. Organic geochemistry of a 6.9-kilometer-deep well, Hinds County, Mississippi. Trans. Gulf Coast Assoc. Geol. Soc., v. 29, p. 352–370.

Price, L.C., Clayton, J.L., and Rumen, L.L., 1981. Organic geochemistry of the 9.6 km Bertha Rogers No. 1 well, Oklahoma. Organic Geochem. v. 3, p. 59–77.

Price, L.C., 1982. Organic geochemistry of core samples from an ultra-deep hot well (300°C, 7 km). Chem. Geol., v. 37, p. 215–228.

Weres, O., and Newton, A.S., 1985. Sampling and organic geochemistry of geopressured fluids. *In* this Annual Report.

Weres, O., and Tsao, L., 1985. Molten salt chemistry of nuclear steam generators. *In* this Annual Report.

Molten Salt Chemistry of Nuclear Steam Generators

O. Weres and L. Tsao

The steam generator is the boiler of a nuclear power plant. It is a tube-and-shell heat exchanger that transfers heat from the primary water loop (which flows through the reactor core) to the secondary water, which boils to produce the steam that drives the turbine.

Most American nuclear power plants have similar steam generators. The primary water flows through the tubes, which are made of the corrosion-resistant alloy Inconel 600. The secondary water boils outside the tubes. The heat exchange tubes terminate in *tube sheets*, typically of carbon steel and about 60 cm thick. For each tube, there is a hole of slightly larger diameter drilled completely through the tube sheet. The tube extends the complete depth of this hole and is tightly swaged to the tube sheet at its end. Because the swaged section is only a few centimeters long, there remains a narrow crevice between the tube and the tube sheet. The length of the crevice is typically about 50 cm, and its width is a fraction of a millimeter.

The temperature in these crevices is equal to primary side temperature, about 317°C on the hot leg of the steam generator. The pressure in the crevices is the secondary side pressure, about 60 bar. This is much less than the primary side pressure, about 108 bar, which is the vapor pressure of pure water at 317°C. Water continually enters the crevices from the main body of the steam generator and boils away. The secondary water is meticulously purified (less than 1 mg/liter total dissolved solids), but evaporation concentrates any nonvolatile solute in the water inside the crevices by a factor of one million or more. This concentration process can convert the ultrapure secondary water into saline sludge.

In many cases, the salts that accumulate in the crevice corrode the Inconel tubing. Eventually, the tubing begins to crack, causing the radioactive primary side water to contaminate the secondary side water. This is unacceptable. A cracked tube requires taking the plant down to plug off the tube, and the cost of the service interruption that results can reach millions of dollars. Recurrent tubing failures usually require that metal liners be welded into the tube ends, at a cost of tens of millions. A complete steam generator overhaul with full retubing would cost hundreds of millions.

Therefore, the details of steam generator crevice chemistry are of some interest to the nuclear industry. Improved knowledge in this area may lead to improved water treatment methods and may save electric utilities and their customers enormous amounts of money.

THE CREVICE ENVIRONMENT

The composition of the liquid phase in the crevice is most important, because it directly controls the corrosion process. The crevice cannot be sampled for analysis, and the solutes in the secondary water are hard to analyze because they are so dilute.

The crevice liquid must have a composition such that it will not dry out at 317°C and 60 bars. Because the boiling point of pure water at 60 bars is 275°C, the salts in the crevice liquid must raise the boiling point of water by 40°C; in the jargon of the nuclear industry, the crevice fluid must "sustain a superheat of 40°C." Very few salts are sufficiently soluble to sustain this superheat; most salt solutions will dry out under these conditions.

For many years, sodium hydroxide (NaOH), potassium hydroxide (KOH), and potassium silicate were held to be the only salts able to sustain this superheat. Because there is usually much less potassium in the secondary water than sodium, a crevice fluid dominated by KOH or potassium silicate is unlikely. Therefore, the crevice fluid must consist largely of molten sodium hydroxide and water, with subordinate amounts of other salts. Less soluble salts will precipitate to form solid crevice deposits. This has been the conventional wisdom since the 19th century, when coal-fired iron boilers were held together with rivets, which, like modern steam generator tubes, also corroded and failed.

Recently, very sensitive ion chromatography has been used to analyze the secondary water. In a few power plants, the crevices have been "flushed" and the "flush water" analyzed to give some indication of the crevice fluid composition. The best data of this kind are from the Ringhals power plant in Sweden. At the Ringhals plant, the flush water contains substantial silicic acid.

The most recent data from Ringhals and other nuclear plants indicate that sodium acetate and other salts of organic acids may be present in the crevices.

RESULTS

We have experimentally determined the vapor pressure of mixtures of various molten salts with water at 317°C. The relationship between water content and water activity for sodium acetate–water liquids is shown in Fig. 1. Pure, anhydrous sodium acetate melts near 324°C. Therefore, it can sustain nearly the same large superheat as sodium hydroxide, which melts at about 318°C. Sodium formate, sodium propionate, and sodium phenoxide have similar melting points and are also capable of sustaining the required superheat.

A successful model that describes the thermodynamic properties of mixtures of water and molten salts has been developed by K.S. Pitzer and his students (Pitzer, 1985). We have used Pitzer's model to represent our experimental water activity data. Doing so allows us to calculate the ion activity coefficients and other thermodynamic functions of the crevice fluid. That sodium acetate appears to be the major component of the crevice fluid is fortunate;

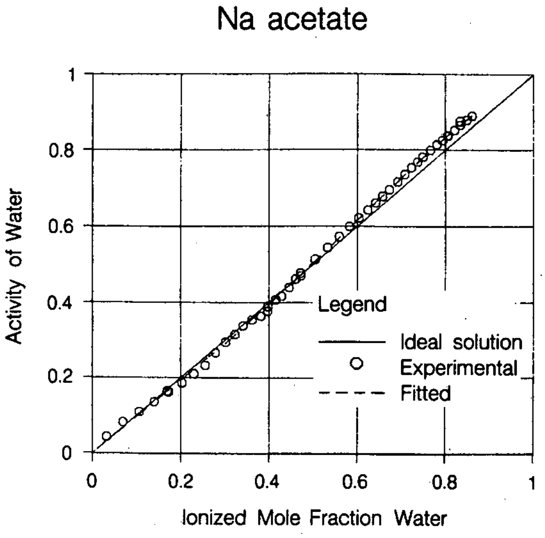

Figure 1. Activity of water in the system H_2O–sodium acetate. Temperature approximately 317°C. "Activity of water" is approximately equal to the vapor pressure of the solution divided by the vapor pressure of pure water at the same temperature. "Ionized mole fraction" = moles H_2O/(moles H_2O + moles Na^+ + moles acetate). Fitted curve derived using Pitzer's (1985) model. [XBL 851-10239]

Fig. 1 shows that sodium acetate and water form a practically ideal solution at 317°C.

Other work has shown that humic acid and other substances that contain aliphatic carboxylic acid groups will decompose to produce acetate ion at this temperature (Weres and Newton, 1985). Probably, some humic acid enters the steam generator system with the make-up water and decomposes at high temperature, releasing acetate and other organic anions. Sodium acetate appears to be stable at 317°C. Sodium formate *is not* stable at this temperature; it slowly decomposes to hydrogen and sodium carbonate. This may be a very significant observation, because sodium carbonate is known to accelerate the corrosion of Inconel in alkaline solutions at high temperature.

The presence of silica in the crevice means that sodium hydroxide cannot be a major component of the crevice fluid. Sodium hydroxide will react with silica to form solid sodium silicates, which are relatively insoluble at 317°C. Depending on the ratio of sodium to silica, the activity of hydroxide ion in the crevice liquid will be controlled by one of two buffering reactions:

$$Na_2Si_2O_5 + 2NaOH \rightarrow 2Na_2SiO_3 + H_2O \qquad (1)$$

$$2SiO_2 + 2NaOH \rightarrow Na_2Si_2O_5 + H_2O \qquad (2)$$

We have experimentally determined the equilibrium relations between sodium silicates and sodium acetate–water liquids. From these data, we were able to calculate the values of sodium hydroxide activity that correspond to the buffering reactions (1) and (2).

As anticipated, potassium silicate can support a large superheat (Fig. 2) (Morey and Fenner, 1917). Sodium silicate cannot. The sodium silicate system is interesting in that two immiscible liquids may coexist: one a dilute solution of sodium silicate in water, the other containing about 75% "dissolved" sodium silicate (Tuttle and Friedman, 1948; Friedman, 1950). The dense liquid has the same vapor pressure as the thin liquid it is in equilibrium with. Therefore, sodium silicate cannot sustain adequate superheat.

The system sodium silicate–potassium silicate–water can sustain a sizable superheat over a wide range of composition (Fig. 3). The flat portion of the curve in Fig. 3 may correspond to a zone of two immiscible liquids, as in the system sodium silicate-water.

The picture that emerges of the crevice chemistry is dominated by a mixture of sodium acetate and water containing smaller amounts of other salts. This liquid coexists with solid sodium silicates, which control the hydroxide ion activity within the liquid, and with other, less important solid phases. If sufficient potassium is present, a potassium silicate–sodium silicate–water liquid may be present.

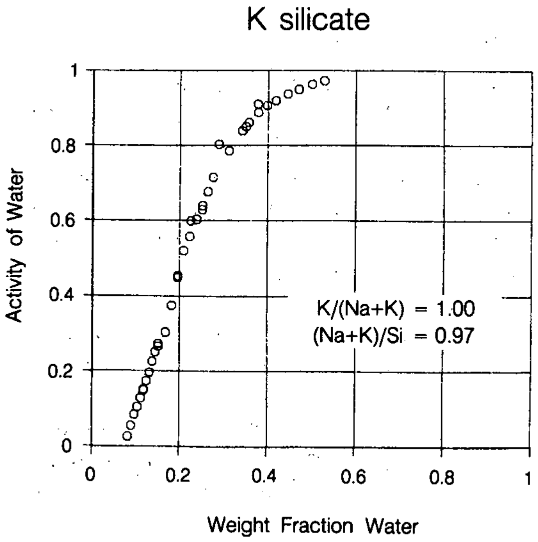

Figure 2. Activity of water in the system potassium silicate–water. Temperature approximately 317°C. [XBL 851-10238]

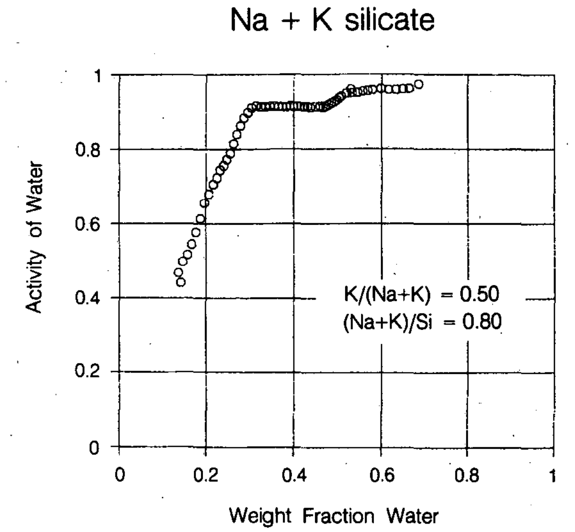

Figure 3. Activity of water in the system sodium silicate–potassium silicate–water. Temperature approximately 317°C. [XBL 851-10237]

ACKNOWLEDGEMENT

This work is supported by the Steam Generator Project Office of the Electric Power Research Institute.

REFERENCES

Friedman, I., 1950. Immiscibility in the system H_2O–Na_2O–SiO_2. J. Am. Chem. Soc., v. 72, p. 4570–4574.

Morey, G.W., and Fenner, C.N., 1917. The ternary system H_2O–K_2SiO_3–SiO_2. J. Am. Chem. Soc., v. 39, p. 1173–1229.

Pitzer, K.S., and Simonson, J.M., 1985. Thermodynamics of multicomponent, miscible ionic systems: Theory and equations. Presented at the 1984 International Chemical Congress of Pacific Basin Societies, December 16–21, Honolulu, Hawaii (LBL-17839).

Tuttle, O.F., and Friedman, I.I., 1948. Liquid immiscibility in the system H_2O–Na_2O–SiO_2. J. Am. Chem. Soc., v. 70, p. 919–926.

Weres, O., and Tsao, L., 1985. Organic chemistry of petroleum generation. *In* this Annual Report.

Sampling and Organic Geochemistry of Geopressured Fluids

*O. Weres and A.S. Newton**

THE DOWNHOLE SAMPLER

A downhole fluid sampler for use in geopressured gas wells has been designed, built, and tested (Michel et al., 1982). This sampler is designed to operate up to 450°F and 20,000 psi gauge pressure. The material of construction is MP35N, imparting great strength and excellent corrosion resistance. The sample volume is 1 liter.

A sample extraction system has been built (Weres et al., 1984) that allows gas and brine to be removed from the sampler, separated, and packaged for shipment, all without exposure to air. This sampler succeeded in bringing up a sample of water from a well in The Geysers geothermal field, where several other samplers had been tested and failed (Michel et al., 1982, Appendix D). Because very little drilling is going on, there has been no opportunity to test the sampler in a geopressured gas well. The sampler is ready to be used in a geopressured gas well.

ANALYSIS OF WELLHEAD SAMPLES

Lacking opportunity to collect downhole samples, we analyzed wellhead fluid samples from geopressured gas wells. We analyzed a geopressured brine (well Prets Unit 1) that was causing a serious water pollution problem. It contained abundant carboxylic acid anions that were responsible for the high biological oxygen demand of the brine. This explanation helped others develop a process to eliminate the problem. The geochemical significance of the organic anions is discussed further by Weres and Newton (1985).

Several of DOE's design geopressured gas wells in Texas and Louisiana have produced small

---

*Applied Science Division, Lawrence Berkeley Laboratory.

amounts of an unusual gas condensate (Table 1 and Fig. 1). The first three analyses in Table 1 are very much alike: aromatics >> cycloalkanes > branched alkanes > *n*-alkanes. Within each group, the concentration decreases rapidly with increasing molecular weight. This distribution of compounds closely parallels their solubility in water.

The condensate from the fourth well (L.R. Sweezy) initially resembled the other gas condensates, but its composition changed with continued production. The Sweezy analysis in Table 1 and Fig. 1b contains 28% alkanes, and the *n*-alkanes are prominent up to C-15. The alkane fraction of this condensate resembles the volatile fraction of paraffinic oil, while the aromatic fraction is practically identical with the other condensates in Table 1. Very likely, it is a mixture of these two components.

With continued production, an increasing amount of paraffinic condensate collected in the water drip pot on the Sweezy well's gas line (Fig. 2a). This material contained 90% alkanes, including 7% cycloalkanes. A small amount of heavy paraffinic oil was recovered from the gas separator of the Sweezy well. This oil resembled the paraffinic condensate, except for its higher-molecular-weight distribution (Fig. 2b). A light paraffinic oil produced from the moderately geopressured Prets well is shown for comparison (Fig. 2c).

Table 1. Composition of aromatic condensates.[a]

Well	Pleasant Bayou	Gladys McCall	Sweet Lake	L.R. Sweezy
Benzene[b]	49.3	56.5	46.6	26.0
Toluene	19.8	18.7	28.5	12.4
C-2 benzenes	14.3	12.4	15.3	19.2
C-3 benzenes	5.3	3.6	4.0	10.4
Naphthalenes	2.7	trace	1.3	3.4
Total aromatics	91.4	91.2	95.7	71.4
Cycloalkanes	6.0	6.9	2.7	5.7
n-alkanes	0.6	0.5	0.4	10.8
Branched alkanes	1.9	1.5	1.2	11.8
Total alkanes	8.5	8.9	4.3	28.3

[a] Reported concentrations proportional to FID response. Methylcyclopentane, isohexane, and *n*-hexane amounting to 5–10% of the total sample are also present but not reported.

[b] Includes cyclohexane, which cannot be resolved from benzene.

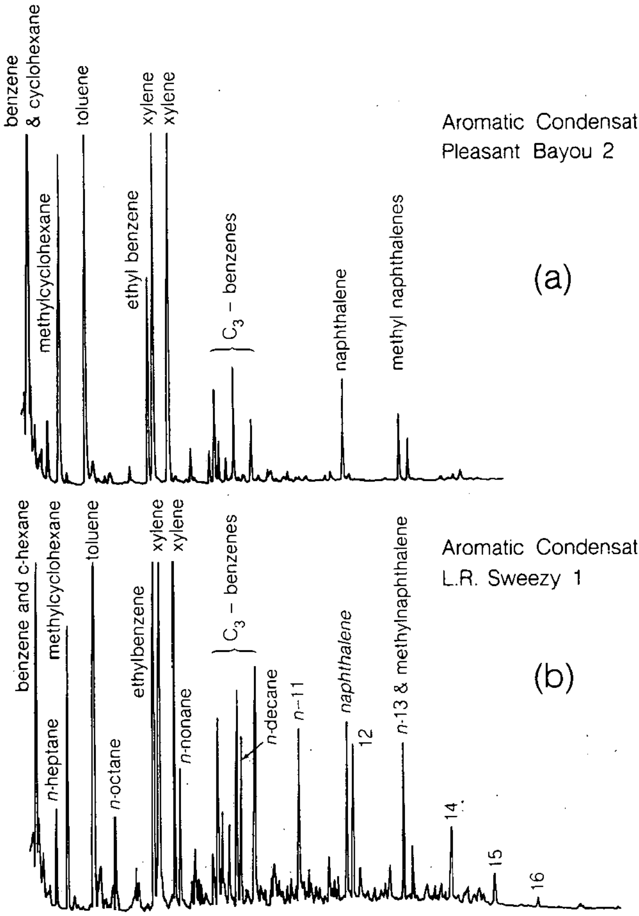

Figure 1. (**a**) Aromatic condensate from geopressured design well Pleasant Bayou 2. (**b**) Aromatic condensate from geopressured design well L.R. Sweezy 1. [XBL 8412-6190]

DISCUSSION

If combined, the alkane fraction of the Sweezy condensate, the paraffinic condensate, and the heavy oil would produce a mixture that resembles the oil from Prets Unit 1. It appears they are fractions of an oil similar to that of Prets Unit 1, separated by fractional condensation in the wellhead equipment.

Probably some oil similar to the Prets oil is present in the rock matrix of all the wells. In the reservoir, the more soluble (i.e., aromatic) hydrocarbons in the oil dissolved in the brine. When a separate gas phase formed in the course of brine production, the hydrocarbons partitioned into the gas phase. At the surface, the aromatic hydrocarbons in the gas were collected in the cold trap to produce the aromatic condensate.

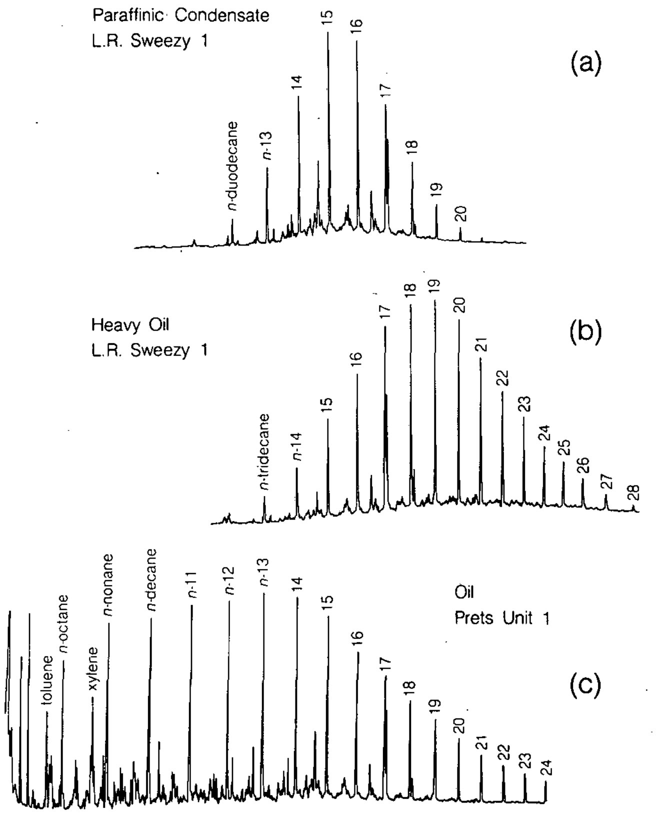

Figure 2. **(a)** Paraffinic condensate from the drip pot at L.R. Sweezy 1. **(b)** "Heavy oil" from the separator at L.R. Sweezy 1. **(c)** Paraffinic oil from Prets Unit 1. [XBL 8412-6189]

The production of the paraffinic condensates requires a different explanation, as liquids of this composition are practically insoluble in water. Conventional theories of oil migration require that enough oil be present to form a continuous oil phase. In the Sweezy well, this is certainly not the case.

The Sweezy well probably produced from a free gas cap, along with gas dissolved in the brine (Weres et al., 1984, p. 37). This gas cap probably developed in response to production and drawdown. The pressure and density in the gas cap were very high, the density of the gas approaching the density of gas condensate. Zhuze et al. (1962) and Price et al. (1983) have demonstrated that at the temperature and pressure that exist at the bottom of the Sweezy well, oil is soluble in natural gas. The water-insoluble alkanes dissolved in the gas and were produced with it. The least volatile fraction of the oil dropped out of the gas when pressure was reduced at the choke; this was the "heavy oil." An intermediate fraction condensed from the gas and collected in the drip pots; this was the paraffinic condensate. The most volatile alkanes remained in the gas with the light aromatics until collected in the cold trap; they formed the paraffinic fraction of the aromatic condensate.

The experience with the Sweezy well suggests that oil may be produced directly from source rock by coupling the processes of gas production and tertiary recovery by gas solution. The method for producing this oil is remarkably simple: draw down a geopressured well until it goes two phase in the formation. At that point, tertiary recovery of oil by solution in supercritical methane will begin.

Price et al. (1979, 1981) and Price (1982) have reported significant hydrocarbons and hydrocarbon potential in cores and cuttings from deep wells with temperatures up to 300°C. Perhaps this oil has not migrated because the pressure in these very deep wells is too high for a free gas phase to exist, making migration by gas solution impossible. Price's observations suggest that there may be an enormous resource of immobile oil in the geopressured zone.

If commercialized, coproduction of oil with geopressured gas could significantly improve the economic prospects for geopressured gas utilization, thereby increasing the economic resource base for both natural gas and oil.

ACKNOWLEDGEMENT

The Gas Research Institute supported this work under Contract No. 5081-212-0552.

REFERENCES

Michel, M. (ed.), Dudak, B., Galbraith, R., Hansen, L., Sverjensky, D., and Weres, O., 1982. Fluid sampling and chemical modeling of geopressured brines containing methane: Final report (March 1980 to February 1981). Lawrence Berkeley Laboratory Report LBL-12832 (GRI-79/0018).

Price, L.C., 1982. Organic geochemistry of core samples from an ultra-deep hot well (300°C, 7 km). Chem. Geol., v. 37, p. 215–228.

Price, L.C., Clayton, J.L., and Rumen, L.L., 1979. Organic geochemistry of a 6.9-kilometer-deep well, Hinds County, Mississippi. Trans. Gulf Coast Assoc. Geol. Soc., v. 29, p. 352–370.

Price, L.C., Clayton, J.L., and Rumen, L.L., 1981. Organic geochemistry of the 9.6 km Bertha Rogers No. 1 well, Oklahoma. Organic Geochem., v. 3, p. 59–77.

Price, L.C., Wenger, L.M., Ging, T., and Blount, C.W., 1983. Solubility of crude oil in methane as a function of pressure and temperature. Org. Geochem., v. 4, p. 201–221.

Weres, O.M., and Newton, A., 1985. Organic chemistry of petroleum generation. *In* this Annual Report.

Weres, O., Michel, M., Harnden, W., and Newton, A., 1984. Downhole sampling of geopressured wells: Final report for 1982–1984. Lawrence Berkeley Laboratory Report LBL-16518.

Zhuze, T.P., Ushakova, G.S., and Yushkevich, G.N., 1962. The influence of high pressures and temperatures on the content and properties of condensate in the gas phase of gas-oil deposits. (Soviet) Geochem., v. 8, p. 797–806. English translation of Geokhimiya, v. 8, p. 689–697.

Radioelements in Groundwater and Rocks of the Long Valley Caldera, California

H.A. Wollenberg, S. Flexser, A.R. Smith, and D.F. Mosier*

In the Long Valley caldera, seismicity has continued essentially uninterrupted since mid-1980, uplift has been documented (Savage and Clark, 1982), and injection of magma has been speculated to be occurring beneath the south moat area. Because of the intense interest in the seismicity and expected magmatism in the region, several geophysical parameters are concurrently being measured in the caldera by federal and state agencies and academic institutions. These parameters include local and regional seismicity, electrical properties, gravity, magnetics, crustal tilting, and horizontal deformation. Hydrogen, helium, and radon in soil gas are also being measured, as are chemical constituents of the groundwater. Thus an excellent opportunity exists for close comparison between variations observed in these parameters and variations in groundwater radon.

Accordingly, we have collected samples of water from hot, warm, and cold springs and have analyzed their radon contents (Wollenberg et al., 1984). A continuous monitoring system to measure waterborne Rn has been installed at a spring at the Hot Creek Fish Hatchery. Rocks encompassing the hydrologic systems feeding the springs of the caldera were analyzed for their radioelement contents in an effort to better understand the distribution of ^{238}U, the source of the ^{222}Rn in the water.

The uranium and thorium contents of rocks through which groundwater percolates control the initial abundances of their daughter products in the groundwater. For this reason, we measured radioelement contents of rocks in the Long Valley region by field and laboratory gamma spectrometry. Results of these analyses are listed in Table 1. Low concentrations of U and Th are evident in basalt of the north and south moats and in Paleozoic carbonate rocks of the Mt. Morrison pendant, which borders the caldera on the south. Mesozoic metavolcanic and Paleozoic clastic metasedimentary rocks to the south and west of the caldera have intermediate radioelement abundances, while the bordering granitic rocks and intracaldera rhyolites are of relatively high radioactivity. Samples of spring deposits have been collected and analyzed from three spring areas. These are predominantly siliceous sinter deposits with low radioelement contents, in keeping with observations of spring deposits in northern Nevada (Wollenberg, 1974), where siliceous sinter is of low radioactivity.

There is an apparent correlation between water ^{222}Rn concentrations and U in the rocks from which the cold springs flow. Radon concentrations are highest in the dilute cold springs in the relatively high radioactivity granitic and metamorphic rocks and are significantly lower in the cool springs flowing from the relatively low radioactivity basalt. This correlation does not hold for the warm and hot springs, for their ^{222}Rn concentrations are most strongly determined by the temperature of the shallow portions of the hydrothermal system and by rock-water interactions (Wollenberg et al., 1985).

Monitoring of groundwater ^{222}Rn continued in a pool at one of the Fish Hatchery springs. The spring system that feeds the pool has been described by Sorey (1976) as being recharged in the southwestern part of the caldera, with the water flowing eastward, primarily through fractured basalt and through the Quaternary glacial debris that underlies the basalt. Sorey (1976) estimated that 1 to 3% of geothermal water mixes with the eastward-flowing water. The

---

*Engineering and Technical Services Division, Lawrence Berkeley Laboratory.

Table 1. Radioelement concentrations of Long Valley rocks.

	U (ppm)	Th (ppm)	K (%)
CALDERA FILL			
Bishop Tuff[a]			
"Early"	6.5	22	4.0
"Late"	2.6	12	4.6
Rhyolite			
Tuffs	4.9	11.2	1.6
Flows and domes	5.6	15.7	4.1
Obsidian, Inyo Domes	6.5	20.4	3.8
Rhyolite of moat	5.0	18.8	3.0
Mean	5.2(± 1.4)	16.6(± 4.5)	3.5(± 1.2)
Basalt			
South moat	0.8	2.0	0.8
North moat	1.3	4.2	1.3
Mean	1.0	3.1	1.1
PRECALDERA ROCKS[b]			
Granodiorite			
Northwest border	6.6	26.1	3.6
South border	4.6	16.3	3.2
Mean	5.6	21.2	3.4
Paleozoic Metamorphics			
Carbonates	1.2	1.7	0.3
Clastics	4.4	7.3	1.8
Mean	2.8	4.9	1.1
Mesozoic metavolcanics	2.9	8.9	2.4

[a] Data from Hildreth (1979).

[b] Data for paleozoic carbonate and clastic rocks of the Mt. Morrison pendant and Mesozoic metavolcanic rock at the south end of the Ritter Range pendant are from Wollenberg and Smith (1970).

spring's temperature (12.5°C) remains essentially constant throughout the year, but flow rates vary by nearly a factor of 2 (about a mean of 150 liters/s), from high flows during spring and early summer to low flows in the late fall and winter. Given the size of the pool and these flow rates, the residence time of water in the pool is a few hours.

The monitoring system consists of a NaI(Tl) gamma detector submerged in the pool so that it is surrounded on all sides by at least 1 m of water. The data are acquired by a gain-stabilized gamma spectrometer whose output is organized into broad gamma-energy windows. The integrals in these windows are recorded hourly as the radon data. The one-hour integration time is appropriate to the several-hour residence time for water in the pool and to the 35- to 40-min half-life for ingrowth of the gamma-emitting daughters of ^{222}Rn. The gamma-ray spectrum from this location (Fig. 1) demonstrates that variations in radioactivity measured in this

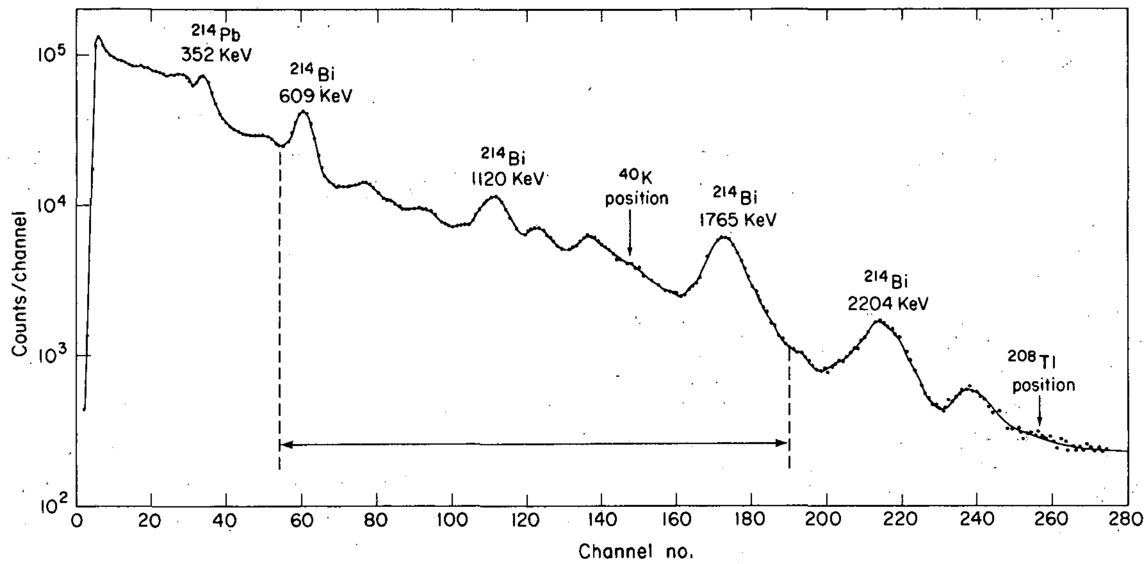

Figure 1. Gamma-ray spectrum measured by a NaI(Tl) detector suspended in water of the Fish Hatchery spring. The arrows delineate the interval measured for radon content. [XBL 8312-2412]

manner are due almost entirely to variations in the ^{222}Rn content of the water. As shown in Fig. 1, the recorded interval in the gamma-ray spectrum consists mainly of contributions from the ^{214}Bi daughter of ^{222}Rn. The absence of appreciable peaks from ^{40}K and ^{208}Tl in this spectrum attests to the effectiveness of the water surrounding the detector in shielding it from radioactivity of the rock that lines the pool.

Continuous monitoring shows that the hourly integrated gamma radioactivity of the spring water has strong semidiurnal peaks ranging in amplitude from 5 to 10% of the average counting rate. Fourier analyses indicate strong 12- and 24-hour periodicities. These radon fluctuations correlate closely with the earth-tidal characteristic, expressed in gravitational units, calculated for the latitude, longitude, and altitude of the Long Valley region, suggesting that radon variations are responding to small changes in stress in the basalt.

Figure 2 shows the hourly integrated record at the Fish Hatchery spring, together with the occurrence of caldera earthquakes of magnitude greater than 1.5 in the fall of 1983. The character of

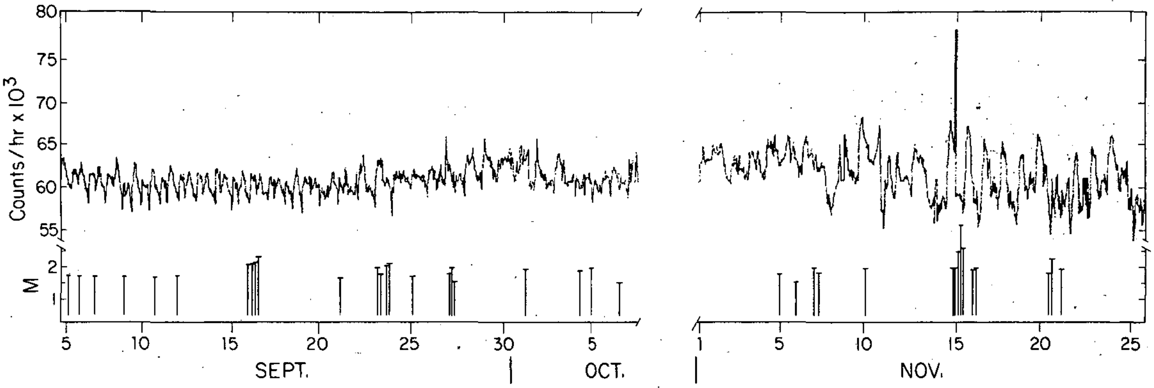

Figure 2. Hourly integrated radon record, September 5–November 25, 1983, at the Fish Hatchery Spring, Long Valley. The break in the record between October 7 and 15 is due to instrumentation problems. The occurrence of earthquakes in the caldera of magnitude >1.5 is shown by the vertical lines below the radon record. [XBL 843-9678]

the radon record for November differs from that prior to the break in the record in October, in that amplitudes are significantly larger after the break. The twice-daily peaks characteristic of September and early October are less apparent in November, and larger-amplitude, longer-period fluctuations appear to precede the period of relatively active seismicity of November 14–16. A large "spike" of radioactivity is nearly coincident with the magnitude 3.4 earthquake of November 14, 1983 (epicenter approximately 5 km southwest of the Fish Hatchery spring). This spike was most likely caused by enhanced emanation of radon in response to ground shaking in the immediate vicinity of the pool. A more regular periodicity of radon fluctuations appears to follow the earthquakes of November 14–16, characterized by daily peaks of relatively large amplitude. Examination of the later record indicates that this character persisted through December and into early 1984.

Conclusions at this stage of the investigation are that

1. Radon in groundwater is readily monitored by an in situ gamma radiometric system. The radioactivity of the water is due almost entirely to its ^{222}Rn content.

2. Radon concentrations of springs in the Long Valley caldera are controlled primarily by the water temperature and to a lesser degree by the U and Th concentrations of the rocks that encompass the hydrologic systems. The cold springs on or near the western, northern, and southern margins of the caldera, which may represent water that is recharging the caldera's hydrothermal system, have high radon concentrations relative to the cool, warm, and hot waters of the caldera.

3. The correspondence between earth-tidal and radon fluctuations suggests that the radon in water at the Fish Hatchery spring is responding to tidal-caused distortions in the basalt flow and glacial deposits that encompass the hydrologic system that feeds the spring. This suggests, in turn, that radon variations are responding to small changes in stress in rocks of the caldera.

REFERENCES

Hildreth, W., 1979. The Bishop Tuff: Evidence for the origin of compositional zoning in silicic magma chambers. Geol. Soc. Am., Spec. Pap. 180, p. 43–75.

Savage, J.C., and Clark, M.M., 1982. Magmatic resurgence in Long Valley caldera, California: Possible cause of the 1980 Mammoth Lakes earthquakes. Science, v. 217, p. 531–533.

Sorey, M.L., 1976. Potential effects of geothermal development on springs at the Hot Creek Fish Hatchery in Long Valley, Mono County, California. U.S. Geol. Survey Open-File Rept. 75-637.

Wollenberg, H.A., 1974. Radioactivity of Nevada hot spring systems. Geophys. Res. Lett., v. 1, no. 8, p. 359–362.

Wollenberg, H.A, and Smith, A.R., 1970. Radiogenic heat production in prebatholithic rocks of the central Sierra Nevada. J. Geophys. Res., v. 75, no. 2, p. 431–438.

Wollenberg, H.A., Smith, A.R., Mosier, D.F., Flexser, S., and Clark, M., 1985. Radon-222 in groundwater of the Long Valley caldera, California. Pure Appl. Geophys., in press.

Naturally Occurring Radioelements and Terrestrial Gamma-Ray Exposure Rates

*H.A. Wollenberg and A.R. Smith**

An assessment of the effects of nuclear reactors and other sources of artificial radioactivity upon the natural gamma radiation environment requires a good understanding of the distribution and abundances of the naturally occurring radioelements uranium and thorium, their decay products, and potassium-40 in rock and soil.

Appreciable data exist, primarily in the geochemical literature, on the distribution and abundance of these elements. A survey of the literature, principally that in English, has resulted in the cataloguing

---

*Engineering and Technical Services Division, Lawrence Berkeley Laboratory.

and characterization of natural radioelements and their associated rock types (Wollenberg and Smith, 1984). A data base has been assembled that incorporates radioelement information classified according to rock type. Formulas relating gamma-ray exposure rates to radioelement contents have been applied to these data. The resulting correlations are expressed as radioelement ratios and plotted as histograms of radioelement content and of calculated terrestrial gamma-ray exposure rates.

The primary impetus for this work is to help in the planning and interpretation of airborne multispectral gamma-radiation surveys to assess the radiation environment in the vicinity of planned and operating nuclear power reactors and other nuclear-energy-related sites. These surveys are conducted by the Aerial Measurements Group of EG&G, Inc. for the U.S. Nuclear Regulatory Commission and the U.S. Department of Energy. The work reported here was supported by EG&G through a memorandum of understanding with the Lawrence Berkeley Laboratory.

Terrestrial sources of gamma radiation are the radioelements ^{238}U, ^{232}Th, their decay products, and ^{40}K. A minor component, presently less than 5%, is from fission-product fallout. At sites of given altitude and geomagnetic latitude, the varying gamma-ray field from these elements in rock and soil is superimposed on a nearly constant gamma field from cosmic radiation. The cosmic-ray-induced gamma field generally contributes 1/4 to 1/3 of the total; the rest is from the terrestrial radioelements. Therefore, major spatial variations in natural gamma radioactivity are caused by variations in the abundance and distribution of U, Th, and K.

Concentrations of U, Th, and K were compiled from the geochemical literature and unpublished data at Lawrence Berkeley Laboratory; these were classified according to rock type on the basis of descriptions in the accompanying articles. The data base presently consists of 2522 entries for U, 2510 for Th, and 2079 for K. The computer program DOSECAL converts these data to gamma-ray exposure rates (at a height of 1 m above the ground surface) using the equations of Beck and de Planque (1968).

The data are summarized by rock class in Tables 1 and 2. Table 1 lists the arithmetic means and ranges in concentration. Table 2 lists the means and ranges of the contributions of the radioelements to the total terrestrial gamma-ray exposure rates.

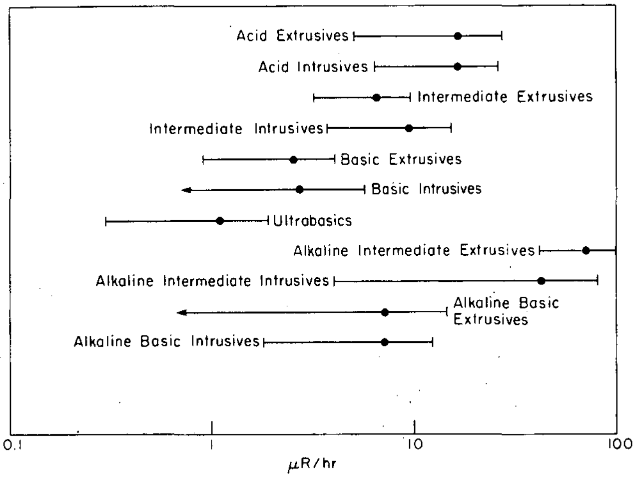

Figure 1. Gamma-ray exposure rates of the igneous rocks. Error bars express standard deviations of the means. [XBL 846-9023]

Figures 1 and 2 illustrate the range of mean values of exposure rates and their large standard deviations. The general variation of radioactivity within the igneous rocks is illustrated in Fig. 1, where mean values are highest in the acidic igneous rocks and range lower through rock types of increasing Fe and Mg and decreasing SiO_2 concentrations. Figure 2 illustrates the range of exposure rates due to sedimentary and metamorphic rocks. Within the sedimentary rocks, shale has the highest mean radioactivity; radioactivities are progressively lower in sandstone and conglomerate, clay, the chemical sediments, and carbonate rocks.

In summary, the compilation of natural radioelement concentrations of the various rock types has shown that

1. The gamma-ray exposure rates of the igneous rocks generally vary with the silica content of the rocks. Exceptions are the high-radioactivity alkali

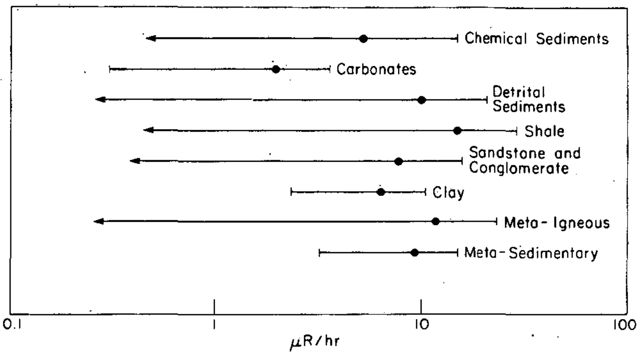

Figure 2. Gamma-ray exposure rates of the sedimentary and metamorphic rocks. Error bars express standard deviations of the means. [XBL 846-9022]

Table 1. Radioelement concentrations.

	U (ppm)			Th (ppm)			K (%)		
Rock class	Mean	Range	*n*	Mean	Range	*n*	Mean	Range	*n*
Acidic extrusives	5.7	0.8–23	131	22.4	1.1–116	131	3.7	1.0–6.2	124
Acidic intrusives	6.3	0.1–30.0	569	27.3	0.1–253	573	3.5	0.1–7.6	573
Intermediate extrusives	2.1	0.2–5.2	71	6.7	0.4–28	71	2.0	0.1–4.2	57
Intermediate intrusives	3.2	0.1–23	271	12.2	0.4–106	273	2.1	0.1–6.2	273
Basic extrusives	0.9	0.03–3.3	77	2.5	0.05–8.8	77	0.7	0.06–2.4	77
Basic intrusives	0.8	0.01–5.7	119	2.3	0.03–15	110	0.8	0.01–2.7	129
Ultrabasics	0.3	0–1.6	31	1.4	0–7.5	30	0.3	0–0.8	28
Alkalic feldspathoidal intermediate extrusives	29.7	1.9–62	138	134	9.5–265	139	6.5	2.0–9.0	36
Alkalic feldspathoidal intermediate intrusives	55.8	0.3–720	75	1.33	0.4–880	75	4.2	1.0–9.9	61
Alkalic basic extrusives	2.3	0.5–12	27	8.9	2.1–60	27	2.2	0.2–6.9	27
Alkalic basic intrusives	2.3	0.4–5.4	8	8.4	2.8–20	8	1.8	0.3–4.8	8
Chemical sedimentary rocks[a]	3.6	0.03–27	243	14.9	0.03–132	239	0.6	0.02–8.4	42
Carbonates	2.0	0.03–18	141	1.8	0–11	131	0.3	0.01–3.5	35
Detrital sedimentary rocks[b]	4.8	0.1–80	412	12.4	0.2–362	411	2.1	0.01–97	298
Clays	4.0	1.1–16	40	8.6	1.9–55	40	0.6	0.1–2.6	29
Shales	5.9	0.9–80	174	16.3	5.3–39	174	3.5	0.9–8.5	126
Sandstones and conglomerates	4.1	0.1–62	198	9.7	0.7–227	198	1.2	0.1–8.5	143
Metamorphosed igneous rocks	4.0	0.1–148	138	14.8	0.1–104	138	2.5	0.1–6.1	138
Metamorphosed sedimentary rocks	3.0	0.1–53	207	12.0	0.1–91	208	2.1	0.4–50	207

[a] Includes carbonates.

[b] Includes clay, shale, sandstone, and conglomerate.

Table 2. Gamma-ray exposure rates (μR/hour).

	U			Th			K			Total		
Rock class	Mean	Range	*n*	Mean	Range	*n*	Mean	Range	*n*	Mean	Range	*n*
Acidic extrusives	3.8	0.5–15	131	7.0	0.3–36	131	6.1	1.6–10	124	16.2	4.2–59	124
Acidic intrusives	5.1	0.1–20	569	8.4	0.03–78	573	5.8	0.2–12	573	18.2	2.7–98	569
Intermediate extrusives	1.3	0.2–4.4	71	2.0	0.1–8.7	71	3.1	0.9–6.2	57	6.5	2.1–20	57
Intermediate intrusives	2.1	0.05–15	271	3.7	0.1–32	273	3.5	0.2–10	273	9.4	0.3–41	271
Basic extrusives	0.6	0.02–2.2	77	0.9	0.02–2.7	77	1.15	0.1–4.0	77	2.65	0.1–8.7	77
Basic intrusives	0.5	0.01–3.7	119	0.7	0.01–4.6	110	1.3	0.1–10	129	2.7	0.2–16	109
Ultrabasics	0.2	0–1.1	31	0.4	0–2.3	30	0.4	0–1.3	28	1.1	0.1–4.0	24
Alkalic feldspathoidal intermediate intrusives	19.4	1.2–40	138	41.1	2.9–81	139	10.7	3.4–15	36	71.5	16.8–117	35
Alkalic feldspathoidal intermediate intrusives	36.5	0.2–470	75	40.7	0.1–491	75	6.9	1.7–16	61	42.7	3.3–323	61
Alkalic basic extrusives	1.5	0.3–7.9	27	2.7	0.6–18	27	3.7	0.3–11	27	7.9	2.8–37	27
Alkalic basic intrusives	1.5	0.3–3.5	8	2.6	0.9–6.0	8	3.0	0.5–7.9	8	7.1	1.6–17	8
Chemical sedimentary rocks[a]	2.4	0.02–18	243	4.6	0.01–40	239	0.9	0.03–14	42	5.2	0.2–45	38
Carbonates	1.3	0.02–12	141	0.6	0–3.3	131	0.5	0.02.5.8	35	1.9	0.2–6.4	32
Detrital sedimentary rocks[b]	3.1	0.05–52	412	3.8	0.1–111	411	3.5	0.02–16	298	9.8	0.4–147	298
Clays	2.6	0.8–10	40	2.7	0.6–17	40	1.0	0.4–4.2	29	6.3	2.1–19	29
Shales	3.9	0.6–52	174	5.0	1.6–12	174	5.7	1.5–14	126	14.5	4.2–63	126
Sandstones and conglomerates	2.7	0.07–41	198	3.0	0.2–70	198	2.0	0.2–14	143	7.7	0.5–101	143
Metamorphosed igneous rocks	2.6	0.1–97	138	4.6	0.02–32	138	4.2	0.22–10	138	11.3	0.8–125	138
Metamorphosed sedimentary rocks	2.0	0.05–35	207	3.7	0.2–28	208	3.4	0.02–8.7	208	9.1	0.4–50	207

[a] Includes carbonates.

[b] Includes clay, shale, sandstone, and conglomerate.

feldspathoidal rocks, which are generally low in SiO_2 but high in Na and K.

2. With the exception of shale, sedimentary rocks generally have low K/U and K/Th ratios compared to most igneous rocks.

3. The radioelement contents of metasedimentary and metaigneous rocks represent well the radioelement contents of their unmetamorphosed precursors.

4. There is an appreciable difference between the overall mean terrestrial gamma-ray exposure rate calculated from rock radioelement contents and the mean exposure rate from measurements over soil. This difference may be explained by effects of the differences in density of soil and rock, the moisture content of soil, and the apparent depletion of U in unsaturated, near-surface soil.

5. One may differentiate between low-radioactivity terranes (carbonates, ultrabasics, and basic igneous rocks) by their K/U and K/Th ratios. High-radioactivity terranes (acid-igneous and alkali feldspathoidal rocks) may also be differentiated by their K/U and K/Th ratios.

6. Airborne gamma-spectrometric surveys may be able to distinguish the general lithologic character of overflown terranes by combining radioelement ratios and concentrations with relative total gamma radioactivity.

REFERENCES

Beck, H., and de Planque, G., 1968. The radiation field in air due to distributed gamma-ray sources in the ground. Health and Safety Laboratory Report HASL-195, U.S. Atomic Energy Commission.

Wollenberg, H., and Smith, A.R., 1984. Naturally occurring radioelements and terrestrial gamma-ray exposure rates: An assessment based on recent geochemical data. Lawrence Berkeley Laboratory Report LBL-18741.

GEOMECHANICS

Topics in geomechanics covered in these reports for fiscal 1984 include the findings of a workshop devoted to rock mechanics issues in waste disposal, current research in hydraulic fracturing, field studies of acoustic-wave propagation in a heated rock mass, laboratory studies of acoustic-wave propagation in porous and fractured media, theoretical studies of the mechanical properties of and elastic-wave propagation in fractured media and discrete fractures, and a theoretical study involving block theory applied to modeling rock mass deformation. The first report discusses the findings of a workshop convened by Lawrence Berkeley Laboratory (LBL), to which hydraulic fracturing experts were invited to review and expand a list of rock mechanics issues involved in waste disposal by hydraulic fracturing. The second describes the laboratory and field studies in which hydraulic fractures induced in salt and granite were monitored by acoustic emission techniques. The third summarizes the results of a field study of acoustic-wave velocities and attenuation in a heated granitic rock mass. The next three reports cover the results of laboratory studies of acoustic-wave velocities and attenuation in fractured and porous rocks. Two theoretical studies follow on elastic-wave propagation in regularly jointed rock masses and across discrete fractures. Results of laboratory experiments are then reported that support the theory developed for elastic-wave propagation across a discrete fracture. Linear elastic fracture mechanics is applied in a report of a theoretical study to determine the effective elastic properties of a solid containing a random distribution of interacting cracks. The final report discusses the use of inverse techniques involving block theory to model the deformation of a rock mass.

These investigations have utilized experimental, analytical, and computational facilities at both LBL and the UC Campus, in particular, laboratories associated with the Civil, Mechanical, and Materials Science and Mineral Engineering Departments. The research effort has been shared by LBL staff, campus faculty, and University graduate students.

Rock Mechanics Issues in Waste-Disposal Fracturing

T.W. Doe

Over the past two decades, the Oak Ridge National Laboratory has developed hydraulic fracturing as a means of permanent disposal of radioactive wastes generated by the processing operations at the site. The predominantly liquid wastes are mixed with fly ash and other additives to make a waste grout. The grout is then injected into hydraulic fractures in the massive shale deposits that underly the site (Fig. 1). Experiments and analyses performed in the late 1960s showed that the grout follows the nearly horizontal bedding planes of the shale and that the grout hardens to form a solid sheet. Gamma-ray logs sense behind the casing of the observation wells (Fig. 2) to detect the depths of the grout sheets. Fluid pressures are monitored in the "rock cover" wells during injections. Oak ridge Laboratory approached Lawrence Berkeley Laboratory (LBL) to evaluate the rock mechanics of the disposal technology in light of the developments in the field in recent years. The results of the review are to be used to develop a research program to support continued use of the technology at Oak Ridge and to assess the feasibility of its use at other sites and for other types of waste.

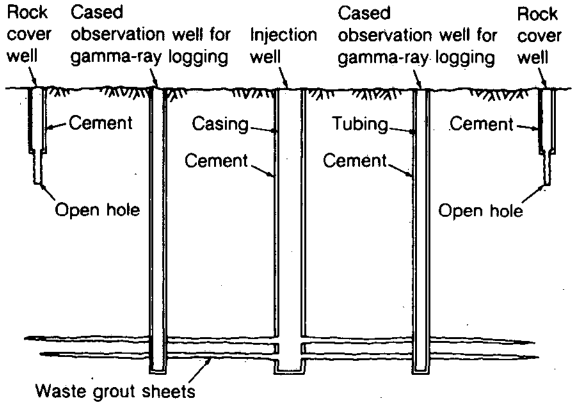

Figure 2. Typical well completions for rock cover and observation wells at Oak Ridge. [XBL 847-9818]

LBL convened a workshop to which hydraulic fracturing specialists were invited to review and expand a list of rock mechanics issues. The results of the workshop have recently been published by LBL (Doe and McClain, 1984). Seven research issues were identified: (1) state of stress at the Oak Ridge site, (2) effect of ground surface on fracture orientation, (3) effect of material anisotropy on controlling fracture orientation, (4) effects of multiple injections in a single hole, (5) pore pressure effects,

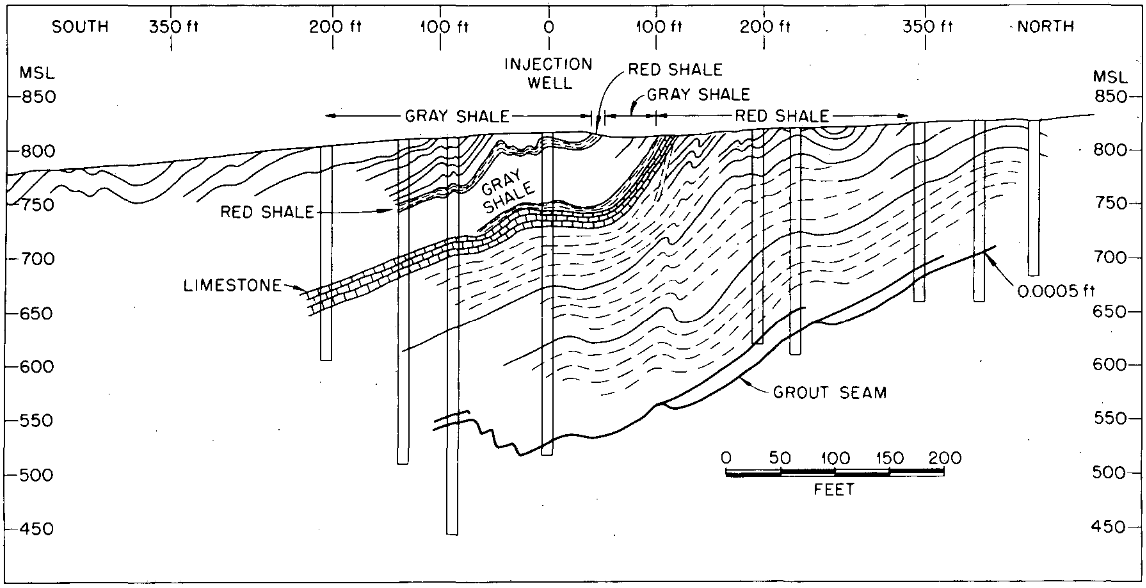

Figure 1. Inferred location of grout seam in first hydraulic fracturing experiment, 4-acre site, Oak Ridge (from De Laguna et al., 1968). [XBL 8410-4292]

(6) effects of discontinuities and heterogeneities on fracture growth, and (7) effects of nonlinear fluid properties on fracture propagation.

ROCK MECHANICS ISSUES

The proposed rock mechanics studies outlined in this report are designed to answer the basic questions concerning hydraulic fracturing for waste disposal. These questions are: (1) How can containment be assured for Oak Ridge or other sites? and (2) What is the capacity of a site? To answer these questions, we have identified several issues that address the questions.

State of stress. The state of stress is the single most important factor in determining whether a hydraulic fracture will be horizontal (and remain confined to the shale bed) or vertical (and pass out of the shale bed to a more permeable strata). Conditions will be favorable for horizontal fracture propagation if the minimum principal stress is vertical.

Effect of ground surface on fracture orientation. The virgin in situ stress field is the main factor controlling the fracture orientation when the fracture size is small relative to its depth. However, as the fracture diameter approaches a value equal to its depth, the ground surface exerts an influence that can cause the fracture to propagate upward. The fracture may then propagate out of the shale into overlying strata. The factors controlling this upward propagation of the fracture must be well understood if this breach of containment is to be avoided.

Effect of material anisotropy on fracture orientation. The bedding and foliation planes impart anisotropic strength and deformational properties to rocks. At Oak Ridge, the bedding of the shales is probably oriented nearly normal to the minimum in situ stress; thus the stress and the bedding both encourage horizontal fracture growth. It is not clear, however, that the bedding planes would control fracture growth if the minimum stress were horizontal. Such could be the case at other potential disposal sites or at greater depths at Oak Ridge.

Effect of multiple injections. In the hydraulic-fracturing waste-disposal operation, several injections are made into a single slot, and several slots may be made in a given well. Each injection deforms the surrounding strata and affects the local stress field, thus altering the in situ conditions for subsequent injections. The optimal size and number of injections, their spacing in the well, and their sequence are not yet known. These factors critically influence the disposal capability of a site.

Pore pressure effects. Pressures as great as 1.0 MPa (145 psi) have been observed in monitoring wells during the injections at Oak Ridge (Fig. 3). These data suggest that the pore fluids are being stressed as the rock accommodates the large volume of grout. Therefore, the mechanics of the rock deformation may not be simply elastic but also may involve poro-elastic factors and transient phenomena related to fluid diffusion. Furthermore, pore pressure buildup may induce additional fracturing or slip on pre-existing fractures in the vicinity of the bedding plane invaded by the grout.

Effect of discontinuities and heterogeneities on fracture growth. The shale strata may contain heterogeneities (such as lenses of carbonates or other rock types) and discontinuities (faults or joints) that influence the propagation of the fracture. When a fracture intersects such a feature, its propagation may be arrested, it may be diverted to another bedding plane in the shale, or it may change orientation. The effects that the several types of discontinuities and heterogeneities have on the propagation of a fracture must be understood.

Effects of fluid properties of grouts. The surface uplift and the potential for upward fracture propagation depend on the pressure distribution in the fracture. This pressure distribution is controlled in part by the fluid properties of the grout, which may be complex because of non-Newtonian behavior.

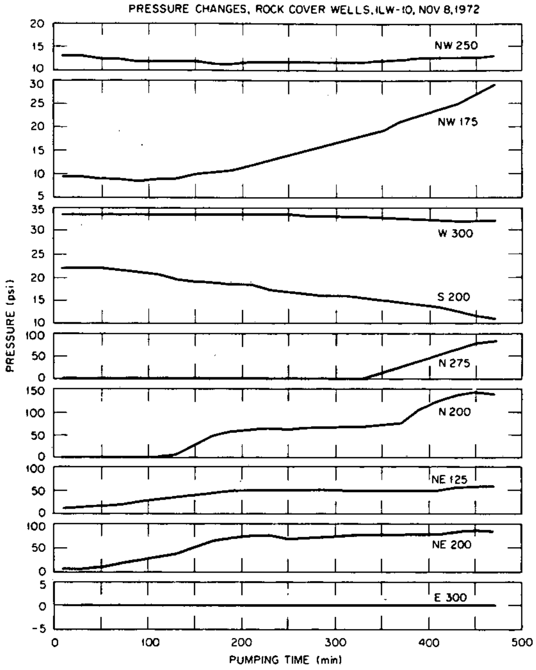

Figure 3. Wellhead pressure changes in rock cover wells during injections. [XBL 8411-4821]

RECOMMENDED RESEARCH

The recommended rock mechanics program consists of four major tasks: (1) numerical modeling, (2) laboratory testing, (3) field testing, and (4) monitoring. These tasks are described below.

Numerical Modeling

The ultimate goal of numerical modeling for hydraulic fracturing waste disposal is development of a fully verified and validated model that completely and accurately simulates all aspects of the process. However, the development of such an inclusive, fully coupled model from the present state of the art would not be cost effective and would not provide timely analysis for the further development of the technique. Instead, the proposed program is to pursue as many as three separate model approaches in order to assess the relative significance of certain issues. The three types of models considered appropriate are (1) deformation mechanics, (2) fracture mechanics, and (3) coupled fluid flow and deformation.

The first step is to develop these existing models to make them more specifically applicable to the waste-disposal process. The required modifications include enlargement to three dimensions; provision for multiple fractures and anisotropic material properties; inclusion of pore-pressure effects, pore compaction, and other nonelastic deformations; and addition of a capability for handling arbitrary discrete discontinuities and inhomogeneities.

As these code developments progress, the codes should be verified (by comparing them with analytical solutions, performing benchmark calculations, etc.), and parametric calculations should be undertaken to assess the individual aspects, such as the effect of the free surface; the effect of bedding-plane anisotropy; and the operating optima for number, size, and sequence of injections.

Later, as data from laboratory simulations, field tests, and monitoring activities become available, the models should be validated and any necessary refinements made. Finally, an evaluation of the numerical modeling effort should be made, including recommendations for the most effective way to proceed with the development of a complete simulation model.

Laboratory Experiments

There are two purposes in performing laboratory experiments. First, measurements of material properties must be made to provide data for the numerical modeling. Second, laboratory-scale simulations of hydraulic fracturing should be performed to validate calculations made by numerical models.

Among the material properties that must be determined for the shales at Oak Ridge are fracture toughness, porosity, permeability, and deformational properties (including moduli for drained and undrained shales). Where possible, the variation of material property values should be determined as a function of orientation relative to bedding. Because shale may rapidly degrade as it loses moisture, cores must be sealed immediately upon their removal from boreholes. The samples tested must be in as undisturbed a state as possible.

Laboratory testing is also a useful means of validating the performance of numerical models. Hydraulic fracturing simulations may be a particularly useful means of studying the influence of bedding-plane orientation relative to the in situ stress directions on the propagation of hydraulic fractures. Laboratory tests may also be used to investigate pore pressure effects around hydraulic fractures and the influence of free surfaces on fracture propagation.

Field Experiments

Field experiments are performed to explore and elucidate the basic rock deformational phenomena and to provide data to validate the numerical calculations. They have advantages over laboratory tests in that they provide data at scales more appropriate than laboratory tests. Field tests are, however, considerably more expensive, and it is more difficult to isolate the effects of specific phenomena or material properties on the overall behavior of the injection. Thus, while field tests are the best simulation experiment, they must be very carefully designed if they are to yield unambiguous results.

We therefore propose a modest effort for designing field tests during the early stages of the program, with a provision for implementing tests at a later time, if appropriate. Results from the modeling program will be incorporated into the field testing plans. Among the considerations to be dealt with in the test planning are (1) the role of smaller-scale tests focused on specific issues (e.g., anisotropy and heterogeneity effects) versus tests that completely simulate a disposal injection, (2) the smallest scale and least depth at which a field experiment can be said to simulate a disposal injection, and (3) the identification of potential sites and their relative advantage.

Monitoring

Much can be learned about fracture behavior using data that has been and will be gathered during the monitoring of injections at Oak Ridge. The monitoring data are of two types: that which has been gathered on previous injections and that which should be gathered during injections performed in the future.

Existing data from the current series of disposals and from previous experimental disposal sites consist mainly of the following: gamma logs of observation wells, pressure measurements in the rock cover wells, and surface leveling data. More recently, feasibility experiments have been performed using tiltmeters and microseismic monitoring arrays. An important task will be to review and compile all existing data, both published and unpublished, and make it accessible for use in the computational program.

Monitoring activities should be expanded for future injections at Oak Ridge. The seismic array should be expanded to allow precise location of events. Packer systems with pressure transducers should be placed at the bottom of the casing of the observation wells to provide rapid response piezometers. If possible, monitoring wells should be drilled and instrumented to provide a profile of pore-pressure change with distance from the hydraulic fracture. The feasibility of using other forms of geophysical monitoring (such as electrical methods) should be investigated. A permanent tiltmeter system should be installed, and surface leveling should continue.

REFERENCES

De Laguna, W., Tamura, T., Weeren, H., Struxness, E., McClain, W., and Sexton, R., 1968. Engineering development of hydraulic fracturing as a method for permanent disposal of radioactive wastes. Oak Ridge National Laboratory Report ORNL-4259, 259 p.

Doe, T.W., and McClain, W.C., 1984. Rock mechanics issues and research needs in the disposal of wastes in hydraulic fractures. Lawrence Berkeley Laboratory Report LBL-17635, 40 p.

Current Research in Hydraulic Fracturing for Stress Measurement

T.W. Doe, E.L. Majer, and G. Boyce

Hydraulic fracturing is a method that uses high-pressure fluids to create fractures in the rock underground. The procedure is to seal off a section of a borehole and pump fluid into it until a fracture is produced in the surrounding rock. First developed as a means of increasing the productivity of oil and gas wells in tight formations, the technique forms the basis of a major service industry within the petroleum industry. Hydraulic fracturing has since been utilized in other areas, including waste disposal, solution mining, geothermal power production, and tectonic stress measurement.

The effectiveness of a hydraulic fracturing job, regardless of its purpose, depends on how large a fracture has been made and what direction it has gone. Laboratory experiments have shown that the tectonic stress determines in large part the fracture direction, as the fracture's favored direction of propagation is normal to the minimum tectonic stress. On a more detailed level, the extent of a fracture depends also on directions of weakness (such as bedding or foliation) and on the presence of other natural fractures.

For the most part, existing fracture technology is capable neither of accurately predicting where a fracture will go nor of monitoring a fracture to determine where it has gone. It is in these two areas of research that the work in hydraulic fracturing at Lawrence Berkeley Laboratory (LBL) has concentrated.

STRESS MEASUREMENT IN SALT

One of the goals of stress-measurement research has been to determine if and under what conditions hydraulic fracturing can be used as a stress-measurement technique in salt. The theoretical basis of hydraulic fracturing as a stress-measurement technique is that the fracture is initiated when the fluid pressure in the hole overcomes the tangential stress concentrations around the hole (the stress acting parallel to the borehole wall) and a tensile strength factor. For rocks that behave nonelastically, like salt, it is not clear whether the elastic stress concentration is appropriate to use in calculating in situ stresses.

We have performed an extensive program of laboratory simulations of hydraulic fracturing stress measurements using salt samples from the Avery Island salt dome in Louisiana. Controlled stresses were applied hydrostatically to 150-mm-diameter cores and nonhydrostatically to prismatic blocks with volumes of 40,000 cm^3. The prismatic samples are loaded in a polyaxial frame that allows us to control the three principal stresses independently. We have studied the effects of applied stress, pressurization rate, time of loading, and hole size on the value of fluid pressure required to fracture the rock.

If the salt behaves in a nonlinear, viscoelastic manner, the stress concentration around the borehole should decrease with time, and the pressure needed to fracture the salt should similarly decrease. If the salt behaves elastically, this breakdown pressure should vary predictably with the level of stress applied to the samples and, for nonhydrostatic tests, should decrease with the difference between the principal stresses normal to the borehole.

Our results show that the breakdown pressures are independent not only of time but also of stress differences. Our current hypothesis is that the stress concentrations around the hole are probably being altered from the elastic values by a time-independent plastic deformation. If this is true, then hydraulic fracturing as it is conventionally applied for stress-measurement work in brittle materials is not applicable in salt.

We did find, however, that the directions of propagation of the fractures are controlled by the direction of the applied minimum stress. This was revealed by using acoustic emissions to locate the fractures in our samples. Acoustic emissions are similar to earthquakes but on a much smaller scale. Methods developed by Majer and McEvilly (1983) for locating and characterizing seismic and microseismic events in the field were readily adaptable to mapping the minute seismic events caused by our laboratory hydraulic fractures (Fig. 1).

ACOUSTIC TRACKING OF HYDRAULIC FRACTURES

In hydraulic fracturing for stress measurement, the orientation of the tectonic stresses is determined from the orientation of the fracture at the borehole wall. The accuracy of this technique has always been somewhat in question because it is never known whether the fracture might, at some distance from the borehole, rotate into some other orientation that would better reflect the minimum stress orientation. Acoustic mapping of stress-measurement hydraulic fractures offers a promising means of removing this doubt.

The acoustic method of tracking hydraulic fractures was used in 1981 to map a series of hydraulic fractures made for stress measurements in the area of LBL's heater tests at the Stripa mine in Sweden. The Stripa experiment (Doe et al., 1983) showed that the acoustic events from field fractures were distinct enough to be mapped, but malfunctions of the tape recorder used for data acquisition restricted us to only 3 of the 12 sensors, thus limiting our ability to locate the event.

Our second opportunity to track a hydraulic fracture in the field came at the Underground Research Laboratory (URL) being developed by Atomic Energy of Canada, Ltd., near Winnipeg, Manitoba. The URL is being developed as a demonstration facility for radioactive waste disposal and has a great advantage over other similar facilities in that it is being excavated especially for the purpose rather than being emplaced in an existing mine.

Our experiment was performed in April 1984, when the shaft of the URL had been advanced to a depth of 15 m. A 30-m hole was drilled in the center of the shaft, and three parallel 25-m holes were drilled around it. At each of the three 25-m holes, we emplaced arrays of sensors. We decided to use dyed water for a fracturing fluid to allow identification of our fractures upon completion of the shaft. Soft rubber impressions were taken of the hydraulic fractures in the borehole wall to determine the directions of the fractures. The seismic data are currently being processed to assess the extent and orientation of the fractures away from the borehole.

Experiments to date have detected high (10–100 kHz) and intermediate (10–1000 Hz) frequency signals, indicating that both shear and tensile failure are associated with hydrofracturing. It appears that low-frequency seismic signals (0.01–0.1 Hz) may also be generated by fracture opening along the total length of a fracture. The interrelation of these phenomena and whatever governs the proportion in which they occur are not totally understood, but seismic monitoring at different scales simultaneously appears to be useful not only for mapping the fracture but for unraveling this coupled fracture-mechanics/fluid-mechanics problem.

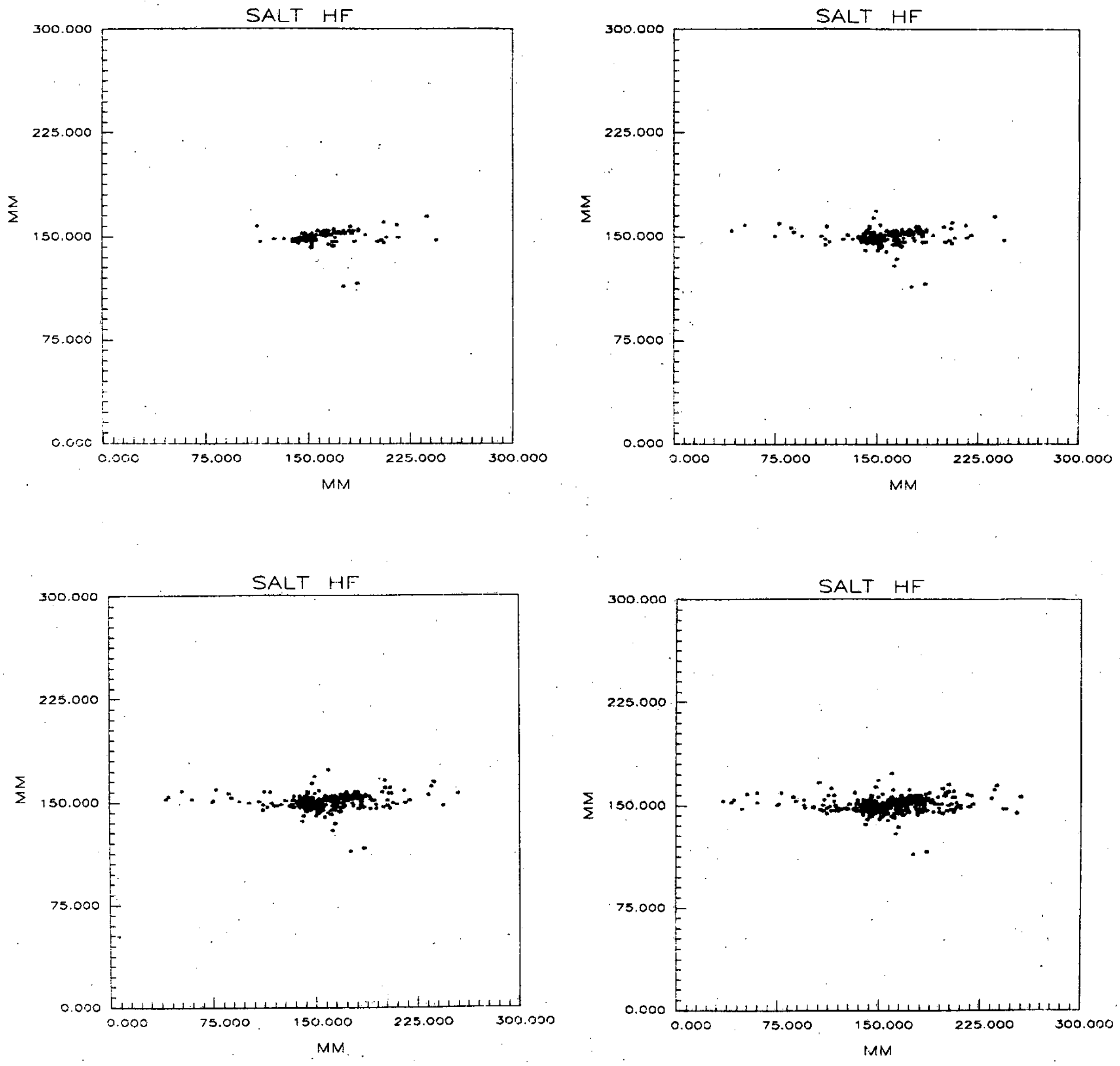

Figure 1. Plan view of acoustic emission locations due to hydraulic fracturing in a salt block. The borehole is at the center of each block. **(Upper left)** First 25% of emissions. **(Upper right)** First 50% of emissions. **(Lower left)** First 75% of emissions. **(Lower right)** All emissions. [XBL 8312-4825]

REFERENCES

Doe, T.W., Ingevald, K., Strindel, L., Leijon, B., Hustrulid, W., Majer, E., and Carlsson, H., 1983. In situ stress measurements at the Stripa mine, Sweden. Lawrence Berkeley Laboratory Report LBL-15009 (SAC-44), 251 p.

Majer, E.L., and McEvilly, T.V., 1983. Stripa acoustic emission experiment. *In* M. Zoback and B. Haimson (eds.), Hydraulic Fracturing Stress Measurements: Proceedings of a Workshop. Washington, D.C., National Academy Press, p. 215–219.

Seismic Velocities and Attenuation in an Underground Granitic Waste Repository Subjected to Heating

B.N.P. Paulsson and M.S. King

The velocities of compressional and shear waves and their attenuation in crystalline rocks containing fissures, fractures, and joints are influenced strongly by the state of stress, changes in temperature, and degree of water saturation in the rock mass. Nur and Simmons (1969) have shown that, at effective stress levels below 100 MPa, the elastic properties of crystalline rocks are controlled mainly by the properties of microcracks and that the application of uniaxial stress to a sample of granite causes elastic-wave anisotropy, with a higher compressional-wave velocity in the direction of the applied stress. Anderson et al. (1974) found that a preferred orientation of open cracks has a marked effect on seismic velocities, with the major reduction in velocity observed perpendicular to the plane of open fractures. King (1984) determined the effects of degree of water saturation on elastic-wave velocities in crystalline rocks and showed that an increase in water saturation increases the velocities of compressional and shear waves in granite.

The use of acoustic measurements made between parallel boreholes for characterizing a rock mass and monitoring changes in rock mass quality have been described by a number of researchers. Grainger and McCann (1977) provided two case histories of cross-hole acoustic measurements for site investigations in rock masses. McKenzie et al. (1982) reported a research program aimed at the in situ assessment of rock properties and quality at a number of Australian mine sites, employing a cross-hole acoustic system to obtain compressional-wave velocity and attenuation. Wong et al. (1983) described an acoustic system using stacking of waveforms for cross-hole seismic imaging in crystalline rocks.

Described in this paper are the results of a cross-hole acoustic investigation of a granitic rock mass subjected to heating (Paulsson and King, 1984).

EXPERIMENTAL PROCEDURES

The investigation was performed in a fractured granitic rock mass (quartz monzonite) at a depth of 340 m. Acoustic monitoring took place between four empty, dry, vertical boreholes of 10 m depth located in the vicinity of a vertical heater borehole in the floor of a drift, a plan of which is shown in Fig. 1 at the plane of the heater center line. Small volumes of water were found to seep continually into the four boreholes, but they were blown out regularly to keep them dry. Oriented core samples from a large number of vertical and horizontal instrumentation boreholes drilled in the vicinity of the heater provide excellent control of the structural geology and fractures within the volume of rock monitored. The cross-hole acoustic equipment has been described by Paulsson and King (1984). The accuracy of the velocity measurements is estimated to be ±0.1% (Paulsson, 1983), resulting in a resolution of ±6 m/s in *P*-wave velocities.

Two categories of acoustic monitoring tests are referred to here: (1) between-hole surveys, for which the transmitter and receiver were positioned at the same depth in a pair of boreholes and then moved down together at 0.25-m intervals between each reading; and (2) between-hole monitoring, for which the transmitter and receiver were positioned in each pair of boreholes at the level of the heater midplane. A reference line was chosen between a pair of boreholes (M6–M9, 1 m below the drift floor) well away from the heater to provide a check on transducer performance and the reproducibility of results.

RESULTS AND DISCUSSION

The velocity and attenuation behavior discussed here is limited to just the two cross sections between the four monitor boreholes shown in Fig. 1. These are M8–M9 and M7–M9, and the boreholes are 4.5 m and 4.2 m apart, respectively. The maximum temperature reached at day 398 (the last day of heater operation) in each of the two sections was quite different. The maximum temperature reached in M8–M9 was slightly more than 40°C, as shown in Fig. 2, while the maximum temperature in M7–M9 was 128°C, as shown in Fig. 3. The reason for these differences is that the two sections are at different distances from the heater borehole wall. The temperature field for the two sections on the last day of heating can be seen in the left-hand side of Figs. 2 and 3. The high temperatures were confined to the immediate vicinity of the heater, where there were sharp thermal gradients. The differences in temperature between the two sections is reflected in large differences in the velocities and the attenuation behavior in space and time. The second active process that influenced the elastic behavior of the rock

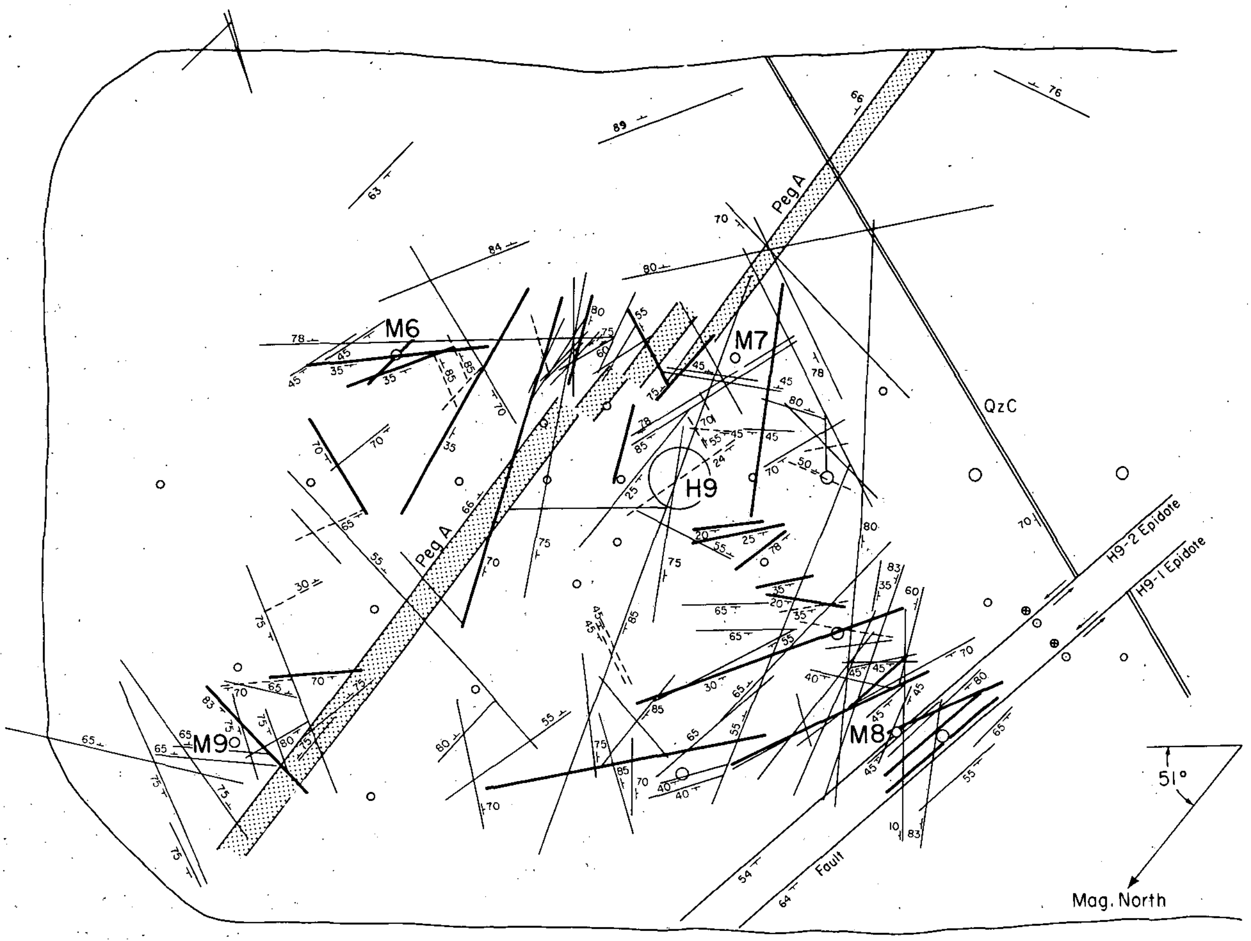

Figure 1. Plan view of borehole locations and geologic features below drift floor at plane of heater center line. [XBL 812-2614]

was dewatering of the rock mass. Dewatering was performed daily by pumping water from the 43 instrumentation boreholes around the H9 heater, as described by Nelson and Rachiele (1982). The dewatering was performed in all the boreholes and affected the whole rock mass around the heater.

The velocities measured during the preheating survey for section M8–M9 (Fig. 2, center) show no large anomalies. At day 343 the *P*-wave velocities had increased by approximately 100 m/s at most depths. The uniform increase of the velocity cannot have been caused by the heating, which was localized to the levels of the heater. The velocity increase in this profile is inferred instead to have been caused by the decrease of pore pressure, which led to a higher effective stress. This inference is confirmed by the nearly uniform increase of the *P*-wave quality factor, Q_α. The uniform increase of Q_α with depth is not seen in Fig. 3, where the velocities and Q_α values for section M7–M9 are plotted. In that section the Q_α values are fairly constant with depth for the preheating survey. The Q_α values continued to increase even after the heater was turned off at day 398. For the two surveys conducted at days 349 and 419 in section M7–M9, the smallest Q_α increase occurred at the level of the heater, indicating that the heated zone was a relatively high attenuation zone. This high attenuation was probably caused by a build-up of pore pressure due to the large thermal expansion of water and a heat-induced sharp reduction in permeability. Paulsson (1983) has shown that the pore pressure could exceed the tensile strength of the unfractured rock for quite modest temperature increases. The zone of low Q_α at the depth of the heater for the survey at day 707 indicates that the rock had been damaged, probably by thermal hydrofracturing. The two peaks of the Q_α values for the survey at day 419 for section M7–M9 were prob-

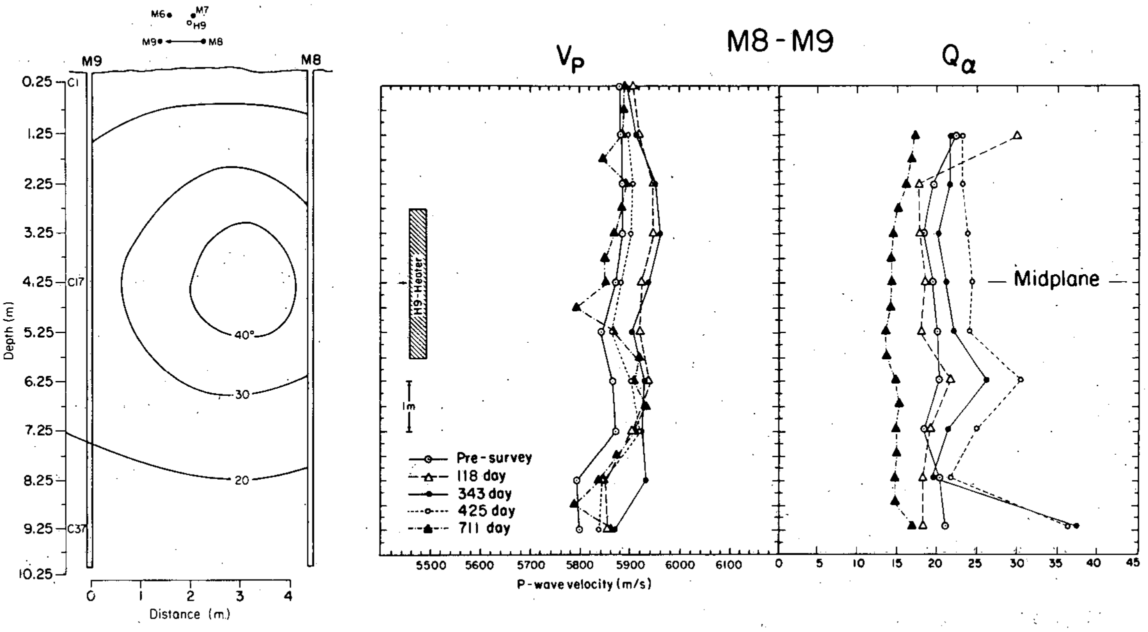

Figure 2. **(Left)** Temperature distribution (°C) immediately before heater shutoff. **(Center, right)** *P*-wave velocity (V_P) and quality factor (Q_α) between boreholes M8 and M9 before, during, and after heating. [XBL 8312-2424]

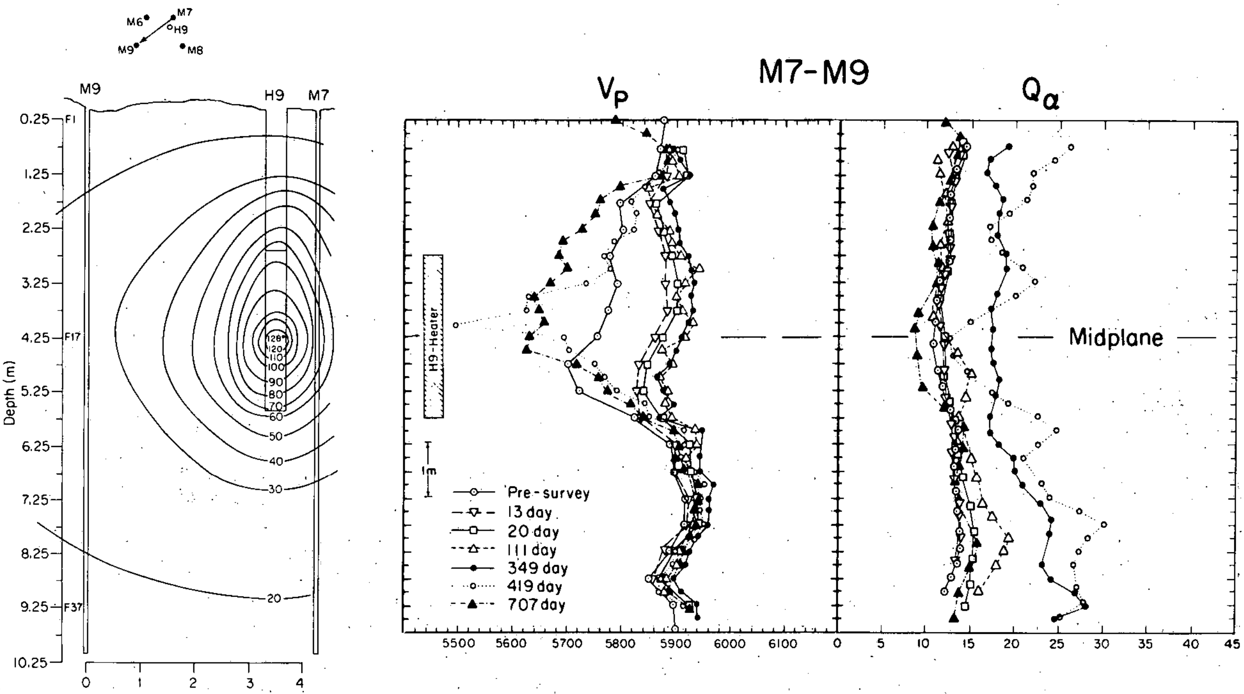

Figure 3. **(Left)** Temperature distribution (°C) immediately before heater shutoff. **(Center, right)** *P*-wave velocity (V_P) and quality factor (Q_α) between boreholes M7 and M9 before, during, and after heating. [XBL 8312-2417]

ably due to water flow into the partially saturated, relatively permeable zone opposite each end of the heater.

CONCLUSIONS

Measurements of the velocity and attenuation properties of high-frequency ultrasonic waves transmitted between boreholes in a heated crystalline rock mass constitute an effective seismic technique for detailed rock mechanics investigations around an underground opening. Compressional-wave velocities can be employed to assess thermal damage of the rock mass and the extent of the heat-disturbed zone. Attenuation properties of compressional waves can provide important information on thermal damage caused by high pore pressures in conjunction with heat-induced reductions in permeability.

The research has demonstrated that a field experiment of comparatively small scale can be successful in monitoring rock parameters that cannot be obtained in the laboratory. As such, it can provide a prototype data base for the implementation of high-frequency acoustic monitoring programs in full-scale waste repositories where the medium integrity must be known and maintained.

REFERENCES

Anderson, D.L., Minster, B., and Cole, D., 1974. The effect of oriented cracks on seismic velocities. J. Geophys. Res., v. 79, p. 4011–4015.

Grainger, P., and McCann, D.M., 1977. Interborehole acoustic measurements in site investigation. Quart. J. Eng. Geol., v. 10, p. 241–255.

King, M.S., 1984. Elastic-wave velocities in quartz monzonite at different levels of water saturation. Int. J. Rock Mech. Min. Sci. Geomech. Abstr., v. 21, p. 35–38.

McKenzie, C.K., Stacey, G.P., and Gladwin, M.T., 1982. Ultrasonic characteristics of a rock mass. Int. J. Rock Mech. Min. Sci. Geomech. Abstr., v. 19, p. 25–30.

Nelson, P.H., and Rachiele R., 1982. Water migration induced by thermal loading of a granitic rock mass. Int. J. Rock Mech. Min. Sci. Geomech. Abstr., v. 19, p. 353–359.

Nur, A., and Simmons, G., 1969. Stress-induced velocity anisotropy in rock: An experimental study. J. Geophys. Res., v. 74, p. 6667–6674.

Paulsson, B.N.P., 1983. Seismic velocities and attenuation in a heated underground granitic repository (Ph.D. thesis). University of California, Berkeley.

Paulsson, B.N.P., and King, M.S., 1984. Seismic velocities and attenuation in an underground granitic waste repository subjected to heating. *In* Proceedings, ISRM Symposium on Design and Performance of Underground Excavations, Cambridge, England, September 3–6, 1984. British Geotechnical Society, p. 477–483.

Wong, J., Hurley, P., and West, G.F., 1983. Crosshole seismology and seismic imaging in crystalline rocks. Geophys. Res. Letters, v. 10, p. 686–689.

Acoustic and Electrical Properties of Cerro Prieto Core Samples

E. Contreras and M.S. King*

Acoustic compressional- and shear-wave velocities have been measured on a suite of 12 sandstone core samples obtained from wells in the Cerro Prieto geothermal field. The samples were tested both when dry and when fully brine saturated at uniaxial stresses up to 15 MPa. Electrical resistivities and associated phase angles have been measured on the same core samples as a function of frequency in the range 10–10^5 Hz under drained conditions at hydrostatic confining stresses up to 10 MPa. The samples were tested in their fully saturated state using brines of two different concentrations.

The techniques used for specimen preparation, saturation with brine, and measurement of acoustic velocities have been described by King (1983, 1984). Those used for measuring the electrical properties have been described by Pandit and King (1979). Porosities were calculated from the dimensions, weights (dry and fully brine saturated), and brine density of the samples.

---

*Instituto de Investigaciones Electricas, Cuernavaca, Morelos, Mexico.

RESULTS AND DISCUSSION

Both compressional- and shear-wave velocities increased with an increase in axial stress; the velocity increase was more pronounced when the samples were dry. Saturating the samples with brine resulted in higher compressional-wave velocities; shear-wave velocities generally remained close in value to those measured dry.

A relationship of the form $1/V_P = A + B\phi$, between compressional-wave velocity (V_P) and porosity (ϕ), with A and B constants, is predicted both by the empirical time-average equation proposed by Wyllie et al. (1956) and by one developed theoretically by Geertsma (1961). Figure 1 shows reciprocal V_P, measured with specimens fully brine saturated at an axial stress of 10 MPa, as a function of ϕ. A relationship of the form given above fits the data well, with the intercept A yielding V_P = 5500 m/s for the solid rock matrix material, as expected for quartz.

Electrical resistivities for the brine-saturated specimens first showed a small decrease as the frequency was increased; the resistivities decreased asymptotically to constant values at frequencies above 200 Hz. The low-frequency behavior was probably due to electrode polarization effects, as referred to by Pandit and King (1979). Small increases in resistivity were observed over the whole range of frequencies for an increase in hydrostatic stress. Formation factors (F) calculated from the resistivities measured with the specimens saturated with brines of two different concentrations showed a small increase with an increase in concentration. This behavior is probably due to the lesser importance of the effect of mineral surface conductivity as the brine saturant resistivity decreased.

An empirical relationship of the form $F = 1/\phi^2$, relating the formation factor and porosity, has been proposed by Archie (Keller and Frischnecht, 1966). Figure 2 shows reciprocal $F^{1/2}$, with specimens fully saturated with brine of resistivity 0.1146 Ω·m and under a hydrostatic stress of 10 MPa, as a function of ϕ. Archie's relationship is seen to be valid for the suite of samples tested.

Wyllie et al. (1958) have demonstrated experimentally that, for sandstones of different porosities, compressional-wave velocities measured under uniaxial stress conditions are very close in magnitude to those measured on the same specimen under similar hydrostatic stress conditions. Figure 3 shows reciprocal V_P, with specimens brine saturated under an axial stress of 10 MPa, plotted as a function of reciprocal $F^{1/2}$, with specimens brine saturated under a hydrostatic stress of 10 MPa. The correlation between the two parameters is good.

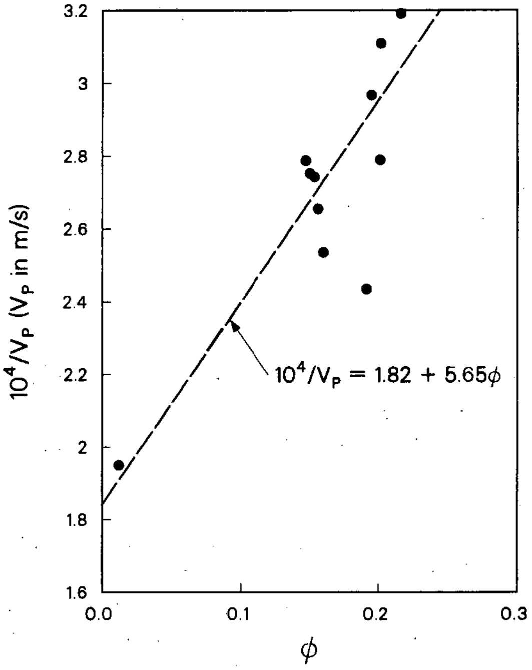

Figure 1. Reciprocal of compressional-wave velocity as a function of porosity. [XCG 8410-13391]

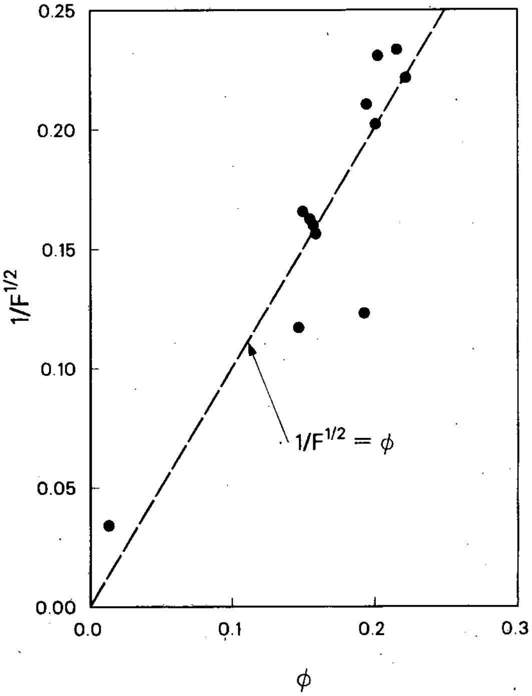

Figure 2. Reciprocal of $F^{1/2}$ as a function of porosity. [XCG 8410-13392]

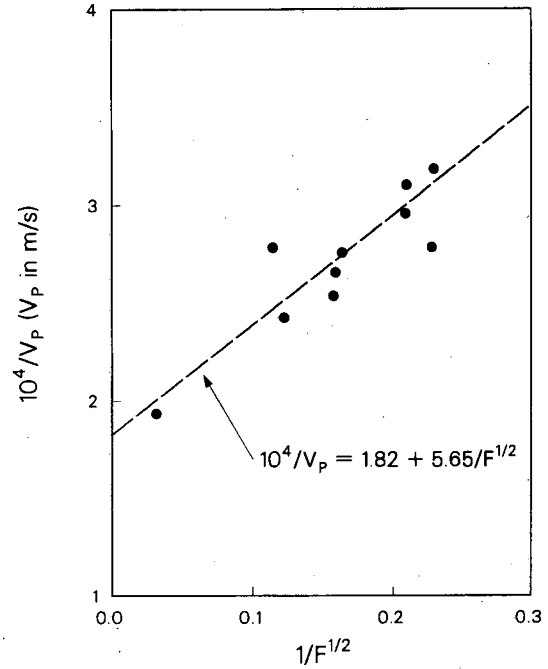

Figure 3. Reciprocal of compressional-wave velocity as a function of reciprocal of $F^{1/2}$. [XCG 8410-13393]

CONCLUSIONS

It is concluded that, provided the brine-saturated rock specimens are subjected to the same state of stress, both compressional-wave velocity and formation factor correlate well with the porosity.

REFERENCES

Geertsma, J., 1961. Velocity-log interpretation: The effect of rock bulk compressibility. Soc. Petrol. Eng. J. v. 1, p. 235–246.

Keller, G.V., and Frischnecht, F.C., 1966. Electrical Methods in Geophysical Prospecting. New York, Pergamon Press, p. 21.

King, M.S., 1983. Static and dynamic elastic properties of rocks from the Canadian Shield. Int. J. Rock Mech. Min. Sci. Geomech. Abstr., v. 20, p. 237–241.

King, M.S., 1984. Elastic wave velocities in quartz monzonite at different levels of water saturation. Int. J. Rock Mech. Min. Sci. Geomech. Abstr., v. 21, p. 35–38.

Pandit, B.I., and King, M.S., 1979. A study of the effects of pore-water salinity on some physical properties of sedimentary rocks at permafrost temperatures. Canad. J. Earth Sci., v. 16, p. 1566–1680.

Wyllie, M.R.J., Gregory, A.R., and Gardner, L.W., 1956. Elastic wave velocities in heterogeneous and porous media. Geophysics, v. 21, p. 41–70.

Wyllie, M.R.J., Gregory, A.R., and Gardner, G.H.F., 1958. An experimental investigation of factors affecting elastic wave velocities in porous media. Geophysics, v. 23, p. 459–493.

Acoustic-Wave Propagation in a Sandstone Saturated with Different Pore Fluids

M.S. King, R.P. Jantz, and B.N.P. Paulsson

The velocities and attenuation of elastic waves in porous sedimentary rocks as a function of stress and pore fluid saturants have been investigated, among others, by King (1966), Toksöz et al. (1976, 1979), and Winkler and Nur (1979). King (1966) measured compressional- and shear-wave velocities in a number of sandstones: dry, water saturated, and kerosene saturated. Toksöz et al., (1976) calculated the velocities of compressional and shear waves theoretically and compared them with laboratory data. Later, Toksöz et al. (1979) formulated models on the basis of various attenuative sources and discussed them within the context of published data. Winkler and Nur (1979) examined the effects of various degrees of water saturation on the velocities and attenuation of elastic waves in a sandstone.

In this study the results are presented of acoustic velocity and attenuation measurements on 16 cylindrical specimens of Berea Sandstone: dry and fully saturated with water, kerosene, and mineral oils of two viscosities. The rock specimens, having an average porosity of 0.21, were tested at uniaxial compressive stresses to 14 MPa under drained conditions. Experimental procedures, including specimen preparation, saturation procedures, and velocity and attenuation measurements, have been described in detail by Jantz (1982).

RESULTS AND DISCUSSION

A study of the acoustic compressional- and shear-wave data indicated that the 16 rock specimens were members of two distinct populations. Thus "high" and "low" velocity groups were formed by inspection. With the creation of two groups, standard deviations of the velocities were reduced, especially at higher stress levels. Figures 1 and 2 show compressional- (V_P) and shear-wave (V_S) velocities for the two groups of sandstone specimens, both dry and saturated with brine (KCl, 5000 ppm), kerosene (viscosity, 4 cp), light oil (viscosity, 17 cp), and heavy oil (viscosity, 60 cp). These figures indicate that at all stress levels, V_P and V_S are less in the dry than in the liquid-saturated specimens. As the axial stress was increased, the differences in velocity between dry and saturated specimens decreased. With its higher bulk modulus, brine saturation might be expected to result in velocities higher than mineral oil saturation. That this is not the case is ascribed to the influence of the strongly wetting liquid (brine) in reducing free surface energy, and thus the acoustic velocities, in comparison with a nonwetting liquid (mineral oil). The behavior observed is consistent with that reported by King (1966) for Berea Sandstone and with the theoretical predictions made by Toksöz et al. (1976) for porous rocks saturated with gas, oil, and water.

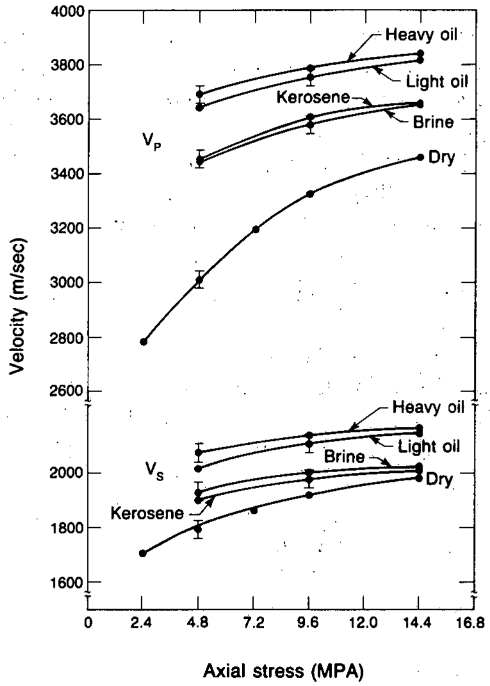

Figure 1. Compressional- and shear-wave velocities as a function of axial stress and different pore fluid saturants. High-velocity group. [XBL 8312-7448]

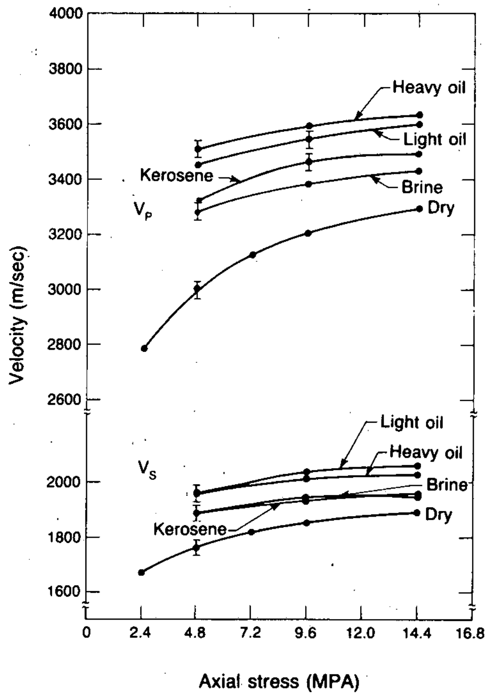

Figure 2. Compressional- and shear-wave velocities as a function of axial stress and different pore fluid saturants. Low-velocity group. [XBL 8312-7447]

The elastic-wave attenuation characteristics of the dry and saturated sandstone were obtained by comparing the Fourier amplitude spectra of the specimens over the frequency range 350–500 kHz with those of an aluminum standard having the same dimensions as the rock samples (Toksöz et al., 1979). The results are plotted in Figs. 3 and 4 in terms of the inverse quality factor Q^{-1} (where $Q = \pi f/\alpha V$, in which f = frequency, V = elastic-wave velocity, and α = attenuation coefficient) as a function of axial stress. While the rock samples were divided into two separate velocity groups, no such distinction could be made concerning the inverse quality factors.

Compressional- and shear-wave attenuation appeared to be less (lower Q^{-1}) in the dry than in the saturated sandstone specimens. As the axial stress was increased, it was observed that, while compressional-wave attenuation (Q_P^{-1}) decreased appreciably, the shear-wave attenuation (Q_S^{-1}) was relatively insensitive to increases in stress. This behavior is consistent with that reported by Toksöz et al. (1979) and Winkler and Nur (1979). It is clear

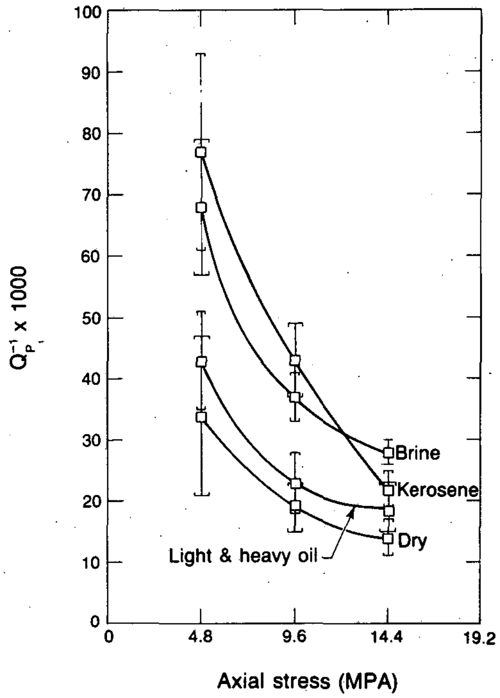

Figure 3. Compressional-wave attenuation as a function of axial stress and pore fluid saturants. [XBL 8312-7445]

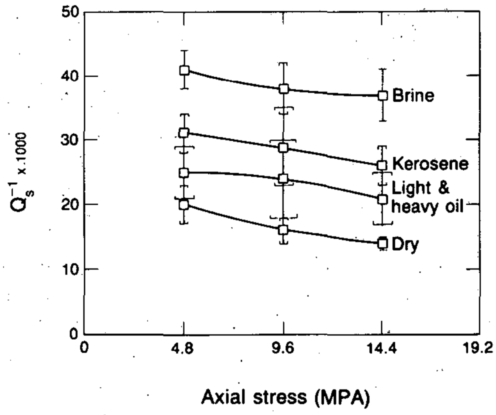

Figure 4. Shear-wave attenuation as a function of axial stress and pore fluid saturants. [XBL 8312-7446]

that the presence of a strongly wetting liquid (brine) in the pore space results in greater attenuation of elastic waves than the presence of a nonwetting liquid (mineral oil). This is particularly true for shear-wave attenuation.

CONCLUSIONS

For the Berea Sandstone tested, it is concluded that

1. The presence of liquid in the pore spaces results in increases in compressional- and shear-wave velocity over those measured in the dry rock, with the increases becoming less pronounced as the axial stress is increased.
2. The presence of liquid in the pore spaces results in increases in compressional- and shear-wave attenuation over those measured in the dry rock. The increase in axial stress results in a pronounced reduction in compressional-wave attenuation but has little effect on shear-wave attenuation.
3. The presence of a wetting liquid in the pore spaces results in increases in compressional- and shear-wave velocity over the dry state that are less than expected, probably because of a reduction in free surface energy. The corresponding increases in attenuation with a wetting liquid in the pore spaces are more pronounced than expected.

REFERENCES

Jantz, R.P., 1966. Velocity and attenuation of seismic waves in a sandstone saturated with different pore fluids (M.S. report). University of California, Berkeley.

King, M.S., 1966. Wave velocities in rocks as a function of changes in overburden pressure and pore fluid saturants. Geophysics, v. 31, p. 50–73.

Toksöz, M.N., Cheng, C.H., and Timur, A., 1976. Velocities of seismic waves in porous rocks. Geophysics, v. 41, p. 621–64.

Toksöz, M.N., Johnston, D.H., and Timur, A., 1979. Attenuation of seismic waves in dry and saturated rocks: Part I. Laboratory measurements. Geophysics, v. 44, p. 681–690.

Winkler, K., and Nur, A., 1979. Pore fluids and seismic attenuation in rocks. Geophys. Res. Letters, v. 6, p. 1–4.

Laboratory Measurements of Acoustic Velocities and Attenuation in Dry and Water-Saturated Basalt

M.S. King and J.J. Rezowalli

Interpretation of the results of a field program involving cross-hole acoustic measurements in a columnar-jointed basaltic rock mass (Rezowalli et al., 1984; King et al., 1984) required laboratory measurements of compressional- and shear-wave velocities and attenuation on intact core samples obtained from the test boreholes. In this study are reported the results of measurements of compressional- and shear-wave velocities and attenuation on 10 cylindrical specimens prepared from core samples recovered from the four 10-m-long horizontal boreholes used for cross-hole measurements in the field program. The rock specimens were tested under uniaxial stresses to 21 MPa, both water saturated and dry. Experimental procedures, including specimen preparation, saturation and drying procedures, and velocity and attenuation measurements, have been described in detail by Rezowalli (1984).

RESULTS AND DISCUSSION

Average values of compressional- (V_P) and shear-wave (V_S) velocities for the 10 intact specimens, dry and water saturated, are shown in Fig. 1 as a function of axial stress up to 21 MPa. It will be observed that V_P measured in the water-saturated state is higher than that in the dry state, with the difference becoming less as the axial stress is increased. V_P measured in the saturated state is relatively insensitive to an increase in axial stress. There is virtually no difference in magnitude between dry and water-saturated V_S. Moreover, V_S is relatively insensitive to an increase in axial stress. Figure 2 shows the Young's modulus and Poisson's ratio for the intact rock, calculated from the acoustic velocities and density of the basalt, as a function of axial stress. The difference in V_P between the dry and water-saturated states results in the significant differences in Young's modulus and Poisson's ratio, dry and water saturated. The acoustic-velocity results are similar to those reported by Nur and Simmons (1969) for rocks containing porosity predominantly in the form of cracks.

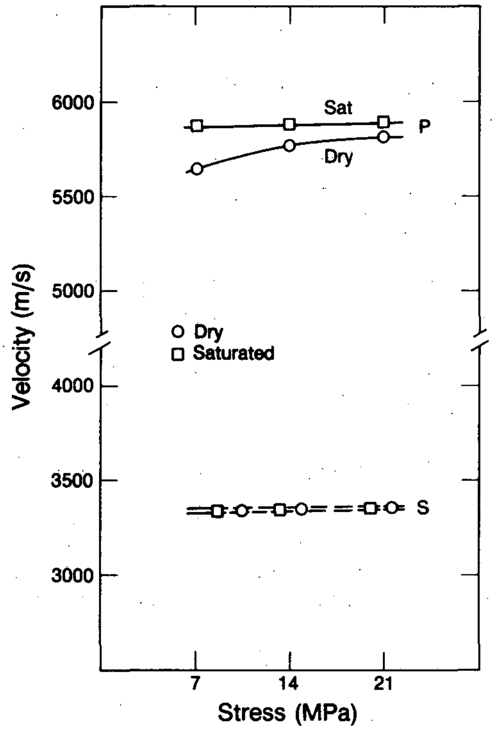

Figure 1. Compressional- and shear-wave velocities in dry and saturated specimens as a function of axial stress. [XBL 844-9746A]

Average values of compressional- and shear-wave quality factor (Q), which is inversely proportional to attenuation, are shown for the 10 specimens, dry and water saturated, in Fig. 3 as a function of axial stress up to 21 MPa. The attenuation characteristics of the dry and water-saturated specimens were obtained by comparing the Fourier amplitude spectra over the frequency range 350–500 kHz with those of an aluminum standard having the same dimensions as the rock specimens (Toksöz et al., 1979). It will be observed that Q_P (for compressional waves) is less, both water saturated and dry, than Q_S (for shear waves), water saturated and dry. It is also worthy of note that Q_P and Q_S are both greater in magnitude for water-saturated than dry specimens. This behavior has also been observed by Paulsson (1984) for dry and water-saturated granite specimens. Figure 3 shows that there is an increase in Q_P and Q_S, both dry and water saturated, as the axial stress is increased.

Laboratory measurements of compressional- and shear-wave velocities and attenuation on intact specimens, dry and water saturated, permitted cer-

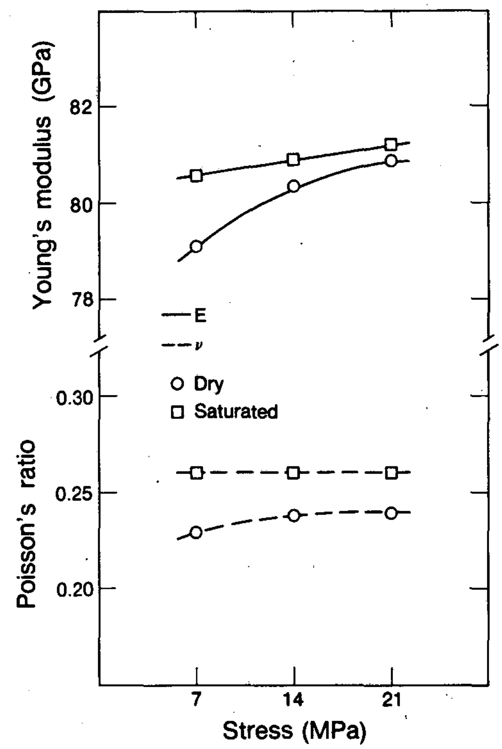

Figure 2. Young's modulus and Poisson's ratio in dry and saturated specimens as a function of axial stress. [XBL 844-9745]

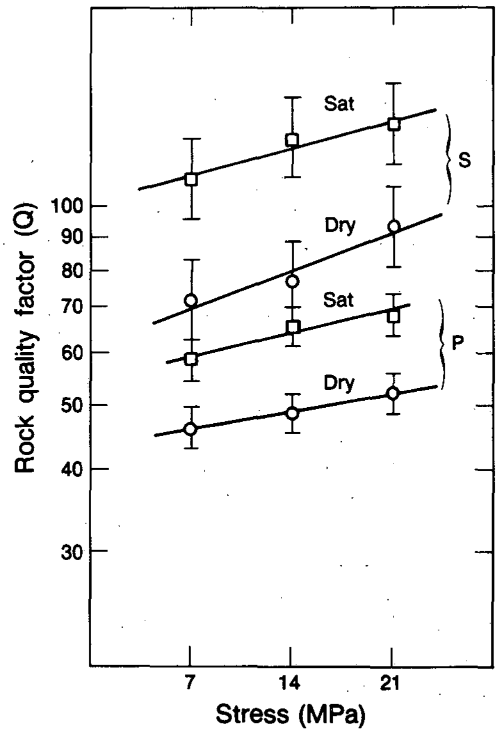

Figure 3. Rock quality factor for compressional and shear waves in dry and saturated specimens as a function of axial stress. [XBL 844-9744A]

tain conclusions to be drawn from the field measurements. Rezowalli et al. (1984) reported consistently high values of Poisson's ratio ($\nu = 0.27$ or higher) from cross-hole measurements made throughout the rock mass. Laboratory values of Poisson's ratio indicate that to yield Poisson's ratios this high, the rock mass was probably water saturated during the field experiments. Laboratory values of Q_P for the water-saturated rock place an upper bound of 60 for Q_P in the field. Paulsson (1984) has shown for granite that, with water saturations less than 60% of the pore volume, Q_P and Q_S are essentially constant. For saturations between 60% and 100%, he showed that Q_P and Q_S increase to their maximum values. Depending on the degree of water saturation of the rock mass in the field, Q_P might be expected to vary between 45 and 60 for cross-hole paths through intact rock. Certainly, cross-hole paths in the vertical direction appear to exist through intact rock in the field (Rezowalli et al., 1984).

CONCLUSIONS

1. Water saturation of dry, intact specimens of basalt results in an increase in V_P but no change in V_S. Both acoustic velocities are relatively insensitive to an increase in axial stress.
2. Water saturation of dry, intact specimens of basalt results in increases in both compressional- and shear-wave quality factor Q. For dry specimens Q_S is approximately 40 percent greater than Q_P.
3. Poisson's ratio calculated from the laboratory measurements of V_P and V_S in dry and saturated specimens of intact basalt indicate the rock mass in the field is probably water saturated.
4. Laboratory measurements of Q_P and Q_S provide an upper bound for cross-hole measurements of each quality factor.

REFERENCES

King, M.S., Myer, L.R., and Rezowalli, J.J., 1984. Cross-hole acoustic measurements in basalt. *In* Proceedings, 25th U.S. Symposium on Rock Mechanics, Evanston, Illinois, June 25–27, 1984. Society of Mining Engineers of AIME, p. 1053–1062.

Nur, A., and Simmons, G., 1969. The effect of saturation on velocity in low porosity rocks. Earth Planet. Sci. Letters, v. 7, p. 183–193.

Paulsson, B.N.P., 1984. A laboratory study of seismic velocities and attenuation of host rocks for a nuclear waste repository. *In* Proceedings, 25th U.S. Symposium on Rock Mechanics, Evanston, Illinois, June 25–27, 1984. Society of Mining Engineers of AIME, p. 1063–1073.

Rezowalli, J.J., 1984. Analysis of cross-hole seismic measurements in columnar-jointed basalt (M.S. thesis). University of California, Berkeley.

Rezowalli, J.J., King, M.S., and Myer, L.R., 1984. Cross-hole acoustic surveying in basalt. Int. J. Rock Mech. Min. Sci. Geomech Abstr., v. 21, p. 213–216.

Toksöz, M.N., Johnston, D.H., and Timur, A., 1979. Attenuation of seismic waves in dry and saturated rocks: Part I. Laboratory measurements. Geophysics, v. 44, p. 681–690.

A Theoretical Study of Elastic Velocities in Regularly Jointed, Dry and Water-Saturated Rock Masses

H.J.P. Yang and M.S. King

Many massive rock masses, particularly carbonates and igneous rocks, which are intrinsically isotropic, have been subjected in the past to regional stresses that have created systems of orthogonal fractures throughout large volumes. Crampin et al. (1984) indicate that elastic-wave propagation through such a fractured rock mass can be simulated by propagation through a homogeneous material having the same velocity variations.

We report here the results of a study of the elastic properties of dry and water-saturated, regularly jointed rock masses, in which orthogonal fracture planes have separated the rock into rectangular blocks. We follow White (1983) in assuming that an elementary cube whose edge dimensions are small compared to the wavelength contains a sufficient number of blocks to yield average properties representative of the fractured rock mass. White further assumed that each fracture plane is slightly irregular and that small movements have displaced the matching surfaces so that contact between contiguous blocks occurs only locally. Because of frictional forces, these local points of contact behave as if they are welded, and they are idealized as circles in the analysis.

The model of the regularly jointed rock proposed by White (1983) employs the force-displacement relations between elastic spheres in contact developed by Hertz for normal forces and by Mindlin for tangential forces. It should be noted in passing that the radius of the sphere does not enter into these force-displacement expressions; only the radius of the contact surface appears.

RESULTS AND DISCUSSION

For simplicity we have chosen first to study an isotropic, orthogonally jointed rock mass with equal joint spacing along each coordinate axis and equal average contact diameter and number of contacts per unit area on each of the planes of discontinuity. The model predicts a dependence of compressional- (V_P) and shear-wave (V_S) velocities on a dimensionless parameter R, where $R = N \cdot D \cdot L$, as well as on the elastic properties of the intrinsic rock and the bulk density of the rock mass. In the expression for R, N represents the number of contacts per unit area on each plane of discontinuity, D represents the average diameter of these discontinuities, and L represents their spacing. Biot's (1956) theory for elastic-wave propagation in a saturated porous medium is used when the rock mass is water saturated. In this case, V_P is found to be a function also of the joint porosity and the saturant bulk modulus. V_S is found to remain essentially independent of the presence of the water saturant.

Figure 1 shows V_P and V_S (normalized to their values for the intrinsic rock) for the dry and water-saturated rock mass. For the saturated rock mass, V_P is a function of the fracture porosity ϕ, which ranges in this study from 0.001 to 0.01. The elastic constants of the solid rock were taken as elastic modulus $E = 80$ GPa and Poisson's ratio $\nu = 0.25$. It will be seen from this figure that, although V_S (sat) and V_S (dry) are approximately the same, there is a considerable increase in V_P upon saturation. This is particularly true at low values of R. The effect of changes in ϕ in the saturated rock is not as pronounced. As expected, the acoustic velocities converge asymptotically to those of the intrinsic rock at high values of R.

Figure 2 shows the ratio of V_P (sat) to V_P (dry) as a function of R for ϕ in the range 0.001–0.01. It is seen that the ratio increases rapidly as R decreases to values below 10. The ratio is relatively insensi-

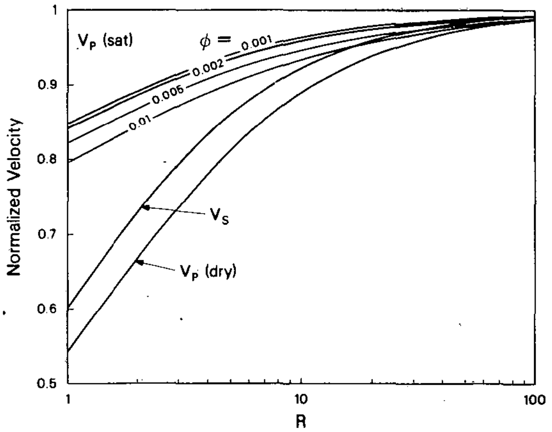

Figure 1. Normalized compressional- and shear-wave velocities in the dry and water-saturated rock mass as a function of the parameter *R* for different values of joint porosity. [XCG 8410-13388]

tive to changes in ϕ. Figure 3 shows the ratio V_P/V_S in the saturated and dry rock mass as a function of *R* for ϕ in the range 0.001–0.01. At high values of *R* the ratios for saturated and dry rock mass converge asymptotically to V_P/V_S. It is clear that for values of *R* less than 10 there are significant differences in the ratio V_P/V_S between the water-saturated and dry rock mass, with the ratio for the saturated rock mass being greater than that for the intrinsic rock and the ratio for the dry rock mass being less. Behavior of this type had been reported by Rezowalli et al. (1984) for a cross-hole acoustic survey in columnar-jointed basalt.

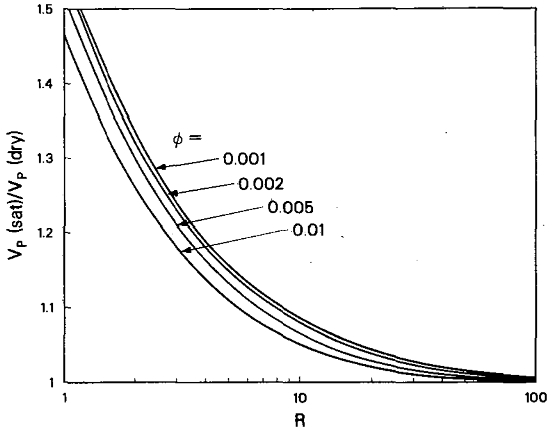

Figure 2. Ratio of compressional-wave velocity in the water-saturated rock mass to that in the dry rock mass as a function of the parameter *R* for different values of joint porosity. [XCG 8410-13389]

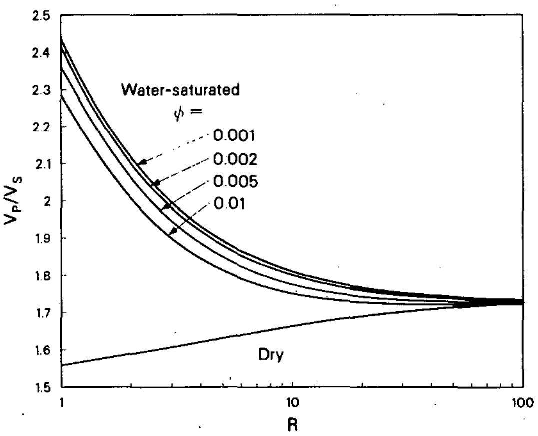

Figure 3. Ratio of compressional- to shear-wave velocity in the rock mass, dry and water saturated, as a function of the parameter *R* for different values of joint porosity. [XCG 8410-13390]

CONCLUSIONS

The results of this study provide insight into the mechanisms of elastic-wave propagation in a jointed rock mass and form the basis for the interpretation of velocity data obtained during seismic surveys in jointed rock masses. Extension of the theory to anisotropic rock masses with different values of the parameter *R* in each direction is expected to provide insight into the variation of body-wave velocities with direction of propagation, the three-dimensional coupling of body waves, and the resulting deviation of group and phase velocity directions and polarized shear-wave birefringence. Thus it will provide a basis for studying by seismic means the elastic properties of anisotropic, jointed rock masses.

REFERENCES

Biot, M.A., 1956. Theory of propagation of elastic waves in a fluid-saturated porous solid; I. Low frequency range. J. Acoust. Soc. Am., v. 28, p. 168–178.

Crampin, S., Chesnokov, E.M., and Hipkin, R.A., 1984. Seismic anisotropy—The state of the art. Geophys. J. Roy. Astron. Soc., v. 76, p. 1–16.

Rezowalli, J.J., King, M.S., and Myer, L.R., 1984. Cross-hole surveying in basalt. Int. J. Rock Mech. Min. Sci. Geomech. Abstr., v. 21, p. 213–216.

White, J.E., 1983. Underground Sound—Application of Seismic Waves. New York, Elsevier, p. 79–81.

Seismic Characteristics of an Interface in Imperfect Contact

G. Chen, S. Coen, N.G.W. Cook, and L.R. Myer

The strength and hydraulic conductivity of strong, impermeable rocks are significantly affected by discontinuities such as joints, fractures, and bedding planes. The opposite surfaces of such discontinuities are in imperfect contact with one another, so that the discontinuity contains a variety of flat, thin voids. Deformation across the discontinuity in response to normal or shear stresses produces a discontinuity in displacement between any two planes parallel to and on opposite sides of the discontinuity. The magnitude of this displacement discontinuity can be characterized by specific normal and shear stiffness. Seismic techniques provide a means of remotely detecting and characterizing discontinuities in rock. On the assumption that a discontinuity in seismic dislacement is proportional to the specific stiffness of a rock joint or fracture, a complete theory has been developed for the reflection and refraction of compressional waves and shear waves of both polarizations by a planar discontinuity. The resulting equations are found to be equivalent to those previously derived by Schoenberg (1980) for nonwelded boundaries between two media.

SPECIFIC STIFFNESS OF A THIN PLANAR DISCONTINUITY

Consider a nearly planar discontinuity in rock, the opposite surfaces of which are in contact over some areas and elsewhere are separated by a small aperture, so that the plane of contact contains voids of negligible thickness perpendicular to the plane of the discontinuity.

Assume that the rock containing this discontinuity is subjected to a normal stress, σ_z, applied both at infinity and inside the voids of the discontinuity. In this state of stress the rock is subjected to a homogeneous strain, and the displacements are everywhere the same as they would be in the absence of the discontinuity.

If the normal stress in the voids is reduced to zero, it can be shown that there is a volumetric displacement of the discontinuity surfaces toward each other. This deformation will manifest itself as a constant-displacement discontinuity between any pair of planes, each of which is on a different side of the discontinuity. If the average magnitude of the displacement discontinuity is Δ, then the instantaneous specific stiffness, K_n, of the discontinuity is defined as

$$\left[\frac{\partial\Delta}{\partial\sigma_z}\right]_\sigma = \frac{1}{K_n}. \tag{1}$$

A similar analysis can be made for a shear stress across a discontinuity to show that there exists a constant-shear displacement discontinuity, Σ, between any pair of planes on opposite sides of the discontinuity. Thus the instantaneous specific stiffness for a discontinuity in shear is given by

$$\left[\frac{\partial\Sigma}{\partial\tau}\right]_\tau = \frac{1}{K_s}. \tag{2}$$

REFLECTION AND REFRACTION OF PLANE WAVES AT AN INTERFACE

Consider two elastic half-spaces divided by an interface with obliquely incident, planar P-, SV-, and SH-waves (Fig. 1). The two elastic media are characterized by density ρ and elastic constants λ and μ. The opposite surfaces of the interface are in partial contact, so that the interface is characterized by specific stiffnesses K_x,K_y,K_z.

The reflection and transmission coefficient follow from solution of the elastodynamics equations for the following boundary conditions (at the interface):

$$K_x(U_x^I - U_x^{II}) = \tau_x^I, \tag{3}$$

$$K_y(U_y^I - U_y^{II}) = \tau_y^I, \tag{4}$$

$$K_z(U_z^I - U_z^{II}) = \tau_z^{II}, \tag{5}$$

$$\tau_x^I = \tau_x^{II}, \tag{6}$$

$$\tau_y^I = \tau_y^{II}, \tag{7}$$

$$\sigma_z^I = \sigma_z^{II}, \tag{8}$$

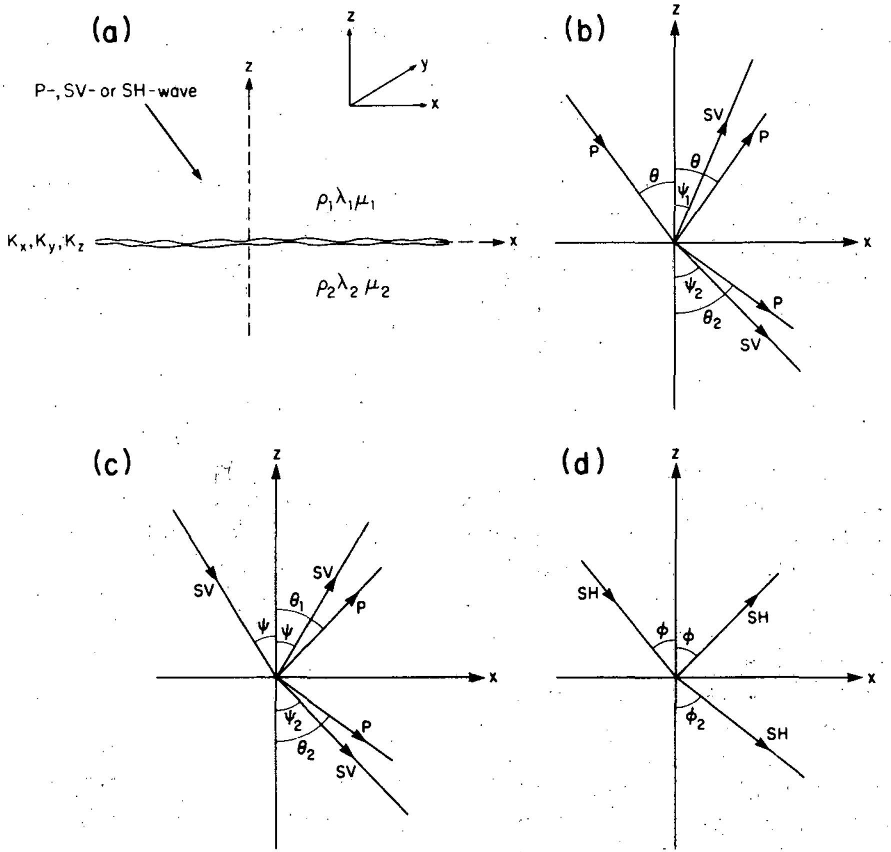

Figure 1. **(a)** Illustration of two elastic half-spaces separated by an interface with partially contacting surfaces. **(b)** to **(d)** Definition of angular relations between incident, reflected, and refracted waves. [XBL 8410-10,000]

where *I* and *II* refer to the media on either side of the interface. These boundary conditions specify continuity of stresses across the interface, but the displacements are discontinuous by an amount equal to the ratio of the imposed stress to the specific stiffness of the interface.

Values of the reflection coefficients, R_P, R_{SV}, R_{SH}, and transmission coefficients, T_P, T_{SV}, T_{SH}, are given by the following set of equations:

$$AX = b_1 \ (P\text{-wave incidence}), \tag{9}$$

$$AX = b_2 \ (SV\text{-wave incidence}), \tag{10}$$

$$BY = b_3 \ (SH\text{-wave incidence}), \tag{11}$$

where

$$A = \begin{bmatrix} -\sin\theta & -\cos\psi_1 & \sin\theta_2 + i\omega \dfrac{Z_{S2}^2}{K_x Z_{P2}} \sin 2\theta_2 & \cos\psi_2 + i\omega \dfrac{Z_{S2}}{K_x} \cos 2\psi_2 \\ \cos\theta & -\sin\psi_1 & \cos\theta_2 + i\omega \dfrac{Z_{P2}}{K_z} \cos 2\psi_2 & -\sin\psi_2 - i\omega \dfrac{Z_{S2}}{K_z} \sin 2\psi_2 \\ \sin 2\theta & \dfrac{Z_{P1}}{Z_{S1}} \cos 2\psi_1 & \dfrac{Z_{P1}}{Z_{P2}} \dfrac{Z_{S2}^2}{Z_{S1}^2} \sin 2\theta_2 & \dfrac{Z_{P1} Z_{S2}}{Z_{S1}^2} \cos 2\psi_2 \\ -\cos 2\psi_1 & \dfrac{Z_{S1}}{Z_{P1}} \sin 2\psi_1 & \dfrac{Z_{P2}}{Z_{P1}} \cos 2\psi_2 & -\dfrac{Z_{S2}}{Z_{P1}} \sin 2\psi_2 \end{bmatrix}$$

$$B = \begin{bmatrix} -1 & 1 + i\omega \dfrac{Z_{S2} \cos\phi_2}{K_y} \\ 1 & \dfrac{Z_{S2}\cos\phi_2}{Z_{S1}\cos\phi} \end{bmatrix}, \quad X = \begin{bmatrix} R_P \\ R_{SV} \\ T_P \\ T_{SV} \end{bmatrix}, \quad Y = \begin{bmatrix} R_{SH} \\ T_{SH} \end{bmatrix},$$

$$b_1 = \begin{bmatrix} \sin\theta \\ \cos\theta \\ \sin 2\theta \\ \cos 2\psi_1 \end{bmatrix}, \quad b_2 = \begin{bmatrix} \cos\psi \\ -\sin\psi \\ \dfrac{Z_{P1}}{Z_{S1}} \cos 2\psi \\ -\dfrac{Z_{S1}}{Z_{P1}} \sin 2\psi \end{bmatrix}, \quad b_3 = \begin{bmatrix} 1 \\ 1 \end{bmatrix}.$$

Angular relations are as defined in Fig. 1, and acoustic impedances, Z, are given by

$$Z_{P1} = \rho_1\alpha_1, \; Z_{P2} = \rho_2\alpha_2,$$

$$Z_{S1} = \rho_1\beta_1, \; Z_{S2} = \rho_2\beta_2,$$

where

$$\alpha_1 = \sqrt{\frac{\lambda_1 + 2\mu_1}{\rho_1}}, \; \alpha_2 = \sqrt{\frac{\lambda_2 + 2\mu_2}{\rho_2}},$$

$$\beta_1 = \sqrt{\frac{\mu_1}{\rho_1}}, \; \beta_2 = \sqrt{\frac{\mu_2}{\rho_2}}.$$

It should be noted that the equations satisfy the laws of conservation of energy, or "lossless" conditions, which, for the case of the same media on both sides of the interface, can be written as

$$|R|^2 + |T|^2 = 1, \tag{12}$$

where | | refers to the magnitude of the complex quantity R or T.

The effects of the magnitude of the specific stiffness of the interface on transmitted acoustic-wave characteristics are shown in Figs. 2 and 3. These figures plot the magnitude and phase of the transmission coefficients given by Eq. (9) for the case of normally incident P-waves and materials with the same acoustic impedance, Z, on either side of the interface. For very large values of K relative to Z, it is seen that the magnitude of the transmission coefficient approaches unity and the phase change approaches zero. Thus large values of K correspond to the "welded" boundary conditions normally assumed in seismologic analysis of multilayer systems. An infinite stiffness means that there is no discontinuity of displacements at the interface, so that if the materials on both sides of the interface are the same, energy is transmitted as if no interface were present at all.

At the other extreme, as K approaches zero, the magnitude of the transmission coefficient approaches zero and the phase shift approaches 90°. Thus very small values of K correspond to the case in which the two surfaces of the interface are nowhere in contact. For all values of K intermediate between the extremes, the magnitude and phase of the transmission coefficient are nonlinear functions of frequency, as shown in Figs. 2 and 3.

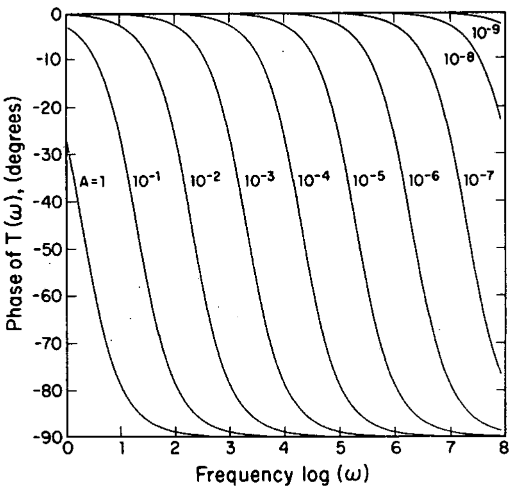

Figure 3. Phase of normally incident P-wave transmission coefficient as a function of frequency for a range in values of A, where A is as defined in Fig. 2. [XBL 8410-9995]

Figures 4 and 5 show the magnitude and phase of reflection and transmission coefficients for a P-wave incident at 60° to an interface. In this case it was assumed that the ratio $\alpha/\beta = 10/7$ and that $K_x = K_z = 1000Z_P$. The media on both sides of the interface have the same properties. Comparison with the previous figures shows the same nonlinear behavior of the magnitude and phase of T_P as a function of frequency. However, because of the oblique incidence of the P-wave, transmitted and reflected shear waves are produced that have magnitude and phase characteristics as shown in Figs. 4 and 5.

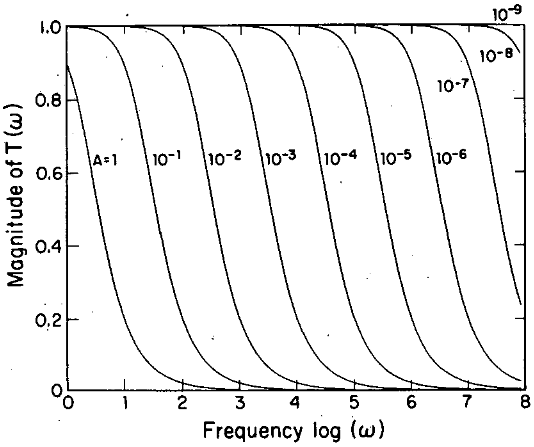

Figure 2. Magnitude of the normally incident P-wave transmission coefficient as a function of frequencies for a range in values of A, where $A = Z/K$, Z is acoustic impedance, and K is specific stiffness. [XBL 8410-9996]

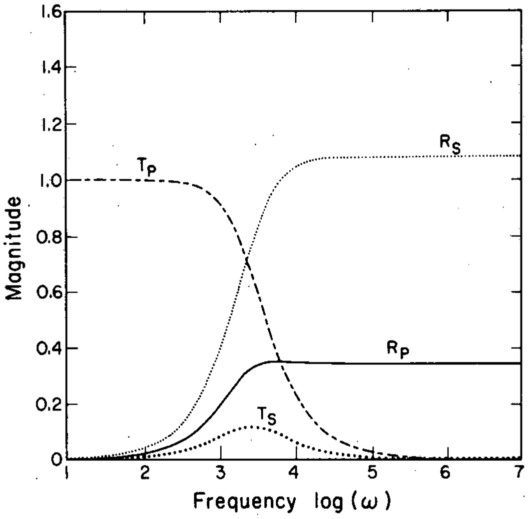

Figure 4. Magnitude of reflection and transmission coefficients for a P-wave incident at 60° to an interface. [XBL 8410-8855]

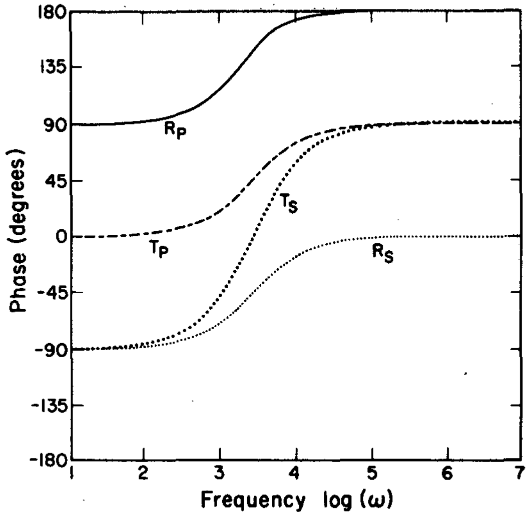

Figure 5. Phase of reflection and transmission coefficients for a *P*-wave incident at 60° to an interface. [XBL 8410-8856]

CONCLUSIONS

A new theory has been developed for the reflection and refraction of seismic waves at an interface whose opposite surfaces are in partial contact. The interface induces a displacement discontinuity of a magnitude proportional to the specific stiffness of the interface. Reflection and transmission coefficients have been found for the general case of obliquely incident planar compressional and shear waves and dissimilar materials on opposite sides of the interface. In general, both the magnitude and phase of these coefficients are nonlinear functions of frequency. For limitingly large values of specific stiffness, this theory is equivalent to the typical seismologic theory for welded boundaries between layers.

REFERENCE

Schoenberg, M., 1980. Elastic wave behavior across linear slip interfaces. J. Acoust. Soc. Am., v. 68, no. 5, p. 1516–1521.

Effects of Contact Area of an Interface on Acoustic-Wave Transmission Characteristics

L.R. Myer, D. Hopkins, and N.G.W. Cook

The detection and characterization of fractures is pertinent to a wide variety of areas of investigation in the geosciences. Particular interest is found in the areas of nuclear waste disposal and geothermal and petroleum reservoir engineering because of the need to analyze fluid flow through rock masses in which fracture flow dominates.

As a group, the seismic methods have proved to be notably applicable to fracture detection. It is known that a single fracture or rock joint will cause a loss of amplitude and a change in phase in a seismic wave incident upon it (Yu and Telford, 1973; Kleinberg et al., 1982; Medlin and Masse, 1984). However, there have been very few attempts to develop quantitative relationships between the physical properties of the fracture and the reflected and refracted waves. Palmer (1982) assumed that a fracture could be represented by two parallel surfaces separated by a thin film. Using the "thin film" approximation of Rayleigh (1945), Palmer was able to model reflections from an air-and-water-filled interface between two polished slabs of granite.

Natural joints and fractures in rock masses are typically in contact over some proportion of the joint surface. To model an interface in partial contact, Chen et al. (1984) proposed that the material properties of an interface can be characterized by a specific stiffness related to the geometry and area of contact of the two surfaces forming the interface. They used their knowledge of the specific stiffness to describe the reflection and refraction of plane waves at the interface.

To test the validity of this theory a set of laboratory experiments were performed in which the effects of the geometry and contact area of an interface on the properties of compressional and shear waves were investigated. The specific stiffness of the interface was evaluated, and the experimental results were compared with theoretical predictions.

EXPERIMENTAL PROCEDURE

An interface with surfaces in partial contact was modeled by placing thin strips of lead (0.03 m thick by 1.0 mm wide) in parallel between two cylinders of steel as shown in Fig. 1. Spacing between the strips was varied to study the effects on the transmitted wave of changing the contact area and specific stiffness of the interface. Very thin lead strips were used to assure that the thickness of the interface was much less than the wavelength of waves incident upon it.

Compressional- and shear-wave piezoelectric crystals with 1-MHz resonant frequency were mounted on the ends of the sample. A pulse generator supplied a short-duration, high-voltage pulse to the crystals on one end of the sample. The signal received by the crystals at the opposite end was digitized by a digital oscilloscope and stored on floppy disk.

RESULTS AND ANALYSIS

The influence of contact area of an interface on characteristics of the transmitted P-wave is illustrated in Fig. 2. In this figure the amplitude spectrum of a reference test with a solid lead disk at the interface is compared with tests in which the interface contained lead strips spaced 1 mm and 2 mm apart. As can be seen in the figure, the peak amplitude decreased by 35% for the 1-mm spacing (corresponding to a 50% reduction in contact area) and 50% for the 2-mm spacing (75% reduction in contact area). It should also be noted that the amplitude reduction was greater at higher frequencies.

The relationships between contact area and the magnitude and phase of the transmitted wave are given explicitly by the theory discussed by Chen et al. (1984). For example, the transmission coefficient (T_P) for an incident P-wave is given by

$$T_P = \frac{2(k/z)}{2(k/z) + i\omega}, \qquad (1)$$

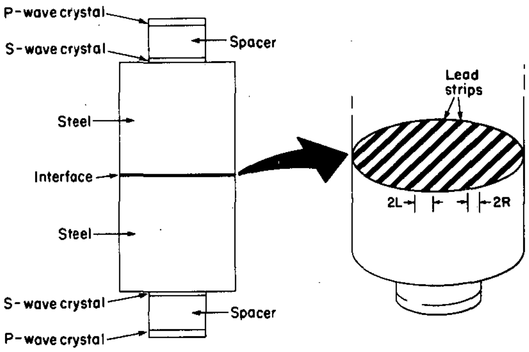

Figure 1. Illustration of experimental configuration. [XBL 8410-9987]

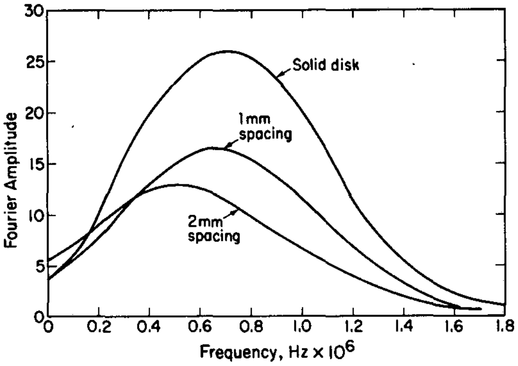

Figure 2. Influence of the contact area of an interface consisting of lead strips on P-wave amplitude spectrum. [XBL 8410-9994]

where $1/k$ is called the specific stiffness of the interface, z is the acoustic impedance of the half-space, and ω is the circular frequency. To verify the theory, predicted values of the magnitude and phase of the transmission coefficients were compared with experimental results.

The concept of specific stiffness of an interface follows from the argument that an interface will produce a discontinuity in the displacement field resulting from the imposed stresses. The magnitude of the displacement discontinuity is related to the imposed stresses by the specific stiffness of the interface. The specific stiffness is therefore equal to the slope of the curve of volumetric deformation of the interface versus imposed stress.

To calculate the specific stiffness of the interface consisting of lead strips, it was assumed that the spaces between the strips could be represented by a series of parallel, thin slits. The total volumetric deformation of the interface was then taken as the sum of the deformation of the slits plus the deformation of the strips. Using an approximation of Salamon (1965) for the deformation in the slits, the specific stiffness of an interface under normal stress was found to be

$$\frac{1}{k} = \left[\frac{-8(1-\nu^2)}{\pi E} \ln \cos \left(\frac{\pi R}{2L} \right) + \frac{Ld}{(L-R)E_\ell} \right], \qquad (2)$$

where E and ν are Young's modulus and Poisson's ratio for steel, $E\ell$ is Young's modulus for lead, d is the thickness of the lead strips, and R and L are as defined in Fig. 1.

Figure 3 is a comparison of the predicted magnitude of T_P, given by Eq. (1), with experimental

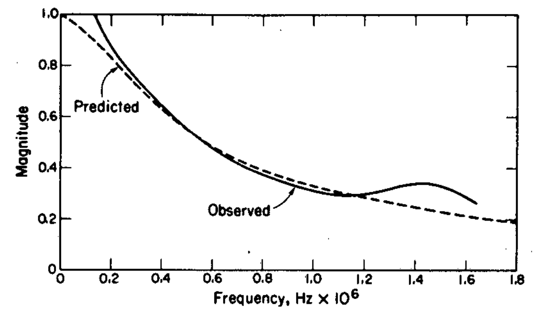

Figure 3. Comparison of observed and predicted magnitude of the P-wave transmission coefficient. [XBL 8411-4823]

results for the case of lead strips spaced 2 mm apart (R = 2.0 in Eq. 2). Note that a magnitude of unity on the ordinate axis means that all energy was transmitted, while a magnitude of zero means that all energy was reflected by the interface. Experimental results are in good agreement with predictions. As predicted, the experimentally observed values of T_P decrease nonlinearly with increasing frequency, meaning that the ratio of reflected to transmitted energy increases with frequency. Other tests verified that the effect of decreasing the spacing of the lead strips, and therefore increasing the specific stiffness, is to increase the amount of energy transmitted by the interface. Outside the frequency range of approximately 0.1–1.4 MHz, the experimental results are questionable because very little source energy was present at very low or very high frequencies.

Figure 4 is a comparison of the phase of T_P given by Eq. (1) and the phase shift induced by the interface for the case of lead strips placed 2 mm apart. As predicted, the experimental results show a shift in phase that is a nonlinear function of frequency. Theory also predicts that the phase of T_P should approach a constant value at high frequencies. The physical interpretation of this result is not clearly understood, though some experimental evidence, as shown in Fig. 4, supports the theoretical prediction.

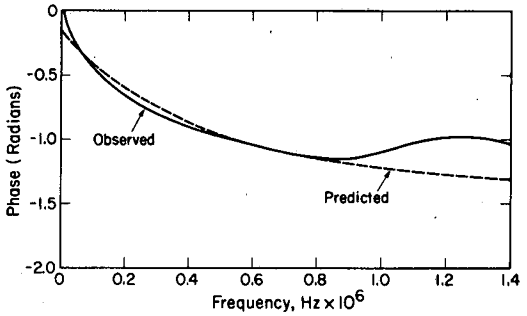

Figure 4. Comparison of observed and predicted phase of the P-wave transmission coefficient. [XBL 8410-9993]

CONCLUSIONS

Laboratory measurements were made of acoustic waves transmitted across an interface that was very thin relative to the wavelength of the incident energy. Results show that the amount of contact area between the surfaces of the interface significantly affects the amount of energy transmitted across the interface. As contact area decreases, the ratio of reflected to transmitted energy increases, with the largest increase being at high frequencies. The experimental results show further that the observed effects of the interface can be predicted by a theory that characterizes an interface by its specific stiffness.

REFERENCES

Chen, G., Coen, S., Cook, N.G.W., and Myer, L.R., 1984. Seismic characteristics of an interface in imperfect contact. *In* this Annual Report.

Kleinberg, R.L., Chow, E.Y., Plona, T.J., Orton, M., and Canady, W.J., 1982. Sensitivity and reliability of fracture detection techniques for borehole application. J. Petrol. Technol., v. 34, no. 4, p. 657–663.

Medlin, W.L., and Masse, L., 1984. Laboratory experiments in fracture propagation. Soc. Petrol. Eng. J., v. 24, no. 3, p. 256–268.

Palmer, S.P., 1982. Fracture detection in crystalline rock using ultrasonic reflection techniques. Lawrence Berkeley Laboratory Report LBL-16347, p. 170–288.

Rayleigh, J.W.S., 1945. The Theory of Sound (Vol. II). New York, Dover Publications, p. 86.

Salamon, M.D.G., 1965. Elastic analysis of displacements and stresses induced by mining of seam or reef deposits, Part IV. *In* Rock Mechanics and Strata Control in Mines. Johannesburg, South Africa, South African Institute of Mining and Metallurgy, p. 148-167.

Yu, T.R., and Telford, W.M., 1973. An ultrasonic system for fracture detection in rock faces. Can. Min. Metall. Bull., v. 66, no. 729, p. 96-101.

Strength, Elastic Moduli, and Nonlinear Deformation of a Cracked Elastic Solid

J. Kemeny and N.G.W. Cook

Using the principles of linear elastic fracture mechanics (LEFM), we calculate the effective elastic moduli, and the strength and stability, of an isotropic elastic solid containing a random distribution of interacting cracks. The relevance of random distributions of interacting cracks to the strength and stability of rocks has been shown by Hallbauer et al. (1973). In order to account for the effects of interacting cracks, we introduce the "anticrack" model as a high-crack-density complement to the noninteracting-crack models of Walsh (1965) and others. The behavior of rock may be seen as progressing from the noninteracting crack models to the anticrack model as cracks extend, interact, and coalesce. The anticrack model is based on the exact analytic solution for two half-spaces connected through a small region referred to as the anticrack. In two dimensions we utilize the analytic expression for the double-edged cracked specimen solved by Bowie (1964), and in three dimensions we utilize the analytic solution for the external circular crack solved by Kassir and Sih (1968). The anticrack models developed from these solutions represent rock structures containing random distributions of interacting microcracks, as well as rock structures containing large, nearly planar discontinuities whose surfaces are separated from one another except at discrete points of contact, such as in jointed or blocky rock.

In rock mechanics, it is more common to encounter displacement-controlled boundary conditions or mixtures of displacement-controlled and load-controlled boundary conditions rather than the pure load-controlled boundary conditions found in other branches of engineering. For this reason, we calculate stress-intensity factors for the anticrack model under displacement-controlled boundary conditions. We also introduce the Griffith locus (Berry, 1960) for the anticrack model, which can determine the onset of fracture and the manner in which fractures extend, under any combination of displacement-controlled and load-controlled boundary conditions.

We consider two general cases of applied loading or displacement that result in crack extension. In the first case, we assume that all cracks will begin to propagate at the same time. We assume that crack extension for this case will occur in the plane of each of the cracks when $K_I \geqslant K_{IC}$, where K_I is the mode I stress-intensity factor and K_{IC} is the fracture toughness for the solid. In the second case, we assume that only cracks with preferred orientations will start to propagate first. For the case in which a single crack begins to propagate first, the preferred orientation is with the crack perpendicular to the maximum principal tensional stress or displacement. We assume that crack extensions for this case will again occur in the plane of the fracture when $K_I \geqslant K_{IC}$.

STRESS-INTENSITY FACTORS UNDER DISPLACEMENT-CONTROLLED BOUNDARY CONDITIONS

To calculate stress-intensity factors for the anticrack model under displacement-controlled boundary conditions, we replace the uniaxial stress σ by $\epsilon\bar{E}$ in the formulas for the stress-intensity factors under load control, where the uniaxial strain ϵ is a constant, and where $\bar{E}$ is the effective Young's modulus for a solid containing a random distribution of anticracks. For the case in which all cracks extend at the same time, we get the following stress-intensity factors under displacement-controlled conditions:

$$K_I = E\epsilon \frac{\sqrt{\pi c}}{1 + \pi \frac{Nc^2}{V}(1 - \nu^2)}, \tag{1}$$

$$K_I = 2E\epsilon \frac{\sqrt{c}}{\sqrt{\pi m}\left[1 + \frac{8Nc^2}{\pi V}\ln(1 + \frac{1}{m})(1 - \nu^2)\right]}, \tag{2}$$

$$K_I = 2E\epsilon \frac{\sqrt{\pi c}}{\pi\left[1 + \frac{16Nc^3}{45V}(1 - \nu^2)\frac{10 - 3\nu}{2 - \nu}\right]}, \tag{3}$$

$$K_I = E\epsilon \frac{\sqrt{c}}{2\sqrt{\pi}m^{3/2}\left[1 + \frac{\pi^2}{15}\,\frac{Nc^3}{V}\,(1 - \nu^2)\,\frac{5 - 4\nu}{m(m + 1)}\right]} \tag{4}$$

for the two-dimensional noninteracting-crack model, two-dimensional anticrack model, three-dimensional noninteracting-crack model, and three-dimensional anticrack model, respectively. Here c is the average crack length, m is the ratio of the average anticrack length to average crack length (relative contact area), N/V is the number of cracks per unit volume, and E and ν represent the intrinsic Young's modulus and Poisson's ratio of the solid with no cracks. Plots of Eqs. (1) and (2) are presented in Figs. 1 and 2, respectively, for various values of N/V. The curve for $N/V = 0$ is the same as the curve for controlled-stress boundary conditions. Crack extension begins at $K_I = K_{IC}$, with stable crack extension occurring for $dK_I/dc < 0$ for the noninteracting-crack model and $dK_I/dm > 0$ for the anticrack model; unstable crack extension occurs when the reverse is true. The results in Figs. 1 and 2 indicate that for the noninteracting-crack model, stable crack propagation can occur under displacement-controlled conditions; for the anticrack model, however, unstable crack propagation occurs for all boundary conditions at all values of K_{IC}.

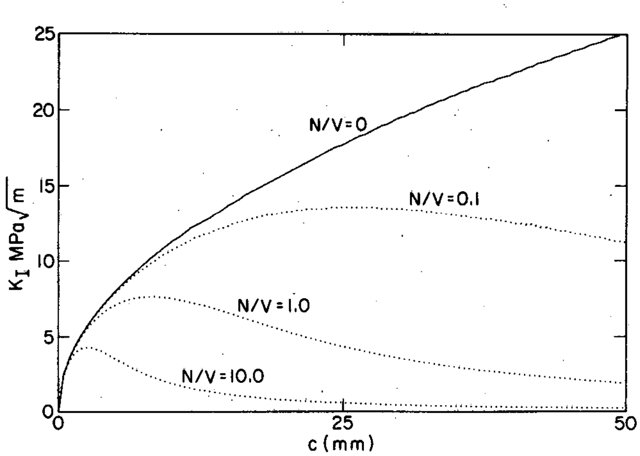

Figure 1. Mode I crack-tip stress-intensity factor for the two-dimensional noninteracting-crack model. [XBL 8410-9997]

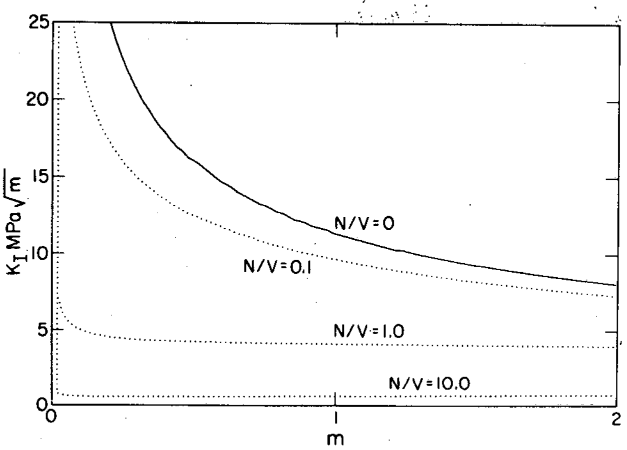

Figure 2. Mode I crack-tip stress-intensity factor for the two-dimensional anticrack model. [XBL 8410-9998]

GRIFFITH LOCI FOR NONINTERACTING-CRACK AND ANTICRACK MODELS

The effective elastic coefficients define, in stress-strain space, lines having various slopes, corresponding to equilibrium elastic deformations for a solid containing various densities of cracks and anticracks. If no cracks or anticracks are present in the solid, then the slope of the line in uniaxial stress-uniaxial strain space is $1/E$. Otherwise the slope corresponds to the reciprocal of the effective Young's modulus. On each of the lines that correspond to a given density of cracks or anticracks, there exists a particular value along the line where crack extension will start to occur, depending on the stress-intensity factors for the particular geometry of cracks and the fracture toughness for the material. The locus of these fracture-initiation points is the Griffith locus. For the case in which all cracks extend at the same time, we get the following Griffith loci:

$$\epsilon = \frac{\sigma_c}{E}\left[1 + \frac{NK_{IC}^4}{V\sigma_c^4\,\pi}\right], \tag{5}$$

$$\epsilon = \frac{\sigma_c}{E}\left[1 + \frac{N8c^2}{V\pi}\ln\left(\frac{\pi K_{IC}^2}{4c\sigma_c^2} + 1\right)\right], \tag{6}$$

$$\epsilon = \frac{\sigma_c}{E}\left[1 + \frac{NK_{IC}^6\,\pi^3\,(10 - 3\nu)}{180V\sigma_c^6\,(2 - \nu)}\right], \tag{7}$$

$$\epsilon = \frac{\sigma_c}{E}\left[1 + \frac{\pi^{7/3}\,Nc^{8/3}\,K_{IC}^{2/3}\,2^{2/3}}{15V\sigma_c^{2/3}}\right] \tag{8}$$

for the two-dimensional noninteracting crack-model, two-dimensional anticrack model, three-dimensional noninteracting crack-model, and the three-dimensional anticrack model, respectively. Here ϵ and σ_c represent the critical strain and stress when crack extension occurs.

The results of Eqs. (5) and (6) are presented in Fig. 3 for various values of *N/V*. Figure 3 shows that as the number of cracks per unit volume, *N/V*, approaches zero, the Griffith loci for both the noninteracting-crack and anticrack models approach the intrinsic elastic moduli, as expected. For larger densities of cracks or anticracks, the noninteracting-crack and anticrack models take on quite different but characteristic shapes. The difference in shape reflects the effect of crack interaction on material behavior.

For the noninteracting-crack model, the Griffith locus is in the form of a rotated hyperbola, with one arm of the hyperbola approaching the intrinsic elastic modulus as the implicit crack length approaches zero and the other arm of the hyperbola approaching zero as the implicit crack length approaches infinity. As a material containing a given density of cracks is loaded, it will follow a stress-strain path given by the effective modulus for that density of cracks until it intersects the Griffith locus, at which point fracture initiation will occur. A solid with a low density of cracks will intersect the Griffith locus on the upper arm of the hyperbola, and a solid with a high density of cracks will intersect the Griffith locus on the lower arm of the hyperbola. Intersection of the Griffith locus anywhere above the point of vertical tangency of the hyperbola will result in initially unstable crack propagation for any boundary conditions, while intersection of the Griffith locus below the point of vertical tangency will result in stable crack propagation for displacement-controlled boundary conditions and some intermediate boundary conditions. An initially unstable fracture propagation may become conditionally stable if, under the proper boundary conditions, the stress-strain path during fracture passes back through the Griffith locus into the stable zone.

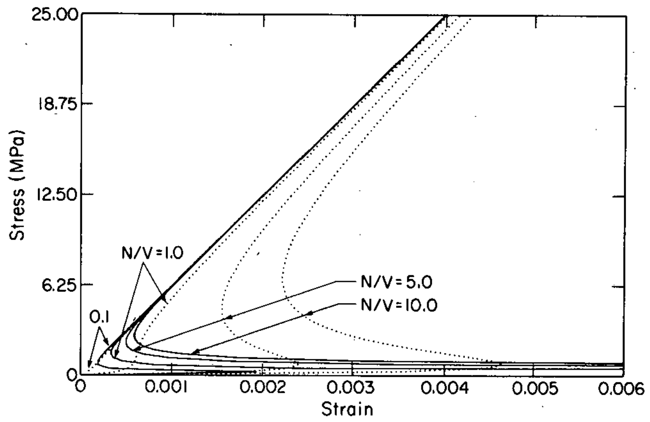

Figure 3. Griffith loci for the two-dimensional noninteracting-crack and anticrack models (anticrack results dotted). [XBL-8410-9999]

The Griffith locus for the anticrack model in two dimensions has a shape similar to that of the Walsh model at high stresses, but at low stresses there is a second point of vertical tangency, and the anticrack locus diverges from the Walsh model after that point. Thus it can be seen that for the anticrack model, unstable fracture propagation will occur under all boundary conditions for a large enough density of anticracks. As a useful model of rock, we consider that a solid with cracks initially follows the Griffith locus given by the Walsh model, and as interaction effects start to dominate, the behavior of the solid switches to the Griffith locus given by the anticrack model. Then it can be seen that in two dimensions, crack interaction causes an initial reduction of stability (slope magnitude change), which is followed by unconditional instability (slope sign change) at a high enough crack density.

REFERENCES

Berry, J.P., 1960. Some kinetic considerations of the Griffith criterion for fracture. I. Equations of motion at constant force. J. Mech. Phys. Solids, v. 8, p. 194–206.

Bowie, O.L., 1964. Rectangular tensile sheets with symmetric edge cracks. J. Appl. Mech., v. 31., p. 208–212.

Hallbauer, D.K., Wagner, H., and Cook, N.G.W., 1973. Some observations concerning the microscopic and mechanical behavior of quartzite specimens in stiff, triaxial compression tests. Int. J. Rock Mech. Min. Sci., v. 10, p. 713–726.

Kassir, M.K., and Sih, G.C., 1968. External elliptical crack in elastic solid. Int. J. Fract. Mech., v. 4, p. 347–356.

Walsh, J.B., 1965. The effect of cracks on the uniaxial elastic compression of rocks. J. Geophys. Res., v. 70, p. 399–411.

Modeling of Rock Mass Deformations Using "Inverse" Techniques

J.P. Tinucci, R.E. Goodman, and G.-H. Shi

Determining the predominant kinematic mode of deformation of a rock mass is the key to assessing stability of underground openings or cut-slope excavations. Simple modes of slope failure, e.g., backward rotation, wedge sliding, or toppling, produce distinctive signals in the displacement field. But more complex modes of failure produce complicated displacement patterns. Thus analysis techniques tend to make limited use of field data on absolute or relative displacements of rocks undergoing deformation. A numerical "inverse" technique has now been developed that solves the set of displacement data, together with input data on the discontinuity system, to untangle the modes of deformation that have affected a discontinuous rock mass. The purposes of using this technique are threefold:

1. To evaluate the modes of deformation that a rock mass has undergone.
2. To determine the magnitude of each individual mode contributing to the total amount of deformation.
3. To predict future localities or zones of potential critical deformation.

The typical rock mass displays so many discontinuities that it can be considered essentially as a collection of separate blocks tightly fitted into a three-dimensional mosaic. The geometry of these blocks can be fairly accurately estimated in two dimensions and extrapolated or simulated into three dimensions. By using the principles of block theory (Goodman and Shi, 1984), not all of the discontinuities forming blocks need to be analyzed. Only certain discontinuities will intersect the excavation in such a way as to produce removable blocks. Of these removable blocks, the first ones to undergo displacements may initiate complete or partial instability of other blocks, unless, of course, they are bolted or supported before they move.

A theorem has been developed (Goodman and Shi, 1982) that allows a search of the list of all possible block types for those that are potentially most critical. Figure 1 shows the five types of blocks that must be searched for: (V) infinite, (IV) tapered, (III) removable but not unstable, (II) removable but stable under side friction, and (I) removable even with frictional resistance. It is the type I blocks that are most likely to move and, as a consequence, invite other blocks to move. The example in Fig. 2 best illustrates this sequential movement. If the key blocks are removed, the number 2 blocks may become unstable. Their displacement would create space for block number 3 to move, and so on.

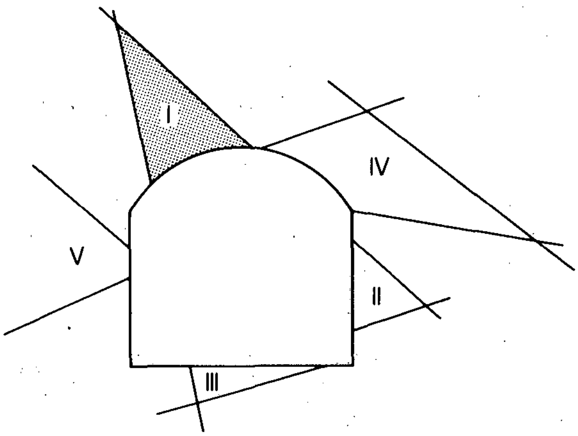

Figure 1. The five types of blocks: (V) infinite, (IV) tapered, (III) removable but stable without friction, (II) removable but stable with friction, and (I) unstable even with friction. [XBL 847-9844]

DISCONTINUOUS DEFORMATION ANALYSIS

To evaluate the modes of deformation that a rock mass has undergone, the discontinuous defor-

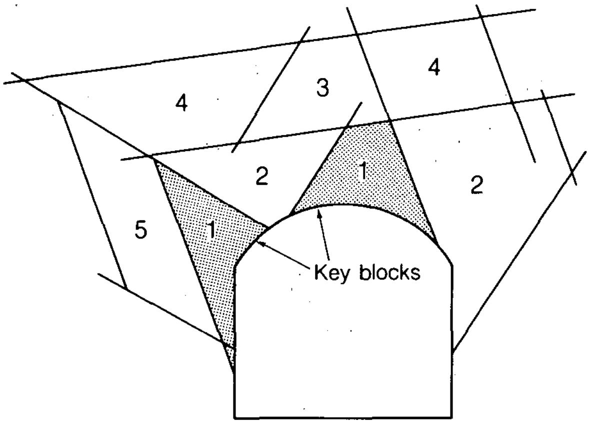

Figure 2. Tunnel with potentially unstable roof blocks. Numbers give order in which blocks may collapse. Note that higher-numbered blocks are unstable only after lower-numbered blocks move. [XBL 847-3589]

mation analysis was developed. From a given geometric description of the discontinuities, the boundaries of each block can be calculated. Also required are the initial coordinates of three gauge points (in two dimensions) per block. Displacement data consist of the magnitude and direction of movement of each gauge point.

For certain simple geometries, the modes of deformation are usually straightforward. However, as seen in Fig. 3, the same geometry may be capable of generating two distinctly different modes of deformation. As shown, either parallel sliding or rotational toppling could occur. An individual block can undergo rigid body translations and rotations as well as nonrigid, body-extensional strains (Shi and Goodman, 1984a). These then sum together to become the "calculated" displacements. A least-squares formulation is used to obtain the best fit by minimizing the sum of the squared deviation between displacements within each block and the squared deviation between two different blocks.

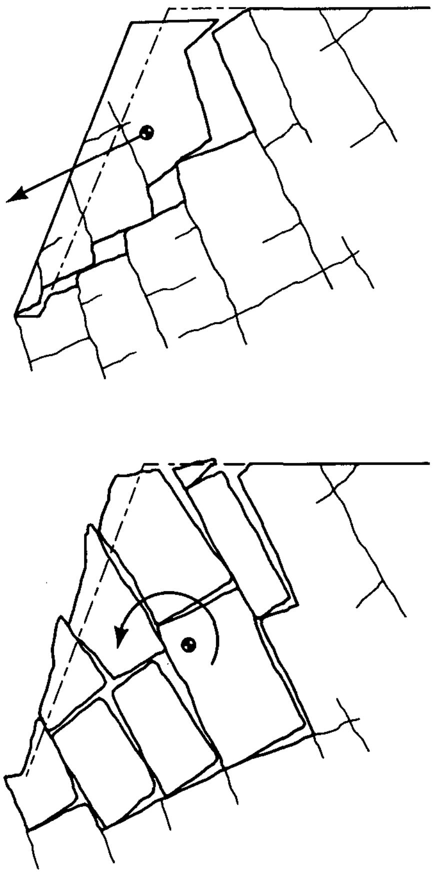

Figure 3. Example of block slope with same geometry undergoing potentially two distinctly different modes of deformation. **(Top)** Parallel sliding. **(Bottom)** Rotational toppling. [XBL 8412-6185]

The least-squares objective function is subject to the constraints that block edges and corners cannot overlap (Shi and Goodman, 1984b). The system of equations is arranged in linear matrix form and then solved simultaneously using a selective equation solver. The technique used in the solver is iterative in the sense that only selective constraint equations are used for each iteration. The constraint equations depend on whether certain blocks overlap the edges of other blocks. An on-off type punishment factor is applied, and the system is solved. The procedure is repeated by checking for violated constraints and then reapplying the punishment factor to the constraint equations. The solution converges faster and more efficiently than with conventional finite-element solvers.

The technique has been extended to higher-order strains and displacements to account for bending behavior observed in longer, more slender blocks. The modification accounts for nonconstant strains and the bending radius of curvature due to the application of bending moments.

APPLICATION AND DISCUSSION

Since the method is purely analytical in origin, many cases have been run on the computer to validate the accuracy of the results. Figure 4 shows a system of blocks that were fit to displacements. In this particular case, random displacements were used as input, and the aperture between blocks was set to zero. This is an extremely effective technique for testing the model, since any magnitude or direction of displacement will cause blocks to overlap unless selective constraint equations are set.

Results from an experiment with a base friction machine were compared using the deformation analysis. The base friction machine allows an experiment to be easily controlled and displacements to be accurately measured. Figure 5 shows a remarkably accurate fit between measured and calculated displacements.

Having determined the deformational components implied in a set of displacement readings, it is then possible to introduce rock properties and to pursue an analysis of stress distributions, permeabilities, or other system properties of the discontinuous rock mass. The reverse is also possible: to introduce measured boundary conditions (such as stress) and then evaluate rock mass properties.

The limitation of the deformation analysis lies in the number of measurement points required; that is, three nonlinear gauge points per block in two dimensions and four nonplanar points in three dimensions. This restriction can be overcome in the following

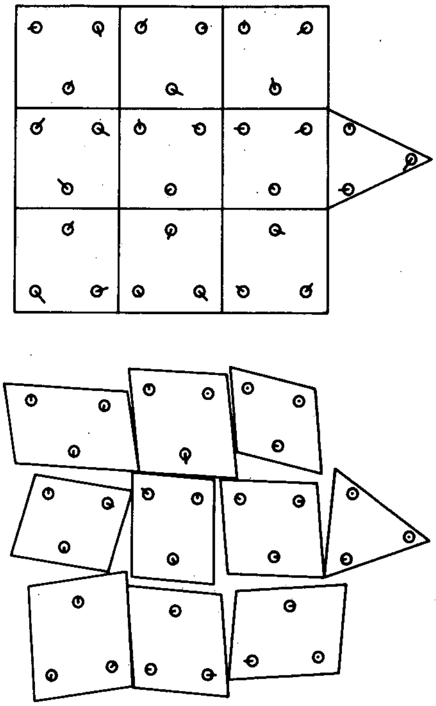

Figure 4. Example of discontinuous deformation analysis. (**Top**) Input: Blocks and randomly input directional displacements (symbols indicate direction and magnitude of displacement). (**Bottom**) Output: Deformed shapes of blocks (symbols indicate direction and magnitude of residual displacements—i.e., those displacements remaining after least-squares "best fit"). [XBL 8412-6187]

two ways. One technique is to restrict the "far-field" blocks to have nonopening discontinuities; the blocks can slide but not open, thus eliminating the need for a minimum number of gauge points in these blocks. The other technique would be to use statistical or numerical interpolation so as to estimate the displacements for a proper number of gauge points per block.

Both the work on block theory and that on discontinuous deformation analysis outlined here are in the early stages of development. Further studies will include statistical simulation to predict future localities or zones of potential deformation given the knowledge of existing deformations.

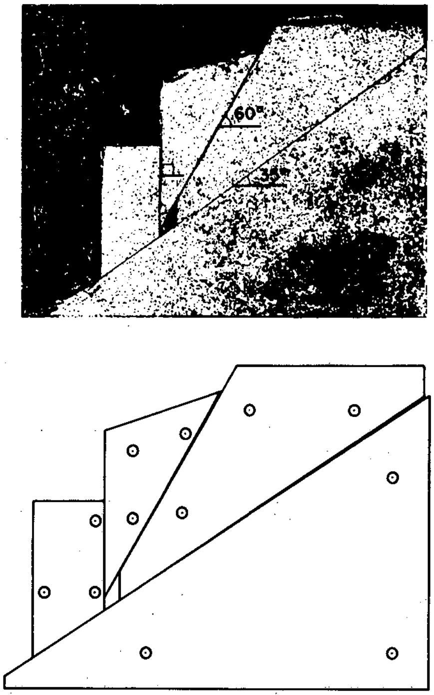

Figure 5. Deformation of blocks in experiment with base friction machine. (**Top**) Photo of blocks after deformation. (**Bottom**) Computer graphics output of "best-fit" deformed shapes of blocks. [XBL 8412-6186]

REFERENCES

Goodman, R.E., and Shi, G.-H., 1984. Block Theory and its Application to Rock Engineering. Englewood Cliffs, New Jersey, Prentice-Hall, Inc., p. 56–97.

Goodman, R.E., and Shi, G.-H., 1982. Geology and rock slope stability—Application of the "Key block" concept for rock slopes. *In* Proceedings, 3rd International Conference on Stability in Surface Mining, Vancouver, B.C., Canada, June 1–3, 1981. Am. Inst. Min. Metal. Petrol. Eng., p. 347–374.

Shi, G.-H., and Goodman, R.E., 1984a. Discontinuous deformation analysis. *In* Proceedings 25th U.S. Symposium on Rock Mechanics, Evanston, Illinois, June 24–27. Society of Mining Engineers of AIME, p. 269–277.

Shi, G.-H., and Goodman, R.E., 1984b. Two dimensional deformation analysis. Num. Methods Geomech., in press.

RESERVOIR ENGINEERING AND HYDROGEOLOGY

The research effort of the Reservoir Engineering and Hydrogeology group is concerned primarily with the movement of mass and energy through rocks. One commonly finds that rock masses are fractured or faulted, and thus it is necessary to analyze the flow phenomena within both the fractures and the matrix. More recently, it has become clear that we must also address the problems of the complex coupling between aspects of the thermal, hydraulic, mechanical, and geochemical behavior of rocks.

The topics that are summarized in this section present the results of research in a number of related areas within the broad fields of reservoir engineering and hydrogeology. Flow has been investigated in fractured, porous media; in single fractures; and in networks of fractures under isothermal and nonisothermal conditions. Systems that are saturated/unsaturated and that involve the complexities of multiphase, multicomponent flows must be considered to enable a realistic handling of practical field situations.

A significant amount of this work is concerned with theoretical studies, but the group also performs field studies that are often used to demonstrate the applicability of the theoretical results. The coupling of field and theoretical studies has revealed the importance of expanding the overall research program to include certain laboratory investigations, such as the measurement of two-phase flow in permeable rocks.

The Effect of Tortuosity on Fluid Flow Through a Single Fracture

Y.W. Tsang and P.A. Witherspoon

Mathematical modeling of flow through a fractured medium invariably requires the assumption of a physical law that governs the fluid movement through a single fracture. Almost without exception, these models assume that each fracture can be represented by smooth, parallel plates separated by a uniform distance (Wang et al., 1983). However, an actual fracture in a real rock mass has rough-walled surfaces, and contrary to the case of parallel plates, portions of a real fracture under stress may be closed while the rest of the fracture remains open. It is not clear whether a physical law that governs the fluid flow through a pair of smooth, parallel plates would be valid for flow through realistic, rough-walled fractures.

Over the past few years, we (Tsang and Witherspoon, 1981, 1983) and other workers (Gangi, 1978; Neuzil and Tracy, 1981; Walsh, 1981) have studied the effect of aperture variation on the movement of fluid through a rock fracture. However, all of those studies neglected the tortuosity of the flow paths. That is, if the rough fracture is represented mathematically by an aperture density distribution, *n(b)*, where *n(b)db* gives the probability of finding apertures with values between *b* and *(b + db)*, the effect of roughness had been incorporated into the fluid flow via the equation

$$\frac{Q}{\Delta h} = C \int_0^\infty b^3 n(b) db = C\langle b^3 \rangle, \qquad (1)$$

where the proportionality constant, *C*, contains information on the dimensions and fluid properties of the flow field. Eq. (1) corresponds to a physical situation in which the openings of the fracture vary only in the direction normal to the externally imposed hydraulic head, resulting in fluid movement along parallel flow paths involving no tortuosity. In a real rock fracture, the variation of *b* is expected to be both normal and parallel to the hydraulic head.

METHOD OF CALCULATION

To analyze quantitatively the effect of tortuosity and connectivity of flow paths on the fluid flow rate, we modeled the variation of fracture apertures by electrical resistances. The method of electrical analogs is an established technique for studying groundwater movement (e.g., Luthin, 1953; Fatt, 1956; Bouwer and Little, 1959; Parsons, 1966). The governing equations for fluid flow and electrical current are identical, giving rise to one-to-one correspondence between (1) the fluid flow rate, *Q*, and the electric current, *i*; (2) the hydraulic head, *h*, and the electrical potential, *V*; and (3) the hydraulic conductivity and the electrical conductivity. The variation of apertures *b* in the rough fracture is modeled by electrical resistors with different resistance values placed on a two-dimensional grid, as shown in Fig. 1a. The resistances take on values of $1/b^3$, with the *b*'s obeying the aperture distribution *n(b)* of the fracture. The electrical analog of the flow situation described by Eq. (1), where tortuosity is absent and fluid movement is along flow paths parallel to the hydraulic head, is a set of resistors connected in parallel, as shown in Fig. 1b. The current through such a set of resistors in parallel is uniquely determined by the given *n(b)*. On the other hand, when the same set of resistors is placed in a two-dimensional grid, as shown in Fig. 1a, the current will vary with different spatial realizations. The spread in the current values with respect to the different spatial realization of resistances, and the discrepancy between these values and the current value through the same set of resistors all connected in parallel, is then a measure of the effect of tortuosity on the flow rate.

Of the aperture distributions used for this study, some were derived from measurements, and others were hypothetical analytical functions. Figure 2 shows an aperture distribution based on fracture surface roughness measurements (S. Gentier, personal communication, 1983). Aperture distributions for

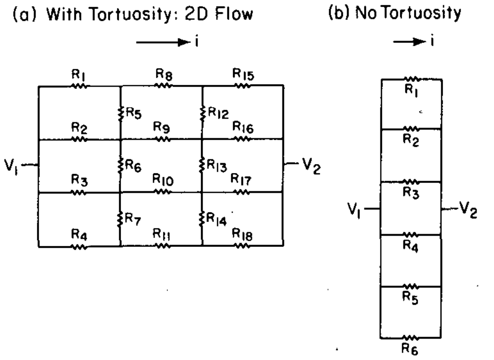

Figure 1. Electrical circuit equivalent of two-dimensional fluid flow **(a)** when tortuosity is present and **(b)** when tortuosity is absent. [XBL 841-9558]

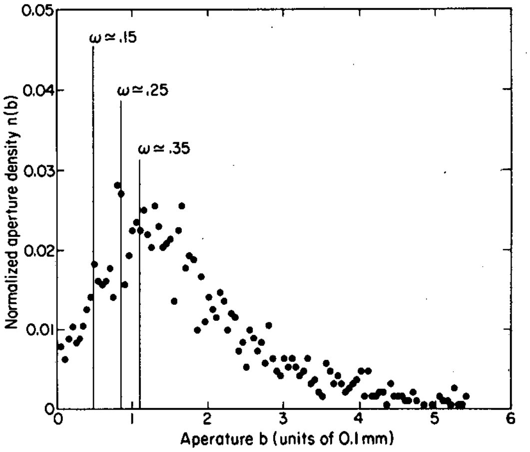

Figure 2. Aperture density distribution *n(b)* derived from 10 sets of surface roughness profiles of a granite fracture. [XBL 841-9556]

different amounts of fracture closure as a result of applied stress may be obtained from the distribution at zero stress by truncation (Tsang, 1984). Indicated in Fig. 2 are the truncations that correspond to fractional contact areas, ω, of 15, 25, and 35% as a result of increasing fracture closure.

RESULTS AND CONCLUSION

Figure 3 displays the calculated results. The horizontal axis is for *N*, the number of resistors used to represent the given *n(b)*. The points on the three lower curves denote average current *i*, and the vertical bars denote one standard deviation *δ*. The points on the upper three curves are the calculated currents through a set of resistors connected all in parallel, the electrical analog of fluid flow in the absence of tortuosity. We note that the average current through a two-dimensional grid of resistors is about one order of magnitude smaller than the current through the same set of resistors connected in parallel when the *n(b)* used corresponds to a fractional contact area of 15%. The reduction of the average current through the two-dimensional grid increases with increasing fracture contact area, giving rise to discrepancies of about two orders of magnitude when the fractional contact area is 35%.

Current calculations are carried out for different analytical forms of aperture distribution. Our results show that the effect of path tortuosity in depressing the fluid flow rate through a rough fracture varies with the roughness characteristics of the fracture. The more small apertures there are in the aperture distribution, the larger is the effect of tortuosity. When the fraction of contact areas between the fracture surfaces exceeds 30%, the aperture distributions are invariably large at small apertures, regardless of the original shape of the aperture distribution. Thus the effect of tortuosity is to depress the fluid flow rate by two or more orders of magnitude. The conclusion that tortuosity depresses fluid flow in a single fracture may appear to be intuitively obvious, yet its impact on the results of numerical modeling in the field of fracture hydrology is nontrivial. Parallel-plate idealization of each rock fracture, the standard assumption in the state-of-the-art numerical modeling of permeability for a fractured medium (Wang et al., 1983), implies that neither fracture roughness nor flow tortuosity affects the movement of fluids. The results of this study suggest that flow rates may have to be corrected by several orders of magnitude because of roughness and tortuosity.

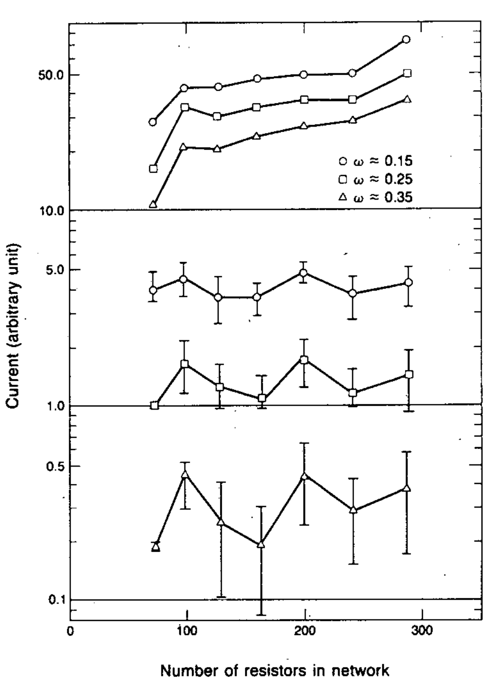

Figure 3. Calculated currents through resistances whose values are governed by the aperture density distributions in Fig. 2. [XBL 8312-7405]

REFERENCES

Bouwer, H., and Little, W.C., 1959. A unifying numerical solution for two-dimensional steady flow problems in porous media with an electrical resistance network. Soil Sci. Soc. Am., Proc., v. 23, p. 91–96.

Fatt, I., 1956. The network model of porous media, II and III. Trans. AIME, v. 207, p. 160–181.

Gangi, A.F., 1978. Variation of whole and fractured porous rock permeability with confining pressure. Int. J. Rock Mech. Min. Sci. Geomech. Abstr., v. 15, p. 249–257.

Luthin, J.N., 1953. An electrical resistance network for solving drainage problems. Soil Sci., v. 75, p. 259–274.

Neuzil, C.E., and Tracy, J.V., 1981. Flow through fractures. Water Resour. Res., v. 17, p. 91–199.

Parsons, R.W., 1966. Permeability of idealized fractured rock. Soc. Petrol. Eng. J., v. 10, p. 126–136.

Tsang, Y.W., and Witherspoon, P.A., 1981. Hydromechanical behavior of a deformable rock fracture subject to normal stress. J. Geophys. Res., v. 86, no. B10, p. 9287–9298.

Tsang, Y.W., and Witherspoon, P.A., 1983. The dependence of fracture mechanical and fluid properties on fracture roughness and sample size. J. Geophys. Res., v. 88 no. B3, p. 2359–2366.

Tsang, Y.W., 1984. The effect of tortuosity on fluid flow through a single fracture. Water Resour. Res., v. 20, p. 1209–1215.

Walsh, J.B., 1981. Effect of pore pressure and confining pressure on fracture permeability. Int. J. Rock Mech. Min. Sci. Geomech. Abstr., v. 18, p. 429–435.

Wang, J.S.Y., Tsang, C.F., and Sterbentz, R.A., 1983. The state of the art of numerical modeling of thermohydrologic flow in fractured rock masses. Environ. Geol., v. 4, p. 133–199.

The Relationship of the Degree of Interconnection to Permeability in Fracture Networks

J.C.S. Long and P.A. Witherspoon

Two of the major goals in fracture hydrology are to determine the permeability of fracture networks and to establish whether those networks behave like porous media. Since fractures are finite, there are three reasons why the network permeability will be smaller than the permeability of extensive fractures. First, some of the fractures may be isolated from the conducting network. Second, a fracture may be a dead end because it is connected to a network only at one end and therefore does not contribute to the permeability of the network. Third, if in fact the fracture does conduct fluid, the contribution of this fracture to the network permeability depends on how it is connected to the rest of the system. Thus the decrease in permeability is due to the degree of interconnection and the degree of heterogeneity of aperture. This paper will examine only the effect of degree of interconnection on the magnitude and nature of permeability. The effect of heterogeneity is currently a topic of research.

In order to study only the effect of interconnection, we have examined two-dimensional networks of fractures in which all fractures have the same aperture and length. Since aperture variation has not been introduced, this study can easily be compared with a study of percolation effects such as those described by Robinson (1982), Englman et al. (1983), and other workers. Percolation theory is primarily used to determine the probability of the network being connected. The focus of this paper is the magnitude and nature of permeability in systems with various degrees of interconnection. That is, we determine the magnitude and direction of the principal permeabilities (i.e., the permeability tensor) that best explain the behavior of the network. At the same time, we evaluate how well that permeability tensor predicts the actual vagaries of the network's behavior. The modeling techniques used to study the relationship between interconnection and permeability are described in Long et al. (1982) and Long (1983).

The modeling techniques used in this study are as follows. Two-dimensional fracture networks are generated, and the permeability is measured in any direction, α, by rotating the boundaries of the flow region α degrees and consequently rotating the direction of the gradient. For a homogeneous, anisotropic medium, $1/K_g(\alpha)$ versus α is an ellipse when plotted in polar coordinates. However, for inhomogeneous fractured media, $1/K_g(\alpha)$ may not plot as a smooth ellipse. A regression technique similar to that of Scheidegger (1954) is employed to interpret quantitatively the directional permeability data by determining a best-fit permeability tensor that in general will be anisotropic. The square of the difference between the values of directional permeability calculated using the best-fit tensor and the actual values calculated from the network model, K_g, divided by the products of the principal permeabilities, K_1 and K_2, is called the NMSE. The NMSE approaches zero as the behavior of the fracture system approaches that of an anisotropic, homogeneous porous medium. The above techniques have been used here to study the permeability of fracture networks with varying degrees of interconnection.

For a given set of fractures, it can be shown (Robertson, 1970; Baecher et al., 1977) that a probabilistic relationship for fracture frequency, λ_L, can be expressed by

$$\lambda_L = \lambda_A \overline{\ell}\, \overline{\cos\theta}, \tag{1}$$

where λ_L is fracture frequency (i.e., the number of fractures in the given set per unit length of sample line); λ_A is areal density, $\overline{\ell}$ is mean length, and θ represents the angles between the sample line and the fracture poles of the given set. This equation indicates that, in two dimensions, the probability of a fracture intersecting a unit length of borehole is proportional to the areal density and the mean fracture length.

Unfortunately, λ_A and $\overline{\ell}$ are difficult, if not impossible, to determine from an examination of borehole data. However, λ_L and θ can be measured, so that if Eq. (1) is rearranged with knowns on one side and unknowns on the other, we have

$$\lambda_L / \overline{\cos\theta} = \lambda_A \overline{\ell} = LD. \tag{2}$$

In all the following examples, the value of LD is the same. The values of λ_A and $\overline{\ell}$ are varied such that the product $\lambda_A \overline{\ell}$ remains a constant equal to the chosen value of LD. Intuition tells us that if all else is held constant, an increase in fracture length will increase the permeability. Conversely, if all else is held constant, a decrease in fracture density will decrease the permeability. However, it is not immediately obvious how permeability will be affected if $\overline{\ell}$ is increased by the same factor by which λ_A is decreased. Some insight can be gained by comparing the parameters used in the length-density study to those commonly used in percolation analysis.

Englman et al. (1983) have generated large numbers of fracture networks similar to those studied here. They (and others) have pointed out that the percolation frequency, ν, which is the ratio of percolative networks to the total number, is a function of sample size and an increasing function of a factor ζ, where

$$\zeta = \pi \lambda_A \overline{\ell^2}. \tag{3}$$

Here ζ represents essentially that fraction of the area of the fracture network in which there are likely to be intersections between fractures. In percolation literature, ζ is called the "effective bond occupation probability." The mean permeability of fracture networks should also increase as ζ increases, although an exact mathematical treatment of the relationship for systems with randomly located fractures is apparently not available. If the product $\lambda_A \overline{\ell} = LD$ is held constant, then ζ is proportional to $\overline{\ell}$. Thus we expect a net increase in permeability when $\overline{\ell}$ is increased and λ_A is decreased such that LD is held constant. Furthermore, since the behavior (as measured by the NMSE) is a function of degree of connection, the NMSE should decrease as $\overline{\ell}$ increases. In fact, as will be discussed below, this is exactly what we have observed.

A question remains as to the appropriate scale for such measurements of permeability. Theoretically, in a homogeneously fractured rock, permeability is not dependent on scale as long as the scale of measurement is large enough to include a statistically representative sample of the fracture network. In analyzing the examples discused below, we attempted to ensure that, from the statistical standpoint, all cases were approximately equally representative statistical samples. However, the method of analysis itself does have a certain scale dependence. If a fracture is truncated by two boundaries of the flow region, it will conduct fluid whether it is connected to the rest of the fracture network or not. This will cause permeability to be somewhat overestimated in every case. For small sample sizes and poorly connected systems, the permeability may be significantly overestimated. We call this truncation error.

On the other hand, percolation frequency is inherently a function of the scale of measurement. Englman et al. (1983) defined a critical value of ζ, called ζ^*. Infinitely large samples with ζ above ζ^* have a percolation frequency, ν, equal to one. Thus all such samples would be conductive. If ζ is below ζ^*, infinitely large samples have ν equal to zero. Above ζ^*, increases in the scale of measurement will increase the percolation frequency. The reason for this is that, especially at small scales of measurement, it is possible to pick a sample that is between fracture clusters. Englman et al. (1983) also observed that, below the critical value, ζ^*, increases in scale of measurement will decrease the percolation frequency. This may be due in part to truncation error, which is especially significant for measurements that are small compared to the size of the fractures and for very poorly connected networks.

For systems in which ζ approaches ζ^*, a finite scale of measurement might give ν less than unity for systems with $\zeta > \zeta^*$ *or* $\zeta < \zeta^*$. As ζ approaches ζ^*, one must examine larger and larger pieces of the system in order to obtain samples for which ν is clearly one or zero. We may expect a similar effect for permeability. However, before making conclusions about the permeability of a fracture network, one must consider the size of the hydrologic problem itself. It is more important to know the behavior of the system on the scale of the problem than on a scale approaching infinity. This is not a trivial matter, since if ζ is near ζ^*, the behavior of the fracture network can depart radically from that of an equivalent porous medium on the scale that is appropriate to the problem at hand. The analysis of such systems is currently a topic of research.

As mentioned earlier, the length-density study was carried out for systems with fractures of uniform aperture and length. The length-density parameter *LD* was arbitrarily held at a fixed value of 0.288 cm for all of the length-density studies presented. Thus input values of fracture density λ_A and length ℓ were calculated using the equation

$$LD = \ell\lambda_A = 0.288. \qquad (4)$$

Figure 1 presents the results for values of length and density from LD2 to LD12. In each part of the figure, the top half shows the networks used to calculate permeability, and the bottom half shows the permeability ellipses for each network. The figure provides a simple visualization of how well the permeability can be represented by a symmetric tensor. Figure 2 is a plot of the values of the principal permeabilities (K_1, K_2) and the NMSE versus fracture length. As ℓ increases from 2 to 24, permeability increases and the NMSE factor decreases.

The effect of scale of measurement was examined in two ways. First, a representative elementary volume (REV) study was performed on LD20 to demonstrate how porous-medium behavior develops with increase in scale. In this study, 14 different scales of measurement were used to calculate permeability. Second, in a series of cases, the flow regions for fracture lengths 10, 12, 14, and 16 were increased in order to examine the effect on NMSE and permeability. All these results are shown in Fig. 3. In this series, each increase in size of flow region requires generation of a new realization of the fracture system. This can introduce vagaries, and the conclusions from this part of the study may be weaker than those from the above REV study. However, all the results support the previously described general concepts about scale effects.

The purpose of this work was to learn whether permeability could be determined from the fracture frequency in a borehole without knowing the actual

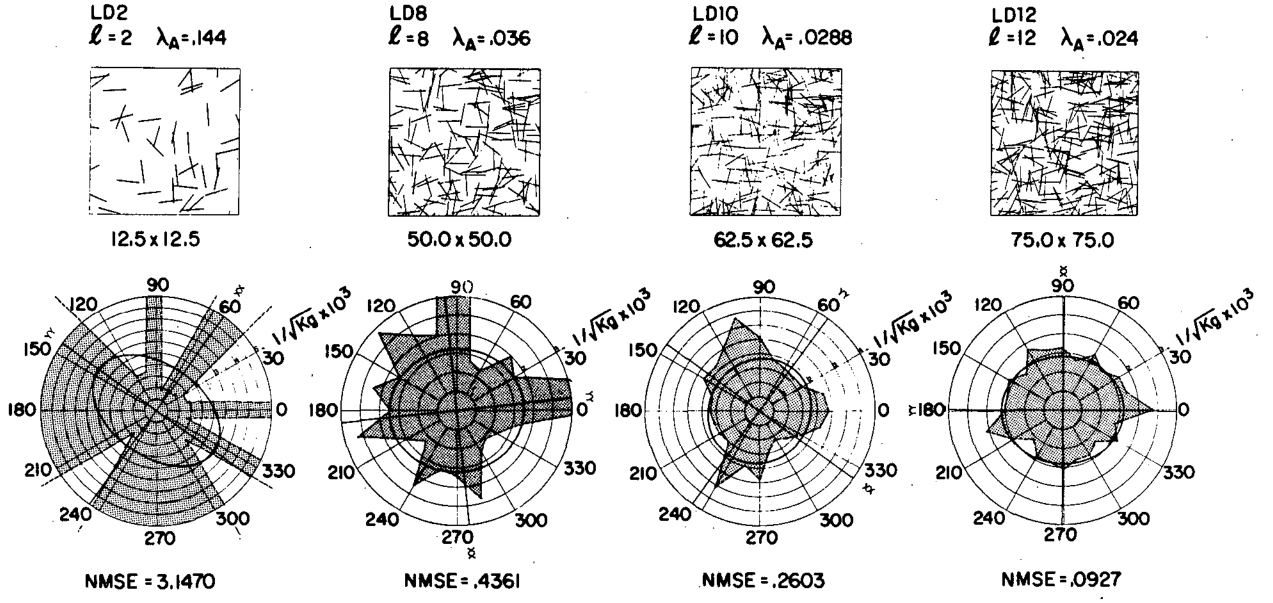

Figure 1. Permeability results for fracture lengths 2, 8, 10, and 12. [XBL 839-2215]

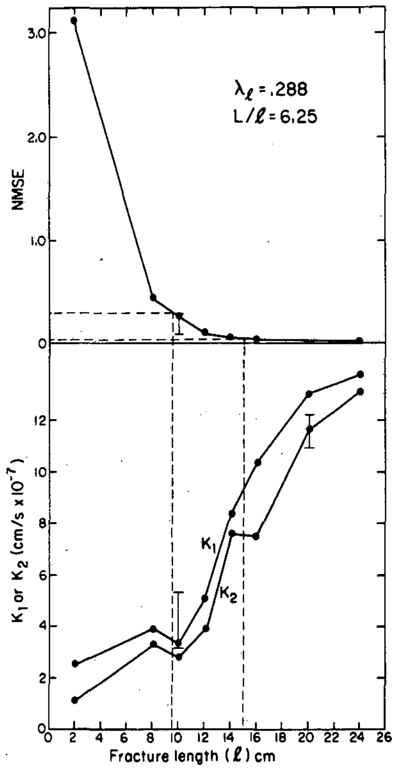

Figure 2. Permeability and NMSE versus fracture length for the first series of length-density studies. [XBL 8210-2566]

lengths and fracture densities. When the fracture length is small, it must be measured in order to predict both permeability and behavior. Networks with shorter fracture lengths and higher density will have lower permeability than those with longer fracture lengths and lower density. Furthermore, systems with shorter fractures behave less like porous media than those with longer lengths. The measured values of permeability and NMSE were much more strongly linked to fracture length than to sample size. Thus, if a fracture system does not behave like a porous medium on one scale, increasing the scale of observation may not improve the behavior. This is not intuitively obvious.

As fracture lengths increase, permeability approaches a maximum. Thus, in systems with fractures longer than a certain minimum, it may not be necessary to specify the length and fracture density exactly. Calculation of the maximum permeability using Snow's (1965) technique would be sufficient.

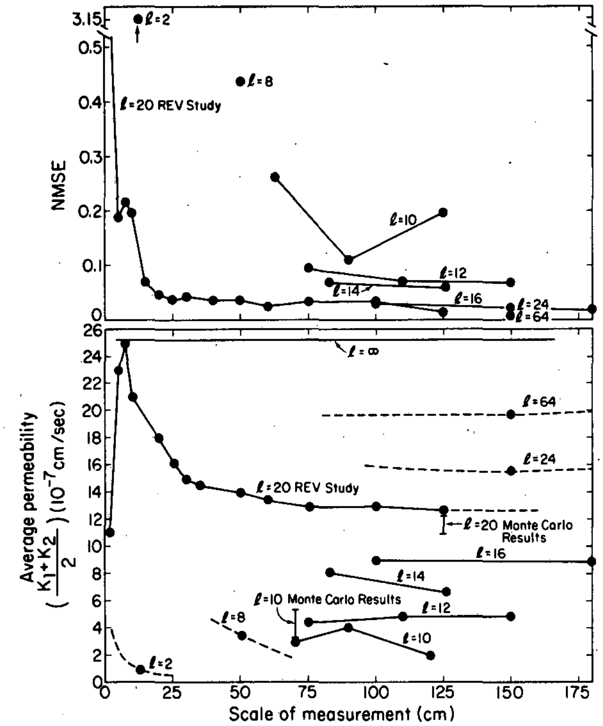

Figure 3. Summary of all permeability results plotted as a function of scale measurement. [XBL 846-9799]

REFERENCES

Baecher, G.B., Lanney, N.A., and Einstein, H.H., 1977. Statistical descriptions of rock properties and sampling. *In* Proceedings, 18th U.S. Symposium on Rock Mechanics, American Institute of Mining Engineers, p. 5C1–5C8.

Englman, R., Gur, Y., and Jaeger, Z., 1983. Fluid flow through a crack network in rocks. J. Appl. Mech., v. 50, p. 707–711.

Long, J.C.S., Remer, J.S., Wilson, C.R., and Witherspoon, P.A., 1982. Porous media equivalents for networks of discontinuous fractures. Water Resour. Res., v. 18, no. 3, p. 645–658.

Long, J.C.S., 1983. Investigation of equivalent porous medium permeability in networks of discontinuous fractures (Ph.D. thesis). University of California, Berkeley.

Robertson, A., 1970. The interpretation of geological factors for use in slope stability. *In* Proceedings, Symposium on the Theoretical Background to the Planning of Open Pit Mines with Special Reference to Slope Stability, p. 55–71.

Robinson, P.C., 1982. Connectivity of fracture systems—Percolation theory approach. Theoretical Physics Division, AERE Harwell, Oxfordshire.

Scheidegger, 1954. Directional permeability of porous media to homogeneous fluids. Geofis. Pura Appl., v. 28, p. 75–90.

Snow, D.T., 1965. A parallel plate model of fractured permeable media (Ph.D. thesis). University of California, Berkeley.

Well-Test Analysis in Fracture Networks

K. Karasaki, J.C.S. Long, and P.A. Witherspoon

Problems concerning flow in fractured media are commonly encountered in oil fields, geothermal fields, groundwater reservoirs, and other geologic media of engineering interest. In recent years, considerable attention has been focused on storage of radioactive wastes in fractured rock. In such a system, fractures are the major conduits of groundwater. Therefore, accurate characterization of the hydrologic behavior of the fractured rock mass is vital to the safety of such an operation.

In general, well testing is one of the most important methods for determining the flow properties of geologic media. Well-testing methodologies in porous media are well established. Although the same well tests are applied in fractured rocks, the analysis of such tests requires that certain assumptions be made about the behavior of the fracture network. A number of studies have been devoted to the method of analysis well tests in two-porosity systems. In these studies, the interconnected fractures are treated as one homogeneous continuum and the rock matrix as another. However, not much is known as to when such assumptions can be employed. The results of the tests may not be meaningful until the transient behavior of fractured rock under well-test conditions is understood.

Well tests have been numerically simulated in models of two-dimensional fracture systems that statistically reproduce the geologic characteristics of fractures in the field. Study shows that the conventional analysis method may fail because of local heterogeneities around the wells. It is also observed that the early-time transient at the pumping well is greatly influenced by the fractures that intersect the well and that, as a result, the late-time, semilog time intersect may not give the correct storage coefficient if the conventional analysis method is used.

A new mathematical model is proposed for analyzing well tests in a purely fractured system. The model consists of two zones. Fractures in the first zone around the well are treated discretely, whereas those in the outer region, are assumed to behave as a continuum. The solution has been obtained in a closed form. By type-curve matching, one can determine the properties of the fractures that intersect the pumping well.

NUMERICAL ANALYSIS

Numerical simulations of well tests in two-dimensional fracture systems have been conducted using the numerical model discussed in Kanehiro et al. (1983). The fracture meshes were generated by the method developed by Long et al (1982). Long has made an extensive study of the behavior of fracture networks under linear flow conditions, but little attention has heretofore been given to the behavior of such networks under well-test conditions (Fig. 1). The following conclusions are the results of a numerical study of well-test behavior. The pressure transient at the pumping well during a constant-flux pumping or injection test is very sensitive to the local fracture characteristics. Therefore, the parameters obtained from analyzing the well test by the conventional method may be quite different from the average system parameters. The locations of observation wells must be chosen such that the distance to the pumping well is far enough to include a representative volume of rock. For systems with permeability anisotropy, three observation wells may not be enough to define the permeability tensor because of local heterogeneities. In sparsely fractured rock, the system may not behave like a continuum at the scale of interest, and the conventional well-testing methodology may fail or provide misleading answers. Hydrologic characterization of such systems may be very difficult.

ANALYTICAL MODEL

In a porous medium, the size of each flow conduit is microscopic, and a large number of conduits are connected to the well. For this reason, the medium appears to behave like a continuum on the scale of the well test. In this case, volumetric averaging and continuum approximations are justified. On the contrary, in a fractured medium, only a small number of fractures may intersect the pumping well. These particular fractures will be stressed by a large gradient under well-test conditions. Therefore, well-test behavior in early time will be dominated by these fractures. Consequently, late-time behavior will also be affected. The volumetrically averaged Darcy flux does not characterize flow in the vicinity of an active well. Instead, the flow in individual fractures must be accounted for. Furthermore, the hydraulic parameters of the few fractures may be quite different from the values averaged over the system. A new analytical model is proposed for well-test problems in fractured media in which the matrix is impermeable. The model accounts for the difference between the flow regime around the active well and

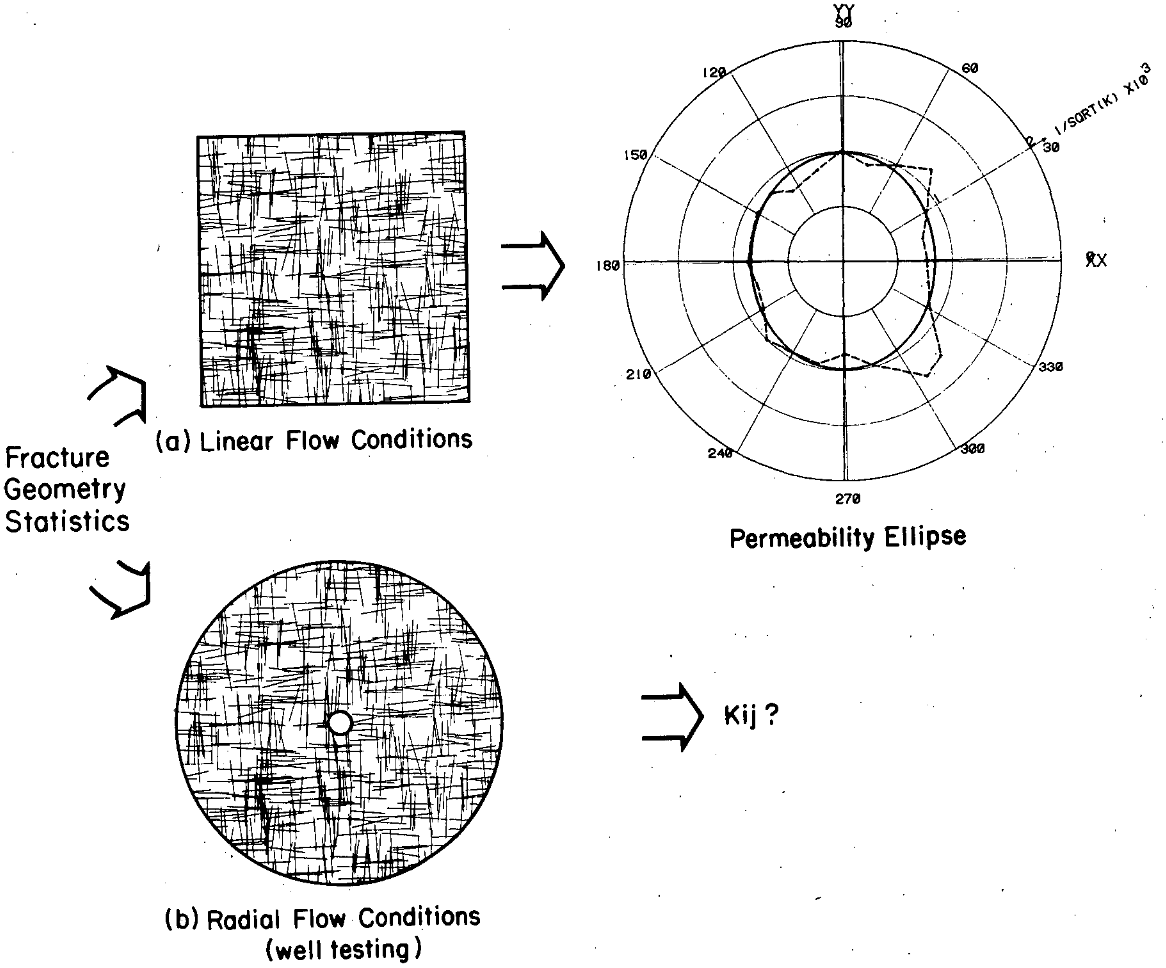

Figure 1. (a) Linear flow model in Long (1982). (b) Well-test model in this study. [XBL 8410-9992]

that of the system as a whole. The fractures are all assumed to be vertical and to extend from the top to the bottom of a formation of uniform thickness. It is further assumed that the rock matrix is impermeable and that all the hydraulic parameters are independent of pressure. The conceptual model of the well test in this system consists of two zones. In the outer region, the usual equivalent porous-medium approximation is assumed to hold; i.e., the flow properties of the fractures are volumetrically averaged, and a single continuum replaces the fractures. The hydraulic conductivity and the storage coefficient for the region are k_2 and S_{s_2}, respectively. The well is located in the center of the inner region and communicates with the outer region through a finite number (n) of fractures in the inner region. The radius of the well is r_w, and the radius of the inner region is r_f. All the fractures in the inner region have the same width b and the hydraulic parameters k_1 and S_{s_1}. It is assumed that there is an infinitesimally thin ring of infinite conductivity between the two regions, so that otherwise incompatible boundaries can be matched. Figure 2 illustrates the model. The following dimensionless parameters are defined:

$$h_D = \frac{2\pi k_2 h}{Q}\,, \qquad t_D = \frac{\alpha_2 t}{r_w^2}\cdot\frac{r_w^2}{r_f^2} = \frac{\alpha_2 t}{r_f^2}\,,$$

$$r_D = \frac{r}{r_f}\,, \qquad r_c = \frac{r_w}{r_f}\,,$$

$$\alpha_c = \frac{\alpha_1}{\alpha_2}\,, \qquad \beta = \frac{nbk_1}{2\pi r_f k_2}\,,$$

where α is the hydraulic diffusivity defined by

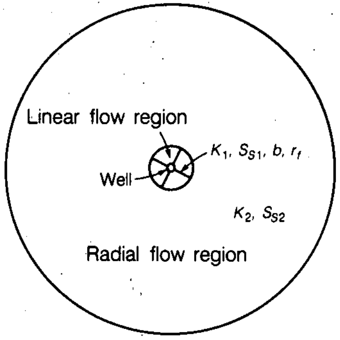

Figure 2. Schematic diagram of the analytical model for well-test problems in purely fractured media. [XBL 8412-6193]

$\alpha = k/S_s$. The governing equation for the inner region is that for one-dimensional unsteady flow:

$$\frac{\partial^2 h_{D_1}}{\partial r_D^2} = \frac{1}{\alpha_c} \cdot \frac{\partial h_{D_1}}{\partial t_D} .$$

For the outer region, the usual radial flow equation describes the flow:

$$\frac{\partial^2 h_{D_2}}{\partial r_D^2} + \frac{1}{r_D} \cdot \frac{\partial h_{D_2}}{\partial r_D} = \frac{\partial h_{D_2}}{\partial t_D} .$$

The initial conditions and the boundary condition for the constant-rate injection test in terms of the dimensionless parameters are

$$h_{D_1}(r_D , 0) = 0 \quad (r_c \leqslant r_D \leqslant 1),$$

$$h_{D_2}(r_D , 0) = 0 \quad (1 \leqslant r_D \leqslant \infty),$$

$$\frac{\partial h_{D_1}}{\partial r_D} = -\frac{1}{\beta} \quad (r_D = r_c) .$$

For the continuity at the boundary of the inner and outer regions,

$$h_{D_1} = h_{D_2} \quad (r_D = 1),$$

$$\frac{\partial h_{D_1}}{\partial r_D} = \frac{1}{\beta} \cdot \frac{\partial h_{D_2}}{\partial r_D} \quad (r_D = 1) .$$

The solutions are

$$h_{D_1} = \frac{4\alpha_c}{\pi^2} \int_0^\infty \frac{1 - \exp(-\mu^2 t_D)}{\mu^3} \cdot \frac{\cos\left[\dfrac{r_D - r_c}{\sqrt{\alpha_c}} \mu \right]}{\Psi^2 + \Theta^2} d\mu \quad (r_c \leqslant r_D \leqslant 1),$$

$$h_{D_2} = -\frac{2\sqrt{\alpha_c}}{\pi} \int_0^\infty \frac{1 - \exp(-\mu^2 t_D)}{\mu^2} \cdot \frac{\Theta \cdot J_0(\mu r_D) + \Psi \cdot Y_0(\mu r_D)}{\Psi^2 + \Theta^2} d\mu \quad (1 \leqslant r_D < \infty),$$

where

$$\Psi = -\sqrt{\alpha_c} J_1(\mu) \cos\left[\frac{1-r_c}{\sqrt{\alpha_c}} \mu \right] + \beta J_0(\mu) \sin\left[\frac{1-r_c}{\sqrt{\alpha_c}} \mu \right] ,$$

$$\Theta = \sqrt{\alpha_c} Y_1(\mu) \cos\left[\frac{1-r_c}{\sqrt{\alpha_c}} \mu \right] - \beta Y_0(\mu) \sin\left[\frac{1-r_c}{\sqrt{\alpha_c}} \mu \right] .$$

The solutions can be presented in a series of type curves for ranges of dimensionless parameters α_c, β, and r_c (Karasaki et al., 1985). If one knows S_{s_1} a priori, k_1, k_2, S_{s_2}, and r_f can be determined by finding the curve that best fits the well-test data. However, there are an infinite number of curves for various combinations of α_c, β, and r_c, so that one has to employ trial and error methods in determining the best fit. By starting with an estimated value for either S_{s_2} or r_f, one can fix one parameter while changing others. The estimated value is checked and updated if necessary using the matching point. Figure 3 illustrates an example of the procedure applied to find r_f from a numerical well-test simulation in the fracture network shown in the figure. The calcu-

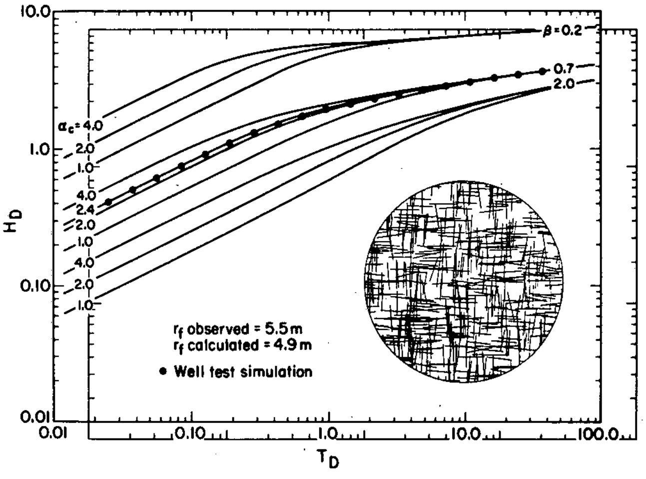

Figure 3. An example of the curve-fitting technique used to find r_f. [XBL 8410-8859]

lated r_f was 4.9 m in this case. In the actual network, the distance to the nearest intersection was 7.3 m in one direction and 3.8 m in the other. If a fit can be found, this analytical model yields accurate determinations of the storage coefficient of a fracture system from one well test (Karasaki et al., 1985), as well as the distance to the nearest fracture intersection, which in turn gives us a clue to the fracture spacing.

REFERENCES

Kanehiro, B.Y., Wilson, C.R., and Karasaki, K., 1983. Transient analysis of groundwater flow in fracture networks. *In* Earth Sciences Division Annual Report 1982. Lawrence Berkeley Laboratory Report LBL-15500, p. 175–178.

Karasaki, K., Long, J.C.S., and Witherspoon, P.A., 1985. A new model for well test analysis in a purely fractured medium. Proceedings, Tenth Workshop on Geothermal Reservoir Engineering, Stanford University, Stanford, California, January 22–24, 1985, in press.

Long, J.C.S., Remer, J.S., Wilson, C.R., and Witherspoon, P.A., 1982. Porous media equivalents for networks of discontinuous fractures. Water Resour. Res., v. 18, no. 3, p. 645.

Design of Well-Testing Programs in Crystalline Rock

T.W. Doe and D. Elsworth

Our efforts to design well-testing programs for crystalline rock have concentrated on two major objectives: improving analytical methods for interpreting well tests in the single fractures that dominate well-test response and developing a rationale for the selection of the numbers and spacings of tests to define the variation in conductivity in the rock mass.

WELL-TEST ANALYSIS

The focus of our work during 1984 has been to investigate the role of turbulence in constant-head test analysis. The constant-head test consists of isolating a test section in a well and injecting water at constant pressure into the test zone. Commonly such tests are analyzed by assuming the flow rate is steady. Doe et al. (1982) have shown that information on the boundaries and interconnections of the fractures can be obtained by looking at the data on transient flow rates. Previous work, however, concentrated only on laminar flow.

Elsworth (1984) has used finite-element modeling methods to describe the effects of turbulence on the well-test flow curves. In turbulent flow, the velocity is not linearly dependent on the gradient. The onset of turbulent flow is favored both by larger roughness in the fracture plane and by elevated pressure gradients in the rock. Where turbulent flow does occur, it may be limited to a narrow collar around the well, beyond which the flow reverts to the laminar condition.

Qualitatively, the onset of turbulence can be diagnosed from the form of the transient flow-rate curve of a constant-pressure injection test. Figure 1 shows the dimensionless discharge for flow in single fractures with either open or closed (finite) outer boundaries. Elsworth (1984) points out that with the inclusion of turbulence, one is no longer able to obtain a unique set of hydrologic parameters from the test and that one needs to perform tests over a range of injection pressures to deduce the hydrologic parameters from the test. Regardless of the number of pressure steps, however, turbulent flow is charac-

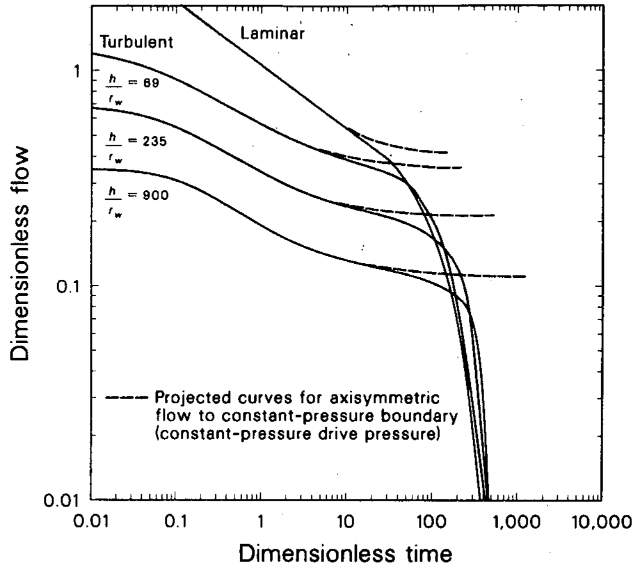

Figure 1. Dimensionless flow versus dimensionless time for a single circular fracture. Dimensionless radius is 10. Curves are given for several ratios of injection head to well radius. [XCG 8412-13490]

terized by a flattening of the early-time portion of the flow curve with respect to the curve for purely laminar flow.

DESIGN OF WELL-TEST PROGRAMS

The major problem in characterizing flow in granitic rocks has been the extreme heterogeneity of the hydraulic conductivity. For example, with water-supply wells in areas of crystalline rock, it is well known that only occasionally do wells provide large yields, and the right locations for drilling such wells are seldom known in advance.

Typically, the statistical distribution of yields from wells is lognormal; that is, the logarithms of the conductivity are normally distributed. This distribution may be very strongly skewed toward lower conductivities, hence most wells are located in relatively low conductivity environments, and large-yield wells are relatively rare. Snow (1970) collected data from Corps of Engineers sources and concluded that lognormal forms fit the data. One goal of our work this past year has been to compile data from the extensive testing efforts that have gone on since Snow's work. The lognormal conductivity distribution is shown clearly in Fig. 2, which is a compilation of well yields from water-supply wells in the Uppland district of Sweden (Carlsson and Olsson, 1977). The graph shows the cumulative distribution function (CDF) plotted on a probability scale. This scaling transforms plots of normally distributed functions into straight lines.

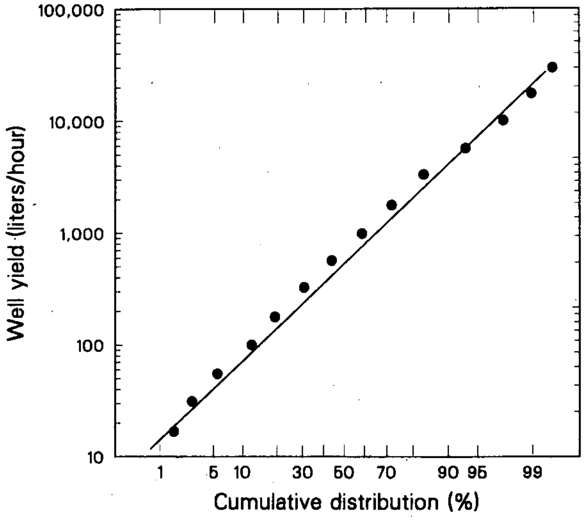

Figure 2. Log-probability plot of water well yields from northern Sweden. [XCG 8412-13491]

A review of conductivity data from numerous sources, including the Swedish repository site characterization program (Ahlbom et al., 1983), the English well-testing work in Cornwall, England (Hodgkinson, 1984), the Stripa program (Gale, 1981), and the test at the Colorado School of Mines test facility (Montazer, 1982), suggests that the lognormal distribution indeed holds. A realistic goal of hydrologic characterization programs may therefore be to obtain the parameters of this distribution to some acceptable level of confidence. Once this level of confidence is defined, the number of tests that should be performed can be readily determined from sampling theory. Performing fewer tests than this number would result in the inadequate characterization of the site; performing more tests might be a waste of money.

REFERENCES

Ahlbom, K., Carlsson, L., and Olsson, O., 1983. Final disposal of spent fuel—Geological, hydrological, and geophysical methods for site characterization. SKBF Technical Report 83–43, 76 p.

Carlsson, A., and Olsson, T., 1977. Hydraulic properties of Swedish crystalline rocks. Bull. Geol. Inst. Univ. Uppsala, v. 7, p. 71–84.

Doe, T., Long, J., Endo, H., and Wilson, C., 1982. Approaches to evaluating the porosity and permeability of fractured rock masses. *In* R. Goodman and F. Heuze (eds.), Issues in Rock Mechanics, Proceedings of the 23rd U. S. Rock

Mechanics Symposium, Berkeley, California, August 25–27, 1982, p. 30–38.

Elsworth, D., 1984. Laminar and turbulent flow in rock fissures and fissure networks (Ph.D. thesis). University of California, Berkeley, 230 p.

Gale, J.E., 1981. Fracture and hydrology data from field studies at Stripa, Sweden. Lawrence Berkeley Laboratory Report LBL-13101, Appendix B-4, p. 227ff.

Hodgkinson, D., 1984. Analysis of steady state hydraulic tests in fractured rock. AERE-Harwel (England) Report DOE/RW/84.076.

Montazer, P., 1982. Permeability of unsaturated, fractured metamorphic rocks near an underground opening (Ph.D. thesis). Colorado School of Mines, 617 p.

Snow, D.T., 1970. The frequency and apertures of fractures in rock. Int. J. Rock Mech. Min. Sci., v. 7, p. 23–40.

Drawdown Around an Off-Centered Constant-Discharge Well in a Closed Circular Region

I. Javandel and P.A. Witherspoon

For more than two decades, salt domes have been studied to determine their suitability for storage of radioactive waste. For various reasons, however, the use of salt domes for radioactive waste isolation seems to have been indefinitely postponed.

Nevertheless, the results of these studies have led certain industries to use salt domes for the storage of other substances that do not require stability over several centuries. One example of such use is the storage of hyrocarbons in cavities generated by the dissolution of salt within the main body of a salt dome. The large volume of brine obtained by dissolution of the salt has to be disposed of in a manner that poses no hazard to the environment. In some cases the brine is reinjected into the caprock.

According to a widely accepted theory, caprocks consist of relatively insoluble impurities that became separated from the original salt body as a result of dissolution by groundwater flow over geologic time. Caprocks are composed of various combinations of anhydrite, gypsum, and limestone.

In general, caprocks differ in shape from one salt dome to another. Many not only cover the top of the salt but extend down the flanks of the salt dome to a considerable depth. Some are axisymmetric relative to the axis of the dome, and others vary in radial extent in different directions. The thickness of caprocks commonly decreases with depth, and in many cases their radial extent is unknown.

Determining the hydraulic connection between a caprock and the rocks surrounding the salt dome is a matter of great importance in evaluating the environmental impact of brine injection in such formations. The hydraulic properties of the caprock and the formations that are in hydraulic contact with it are needed for the study of the behavior of the caprock as a receiving medium for brine. In response to these needs, a new solution is developed to address the following questions.

1. If we consider the caprock to be circular in shape, what is its representative radius?
2. What are the caprock's hydraulic properties?
3. Is the caprock hydraulically closed, or is it connected to one or several other permeable media surrounding the dome?

Most of the available literature pertaining to pressure transient studies of a region bounded by a circular discontinuity addresses the cases in which the injection or pumping well is located at the center of the circular region. In actual field cases, injection wells are located all over the region. Therefore, the following solution is developed for the general case in which the injection well is located anywhere within a circular region. In this development the assumption is made that the region is of constant thickness and is composed of geologic materials that behave like a porous medium.

THEORY

Let us consider a circular region of porous medium with uniform thickness b and radius a (see Fig. 1). This region is surrounded by an impermeable boundary that does not allow any flow out of the region. Furthermore, the region is confined by impermeable layers at both top and bottom. A well located at a distance r_1 from the center of the region

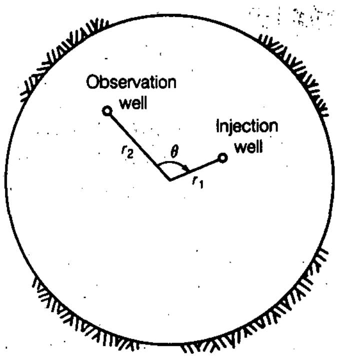

Figure 1. Schematic diagram showing arbitrary locations of injection and observation wells in a closed circular region. [XBL 8412-6192]

is open along the total thickness b and is being recharged with a fluid at a constant rate of Q. Assuming that the hydraulic head is initially uniform over the whole region, by analogy with heat conduction (Carslaw and Jaeger, 1959), the change in hydraulic head with time at an arbitrary well that (1) is open in the same formation, (2) is located at a distance r_2 from the center of the region, and (3) makes an angle θ with the injection well is given by

$$\Delta h = \frac{Q\mu}{2\pi k b \gamma}\left\{\frac{2\alpha t}{a^2} + \frac{r_1^2 + r_2^2}{2a^2}\right.$$

$$- \frac{3}{4} - \frac{1}{2}\ln\left(1 - \frac{2r_1 r_2}{a^2}\cos\theta + \frac{r_1^2 r_2^2}{a^4}\right)$$

$$- \frac{1}{2}\ln\left(\frac{r_1^2}{a^2} - \frac{2r_1 r_2}{a^2}\cos\theta + \frac{r_2^2}{a^2}\right)$$

$$- \sum_{n=0}^{\infty} 2\epsilon_n \cos n\theta \sum_{m=1}^{\infty} \exp(-\alpha\beta_{n,m}^2\, t/a^2)$$

$$\left.\cdot \frac{J_n(r_1\beta_{n,m}/a)J_n(r_2\beta_{n,m}/a)}{(\beta_{n,m}^2 - n^2)J_n^2(\beta_{n,m})}\right\}, \qquad (1)$$

where, $\beta_{n,m}$ are the positive roots of

$$J_n'(\beta) = 0, \qquad (2)$$

and $\epsilon_n = 1$ (if $n = 0$), $\epsilon_n = 2$, (if $n = 1,2,3,\ldots$), k and α are the permeability and hydraulic diffusivity of the porous medium, γ and μ are the unit weight and viscosity of the fluid, and J_n is the Bessel function of the first kind and order n.

By introducing the dimensionless parameters

$$P_D = \frac{2\pi k b \gamma \Delta h}{Q\mu},\ t_D = \frac{\alpha t}{r^2},\ r_{D_1} = \frac{r_1}{a},$$

$$r_{D_2} = \frac{r_2}{a},\ r_D = \frac{r}{a},$$

where

$$r = (r_1^2 + r_2^2 - 2r_1 r_2\cos\theta)^{1/2} \qquad (3)$$

is the distance between the observation and injection wells, Eq. (1) may be written as

$$P_D = 2t_D r_D^2 + \frac{r_{D_1}^2}{2} + \frac{r_{D_2}^2}{2} - \frac{3}{4} - \frac{1}{2}$$

$$\cdot \ln(1 - 2r_{D_1} r_{D_2}\cos\theta + r_{D_1}^2 r_{D_2}^2) - \frac{1}{2}\ln r_D^2$$

$$- \sum_{n=0}^{\infty} 2\epsilon_n \cos n\theta \sum_{m=1}^{\infty} \exp(-t_D r_D^2 \beta_{n,m}^2)$$

$$\cdot \frac{J_n(r_{D_2}\beta_{n,m})J_n(r_{D_1}\beta_{n,m})}{(\beta_{n,m}^2 - n^2)J_n^2(\beta_{n,m})}. \qquad (4)$$

For the special case in which the injection well is located at the center of the circular aquifer, r_1 becomes zero and r_2 equals r. In this case, Eq. (4) simplifies to

$$P_D = 2t_D r_D^2 + \frac{r_D^2}{2} - \frac{3}{4} - \ln r_D$$

$$- 2\sum_{m=1}^{\infty} \exp(-t_D r_D^2 \beta_{0,m}^2)\frac{J_0(r_D\beta_{0,m})}{\beta_{0,m}^2 J_0^2(\beta_{0,m})}, \qquad (5)$$

which is the solution given by Muskat (1946).

The following steps can be used to answer the set of questions raised earlier.

1. Make a log-log plot of the pressure build-up produced at a given observation well by injection at another well.

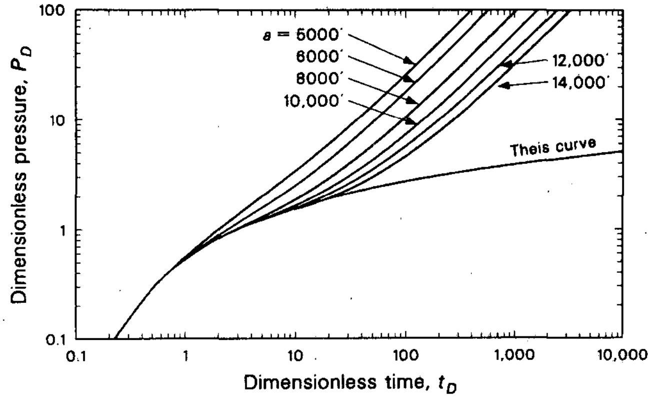

Figure 2. Type curves for pressure build-up due to off-center injection in a closed circular region showing the effect of radius of the region on pressure build-up for r_1 = 1700 ft, r_2 = 3000 ft, and θ = 27°. [XCG 8411-13489]

2. Assuming that the caprock is circular in shape with its center at the centroid of the dome's plan view (unless further information is available), determine the radial distances to the injection and observation wells. The corresponding dimensionless radii depend on the value of *a*. Figure 2 shows type curves prepared from Eq. (4) for different values of *a* and for the positions of the injection and observation wells, r_{D_1} and r_{D_2}

3. Obtain an estimate of caprock effective radius and hydraulic properties by superimposing the field data upon the corresponding family of type curves, like those shown in Fig. 2.

4. After the plot of field data departs from the Theis curve, if the slope of the plot is less than those for the closed boundary curves, then that indicates that the boundary is not completely impermeable. The position of the section of the plot in between the Theis curve and the corresponding curve for a tight boundary is an indication of the conductivity ratio of the outside and inside materials of the circular region.

REFERENCES

Carslaw, H.S., and Jaeger, J.C., 1959. Conduction of Heat in Solids. London, Oxford Univ. Press, 510 p.

Muskat, M., 1946. The Flow of Homogeneous Fluids Through Porous Media. Ann Arbor, J.W. Edwards, Inc.

Development of RESSQ: A Semianalytical Model for Two-Dimensional Contaminant Transport in Groundwater

C. Doughty, C.F. Tsang, and I. Javandel

The computer program RESSQ, introduced in last year's Annual Report (Javandel et al., 1984a,b), uses semianalytical methods to calculate two-dimensional contaminant transport by advection and adsorption in a homogeneous, isotropic, confined aquifer of uniform thickness under steady-state flow conditions. The calculation can include uniform regional flow; multiple point sources and sinks, such as recharge and extraction wells; extended sources, such as waste storage ponds; and a linear no-flow or constant-pressure boundary condition. RESSQ calculates the streamline pattern in the aquifer by following the paths of contaminant particles emanating from sources. From the streamline pattern, one can readily obtain the location of contaminant fronts around sources at various times and the variation of contaminant concentration with time at sinks. The calculation is based on the theory of the complex velocity potential. RESSQ is presently being used by a number of researchers inside and outside Lawrence Berkeley Laboratory to study a variety of contaminant transport problems. On the basis of our experience and the comments of others, we have recently added several new features to RESSQ to broaden its range of applicability. We have considered nonsteady-flow fields, variable injection concentrations, and the calculation of pressure change at selected observation points.

NONSTEADY-FLOW FIELDS

The complex-velocity-potential formulation on which RESSQ is based applies to steady-state fluid flow. In typical groundwater aquifers, steady flow conditions are achieved quickly after pumping begins, so that the error made by RESSQ in ignoring the short transient period is small. It follows also that steady conditions are quickly re-established after a change in pumping rate. Thus, if a variable pumping rate can be represented by a series of constant steps, then the resulting variable-flow field can be closely approximated by a piecewise-steady-flow field. Each time there is a change in the pumping rate of any well penetrating the aquifer, a new steady-flow field is calculated, giving a new streamline pattern. A contaminant particle emanating from a source follows a given streamline until some pumping rate in the aquifer changes, at which time the contaminant particle shifts to the new streamline. A plot of the particle's flow path through the aquifer shows segments of smooth streamline joined at kinks. Figure 1a shows the streamline pattern for an injection/production well pair pumping at constant, equal rates. Figure 1b shows the flow paths that form when the injection well is pumped at constant rate and two production wells are pumped discontinuously. When the contaminant particles whose flow paths are shown leave the injection well, a production well at point *P* is pumping. A short time later, the well at *P* is shut in and a production well at point *P′* begins to pump. Still later, the well at *P′* is shut in and the well at *P* recommences pumping. In general, contaminant particles found at the same location in the aquifer at different times will not follow the same flow path if any pumping rate in the aquifer has changed in the interim. This leads to the possibility of crossing flow paths. Note in Figure 1b that the lowermost flow path from *I* to *P* passes through point *P′* without being captured, as are the two flow paths above it. Thus the particle following the lower flow path passed by *P′* later than the others, when the production well there was no longer pumping. A number of plots, showing the flow paths of particles emanating from a source at different times, are necessary to follow the course of all the contaminant from a source. Variation of contaminant concentration at production wells is more complicated to calculate than in the original version of RESSQ and is the subject of current study.

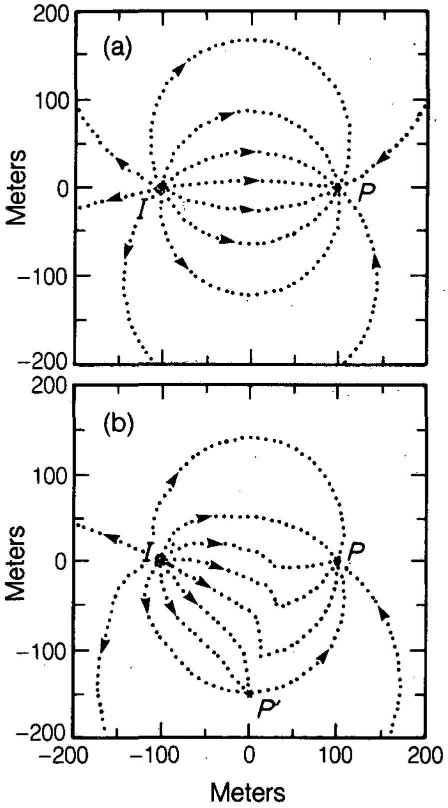

Figure 1. **(a)** The streamline pattern for an injection well *(I)* and a production well *(P)* pumping at constant rates. **(b)** The flow paths for the case when *I* is pumped at a constant rate but *P* and P′ are pumped discontinuously. [XBL 8412-6188]

VARIABLE INJECTION CONCENTRATION

When pumping rates are constant but injection concentration varies, a straightforward extension of the original version of RESSQ is used to calculate contaminant concentration at production wells. An example of these conditions is a two-well tracer test. An injection well and a production well are separated by some distance and pump at equal rates from an aquifer. The streamline pattern is shown in Fig. 1a. During a period of time, a slug of tracer is added to the injected water. The variation in tracer concentration at the production well, the breakthrough curve, is studied to learn about the aquifer properties. If the produced water is subsequently reinjected, the test is called a recirculation test. Figure 2 shows the breakthrough curves for a slug tracer test and a recirculation tracer test. Note that RESSQ does not calculate dispersion or diffusion. The gradual variation in the breakthrough curve is due to the difference in travel times for tracer particles following the various streamlines joining the injection and production wells.

CALCULATION OF PRESSURE CHANGE

The long-time solution of the Theis equation is used to calculate the drawdown at all injection and production wells and at additional observation points if desired. The pressure change is calculated as

$$\Delta P = \sum_{j=1}^{J} \frac{q_j \mu}{4\pi kh} \ln \frac{(\gamma \phi \mu C r_j^2)}{4kt},$$

where ΔP = pressure change, q_j = volumetric flow

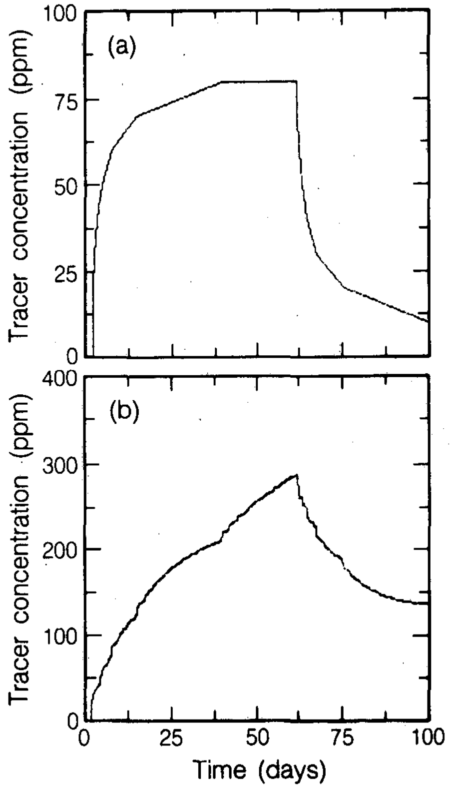

Figure 2. The variation of tracer concentration at the production well of a two-well tracer test for a slug test **(a)** and a recirculation test **(b)**. The tracer is added to the injected water for 50 days at a concentration of 100 ppm. For the recirculation test, the produced fluid is immediately reinjected. [XBL 8412-5801]

rate of the jth well, μ = dynamic viscosity, k = intrinsic permeability, h = aquifer thickness, γ = Euler's constant = 1.78, ϕ = porosity, C = matrix compressibility, r_j = distance from observation point to jth well, t = time at which drawdown is calculated, and J = total number of wells. This expression can be rewritten as

$$\Delta P = \frac{\mu}{4\pi kh}\ln\left(\frac{\gamma\phi\mu C}{4kt}\right)\sum_{j=1}^{J} q_j$$

$$+ \frac{\mu}{4\pi kh}\sum_{j=1}^{J} q_j \ln(r_j^2).$$

When the net flow into and out of the aquifer is zero, i.e., when

$$\sum_{j=1}^{J} q_j = 0,$$

the first term becomes zero and the time dependence drops out of the expression for the pressure change, so that true steady-state conditions prevail. When the net flow is nonzero, an overall drawdown or buildup occurs, given by the first term, but local variations in pressures, given by the second term, remain constant, so that fluid flow, which is proportional to the spatial derivative of pressure, is steady.

The calculated drawdowns can be compared to measured drawdowns, providing a convenient means of validating the mathematical model—i.e., to assess whether the model's idealizations adequately represent conditions in the field.

REFERENCES

Javandel, I., Doughty, C., and Tsang, C.F., 1984a. The use of mathematical models for subsurface contaminant transport assessment. *In* Earth Sciences Division Annual Report 1983. Lawrence Berkeley Laboratory Report LBL-16920, p. 47–50.

Javandel, I., Doughty, C., and Tsang, C.F., 1984b. Groundwater Transport: Handbook of Mathematical Models. (Water Resources Monograph Series Vol. 10). Washington D.C., American Geophysical Union, p. 35–67, 175–204.

Preliminary Mathematical Modeling of the SPEOS Aquifer Thermal Energy Storage Field Experiment

C. Doughty and C.F. Tsang

Project SPEOS, sponsored by the International Energy Agency, considers the seasonal storage of warm water in a shallow aquifer. Between 1982 and 1984 a two-cycle field experiment was conducted at Dorigny, near Lausanne, Switzerland (IENER, 1983). This report describes the preliminary mathematical modeling of the first injection-storage-production cycle carried out by Lawrence Berkeley Laboratory

(LBL). The basic SPEOS design includes a vertical central well with two levels of horizontal radial drains separated by a vertical interval. During the injection period, water is extracted from the lower-level "supply" drains, heated, and then injected into the upper-level "storage" drains. Hot water flow is by downward piston action, thus minimizing the effects of natural convection. During the production period, the flows are reversed.

At the Dorigny site, the 25-m-long, horizontal upper supply drains and lower storage drains are separated by a vertical distance of 17 m. Unfortunately, a less permeable clay layer has been discovered that separates the upper and lower permeable layers, effectively dividing the system into two aquifers. During injection, hot water spreads laterally around the upper drains and does not move downward through the clay layer. This creates an elongated plume (upper aquifer thickness is 6.5 m) with large surface area and high heat loss.

The numerical model PT (Bodvarsson, 1982), developed at LBL, was used to calculate the coupled mass and heat transfer in the water-saturated upper aquifer for the first cycle. In this preliminary study, the aquifer was modeled as a single homogeneous layer of uniform thickness. An analytical solution for conductive losses to the underlying clay layer was included in the numerical model. Heat losses to the ground surface through the unsaturated zone overlying the upper aquifer were expressed by a linear "radiation" heat flow, $Q = h(T - T_0)$. The unknown heat transfer coefficient, h, which combines the effects of the unsaturated zone and the ground surface, was used as a fitting parameter to match experimental and calculated energy recovery factors. A regional groundwater flow was included in the model, and an irregular calculational mesh that makes a gradual transition from circular to rectangular geometry was used, as shown in Fig. 1. The mesh was generated using the computer code OGRE (Weres and Schroeder, 1978), developed at LBL. To avoid the short time-steps necessary for calculating sharp temperature gradients, the six radial drains were approximated by a uniform disk.

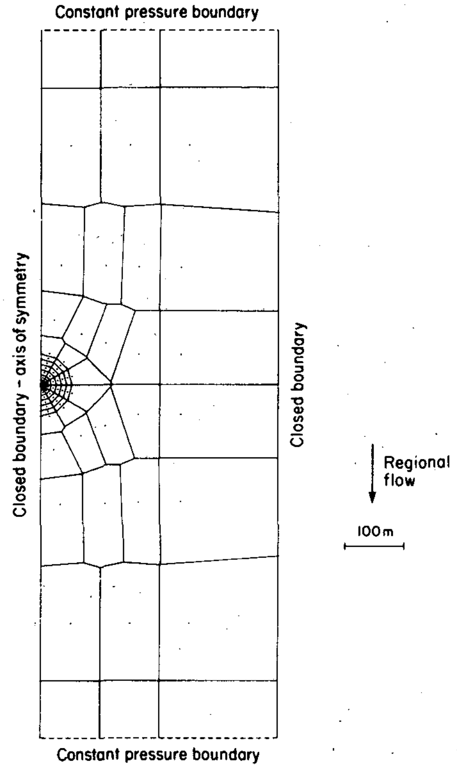

Figure 1. Single-layer calculational mesh used for the preliminary mathematical modeling of the SPEOS first cycle. [XBL 849-9957]

Between July and December 1982, 14,743 m^3 of water at an average temperature of 59.3°C was injected. From mid-January to April 1983, 18,280 m^3 of water was extracted. In total, 42% of the injected energy was produced, and the volume extracted was 1.24 times the volume injected. By adjusting the surface heat transfer coefficient, the calculated recovery factor was matched to the experimental value. The experimental and calculated production temperature curves are shown in Fig. 2. The reason for the increase in observed production temperature between days 198 and 219 is that the two drains most upstream were closed during that time period. The drain closure was modeled by producing only from the downstream portion of the injection disk. The good match between experimental and calculated production temperatures indicates that even with a simple one-layer model, many essential features of the SPEOS problem can be studied. Several additional calculations were made in

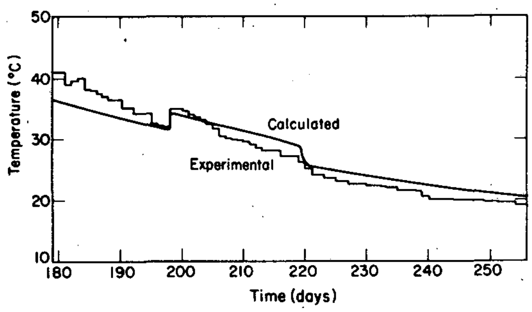

Figure 2. SPEOS first-cycle experimental and calculated production temperatures versus time. [XBL 849-9958]

order to study the relative importance of various heat-loss mechanisms. These are summarized in Table 1.

Three general conclusions can be made on the basis of our preliminary modeling studies:

1. The unfavorably large aspect ratio (radius divided by thickness of the hot plume), caused by the low-permeability clay layer, appears to be the dominant factor affecting heat loss. Current work at the SPEOS site, which involves drilling vertical drains into the clay layer to increase permeability, could prove helpful if the aspect ratio of the resultant thermal plume were reduced.
2. Regional flow appears to have a secondary effect in this case.
3. Because a clay layer is present in the middle of the storage system, the relatively low recovery factor does not disprove the SPEOS concept. Furthermore, the experiment does provide valuable field data to validate numerical models.

Future mathematical modeling work is planned along three lines:

1. Refine the present study by using a multilayered calculation mesh. Detailed comparison of experimental and calculational data will be carried out.
2. Study ways to optimize the energy recovery factor at the Dorigny site.
3. Assuming the absence of the clay layer, perform parameter studies to estimate typical energy recovery factors for SPEOS systems at other sites.

Table 1. SPEOS parameter sensitivity studies.

Case	Recovery factor	Comments
Base case	0.42	Surface heat transfer coefficient has the value 0.0892 W/m$^2 \cdot$ °C.
No regional flow	0.46	Recovery factor similar to base case
No regional flow; no vertical heat loss	0.71	Recovery factor much larger than base case. Vertical heat losses important because of large aspect ratio of plume
Injection into upstream drains; production from downstream drains	0.48	Selective injection/production to counteract regional flow and improve aspect ratio during injection

REFERENCES

Bodvarsson, G.S., 1982. Mathematical modeling of the behavior of geothermal systems under exploitation (Ph.D. thesis). Lawrence Berkeley Laboratory Report LBL-13937, p. 18–48.

IENER (Institute d'economie et aménagements ènergetiques), 1983. Premier cycle d'exploitation de l'installation pilote SPEOS. IENER No. 703.217.

Weres, O., and Schroeder, R.C., 1978. Documentation for program OGRE. Lawrence Berkeley Laboratory Report LBL-7060, 58 p.

A New Method for Evaluating Composite Reservoir Systems

S.M. Benson and C.H. Lai

Increased interest in complex hydrogeologic and hydrocarbon systems has stimulated the development of advanced pressure transient techniques for evaluating reservoir heterogeneity. For example, techniques for enhanced recovery of energy and fluid from oil and geothermal reservoirs require injection of fluid to sweep the in situ resources to production wells. Once fluid is injected, the system is nonuniform, and the effects of the nonuniformity must be considered if information is to be gained by analyzing pressure transient data obtained from such systems. Other examples of complex hydrogeologic systems are met in the assessment of naturally fractured geologic settings under consideration for isolation of nuclear waste and in the evaluation of the natural state of fractured geothermal systems.

Common types of heterogeneity can be broadly grouped as areally distributed or areally limited heterogeneities. The difference between the two groups depends on whether (1) the heterogeneity is distributed over the system (e.g., reservoir layering and uniformly fractured rock) or (2) the heterogeneity has well-defined spatial limits (e.g., an isolated fracture zone or the region behind a flood front). Categorization of heterogeneity also depends to some extent on the scale of the problem considered. For pressure transient testing, the scale is a temporal one, governed by the diffusivity ($k/\phi\mu c$) of the rock/fluid system. For instance, during a short-term test, the reservoir may behave as a uniform system, but a long-term test might be influenced by a nonuniformly distributed heterogeneity.

One of the important tasks of evaluating a system is to establish the nature of the geologic heterogeneity. The difficulty arises because many of the common types of heterogeneity have similar "pressure transient signatures," and analysis usually relies on the details of these signatures to extract information from the data. For instance, the shape of a pressure drawdown curve versus time may be nearly identical for composite reservoir systems and double-porosity systems. The pressure transient data from such heterogeneous systems can be easily misinterpreted and the actual nature of the heterogeneity go undetected.

Conventional analysis techniques rely heavily on the shape of the early-time pressure transient response. Early-time data are influenced by the region close to the active well. Therefore, local heterogeneities dominate the pressure transient response and, if properly interpreted, can yield valuable information about the system. However, two difficulties are encountered when relying on early-time data. First, as mentioned previously, the "pressure transient signature" may be nonunique. Second, early-time data are strongly influenced by flow-rate variations and pressure measurement errors.

For composite systems (see Fig. 1), these difficulties can be avoided by analyzing the late-time pressure transient response rather than the early-time response. The late-time response is influenced by a much larger rock volume than is the early-time response. Therefore, small-scale heterogeneities (far from either the production well or the observation well) have little influence on the response, and the system behaves in a relatively uniform manner. Nevertheless, information about the local heterogeneity *is* contained in the data, but it must be extracted in a different manner. The following discussion outlines a simple graphical procedure for evaluating composite reservoir systems when data from several observation wells are available. The procedure can be used to calculate the mobility-thickness of the inner and outer regions, as well as the radial distance to the discontinuity separating the two regions. The technique is most useful in composite systems created by injection and production wells because it assumes that the active well is concentrically located in the inner region. However, it is also applicable to natural geologic systems in which the heterogeneity is roughly cylindrical and the active well is near the middle of the inner region.

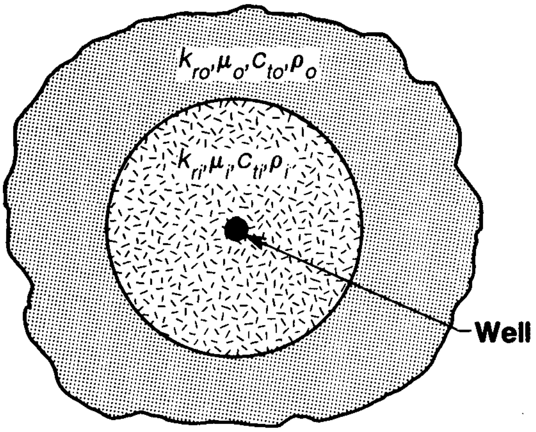

Figure 1. Schematic diagram of a composite reservoir. [XBL 854-10434]

COMPOSITE RESERVOIR ANALYSIS

The analytical procedure described below is based on the late-time asymptotic solutions developed by Ramey (1970) for drawdown (or buildup due to injection) in a composite reservoir. These solutions (one for the inner region and one for the outer region) are correct to within 1% for times (in seconds) greater than that given by

$$t > \frac{a^2}{0.04}\,\frac{1}{\eta_i}(1 - \eta_i/\eta_o), \tag{1}$$

where a is the radial distance to the discontinuity and η is the diffusivity ($k/\phi\mu c$). The subscripts i and o refer to the inner and outer region, respectively. The late-time asymptotic solutions for the drawdown in observation wells in the inner and outer regions are given by Eqs. (2) and (3):

$$\Delta p_i(r,t) = \frac{2.303q}{4\pi\lambda_o h} \cdot \left\{ \frac{\lambda_o}{\lambda_i} \log\left(\frac{a}{r}\right)^2 + \log t + \log \frac{\lambda_o}{\phi_o c_o a^2} + 0.351 \right\} \tag{2}$$

and

$$\Delta p_o(r,t) = \frac{2.303q}{4\pi\lambda_o h} \cdot \left\{ \log t + \log \frac{\lambda_o}{\phi_o c_o r^2} + 0.351 \right\}. \tag{3}$$

From the form of both equations, it is clear that a plot of the late-time data falls on a semilog straight line whose slope is proportional to the mobility (λ) of the outer region. For example, Fig. 2 shows a typical response for a well in the inner region. The early-time data show the influence of the inner region. The late-time transients, influenced by the outer region, fall on a semilog straight line.

For wells in either the inner region or the outer region, this semilog straight line can be extrapolated back to the point where $\Delta p = 0$ in order to evaluate t_o (see Fig. 2). From the value of t_o, the storativity (ϕch) can be calculated by

$$(\phi ch)_o = 2.24 \frac{t_o}{r^2} \lambda_o h \tag{4}$$

for the outer region or by

$$(\phi ch)_o = 2.24 \frac{t_o}{r^2} \lambda_o h (\frac{r}{a})^{2(1 - \lambda_o/\lambda_i)} \tag{5}$$

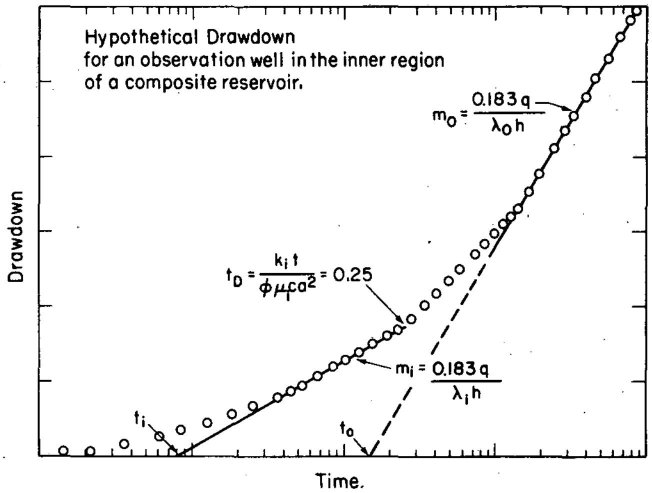

Figure 2. Semilog plot of the hypothetical drawdown for an observation well located in the inner region of a composite reservoir. [XBL 853-10373]

for the inner region. From the form of Eq. (5) it is clear that if $(\phi ch)_o$ is to be calculated using the late-time solution, an estimate of both the mobility of the inner region and the radius to the discontinuity are required. In general, this information is not available. However, if pressure transient data are available from more than one well in the inner region and one well in the outer region, the following procedure can be used to calculate the distance to the discontinuity and the mobility of the inner region. First, calculate λ_o and $(\phi ch)_o$ for the well in the outer region. Next, calculate λ_o and ϕch_a for wells in the inner region, where ϕch_a is defined by

$$\phi ch_a = 2.24 \lambda_o h \frac{t_o}{r_2}. \tag{6}$$

Next, note that by taking the logarithm of both sides of Eq. (5), we find that

$$\log(\phi ch_o / \phi ch_a) = 2(1 - \lambda_o/\lambda_i) \log(r/a). \tag{7}$$

This implies that on a log-log plot of $(\phi ch / \phi ch_a)$ versus r (r is the distance to the observation well), all of the data points from wells located in the inner region lie on a straight line with a slope of

$$b = 2(1 - \lambda_o/\lambda_i). \tag{8}$$

The mobility ratio between the inner and outer regions can be calculated from

$$\lambda_o/\lambda_i = 1 - b/2. \tag{9}$$

The radius of the inner region is calculated by extrapolating the straight line drawn through the data points to the point where

$$\phi ch / \phi ch_a = 1 \text{ and, therefore, } a = r. \tag{10}$$

EXAMPLE

The following data come from an interference test conducted in the Klamath Falls, Oregon, geothermal system (Benson, 1984; Benson and Lai, 1984; Benson et al., 1984). On the basis of geologic evidence, the system was initially thought to be a double-porosity reservoir in which fractures acted as high-permeability conduits and lower-permeability basaltic flows and volcanic sediments provided fluid storage capacity. The data were analyzed by means of a procedure in which the late-time asymptotic solution is used to evaluate the bulk characteristics of double-porosity reservoirs. The double-porosity parameters are evaluated by history-matching the early-time data (Lai et al., 1983). Consistency between the values of λh calculated for each of the observation wells indicated that, overall, the system behaved in a uniform manner. However, ϕch values range from 5.0×10^{-3} to 0.79 ft/psi. This large variation and the unreasonably high values of ϕch indicate that, for some of the wells, the double-porosity interpretation is incorrect.

The data were re-analyzed using the procedure described here. Figure 3 is a graph of $\phi ch_o/\phi ch_a$ versus distance from the pumped well. The data points fall on a fairly well defined straight line with a slope of 1.73. This indicates that $\lambda_i/\lambda_o = 7.4$. As shown in the figure, the radius of the inner region is 1600 ft. Re-evaluation of the hydrogeologic setting confirmed this interpretation to be the correct one (Benson and Lai, 1984; Benson and Lai, 1985).

CONCLUSION

A very simple graphical technique has been developed for evaluating composite reservoir systems. The technique relies on using the late-time data, thereby avoiding difficulties associated with relying heavily on the interpretation of the early-time pressure transient data. In addition to providing a new analysis technique, evaluation of the theory behind the technique shows that apparent variations in storativity can be sensitive indicators of variations in the reservoir mobility. Thus it provides another means for developing insight into the behavior of heterogeneous hydrogeologic systems.

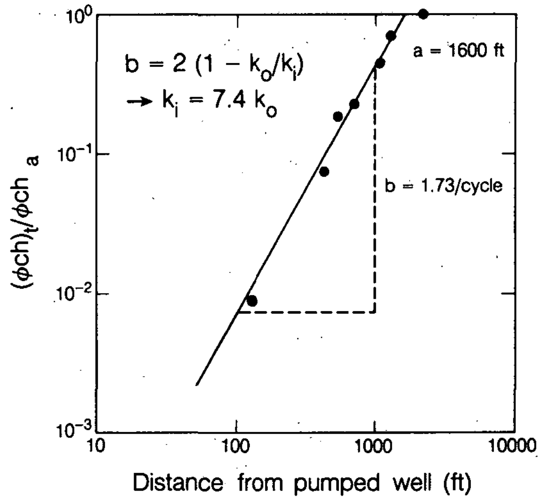

Figure 3. Composite reservoir analysis for the Klamath Falls interference data. [XBL 853-10370]

REFERENCES

Benson, S.M. (principal author), 1984. Data from pumping and injection tests and chemical sampling in the geothermal aquifer at Klamath Falls, Oregon. U.S. Geol. Surv. Open-File Report 84-146.

Benson, S.M., and Lai, C.H., 1984. Analysis of interference data in a highly heterogeneous and naturally fractured geothermal system. Presented at the 59th Annual Technical Conference and Exhibition of the Society of Petroleum Engineers of AIME, Houston, Texas, September 16–19, 1984 (SPE-11137).

Benson, S.M., and Lai, C.H., 1985. Interpretation of interference test data from the Klamath Falls, Oregon, geothermal system. *In* this Annual Report.

Benson, S.M., Sammel, E.N., Solbau, R.D., and Lai, C.H., 1984. Analysis and interpretation of the data obtained in tests of the geothermal aquifer at Klamath Falls, Oregon. *In* U.S. Geol. Surv. Open-File Report 84-4216, p. 5–1 to 5–23.

Lai, C.H., Bodvarsson, G.S., and Witherspoon, P.A., 1983. A new model for well-test data analysis in naturally fractured reservoirs. Presented at the 1983 California Regional Meeting of the Society of Petroleum Engineers of AIME, Ventura, California, March 23–25, 1983 (SPE-11688).

Ramey, H.J., Jr., 1970. Approximate solutions for unsteady liquid flow in composite reservoir. J. Can. Petrol. Technol., March, p. 32–37.

Interpretation of Interference Test Data from the Klamath Falls, Oregon, Geothermal System

S.M. Benson and C.H. Lai

It has long been recognized that interference testing is a valuable technique for evaluating reservoir properties. Pressure changes, measured in a passive well in response to pumping a nearby well, can be used to determine the permeability-thickness (*kh*) and the storativity (ϕch) of the formation. In addition, reservoir heterogeneities such as layering, double-porosity, boundaries, and anisotropy can be detected.

During the summer of 1983, a 7-week interference test, in which over 50 wells were monitored, was conducted in the Klamath Falls, Oregon, geothermal aquifer (Benson, 1984). The Klamath Falls geothermal anomaly is a shallow (< 2000 ft), moderate-temperature (100°C) geothermal system situated in rocks of primarily volcanic origin. Over 450 wells have been drilled into the aquifer. These show that the porosity and permeability of the system are attributable to both andesitic flows and lacustrine volcanic sediments.

Although many wells have been drilled and considerable effort has been devoted to developing a geologic model of the area, the hydrogeologic characteristics of the reservoir remain ill defined because correlation of individual rock strata is often difficult, if not impossible, even over distances as short as 100 ft. The central area of the geothermal anomaly is transected by a northwest-trending normal fault that is presumably the primary conduit along which thermal fluids rise from great depths to the surface. The geologic complexity is believed to be the result of a varying depositional environment and faulting.

One of the objectives of the interference test was to determine the effect of the geologic heterogeneity of the hydrologic behavior of the geothermal reservoir. As mentioned above, interference testing can be a useful tool for detecting hydrologic heterogeneity. However, since the pressure responses for many of the common types of reservoir heterogeneity are very similar, a sufficiently accurate geologic model is required for an accurate analysis of the interference data. In Klamath Falls, the complexity of the system precludes development of a hydrogeologic model based on geologic data alone. Therefore, only by combining both types of data is it possible to develop a convincing model of the system.

INTERFERENCE TEST

The interference test, which covered a 7-week period in July–August 1983, consisted of measuring water level changes in 52 wells while pumping and injection operations were in progress in two other wells. For the first 3 weeks, city well 1 (CW-1) was pumped at a rate of 24,700 bbl/day (43.5 kg/s). For the final 4 weeks, water was pumped from CW-1 and concurrently reinjected into the County Museum well. Figure 1 shows the pumping and reinjection schedule. The figure also shows the downhole pressure response at one of the observation wells. During the first phase of the test, the pressure dropped (approximately 1.7 psi in this well). After reinjection began, the pressure gradually increased to within 0.4 psi of the original value. This response is typical of all of the observation wells.

Wells extending over an area of about a square mile were monitored during the interference test. Observation, pumping (CW-1), and injection

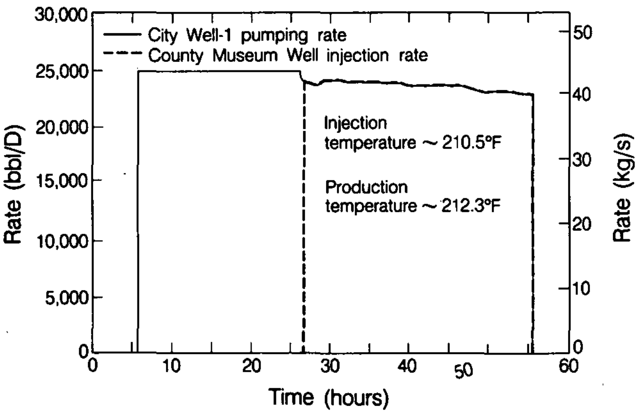

Figure 1. Pumping, injection, and observation well data from the interference test. [XBL 849-9920]

(County Museum) well locations are shown in Fig. 2. Well depths range from 250 ft to over 1200 ft. However, each well penetrates at least part of the same reservoir (as is evident from the test and drilling data).

DATA ANALYSIS

The layered and fractured nature of the reservoir rock, the interpretation of previous short-term tests, and the shape of the drawdown curves (e.g., see Fig. 3) indicate that a double-porosity or layered model describes the system best. Therefore, all of the interference test data were analyzed with two techniques applicable to such systems: a type-curve-matching technique developed by Deruyck et al. (1982) and a semilog history-matching technique developed by Lai et al. (1983).

The analysis shows that, overall, the individual wells behaved in a remarkably uniform manner (Benson et al., 1984b). All of the interference data show that the permeability-thickness is approximately 1.4×10^6 millidarcy·feet (md·ft). On the other hand, calculated values for ϕch varied by over two orders of magnitude, from 5.0×10^{-3} ft/psi to 0.79 ft/psi. The double-porosity model cannot explain the high values of ϕch or the large range of values.

Closer inspection of the values of ϕch showed that they vary in a systematic manner. For wells close to the pumped well (CW-1), ϕch appears to increase with decreasing distance to the observation well. This type of behavior indicates that some of the wells are influenced by a composite reservoir system (see Fig. 1 of preceding article) rather than a double-porosity system (Benson and Lai, 1984). Using a new analysis technique in which the data are analyzed on the basis of the late-time asymptotic solution for a composite reservoir, it is possible to calculate the kh of the outer and inner regions, the ϕch of the outer region, and the radial distance to the boundary between two regions (Benson and Lai, 1984, 1985). This analysis indicates that the outer region has a permeability-thickness of approximately 1.4×10^6 md·ft and a ϕch of 5×10^{-3} ft/psi. The inner region, which has a radius of approximately 1600 feet, is centered on CW-1 and is 7.5 times more permeable than the outer region.

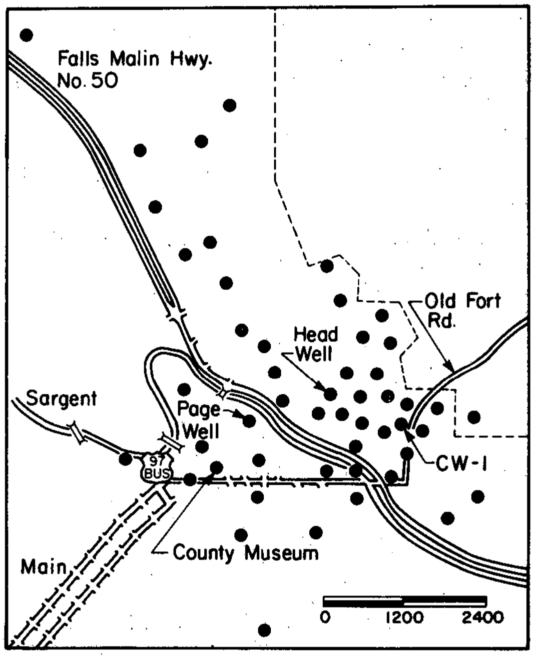

Figure 2. Location map showing observation wells. [XBL 853-10374]

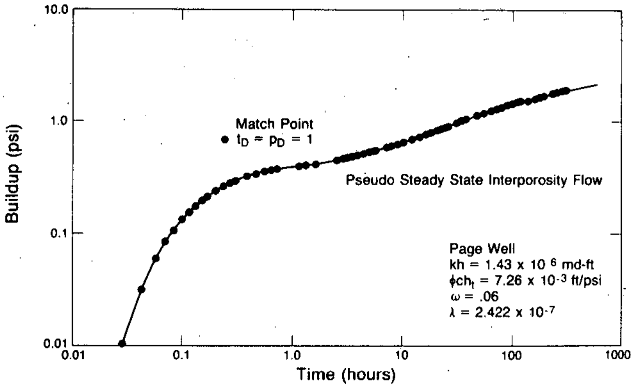

Figure 3. Double-porosity type-curve match for the Page well (no. 177) build-up. [XBL 844-10484]

Geologic data alone give no indication of the composite nature of the reservoir. Therefore, in light of the unanticipated results, additional evidence was sought for the existence of a high-permeability region. One such evidence comes from a graph of observation well drawdown versus distance to the pumped well. For a homogeneous reservoir at semi-steady state, all of the data points should fall on a single straight line whose slope is inversely proportional to kh. Figure 4 shows the drawdown at several of the wells after 336 hours of pumping. The data points do not fall on a single straight line. Instead, with the exception of one data point, the data fall on two straight lines. The permeabilities of these two regions, calculated from the slopes of these lines, are 1.06×10^7 and 1.43×10^6 md·ft, respectively. The permeability calculated for the outer region agrees well with the average formation permeability calculated from the pressure transient

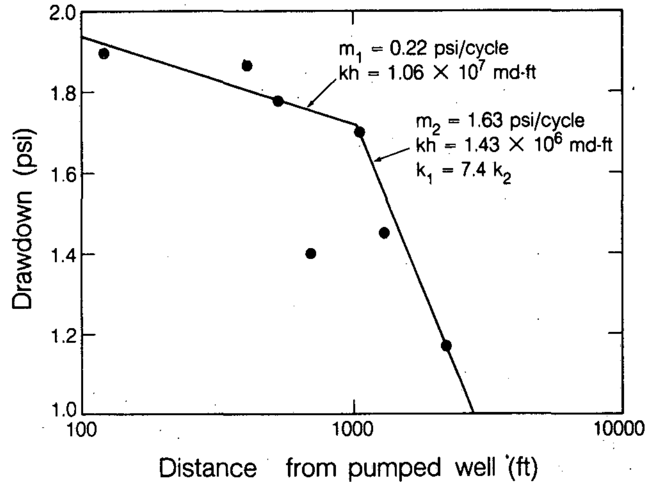

Figure 4. Pressure drawdown (at 336 hours) versus distance to the pumping well. [XBL 848-9913]

analysis. Furthermore, the ratio of the inner to outer region permeability is approximately 7.4, the same value as that obtained from the above analysis.

Consideration of the geologic setting gives additional validity to this interpretation. A major range-front normal fault is known to transect the area. It was anticipated that the fault would manifest itself either as a constant-pressure or no-flow linear boundary. Instead, the fault was essentially invisible to hydrologic testing. It is proposed that, within a limited area, the fault is not a single linear fracture but a broad region coincident with the high-permeability region detected by the interference test.

CONCLUSIONS

The results of the analysis can be summarized as follows. Interference data from the Klamath Falls geothermal reservoir indicate that it is both a double-porosity and composite reservoir. Representative values of the formation parameters calculated from these models are $kh = 1.4 \times 10^6$ md·ft, $\phi ch = 5 \times 10^{-3}$ ft/psi, $\lambda = 1 \times 10^{-7}$, and $\omega = 1 \times 10^{-2}$. The pumped well is located in a region that is approximately 7.5 times more permeable than the rest of the reservoir. This region is believed to coincide with a broad fault zone that transects the area.

REFERENCES

Benson, S.M. (principal author), 1984. Data from pumping and injection tests and chemical sampling in the geothermal aquifer at Klamath Falls, Oregon. U.S. Geol. Surv. Open-File Report 84-146.

Benson, S.M., and Lai, C.H., 1984. Analysis of interference data in a highly heterogeneous and naturally fractured geothermal system. Presented at the 59th Annual Technical Conference and Exhibition of the Society of Petroleum Engineers of AIME, Houston, Texas, September 16–19, 1984 (SPE-11137).

Benson, S.M., and Lai, C.H., 1985. A new method for evaluating composite reservoir systems. *In* this Annual Report.

Benson, S.M., Sammel, E.N., Solbau, R.D., and Lai, C.H., 1984. Analysis and interpretation of the data obtained in tests of the geothermal aquifer at Klamath Falls, Oregon. *In* U.S. Geol. Surv. Open-File Report 84-4216, p. 5-1 to 5-23.

Deruyck, B.G., Bourdet, D.P., Da Prat, G., and Ramey, H.J., Jr, 1982. interpretation of interference tests in double-porosity reservoirs—Theory and field example. Presented at the 57th Annual Meeting of the Society of Petroleum Engineers of AIME, New Orleans, Louisiana, September 26–29, 1982.

Lai, C.H., Bodvarsson, G.S., and Witherspoon, P.A., 1983. A new model for well-test data analysis in naturally fractured reservoirs. Presented at the 1983 California Regional Meeting of the Society of Petroleum Engineers of Aime, Ventura, California, March 23–25, 1983 (SPE-11688).

Geologic Interpretation of East Mesa from Well-Log Analysis

S.E. Halfman

The moderate-temperature, low-salinity, liquid-dominated East Mesa geothermal field (Fig. 1) is located in the Imperial Valley, southern California, about 110 miles east of the San Diego metropolitan area. This valley is part of the Salton trough—an actively developing structural depression that hosts a number of geothermal systems, some of which are under development for electrical power generation.

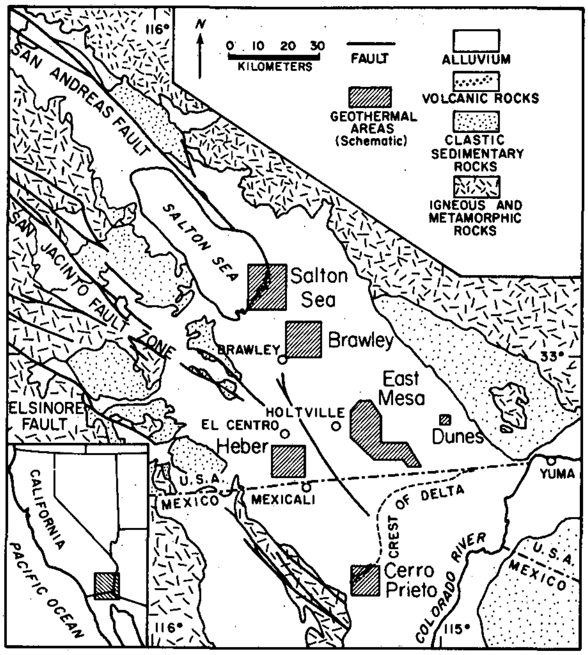

Figure 1. Location of geothermal areas in the Salton trough (after Elders et al., 1978). [XBL 7912-13479]

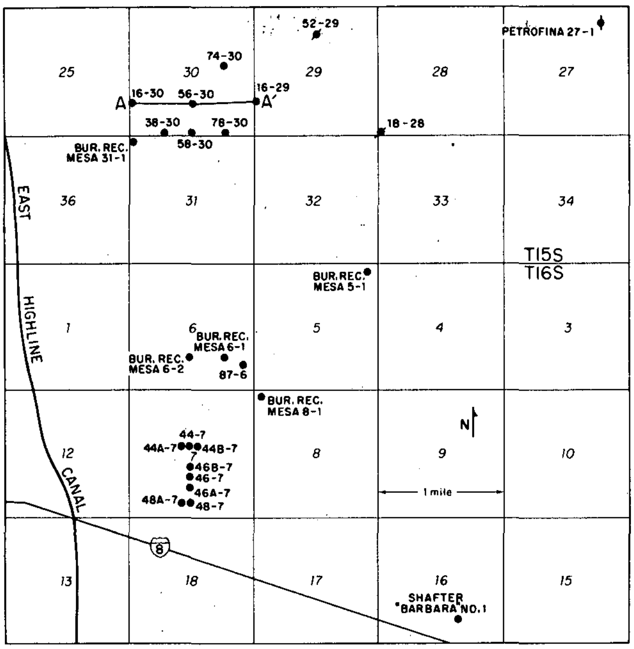

Figure 2. Location of wells and cross section A–A′ at East Mesa. [XBL 8412-6184]

At East Mesa, power production began in 1982 with a 10-MW binary plant owned by Magma Power Company.

A geologic model of part of this geothermal field was developed to allow prediction of fluid and heat movement. This model was then used to help plan a nonisothermal injection study for well 56-30 (Fig. 2). The subsurface stratigraphy at East Mesa is characterized mainly by complex interfingering of late Cenozoic Colorado River delta deposits (van de Kamp et al., 1978). The well logs from the northern portion of the field (in the vicinity of well 56-30) were analyzed to develop a geologic model, to determine geologic factors that are influencing the flow of geothermal fluids, and to identify postdepositional changes in the sedimentary rocks for this portion of the field. The approach used to analyze the well logs is similar to the one applied to study the high-temperature (up to 370°C) Cerro Prieto geothermal field of Baja California, Mexico (Halfman et al., 1984, Fig. 1). At Cerro Prieto it was shown that the upward subsurface movement of the geothermal fluids is controlled by the continuity of the shale layers and by major normal faults. Similar results were expected at East Mesa.

METHODOLOGY

On the basis of wire-line log data, the East Mesa sedimentary column was divided into three lithofacies groups: sandstone, sandy-shale, and shale. Basically, sandstone beds are thick, permeable, and well defined (with some interbedded shales) in the sandstone group, but are thinner and less permeable (with a higher percentage of intercalated shales) in the sandy-shale group, and even thinner (usually < 10 ft) in the shale group. After assigning the beds to different lithofacies groups, lithofacies cross sections were constructed, incorporating faults determined from the correlation of certain stratigraphic layers. To establish possible fluid flow patterns, downhole temperature profiles (Kassoy and Goyal, 1979; P. Parmentier, personal communication, 1984) and depth of well-production intervals (Narasimhan et al., 1977; P. Parmentier, personal communication, 1984) were superimposed on these cross sections.

RESULTS

The geologic cross section A–A′ (Fig. 3) shows that the upper 4200 ft of the sedimentary column corresponds predominately to the shale lithofacies group, with smaller percentages of interbedded sandstone and sandy-shale groups. The lower portion of this section consists mostly of deposits of the sandstone group (about 2500–3000 ft thick), which are underlaid mainly by deposits of the shale group.

With the incorporation of temperature data and depths of production intervals, a conductive heat zone can be identified above a depth of 2500 ft and a

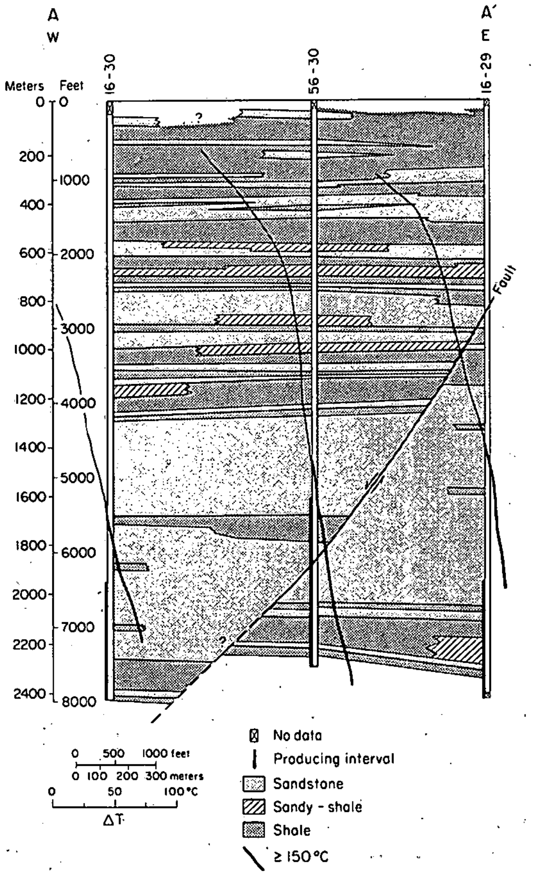

Figure 3. Lithofacies cross section A–A′, showing well locations, lithofacies groups, faults, temperature profiles, and producing intervals. On the temperature profiles, points corresponding to 150°C are placed under the location of the respective wells. Parts of temperature profiles shown by heavy lines indicate temperatures of 150°C or higher. [XBL 8410-9989]

zone of heat convection below that depth. The explanation for this difference in heat transfer may be that the shale layer at 2500 ft deep acts as a caprock to the upward flow of geothermal fluid. However, the well-log characteristics for this layer are quite different from those of the (discontinuous) caprock identified at Cerro Prieto. The shale layer at East Mesa lacks the highly densified sediments (as interpreted from well-log data) so characteristic of the Cerro Prieto caprock (Halfman et al., 1984). The difference in the densification of these shale layers is due to the lower subsurface temperature at East Mesa; the temperature at the base of the caprocks is about 120°C at East Mesa and about 300°C at Cerro Prieto.

At East Mesa, heat convection occurs predominately in a thick sandstone group shown in the lower portion of cross section A–A′ and in the sandy-shale part of the underlying shale group. Although geothermal fluid (about 150°C) flows through the lower parts of this section, the direction of flow cannot be discerned. Surprisingly, the fault shown in Fig. 3 does not seem to affect the migration of geothermal fluid, as is the case for faults at the Cerro Prieto field.

HYDROTHERMAL ALTERATION OF THE EAST MESA SEDIMENTS

The correlation of wire-line well-log data with hydrothermal alteration of sedimentary rocks has been studied at Cerro Prieto. Results show that the onset of hydrothermal alteration is marked by a density increase in both sandstones and shales, the relative changes being greater in the shales (Lyons and van de Kamp, 1980). Furthermore, the degree of alteration reflected by the change in the mineralogy of the sediments can be correlated with changes in the character of the wire-line well logs (Seamount and Elders, 1981). At Cerro Prieto, it is possible to identify from the logs the general transition from a zone of unaltered montmorillonite ($T < 150°C$) to hydrothermally altered zones of illite (150–230° to 245°C), chlorite (235–300°C), and feldspar (> 300°C).

On the basis of the preceding results, it was possible to determine zones of hydrothermal alteration at East Mesa from the wire-line logs. For example, the onset of hydrothermal alteration can be seen in well 56-30 at about 3600 ft depth (Fig. 4), as evi-

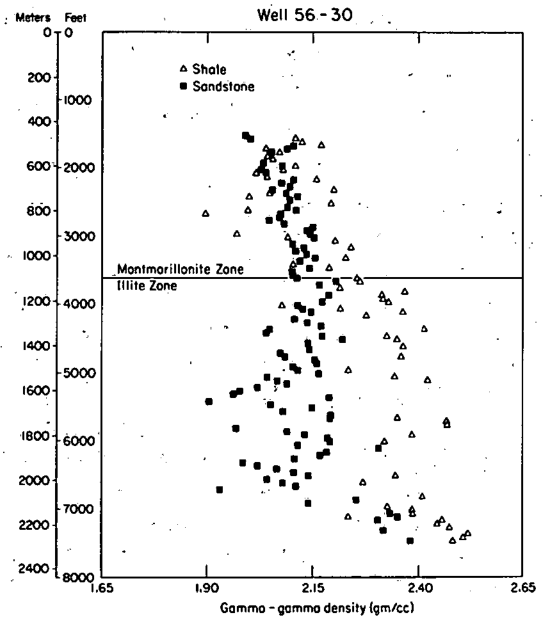

Figure 4. Density-depth plot in East Mesa well 56-30, illustrating the marked increase in shale densities with the onset of hydrothermal alteration, indicated by the top of the illite zone. [XBL 8410-9988]

denced by the noticeably increased shale densities. Above that depth, there is the unaltered montmorillonite zone; below it, the altered illite zone. The depth to the zone of hydrothermal alteration is also indicated by other wire-line log data (e.g., deep induction logs). The wire-line well-log data do not indicate the presence of higher-temperature alteration zones, suggesting that East Mesa has always been a moderately low temperature geothermal system, which is consistent with the present-day temperatures measured in the field.

REFERENCES

Elders, W.A., Hoagland, J.R., Olson, E.R., McDowell, S.D., and Collier, P., 1978. A comprehensive study of samples for geothermal reservoirs. Riverside, University of California Report UCR/IGPP-78/26, 264 p.

Halfman, S.E., Lippmann, M.J., Zelwer, R., and Howard, J.H., 1984. Geologic interpretation of geothermal fluid movement in Cerro Prieto field, Baja California, Mexico. Am. Assoc. Petrol. Geol. Bull., v. 68, p. 18–30.

Kassoy, D.R., and Goyal, K.P., 1979. Modeling heat and mass transfer at the East Mesa geothermal anomaly, Imperial Valley, California. Lawrence Berkeley Laboratory Report LBL-8784, 171 p.

Lyons, D.J., and van de Kamp, P.C., 1980. Subsurface geological and geophysical study of the Cerro Prieto geothermal field, Baja California, Mexico. Lawrence Berkeley Laboratory Report LBL-10540, 95 p.

Narasimhan, T.N., Schroeder, R., Goranson, C., McEdwards, D.G., Campbell, D.A., and Barkman, J.H., 1977. Recent results from tests on the Republic geothermal wells at East Mesa, California. *In* Proceedings, 3rd Workshop on Geothermal Reservoir Engineering, Stanford University, Stanford, California, December 14–16, 1977. Stanford Geothermal Program Report SGP-TR-30, p. 116–124.

Seamount, D.T., and Elders, W.A., 1981. Use of wireline logs at Cerro Prieto in identification of the distribution of hydrothermally altered zones and dike locations, and their correlation with reservoir temperatures. *In* proceedings, Third Symposium on the Cerro Prieto Geothermal Field, Baja California, Mexico, March 24–26, 1981. Lawrence Berkeley Laboratory Report LBL-11967, p. 123–133.

van de Kamp, P.C., Howard, J.H., and Graf, A.N., 1978. Geology (Section 1). *In* J.H. Howard (principal editor), Geothermal resource and reservoir investigations of U.S. Bureau of Reclamation leaseholds at East Mesa, Imperial Valley, California. Lawrence Berkeley Laboratory Report LBL-7094, p. 1–32.

Analysis of Production Data from the Krafla Geothermal Field, Iceland

K. Pruess and G.S. Bodvarsson

Many high-temperature geothermal fields contain boiling fluids. When the pore space is filled with a mixture of vapor and liquid phases, the flow of one phase is impeded by the presence of the other. The permeability reduction for each phase is customarily expressed by relative permeability functions, which are thought to depend primarily upon phase saturations (volume fractions of gas and liquid phases). Numerous studies have shown that predictions of geothermal reservoir behavior are strongly dependent upon the choice of relative permeability functions. There is an extensive literature on gas-oil and oil-water relative permeabilities, but steam-water relative permeabilities are poorly known. In this study we have used production data from the Krafla geothermal field, Iceland, to obtain insight into relative permeabilities and other reservoir parameters.

PRODUCTION DATA

Krafla wells completed in two-phase zones show strong transients in flow rate and enthalpy when first put into production. As a typical example of this behavior, Fig. 1 shows production data from well 12. Initially the well produced approximately 14 kg/s of water and 20 kg/s of steam from a reservoir at a temperature of approximately 320°C. Within a few days water production ceased, and steam production

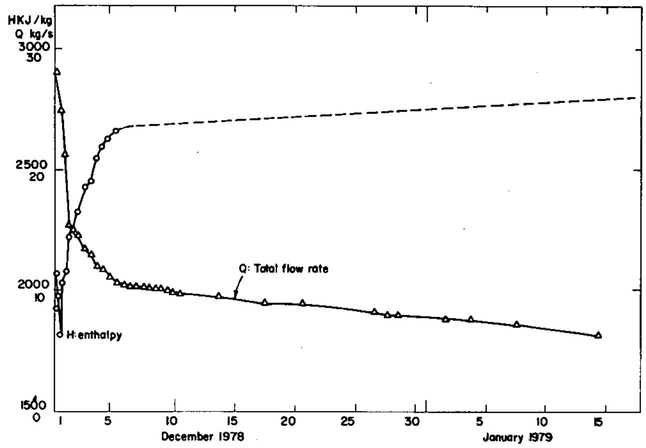

Figure 1. Production data for well 12. [XBL 837-1916]

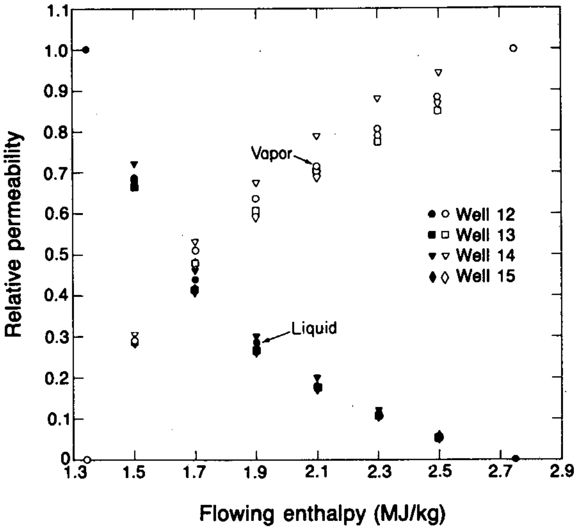

Figure 2. Relative permeability obtained from smoothed field data. [XBL 8312-7415]

dropped to approximately 10 kg/s. After three months steam production had declined to 6 kg/s, while enthalpy continued to increase slowly.

When plotting the flow-rate data versus flowing enthalpy, most data points fall on smooth curves. We have used smoothed field data to study the relative permeability behavior of wells 12 through 15. Using the analysis method of Grant (1977), we obtained relative permeability curves that are rather different for the different wells. Grant's method assumes a well index independent of flowing enthalpy. This appears to be a poor approximation, because flowing downhole pressures are known to vary considerably with flowing enthalpy. Assuming a linear dependence of well index upon flowing enthalpy, we obtained the relative permeabilities shown in Fig. 2. The results for wells 12, 13, and 15 practically collapse into single curves, with well 14 showing a somewhat different behavior. Figure 2 also shows that the sum of liquid and vapor relative permeabilities is close to 1 over the entire range of flowing enthalpies. A similar conclusion was reached by Bodvarsson et al. (1983) on the basis of steam-rate transients observed at the separators for well 13 in response to water injection into nearby well 7. It is also interesting to note that the relative permeability curves shown in Fig. 2 are rather similar in shape to the theoretical streamtube model predictions of Menzies (1982) and Gudmundsson et al. (1983).

It should be emphasized that the relative permeability information obtained from the above analysis remains incomplete, because the in-place vapor saturations corresponding to different flowing enthalpies are unknown. Indeed, any relative permeability functions $k_{r\beta}$ (β = liquid, vapor) with monotonic dependence upon vapor saturation S are compatible with the results of our analysis, as long as the constraint $k_{r\ell}(S) + k_{rv}(S) \approx 1$ is satisfied.

FLOW RATE AND ENTHALPY TRANSIENTS

The foregoing relative permeability analysis employs only the observed correlation between flow rates and enthalpies. Additional information can be extracted from the actual time dependence of these parameters. Using our numerical simulators SHAFT79 and MULKOM, we have modeled the flow rate and enthalpy transients for well 12. An extensive parameter search was made in an effort to match observed transients with a model of uniform vapor saturation. It was found that calculated enthalpies rise much more rapidly than observed in the field in all cases. By switching to a model of nonuniform vapor saturation, with larger liquid content near the well, several excellent matches were obtained with both flow rates and enthalpies (Figs. 3 and 4). Thus for many formation parameters it is not possible to obtain an unambiguous identification from the production data (see Table 1). The only unambiguous piece of information appears to be the "excess mass," M_{ex}, present near the well because of the larger liquid saturation there. It is interesting to note that M_{ex} compares favorably with the amount of water injected at the end of drilling into Krafla wells to stimulate production and to facilitate well logging. The total injectate has been estimated at 3000–5000 tons on the average (S. Benediktsson, personal communication, 1982; no specific figure for well 12 is available). Thus it appears that the water

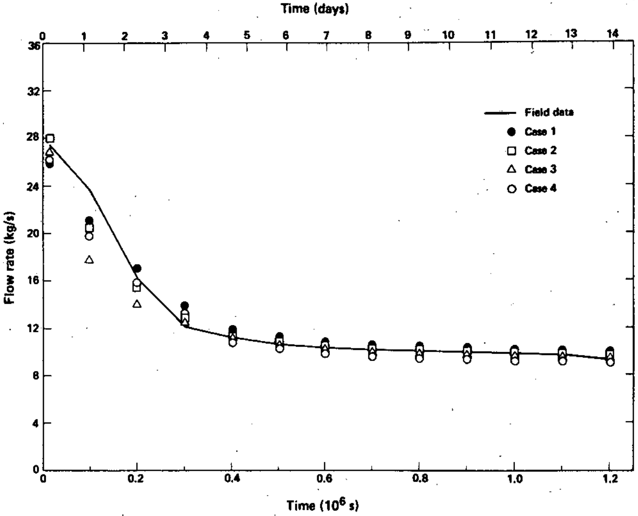

Figure 3. Comparison between calculated and observed flow rates for well 12. [XBL 8210-4728]

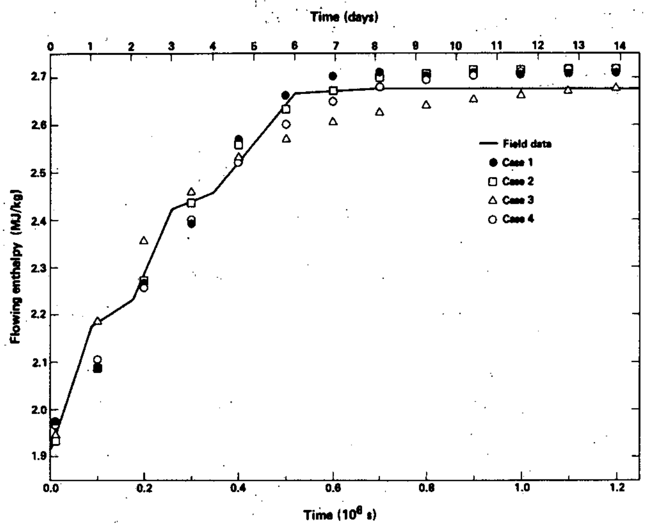

Figure 4. Comparison between calculated and observed enthalpies for well 12. [XBL 8210-4727]

Table 1. Parameters used in matching transients.

Parameter	Case 1	Case 2	Case 3	Case 4
Relative permeability functions	Smoothed linear	Smootheed linear	Corey	Smoothed linear
Irreducible liquid saturation	0.40	0.50	0.30	0.40
Irreducible steam saturation	0.05	0.05	0.0	0.05
Vapor saturation at distance from the well	0.65	0.55	0.50	0.65
Vapor saturation near well	0.24	0.16	0.06	0.24
Porosity	0.015	0.06	0.06	0.06
Radius of near zone (m)	20	10	10	10
"Excess" mass (10^6 kg)	4.66	4.43	5.00	4.66

injected into the well during drilling and completion remains in the vicinity of the well bore during several weeks of warmup.

REFERENCES

Bodvarsson, G.S., Pruess, K., and O'Sullivan, M.J., 1983. Injection and energy recovery in fractured geothermal reservoirs. Presented at the 53rd California Regional Meeting of the Society of Petroleum Engineers of AIME, Ventura, California, March 23–25,1983 (SPE-11689).

Grant, M.A., 1977. Permeability reduction factors at Wairakei. Presented at AICHE–ASME Heat Transfer Conference, Salt Lake City, Utah, August 1977 (77-HT-52).

Gudmundsson, J.S., Menzies, A.J., and Horne, R.N., 1983. Streamtube relative permeability functions for flashing steam-water flow in fractures. Presented at the 53rd California Regional Meeting of the Society of Petroleum Engineers of AIME, Ventura, California, March 23–25, 1983 (SPE-11686).

Menzies, A.J., 1982. Flow characteristics and relative permeability functions for two-phase geothermal reservoirs from a one dimensional thermodynamic model. Stanford Geothermal Program Report SGP-TR-59.

Studies of Enthalpy and CO_2 Transients

G.S. Bodvarsson

For wells penetrating a two-phase reservoir with both phases (liquid and steam) mobile, significant transient changes in enthalpy and CO_2 content of the produced fluids can occur. Model studies have shown that for a constant rate of production the enthalpy will increase at early times and then stabilize (Sorey et al., 1980; O'Sullivan, 1981). The rise in flowing enthalpy depends on various factors such as porosity, permeability (or flow rate), initial vapor saturation, and relative permeabilities (Bodvarsson et al., 1980; Sorey et al., 1980). Enthalpy increases of over 1000 kJ/kg have been observed for some wells completed in the Krafla reservoir in Iceland (Stefansson and Steingrimsson, 1980). Many wells that exhibit a large, early enthalpy rise will show a gradual decline in the long run.

In general, little is known about the transient behavior of noncondensible gases in produced fluid. Many reservoirs contain large amounts of noncondensible gases, particularly CO_2. Pritchett et al. (1981) studied the transient CO_2 content during the discharge of a well completed in a homogeneous porous-medium reservoir. They found that the CO_2 content of the produced fluids cannot readily be correlated with the in situ content and may be either more or less than that in situ. O'Sullivan et al. (1983) state that the CO_2 content of the produced fluids, like the enthalpy, will reach a stable value after an initial short transient period (see also Grant, 1979). They also found that the stable CO_2 content does primarily depend upon the initial partial pressure of CO_2, the relative permeability functions, and the initial vapor saturation. The effects of porosity and flow rate on the stable CO_2 content are secondary.

Grant and Glover (1984) present enthalpy and CO_2 transient data from well BR-21 in Broadlands, New Zealand. They investigate various models, including homogeneous porous-medium and fracture models, in order to analyze the data. They conclude that the enthalpy transients can be explained only in terms of a fracture model because of the long period of enthalpy rise.

Most of the work to date on enthalpy and CO_2 transients has considered only constant-rate testing in homogeneous porous media. The purpose of this paper is to investigate enthalpy and CO_2 transients in more heterogeneous formations, allowing for variable flow rates. Some of the questions addressed are:

1. How do variations in hydrologic parameters such as porosity and permeability affect the stable enthalpy and CO_2 content?
2. Can enthalpy and CO_2 data give an estimate of the extent of the two-phase zone?
3. How do enthalpy and CO_2 transients for constant-pressure production differ from those observed during constant-rate production?

In order to answer some of these questions, numerical modeling techniques are employed.

APPROACH

A single-layer radial model is used for the simulations. It is a composite reservoir model, with two zones having different hydrologic properties (porosity and permeability) or initial vapor saturation (Fig. 1). The radial distance to the boundary between the two zones is fixed at r = 100 m. The reservoir parameters and initial conditions of the inner zone are the same in all simulations and are given in Table 1. Various cases are considered in which the properties of the outer zone are varied and the resulting enthalpy and CO_2 transients calculated. As a base case for comparison, the homogeneous reservoir case (identical properties for inner and outer zones) is modeled. In addition, the two extreme cases of no-flux and constant-pressure inner boundary (at r = 100 m) are simulated. In the work described here, the multicomponent simulator MUL-

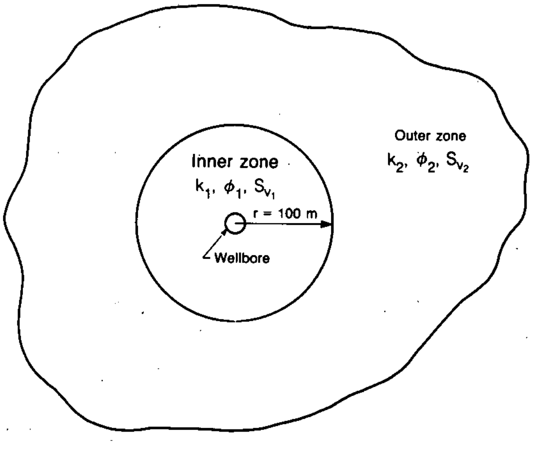

Figure 1. Radial model for simulation studies. [XBL 844-10435]

Table 1. Reservoir parameters and initial conditions of the inner zone.

Parameters	Initial conditions
Permeability	1.5×10^{-14} m^2 (15 md)
Porosity	2%
Rock density	2650 kg/m^3
Rock heat capacity	1000 J/kg
Thermal conductivity	2.0 W/m·°C
Initial pressure	97 bars
Initial vapor saturation	0.10
Initial partial pressure CO_2[a]	10 bars

[a] Used only when CO_2 transients are considered.

KOM (Pruess, 1983) is used with an equation of state for H_2O–CO_2 mixtures developed by O'Sullivan et al. (1985).

ENTHALPY TRANSIENTS

In this summary, only constant-pressure production is considered; similar constant-rate production studies are described elsewhere (Bodvarsson, 1984). Most geothermal wells are produced at constant downhole pressure.

The cases modeled are listed in Table 2. Note that for Cases B through F all parameters are identical to those of the base case except for the parameter value given. Figures 2 and 3 show results obtained for the enthalpy and CO_2 transients, respectively. If we first consider the base case, it can be seen that the enthalpy rises very rapidly because of the high flow rates at early times (a result of the constant-pressure production). After a short time the enthalpy starts to decline because of the decreasing flow rate. It should be noted that the enthalpy never reaches a stable value, as in the case of constant-rate production (Sorey et al., 1980; O'Sullivan, 1981), and the enthalpy decline becomes nearly linear on the semilog time plot. Note also in Fig. 2 that the rise in enthalpy occurs very early because of the rapid thermal equilibrium in porous media. Enthalpy transients for wells completed in fractured reservoirs can last much longer (Grant and Glover, 1984). In many cases the enthalpy transients may be prolonged because of nonuniform vapor saturation conditions near wells that have just come on line, particularly if drilling fluids and injected water remain in the vicinity of the well during the heating-up period (Pruess et al., 1983).

As shown in Fig. 2, all of the cases show identical response until the effects of the outer zone are felt (radius of influence exceeds 100 m). For the no-flux boundary conditions (Case B), the results are as expected: a rapid pressure decline is observed along with a rapid increase in enthalpy of the produced fluids. Also as expected, the effect of the constant-pressure boundary is to stabilize the well pressure and lower the flowing enthalpy, since the recharge enthalpy from the boundary will equal the initial flowing enthalpy in the system. When the outer zone has a higher initial vapor saturation (Case C), the pressure decline is slightly higher than that of the base case as a result of the reduced overall mobility

Table 2. Different cases simulated.

Case	Value for outer zone/boundary conditions
A	Base case
B	No-flux boundary (r = 100 m)
C	Initial vapor saturation 0.20
D	Permeability 30 md
E	Porosity 0.10
F	Constant-pressure boundary (r = 100 m)

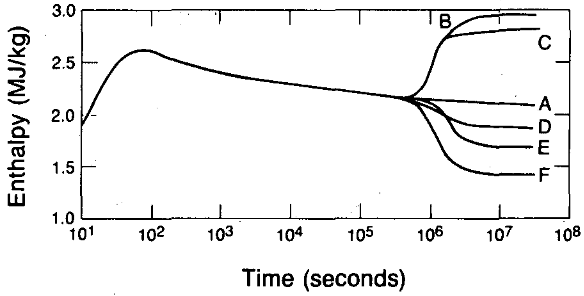

Figure 2. Constant-pressure production. Enthalpy variations with time for the different cases. [XBL 844-10382]

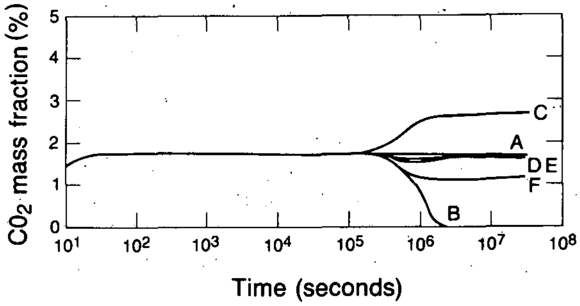

Figure 3. Constant-pressure production with CO_2, showing variations in CO_2 content with time for the different cases. [XBL 844-10386]

caused by the increasing vapor saturation. The enthalpy reaches a stable value that is identical to that observed if the vapor saturation is initially 20% everywhere.

The effects of porosity and permeability on enthalpy transients were studied by Sorey et al. (1980) and Bodvarsson et al. (1980). In general, the rise in enthalpy is inversely proportional to permeability but directly proportional to $(1 - \phi)/\phi$, where ϕ is the porosity (Bodvarsson et al., 1980). This is evident in Fig. 2, as both doubling the permeability and increasing the porosity of the outer zone cause a large decrease in the stable enthalpy.

We also studied a case in which a uniform porosity of 10% was specified for the entire reservoir (Bodvarsson, 1984). The results were interesting, since the long-term behavior in this case is identical to that in Case E (inner region porosity of $\phi = 0.02$). This implies that the long-term flow characteristics of a well are independent of the near-well porosity, although it dominates the early-time enthalpy rise.

In summary, spatial variations in porosity, permeability, and vapor saturation can greatly affect the enthalpy of the produced fluids. Proper analysis of such enthalpy transient data may give useful information on reservoir conditions: e.g., the extent of two-phase zones. Because of uncertainties about relative permeabilities, the enthalpy transients cannot give quantitative information on changes in the hydraulic parameters.

CO_2 TRANSIENTS

In the simulations a partial pressure of CO_2 of 10 bars is assumed; this corresponds to approximately 0.008% CO_2 per mass, which is the estimated CO_2 content of reservoir fluids at the Baca field, New Mexico (Pritchett et al., 1981).

Figure 3 shows that for the base case the stable CO_2 content exceeds that in situ; the rise in the CO_2 content is 0.5%. For the closed reservoir (Case B), the CO_2 content goes to zero when the vapor saturation approaches unity. On the other hand, the CO_2 content increases greatly when the effects of the higher vapor saturation in the outer zone are felt (Case C). In this case the stable CO_2 content increases by 1.1% for a change of only 0.1 in the initial vapor saturation. This increase is due to the low solubility of CO_2 in the liquid phase; most of the CO_2 is in the gas phase. Also of interest is the fact that the stable CO_2 content does not significantly depend upon the porosity and permeability of the medium. This is consistent with results of O'Sullivan et al. (1983). Theoretically this implies that careful monitoring of enthalpy and CO_2 content of the produced fluids can help identify changes in radial vapor saturation or in hydrologic parameters. If the enthalpy changes but the CO_2 content remains the same, spatial variations in the hydrologic parameters may be the cause. However, if the CO_2 content also changes, this would imply spatial changes in vapor saturation.

CONCLUSIONS

From the numerical simulation studies, the following conclusions can be made (for details see Bodvarsson, 1984):

1. Radial variations in hydrologic parameters and vapor saturation have a large effect on the enthalpy of the produced fluids.
2. The near-well porosity and vapor saturation have strong effects on the rise in flowing enthalpy, but the long-term stable enthalpy is independent of both.
3. The enthalpy transients for a well produced at a constant bottom-hole pressure show a sharp initial rise due to high flow rates but a gradual decline thereafter. This is consistent with data from many geothermal wells.
4. Radial variations in hydrologic parameters cause rapid changes in flow rates for wells produced at constant pressure. Most of the flow-rate changes are due to mobility effects.
5. Radial variations in vapor (gas) saturation have a large effect on the CO_2 content of produced fluids, but the CO_2 content is unaffected by variations in permeability and porosity.
6. Careful monitoring of both enthalpy and CO_2 content of produced fluids may help determine the extent of two-phase zones and variations in hydrologic parameters.

REFERENCES

Bodvarsson, G.S., 1984. Numerical studies of enthalpy and CO_2 transients in two-phase wells. Geothermal Resour. Counc., Trans., v. 8, p. 289–294.

Bodvarsson, G.S., O'Sullivan, M.J., and Tsang, C.F., 1980. The sensitivity of geothermal reservoir behavior to relative permeability parameters. *In* Proceedings, 6th Workshop on Geothermal Reservoir Engineering, Stanford University, Stanford, California, December 16–18, 1980. Stanford Geothermal Program Report SGP-TR-50, p. 224–237.

Bodvarsson, G.S., Pruess, K., Stefansson, V., and Eliasson, E.T., 1984. The Krafla geothermal field, Iceland. 2. The natural state of the system. Water Resour. Res., v. 20, no. 11, p. 1531–1544.

Grant, M.A., 1979. Water content of the Kawah Kamojang geothermal reservoir. Geothermics, v. 8, p. 21–30.

Grant, M.A., and Glover, R.B., 1984. Two-phase heat and mass transfer experiment at well BR-21, Broadlands. Geothermics, in press.

Grant, M.A., and Sorey, M.L., 1979. The compressibility and hydraulic diffusivity of water-steam flows. Water Resour. Res., v. 15, no. 3, p. 684-686.

O'Sullivan, M.J., 1981. A similarity method for geothermal well test analysis. Water Resour. Res., v. 17, no. 2, p. 390–398.

O'Sullivan, M.J., Bodvarsson, G.S., Pruess, K., and Blakeley, M.R., 1985. Fluid and heat flow in gas-rich geothermal reservoirs. Soc. Petrol. Eng. J., v. 25, no. 2, p. 215–222.

Pritchett, J.W., Rice, M.H., and Riney, T.D., 1981. Equation-of-state for water-carbon dioxide mixtures: Implications for Baca reservoir. La Jolla, California, Systems, Science, and Software Report DOE/ET/27163-8.

Pruess, K., 1983. Development of the general purpose simulator MULKOM. *In* Earth Sciences Division Annual Report 1982. Lawrence Berkeley Laboratory Report LBL-15500, p. 133–134.

Pruess, K., Bodvarsson, G.S., and Stefansson, V., 1983. Analysis of production data from the Krafla geothermal field, Iceland. *In* Proceedings, Ninth Annual Workshop on Geothermal Reservoir Engineering, Stanford University, Stanford, California, December 13–15, 1983, p. 345–351.

Sorey, M.L., Grant, M.A., and Bradford, E., 1980. Nonlinear effects in two-phase flow to wells in geothermal reservoirs. Water Resour. Res., v. 16, no. 4, p. 767–777.

Stefansson, V., and Steingrimsson, B., 1980. Production characteristics of wells tapping two-phase reservoirs at Krafla and Namafjall. *In* Proceedings, 6th Workshop on Geothermal Reservoir Engineering, Stanford University, Stanford, California, December 16–18, 1980. Stanford Geothermal Program Report SGP-TR-50, p. 49–59.

Modeling Studies of the Interaction Between Geothermal Reservoirs and Shallow, Unconfined Aquifers

G.S. Bodvarsson and K. Pruess

Numerical simulators developed for geothermal reservoir engineering applications generally consider only systems that are saturated with liquid water, steam, or both. However, most geothermal fields are in hydraulic communication with shallow aquifers having a free surface (water table), so that production or injection operations will cause movement of the surface and of the air in the pore spaces above the water table. In some geothermal fields the water table is located hundreds of meters below the surface [e.g., Olkaria, Kenya (Bjornsson, 1978)], so that an extensive unsaturated zone is present. In others the caprock may be very leaky or nonexistent [e.g., Klamath Falls, Oregon (Sammel, 1976); Cerro Prieto, Mexico (Grant et al., 1984)], in which case there is good hydraulic communication between the geothermal reservoir and shallow, unconfined (free-surface) aquifers. Thus there is a need to explore the effect of such aquifers on reservoir behavior during production or injection operations.

The water table in a free-surface aquifer moves in response to recharge or discharge. This results in a high overall storativity, typically two orders of magnitude higher than that of compressed liquid systems but one or two orders of magnitude lower than that for liquid–steam reservoirs. Consequently, various data analysis methods developed for compressed-liquid aquifers (such as conventional well-test analysis methods) are not applicable to aquifers with a free surface (Bodvarsson and Zais, 1982).

We have developed a numerical simulator for the modeling of air–steam–water systems. In this report we apply the simulator to various problems involving injection into or production from a geothermal reservoir in hydraulic communication with a shallow, free-surface aquifer. We first consider a one-dimensional column problem and study the water level movement during exploitation using different capillary pressure functions. Next we use a two-dimensional radial model to study and compare reservoir depletion for cases with and without a free-surface aquifer. Finally, we investigate the contamination of a shallow, free-surface aquifer due to cold water injection. The primary aim of these studies is to obtain an understanding of the response of a reservoir in hydraulic communication with an unconfined aquifer during exploitation or injection and to determine the circumstances under which conventional modeling techniques (fully saturated systems) can be applied to such systems.

METHODOLOGY

In our modeling studies we employ a numerical simulator called TOUGH (Pruess, 1984), which treats the two-phase flow of water and air in liquid and gaseous phases, together with heat flow, in a fully coupled way. The governing equations account for Darcy flow with relative permeability and capillary pressure effects. Gaseous diffusion can be handled also but has been omitted in the calculations presented here. The energy balance includes the latent heat effects of vaporization and condensation, along with conductive and convective heat flow. Water, air, and rock are assumed to be in local thermodynamic equilibrium at all times. The flow domain can include liquid, gaseous, and two-phase regions. The thermophysical properties of water substance are accurately represented by the steam table equations as given by the International Formulation Committee (1967). Air is approximated as an ideal gas, and additivity of partial pressures is assumed for air–vapor mixtures. The (small) solubility of air in liquid water is represented by Henry's law.

PRODUCTION FROM A VERTICAL COLUMN

The first problem considered consists of a vertical column with a main reservoir, a caprock, a shallow, unconfined aquifer, and an unsaturated zone. The grid used and the permeabilities assigned to different zones are shown in Fig. 1. The water table is located at a depth of 200 m; below that there is a shallow aquifer. The aquifer is separated by a 200-m-thick caprock from a 600-m-thick geothermal reservoir. Atmospheric conditions are maintained at the ground surface (P = 1 bar, T = 10°C). Parameters that do not vary spatially are given in Table 1.

The capillary pressure and the relative permeabilities are assumed to depend linearly on saturation. In general, capillary pressure functions depend greatly on the pore size distribution of the rocks, with larger capillary pressure for smaller pore size. We assume a maximum capillary pressure of 15 bars, which was chosen rather arbitrarily, but may be reasonable for the small pores typically found in volcanic rocks. The relative permeability functions used are linear, with 30% irreducible liquid saturation and 5% irreducible gas saturation. We have found that these functions are compatible with field data from the Krafla geothermal field, Iceland (Pruess et al., 1983).

Before exploitation, stable initial conditions were obtained for a constant heat flux of 0.75 W/m^2. Two cases were considered: capillary effects were neglected in one case and included in the other. Figure 2 shows that capillary effects tend to reduce sharp saturation gradients and expand the two-phase zone. On the other hand, when capillary effects are neglected, the gas saturation tends to stabilize at the irreducible liquid saturation (S = 0.7 for our relative

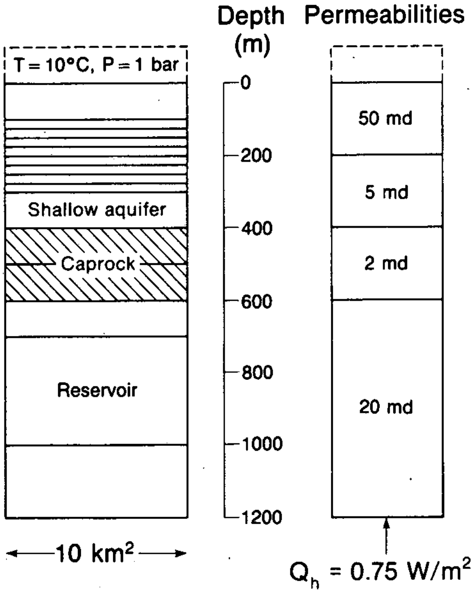

Figure 1. Schematic diagram of a one-dimensional, vertical-column model. [XBL 8312-7441]

Table 1. Specifications for column problems: parameters that do not vary spatially.

Parameters	Values
Porosity	10%
Rock grain density	2650 kg/m^3
Rock specific heat	1000 J/kg
Heat conductivity	2.0 W/m ·°C
Rock compressibility	0 Pa^{-1}

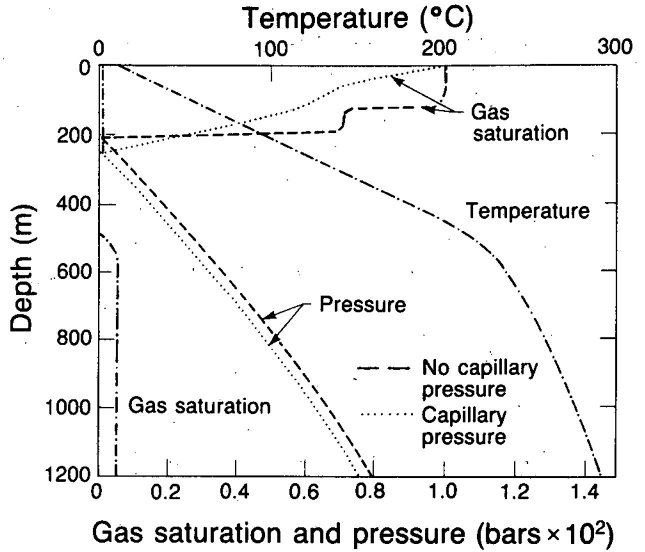

Figure 2. Initial thermodynamic conditions for the column problem. [XBL 8312-7437]

permeability curves). Because of the expanded unsaturated zone with pressure close to 1 bar, the case with capillary effects always has a slightly lower pressure. The temperature profile (identical for both cases) shows the two possible heat transfer mechanisms for this problem. In the upper part of the system the heat is transported mainly by conduction, resulting in a linear temperature profile with a large gradient. The main reservoir beneath the caprock is two phase, and heat is transported mainly by counterflows of steam and water with a smaller temperature gradient.

During exploitation 500 kg/s of fluid was produced from the reservoir (approximately equivalent to 50 MW_e). The results show that during exploitation the water level declines and steam saturation increases in the reservoir. When capillary pressure effects are neglected, there is a distinct minimum in the gas saturation in the caprock. When capillary pressure effects are included, the gas saturation in the caprock is much higher, as they tend to diminish saturation differences. Near the bottom of the reservoir, the capillary pressure effects tend to hold onto the liquid, resulting in lower gas saturations at late times (30 years). However, vapor static conditions develop in the reservoir at late times.

Of major interest is the total fluid recharge from the shallow, free-surface aquifer to the reservoir for the two cases (with and without capillary pressure effects). In both cases a rapid rise in the recharge rate is observed, reflecting the pressure decline in the reservoir, but the maximum recharge rate occurs later when capillary effects are included. The reason for this is that capillary effects tend to slow the release of water present in the caprock and in the shallow aquifer. The recharge rate declines at later times in response to the lowering of the water table and the increasing gas saturation in the shallow zones. Detailed results of similar two-dimensional calculations are given by Bodvarsson and Pruess (1983).

INJECTION INTO A RESERVOIR WITH A FAULT CONNECTION TO A SHALLOW AQUIFER

In this section we discuss the effects of reinjection into a liquid-dominated geothermal reservoir that is hydraulically connected to a shallow, unconfined aquifer by means of a vertical fault. Of particular interest in this type of problem is the migration of reservoir water into the shallow aquifer as a consequence of reinjection, which may create environmental hazards.

The injection configuration and the overall geometry of the flow system are shown in Figs. 3 and 4. The injectors are placed in a "line drive" pattern at 100-m spacing. At a distance of 126 m from the

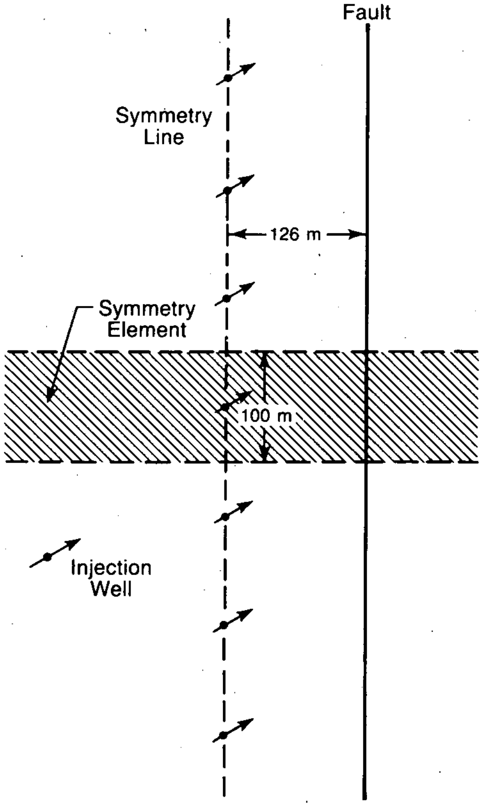

Figure 3. Schematic diagram of the injection well configuration and the leaky fault. [XBL 8312-7411]

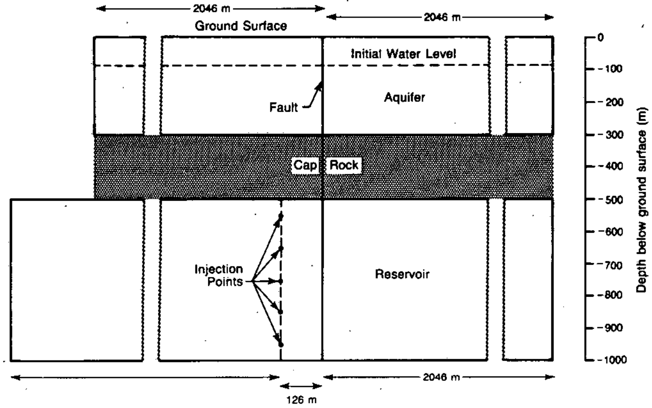

Figure 4. A vertical cross section of the interconnection between the shallow aquifer and the reservoir. [XBL 8312-7410]

injection line, there is a vertical fault. The line connecting the injection wells is an approximate line of symmetry, because problem parameters were chosen in such a way (see Table 2) that the rate of flow up the fault is negligibly small compared to lateral flow in the reservoir (less than 5%). We model one symmetry element, which is a vertical slice with a thickness of 100 m, as shown in Fig. 3. The reservoir is represented by five grid layers, each 100 m thick. The injection rate into each grid layer is constant at 10 kg/s. Constant-pressure boundary conditions, corresponding to the initial gravity-equilibrated pressure distribution, are assumed at the left and right boundaries of reservoir and aquifer. The lower boundary of the reservoir, and the boundaries of the caprock, are assumed "no flow." Boundary conditions of $P = 1$ bar and $T = 20°\mathrm{C}$ are maintained at the ground surface. Detailed problem parameters are given in Table 2.

In response to injection, pressures in the reservoir increase, causing some upflow of water in the fault zone. The water levels in the fault zone and the shallow aquifer rise above their initial depth of −90 m. Figure 5 shows the water levels at various times as a function of the distance from the fault. For comparison we have also carried out a simulation using a fully saturated system, i.e., placing the upper boundary of the system at the initial water level of −90 m. (This corresponds to treating the aquifer as fully confined.) Figure 6 shows velocities of water migration up the fault for the two cases. The velocities differ by as much as 50%. Nonreactive solids dissolved in the reservoir water will begin to reach the shallow aquifer approximately 25 days after injection has started. In the confined case, pressures near the top of the aquifer rise to approximately 9.5 bars, whereas pressures remain near 1 bar at the free water surface in the unconfined case. Pressures and temperatures in the reservoir differ by no more than 1–2% between the two cases. Thus an explicit treatment of the free surface is not necessary if only predictions of reservoir behavior are desired. However, reliable predictions of effects of injection on the shallow aquifer are possible only when a two-component air–water approach is used.

Table 2. Parameters for injection problems.

	Aquifer	Fault	Reservoir
Formation parameters			
Permeability (m^2)	100×10^{-15}	400×10^{-15}	50×10^{-15}
Porosity (%)	20	20	10
Initial conditions			
Initial temperature (°C)	20	20/250	250
Initial pressure (bars)	Gravity equilibrium, with 1 bar at ground surface		
Initial water level (m)	-90	-90	
Injection			
Total rate (kg/s)			50
Enthalpy (kJ/kg)			419
Width of fault (m)		1.0	

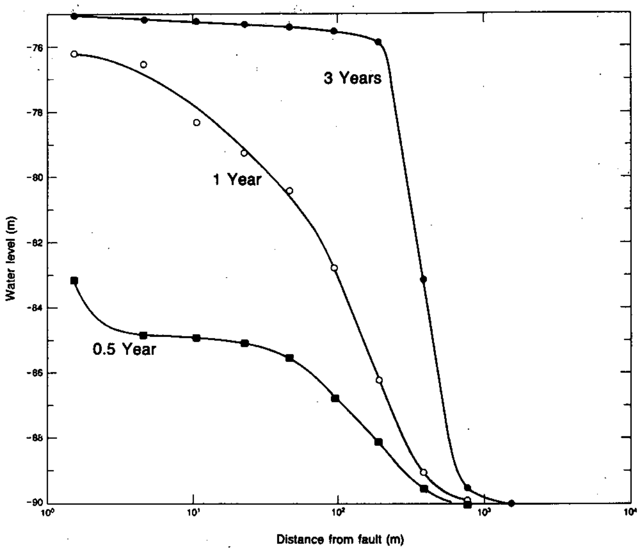

Figure 5. The rise of the water level in the shallow aquifer versus time during injection. [XBL 8312-7413]

SUMMARY AND CONCLUSIONS

We solve some reservoir problems involving an unconfined shallow aquifer. These simulations have a twofold purpose:

1. To obtain some understanding of the interaction between geothermal reservoirs and shallow, unconfined aquifers and of the capillary pressure effects for such problems.

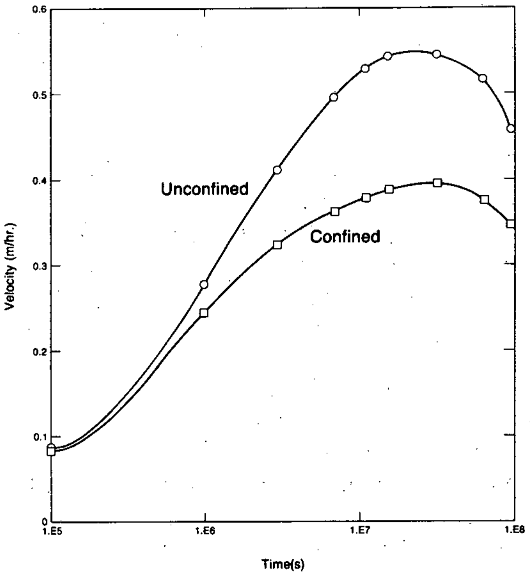

Figure 6. The velocity of the fluid migration up the fault as a function of time. [XBL 8312-7412]

2. To study the extent to which conventional geothermal simulators for fully saturated media can be applied to problems involving free-surface aquifers.

The results obtained indicate that capillary pressure effects tend to enlarge the two-phase zone and smooth out large gas-saturation gradients within the zone. Free-surface aquifers provide recharge to the main geothermal reservoir, and if a rigorous air–water simulator is not used, the recharge rate may be underestimated. This can have serious implications, especially where the caprock is very leaky and recharge of fluids from above can cool the reservoir. However, for most reservoir problems, our results show that conventional single-component geothermal simulators give reasonable results for modeling the interaction of a shallow, unconfined aquifer with a reservoir under exploitation. This is especially true for cases in which exploitation causes boiling in the reservoir or in the shallow aquifer, because in these cases the reservoir response is dominated by the two-phase zone. On the other hand, our results indicate that for an assessment of possible contamination of shallow, unconfined aquifers during injection, one must use a rigorous air–water model for a detailed analysis. In these cases, neither the discharge rate to the shallow aquifer nor its pressure distribution during injection can be accurately calculated with a model for a saturated medium. As the discharge rate to the shallow aquifer is the most important parameter for contamination studies, it appears that air–water models are necessary for such problems.

REFERENCES

Bjornsson, S., 1978. Estimation of the reservoir potential of the Olkaria geothermal field in Kenya. *In* Proceedings, Nordic Symposium on Geothermal Energy, Goteborg, Sweden.

Bodvarsson, G., and Zais, E.J., 1982. Geothermal reservoir testing by piezometric surface drawdown/buildup. Paper presented at the 57th Annual Meeting of the Society of Petroleum Engineers of AIME, New Orleans, September 26–29, 1982 (SPE-11142).

Bodvarsson, G.S., and Pruess, K., 1983. Modeling studies of geothermal systems with a free water surface. *In* Proceedings, Ninth Workshop on Geothermal Reservoir Engineering, Stanford, December 13–15, 1983. Stanford Geothermal Program Report SGP-TR-74, p. 351–356.

Grant, M.A., Truesdell, A.H., and Mañón, A., 1984. Production induced boiling and cold water entry in the Cerro Prieto geothermal reservoir indicated by chemical and physical measurements. Geothermics, v. 13, p. 117–140.

International Formulation Committee, 1967. A formulation of the thermodynamic properties of ordinary water substance. Dusseldorf, Germany, IFC Secretariat.

Pruess, K., 1984. TOUGH—A numerical model for strongly heat driven flow in partially saturated media. *In* Earth Sciences Division Annual Report 1983. Lawrence Berkeley Laboratory Report LBL-16920, p. 39–41.

Pruess, K., Bodvarsson, G.S., Stefansson, V., and Eliasson, E.T., 1983. The Krafla geothermal field, Iceland. 4. History match and prediction of individual well performance. Water Resour. Res., v. 20, no. 11, p. 1561–1584.

Sammel, E.A., 1976. Hydrologic reconnaissance of the geothermal area near Klamath Falls, Oregon. Menlo Park, California, U.S. Geol. Surv. Report WRI-76-127, 129 p.

The Heber Geothermal Field: Exploitation Modeling Studies

M.J. Lippmann and G.S. Bodvarsson

The Heber field is located in the southern part of the Imperial Valley, California, about 7 km north of the Mexican border (Fig. 1). In the 1970s, exploration drilling, mainly by Chevron Geothermal Co. and Union Geothermal Co., delineated this moderate-temperature (< 200°C), liquid-dominated geothermal system. Chevron Geothermal Co., the operator of the field, estimates that the Heber system can support a power generation of 500 MW_e for at least 30 years (Salveson and Cooper, 1981; California Division of Oil and Gas, 1983a).

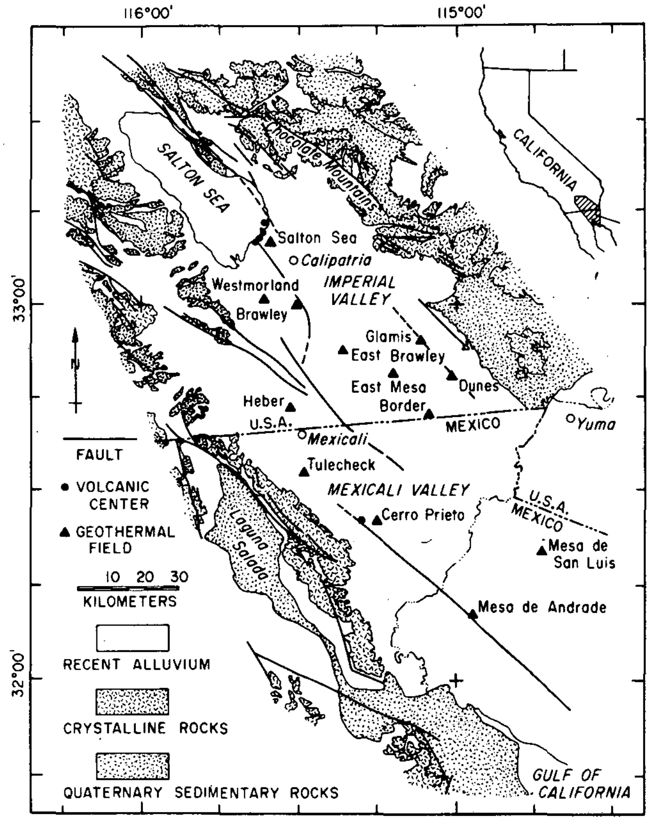

Figure 1. Location of geothermal areas in the Salton trough. [XBL 845-1692]

Construction of the first two power plants—a 45-MW_e (net) binary plant and a 47-MW_e (net) dual-flash plant—has recently begun. The plants are scheduled to be complete in mid-1985. The production and injection wells for the two projects are being drilled directionally from drilling "islands." Initially, 13 production and 9 injection wells are proposed for the binary plant and 9 production and 8 injection wells for the dual-flash plant (California Division of Oil and Gas, 1983b).

In late 1980, San Diego Gas and Electric Company and the Department of Energy (DOE) signed a cooperative agreement calling for DOE to share in the cost of the Heber Geothermal Binary Demonstration Project (Allen and Nelson, 1983). The purpose of our work at Lawrence Berkeley Laboratory (LBL), as advisors to DOE, is to study carefully the response of the field to exploitation and identify potential reservoir problems at Heber. For example, excessive declines in reservoir pressure can seriously affect the economics of the project, since the Heber wells must be pumped because of the low reservoir temperature. Moreover, the limited size of the thermal anomaly could result in a rapid fluid temperature decline during production, which would greatly reduce the efficiency of the heat exchangers. Consequently, the reservoir behavior should be carefully evaluated under different exploitation schemes.

RESULTS

In studying the response of the Heber system to exploitation, we used the numerical simulator PT, developed at LBL (Bodvarsson, 1982), and the same multilayer axisymmetric model (Fig. 2) that was used in the natural-state simulations described in Lippmann and Bodvarsson (1984, 1985). The rock properties of the different reservoir regions and the boundary conditions used are those determined by the natural-state model. However, instead of prescribing a constant mass and energy flux into the system through the bottom of the 1000-m-radius upflow zone, as we did in the natural-state model, we allow pressure-dependent recharge from a node (at a depth of about 5 km) with a constant temperature and pressure of 244.5°C and 45.67 MPa, respectively. Under natural-state conditions, this approach results in a mass recharge through the lower part of the upflow zone equal to 14.6 kg/s, as in the best model of the natural-state system. During simulation of the exploitation of the field, this rate of recharge will increase with time as the reservoir pressure in the upflow zone decreases. Thus, in general, the assumption that the upflow zone can be modeled using a constant-pressure boundary is an optimistic one, but we found that in our work it has only minor effects on the overall response of the system. The initial temperature and pressure conditions used in simulating the exploitation of the field correspond to those of the natural-state model.

The main objective of this study is to find out what fluid extraction rates (i.e., generating capacity) are possible at Heber for different production-injection scenarios. It is assumed that during a 10-year period the installed generating capacity in the field increases linearly with time, from zero MW_e at $t = 0$ to a maximum value at 10 years. From then on, the electrical power generation remains constant at the maximum level.

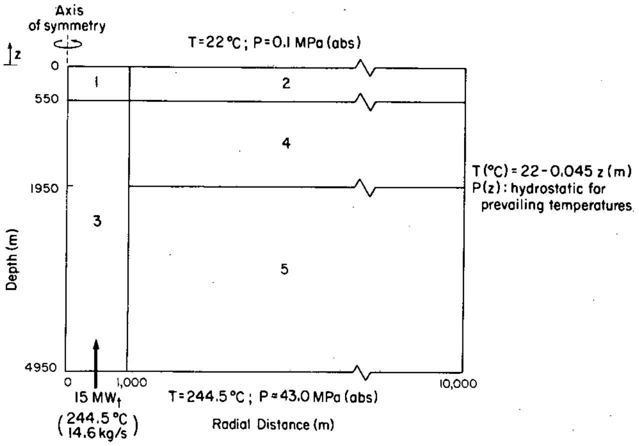

Figure 2. Zones and boundary conditions used in the model. The upper and lower boundaries (except the bottom of zone 5) are closed to fluid flow and opened to heat flow. The outer radial boundary is open to heat and fluid flow. [XBL 847-9833]

The simulations are carried out to 100 years or until boiling is observed in some part of the system (this always occurs in the shallow reservoir region near the axis). When boiling occurs, the reservoir pressure in the upper part of the production zone (at 750 m depth in Cases 1 and 2; Table 1) has generally dropped about 4 MPa—a drawdown considered to be excessive for a pumped system like that planned at Heber. On the basis of the published data, it is assumed that 1000 kg/s of geothermal fluid is required to generate 50 MW_e.

Fluids are produced uniformly from part of the 1000-m-radius upflow zone (zone 3; Fig. 2). In two of the six cases studied (Cases 1 and 2), production is uniformly distributed between 650 m and 2950 m depth; the plan is similar to that described by Salveson and Cooper (1981). In Cases 3 and 4, the production is assumed to be restricted to deeper formations (the depth interval 1950–2950 m) facing the higher-permeability zone 5 (Fig. 2). Finally, Cases 5 and 6 evaluate an intermediate situation. Twenty-five percent of the produced fluid is extracted from the shallower depth interval (650–1950 m) and 75% from the deeper one (1950–2950 m).

One hundred percent of the fluid extracted from the reservoir is reinjected. In Cases 1 to 4, the same mass of fluid is injected at each depth interval as is produced. In Cases 5 and 6, 75% of the extracted fluid is injected into the upper depth interval (650–1950 m) and 25% into the lower one (1950–2950 m).

Reinjection is considered at several radial distances from the axis of the system. Two extreme situations are discussed here.

Table 1. Reservoir development plans studied for the Heber field.

Case	Production/injection depth intervals (m)	Average radial distance to injection zones (m)
1 and 5	650–2950	2250
2 and 6	650–2950	4250
3	1950–2950	2250
4	1950–2950	4250

Note: In all cases fluid is produced from a 1000-m-radius axial cylinder.

Near Injection: Uniform injection into an annular region located between 2000 and 2500 m from the axis (Cases 1, 3, and 5).

Far Injection: Uniform injection into an annular region located between 4000 and 4500 m from the axis (Cases 2, 4, and 6).

These two extremes bound the radial distances indicated by Salveson and Cooper (1981) for the location of the injection zone, i.e., 2.4–4.0 km. Following Allen and Nelson (1983), it is assumed that the injected fluid has a temperature of 72.2°C.

Table 1 lists the possible reservoir development cases. Table 2 summarizes the production characteristics after 40 years of development for the same cases.

Reservoir Pressures

The pressure versus time curves for the production nodes (Figs. 3 to 8) depict the assumed field development plan. During the first 10 years, the total fluid production rate increases linearly with time, from zero to a maximum rate at 10 years.

Table 2. Production characteristics after 40 years.

Fluid production rate (kg/s)	Generating capacity (MW_e)	Reservoir pressure[a] (MPa)	ΔP (MPa)	Average temperature of produced fluids (°C)	$\Delta \overline{T}$ (°C)
Case 1					
4000	~200	5.55	−2.31	168.0	−10.7
5000	~250	4.93	−2.94	165.8	−12.9
6000	~300	4.28	−3.59	163.6	−15.1
7000[b]	~350	—	—	—	—
Case 2					
2000	~100	5.91	−1.96	172.7	−6.0
3000	~150	4.91	−2.96	170.1	−8.6
4000[c]	~200	—	—	—	—
Case 3					
6000	~300	23.46	−1.97	144.1	−33.6
10,000	~500	21.74	−3.70	126.8	−51.0
Case 4					
3000	~300	24.24	−1.20	159.2	−18.5
10,000	~500	21.27	−4.17	146.0	−31.8
Case 5					
6000	~300	10.92	+3.05	160.9	−17.3
10,000	~500	12.86	+4.99	154.2	−24.0
Case 6					
3000	~150	7.82	− 0.05	166.1	−12.1
5000	~250	7.77	− 0.10	161.5	−16.7
10,000	~500	7.62	− 0.25	154.7	−23.5

[a] For Cases 1, 2, 5, and 6 reservoir pressures correspond to the production node at $r = 100$ m and $z = -750$ m; for Cases 3 and 4, to the node at $r = 100$ m and $z = -2700$ m.

[b] Boiling occurs in the system at about 25 years.

[c] Boiling occurs in the system at about 12 years.

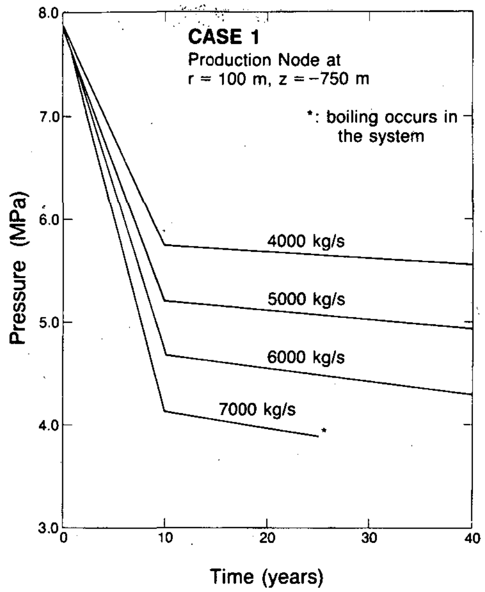

Figure 3. Case 1. Pressure in production node at *r* = 100 m, *z* = −750 m. [XBL 8311-3443]

This causes a large pressure decline at early times. Later on, pressures tend to stabilize as a result of the constant extraction rate and 100% reinjection.

In Cases 1 and 2 the drawdown in the upper part of the production zone (Figs. 3 and 4) is much greater than that in the lower part (Figs. 5 and 6). The main reason for this is that lateral recharge to the upper part of the production zone is limited by the relatively low horizontal permeability of zone 4 (10×10^{-15} m^2). Recharge to the lower part of the production zone takes place at a faster rate because neighboring zone 5 has a horizontal permeability of 115×10^{-15} m^2.

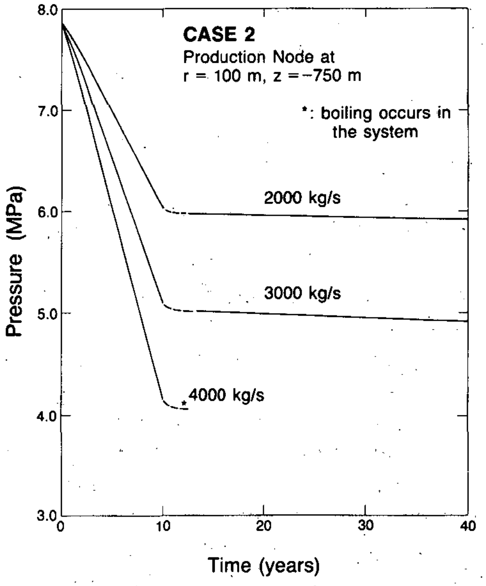

Figure 4. Case 2. Pressure in production node at *r* = 100 m, *z* = −750 m. [XBL 8311-3442]

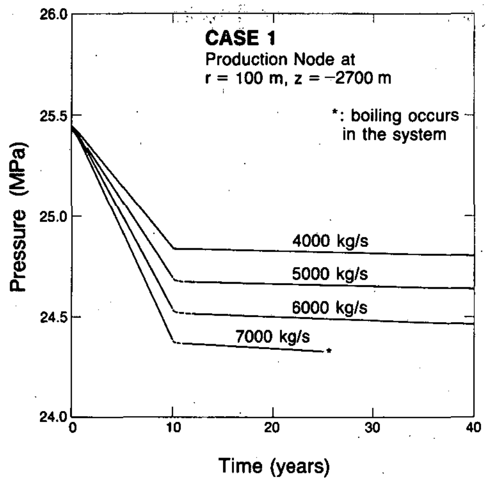

Figure 5. Case 1. Pressure in production node at *r* = 100 m, *z* = −2700 m. [XBL 8311-3444]

In order to circumvent the effect of lower-permeability zone 4 in Cases 3 and 4, production and injection were restricted to the depth interval between 1950 and 2950 m (Table 1). In these cases, even though the fluid extraction rate per unit volume of production zone is more than twice that for Cases 1 and 2, less drawdown is observed. No boiling occurs in the system, even when the production rate is as high as 10,000 kg/s (Figs. 7 and 8).

In Cases 5 and 6 we assume 25% production and 75% injection from and into the upper zones (between 650 and 1950 m) and 75% production and

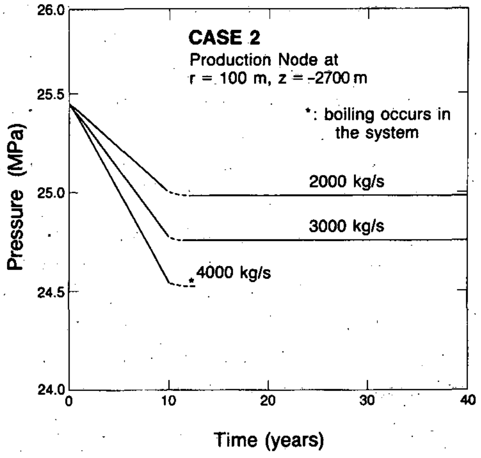

Figure 6. Case 2. Pressure in production node at *r* = 100 m, *z* = −2700 m. [XBL 8311-3441]

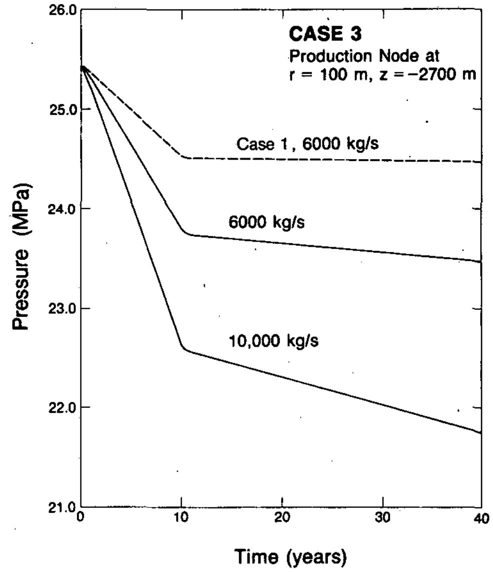

Figure 7. Case 3. Pressure in production node at $r =$ 100 m, $z = -2700$ m. [XBL 8311-3439]

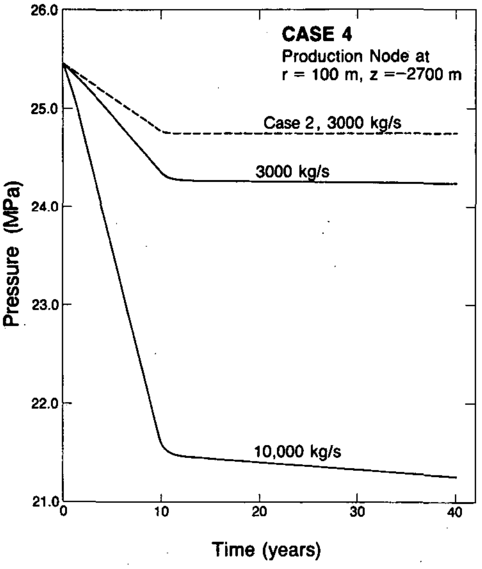

Figure 8. Case 4. Pressure in production node at $r =$ 100 m, $z = -2700$ m. [XBL 8311-3445]

25% injection from and into the lower zones (1950–2950 m). The purpose of this case is to attempt to limit the pressure decline in the upper part of the production zone. As expected in Cases 5 and 6, the pressure does not drop as fast as in Cases 1 and 2; it actually increases in Case 5 (Table 2). However, the difficulty with this reservoir development plan is that the pressures in the injection region rise to excessive levels because of the relatively low permeability of zone 4. For Case 5 ($Q =$ 6000 kg/s) at the end of the 40-year period, the pressure in the injection node located at $r = 2250$ m and 750 m depth has risen 7.60 MPa to 15.33 MPa. The injection pressure for Case 6 (Q = 5000 kg/s) is also high; i.e., at $r = 4250$ m and 750 m depth, the pressure rises to 12.85 MPa, an increase of 5.23 MPa; for Case 6 ($Q = 3000$ kg/s), $\Delta P = 3.13$ MPa. This suggests that most of the fluid must be injected into the deeper, more permeable zone.

The reservoir pressure support of the reinjection operations is clearly evident when one compares the 4000-kg/s examples for Cases 1 and 2 (Figs. 3 to 6). The closer to the production zone injection takes place, the greater is the pressure support. However, if fluid is injected too close to the production zone, detrimental decreases in the temperature of the produced fluid may occur (see below).

Average Production Temperature

The temperatures reported here are the average temperatures of the produced fluid at the reservoir level. To obtain the temperature of the fluid at the inlet to the power plant, one must consider the heat losses in the well bore and those in the hot water transmission pipes at the surface.

With production uniformly distributed over the 1000-m-radius cylinder, the initial average temperature of the produced fluid (weighted by mass) is 178.7° for Cases 1 and 2, 177.8°C for Cases 3 and 4, and 178.2°C for Cases 5 and 6. Because of the characteristic mushroom shape of the isotherms in the reservoir under natural conditions (Lippmann and Bodvarsson, 1984, 1985), these average initial temperatures would be a few degrees higher if production were increased toward the axis of the system and would be correspondingly reduced if increased in the outer regions of the production cylinder. The changes in average fluid production temperatures with time for the first four cases are given in Figs. 9 to 12. For most of the cases studied the temperature decline of the produced fluid is due entirely to the flow of colder fluid into the production area from the outer regions of the system, and not to injection. This is evident when we compare the temperature decline for near and far injection (Table 2). In Case 3, however, the observed temperature decline is due to the advance of the injected fluids (compare Figs. 11 and 12), which reflects the higher extraction/injection rates employed. Note that in our studies we do not model in detail the layering of sandstones and shales, hence the breakthrough times could be shorter than what we predict.

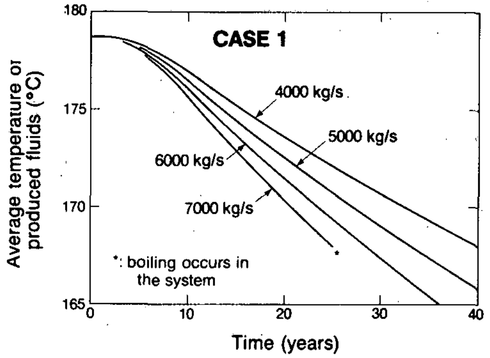

Figure 9. Case 1. Average temperature of produced fluids. [XBL 8311-2385]

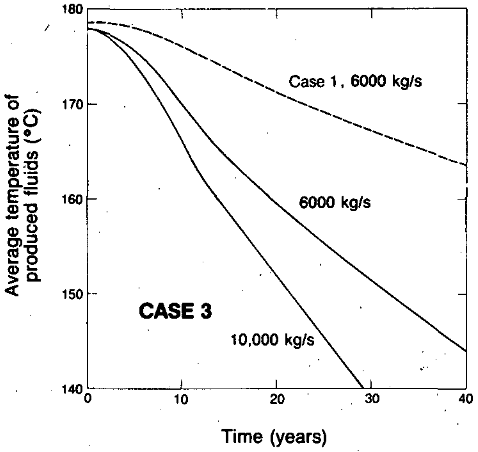

Figure 11. Case 3. Average temperature of produced fluids. [XBL 8311-3440]

As one would expect from the production-injection scheme of Cases 5 and 6, the temperature of the produced fluids falls between those of Cases 1 and 2 and Cases 3 and 4 (Table 2).

For most cases the temperature of the produced fluid is not significantly affected if the temperature of the injected fluid is increased slightly (e.g., 100°C instead of 72.2°C). For example, in Case 1 (6000 kg/s) the increase in average temperature after 40 years is only 0.3°C (from 163.6 to 163.9°C). However, because 100°C fluids have significantly lower viscosity than 72.2°C fluids, injection of higher-temperature fluids is preferred for pressure support. In Case 1 (6000 kg/s) the 100°C injection delays the start of boiling in the system for about 12 years.

THE GENERATING CAPACITY OF THE FIELD

In evaluating the generating capabilities of the field, we must develop some criteria for maximum allowable pressure drop and temperature decline. The criteria we selected are as follows:

1. Maximum allowable pressure drop is 4 MPa (corresponds to boiling starting in shallow zones).
2. Temperature of produced fluids must exceed 160°C, which is the economic fluid temperature limit for the power plant (Tansev and Wasserman, 1978). Note, however, that we neglect heat losses during transport of the fluids in the well bore and surface pipes.

Most of the results for the Heber reservoir show that the maximum extraction rates for near and far injection are 6000 and 3000 kg/s, respectively, which correspond to power outputs of 300 and 150 MW_e. In Cases 1 and 2 the limiting factor is the pressure drop in the reservoir, whereas in Cases 3 and 4 the temperature decline limits the generating capacity. However, the results from Case 6 indicate that optimum proportioning of the extraction/injection

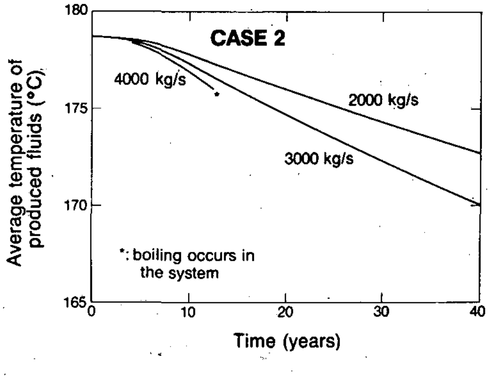

Figure 10. Case 2. Average temperature of produced fluids. [XBL 8311-2386]

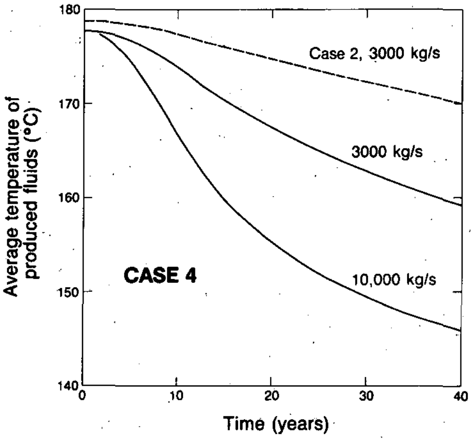

Figure 12. Case 4. Average temperature of produced fluids. XBL 8311-3446]

rates between different depth zones may enable 250 MW_e power production in the case of far injection. In this case one would expect larger pressure increases due to injection in shallow regions.

Our results are more conservative than those of Chevron, the operator of the Heber field. They estimate a generating capacity of 500 MW_e; our modeling study indicates a maximum of 300 MW_e. Because the details of their modeling effort are not in the public domain, we cannot directly compare our results with theirs. Our model shows that the relatively low permeability of the upper outer zone (zone 4; 10×10^{-15} m^2 horizontal; 0.1×10^{-15} m^2 vertical) is the main limiting factor for the generating capacity of the Heber field. This low-permeability zone was established from the modeling of the natural state of the system. It is possible that recently completed wells at Heber may give a higher temperature distribution in the system. In that case the permeability of zone 4 (and the strength of the convective source) would be higher, thus increasing the maximum allowable generating capacity of the field.

REFERENCES

Allen, R.F., and Nelson, T.T., 1983. Heber geothermal binary demonstration project. *In* Proceedings, Geothermal Program Review II. Washington, D.C., U.S. Department of Energy, CONF-8310177, p. 235–241.

Bodvarsson, G.S., 1982. Mathematical modeling of the behavior of geothermal systems under exploitation (Ph.D thesis). Lawrence Berkeley Laboratory Report LBL-13937, p. 18–48.

California Division of Oil and Gas, 1983a. Chevron, Dravo, may be partners in Heber dual flash project. Geothermal Hot Line, v. 13, no. 1, p. 7–8.

California Division of Oil and gas, 1983b. Heber power plant projects underway. Geothermal Hot Line, v. 13, no. 2, p. 50–51.

Lippmann, M.J., and Bodvarsson, G.S., 1984. A modeling study of the natural state of the Heber geothermal field, California. *In* Earth Sciences Division Annual Report 1983. Lawrence Berkeley Laboratory Report LBL-16920, p. 18–22.

Lippmann, M.J., and Bodvarsson, G.S., 1985. The Heber geothermal field, California: Natural state and exploitation modeling studies. J. Geophys. Res., v. 90, no. B1, p. 745–758.

Salveson, J.O., and Cooper, A.M., 1981. Exploration and development of the Heber geothermal field, Imperial Valley, California. *In* Proceedings, 1981 New Zealand Geothermal Workshop, University of Auckland, Auckland, New Zealand, November 9–11, 1981, p. 3–6.

Tansev, E.O., and Wasserman, M.L. 1978. Modeling the Heber geothermal reservoir. Geothermal Resour. Counc., Trans., v. 2, p. 645–648.

Recent Developments at the Cerro Prieto Geothermal Field

*M.J. Lippmann and A. Mañón**

As part of its program in geothermal energy (Table 1), funded by the Division of Geothermal and Hydropower Technologies of the U.S. Department of Energy (DOE) under the Reservoir Definition Program, Lawrence Berkeley Laboratory (LBL) has continued to carry out studies of the Cerro Prieto geothermal system (Fig. 1) and has kept abreast of the latest developments at the field. The fiscal 1984 effort has been significantly smaller than in previous years because of the lack of a formal agreement for continued technical cooperation between DOE and the Comisión Federal de Electricidad of Mexico (CFE), operator and manager of the Cerro Prieto field. The earlier agreement (Witherspoon et al., 1978) expired in July 1982; a new 3-year agreement is expected to be signed during the first half of 1985.

Recent LBL studies on Cerro Prieto have been restricted mainly to analyzing field data gathered earlier and to updating the models of this geothermal field on the basis of new well data and studies performed by CFE.

RECENT FIELD ACTIVITIES

By late 1984 the two 110-MW_e turbogenerators of power plant CPII had been commissioned, increasing the installed generating capacity at Cerro

---

*Comisión Federal de Electricidad, Mexicali, Baja California, Mexico.

Table 1. Geothermal projects, Earth Sciences Division, fiscal years 1984 and 1985.

Well-test analysis
- Single/multiple well
- Injection/production tests

Relative permeability laboratory experiments and field data analysis

Modeling reservoir behavior
- Natural state
- Under exploitation
- Temporal and spatial variations in concentrations of noncondensible gases

Study optimization of heat extraction

Modeling migration of injected fluids in fractured/porous rocks

Development of modeling capabilities for transport of heat, mass, and chemical species in rock masses
- Porous/fractured media
- Saturated/unsaturated media
- One/two phases
- Single/multicomponent fluids
- Fluid/rock interactions

Fault and fracture mapping
- Numerical and scale modeling of electrical/EM methods
- Evaluation of vertical seismic profiling and cross-hole seismic tomography

Development of surface and downhole instrumentation

Well-log analysis

Multidisciplinary field case studies
- Klamath Falls (Oregon)
- Cerro Prieto/Los Azufres (Mexico)
- Salton Sea Scientific Drilling Project (California)
- Heber (California)
- Cascades (California, Oregon, Washington)
- Krafla (Iceland)

Magma energy development (assistance to SNL)
- Geological and geophysical evaluation of probable sites

Prieto to 400 MW_e. The construction of power plant CPIII continued; it should be operational before the end of 1985, bringing the total installed capacity at the field to 620 MW_e.

The drilling activity at Cerro Prieto continued at full pace. New production wells were drilled to replace older ones and to supply steam to the new power plants. Deep exploration wells were drilled to outline the boundaries of the thermal anomaly and to locate more precisely the hot-fluid recharge area. Between April 1983 and September 1984 sixteen wells were completed (Figs. 2 and 3; Table 2).

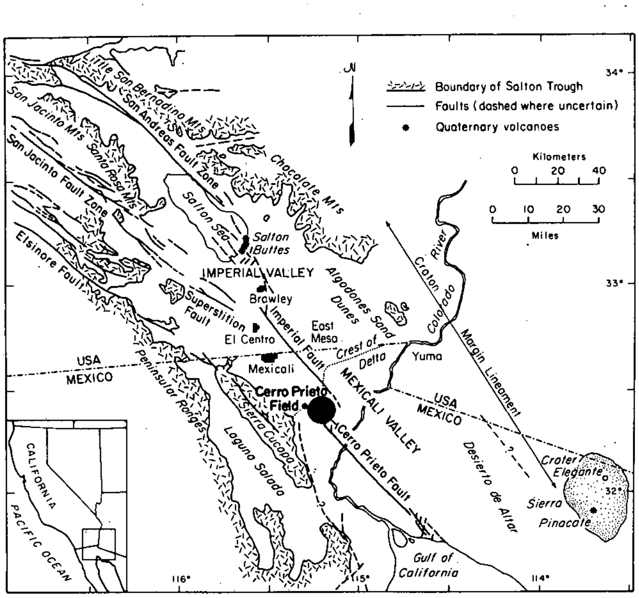

Figure 1. Regional geology of the Salton trough and location of the Cerro Prieto field. [XBL 801-6718A]

The wells of the E-series in the western part of the field tap the lower reservoir in that area, replacing or supplementing the fluid output of older, shallower wells. The 200-series wells drilled in the eastern part of the system are exploratory. Well M-203 is presently the deepest at Cerro Prieto, with a total depth of 3995 m. Data from these wells were used to make a map showing the depth to the 300°C isotherm (Fig. 4).

The rate of fluid production and the average enthalpy of the produced fluid have remained relatively constant since late 1982, varying between 4300 and 4700 tonnes/hour and between 1410 and 1450 kJ/kg, respectively (Figs. 5 and 6). The rate of fluid production has increased since July 1984, when one of the new turbogenerators in power plant CPII came on line.

In response to fluid extraction (with no brine reinjection), the pressure in the shallow western reservoir has been gradually dropping. This is indicated by changes in the water level in well M-6 (Fig. 7), located west of the production region.

Apart from activities related to electrical power production, CFE has recently begun at Cerro Prieto a number of demonstration projects related to the direct use of geothermal fluids (Mañón, 1984). Among them are fish farming, greenhouse agriculture, absorption refrigeration, and mineral extrac-

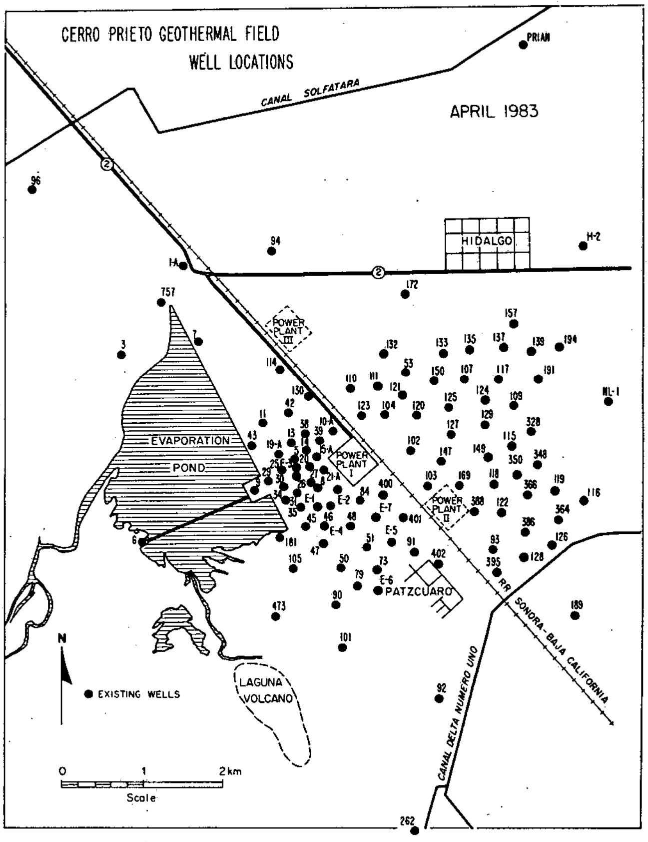

Figure 2. Location of wells in the Cerro Prieto field as of April 1983. [XBL 835-1804A]

Table 2. Wells completed at Cerro Prieto between April 1983 and September 1984.

Well	Total depth (m)	Open intervals (m)
E-8	1796	1513–1794
E-9	1714	1479–1702
E-10	1814	1515–1807
M-108	2211	1896–2211
M-112	3622	2409–2801, 3370–3622
M-113	2041	1771–2040
M-155	2526	2358–2525
M-192	2906	2596–2906
M-193	2226	1924–2226
M-197	2790	2578–2786
M-198	2797	2494–2622
M-200	2841	2482–2834
M-201	3610	—
M-202	3987	3712–3987
M-203	3995	3537–3993
T-394	3019	2684–3013

Note: Data from F.J. Bermejo and C.A. Esquer, personal communications, 1984.

tion. CFE recently granted a license to a private company to utilize the geothermal waste heat for food production and industrial use. The Baja California state government and a private concern are working on an agreement to establish farms and industries that require low-cost process heat. A plant for extracting 100,000 tonnes/year of potassium chloride from the separated brines is being built west of the Cerro Prieto wellfield. Construction of the evaporation ponds for this plant is nearly complete (Mañón, 1984).

RECENT STUDIES

Over the past 7 years great advances have been made toward understanding the Cerro Prieto system, both in its natural state and under exploitation. A

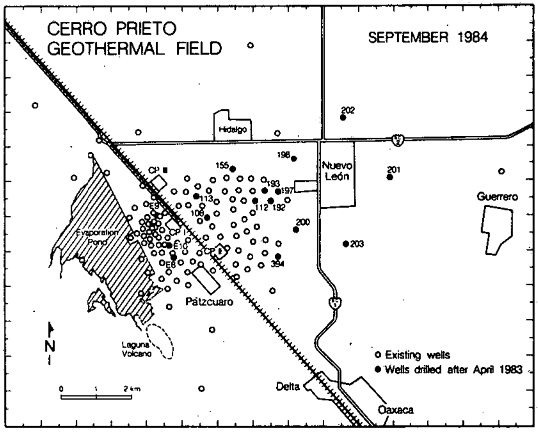

Figure 3. Location of wells drilled between April 1983 and September 1984 (from Mañón, 1984). [XBL 849-9922]

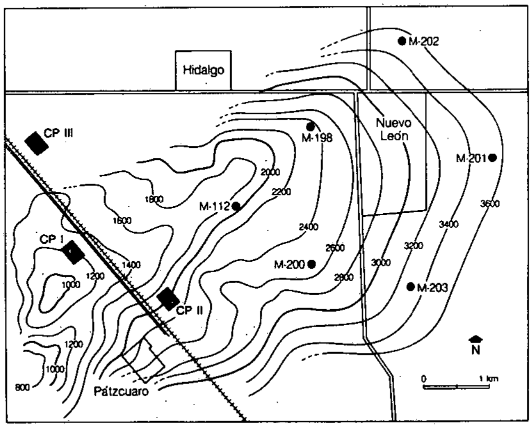

Figure 4. Depth to the 300°C isotherm (from Mañón, 1984). [XBL 8410-9972]

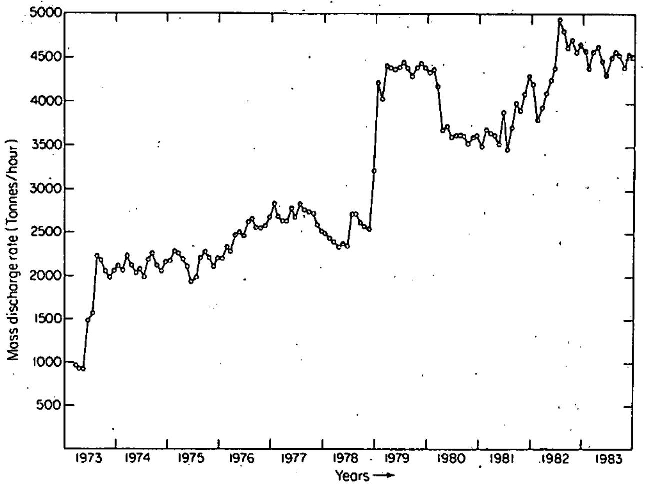

Figure 5. Mass production rate at Cerro Prieto (data from F.J. Bermejo, personal communication, 1984). [XBL 837-2129]

large body of information is included in the numerous reports and papers published since 1977. Most of these are included in the proceedings of the four symposia held on Cerro Prieto (LBL, 1978, 1981; CFE, 1979, 1982), and many have recently been summarized in three review papers (Lippmann, 1983; Lippmann et al., 1974; Mañón, 1984). Discussed below are the findings of some later studies that are not included in these publications.

Work has continued on updating the hydrogeologic model for Cerro Prieto developed by Halfman et al. (1984a). Data obtained from recently completed wells confirm the soundness of that model. The depositional environments of the various sedimentary units found at the reservoir level were derived from the study of dipmeter logs. They were shown to correspond to a coastal system (Halfman et al., 1984b). Along a west-to-east line, one would find, in succession, longshore current, shoreline, and protected embayment deposits (Fig. 8). By establishing the characteristics of the coastal environment of deposition of the sedimentary rocks forming the Cerro Prieto geothermal reservoir and its caprock, it was simple to explain the change in lithology and disappearance of different units. This new analysis should be useful for locating and designing the completion of new wells in the field.

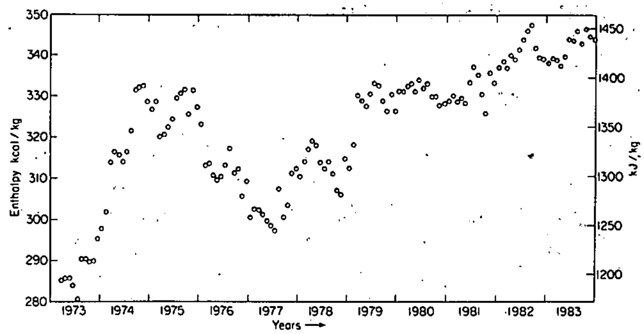

Figure 6. Average enthalpy of the fluids produced at Cerro Prieto (data from F.J. Bermejo, personal communication, 1984). [XBL 837-2128]

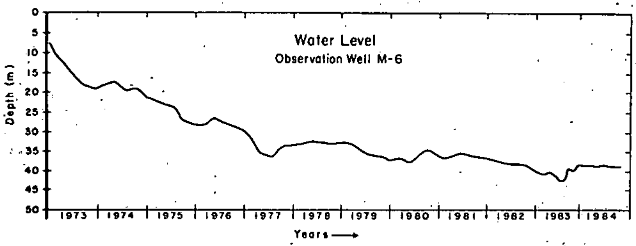

Figure 7. Change of water level in Cerro Prieto well M-6 (data from F.J. Bermejo, personal communication, 1984). [XBL 8411-6156]

The results of an extensive geologic study were reported by Cobo et al. (1984). On the basis of cut-

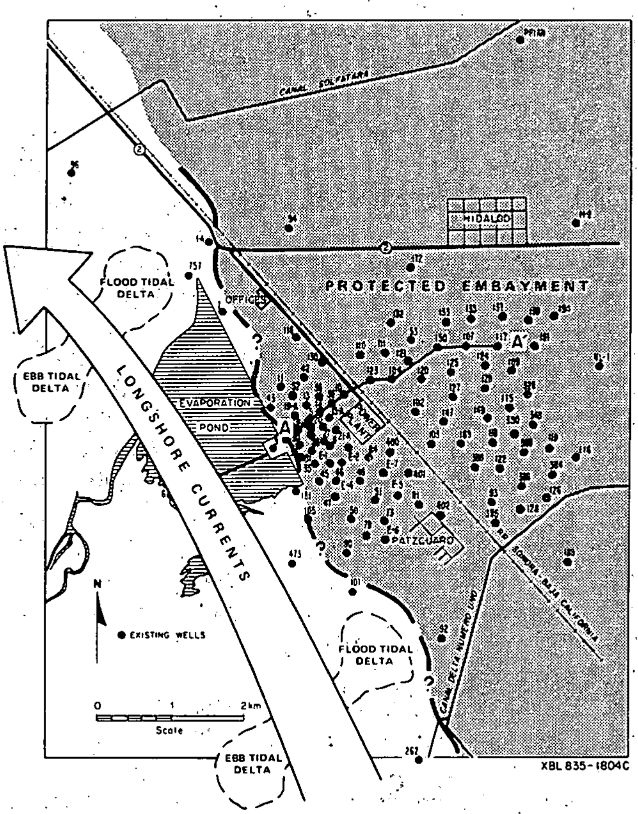

Figure 8. Schematic paleoenvironmental map of the deeper part of the Cerro Prieto section (from Halfman et al., 1984b). [XBL 835-1804C]

tings, cores, and wire-line log data, they developed a geologic model of the Cerro Prieto field. Their model suggests that a major fracture and a set of radial faults might be the main conductors of geothermal fluids in the system. Some features of this model disagree with those developed by Halfman et al. (1984a); efforts will be made to integrate features of both into a single hydrogeologic model of the field.

On the basis of whole rock analyses, Reed (1984) suggests that the Cerro Prieto volcano is derived from the partial melting of granitic basement rocks and not from differentiation of gabbroic intrusions. The small magma chamber associated with the volcano had insufficient volume to retain the heat to drive the present hydrothermal system. Reed contends that the volcanism and the current hydrothermal activity are both the result of heat transferred to the crust by gabbroic intrusions.

On the basis of geochemical and reservoir engineering, Truesdell et al. (1984) conclude that the localized boiling occurring in the shallow western Cerro Prieto reservoir has produced excess steam and increased the enthalpy of the produced fluids. This boiling also caused mineral deposition around the wells, thereby decreasing the permeability and the fluid flow. In the shallow western reservoir the inflow of colder waters has limited the extent of aquifer boiling and permeability loss. However, according to these authors, such recharge might not occur in the deeper reservoir at Cerro Prieto, and injection of waste brine might be required to decrease boiling and prevent loss of production due to mineral precipitation.

Wilt et al. (1984) continued their analysis of dipole-dipole resistivity data. The trend of increasing apparent resistivity associated with the shallow reservoir in the western part of Cerro Prieto was reversed in the period between Fall 1981 and Spring 1983. This change is interpreted to be caused by the collapse of boiling zones around the production wells due to a progressive cooling of the reservoir by the influx of cold recharge waters. On the other hand, in the eastern part of the field, the decrease in resistivity intensified, possibly as a result of the continuing influx of hotter, saline waters from depths greater than 3 km.

The analysis by Grannell et al. (1984) of gravity and leveling data obtained since 1978 at Cerro Prieto indicates that subsidence persists, possibly as a result of fluid production and partial recharge. Modeling of the gravity changes indicates a probable density increase, perhaps due to compaction within the reservoir.

Extensive reprocessing of the Cerro Prieto seismic reflection data (Blakeslee, 1984) has shown that the production region coincides with a zone of reflection attenuation and that a region of high-velocity events rimmed that zone. Blakeslee suggests that this concurrency may prove to be a valuable discriminant for locating geothermal reservoirs using seismic reflection.

Other recent papers have analyzed or summarized some of the reservoir engineering data collected on Cerro Prieto. A method to compute the bottom-hole enthalpy in a well and its change with wellhead conditions has been developed by Hiriart and Sânchez (1984) and applied to Cerro Prieto well M-147. Iglesias et al. (1983) have described a method for using productivity curves to determine the reservoir pressure, mass productivity index, thermal power productivity index, and radius of influence of liquid-fed geothermal wells. They applied their method to a number of Cerro Prieto wells. The petrophysical properties of Cerro Prieto reservoir sandstones were discussed by Contreras et al. (1984) and summarized in a review paper.

The results of numerical modeling studies of the field (Ayuso et al., 1984) suggest that the planned 620-MW_e generating capacity could be maintained through the year 1998. These studies are still in progress.

FINAL REMARKS

The joint U.S.-Mexican studies on Cerro Prieto (and Los Azufres) are expected to intensify once the new DOE/CFE agreement on geothermal energy is signed. This agreement includes cooperative activities in geology and hydrogeology, geophysics, geochemistry, reservoir engineering, reinjection, subsidence and induced seismicity, geochemical engineering and materials, energy conversion technology, and information exchange. Soon we hope to be able to report on the new results obtained under this international cooperative effort.

REFERENCES

Ayuso, M.A., Mârquez, R., Esquer, C.A., and Negrin, G., 1984. Modeling studies in the Cerro Prieto geothermal field. Geothermal Resour. Counc., Trans., v. 8, p. 175–181.

Blakeslee, S., 1984. Seismic discrimination of a geothermal field: Cerro Prieto. Geothermal Resour. Counc., Trans., v. 8, p. 183–188.

Cobo, J.M., Cobo, F.J., and Bermejo, F.J., 1984. Geological model of the geothermal field at

Cerro Prieto, Baja California. Geothermal Resour. Counc., Trans., v. 8, p. 189–192.

Comisiôn Federal de Electricidad, 1979. Proceedings, Second Symposium on the Cerro Prieto Geothermal Field, Baja California, Mexico, October 17–19, 1979. Mexicali, Comisiôn Federal de Electricidad.

Comisiôn Federal de Electricidad, 1982. Proceedings, Fourth Symposium on the Cerro Prieto Geothermal Field, Baja California, Mexico, October 10–12, 1982. Mexicali, Comisiôn Federal de Electricidad, in preparation.

Contreras, E.A., Iglesias, E.R., and Bermejo, F., 1984. Geothermal Resour. Counc., Trans., v. 8, p. 193–202.

Grannell, R.B., Zhou, H.W., and Wyman, R.M., 1984. Modeling of repetitive gravity observations at Cerro Prieto geothermal field. Geothermal Resour. Counc., Trans., v. 8, p. 203–206.

Halfman, S.E., Lippmann, M.J., Zelwer, R., and Howard, J.H., 1984a. Geological interpretation of geothermal fluid movement in Cerro Prieto field, Baja California, Mexico. Am. Assoc. Petrol. Geol. Bull., v. 68, p. 18–30.

Halfman, S.E., Lippmann, M.J., and Gilreath, J.A., 1984b. Cerro Prieto case history: Use of wireline logs to characterize a geothermal reservoir. *In* Proceedings, 1984 California Regional Meeting of the Society of Petroleum Engineers of AIME, Long Beach, California, April 11–13, 1984, p. 113–122 (SPE-12739).

Hiriart, G., and Sânchez, E., 1984. Thermodynamic considerations about the well M-147 at Cerro Prieto. Geothermal Resour. Counc., Trans., v. 8, p. 207–210.

Iglesias, E., Arellano, V., and Molinar, R., 1983. A method to recover useful geothermal-reservoir parameters from production characteristic curves. (2) Hot water reservoirs. *In* Proceedings, Ninth Workshop on Geothermal Reservoir Engineering, Stanford Geothermal Program Report SGP-TR-74, p. 291–297.

Lawrence Berkeley Laboratory, 1978. Proceedings, First Symposium on the Cerro Prieto Geothermal Field, Baja California, Mexico, September 20–22, 1978. Lawrence Berkeley Laboratory Report LBL-7098.

Lawrence Berkeley Laboratory, 1981. Proceedings, Third Symposium on the Cerro Prieto Geothermal Field, Baja California, Mexico, March 24–26, 1981. Lawrence Berkeley Laboratory Report LBL-11967.

Lippmann, M.J., 1983. Overview of Cerro Prieto studies. Geothermics, v. 12, no. 4, p. 267–289.

Lippmann, M.J., Goldstein, N.E., Halfman, S.E., and Witherspoon, P.A., 1984. Exploration and development of the Cerro Prieto geothermal field. J. Petrol. Technol., v. 36, p. 1579–1591.

Mañôn, A., 1984. Recent activities at Cerro Prieto. Geothermal Resour. Counc., Trans., v. 8, p. 211–216.

Reed, M.J., 1984. Relationship between volcanism and hydrothermal activity at Cerro Prieto, Mexico. Geothermal Resour. Counc., Trans., v. 8, p. 217–221.

Truesdell, A.H., D'Amore, F., and Nieva, D., 1984. The effects of localized aquifer boiling on fluid production at Cerro Prieto. Geothermal Resour. Counc., Trans., v. 8, p. 223–229.

Wilt, M., Goldstein, N.E., and Sasaki, Y., 1984. Long-term dipole-dipole resistivity monitoring at the Cerro Prieto geothermal field. Geothermal Resour. Counc., Trans., v. 8, p. 235–240.

Witherspoon, P.A., Alonso, H., Lippmann, M.J., Mañôn A., and Wollenberg, H.A., 1978. Mexican-American cooperative program at the Cerro Prieto geothermal field. Lawrence Berkeley Laboratory Report LBL-7095.

The Numerical Simulator PTC

C.H. Lai and G.S. Bodvarsson

The numerical simulator PTC was developed to analyze the coupled hydrological-thermal-chemical processes encountered in subsurface geologic formations. These complex processes often exhibit nonlinear behavior, thus requiring numerical methods for solution. Applications include simulation of geothermal systems under exploitation, assessment and cleanup of dumpsites, and performance predictions of nuclear waste disposal sites. PTC has the capability to simulate nonisothermal, two-dimensional tracer transport as well as the kinetics of silica-water reactions in fractured porous media.

Development of the code PTC was based on the code PT (Bodvarsson, 1982), which handles the coupled fluid and energy transport processes in fractured porous media. In PT, the fluid and energy transport equations are derived by combining the law of conservation of mass and energy and an equation of state describing the pressure-volume and temperature-volume relationships. The resulting equations involve two independent variables, pressure and temperature, and are solved simultaneously with a noniterative numerical scheme using a sparse, direct matrix solver (Duff, 1977). At each time-step, the fluid properties are functions of pressure and temperature and are explicitly determined from the previous time-step.

In addition to the fluid and energy transport equations, the code PTC solves the one-component chemical transport equation, including the effects of convection, dispersion, kinetics of silica-water reactions, and source terms. For an isotropic porous medium, Scheidegger (1961) has shown that the dispersion coefficient is a tensorial quantity proportional to the product of the dispersivity and magnitude of the fluid velocity. PTC considers tensorial dispersion, with the surface dispersion flux calculated using two components: one normal to the surface and the other parallel to the surface. The flux normal to the surface is treated in the same manner as the diffusion term in the energy equation. The parallel flux is calculated from the gradient of chemical potential parallel to the surface, which is approximated by the central-difference scheme presented by Peaceman (1966). Therefore, in the numerical computation, the calculations of the dispersion terms will include more nodal points than the diffusion terms and consequently will result in greater computational effort. Convection in the chemical transport equation is handled the same as in the energy transport equation.

In problems involving hydrothermal systems and nuclear waste repositories, a well-known problem is silica dissolution and precipitation. This can alter the formation permeability, thus changing the flow field. The kinetic rates depend on the fluid temperature, the silica concentration, presence of other dissolved chemical species, and the ratio of quartz surface area to the fluid mass available for reaction. The model for the kinetics of silica-water reactions proposed by Rimstidt and Barnes (1980) has been incorporated in the code PTC.

CODE VALIDATION

The validity of the code has been tested against several simple problems, for which exact or approximate analytical solutions are available.

Case 1: One-dimensional convection-diffusion problem

Here we assume that a semi-infinite, homogeneous, isotropic porous medium has a constant concentration C_0 maintained at $x = 0$ and a uniform initial concentration of zero. The isothermal fluid flow has a constant velocity, V/ϕ; the longitudinal dispersion coefficient, D_L, is assumed to be constant. The chemical transport equation then becomes

$$D_L \frac{\partial^2 C}{\partial x^2} - \frac{V}{\phi} \frac{\partial C}{\partial x} = \frac{\partial C}{\partial t}. \tag{1}$$

The solution to Eq. (1) for the given boundary and initial conditions is given by Carslaw and Jaeger (1959) as

$$\frac{C}{C_0} = \frac{1}{2} \left[\operatorname{erfc}\left(\frac{x - Vt/\phi}{2\sqrt{D_L t}} \right) + \exp\left(\frac{Vx/\phi}{D_L} \right) \operatorname{erfc}\left(\frac{x + Vt/\phi}{2\sqrt{D_L t}} \right) \right]. \tag{2}$$

In this test problem, the central-difference scheme is employed. A comparison of numerical and analytical solutions shows very good agreement, as can be seen in Fig. 1.

Case 2: Two-dimensional convection-diffusion with longitudinal and transverse dispersion

In this case, we assume a rectangular, homogeneous, isotropic porous medium with constant concentration C_0 maintained over a portion of the boundary ($0 \leqslant y \leqslant b$) and zero concentration maintained over the rest of the boundary ($b < y \leqslant L$). A uniform initial concentration of zero is assumed. The isothermal flow velocity, V/ϕ, longitudinal dispersion coefficient, D_L, and transverse dispersion coefficient, D_T, are assumed constant. The chemical transport equation can now be expressed as

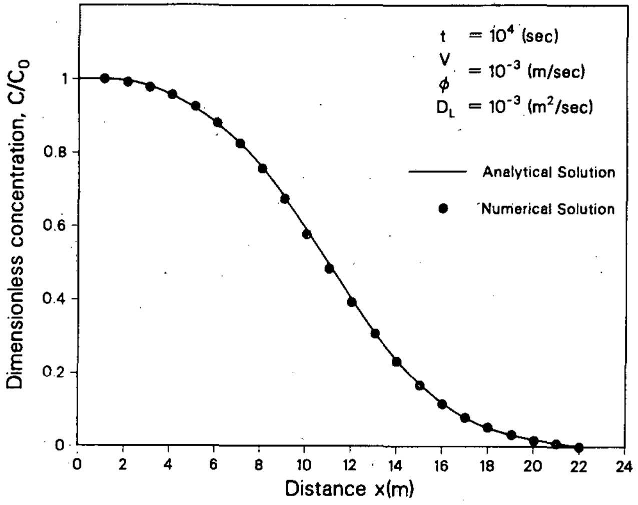

Figure 1. Comparison between numerical and analytical solutions for the one-dimensional convection-diffusion problem. [XCG 8411-13458]

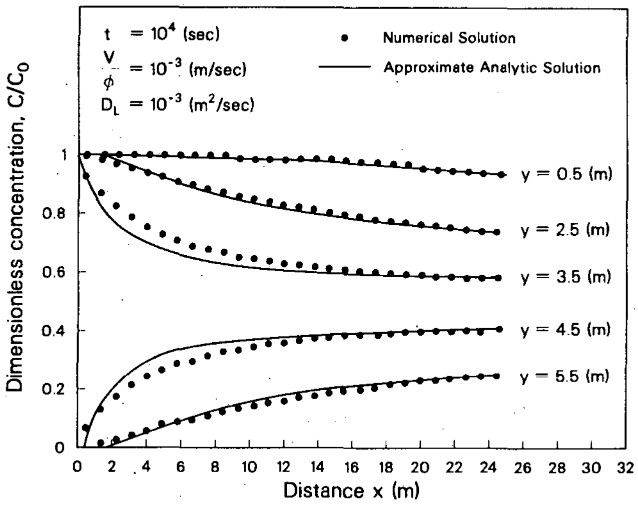

Figure 2. Comparison between numerical and analytical solutions for two-dimensional convection-diffusion problem. [XCG 8411-13459]

$$\frac{\partial C}{\partial t} = D_L \frac{\partial^2 C}{\partial x^2} + D_T \frac{\partial^2 C}{\partial y^2} - \frac{V}{\phi} \frac{\partial C}{\partial x}. \qquad (3)$$

When the input concentration is maintained at the boundary for a long enough time, the concentration distribution approaches the quasi-steady state. Harleman and Rumer (1963) neglected the longitudinal dispersion and transient terms to solve the steady-state problem. Their approximate solution can be expressed as

$$\frac{C}{C_o} = \frac{1}{2} \operatorname{erfc} \left(\frac{y - b}{2\sqrt{D_T X \phi / V}} \right). \qquad (4)$$

Here again we use the central-difference scheme to avoid numerical dispersion. Comparison of numerical and approximate analytical solutions is shown in Fig. 2. The solutions agree well except in the region near $x = 0$. The discrepancy between these results is to be expected, since the approximate analytical solution assumes $\partial^2 C/\partial x^2 = 0$. The discrepancy is largest in the curves for $y = 3.5$ and $y = 4.5$ because the curvature is larger, and hence $\partial^2 C/\partial x^2 >> 0$.

We have attempted to verify the accuracy of the dispersion tensor terms. Theoretically, one would expect that if the grid were oriented at 45° with respect to the flow lines, the dispersion tensor terms would make the results identical to those observed in this case. However, we found that numerical diffusion errors in this case dominate the physical diffusion. Consequently, the validity of the dispersion tensor formulation could not be verified.

Case 3: Numerical Diffusion Problem

In the past decade, many numerical schemes have been designed to solve nonlinear hyperbolic equations. Most of these schemes cannot avoid numerical diffusion or oscillation behind a shock front. Sod (1978) published a survey of finite-difference methods for systems of nonlinear hyperbolic conservation laws. He pointed out that Glimm's sampling method (1965), which was developed by Chorin (1976, 1977) into an effective numerical method, has many advantages over the conventional finite-difference methods and has the ability to track the sharp front in wave-propagation problems. Recently Colella (1982) developed a more accurate sampling procedure that is based on the Van der Corput sampling sequence and used it to solve Riemann problems. Concus and Proskurowski (1979) and Li (1983) have applied this method to porous-media problems.

To apply Glimm's method to the convection-diffusion equation, the operator-splitting method is employed. In the first fractional step, only the convection equation (without diffusion) is solved, using Colella's sampling procedure (sampling once per zone per time-step). After that, the diffusion equation is solved with the conventional finite-difference method.

In order to demonstrate the effectiveness of this approach, the one-dimensional convection-diffusion problem (see Case 1) is again considered. Figure 3 compares the numerical and analytical solutions. It is found that, with a wide range of Peclet numbers, there is no numerical diffusion or oscillation in the

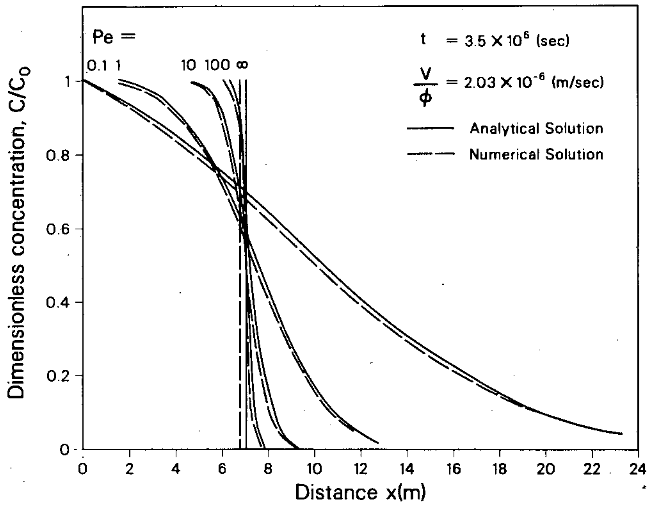

Figure 3. Comparison between analytical and numerical results for several different Peclet numbers. In the numerical work, Glimm's method is used with the van der Corput sampling sequence. [XCG 8411-13457]

numerical solution. Although location of the front in comparison with the analytical solution is not exact, because of the sampling process, it will be correct on the average. We are currently extending this approach to multidimensional problems by using the operator-splitting method.

APPLICATIONS

We have applied the code to various problems in which the coupling between mass, energy, and chemical transport equations is important. Examples include simulations of chemical and thermal changes during exploitation of geothermal systems, predictions of plume movement in contaminated aquifers, and assessment of the thermal regime around a nuclear waste repository.

REFERENCES

Bodvarsson, G.S., 1982. Mathematical modeling of the behavior of geothermal systems under exploitation (Ph.D. thesis). Lawrence Berkeley Laboratory Report LBL-13937, p .18–48.

Carslaw, H.S., and Jaeger, J.C., 1959. Conduction of Heat in Solids (2nd ed.). London, Oxford University Press, p. 388.

Chorin, A.J., 1976. Random choice solution of hyperbolic systems. J. Comp. Phys., v. 22, p. 517–523.

Chorin, A.J., 1977. Random choice method with application to reacting gas flow. J. Comp. Phys., v. 25, p. 253–272.

Colella, P., 1982. Glimm's method for gas dynamics. SIAM J. Sci. Stat. Comp., v. 3, p. 76–109.

Concus, P., and Proskurowski, W., 1979. Numerical solution of a nonlinear hyperbolic equation by a random choice method. J. Comp. Phys., v. 30, p. 153–166.

Duff, I.S., 1977. MA28—A Set of Fortran subroutines for sparse unsymmetric linear equations. AERE Harwell Report R8730, p. 153.

Glimm, J., 1965. Solution in the large for nonlinear hyperbolic systems of equations. Commun. Pure Appl. Math., v. 18, p. 697–715.

Harleman, D.R.F., and Rumer, R.R., 1963. Longitudinal and lateral dispersion in an isotropic porous medium. Fluid Mech., v. 16, no. 3, p. 385–394.

Li, K.M.G., 1983. Random choice method for treating the convection-diffusion equation. *In* Proceedings, Seventh SPE Symposium on Reservoir Simulation, San Francisco, California, November 16–18, 1983, p. 33–40.

Peaceman, D.W., 1966. Improved treatment of dispersion in numerical calculation of multidimensional miscible displacement. Soc. Petrol. Eng. J., September, p. 213–216.

Rimstidt, J.D., and Barnes, H.L., 1980. The kinetics of silica-water reactions. Geochem. Cosmochim. Acta, v. 44, p.1683–1699.

Scheidegger, A.E., 1961. General theory of dispersion in porous media. J. Geophys. Res., v. 66, no. 10, p. 3273–3278.

Sod, G.A., 1978. A survey of general finite difference methods for systems of nonlinear hyperbolic conservation laws. J. Comp. Phys., v. 27, p. 1–31.

Coupled Thermal-Hydraulic-Mechanical Phenomena in Saturated, Fractured, Porous Rocks—Numerical Approach

J. Noorishad, C.F. Tsang, and P.A. Witherspoon

The presence of heat in a liquid-saturated geologic medium brings about a chain of events that is caused by what are referred to as coupled thermal-hydraulic-mechanical phenomena. The interdependence of each of these three phenomena leads to a coupled behavior that is very complex. However, recent progress in coupled analyses among pairs of these three phenomena provides a basis for treating all three phenomena in a fully coupled manner.

This work is the result of our effort to treat the fully coupled problem of thermohydroelasticity and is a natural outgrowth of our earlier work. We first develop the fundamental equations and then define the initial and boundary conditions. Because of the complexity of the problem, we have not attempted an analytical solution. Thus we have developed the finite-element code ROCMAS, which is based on a mixed variational and Galerkin approach. Fundamental laws governing the static equilibrium, flow of fluid, and flow of heat are coupled through the dependent variables of solid displacement vector, fluid pressure, and temperature of the medium. These governing laws were developed to provide the complete mathematical formulation of the linear thermohydroelastic phenomena in saturated porous media and to define the mixed initial-boundary-value problem of thermohydroelasticity, for which a numerical solution is suggested.

Because other methods were not available, full-capability verification of ROCMAS was not possible. A recent publication by Aboustit et al. (1982), however, provided an opportunity for the code-to-code verification that is presented below. A scoping study was performed to simulate the effect of the emplacement of a thermal source in fluid-saturated, fractured rock.

VERIFICATION—THERMOELASTIC CONSOLIDATION OF A SAND COLUMN

Aboustit et al. (1982) used a nonconvective, coupled, variational finite-element approach to analyze the thermoelastic consolidation of a sand column. Table 1 gives the data used in this problem. Results of their analysis have been reproduced in Fig. 1 along with our solution of the same problem. There is almost perfect agreement between the two solutions. The slight discrepancy is due to the interlaced solution scheme of the present work, in which temperature solution lags one step behind the hydromechanical calculations. Reduction of the time-step size will decrease the difference. In solving this problem, the advection of energy along with the effects of fluid compressibility, thermal expansivity, and viscosity variations were assumed to be negligible. All of these assumptions, in addition to those

Table 1. Data used in sand column consolidation analysis.

Material	Property	Value
Rock	Porosity (ϕ)	2.0×10^{-1}
	Young's modulus (E_s)	6×10^3 Pa
	Poisson's ratio (ν_s)	4.0×10^{-1}
	Thermal expansion coefficient (β_t)	3.0×10^{-7}
	Matrix heat capacity (ρC)	167.2 KJ/m^3·°C
	Solid-fluid-thermal conductivity (K_M)	8.36×10^{-1} kJ/m·s·°C
	Permeability (k_f)[a]	4.0×10^{-6} m/s
	Biot's coupling coefficient (α)	1.0

[a] Fluid properties are assumed to be constant in this problem.

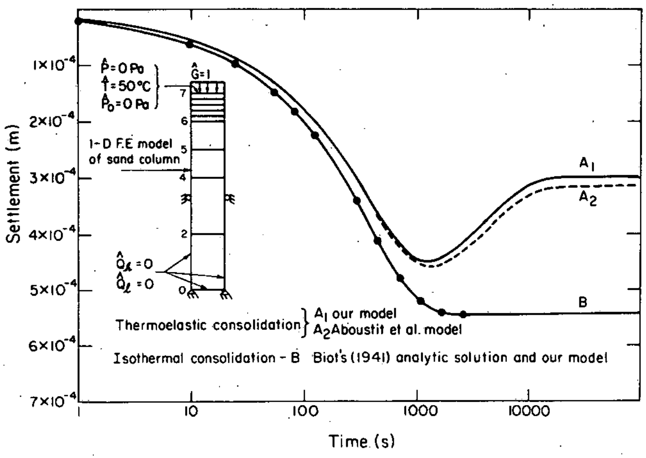

Figure 1. Consolidation history for the one-dimensional finite-element model. [XBL 835-921]

that pertain to linear material behavior, can be relaxed at will in the program ROCMAS.

APPLICATION—A SCOPING ANALYSIS OF THE OCCURRENCE OF COUPLED THERMAL-HYDRAULIC-MECHANICAL PHENOMENA NEAR A HEATER

To demonstrate the ability of ROCMAS to simulate the thermohydromechanical environment around a waste canister or heater, we have studied the changes induced in the inflow of fluid to a heater borehole by increasing temperature. A 5-kW heater is located at a depth of 350 m in granite. A horizontal fracture is assumed to lie 3 m below the heater midplane and to extend from the heater borehole to a hydrostatic boundary at a radial distance of 20 m from the borehole. The properties of rock and fracture are given in Table 2, and the two-dimensional axisymmetric (r,z) finite-element grid is shown in Fig. 2. The heater drift, approximated by the cylindrical hatched area, is simulated by assigning a very low value of Young's modulus to the elements. Before the heater raises the temperature of a large

Table 2. Data used for analysis of fracture fluid flow to a heater borehole.

Material	Property	Value
Rock	Mass density (ρ_s)	2.6×10^3 kg/m^3
	Porosity (ϕ)	5.0×10^{-2}
	Young's modulus $(\dot{E}_s)$	51.3 GPa
	Poisson's ratio (ν_s)	0.23
	Thermal expansion coefficient (β_t)	8.8×10^{-5}/C°
	Specific heat (C_{vs})	2.1×10^{-1} KJ/kg·°C
	Thermal conductivity (K_M)	3.18×10^{-3} KJ/m·s·°C
	Permeability (k_f)	1.0×10^{-18} m^2
	Biot's storativity constant (1/M)	5.0 GPa
	Biot's coupling constant (α)	1.0
Fracture	Initial aperture $(2b)$	10^{-1} m
	Biot's storativity constant (1/M)	5.0 GPa
	Initial normal stiffness (K_N)	85 GPa/m
	Initial tangential stiffness (K_S)	0.85 MPa/m
	Friction angle (ψ)	30°
	Cohesion (C)	0.0
	Porosity, (ϕ)	1.0

Note: For the sake of brevity, the developments presented in this paper do not contain the expansions needed for the inclusion of the nonlinear fracture element. Those expansions are discussed in Noorishad et al. (1982).

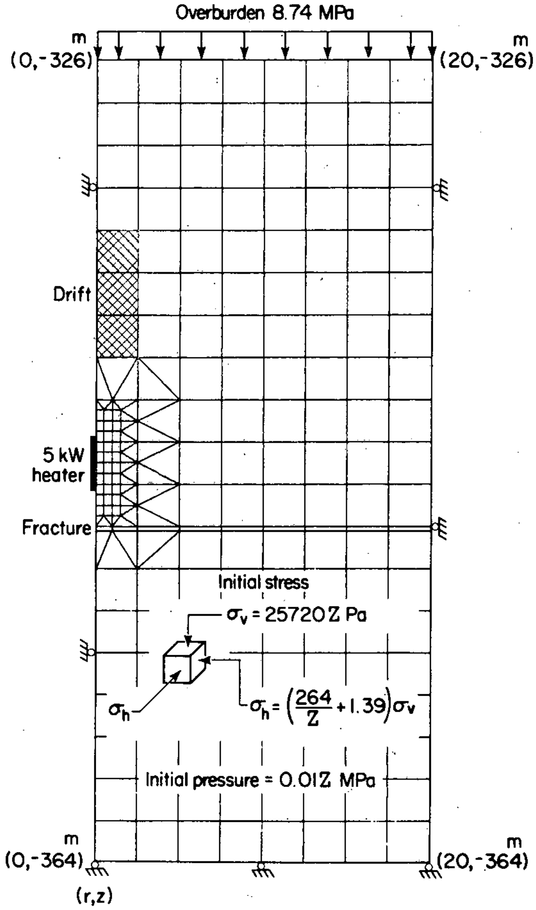

Figure 2. Finite-element model of the heat source environment. [XBL 8210-4847]

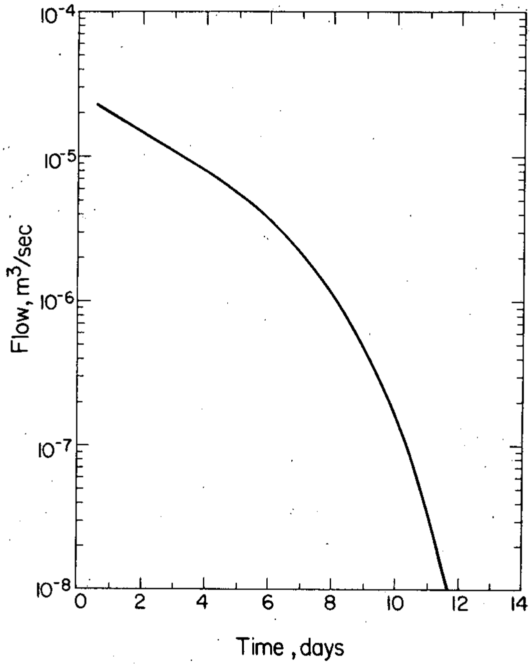

Figure 3. Variation of fluid inflow to the heater borehole as a function of time. [XBL 8210-4843]

volume of the rock, the flow from the hydrostatic outer boundary to the atmospheric ("zero" hydraulic pressure) borehole is high. Later in time, with the heated rock above the fracture expanding and the fracture aperture near the heater borehole closing, the flow decreases sharply, as shown in Fig. 3. The evolution of the fracture aperture profile, together with the variations of the pressure and temperature distributions, are shown in Fig. 4. As may be seen in the pressure-distance graph of this figure, before the tapping of the fracture at 0-day, full hydrostatic pressure prevails in the fracture. This pressure diminishes rapidly at 0.25-day before major development of the thermal front. However, as thermal stresses are established, the fracture starts closing. As a result the pressure inside the fracture starts rising, thus leading to the establishment of full pressure in the fracture at 14-day, similar to the situation at 0-day. These results may provide a better understanding of some of the observations made in the in situ heater experiments in the Stripa granite. The delayed responses of the extensometers in these experiments (Witherspoon et al., 1981) may be explained by the closing of the fracture. Similarly, gradual stoppage of the water inflow into the heater boreholes (Nelson et al., 1981) can be explained by the same phenomena.

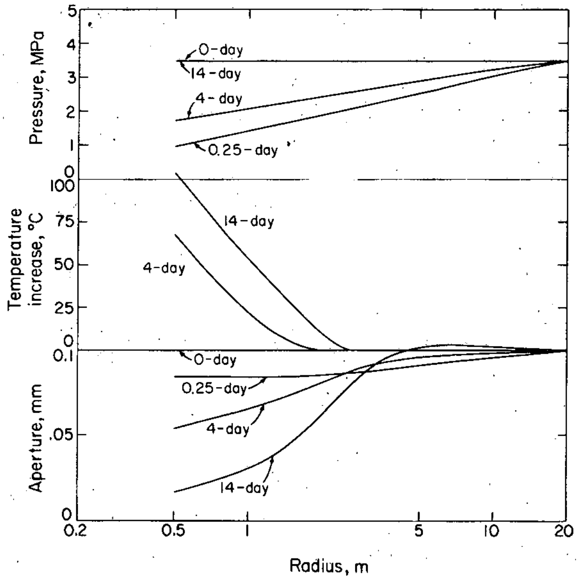

Figure 4. Pressure and aperture profiles in the fracture for various durations and temperature profiles along the heater midplane. [XBL 8210-4848]

The work summarized here provides a new technique for investigation of thermal-hydraulic-mechanical behavior of fractured porous rocks. The work is based on the fundamentals of consolidation and thermoelasticity, which are recast into what we call thermohydroelasticity theory. The results of a code-to-code verification of the triple analysis capability of ROCMAS are presented. In a scoping analysis, thermohydromechanical simulation of fracture fluid flow near a heater was performed. It was shown that the nonlinear fracture behavior activated by coupling effects can change fluid flow behavior in the rock dramatically.

REFERENCES

Aboustit, B.L., Advani, S.H., Lee, J.K., and Sandhu, R.S., 1982. Finite element evaluation of thermo-elastic consolidation. *In* Proceedings, 23rd U.S. Congress on Rock Mechanics, Berkeley, California, August 25–27, 1982, p. 587–595.

Nelson, P.H., Rachiele, R., and Remer, J.S., 1981. Water inflow into boreholes during the Stripa heater experiments. Lawrence Berkeley Laboratory Report LBL-12574.

Noorishad, J., Ayatollahi, M.S., and Witherspoon, P.A., 1982. A finite element method for coupled stress and fluid flow analysis of fractured rocks. Int. J. Rock Mech. Min. Sci. Geomech. Abstr., v. 19, p. 185–193.

Witherspoon, P.A., Cook, N.G.W., and Gale, J.E., 1981. Geologic storage of radioactive waste: Field studies in Sweden. Science, v. 211, p. 894–900.

Multiple Species Chemical Transport with Precipitation and Dissolution: A Case History

T.N. Narasimhan, A.F. White, and T.K. Tokunaga

The inactive uranium mill-tailings pile at Riverton, Wyoming, has been in existence for about 25 years. Earlier field work (Narasimhan et al., 1984; Tokunaga and Narasimhan, 1984; White et al., 1984a,b,c) has established that significant quantities of water infiltrate the tailings, transporting tailings water to the groundwater system below; consequently, the shallow groundwater reservoir contains well-defined plumes of sulfate, uranium, and molybdenum. The purpose of our work is to develop a mathematical model of the geochemical regime in and around the tailings. The model will eventually be of use in preparing proper engineering designs to implement remedial measures for long-term protection of the groundwater system.

THE PROBLEM

Our approach to the problem is fourfold:

1. Use climatologic data at the site to model the fluid potential distribution within the tailings so as to obtain estimates of time-dependent fluid fluxes through the tailings.
2. Use the fluxes so obtained to model the dilution front within the top 2 m of the tailings.
3. Use the same fluxes in conjunction with the natural groundwater velocities to investigate the mixing of tailings water with fresh water leading to the development of the contaminant plume.
4. Monitor the migration of the plume of a single species, such as sulfate, toward the Little Wind River to the southeast.

METHODOLOGY

We divide the overall simulation problem into three parts, arranged in the following sequence: (1) fluid flow analysis, (2) multiple species transport with precipitation dissolution, and (3) migration of the plume of a single species. We choose this scheme to make the overall problem computationally tractable. The first and third parts can be readily handled with off-the-shelf computer programs, but the second part requires the development of a new algorithm (Narasimhan, 1984).

The fluid flow problem is solved first using the computer program TRUST (Narasimhan et al., 1978), which solves for saturated-unsaturated flow in deformable porous media. The forcing function for this phase of the simulation originates in the cyclic rainfall-evaporation boundary conditions summarized from climatic data (Tokunaga and Narasimhan, 1985). The outcomes are the time-dependent fluid fluxes and fluid saturations within the tailings.

The program DYNAMIX solves for multiple species chemical transport with advection, dispersion, and diffusion and the neutralization reactions that occur when water of contrasting chemical quality and pH mix with each other. The DYNAMIX code is used to solve two separate problems. The first is the migration of the dilution front that occurs within the upper 2 m of the tailings as fresh rainwater sweeps downward. Field evidence indicates that the dilution front has migrated only part way into the tailings and that the lower part of the tailings is still undiluted by rainwater. Therefore we treat the mixing of the tailings water with the shallow aquifer below as a distinct second problem.

Figure 1 shows the setup for the mixing problem. The aquifer immediately below the 800 m × 340 m tailings is treated as a slab 800 m by 350 m by 10 m. The regional groundwater velocity is estimated to be 20 m/year toward the southeast. Tailings water filters downward into the aquifer at a rate varying from 1 m/year during the 5 active years of the dump site to about 1 cm/year at the present time, as indicated by the TRUST simulations. The shallow aquifer is divided into seven elemental volumes oriented northeast-southwest and disposed normal to the direction of regional groundwater flow. The tailings water and the groundwater composition are given in Table 1. The mixing of the waters is carried out under the assumption that an abundance of calcite buffer is present in the solid matrix of the shallow aquifer.

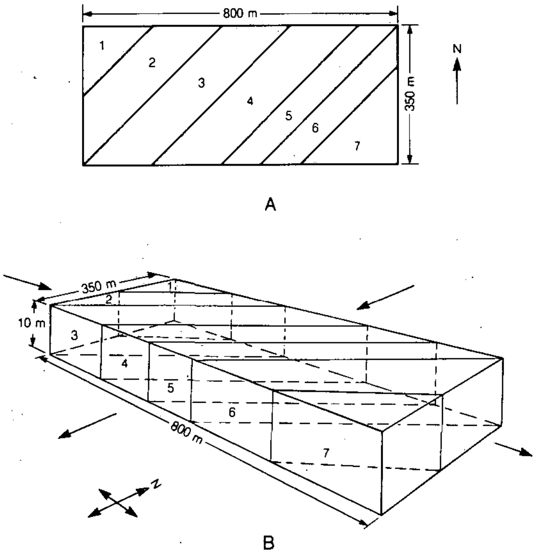

Figure 1. Schematic diagram of mesh used for DYNAMIX simulations. **(A)** Plan view. **(B)** Three-dimensional perspective view. [XBL 8412-5142]

Table 1. Compositions of groundwater and tailings water.

Chemical species	Concentration, mmoles/liter (moles/m^3)	
	Groundwater	Tailings water
Ca	1.76	3.70
Mg	0.905	78.60
Na	3.93	8.00
K	0.105	0.0056
Fe	0.003	773.00
Al	0.001	431.00
Si	0.548	1.53
Cl	0.8174	3.25
C (Total alkalinity)	4.73	0.001
SO_4	2.34	1757.00

Note: Groundwater has pH = 7.60, tailings water pH = 1.43.

The outcomes of this phase of the simulation are the time-dependent aqueous concentrations of the 10 species considered (Ca, Mg, Na, K, Fe, Al, SiO_2, Cl, CO_3, and SO_4) and the pH as a function of location within the aquifer and immediately below the tailings. In addition, the DYNAMIX outputs yielded the time-dependent rates of precipitation of SO_4, $Fe(OH)_3$, and Al_2O_3 and the dissolution rates of calcite.

The final phase of the simulations was to model the time-dependent migration of the sulfate plume. For this purpose a two-dimensional areal mesh was set up (Fig. 2), with the volume elements arranged in the expected direction of regional flow (southeast). The regional groundwater velocity was assumed to be 20 m/year, and the vertical infiltration over the area was assumed to decline from about 1 m/year to about 1 cm/year over 25 years. Both molecular diffusion and hydrodynamic dispersion were considered. A longitudinal dispersivity of 1 m and a transverse dispersivity of 0.1 m were used. Figure 3 gives the precipitation rates for sulfate calculated with the DYNAMIX code. These rates constitute the nonlinear sink terms for the plume-definition problem. This final phase yielded spatial and temporal distributions of aqueous sulfate concentrations

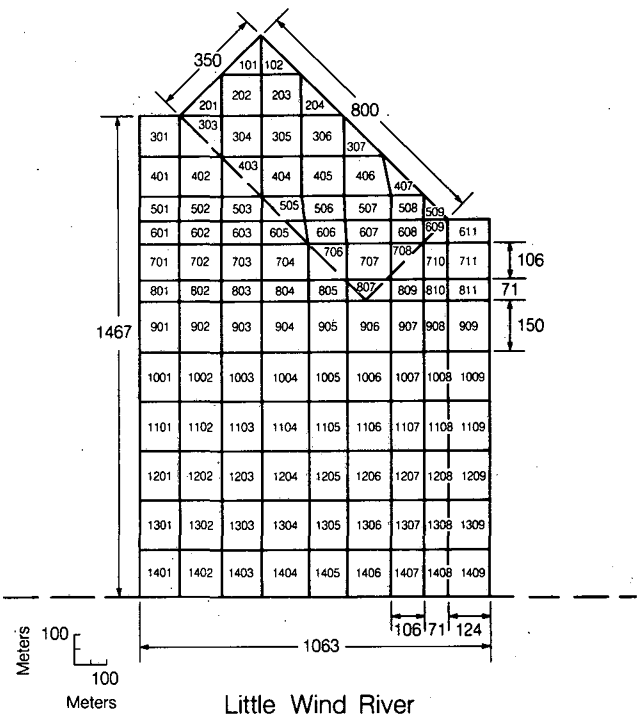

Figure 2. Mesh used in the DYNAMIX simulation. The mesh is oriented parallel to the northwest-southeast direction of regional groundwater flow. [XBL 8410-8901]

that determine the time-dependent disposition of the sulfate plume. The plume-definition calculations were carried out with program TRUMP (Edwards, 1976).

RESULTS

Figure 4 shows the results for the dilution calculations within the upper 2 m of the tailings compared with field observations for Fe, SO_4, and pH. In these calculations a gross annual average infiltration rate of 2 cm/year was assumed over a 20-year period. The results compare favorably except for the fact that the field data indicate a sharper front than that computed.

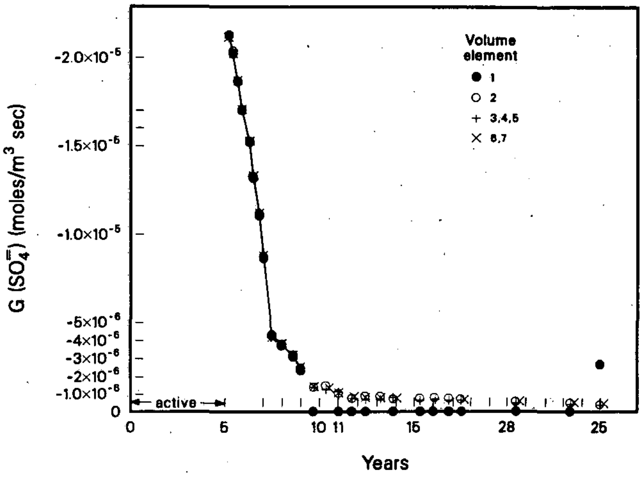

Figure 3. Rate of precipitation of gypsum as a function of time. [XCG 8410-13359]

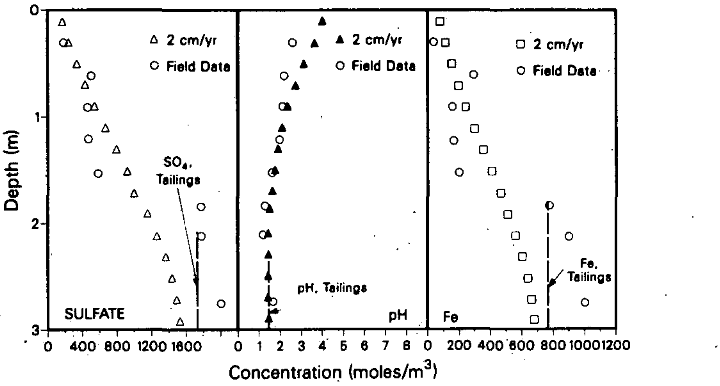

Figure 4. Comparison of observed and computed dilution fronts in the upper part of the tailings. [XCG 8410-13361]

Figure 5 compares the plume as it appears today with that computed for the 25-year case. It is seen that the observed 21 moles/m^3 contour agrees rea-

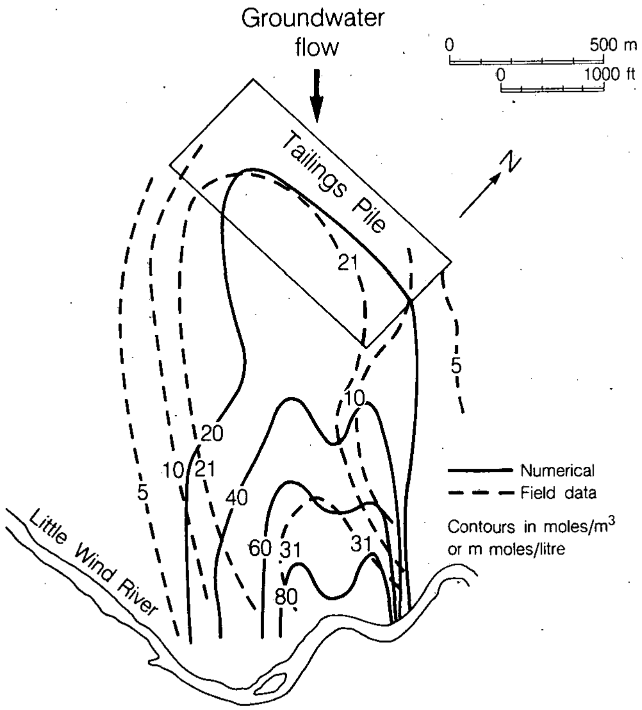

Figure 5. Riverton sulfate plume 20 years after abandonment of the tailings pile. Comparison of TRUMP results with field data (entire plume). [XBL-851-1050]

sonably well with the computed 20 moles/m^3 contour. However, toward the southeast, near the river, the computed values are in excess of the observed values by a factor of about 2.

CONCLUSIONS

The mathematical modeling methodology developed here has established that we can now quantify hydrogeochemical systems in which precipitation/dissolution phenomena are input. The methodology has direct application to such diverse processes as ore genesis (supergene sulfide enrichment), acid rain (response of surface water bodies to acid rain), and radioactive waste disposal.

REFERENCES

Edwards, A.L., 1976. TRUMP: A computer program for transient and steady-state temperature distributions in multidimensional systems. Lawrence Livermore Laboratory Report UCRL-14754, Rev. II, p. 263.

Narasimhan, T.N., 1984. DYNAMIX, A computer program for multiple species chemical transport with precipitation and dissolution. *In* Earth Sciences Division Annual Report 1983. Lawrence Berkeley Laboratory Report LBL-16920, p. 77–78.

Narasimhan, T.N., Witherspoon, P.A., and Edwards, A.L., 1978. Numerical model for saturated-unsaturated flow in deformable porous media. Part 2. The algorithm. Water Resour. Res., v. 14, no. 2, p. 255–261.

Narasimhan, T.H., Tokunaga, T., White, A.F., and Smith, A.R., 1984. Mathematical simulation of contaminant distribution in and around the uranium mill tailings pile, Riverton, Wyoming. *In* Proceedings, Sixth Symposium on Management of Uranium Mill Tailings, Low Level Waste and Hazardous Waste, Colorado State University, Fort Collings Colorado, February 1-3, 1984, p. 197–210.

Tokunaga, T., and Narasimhan, T.H., 1984. Simulation of evaporation from the uranium mill tailings pile at Riverton, Wyoming. *In* Earth Sciences Division Annual Report 1983. Lawrence Berkeley Laboratory Report LBL-16920, p. 75–76.

Tokunaga, T.K., and Narasimhan, T.N., 1985. Hydrologic studies of the Riverton uranium mill-tailings pile. *In* this Annual Report.

White, A.F., Delany, J.M., Narasimhan, T.H., and Smith, A.R., 1984a. A chemical mixing model describing groundwater contamination from an inactive uranium mill tailings pile. *In* Earth Sciences Division Annual Report 1983. Lawrence Berkeley Laboratory Report LBL-16920, p. 196–198.

White, A.F., Yee, A., Narasimhan, T.N., and Smith, A.R., 1984b. Groundwater contamination at the inactive Riverton, Wyoming, uranium mill tailings. Proceedings, Sixth Symposium on Management of Uranium Mill Tailings, Low Level Waste and Hazardous Waste, Colorado State University, February 1–3, p. 185–196.

White, A.F., Delany, J.M., Narasimhan, T.N., and Smith, A.R., 1984c. Groundwater contamination from an inactive uranium Mill tailings pile. I. Application of a chemical mixing model. Water Resour. Res., v. 20, no. 11, p. 1743–1752.

Hydrologic Studies of the Riverton Uranium Mill-Tailings Pile

T.K. Tokunaga and T.N. Narasimhan

In order to understand the processes involved in contamination of the shallow aquifer underlying the Riverton uranium mill-tailings pile, numerical simulations of tailings water flow were performed. Information gained from these studies on the movement of tailings pore water is used in models developed to study contaminant migration from the pile (Narasimhan et al., 1985). Three separate methods have been used to model the infiltration and evaporation into and from the tailings pile. They include two previously reported (Tokunaga and Narasimhan, 1984) methods of arbitrarily step-changed surface potentials and the coupling of climatic influences to surface-pressure-potential-dependent evaporation rates developed by Staple (1974). A third evaporation model (Morton, 1978), based on the complementary relationship areal evaporation (CRAE) approach, has also been considered in a modified form. Finally two-dimensional simulations of vertical transects across the tailings pile were conducted to assess the possible effects of lateral flow of groundwater through the bottom portions of the pile. The program TRUST (Narasimhan et al., 1978) was used for all of these models. The results of simulations from both the modified Morton method and the two-dimensional model are presented here. Defects in both the step-changed surface potential method and the Staple methods will also be reviewed.

The method of step-changed surface potentials consists of using pressure heads of −6 and +0.001 m H_2O to model evaporation and infiltration, respectively, at the upper boundary of vertical tailings columns. Although this model was successful in matching the field-observed hydraulic head profiles in the bulk of the pile, the arbitrary nature of the surface boundary conditions made it unsatisfactory.

In the method developed by Staple, the vapor pressure of pore water in the upper surface is used to calculate evaporation rates according to the Penman formula. This approach couples climatic effects with a pressure-potential-dependent evaporation rate. Although this procedure is more physically reasonable than the step-changed surface-potential method, the results of simulations using Staple's method clearly contradict the field observations. Specifically, even after simulations to only 3 years of drainage and evaporation from initially full saturation, the model predicts excessive desaturation of the tailings pile.

A detailed description of the CRAE method is found in Morton (1978). Very basically, the model predicts that actual evaporation from a region is related in a complementary way to potential evaporation, such that increases in one are coupled to decreases in the other and vice versa. Calculations from this method overestimated evaporative losses for the Riverton tailings pile, as predicted evaporation exceeded precipitation. This is contrary to the nearly steady recharge observed through the tailings pile. As noted previously (Tokunaga and Narasimhan, 1984), this discrepancy may be due largely to the fact that the CRAE calculations are regional estimates, whereas the sparse cover of vegetation on the tailings pile is probably evapotranspiring at a rate below the regional average. Scaling down the CRAE calculations by a factor of 0.55 results in annual losses of 20 cm due to evapotranspiration, leaving 2 cm/year to net infiltration (based on a mean annual precipitation of 22 cm in Riverton). From previous studies (Tokunaga and Narasimhan, 1982) a recharge of 2 cm/year through the tailings appeared reasonable. Therefore, one-dimensional simulations of the tailings pile were performed using 55% of the CRAE-calculated evaporation rates. These reduced CRAE evaporation rates (referred to as 0.55 × E(Morton)) were applied in both a detailed form between 44 yearly precipitation events and in a simplified form in which evaporation and precipitation were averaged over 3-month periods. In both approaches the initial condition was that of full saturation, and the lower boundary condition at 6.75 m depth was that of a fixed water table.

Hydraulic head profiles from the detailed 0.55 × E(Morton) model are shown in Fig. 1, along with field data from July 1982. The displacement of the simulated profiles from that of the field observations are actually due to mass balance errors incurred with the large number of saturation-desaturation cycles. While a net yearly surface influx of 2 cm was specified by this model, water table recharge rates stabilized at over 4 cm/year.

Results from the quarterly averaged 0.55 × E(Morton) model show much better agreement with field observations (Fig. 2). Furthermore, mass balance errors are eliminated. As seen in Fig. 3, groundwater recharge rates settle to the 2 cm/year net surface input by about the 20th year. Oscillations reflect seasonal variations in evaporation and precipitation. Also shown in Fig. 3 are recharge rates from the detailed 0.55 × E(Morton) method and water table recharge rates due to a steady surface source of 2 cm/year superimposed on drainage of the initially saturated tailings.

The two-dimensional transect model of the Riverton tailings pile was developed to determine

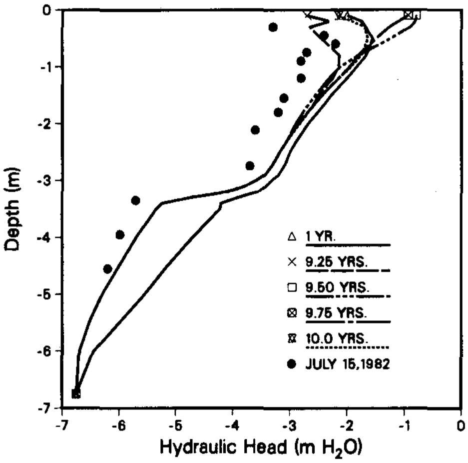

Figure 1. Riverton site B, with 0.55 × E(Morton) and forty-four 0.5-cm rains/year at 1 and 10 years after initial desaturation. [XCG 841-13004]

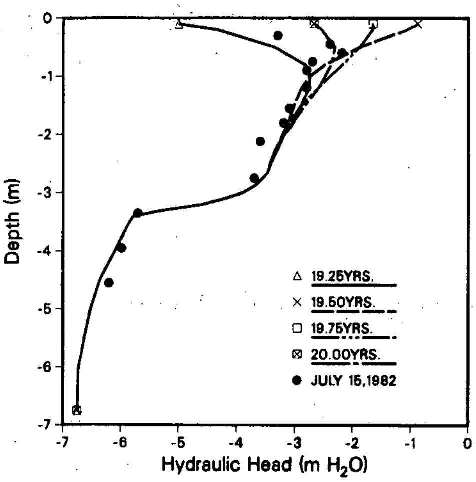

Figure 2. Riverton site B, with 0.55 × E(Morton) and quarterly sink/source, 20th year. [XCG 841-13005]

the extent to which lateral flow from the shallow aquifer occurs in the deeper regions of the pile. The possibility of significant lateral flow within the tailings was suggested by observations of dilution of trace metal concentrations in the bottom meter of tailings pore waters (White et al., 1984). The transect chosen was through the 750-m east-west center line of the pile. The vertical component of this model includes the tailings pile, underlying soil, and shallow aquifer. Upstream and downstream boundaries correspond to the west and east edges of the system, respectively. The boundary conditions used along these surfaces are those of prescribed potentials, allowing various configurations for the piezometric surface. A steady recharge of 1 cm/year was supplied at the upper tailings surface. A recharge rate of a 1 cm/year (rather than the 2 cm/year used previously) was chosen to enhance possibilities for observing lateral flow.

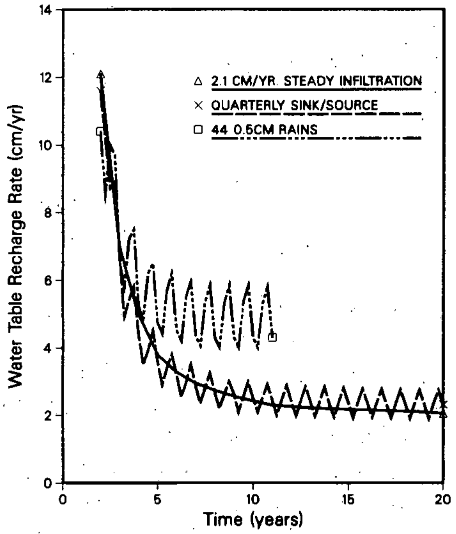

Figure 3. Riverton site B, with 22.0 cm/year precipitation and 0.55 × E(Morton) = 19.9 cm/year evaporation. [XCG 841-13006]

The results of a variety of possible configurations of the two-dimensional system all reveal insignificant components of lateral flow within the tailings pile. The lateral component to the hydraulic head gradients were at most about 3 m/m. Along with a high value for the unsaturated hydraulic conductivity of the lower tailings of 10^{-9} m/s, an upper limit on lateral flow of 10^{-4} m/year is obtained. Such low flux densities are incapable of accounting for the zone of trace metal dilution in the bottom regions of the tailings pile.

REFERENCES

Morton, F.I., 1978. Estimation of evapotranspiration from potential evaporation: Practicality of iconoclastic approach. J. Hydrol., v. 38, p. 1–32.

Narasimhan, T.N., Witherspoon, P.A., and Edwards, A.L., 1978. Numerical method for saturated-unsaturated flow in deformable porous media. Part 2. The algorithm. Water Resour. Res., v. 14, no. 2, p. 255–261.

Narasimhan, T.N., White, A.F., and Tokunaga, T.K., 1985. Hydrology and geochemistry of the uranium mill-tailings pile at Riverton, Wyoming. Part II. History matching. Lawrence Berkeley Laboratory Report LBL-18526, in preparation.

Staple, W.J., 1974. Modified Penman equation to provide the upper boundary condition in computing evaporation from soil. Soil Science Soc. Am., Proc., v. 38, p. 837–839.

Tokunaga, T., and Narasimhan, T.N., 1982. Recent hydrologic observations from the Riverton and Maybell tailings piles. Proceedings, 5th Uranium Mill Tailings Management Symposium, Colorado State University, Ft. Collins, Colorado, December 9–10, 1982. Civil Engineering Department, Colorado State University, p. 463–474.

Tokunaga, T., and Narasimhan, T.N., 1984. Simulation of evaporation from the uranium mill tailings pile at Riverton, Wyoming. *In* Earth Sciences Division Annual Report 1983. Lawrence Berkeley Laboratory Report LBL-16920, p. 75–77.

White, A.F., Delaney, J.M., Narasimhan, T.N., and Smith, A.R., 1984. A chemical mixing model describing groundwater contamination from an inactive uranium mill tailings pile. *In* Earth Sciences Division Annual Report 1983. Lawrence Berkeley Laboratory Report LBL-16920, p. 196–199.

Porous-Media Gas Diffusivity from a Free-Path Distribution Model

T.K. Tokunaga

The concepts of free-path distributions and "dusty gas" approximations have been used in a variety of studies on gas diffusion in porous media (Pollard and Present, 1948; Evans et al., 1961; Strieder, 1971; Ho and Strieder, 1979, 1980). Here a model for the effective diffusivity D_e in porous media is developed from simple consideration of the effects of gas-solid surface collisions on the free-path distribution. This derivation is analogous to those used in free-path models for electron and phonon diffusion in solids. The well-known Bosanquet formula for D_e obtained from various approaches (Pollard and Present, 1948; Evans et al., 1961; Spiegler, 1965; Strieder, 1971; Ho and Strieder, 1980) also results from the model presented here.

Beginning with the self-diffusion coefficient D_0 in a purely gaseous system, simple kinetic theory predicts $D_0 = \overline{v}l_0/3$, where $\overline{v}$ is the mean speed of gas molecules and l_0 is the mean free path. In a porous system D_0 is decreased in two ways. First D_0 is reduced by a factor $f(\epsilon)$ that accounts for porosity ϵ and tortuosity. The nature of $f(\epsilon)$ will not be addressed here. A second reduction in D_0 for porous systems is associated with the decrease of l_0 due to collisions of gas molecules with the solid matrix (more generally the condensed phase). From these considerations the effective diffusivity in an isotropic porous system is

$$D_e = \frac{1}{3} f(\epsilon)\, \overline{v} l_e, \tag{1}$$

where l_e is the mean free path for gas molecules in the porous system. This note focuses on the form of l_e.

In a simple gas system the probability that a molecular trajectory will traverse a distance greater than l is approximately e^{-l/l_0}. More refined calculations accounting for the Maxwell speed distribution still provide nearly the same result (Jeans, 1940). The probability that a molecule will travel a distance l between collisions is therefore approximated by

$$p(l) = \frac{1}{l_0} e^{-l/l_0}. \tag{2}$$

By introducing a solid at a distance l_s along a particular trajectory from a point in a pore, Eq. (2) is modified in the following ways for such trajectories. The probability that $l = l_s$ becomes

$$p(l) = \frac{1}{l_0} \int_{l_s}^{\infty} \exp(-l/l_0)\, dl. \tag{3}$$

The probability that $l > l_s$ clearly becomes zero. The mean free path of these trajectories is therefore

$$l_e(l_s) = \frac{1}{l_0}\left[\int_0^{l_s} l \exp(-l/l_0)\, dl + l_s \int_{l_s}^{\infty} \exp(-l/l_0) dl\right], \tag{4a}$$

$$l_e(l_s) = l_0 \left[1 - \exp(-l_s/l_0)\right]. \tag{4b}$$

The probability distribution of distances along all possible trajectories to solid surfaces $p(l_s)$ is required to obtain the average l_e. The form of $p(l_s)$ is suggested by considering molecular trajectories originating from random positions in the pore space in the Knudsen limit. In this limit, where l_0 is much larger than characteristic pore dimensions, molecules collide essentially only with solid surfaces. Let $P(l_s)$ be the probability that Knudsen limit trajectories exceed l_s from arbitrary starting positions in the pore space. The probability that no surface collision will occur between distances l_s and $l_s + dl_s$ is $1 - kdl_s$, where K is a positive constant. Since averaging for $P(l_s)$ is taken over a macroscopically homogeneous space, the probability $P(l_s + dl_s)$ is equal to the product of the independent probabilities $P(l_s)$ and $P(dl_s)$. This results in

$$\frac{d}{dl_s} P(l_s) = -KP(l_s), \tag{5}$$

which upon integration gives $P(l_s) = \exp(-Kl_s)$. The distribution of interest is

$$p(l_s) = \frac{-d}{dl_s} P(l_s) = \frac{1}{r_0} \exp(-l_s/r_0), \tag{6}$$

where r_0, equal to the mean value of l_s, replaces $1/K$.

The porous-media mean free path results from the integration of the product of Eqs. (4b) and (6) over all possible l_s:

$$l_e = \frac{l_0}{r_0} \cdot \int_0^\infty \left[\exp(-l_s/r_0) - \exp\left(-l_s \left(\frac{l_0 + r_0}{l_0 r_0} \right) \right) \right] dl_s, \tag{7a}$$

$$l_e = \frac{l_0 r_0}{l_0 + r_0}, \tag{7b}$$

$$l_e^{-1} = l_0^{-1} + r_0^{-1}. \tag{7c}$$

Combining Eqs. (1) and (7b) provides the final equations:

$$D_e = \frac{1}{3} f(\epsilon)\bar{v} \frac{l_0 r_0}{l_0 + r_0} = \frac{f(\epsilon) D_0}{1 + Kn}, \tag{8a}$$

$$D_e^{-1} = \left[f(\epsilon) D_0 \right]^{-1} + \left[\frac{1}{3} f(\epsilon)\bar{v} r_0 \right]^{-1}. \tag{8b}$$

The Knudsen number in Eq. (8a) is $Kn = l_0/r_0$. By equating the last term in Eq. (8b) to D_k^{-1}, the inverse of the Knudsen diffusivity, the Bosanquet result is obtained.

As a final observation it is noted that the form of l_e shown in Eq. (7c) is analogous to those of the free-path models for phonon and electron transport in solids (Wert and Thomas, 1963). In each case l_e displays inverse additivity of interparticle effects (interquasiparticle effects in the case of phonons) and particle-matrix effects.

REFERENCES

Evans, R.B., Watson, G.M., and Mason, E.A., 1961. Gaseous diffusion in porous media at uniform pressure. J. Chem. Phys., v. 35, p. 2076.

Ho, F.G., and Strieder, W., 1979. Asymptotic expansion of the porous medium, effective diffusion coefficient in the Knudsen number. J. Chem. Phys., v. 70, p. 5635.

Ho, F.G., and Strieder, W., 1980. Numerical evaluation of the porous medium effective diffusivity between the Knudsen and continuum limits. J. Chem. Phys., v. 73, p. 6296.

Jeans, J., 1940. An Introduction to the Kinetic Theory of Gases. Cambridge Univ. Press.

Pollard, W.G., and Present, R.D., 1948. On gaseous self-diffusion in long capillary tubes. Phys. Rev., v. 73, p. 762.

Spiegler, K.S., 1965. Diffusion of gases across porous media. Ind. Eng. Chem. Fundam., v. 5, p. 529.

Strieder, W., 1971. Gaseous self-diffusion through a porous medium. J. Chem. Phys., v. 54, p. 4050.

Wert, C.A., and Thomas, R.M., 1963. Physics of Solids. New York, McGraw-Hill.

Numerical Modeling of Gas Reservoirs and Gas–Condensate Reservoirs

M.F. Amin, T.N. Narasimhan, and W.H. Somerton

Gas–condensate reservoirs are characterized by the special feature that, as the pressure in the gas phase declines below the dew point pressure, which is a function of gas composition and temperature, a portion of the gas will condense to form a condensate liquid, so that both gas and liquid phases will coexist (Fig. 1). In a system at constant temperature, a further decrease in pressure will increase the volume of condensate as shown in Fig. 2. However, at some lower pressure (point *A* in Fig. 2), condensation will stop, and gas will begin to bubble out of the condensate phase once again. Such a phenomenon is known as retrograde condensation. It is of considerable practical interest to develop mathematical models to simulate gas flow in such reservoirs. The purpose of the work summarized here is to develop such a model.

THEORY

We consider a gas reservoir in which the gas component is characterized as a 12-component system consisting of methane (C1), ethane (C2), propane (C3), isobutane (i-C4), normal butane (n-C4), isopentane (i-C5), normal pentane (n-C5), hexane (C6), heptane plus (C7+), hydrogen sulfide (H_2S), carbon dioxide (CO_2), and nitrogen (N_2). We consider this system to be under a given constant temperature but allowed to experience change in pressure. We assume that the reservoir rock may have a prescribed water saturation below the residual saturation so that water is immobile. We also assume that the condensate is immobile. Considering that the range of pressure manifested by a gas reservoir as it changes from a pure gas reservoir to a gas–condensate reservoir is about a few thousand pounds per square inch, one would expect the reservoir to experience significant pore compression due to significant increases in effective stress. Thus the model will also have to consider the porous-medium deformation accompanying the pressure reduction.

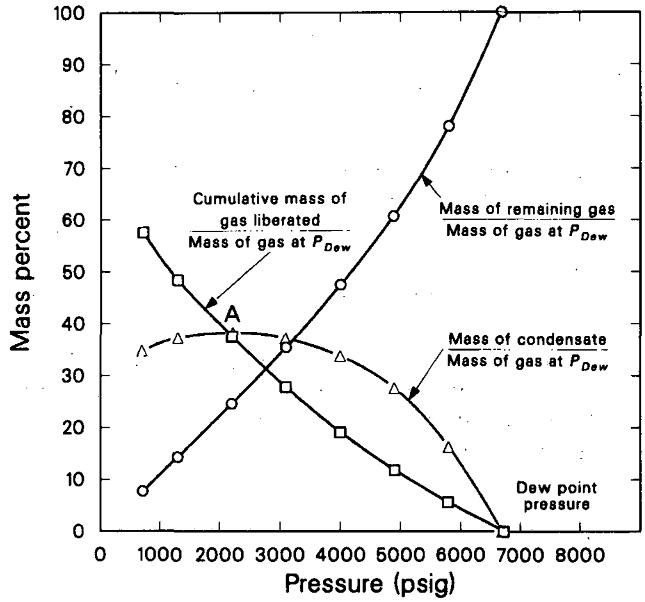

Figure 2. Mass percent of cumulative gas liberated, gas remaining in pore spaces, and condensate formed with respect to the total mass of gas at dew point pressure versus pressure. [XCG 8412-13488]

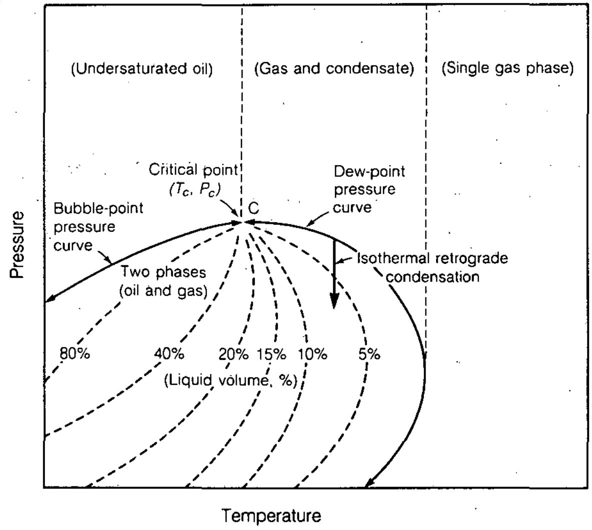

Figure 1. A typical pressure-temperature phase diagram for a multicomponent hydrocarbon system. [XBL 8412-6191]

The general equation for the transport of multicomponent condensate–gas systems can be derived from the principle of mass conservation (embellished by the equation of motion and the equation of state for nonideal gases). This equation may be expressed by the following continuity statement:

$$\sum \text{mass flux} + \text{source (or sink) term}$$
$$= \text{rate of change of mass.} \qquad (1)$$

We now use an integral form of Darcy's law (Narasimhan, 1985) for the flow of fluids through a tube of nonuniform cross-sectional area and the following expression for the mass flux of gas, m_g, for the special case of a radial system:

$$\dot{m}_g = \rho_g q A(r)$$
$$= \frac{-2\pi h M k k_{rg} \, (P_{i+1}^2 - P_i^2)}{2RT\mu(P)z(P) \ln(r_{i+1}/r_i)}, \qquad (2)$$

where $\rho_g = MP/[z(P)RT]$ = density of gas, M = gas molecular weight (a function of composition), P = pressure, $z(P)$ = gas deviation factor (a function of pressure and gas composition), R = universal gas constant, T = average reservoir temperature, $q = [-kk_{rg}/\mu(P)](\partial P/\partial r)$ = Darcy's equation for laminar flow, k = absolute permeability, k_{rg} = relative permeability to gas, $\mu(P)$ = viscosity (a function of pressure and gas composition), r = radial distance between nodal point and interface, and $A(r)$ = cross-sectional area of the interface. In addition to the accumulation of gas in an elemental volume as dictated by Darcy's Law, the condensation of gas in the two-phase region needs to be considered. To account for this condensation process, we use a pressure-dependent, nonlinear source/sink term in the governing equation. The strength of this source term is related to the gas–condensate mass-fraction curve given in Fig. 2.

We now consider the term for the rate of change of mass on the right-hand side of Eq. (1). The rate of change of mass in an elemental volume will be governed by both the change in the void volume of the element (controlled by the compressibility of the rock) and the change in density and saturation of the gas (controlled by the change in pressure and composition). Thus the rate of change of mass of gas is given by

$$\frac{\partial M_g}{\partial t} = V_s \frac{\partial(\rho_g e S_g)}{\partial t} = \frac{MV_s}{2z(P)RT}$$
$$\cdot \left[S_g a_v + e\frac{\partial S_g}{\partial P} + S_g \frac{e}{P} - S_g \frac{e}{z}\frac{\partial z}{\partial P} \right] \frac{\partial P^2}{\partial t}, \qquad (3)$$

where M_g = mass of gas in an elemental volume, t = time, V_s = bulk volume, $S_g = (1.0 - S_w - S_o)$ = gas saturation, S_w = water saturation, S_o = oil saturation, a_v = coefficient of rock compressibility, and e = void ratio. Combining Eqs. (2) and (3), we arrive at the following equation for a discretized radial flow system:

$$\sum_i \frac{-2\pi h M k k_{rg} \, (P_{i+1}^2 - P_i^2)}{2RT\mu(P)z(P) \ \ln(r_{i+1}/r_i)}$$
$$+ \text{ source (or sink) term } = \frac{MV_s}{2z(P)RT}$$
$$\cdot \left[S_g a_v + e\frac{\partial S_g}{\partial P} + S_g \frac{e}{P} - S_g \frac{e}{z}\frac{\partial z}{\partial P} \right] \frac{\partial P^2}{\partial t}. \qquad (4)$$

The source term in Eq. (4) is a function of the average gas pressure during an interval of time t and is determined by the slope of the gas–condensate mass fraction curve in Fig. 2.

A computer program called GASFLOW has been developed to solve Eq. (4) using an implicit method. The resulting matrix of linear equations is solved with a direct solver. GASFLOW is an extension of an earlier algorithm of the same name developed by C.H. Lai (personal communication, 1981).

THE EQUATION OF STATE

It is of particular interest to discuss briefly the equation of state for a gas in the gas reservoirs and gas–condensate reservoirs. As long as the reservoir pressure is above the dew point pressure, the gas will remain in a single phase and its composition will remain constant. The gas deviation factor, $z(P)$, and viscosity, $u(P)$, in the governing equation are dependent only upon pressure. An equation of state that accurately represents the Standing-Katz z-factor chart was presented by Hall and Yarborough (1971):

$$z(P) = \frac{0.06125Pt \exp[-1.2(1 - t)^2]}{P_c X}, \qquad (5)$$

where $t = T_c/T$, T_c = critical temperature, and X is determined from the following nonlinear equation when $F = 0$ is satisfied:

$$
\begin{aligned}
F = {} & -0.06125\frac{Pt}{P_c}\exp[-1.2(1-t)^2] \\
& + \frac{X + X^2 + X^3 - X^4}{(1-X)^3} \\
& - (14.76t - 9.76t^2 + 4.58t^3)X^2 \\
& + (90.7t - 242.2t^2 + 42.2t^3)X^{(2.18 + 2.82t)} \\
& = 0.0.
\end{aligned}
$$

The following equation for gas viscosity, $\mu(P)$, was presented by Lee et al. (1971):

$$
\begin{aligned}
\mu(P)\,[\text{micropoise}] = {} & \frac{(9.4 + 0.02M)T^{1.5}}{(209 + 19M + T)} \\
& \cdot \exp\left\{\left(3.5 + \frac{986}{T} + 0.01M\right)\right. \\
& \left. \cdot\, \rho_g\left(2.4 - 0.2\left[3.5 + \frac{986}{T} + 0.01M\right)\right]\right\}. \qquad (6)
\end{aligned}
$$

During retrograde condensation in the two-phase flow region, the compositions of both gas and liquid change with pressure according to the equilibrium ratios or K values of each component of the hydrocarbon mixtures. Thus M, $z(P)$, and $\mu(P)$ in the governing equation are dependent on both pressure and composition of the hydrocarbon mixtures. In this case, where significant interphase mass transfer occurs, compositional modeling is required to predict the compositional changes and flow performance.

In compositional modeling, the reliability and accuracy of the numerical model is strongly dependent upon the accuracy of the K values. Considerable efforts have been directed toward the development, modification, and application of the equation of state to determine K values for predicting phase behavior. The most widely used are the cubic equations of state of Redlich and Kwong (1949), modified by Soave (1972), Zudkevitch and Joffe (1970), and Peng and Robinson (1976). Whitson and Torp (1981) and Bashbush (1981) have shown that a reasonably accurate set of K values can also be determined by material balance from the constant-volume depletion (CVD) data. We calculate our K values from CVD data obtained from reports of *PVT* analyses of the hydrocarbon system to be studied.

MODEL VALIDATION

Program GASFLOW can simulate the flow of an ideal gas or a real gas in multidimensional, isothermal gas, or gas–condensate reservoir systems. The following parameters need to be specified:

Gas reservoirs:

Ideal gas – IDEAL = 1 and PDEW = 0.0,
Real gas – IDEAL = 0 and PDEW = 0.0.

Gas–condensate reservoirs:

Ideal gas – IDEAL = 1 and PDEW = P_{sat},
Real gas – IDEAL = 0 and PDEW = P_{sat}.

The model has been validated successfully against a numerical solution by Jenkins and Aronofsky (1953) for solutions of ideal gas flow (Fig. 3).

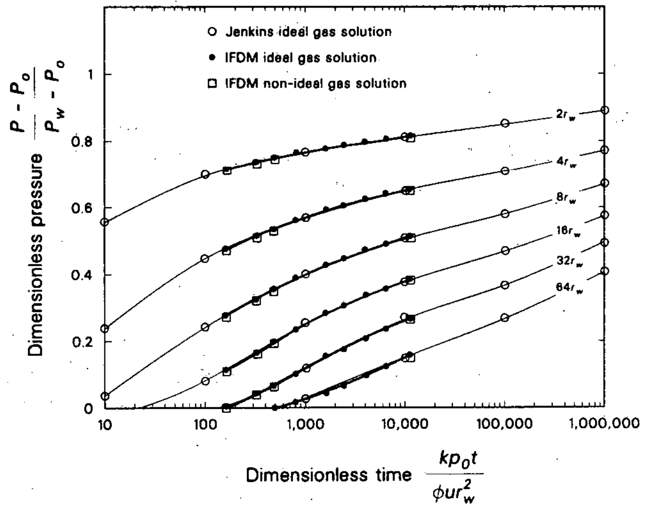

Figure 3. Dimensionless pressure distribution for radial gas flow. Comparison of Jenkins' ideal gas solution with IFDM ideal and nonideal gas solutions. [XCG 8412-13487]

REFERENCES

Bashbush, J.L., 1980. A method to determine K-values from laboratory data and its applications. Presented at the 56th Annual Fall Technical Conference and Exhibition of the Society of Petroleum Engineers of AIME, San Antonio, Texas, October 5–7, 1981 (SPE-10127).

Hall, K.R., and Yarborough, L., 1971. A new equation of state for z-factor calculations. Oil Gas J., June 18, p. 82–82 (SPE Reprint Series No. 13, p. 227).

Jenkins, R., and Aronofsky, J.S., 1953. Unsteady radial flow of gas through porous media. J. Appl. Mech., v. 20, p. 210.

Lee, A.L., Gonzalez, M.H., and Eakin, B.E., 1971. The viscosity of natural gases (SPE Reprint Series No. 13, p. 201).

Narasimhan, T.N., 1985. Geometry-imbedded Darcy's law and transient subsurface flow. Water Resour. Res., in press.

Peng, D.Y., and Robinson, D.B., 1976. A new two-constant equation of state. Ind. Eng. Chem. Fundam., v. 15, no. 1, p. 59–64 (SPE Reprint Series No. 15, p. 46).

Redlich, O., and Kwong, J.N.S., 1949. On the thermodynamics of solutions—An equation of state. Fugacities of Gaseous Solutions. Chem. Rev., v. 44, p. 233–244 (SPE Reprint Series No. 15, p. 52).

Soave, G., 1972. Equilibrium constants from a modified Redlich-Kwong equation of state. Chem. Eng. Sci., v. 27, no. 6, p. 1197–1203 (SPE Reprint Series No. 15, p. 64).

Whitson, C.H., and Torp, S.B., 1981. Evaluating constant volume depletion data. Presented at the 56th Annual Fall Technical Conference and Exhibition of the Society of Petroleum Engineers of AIME, San Antonio, Texas, October 5–7, 1981.

Zudkevitch, D., and Joffe, J., 1970. Correlation and prediction of vapor–liquid equilibria with the Redlich-Kwong equation of state. Am. Inst. Chem. Eng. J., v. 19, no. 1, p. 1120–1129.

Benchmarking of the TRUST Code for Nuclear Waste Isolation

M. Alavi and T.N. Narasimhan

The Nevada Nuclear Waste Storage Investigation project (NNWSI), managed by the Nevada operations office of the U.S. Department of Energy, is investigating the possibility of siting a repository for high-level nuclear wastes at Yucca Mountain. This necessitates studying the long-term effects of radionuclide containment on the hydrologic and geochemical systems at Yucca Mountain. Such study requires the use of computer codes, which must be benchmarked and eventually validated against laboratory and field data. One of the codes chosen for the benchmarking activity is TRUST, which is being used as part of the Nuclear Regulatory Commission system (Narasimhan et al., 1978; Reisenauer et al., 1982).

TRUST is a three-dimensional, isothermal, fluid-flow code that can be used as a tool to solve fluid-flow problems in variably saturated, deformable porous media. It uses an integrated finite-difference scheme combined with a mixed explicit-implicit numerical procedure in which the time-step is internally set. The latest version of the TRUST code, TRUST84, incorporates additional automatic control on time-stepping to eliminate user judgement, especially when convergence problems arise.

BENCHMARKING

As the first step in certifying the codes to be used in the NNWSI performance assessment, six codes were chosen by the NNWSI Repository Performance Assessments group at Sandia National Laboratories, Albuquerque, to participate in the code verification activity (COVE).

The COVE benchmarking activity consisted of three cases of a hypothetical tile-drainage problem. The flow region considered is a box of soil 150 cm deep, 500 cm wide, and 1 cm thick, with the tile located at a depth of 75 cm on the right-hand side (Fig. 1).

The first case, called COVEIN, is the problem solved by Pickens et al. (1979). The soil is a medium-grained sand having a saturated hydraulic conductivity of 5.833×10^{-3} (cm/s) and a dry bulk density of 1.650 (g/cm^3). The boundary conditions specify no flow everywhere except at the tile, where constant atmospheric pressure is imposed. Initially the system is fully saturated (Fig. 1a). The tile is modeled as a 5-cm by 10-cm rectangle, and the system is allowed to drain for a period of 24 hours. Comparison of water table decline midway between the tile lines shows TRUST to be in excellent agreement with Pickens (Fig. 2). The mass balance is defined as the difference between the sum of the cumulative boundary fluxes and the change in the mass of fluid in the system normalized by the original mass of fluid in the system. Defining the mass balance in this way results in an error of less than 0.38%.

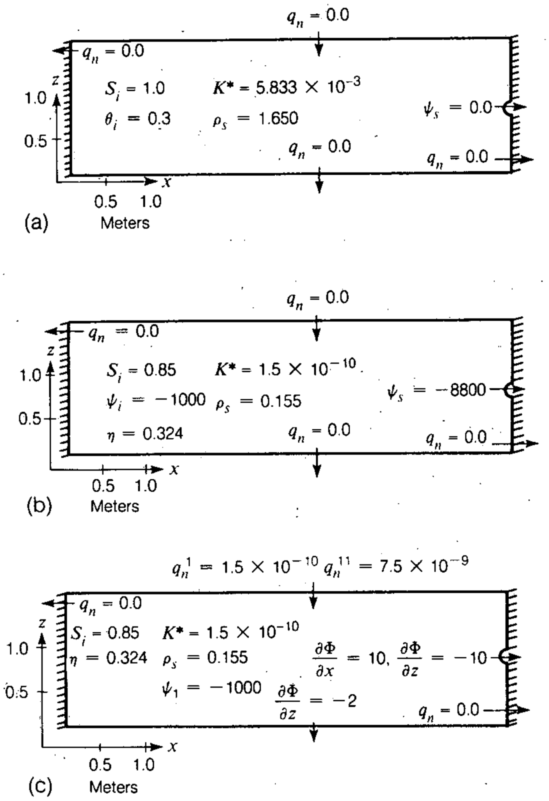

Figure 1. Geometry, boundary conditions, and hydrologic conditions for the three cases studied in the tile-drainage problem. **(a)** COVEIN. **(b)** COVEIYMa. **(c)** COVEIYMb. [XBL 851-10247]

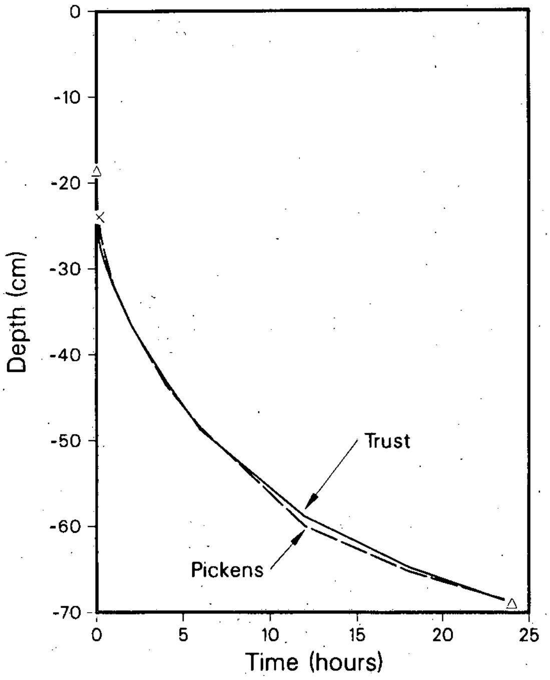

Figure 2. Water table decline at the point midway between tile lines (rectangular tile). [XCG 8312-4929]

The second case, COVEIYMa, has the same geometry as COVEIN, but the material properties and boundary and initial conditions of the system represent those of an unsaturated tuff unit at Yucca Mountain. The dry bulk density is 0.155 g/cm^3, the porosity 0.324 cm/s, the saturated hydraulic conductivity 1.5×10^{-10} cm/s, and the initial saturation state 0.85. The boundary conditions specify no flow everywhere and a pressure head of −8800 cm at the tile (Fig. 1b). In this case the tile was modeled the same way as in COVEIN. The system is allowed to drain for 20,000 years. The pressure head throughout the system declines with time (Fig. 3). Calculating the mass balance in the same manner as in COVEIN gives an error of less than 0.06%.

The third case, COVEIYMb, has the same geometry, material properties, and initial saturation state as COVEIYMa. The boundary conditions specify a combination of fluid-potential gradients at the tile and the bottom, no flow at the left boundary, and a variable infiltration rate at the top. The infiltration rate varies in the following manner:

$$q_n' = 1.5 \times 10^{-10}\ \text{cm/s}$$

for $t \leqslant 5000$ years and $t > 5000$ years + 1 week,

$$q_n' = 7.5 \times 10^{-9}\text{cm/s}$$

for 5000 years $< t \leqslant$ 5000 years + 1 week.

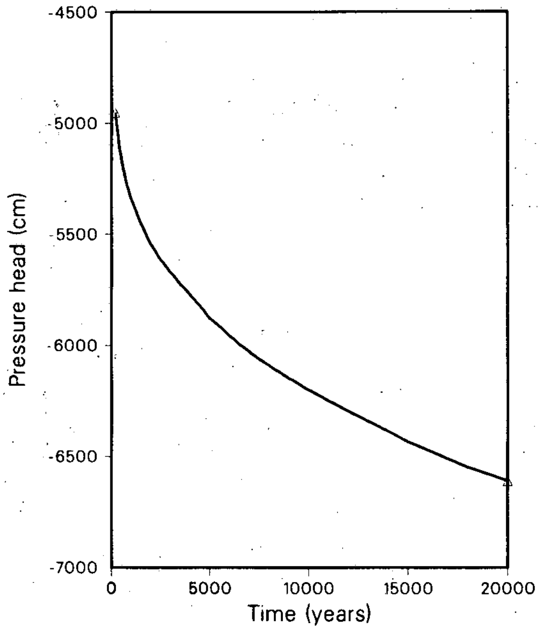

Figure 3. Fluid pressure at tile drain (Yucca Mountain, Case a; x = 492.50 cm, z = 75 cm). [XCG 843-13024]

Table 1. Mass balance and CPU listing for the codes used in the benchmarking activity.

	Mass balance			CPU		
Code	IN	IYMa	IYMb	IN	IYMa	IYMb
TRACR3D	—	< 0.05%	< 4.2%	2700[f]	1920[d,f]	814[d,e,f]
SAGUARO	< 1%	< 1%	< 1%	493[f]	226[d,f]	760[d,e]
TRUST	< 0.38%	< 0.06%	< 0.25%	120[c]	68[c,d]	67[c,e]
GWVIP	< 0.01%	< 0.03%	—	1700[a,b]	650[a,b]	—

[a] Calculation ran to 10,000 years.

[b] Calculated on Harris 800 computer.

[c] Calculated on CDC 7600 computer.

[d] Calculation to 20,000 years.

[e] Did not include transient pulse.

[f] Calculated on CRAY computer.

The tile was modeled in the same fashion as in the two previous cases. The system is allowed to drain for 20,000 years, but the steady-state criteria are satisfied after 2167 years. The calculated mass balance error was less than 0.25%.

SUMMARY

It was reported by Sandia's NNWSI Repository Performance Assessments group that all calculations for COVEIN almost exactly match those of Pickens et al. (1979) for water table decline midway between the tile lines. The water content contours predicted by all of the participating codes are nearly indistinguishable for all times. Qualitative agreement is seen for hydraulic head contours calculated by all codes, and the tile exit geometry affects SAGUARO results by the same amount as it affects TRUST results. As far as COVEIYMa and COVEIYMb are concerned, only mass balances and CPU times (Table 1) are available at this time.

REFERENCES

Narasimhan, T.N., Witherspoon, P.A., and Edwards, A.L., 1978. Numerical model for saturated-unsaturated flow in deformable porous media. Part 2. The algorithm. Water Resour. Res., v. 14, no. 2, p. 255–261.

Pickens, J.F., Gillham, R.W., and Cameron, D.R., 1979. Finite-element analysis of the transport of water solutes in tile-drained soils. J. Hydrol., v. 40, p. 243–264.

Reisenauer, A.E., Key, K.T., Narasimhan, T.N., and Nelson, R.W., 1982. TRUST: A computer program for variably saturated flow in multidimensional, deformable media. U.S. Nuclear Regulatory Commission Report NUREG/CR-230.

Fluid Flow in Partially Saturated, Fractured, Porous Media

J.S.Y. Wang and T.N. Narasimhan

Fluid flow in partially saturated, fractured tuff is different from the fluid flow in saturated media. In saturated, fractured zones, fluid generally moves along fractures. Because fractures generally have apertures that are large relative to the size of the matrix pores and because the capillary forces are strong enough to hold fluid in the smaller pores, fractures in the unsaturated zone tend to desaturate more easily than do the pores in the rock matrix during a drainage process. As a result, the bulk of the fluid moves through interconnected pores in the matrix. Within a partially drained fracture, the presence of a relatively continuous air phase will produce a nearly infinite resistance to liquid flow in the direction parallel to the fracture. The residual liquid will be held by capillary forces in regions around fracture contact areas, where the apertures are small. Normal to the fracture surfaces, the drained portions of the fractures will reduce the effective area for liquid flow from one matrix block to another matrix block. This report summarizes a general statistical theory for flow along the fracture and for flow between the matrix blocks (across the fractures) under partially saturated conditions. Results are obtained from an aperture distribution model for fracture saturation, hydraulic conductivity, and effective matrix-fracture flow areas as functions of pressure. Drainage from a fractured tuff column is simulated. The tuff column represents the partially saturated, fractured Topopah Spring Member at Yucca Mountain, on and adjacent to the Nevada Test Site. Yucca Mountain is being evaluated as a possible repository site for high-level nuclear wastes.

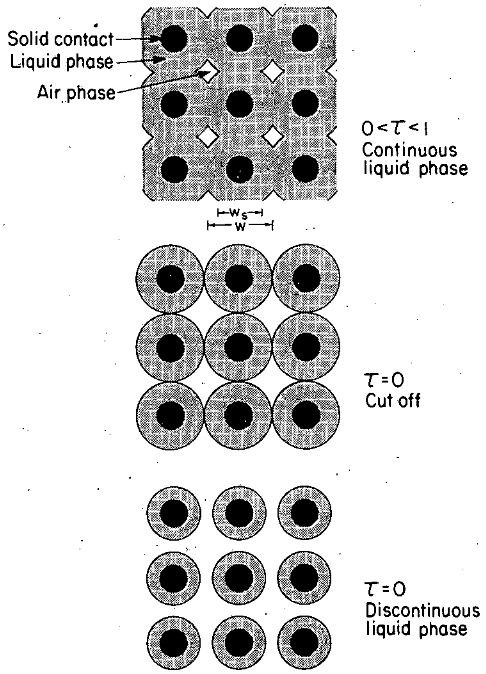

Figure 1. Desaturation of fracture surface, showing schematically the changes in the configuration of the liquid phase (shaded areas) around contact areas in the fracture plane (black areas). [XBL 842-9615]

DESATURATION OF ROUGH-WALL FRACTURES

If the capillary theory is applied to real fractures with rough walls and variable apertures, the sections of large aperture will drain first as the magnitude of the capillary suction increases (or the pressure head becomes more negative). Two important phenomena will occur as the fractures desaturate: (1) air pockets will form along fracture surfaces, thereby reducing the fractures' effective permeability for liquid flow, and (2) flow between adjacent matrix blocks and normal to the fractures will occur only through sections of the fractures that remain saturated. Unsaturated portions within the fractures will then become barriers to liquid flow, both along the fractures and normal to the fractures. Figure 1 shows schematically the changes of liquid phase configuration on a fracture surface during the desaturation process. If the liquid phase is continuous (Fig. 1, top), the liquid can flow along the fracture plane with effective width of flow determined by the width of the neck (W_s in Fig. 1) between nearest-neighbor dry areas (air pockets). The ratio $\tau = W_s/W$, where W_s is the neck width and W is the nearest-neighbor distance, can be quantified as an effective phase-separation constriction factor to take into account the blockage of flow by the air pockets and the change of flow paths in swinging around these dry areas. If the liquid phase is discontinuous on the fracture surface, liquid cannot flow along the fracture (Fig. 1, bottom). Therefore, $\tau = 0$ determines the cutoff for fracture flow for a partially saturated fracture (Fig. 1, middle).

Figure 2 compares the discrete fracture permeabilities with and without the phase-separation constriction factor taken into account. The case in which $\tau = 1$ ignores the blockage effects and takes into account only the generalized cubic law for fracture flow. With $\tau = 1$, we overestimate the fracture permeabilities and ignore the zero-fracture permeability cutoff. The effects of this phase-separation constriction factor will be discussed in the simulation results. The discrete fracture permeabilities as functions of pressure are derived from fracture-aperture distribution functions for the vertical and horizontal fracture sets in the partially saturated Topopah Spring tuff formation. The parameters of the distributions are deduced from fracture surface characteristics, spacings, and orientations determined from core analyses (Spengler and Chornack, 1984). Zeolites, clays, and calcite coat 12% of the fracture surfaces in the core. We identify the fracture coating ($\omega = 12\%$) with the fraction of contact area on the

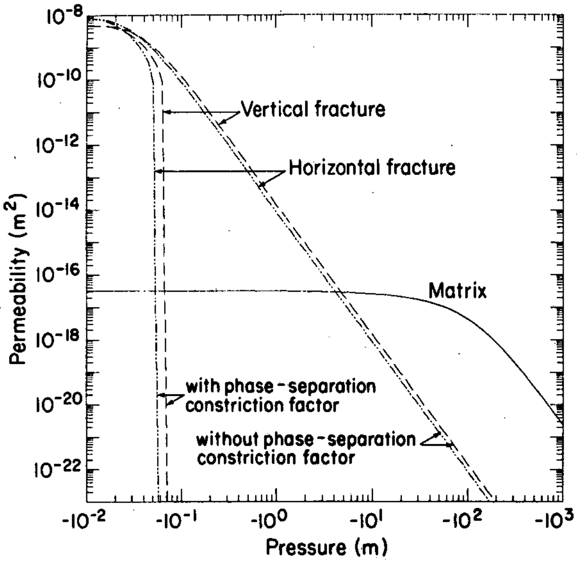

Figure 2. Permeabilities of partially saturated discrete fractures and tuff matrix with parameters derived from data on the Topopah Spring Member [XBL 842-9620]

assumption that hydrochemical alterations occur in contact areas that remain in continuous contact with water for a long time.

Figure 2 also shows that the fracture permeabilities are very sensitive to suction. If fully saturated, the permeability of each discrete fracture is eight orders of magnitude greater than the matrix permeability. With small suctions in the range -10^{-1} to -10^{1} m, the discrete fracture permeabilities decrease drastically. The matrix permeability decreases much more gently as the pressure head becomes more negative. Fractures that are almost fully saturated will control the fluid flow. As desaturation proceeds and the fracture permeability of each discrete fracture becomes less than the matrix permeability, the matrix will control the flow. For in situ suction of -111.6 m in the Topopah Spring Member with matrix saturation of 80%, fracture flow is negligible and matrix flow dominates.

The matrix flow also will be impeded when it crosses the fractures. The matrix-fracture flow is limited by the fracture surface area available for transmission of fluid. The effective fracture-matrix flow area decreases and quickly approaches the limiting fraction of contact area ω as the pressure head decreases. The decrease in effective fracture-matrix flow area reduces the available area for matrix flow across the matrix-fracture interfaces. With liquid flow from one matrix block to another restricted in this way, the flow lines will bunch around asperities, and flow paths will be more tortuous in the partially saturated, fractured porous medium.

SIMULATIONS OF FRACTURED TUFF COLUMN

A test case was set up to simulate the fluid flow in partially saturated, fractured, porous tuff. Simulations of vertical drainage within the Topopah Spring Member were performed. Two vertical fracture sets and one horizontal fracture set partitioned the tuff formation into blocks. To simulate vertical drainage, we modeled one vertical column bounded by four vertical fractures. By symmetry, the midplanes of the bounding vertical fractures are no-flow boundaries. The horizontal fractures, normal to the direction of general flow, are explicitly simulated. On the local scale, lateral flow is allowed between the vertical fractures and the matrix blocks. Three blocks with two horizontal fractures are simulated. The upper boundary is a no-flow boundary, and the lower boundary is a constant-suction boundary. The suction head is maintained at -111.6 m, the in situ suction. Initially the system is fully saturated, with pressure determined by hydrostatic equilibrium. The potential everywhere is zero, and fluid is stationary. At $t = 0^+$, the negative suction head at the lower boundary begins to induce transient changes in the fluid flow field throughout the fractured, porous tuff column.

Five cases of flow in fractured, porous tuff were studied: (1) a fractured, porous column with the phase-separation constriction factor taken into account $(0 \leq \tau(h) \leq 1)$, (2) a fractured, porous column without the phase-separation constriction factor $(\tau = 1)$, (3) a matrix column without fractures, (4) a discrete fracture network without a matrix and with the τ factor, and (5) a discrete fracture network without a matrix and without the τ factor. The results are presented in plots of pressure head, saturation, permeability, effective fracture-matrix flow area, and Darcy velocity versus time at different locations (Wang and Narasimhan, 1984).

Figure 3 illustrates the changes in Darcy velocities across the fracture-matrix interfaces at the midpoints of fractures. Before the fractures desaturate, the fluid in the matrix flows toward the fractures to supply the fluid in the fractures, which is drained rapidly by the suction. At the saturated-desaturated transition, these matrix-fracture flows change drastically. After the transition, the fluid mainly moves vertically—from upper matrix blocks across horizontal fractures and into lower matrix blocks. The horizontal flow also reverses direction from an initial

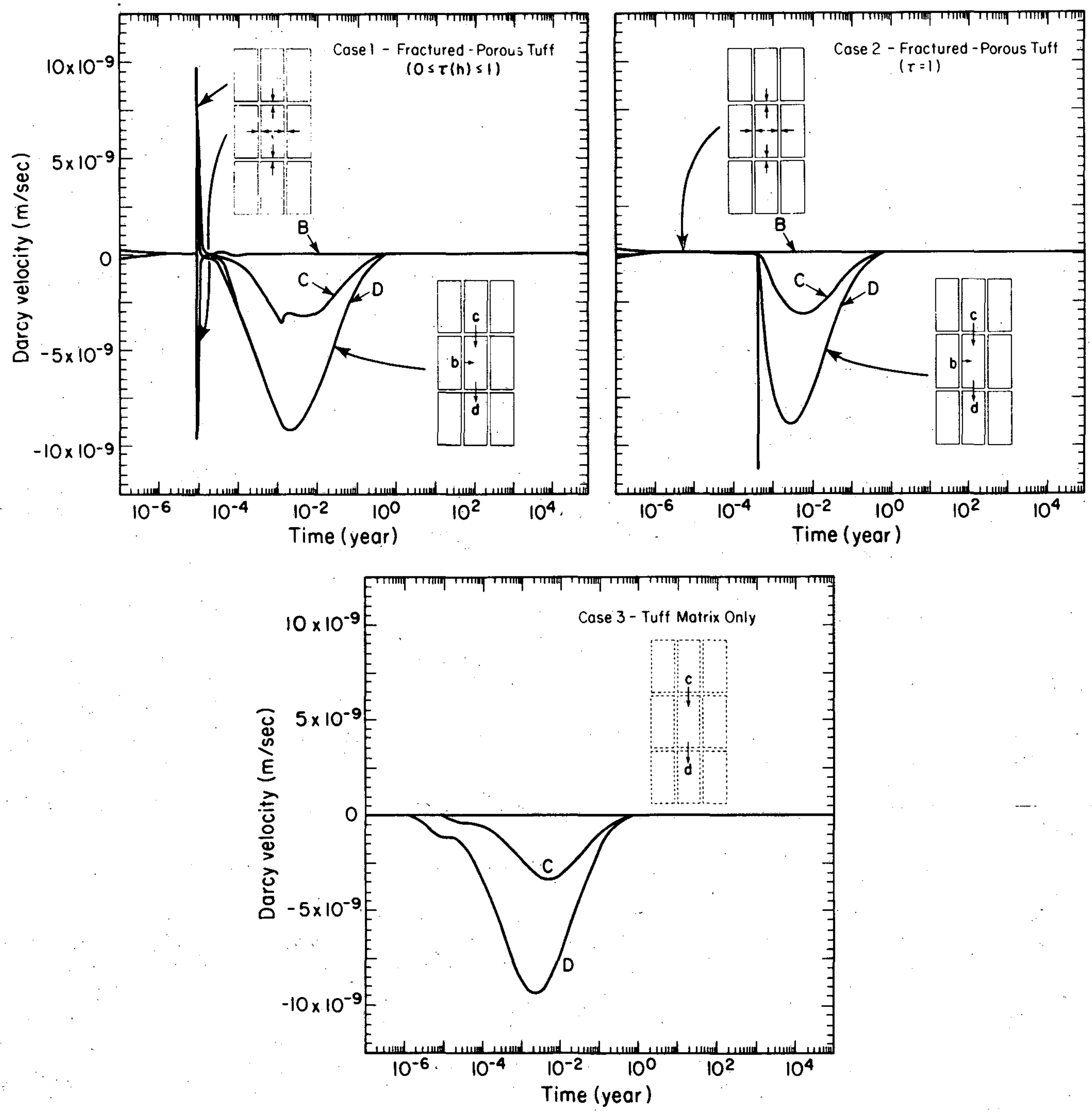

Figure 3. Darcy velocities at the fracture-matrix interfaces. Sign convention for horizontal flow: positive = matrix into fracture; negative = fracture into matrix. Sign convention for vertical flow: positive = upward; negative = downward. [XBL 853-10356].

matrix-to-fracture flow to a small but significant fracture-to-matrix flow. After the transition, the fractures no longer transmit fluid and become small fluid storage sources, which feed the matrix blocks as they drain.

After the fractures desaturate, the Darcy velocities in matrix blocks on opposite sides of a fracture are essentially the same as those calculated by a matrix-only model, as illustrated in Fig. 3 (case 3) for a tuff matrix column without fractures. The agreement among the velocities in Cases 1, 2, and 3 gives a strong indication that the quasi-steady fluid flow field of a partially saturated, fractured, porous formation can be simulated without taking fractures into account if the transition region from saturated to unsaturated conditions is of no concern. However, the highly transient changes in flow from fully saturated conditions to partially saturated conditions are extremely sensitive to the fracture-phase-separation constriction factor. Detailed information on fracture network geometry and discrete fracture characteristics is needed to understand fully the responses of a fractured-porous system to extreme perturbations such as a major flood event, which may cause transitions between partially saturated and fully saturated conditions.

REFERENCES

Spengler, R.W., and Chornack, M.P., 1984. Stratigraphic and structural characteristics of volcanic rocks in core hole USW-G4, Yucca Mountain, Nye County, Nevada, with a section of geophysical logs by D.C. Muller and J.E. Kibler. U.S. Geol. Surv. Report USGS-OFR-84-789.

Wang, J.S.Y., and Narasimhan, T.N., 1984. Hydrologic mechanisms governing fluid flow in partially saturated, fractured porous tuff at Yucca Mountain. Lawrence Berkeley Laboratory Report LBL-18473.

Heat-Driven Flow in Partially Saturated, Fractured Rock

K. Pruess, Y.W. Tsang, and J.S.Y. Wang

Various rock types and geologic settings are currently being studied in the U.S. to evaluate their suitability as a disposal medium for high-level nuclear wastes. The most likely mechanism by which radionuclides could reach the biosphere, should they ever escape from the engineered repository system, is through transport in groundwater. Therefore, the hydrologic characteristics and mechanical stability of the host rock are of primary concern in the assessment of potential repository sites.

Among the candidate sites currently under investigation, the tuff formations at the Nevada Test Site are unique in that the potential repository horizon is located above the water table in partially saturated rock. The tuffs have both matrix and fracture porosity and permeability. At the potential repository horizon, 390 m below the ground surface, approximately 80% of the pore volume contains water, which is held in place by capillary suction. The remaining voids contain air and a small amount of water vapor at ambient pressures. Our research in support of the Nevada Nuclear Waste Storage Investigations project (NNWSI) aims at developing concepts and computational tools for understanding fluid and heat flow, and chemical transport, in this kind of environment. This article specifically addresses the thermal and hydrologic effects of waste package emplacement in partially saturated, fractured rock.

HEAT-DRIVEN FLOW

Emplacement of high-level nuclear waste in partially saturated rock presents a "strongly" heat driven problem. The "conventional" description of unsaturated flow, as recently reviewed by Narasimhan (1982), is not applicable to the processes in the vicinity of the waste packages. Rock temperatures are expected to rise beyond 100°C, so that vigorous boiling with pressurization of the gas phase and forced convection will take place. As the vapor flows away from the vicinity of the waste packages, it will condense on cooler rock.

To describe these phenomena, it is necessary to employ a multiphase approach to fluid and heat flow that fully accounts for the movement of gaseous and liquid phases, their transport of latent and sensible heat, and phase transitions between liquid and vapor. The gas phase will in general consist of a mixture of vapor and air, and both of these components must be accounted for separately.

COMPUTER CODE TOUGH

We have developed a numerical model called TOUGH, which can represent most of the physical processes of significance in two-phase flow of water and air with simultaneous heat transport. Table 1 summarizes the physical effects that impact on fluid and heat transport. Check marks indicate processes or effects that are accounted for by the heat- and

Table 1. Physical processes in strongly heat driven flow in partially saturated rocks.

Process		Depends on	
Fluid Flow	✓	Pressure forces	
	✓	Viscous forces	
		Inertial forces	
	✓	Gravity	
	✓	Interference between liquid and gas	
	✓	Dissolution of air in liquid	liquid
	✓	Capillarity and adsorption	
		Differential heat of wetting	
		Chemical potential gradients	
	✓	Mixing of vapor and air	gas
	✓	Vapor pressure lowering	
	✓	Binary diffusion	
		Knudsen diffusion	
		Thermodiffusion	
Heat flow	✓	Conduction	
	✓	Flow of latent and sensible heat	
		Radiation	
Vaporization and condensation	✓	Temperature and pressure effects	
	✓	Capillarity and adsorption	
Changes in rock mass	(✓)	Thermal expansion	
	(✓)	Compression under stress	
		Thermal stress cracking	
	(✓)	Change in porosity and permeability	

mass-transport equations solved by the TOUGH simulator. Processes checked off in parentheses are at present implemented in an approximate way. Other effects currently not accounted for in the computer model may be significant and are being studied. The most important of these is probably Knudsen diffusion, which at low pressures is a more effective mechanism for gas transport in small pores than Darcy flow (Hadley, 1982; personal communication, 1984). However, as most gas phase flow in the tuff takes place in fractures, the overall effects of Knudsen diffusion may well be minor.

The system of equations representing the various fluid and heat flow mechanisms is highly nonlinear because of order-of-magnitude changes in parameters during phase transitions and because of nonlinear material properties (chiefly relative permeability for gas and liquid phases and capillary pressures). Furthermore, the mass- and energy-balance equations are strongly coupled.

Because of these features of the equation system, TOUGH performs a completely simultaneous solution of the discretized mass- and energy-balance equations, taking all coupling terms into account. Time is discretized fully implicitly as a first-order finite difference to obtain the numerical stability needed for an efficient calculation of flow in fractures with extremely small volumes. Newton-Raphson iteration is performed to handle the nonlinearities. The linear equations arising at each iteration step are solved directly using Gaussian elimination and sparse storage techniques (Duff, 1977).

POROUS-MEDIUM CALCULATIONS

The accuracy of the mathematical and numerical formulation used in TOUGH was verified by running a number of isothermal saturated-unsaturated flow problems and single-component (no air) geothermal reservoir problems for which analytical or numerical solutions are available in the literature. We also performed test calculations to demonstrate that TOUGH can handle the appearance and disappearance of any phase and component, as well as extremely nonlinear characteristic curves. Parametric studies were then initiated to investigate the drying of partially saturated rock in which high-level waste packages have been emplaced (Pruess and Wang, 1984).

Figure 1 shows a highly idealized emplacement configuration for which preliminary calculations of thermohydrologic conditions in the rock have been made for a period of 1000 years. Problem parameters were provided to us by Sandia National Laboratories. Figure 2 shows results for temperatures in the rock at a few centimeters distance from the waste package hole. Several cases were simulated with different capillary pressure curves and different boundary conditions at the emplacement hole. Temperatures are similar in all cases, indicating that fluid flow effects on heat transport are small.

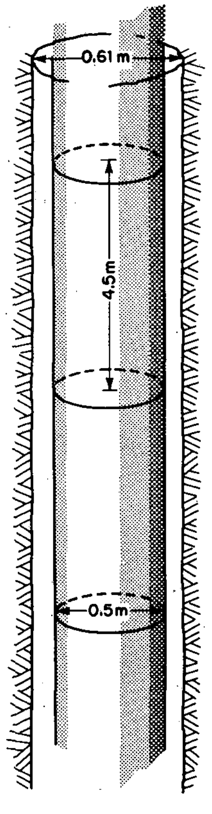

Figure 1. Idealized emplacement configuration with an infinite linear string of waste packages. [XBL 8311-2313]

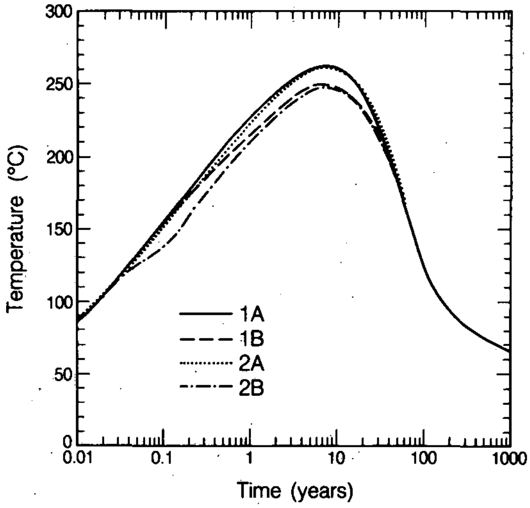

Figure 2. Simulated temperatures at a distance of r = 0.3355 m from the canister center line for different boundary conditions and capillary pressures (idealized porous-medium model). [XBL 847-9846]

In these calculations fracture flow effects were neglected, even though it is expected that they will strongly impact on the response of the rock mass to heating. The rationale for performing a highly simplified porous-medium calculation was primarily to evaluate and demonstrate computational capabilities for a test problem of reasonable complexity and to provide a benchmark case against which other numerical models can be compared. Calculations recently performed by R. Hadley with his PETROS code show good agreement with the TOUGH results (Hadley, personal communication, 1984).

FRACTURE EFFECTS

Subsequent simulations were aimed at exploring the complex flow effects caused by the presence of fractures. By idealizing fracture geometry and emplacement configuration as shown in Fig. 3, it is necessary to model only one symmetry element (indicated by broken lines). The hydrologic parameters for the fractures are poorly known, and several hypothetical cases were studied to explore possible system behavior. The general pattern of simulated fluid flow processes is shown in Fig. 4. Liquid is vaporized in the rock matrix near the waste canisters. The vapor is discharged into the fractures, flowing through them until it condenses on the cooler fracture walls. System behavior is strongly dependent upon liquid mobility in the fractures. If liquid water is immobile in the fractures, the condensate is sucked back into the matrix by capillary and

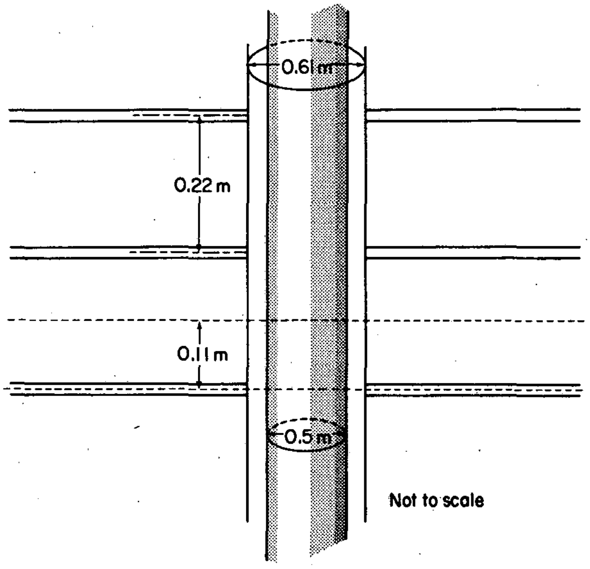

Figure 3. Idealized emplacement configuration. An infinite linear string of waste packages is intersected by fractures with 0.22-m spacing. [XBL 847-9831]

adsorptive forces. Liquid in the matrix flows up the saturation gradient, i.e., toward the heat source. If liquid is mobile in the fractures, however, the condensate is rapidly distributed over the fracture walls. This gives rise to a countercurrent two-phase flow in the fractures between heat source and condensation zone, which provides a very efficient heat transport mechanism known as a "heat pipe" (Eastman, 1968). As pressure in the fractures remain near ambient (1 bar) in all cases, the heat pipe keeps maximum temperatures near 100°C. Temperatures rise above 200°C when liquid is immobile in the fractures, and the vicinity of the waste packages dries up completely. Detailed information about problem parameters and results are available in the original papers (Pruess et al., 1984, 1985).

EQUIVALENT CONTINUUM

Calculations with an explicit representation of fractures, as sketched above, are useful for fundamental studies, but they are not practical for the time—and space—scales of interest in actual performance assessment. We have developed "equivalent" continuum models, which are able to provide an approximate description of fluid and heat flow in a fractured porous medium at reduced computational expense. In the equivalent continuum, fracture-flow effects are represented by large effective relative permeabilities. In this way, rather good agreement can be obtained with thermohydrologic conditions calculated in explicit fracture models. As an example, Fig. 5 shows simulated flow rates of the gas phase for a fractured porous medium and for an equivalent continuum (labeled "porous matrix with large effective gas permeability"). Also shown for comparison are results of a simulation without any allowance for fracture effects.

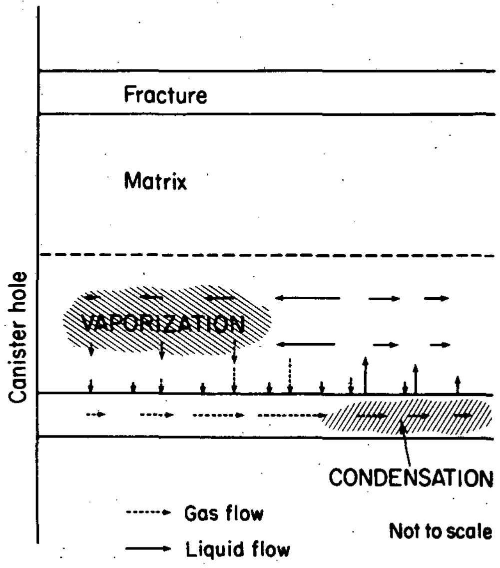

Figure 4. Response of fractured porous medium to heat load for case with immobile liquid in fractures. [XBL 847-9830]

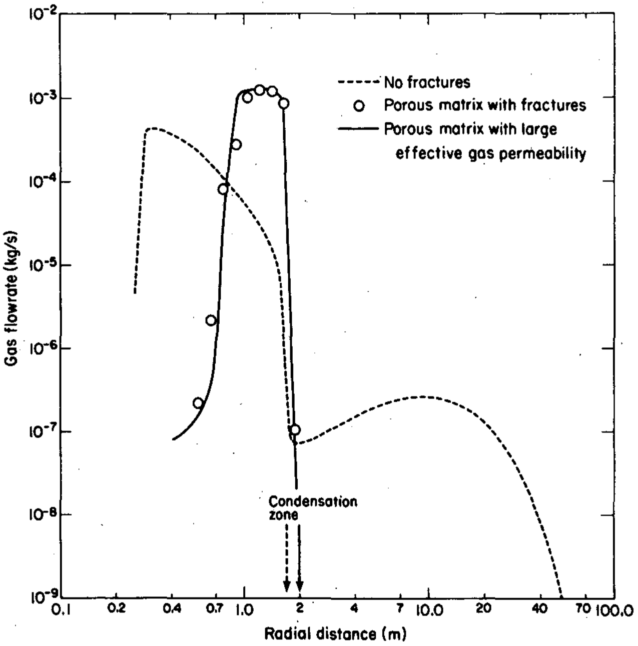

Figure 5. Simulated rates of radial gas flow per waste package at t = 160 days. [XBL 847-9824]

The equivalent continuum results are encouraging, but many problems remain. The equivalent continuum parameters depend not only on formation properties but also on the particular flow process considered. For some processes of interest, e.g., major flood events, it may not be possible at all to obtain an equivalent continuum description. Even for cases in which the continuum approximation works, its applicability is limited. A continuum provides only a single velocity field, which will either underestimate flow velocities in the fractures or overestimate flow velocities in the matrix. Therefore, the utility of continuum models for predicting contaminant transport is uncertain at the present time.

ACKNOWLEDGEMENTS

In addition to the support from the U.S. Department of Energy, this work received funding from Sandia National Laboratories.

REFERENCES

Duff, I.S., 1977. MA28—A set of FORTRAN subroutines for sparse unsymmetric linear equations. AERE Harwell Report R8730.

Eastman, G.Y., 1968. The heat pipe. Scientific American, v. 218, no. 5, p. 38–46.

Hadley, R.G., 1982. Theoretical treatment of evaporation front drying. Int. J. Heat Mass Transfer, v. 25, no. 10, p. 1511–1522.

Narasimhan, T.N., 1982. Physics of saturated-unsaturated subsurface flow. *In* T.N. Narasimhan (ed.), Recent Trends in Hydrogeology. Geol. Soc. Am., Spec. Pap. 189, p. 3–23.

Philip, J.R., 1955. Numerical solution of equations of the diffusion type with diffusivity concentration dependent. Trans. Faraday Soc., v. 51, p. 885–892.

Pruess, K., and Wang, J.S.Y., 1984. TOUGH—A numerical model for nonisothermal unsaturated flow to study waste canister heating effects. *In* G.L. McVay (ed.), Scientific Basis for Nuclear Waste Management (Proceedings, Materials Research Society; Vol. 26). New York, North Holland, p. 1031–1038.

Pruess, K., Tsang, Y.W., and Wang, J.S.Y., 1984. Numerical studies of fluid and heat flow near high-level nuclear waste packages emplaced in partially saturated fractured tuff. Lawrence Berkeley Laboratory Report LBL-18552.

Pruess, K., Tsang, Y.W., and Wang, J.S.Y., 1985. Modeling of strongly heat driven flow in partially saturated fractured porous media. Presented at the IAH 17th International Congress on the Hydrogeology of Rocks of Low Permeability, University of Arizona, January 7–12, 1985.

Development of Analytical Methods and Field Test Designs for the Study of Unsaturated, Fractured Tuffs at Yucca Mountain, Nevada

C.F. Tsang, G.S. Bodvarsson, J. Noorishad, J.C.S. Long, J. Rulon, and K. Karasaki

The Department of Energy is currently supporting comprehensive studies to determine the feasibility of placing a repository for high-level radioactive waste in the unsaturated tuffs at the Nevada Test Site. The investigations have focused on Yucca Mountain, along the western border of the site. The responsibility of characterizing the hydrogeology of Yucca Mountain was assigned to the USGS at Denver. The USGS has asked Lawrence Berkeley Laboratory (LBL) to participate in a number of tasks related to the test site:

1. Modeling studies of the unsaturated flow system at Yucca Mountain.
2. Development of a kinetic-equilibrium chemical transport code.
3. Well-test analysis of fracture networks in the saturated zone.

Some recent results for these three tasks are summarized below.

NUMERICAL MODELING OF THE UNSATURATED FLOW SYSTEM AT YUCCA MOUNTAIN

Yucca Mountain consists of fault blocks composed of alternating layers of highly fractured, welded tuff and relatively unfractured, nonwelded tuff, as illustrated in Fig. 1. The proposed repository unit is a thick welded unit called the Topopah Spring Member. At Yucca Mountain, the unsaturated zone is 500–750 m thick (Robison, 1984); recharge is estimated to be between 0.5 and 4.5 mm/year (Montazer and Wilson, 1984). We are therefore faced with a complex hydrogeologic problem that requires an understanding of flow through heterogeneous, unsaturated, fractured, and unfractured rock systems in an arid environment.

A conceptual model has been proposed by Montazer and Wilson (1984). It features vertical flow through the welded units, lateral flow at the base of the welded units and within the nonwelded units, and convection cells within the Topopah Spring Member. This model is a working hypothesis based on the available data and an understanding of the mechanisms governing flow in systems such as Yucca Mountain. To test the conceptual model, we have performed numerical simulations with the code TOUGH (Pruess, 1983). With TOUGH, we are able to model three-dimensional, nonisothermal, unsaturated, air-liquid-tracer flow through fractured and porous media. However, our initial studies are constrained by the availability of data and, as a result, have been kept as simple as possible. To date, we have used TOUGH to model two-dimensional, isothermal, unsaturated liquid flow through porous media. As more information becomes available, the numerical studies will be extended to include the effects of fracture flow, faults, and the convective flow of vapor due to thermal effects.

One-dimensional studies were performed to test the model and to determine if predictions based on steady-state, one-dimensional flow would match the data available to characterize the natural state of the system. Four simulation calculations were made, each with a different infiltration rate: Q = 0.001, 0.01, 0.1, and 1.0 mm/year. The solutions were consistent with the unsaturated hydraulic properties of the units. For all infiltration rates, the moisture tension in the Topopah Spring Member was essentially depth invariant and less than 2.2 bars. This result, however, is entirely dependent upon the nature of the characteristic curves and must be interpreted with caution. The one-dimensional simulations, in which infiltration rates were less than 1 mm/year, agree best with the measured liquid saturation profile.

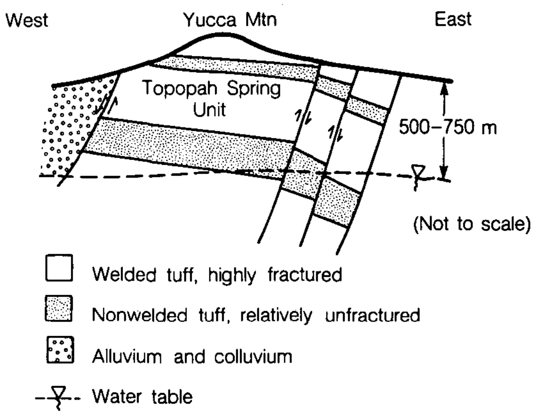

Figure 1. Conceptual cross section through the Yucca Mountain site. [XBL 854-10463]

Two-dimensional studies were also made to demonstrate the ability of the mathematical model to predict the long-term behavior of the system and to investigate the general flow patterns predicted on the basis of the available data. The results of our simulations support the concept of lateral flow above the repository unit. If flow through the welded units is controlled by the matrix permeability, then a significant amount of flow occurs above the Topopah Spring unit. However, if the welded units are modeled with relatively transmissive properties, then the majority of the lateral flow occurs beneath the repository unit.

DEVELOPMENT OF A KINETIC-EQUILIBRIUM CHEMICAL TRANSPORT CODE

Almost all reactive solute transport codes use the assumption of local chemical equilibrium. The lack of kinetic constraints on chemical reactions can be a serious deficiency in applications of certain chemical systems. Our studies take into account the kinetics of calcite dissolution and precipitation. Experimental data for these time-dependent processes have been reported by Plummer et al. (1978).

The kinetics is described by a simple nonlinear differential equation of first order, which replaces the equilibrium ion activity product for dissolution/ precipitation. We begin with the computer code CHEMTRN, developed by Miller and Benson (1983). A subroutine was added for calculation of nonlinear rate equations. The input-output part of the code and a number of other subroutines were also modified.

Two kinetic problems have been solved with TRANK using the rate equation provided by Plummer et al. (1983). In the first, we modeled the dissolution of the calcite lining of a tube by inflow water containing carbonic acid. In the second, we fed the equilibrated outflow of the first problem into a tube lined with calcium-loaded smectite. Ion exchange in the tube causes sodium to displace calcium from the lining, thereby reversing the direction of the rate equation and causing precipitation of calcium carbonate. The models of both problems showed expected behavior, thus providing confidence in the implementation of kinetics.

WELL-TEST ANALYSIS OF FRACTURE NETWORKS IN THE SATURATED ZONE

For several years LBL has been examining the behavior of fracture networks under the linear gradient conditions that might characterize regional flow. In order to understand how these same networks respond to well-test conditions, we have made numerical and analytical studies of well tests in fracture networks. The numerical aspects of this work include the use of a model for transient flow in fracture networks and the incorporation of circular boundary conditions into the fracture networks. With these tools we have performed numerical simulation of well tests. We have also developed new analytical solutions for well behavior that account for the way in which the fractures intersecting the well dominate the early-time behavior.

Two types of fracture networks have been tested in numerical simulation. First, we have tested continuous, or infinite, fractures. These simulations have shown that well-test analysis would predict the same value of permeability as would be calculated by Snow's method (Snow, 1969). However, unless the well is large compared to the fracture spacing, one cannot predict the correct values of storage coefficient. Second, we performed some well-test simulations on discontinuous networks with varying degrees of interconnection. For cases in which the network is well connected, the numerical results show that the observed permeability tensor is highly dependent on the choice of observation wells. For cases in which the network is not well connected, the results of well tests were not interpretable.

To improve the interpretation of well tests, we have developed an analytical solution based on a composite model of the fracture network. In this model the inner zone near the well consists of a finite number of fractures that intersect the well itself. These are connected to an outer zone of porous material by an infinitesimal annulus of infinite permeability. The solution is in terms of five dimensionless parameters, which are functions of the permeability and storage coefficients for the inner and outer zones and the radius for the inner zone. If a match can be found, one can determine the average system parameters, i.e., the permeability and storage coefficient of the outer zone. Furthermore, if one knows the number of fractures intersecting the test zone in the well, one can determine the average permeability of those fractures and the approximate distance to the first fracture intersection. In this way the well-test analysis may provide information about the fracture lengths. We have simulated a well test in a fracture network and found excellent agreement between the radius of the inner zone as predicted by the well-test analysis and the actual distance to the nearest fracture intersections.

REFERENCES

Miller, C.W., and Benson, L.V., 1983. Simulation of solute transport in a chemically reactive heterogeneous system. Model development and applications. Water Resour. Res., v. 19, p. 318–391.

Montazer, P., and Wilson, W.E., 1984. Conceptual hydrologic model of flow in the unsaturated zone, Yucca Mountain, Nevada. U.S. Geol. Surv. Water-Resour. Invest. Report 84-4345, p. 55.

Plummer, L.N., Wigley, T.M.L., and Parkhurst, D.L., 1978. The kinetics of calcite dissolution in CO_2-water systems at 5° to 60°C and 0.0 to 1.0 atm. CO_2. Am. J. Sci., v. 278, p. 179–216.

Pruess, K., 1983. TOUGH: A numerical model for strongly driven heat flow in partially saturated media. Earth Sciences Division Annual Report 1983. Lawrence Berkeley Laboratory Report LBL-16920, p. 39–41.

Robinson, J.H., 1984. Ground-water level data and preliminary potentiometric-surface maps of Yucca Mountain and vicinity, Nye County, Nevada: U.S. Geol. Surv. Water-Resour. Invest. Report 84-4197, p. 8.

Thermohydromechanical Considerations in the Performance Assessment of High-Level Waste Repositories

J. Noorishad and C.F. Tsang

In attempting to assess the influence of various coupled processes in the performance of high-level waste repositories, three key requirements must be met. First, the phenomena occurring at the microscopic and macroscopic scales in the rock mass must be adequately understood. Second, appropriate data must be obtained for the full range of conditions in the life of a repository. Third, the method of mathematical analysis employed must be capable of producing a realistic repository model.

A search of the literature reveals a body of knowledge about macroscopic and microscopic thermal-hydrological-mechanical-chemical (THMC) phenomenological effects and events. These phenomena can be attributed to one or a combination of certain causative mechanisms. Tables 1 and 2 list the important effects and events; Table 3 enumerates some of the causative mechanisms. To be able to explain the phenomenological effects and events, one needs to describe mathematically the physics and chemistry of the THMC processes at microscopic or crystalline levels. However, considering some of the causative mechanisms, such as microfracturing, intracrystalline slip, and recrystallization, the task is rather formidable because of the lack of knowledge about the inherent characteristics of media at microscopic levels. Therefore, the mathematical description of the THMC system has to be done at the macroscopic level. However, in doing so it becomes essential to use constitutive models that are based on material properties obtained in coupled thermal, mechanical, hydraulic, and chemical laboratory and field tests. This way the *microphenomenological effects*—namely, varia-

Table 1. Coupled THMC phenomena. Microscopic phenomenological effects.

- Variations in thermal properties (fluid-solid)
- Variations in deformation moduli
- Variations in strength characteristics (effects on cohesion and friction angle)
- Variations in chemical transport properties
- Variations in hydrologic properties
- Time-dependent inelasticity (creep)
- Pressure solution
- Stress corrosion
- Thermal diffusion, thermal and chemical osmosis, and ultrafiltration
- Phase change with release of latent heat

Table 2. Macroscopic phenomenological events.

- Variations in fluid pressure
- Buoyancy
- Development of fracture permeability
- Changes in fracture permeability
- Transport of heat, fluid, and solutes
- Variations in strength (dilation of fractures)
- Spalling
- Slabbing
- Cave-ins
- Dilatation
- Closing in
- Failure (away from the openings)
- Induced seismicity

Table 3. Potential causative mechanisms.

- Microcracking: anisotropic thermal expansion
- Macrocracking: inhomogeneous thermal expansion; constrained thermal expansion
- Microcrack and macrocrack deformations
- Dissolution-precipitation
- Chemical alteration
- Hydration-dehydration
- Recrystallization-thermodynamic instability
- Phase changes
- Saturation changes
- Chemical effects of water-phase separation
- Gamma radiation
- Chemical reactions

tions of the material properties as a function of the main external physical parameters (temperature, confining pressure, deviatoric stresses, and time)—serve as input for the analysis of the macroscopic THMC phenomenological events. To describe the macroscopic phenomena (processes), the laws of conservation of mass, momentum, and energy must be applied to each single phenomena involved in THMC while considering cross contributions among them. Constitutive laws for each phenomenon, utilizing proper coupled material properties, supplement the conservation laws to describe the THMC system completely. The mathematical description of the phenomena and the appropriate initial and boundary conditions, along with the coupled material properties, provide the necessary and sufficient conditions for the analysis of the physicochemical system. Our research, however, addresses much less complicated phenomena; we are concerned only with those thermal-hydraulic-mechanical (THM) processes that pertain to the performance assessment of a nuclear waste repository. This work benefits from the state-of-the-art progress being made in the areas of numerical computer codes aimed at solving THM problems and other important needs of modeling studies of a deeper geotechnical structure.

Key Issues in Coupled Processes Associated with Geologic Disposal of Nuclear Waste

C.F. Tsang, J. Noorishad, K. Pruess, C.L. Carnahan, M.J. Lippmann, and T.N. Narasimhan

The assessment of the long-term performance of a nuclear waste repository involves the evaluation of the travel time and rate of transport of radioactive elements from the repository to the accessible environment. Accurate prediction of the mass transport rates and travel times requires a comprehensive view of the major physical processes likely to occur. The basic phenomena are thermal (T), hydrological (H), mechanical (M), and chemical (C), which may act together in a coupled way. The thermal processes may be due either to the natural geothermal gradient or to the heat released from the decay of nuclear waste in the repository. The thermal input, in turn, causes mechanical movements of the rocks and thermohydraulic flow of the formation water. The water carries chemical solutes that may react with the surfaces of rock pores or fractures. The need to focus on the coupled interactive effects of these four phenomena for a proper study of groundwater transport was pointed out by Tsang (1980) and Tsang et al. (1982).

If we consider the four-way coupling of different major processes, we realize that there can be only 11 (i.e., $2^4 - 5$) couplings of various degrees of importance. They may be conveniently summarized as in Table 1, which also gives one example of a coupled process for each. This table formed the starting point of discussions by an LBL Panel that was convened on January 25–27, 1984. A great number of coupled processes with various degrees of importance for geologic repositories were identified and arranged into these 11 types (Table 2). For further

Table 1. Types of coupled processes.

Types	Examples
T = C	Phase changes
T = H	Buoyancy flow
T = M	Thermally induced fractures
H = C	Solution and precipitation
H = M	Hydraulic fracturing
M — C	Stress corrosion
	Chemical reactions and transport in hydrothermal systems
	Thermomechanical effects with change of mechanical strengths due to thermochemical transformation
	Thermally induced hydromechanical behavior of fractured rocks
	Hydromechanical effects in fractures that may influence chemical transport
	Chemical reactions and transport in fractures under thermal and hydraulic loading

Note: T = thermal, M = mechanical, H = hydrological, C = chemical. Single lines indicate weak coupling; double lines, strong coupling.

Table 2. List of coupled processes.

Thermochemical (TC)

- Thermal diffusion
- Phase changes (equation of state of solids)
- Solid solution
- Metastable phases

Thermohydrological (TH)

- Convection currents (one or two phases) including buoyancy flow
- Phase changes and interference
- Thermophysical property changes
- Thermal osmosis
- Gas diffusion
- Binary
- Knudsen
- Thermal
- Coupled
- Capillary-adsorption

Thermomechanical (TM)

- Induced cracking
- Fracture deformation
- Thermal spalling
- Thermal creep
- Thermal expansion

Hydrochemical (HC)

- Speciation
- Complexation
- Solution
- Deposition
- Sorption/desorption
- Redox reactions
- Hydrolysis
- Acid-base reactions
- Diffusion
- Chemical osmosis and ultrafiltration
- Isotopic exchange
- Coprecipitation

Hydromechanical (HM)

- Hydraulic fracturing
- Pore pressure change
- Hydraulic erosion of fractures
- Sedimentation of particles
- Shear effect causing abrasion
- Variation of fracture apertures
- Filtration of particles
- Ultrafiltration

Mechanical-Chemical (MC)

Because these processes are modified by hydrological and thermal effects, they are included under the next two types

Thermohydrochemical (THC)

- Solution/precipitation
- Time-dependent solution and precipitation
- Fluid transport by osmotic effect
- Chemical transport in gas phase
- Partition between gas and solid
- Particle transport (colloids)
- Equation of state
- Thermal diffusion (Soret effect)
- Thermal osmosis

Thermomechanical-Chemical (TMC)

- Phase change in mineral phases
- Dehydration
- Creep
- Hydration and swelling

Thermohydromechanical (THM)

- Hydraulic fracturing
- Triggering of latent seismicity
  - Stress redistribution
  - Pore pressure
- Opening and closing of joints
  - Stress redistribution
  - Thermal coupling
  - Pore pressure
- Spalling
- Change of strength
  - Stress corrosion
  - Hydrolitic weakening
- Hydration

Hydromechanical-Chemical (HMC)

These processes were eliminated from consideration because without thermal effects the mass transport is not sufficient to change the geometry except for low-temperature precipitation, stress corrosion, and ion-exchange-producing swelling (e.g., Na for Ca in smectites) at approximately 50°C or below

Thermohydromechanical-Chemical (THMC)

- Piping
  - Selected dissolution and tunnel corrosion inhomogeneous leaching
- Precipitation
  - In fractures
  - In matrix
- Hydrothermal alteration of rock
- Vertical vapor-liquid cycling near canisters
- Pressure solution

details, readers are encouraged to refer to the Panel report (LBL Panel, 1984).

Questions concerning the prediction of long-term performance of a nuclear waste geologic repository have opened up a new field of research. In this new field, it is essential to have a multidisciplinary effort involving hydrologists, geochemists, geophysicists, as well as researchers in rock mechanics and thermodynamics. Considerable research that couples two of the four (T, H, M, C) phenomena has been carried out, e.g., in geothermal and thermomechanical studies. However, three- or four-way coupled processes present a major challenge. Much work in theoretical, laboratory, and field studies, using a close multidisciplinary approach, must be done to advance our current state of understanding.

REFERENCES

LBL Panel (C.F. Tsang and D.C. Mangold, eds.), 1984. Panel report on coupled thermo-mechanical-hydrochemical processes associated with a nuclear waste repository. Lawrence Berkeley Laboratory Report LBL-18250.

Tsang, C.F., 1980. A review of the state of the art of thermomechanical-hydrochemical modeling of a hardrock waste repository. *In* Proceedings, ONWI/LBL Workshop on Thermomechanical-Hydrochemical Modeling for a Hardrock Repository, Berkeley, California, July 29–31, 1980. Lawrence Berkeley Laboratory Report LBL-11204, p. 16–21.

Tsang, C.F., Noorishad, J., and J.S.Y., Wang, 1983. A study of coupled thermomechanical, thermohydrological and hydromechanical processes associated with a nuclear waste repository in a fractured rock medium. *In* D.G. Brookins (ed.), Scientific Basis for Nuclear Waste Management (vol. 6). New York, North Holland, p. 515–522.

Convection in the Oceanic Crust: Simulation of Observations from DSDP Hole 504B, Costa Rica Rift

T.N. Narasimhan and C.F. Williams

The Deep Sea Drilling Project (DSDP) hole 504B is located about 100 km south of the Costa Rica Rift (Fig. 1), the water depth at this location being nearly 4000 m. Between 1979 and 1982, hole 504B was drilled in three stages, reaching a total depth of 1350 m. The uppermost 275 m comprised oozes, chalk, and chert; the remaining 1075 m consisted of oceanic basalt. In addition to providing as extensive a set of geophysical logs and televiewer studies as has yet been run on any DSDP hole, a unique achievement of hole 504B was the measurement of permeability and pore pressure (Anderson and Zoback, 1982), leading to the acquisition of a rare set of in situ hydrogeologic data from such a remote environment.

The hydrogeologic data show that the observed fluid pressure in the basalt at a depth of 450 m below the ocean bottom is significantly lower than the hydrostatic head of ocean water that could be expected at that depth (~4450 m). The actual "underpressuring" was computed to be about 8 bars, or about 2% of the expected hydrostat. Anderson and Zoback (1982) suggest that the underpressuring

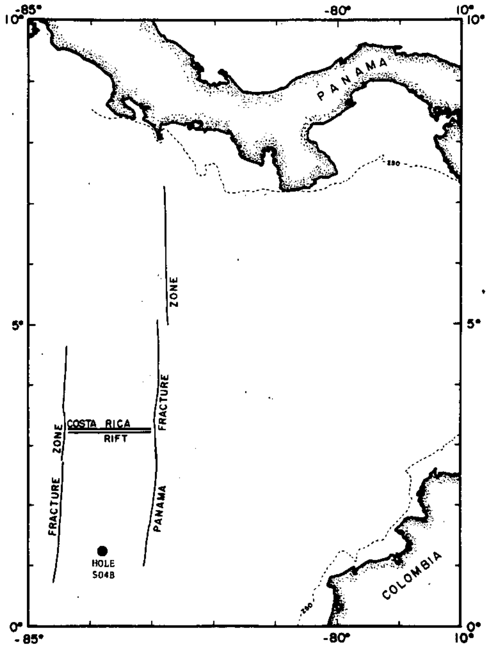

Figure 1. Location of DSDP hole 504B. [XBL 8411-4816]

could be the result of convective flow of water within the basalt aquifer. The purpose of the work reported on here is to test this convection hypothesis through mathematical modeling.

THE MODEL

The convection problem requires the transient transfer of water and heat in a geologic system. To handle such a system the code PT (Bodvarsson, 1982) was used. This code, based on the integral finite-difference method (Narasimhan and Witherspoon, 1976) solves the coupled mass-energy transport equation in three dimensions.

On the basis of symmetry considerations, the geologic system near hole 504B is idealized as a three-dimensional region, as shown in Fig. 2 (Williams et al., 1984). This system, measuring 4000 m by 4000 m by 1300 m, consists of four materials (uppermost chert is underlain by three basalt layers with permeability decreasing with depth in the basalt). Their in situ material properties are given in Table 1. The system has been discretized into 234 volume elements arranged in 13 rows with 18 elements in each row. The vertical surfaces of the region are bottom surface is assumed to be impermeable but with prescribed heat flux varying spatially from 209 MW/m^2 to about 215 MW/m^2. The upper boundary, representing the interface between the chert layer and the ocean, is treated as a constant-pressure, constant-temperature (0°C) boundary. The initial conditions consist of the observed temperature profiles in conjunction with hydrostatic pressure distribution.

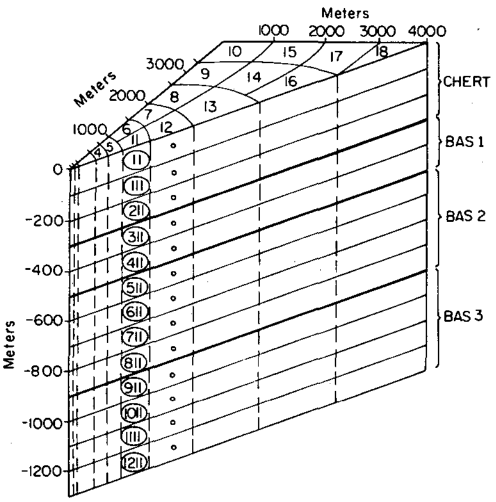

Figure 2. Three-dimensional mesh used for the mathematical model. [XBL 8411-4817]

Table 1. Summary of properties of mesh materials.

Material	Permeability (md)[a]	Porosity (%)	Thermal conductivity (W/m·K)
Chert	0	1	1.26
Basalt 1	100	11	1.67
Basalt 2	0.4	8	1.67
Basalt 3	0.2	3	2.20

[a] 1 md $\approx 10^{-15}$ m^2.

RESULTS

The computed pressure-depth profile is given in Fig. 3. The solid symbols in this figure denote the pressure profile computed using the permeability-, porosity-, and thermal conductivities measured in situ in the field (Table 1). The open circles show what might happen if the chert had a small permeability of 0.1 md instead of being impermeable. Clearly, a leaky chert is conducive to a hydraulic connection between the ocean and the basalt, leading to a profile that is closer to hydrostatic than the previous case. Conversely, if the permeability of the entire basalt aquifer is higher (Case 3, Table 2), then there is increased convection, which tends to accentuate the underpressuring (open squares, Fig. 3). Thus the calculations show that a caprock such as chert is essential for the development of underpressuring whereas increased convection accentuates it.

The simulated and measured temperature profiles are compared in Fig. 4. Again the comparison is good.

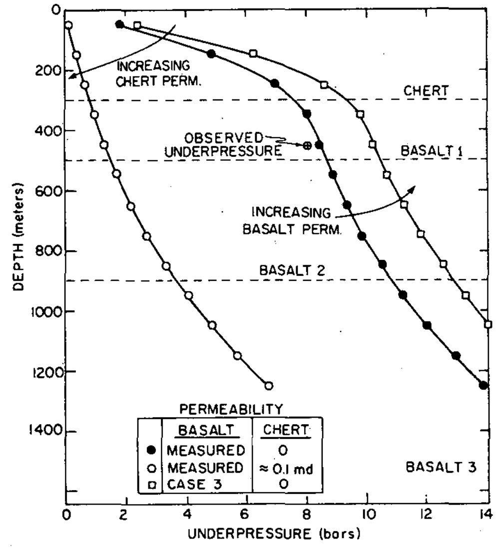

Figure 3. System under pressure as a function of depth for various permeability variations. Permeable caprock attenuates underpressuring whereas permeable basalt accentuates it. [XBL 8411-4818]

Table 2. Basalt permeability variations.

Material	Permeability (md)[a] Case 1	Case 2	Case 3
Basalt 1	200	200	500
Basalt 2	0.8	0.8	2.0
Basalt 3	0.4	0.8	1.0

[a] 1 md $\approx 10^{-15}$ m^2.

The computed heat fluxes at the ocean bottom for several cases (Tables 1 and 2) are compared in Fig. 5. It is seen that the heat fluxes computed with the measured parameters (Table 1) are very close to those for a purely conductive regime, which agrees with field measurements. The data in Fig. 5 show that as convection increases because of increased permeability, the surface heat flux tends to assume a pronounced peaked distribution. This result suggests that heterogeneity may be a cause of at least some of the heat flux peaks observed on the ocean floor.

Other results, presented in Williams et al. (1984), indicate that (1) the convection cells break up into smaller cells as the horizontal dimensions of the flow region are increased or as the permeability of the basalt is increased and (2) there is a continuous inflow of ocean water into the basalt aquifer, the rate of inflow declining exponentially with time, with good agreement between the computed values and the in situ measurements.

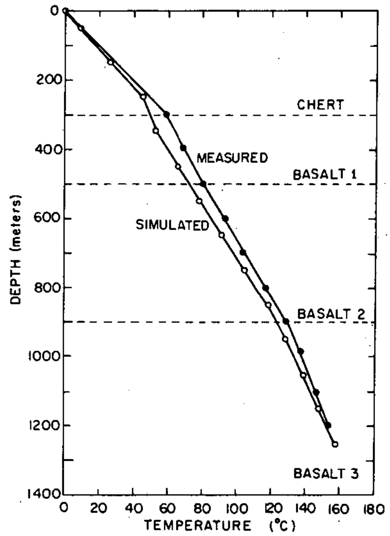

Figure 4. Comparison of downhole temperature profiles for simulated and measured equilibrium conditions. [XBL 8411-4819]

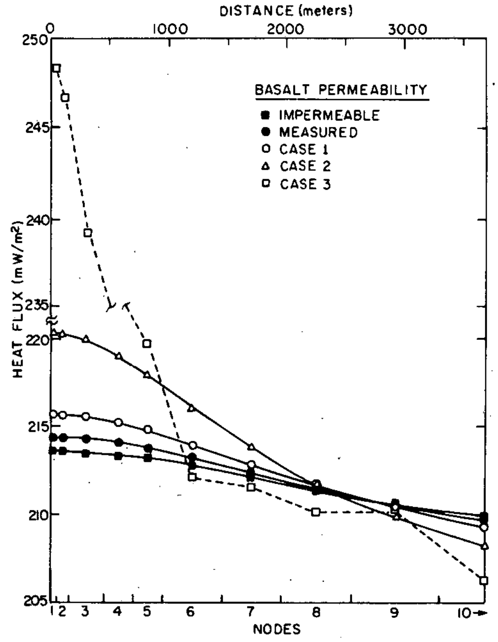

Figure 5. Plot of surface heat flux for five permeability variations. [XBL 8411-4822]

CONCLUSIONS

The investigation has established that pronounced underpressuring should be of widespread occurrence in the oceanic crust wherever a tight caprock is present. Furthermore, the numerical model can be a valuable tool in quantitatively studying the evolution of these systems.

REFERENCES

Anderson, R.N., and Zoback, M.D., 1982. Permeability, underpressures and convection in the oceanic crust near the Costa Rica Rift, eastern equatorial Pacific. J. Geophys. Res., v. 87, p. 2860–2868.

Bodvarsson, G.S., 1982. Mathematical modeling of the behavior of geothermal systems under exploitation (Ph.D. thesis). Lawrence Berkeley Laboratory Report LBL-13927, p. 18–48.

Narasimhan, T.N., and Witherspoon, P.A., 1976. An integrated finite difference method for analyzing fluid flow in porous media. Water Resour. Res., v. 12, no. 1, p. 57–64.

Williams, C.F., Narasimhan, T.N., Anderson, R.N., Zoback, M.D., and Becker, K., 1984. Convection in the oceanic crust: Numerical simulation of observations from DSDP hole 504B, Costa Rica Rift. Lawrence Berkeley Laboratory Report LBL-18564.

GEOPHYSICS

The geophysical program at Lawrence Berkeley Laboratory (LBL) is strongly applied, having its origins in the Geothermal Exploration Technology Development Program that was started under the Atomic Energy Commission and the Energy Research and Development Administration. For this reason, the geophysical program has an orientation toward techniques for resource definition and the monitoring of subsurface processes. Research efforts concentrate on developing better field instrumentation and techniques and on interpretation of seismic and electromagnetic data. The success of the geophysical program has been due to the effective collaboration between LBL staff scientists and engineers and the UC Berkeley faculty associates and graduate students. Many students from the Department of Materials Science and Mineral Engineering (College of Engineering) and from the Department of Geology and Geophysics (College of Letters and Science) have completed or are currently doing their graduate research in support of LBL projects.

As evidenced by the geophysical research summaries that follow, most of the geophysical projects fall into the categories of seismology or electromagnetics. Since the creation of the Center for Computational Seismology (CCS) in 1982, the number and diversity of seismological projects has increased; these projects range in scope from earthquake mechanisms and elastic-wave propagation to mapping faults and hydrofractures and thermally induced stresses. CCS also has a supporting role in developing a seismic data base for the Defense Advanced Research and Projects Administration (DARPA).

In electromagnetic studies, the emphasis is on improving instrumentation and techniques for interpreting electromagnetic sounding data. As part of this interpretation, serious efforts were made to develop laboratory facilities in which scale modeling can be applied to problems that cannot be solved numerically. A new direction of our research has been to evaluate seismic and electromagnetic techniques in the detection and characterization of man-made hydrofractures.

CCS: Center for Computational Seismology

E.L. Majer, T.V. McEvilly, and L.R. Johnson

In the past year the Center for Computational Seismology (CCS) has made significant progress toward achieving its goal of becoming a user-oriented center based upon maximizing user convenience, program management, and systematic advances in computing technology applied to a wide range of problems in seismology. CCS is designed to provide a focused environment for computational seismology that traditionally has been distributed among many research groups.

Two of the most basic problems we have been addressing are data compatibility and an integrated analysis system. Seismologists not working with conventional reflection data have devised numerous formats for their data. Each group or person who desires to work with these data must either write or obtain a large body of software just to access and archive the data. As a step in streamlining data exchange, CCS is interacting with the Lawrence Livermore National Laboratory (LLNL), the U.S. Geological Survey (USGS), and the Defense Advanced Research Project Agency (DARPA) in establishing a mutually acceptable data-exchange format. The goal is to establish a "universal" format, just as the commercial reflection industry has established the SEG formats. Once adopted, the format will open new avenues to the exchange of important data sets. With the new large-scale cooperative initiatives in seismology, it is now extremely important to do so as soon as possible.

A second goal at CCS is to organize the myriad of analysis and graphical routines that are typically in use within any large group of seismologists (usually two or more routines will suffice). Although no one package can hope to solve all computational problems, there are basic routines that almost all seismologists use, i.e., trace manipulation and display, windowing, FFT, phase picking, filtering, event location and display, and fault-plane determinations, just to name a few. These routines are often duplicated many times as groups or individuals set out to analyze data for the first time. Lawrence Berkeley Laboratory (LBL), in collaboration with UC Berkeley (UCB) faculty members, has developed such a package for DEC/VMS called the New Seismic Analysis System, or NSAS; LLNL has its Seismic Analysis Code, or SAC. To be useful an analysis system must be modular and expandable; it also must work at the system level for maximum efficiency and be compatible with a wide variety of operating systems. Since the SAC code at LLNL most closely fits this description, we have adopted it as our basic analysis package. LLNL has ported SAC from the original PRIME operating system to DEC/VMS, UNIX[1], and IBM. LBL is developing modules that will expand SAC's analysis capabilities and improve its flexibility by integrating NSAS into it. We are also responsible for writing the code that will interface the "universal" format with SAC.

A third goal at CCS is of course to conduct research in seismology. A broad range of research is carried out by LBL staff, UCB students and faculty, and visiting scientists. This report presents brief descriptions of those research activities.

NEAR-SURFACE VELOCITY STRUCTURE BENEATH PAHUTE MESA, NEVADA TEST SITE

—M.A. Leonard

Ground motion data recorded at stations close to several explosions in Pahute Mesa have been used to investigate the shallow velocity structure of that region. Three-component data from seven explosions of approximately the same depth (Chancellor, Harzer, Serpa, Farm, Colwick, Pipkin, and Emmenthal) have been combined to form composite record sections. Recordings from 42 randomly located stations are combined in sections extending to a maximum epicentral distance of 14 km.

Because of the heterogeneities inherent in the azimuthal variations of source-receiver combinations, travel-time data show considerable scatter out to distances of 54 km. However, the scatter is less pronounced at larger distances, perhaps indicating a lesser degree of structural heterogeneity at depth.

The data have been interpreted initially in terms of an average model. The travel-time data can be fitted with a model having strong velocity gradients at shallow depths, the P velocity increasing from 1 km/s at the surface to 4.2 km/s at a depth of 2 km. The data have been subjected to the standard processing techniques of reflection seismology in a search for later arrivals. Synthetic seismograms have also been used in the interpretation.

---

[1] UNIX is a Bell Laboratory trademark.

PROGRESSIVE INVERSION FOR *P*-WAVE AND *S*-WAVE VELOCITY STRUCTURE AND HYPOCENTERS: APPLICATION TO THE GEYSERS GEOTHERMAL FIELD

—D.R. O'Connell

A progressive inversion method is extended to include *S*-wave data. *P*-wave and *S*-wave arrival times can be used together to estimate hypocenters, to estimate *P*-wave and *S*-wave station corrections, and to construct new *P*-wave and *S*-wave velocity models. Addition of *S*-wave arrival times reduces hypocentral uncertainties, removes the tradeoff between origin time and hypocentral depth, and eliminates the tradeoff between *P*-velocity dc level and origin time.

The Geysers, California, is the world's most productive geothermal field and the site of intense microseismicity. To study its velocity structure and seismicity, a nine-station array of three-component digital event recorders was deployed at The Geysers during late July and early August of 1982. Data from these stations were supplemented by data from eight USGS Calnet stations in The Geysers area. Only stations in or on the edge of the geothermal field were used in the progressive inversion; the ray paths were confined to the production zone. *P*-wave arrival times were obtained from all stations. *S*-wave arrival times were read from the 10 three-component stations. We estimated the *P*-wave velocity, V_P, S-wave velocity, V_S, and V_P/V_S as a function of depth to help characterize the reservoir properties (fracture density, degree of fluid saturation) and to facilitate the calculation of Greens functions for use in source studies of the microseismicity.

APPLICATIONS OF ALGEBRAIC RECONSTRUCTION TECHNIQUES TO CROSS-HOLE SEISMIC DATA

—J.E. Peterson, Jr.

Tomographic imaging techniques have been applied to cross-hole data sets to determine the velocity structures and the reliability and resolution of the algorithms. The data used in this work come from experiments carried out at the Retsoff salt mine in New York and at the underground radioactive waste study facility at the Stripa mine in Sweden. The travel times at Retsoff were of high quality and obtained over ray paths of up to 500 m in length. The structure is quite complicated, with velocity contrasts up to 50%. The Stripa facility is in granitic rock, with velocity contrasts of only a few percent. The dimensions of the experiment were small, with maximum ray lengths of just over 10. The data were collected with very high accuracy, with source and receiver locations measured to 0.1 mm and travel times read to 0.001 ms.

We have applied to the data a number of algorithms similar to the Algebraic Reconstruction Techniques (ART) used in medical imaging. Some modifications of the algorithms, such as the application of weighting schemes, damping parameters, and ray-path bending, were performed. The resulting velocity fields were compared with the known fields and with each other to determine an optimal method. We found the algorithms to be a rapid, reliable means of reconstructing the slowness field of real data. Low-velocity zones were recovered with accuracy in location and value. We also found that great care is required in applying techniques, in that proper damping parameters must be used and the proper number of iterations taken.

SEISMIC-WAVE SCATTERING AND ATTENUATION ACROSS THE SAN ANDREAS FAULT ZONE IN CENTRAL CALIFORNIA

—J. Scheiner

Expanding on a previously reported diffusion approach to the problem of crustal-wave scattering and attenuation, we are now developing an approach based on a weak-scattering model. The study area is the San Andreas fault zone in central California. Local microearthquake data and seismic reflection data from a 16-km-long Vibroseis line across the fault are being investigated; the parameters of interest are the apparent (coda) *Q* factor and several scattering parameters. It is anticipated that an understanding of the scattering properties as a function of position and frequency will in turn lead to an understanding of the relative contributions to the apparent attenuation from intrinsic and nonintrinsic elastic mechanisms. The method depends on a judicious windowing of the data; this is especially difficult with reflection data because the theory depends on the identification of a primary arrival and its coda. Tests have shown that in "well-behaved," layered media, a clear and coherent arrival can be discerned and its coda analyzed, whereas in extensively fractured or strongly inhomogeneous media, such coherent primary arrivals are not clearly present. Other methods of determining the attenuation characteristics are also being studied, such as the spectral ratio technique; comparison of these inverse methods (using both reflection data and microearthquake data) with the results of forward modeling should provide adequate bounds on the crustal attenuation and scattering characteristics of this important region of the San Andreas fault.

LOWER MANTLE TAU ESTIMATES FOR A REGIONALIZED EARTH

— *D.M. Tralli*

Estimates of tau functions are obtained for seven tectonic regions of the earth to study the correlation of potential lateral variation in lower-mantle *P*-wave velocities with recognized surface heterogeneity. Statistical analysis establishes constraints on the significance and interpretation of differences in these tau estimates and provides a check on the consistency of the regionalization.

A simple algebraic formulation using data from the Bulletin of the International Seismological Centre (a set of over 1.25 million ray paths) defines a tau estimate as the sum of the contributions from the turning point of the ray path and two end-point perturbations. The travel paths are characterized by the regions associated with the epicenter, the station locations, and the surface projection of the path turning point. This scheme allows for the independent determination of epicenter and station corrections, the isolation of a tau value corresponding to the turning-point path segment, and the derivation of a "pure region" tau function from an otherwise uneven sampling of the earth. The correction terms permit estimating a possible regional bias that may be present in the hypocentral parameters.

Station and epicenter corrections determined thus far are small, generally less than 0.5 s and never more than 2 s, and may be fit by smooth functions of the slowness parameter. Oceanic ridge corrections imply that source locations are systematically too shallow or that origin times are too late. In comparison, continental shields indicate locations that are systematically too deep or origin times that are too early. Differences between the "pure region" tau functions and a weighted mean, which takes into account the fractional surface area of the tectonic regions, indicate that although differences in the tau estimates are small, they are statistically significant and upon inversion may yield interesting features in the *P*-wave velocity profiles of the individual teconic regions.

EXTREMAL INVERSION OF VERTICAL DISPLACEMENTS, LONG VALLEY CALDERA, CALIFORNIA, 1982-1983

—*D.W. Vasco*

Vertical displacement data from August 1982 and August 1983 leveling surveys in Long Valley caldera are examined using extremal inversion techniques. Bounds on the depth to the top of the body and on the width of the body are produced. Random leveling errors are included in the inversions. Any volume source satisfying the August 1982 leveling data must include some volume change above 12 km. For the August 1983 data some volume change must have occurred at or above 11 km. The bounds on the east-west extent of the source have not changed from 1982 to 1983. However, the north-south bounds have moved northward during this interval. It is found that these estimates do not depend on the Poisson's ratio of the region or on the exact boundaries of the region modeled.

Utilizing Seismologic Techniques to Map Hydrofractures

E.L. Majer, T.V. McEvilly, and T.W. Doe

During the past several years Lawrence Berkeley Laboratory (LBL) has been studying the processes by which rocks fail when hydrofractured. A key component in this study has been the use of seismological techniques to detect the release of seismic energy during the fracturing process. Over the past year several different experiments at various scales have been carried out to determine the seismic signatures associated with energy release during the hydrofracture process.

At the smallest scale was an experiment in which a salt block (300 mm × 300 mm × 450 mm) was hydrofractured using oil at triaxial confining pressures up to 205 bars (3000 psi). Five acoustic emission (AE) sensors were placed on the block surrounding the hydrofracture. The bandwidth of the recorded data was from 300 Hz to 300 kHz. The data were analyzed for discrete events or acoustic emission activity to determine source location, size, mechanism, and occurrence rate. Figure 1 shows the results of one of the tests; the discrete event locations are plotted in plan view. The borehole is in the center of the block. Each frame shows successive numbers of events, the last frame including 100% of the events located. As can be seen, the events migrated away from the borehole in an east-west direction (north is up). The fracture fluid was dyed to make the fracture more visible afterward, and the visible fracture agreed in direction with the AE analysis. Of note is the fact that in this dry sample only tensile events were detected. The source sizes inferred from the seismic data were on the order of 1–5 mm, or about the size of individual grains. It is clear from this experiment that, even in a semiductile material (salt is ductile at these pressures), discrete fractures occur in a sequence that defines the extent of the fluid.

At a slightly larger experimental scale, a hydrofracture in saturated granite was carried out at a depth of 50 m in a mine (Underground Research

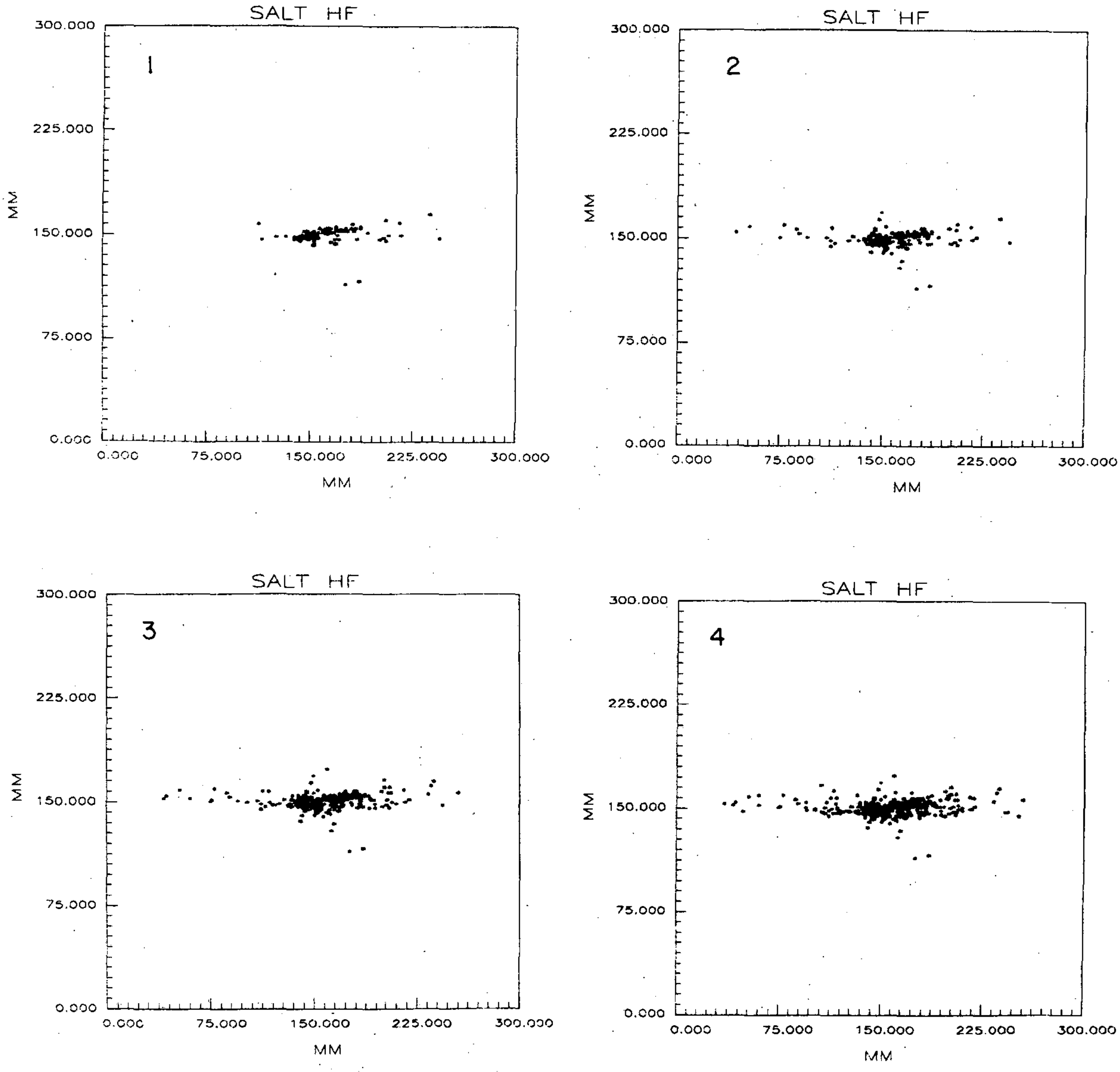

Figure 1. Plan view of acoustic emission locations due to hydraulic fracturing in a salt block. **(Upper left)** First 25% of emissions. **(Upper right)** First 50% of emissions. **(Lower left)** First 75% of emissions. **(Lower right)** All emissions. [XBL 8312-4825]

Laboratory in Canada). Twelve AE sensors in three boreholes, each located 3 m from the hydrofracture hole, were arrayed to detect the signals associated with several hydrofractures. The fracture fluid used in this case was water containing a blue dye. The bandwidth of recording was again 300 Hz to 300 kHz. The idea was to map the fracture seismically and then mine it out for confirmation. Two different types of events were detected: (1) impulsive, discrete, high-frequency (100–150 kHz) events and (2) emergent, lower-frequency (10–50 kHz) events. It is assumed that the high-frequency events were due to fracture extension from tensile failure and the low-frequency events due to shear failure on oblique planes or to slower tensile extension of the fracture. Whatever the case, it is clear that seismic activity was also occurring at a scale 10 times larger than the laboratory scale with a frequency range broader than that of the lab scale.

At the largest scale, two hydrofractures were monitored at 350 m depth with array dimensions of the same order as in the previous case. One hydrofracture was in a sandstone and the other in a shale. The sandstone was fractured with water and later with a gel. The shale was fractured with grout. In both cases the array geometry consisted of two borehole geophone strings to 200 m depth (about 150–0200 m horizontally from the top of the hydrofracture well) and surface strings of geophones. In addition, long-period instruments were deployed at the surface, thus covering a bandwidth from 500 to 0.02 Hz. In both cases signals were observed across the total bandwidth. The higher-frequency events (80–200 Hz) in the shale were observed to be impulsive, with clearly defined *P*- and *S*-waves continuing after pumping for nearly a month. These events are most likely shear events associated with either fluid leak-off or pore pressure build-up due to formation compaction or fluid build-up. A surprising result was the number of long-period (LP) events observed in the shale experiment. (LP events were also observed in the sandstone in addition to just a few discrete events.) The LP events could clearly be correlated with major pressure drops in the uphole pressure records. It is thought that these LP events are reflecting the surface deformation associated with fracture flexure. Even at laboratory scales the opening time for fractures is a few seconds (Medlin and Massé, 1984). Thus on a larger scale the opening time may be much slower, resulting in an LP fracture displacement that is propagated to the surface. Monitoring an LP signal offers the advantage of low attenuation over large distances, but resolution is lower.

As a result of these larger-scale experiments, it has become evident that such problems as pump noise, attenuation, and tube waves, make it very difficult to pick up the high-frequency "nano" earthquakes associated with the fracturing process. It is evident from the smaller-scale experiments, however, that seismic activity is occurring; the trick is to detect it. In some optimal cases the activity may be quite easily detectable, but in most instances sophisticated data processing will be required. Borrowing from the techniques of seismic reflection processing may be an answer. Shown in Fig. 2 is a frequency-wavenumber (*F-k*) plot of a segment of array data. In this case a vertical string of nine geophones, at 30-ft intervals in a borehole, detected the signals from a perforation shot at the fracture zone. The actual event segments (200 ms) are shown on the right-hand side of Fig. 2. Contoured in Fig. 2 is the energy as a function of frequency and wavenumber. As can be seen the energy dominates the right-hand side, which indicates that the energy is originating from below the array, or the direction of the shot. The peak energies for the *P*-waves (110 Hz) and *S*-waves (30 Hz) arrive just to the left of the *P* and *S* lines, indicating that the apparent velocity is greater than the true velocity. The wave is therefore coming at an angle to the array, or in this case at exactly 27°. By measuring arrivals from several arrays, the azimuth of the energy can be obtained. For mapping purposes one would monitor in real time the direction of arrival of the principal energy. If this direction is systematic one could track the direction of microfracturing. The next step is to isolate the peaks in energy in the *F-k* domain, velocity filter the time domain to bring out the arrivals, and then move the waveforms to their origin. In any case, it seems possible to apply to this problem of fracture mapping a body of processing expertise that was once applied only to reflection seismology.

In conclusion, experiments to date indicate that both shear and tensile failure are associated with hydrofracturing. It appears that low-frequency seismic signals may also be generated by fracture opening along the total length of the fracture. The interrelation of these phenomena and whatever it is that governs the proportion in which they occur are not totally understood, but seismic monitoring at different scales appears to be useful not only for mapping the fracture but for unraveling this coupled fracture-mechanics/fluid-mechanics problem.

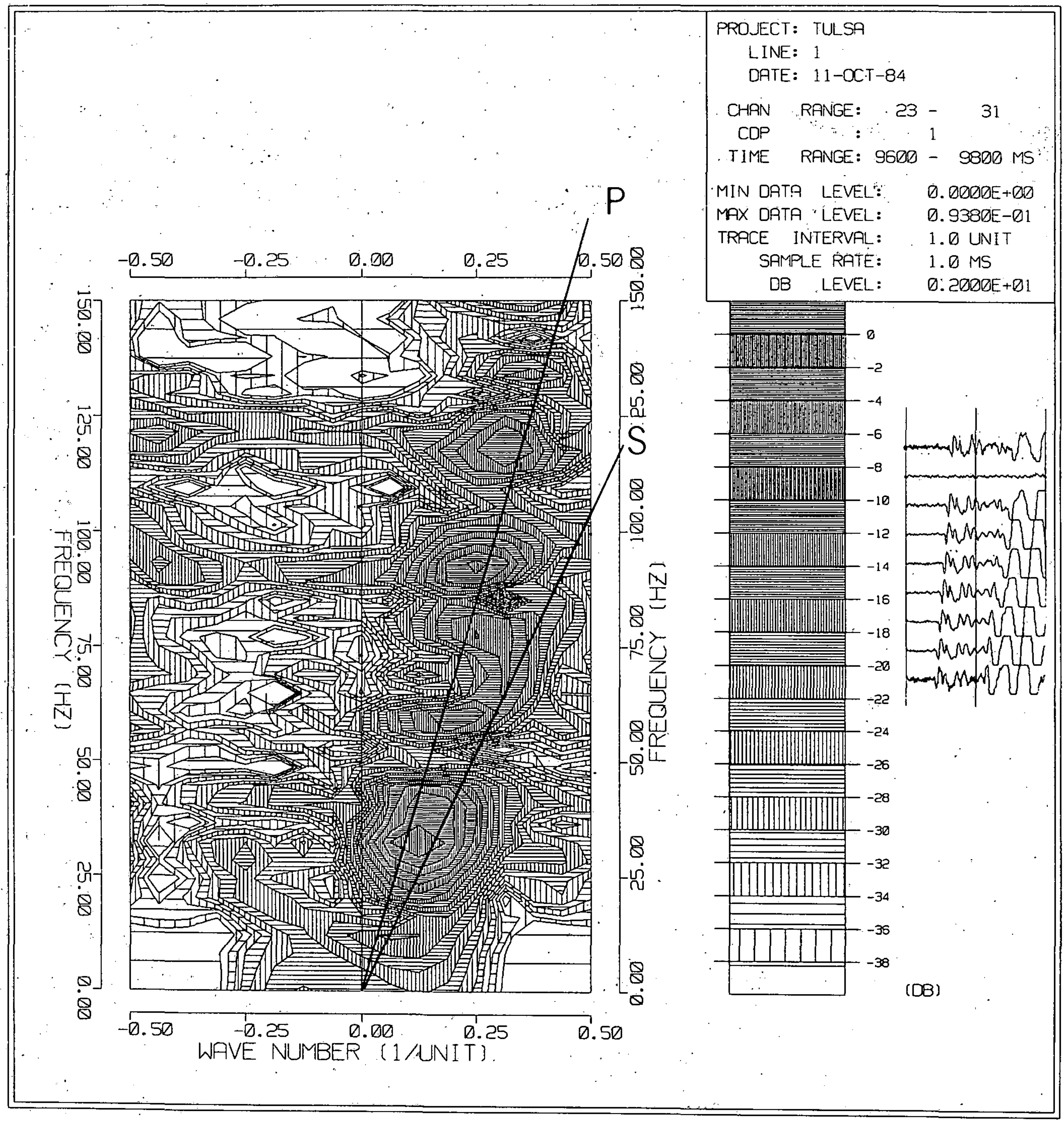

Figure 2. *F-k* plot of energy arriving along a borehole array from a perforation shot below the array. See text for details. [XBL-8412-5221]

REFERENCE

Medlin, W.L., and Massé, L., 1984. Laboratory experiments in fracture propagation. Soc. Petrol. Eng. J., v. 24, no. 3, p. 256–268.

Controlled-Source Electromagnetic Soundings in Basalt-Covered Areas

N.E. Goldstein, H.F. Morrison, M.J. Wilt, and K.H. Lee

The controlled-source electromagnetic (CSEM) technique has been recently applied by various workers to the problem of mapping sedimentary rocks beneath a thick volcanic sequence. The interest in this technique derives from the fact that conventional reflection seismology has not provided needed information in such regions as the Columbia Plateau, where thick sequences of massive basalt and sedimentary interbeds blanket possible oil- and gas-bearing sedimentary rocks to depths of several kilometers. Electromagnetic techniques should be capable of mapping the depth and configuration of these underlying sedimentary units because volcanic rocks have a relatively high resistivity (~ 100 ohm·m) compared to sedimentary rocks (< 10 ohm·m), a fact known from geophysical well logs and published sounding results.

Keller et al. (1984) report on sounding studies performed near Yakima and Ellensburg, Washington, with a time-domain (TDEM) system that uses a long, grounded dipole-transmitter to energize the earth with an 80-s square-wave current pulse of 610 A, peak to peak. Lawrence Berkeley Laboratory (LBL) conducted studies in a nearby area using the EM-60 frequency-domain system, which energizes the earth with a horizontal loop transmitter. This system has been described by Wilt et al. (1983); the field results are summarized here.

NUMERICAL ANALYSIS

Before and after the field survey, a number of 1-D and 2-D models were computed (Lee and Morrison, 1985) to determine the sensitivity of electromagnetic and magnetotelluric parameters to a conductive wedge (the sediments sought) in a more resistive, layered half-space. For the example of a 2-D resistivity model shown in Fig. 1, we attempted to determine how accurately a 2-D sedimentary unit could be resolved from 1-D inversions of the normalized vertical and horizontal magnetic field amplitudes (in phase and quadrature) and from the ellipticity of the polarization ellipse traced out by H_z and H_r (Morrison et al., 1985). In such an exercise the transmitter-receiver separations are a constant 2 km, and the inversion is plotted midway between the transmitter and the receiver. The data set for the inversions consists of results at only five frequencies (0.05, 0.1, 0.3, 0.5, and 1.0 Hz), and it is clear that much information is lost because the EM response cannot be calculated at frequencies above 1 Hz for the finite-element mesh used. Nevertheless, as Fig. 2 shows, the three-layer inversions of all three EM parameters resolve the conductive sediments and

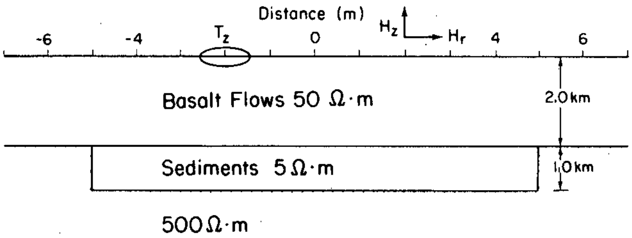

Figure 1. Two-dimensional resistivity model used to evaluate the resolution of a sedimentary unit by means of controlled-source EM soundings and 1-D inversions. [XBL 8312-2429]

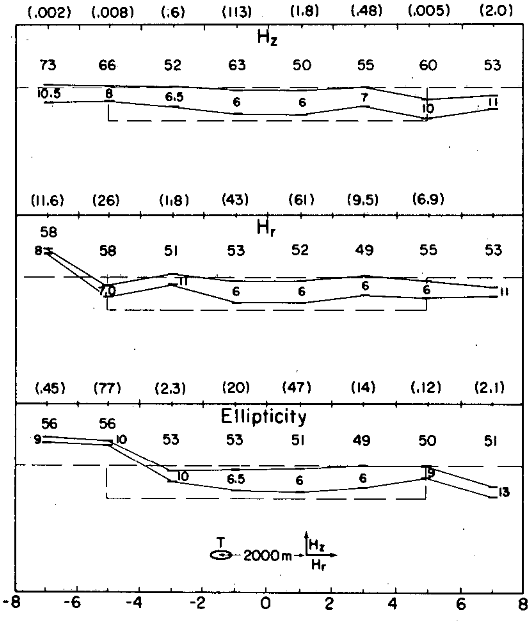

Figure 2. Results of three-layer 1-D inversions of **(top)** the complex vertical magnetic field (H_z), **(middle)** the complex horizontal magnetic field (H_r), and **(bottom)** the ellipticity of the polarization ellipse traced out by H_z and H_r. Inversions are plotted midway between transmitter and receiver. [XBL 8312-2434]

give a fairly accurate depth of the conductor. The conductor thickness is underestimated in each case, and the width of the conductor is poorly resolved. The numbers in parentheses in Fig. 2 are called the weighted cumulative squared differences (WCSD). These are a measure of the closeness of fit between the inversion model data and the original data at all five frequencies. The WCSD values are difficult to assess because some of the smallest values, indicating good fits, occur at stations where the 1-D inversions are obviously in serious error.

DATA ACQUISITION

The field survey consisted of 38 frequency-domain EM soundings made principally along a single traverse line 30 km in length and oriented in a northeast-southwest direction, or perpendicular to the fold structures in the Columbia River basalt group near Yakima. Five horizontal-loop transmitters were used; these were typically two turns of No. 6 welding cable laid out in a square 0.4–0.5 km on a side and connected in parallel. The inclination of each loop corner was determined by means of an altimeter. The observed fields, and hence interpretations, are sensitive to loop orientation.

Figure 3 shows the data acquisition system. The EM-60 transmitter impresses into the loop a peak current of 35–65 A, depending on the resistive load. The fundamental frequency of the square-wave current is controlled by one of a pair of synchronized quartz clocks. The other clock, located in the processing van, is used as the phase reference between transmitter current and detected signals. At frequencies above 100 Hz, the loop inductance causes the waveform to become quasi-sinusoidal. Because each loop has a unique inductive reactance, the frequency-dependent characteristics of each loop are measured so that the effects can be removed from the data prior to interpretation. In this survey, loop characteristics were obtained by making magnetic field measurements 50 m from one edge of the loop to observe the primary fields, i.e., those due solely to current flowing in the loop.

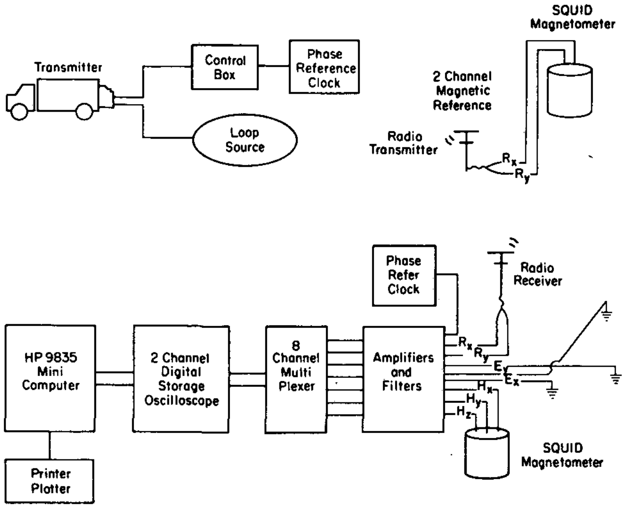

Figure 3. Schematic diagram of the horizontal-loop EM-60 system. In the work described here, we did not measure the electric field components, E_x and E_y. [XBL 818-3383A]

Receiver sites were located at distances ranging from 1 to 5.5 km from the transmitters. Since the depth of exploration is mainly a function of the transmitter-receiver separation (the offset distance), the closer sites provide controls on the near-surface resistivities and the more distant sites provide information to greater depths. As a general rule, the depth of investigation varies from half to the full offset distance.

At each receiver site three orthogonal components of the magnetic field were measured by means of SQUID magnetometers oriented to obtain vertical, radial, and tangential fields with respect to the loop. Data were taken over the frequency range 0.05–500 Hz at two sites simultaneously. Signals from one magnetometer ("local") were brought to the processing van via a 100-ft cable. The other magnetometer ("remote") was located 1–3 km from the van and linked to the van via FM radio telemetry. Background geomagnetic fields were simultaneously measured with induction coil magnetometers for the purpose of noise cancellation. Sites for background measurement were located 15 km or more from the transmitters. Field data were processed on site and in real time by means of an HP 9835 desktop computer. Field processing yielded initial EM parameter estimates, data quality evaluations, and apparent resistivity calculations. Between two and four soundings could be obtained per 12-hour field day by the 4-man crew.

DATA PROCESSING

On-site data processing consists of calculating auto- and cross-power spectra, correcting those spectra for calibrations and gains, and calculating EM parameters and their statistical errors. The uncorrected power spectra are stored on cassette tapes for reprocessing at the laboratory. Post-field processing consists primarily of reaveraging data segments (i.e., deleting the noisier data) and applying final calibration corrections and any adjustments for clock drift or transmitter-receiver separation. Once a final working data set is obtained for a station, the data are sent to the LBL CDC 7600 mainframe computer for interpretation. A data set can consist of eight spectra:

1. Normalized vertical field amplitude.
2. Vertical field phase.
3. Normalized radial magnetic field amplitude.
4. Radial field phase.
5. Ellipticity of the polarization ellipse traced out by the vertical and radial fields.
6. Inclination of the polarization ellipse from the vertical.
7. Wavetilt (the ratio of parameters 3 and 1)
8. Wavetilt phase (the difference between parameters 4 and 2).

INVERSION OF FIELD DATA

Layered-model interpretations are obtained for EM soundings by a least-squares inversion of field spectra. The inversion program, which uses a Marquardt algorithm, can use any combination of the eight field spectra or partial spectra from a station.

Individual data points used in inversions are weighted in proportion to their measurement error. Measurement error consists of the effects of random noise in combination with calibration errors, clock drift, and imprecise knowledge of transmitter-receiver separation and transmitter current. Typically these errors are larger at higher frequencies (> 10 Hz), where the primary field is less strong, cultural noise more severe, and calibration errors largest. In spite of our attempt to cancel geomagnetic noise using a distant reference magnetometer, errors may also be significant at low frequencies if geomagnetic noise levels are very high. Because easily calculated random error in the data probably underestimates the true error, we typically assign a 1% error to the spectral points, which is about twice as large as the error due to random noise alone. The amplitude spectra have values that range over two orders of magnitude, and weighting all amplitude data equally may bias the results because the inversion algorithm tends to fit the large-valued points in preference to the low-valued points. To obtain a better overall fit we may assign higher errors to the larger-valued data points.

SURVEY RESULTS

To illustrate how well the EM resolves stratigraphic units and determines layer resistivities, we averaged the results from a cluster of four soundings made around a deep well in the area and plotted the results against a smoothed version of resistivities read from the geophysical well log (Fig. 4). The agreement in the two curves is reasonably good. The EM soundings cannot resolve small layers, nor can they resolve the thickness of the lowermost (sedimentary) layer, which drilling indicates exceeds a depth of 4.5 km. The upper two layers are probably both volcanic units. The third and conductive layer is probably mostly pre-basalt sedimentary units. We also plot a layered interpretation for a station at the Santa Rosa dam site on the Yakima River. This result was obtained from a TDEM sounding made by Keller et al. (1984).

Figure 5 shows a selected segment of the interpreted results from the 30-km traverse line. The 1-D inversion results are plotted midway between the transmitter (two solid circles at the surface) and the magnetometer stations (the x's). The CSEM soundings seem to define clearly the conductive sediments below the basalt sequence. Agreement between adjacent and overlapping soundings is good, and the 1-D interpretation shows a structural high in the volcanic-sedimentary contact that may be related to an anticlinal fold.

Two-dimensional interpretations of the data set have not been made. The most significant 2-D effects are believed to be the surface conductors, such as the one in Badger Pocket. Scale modeling

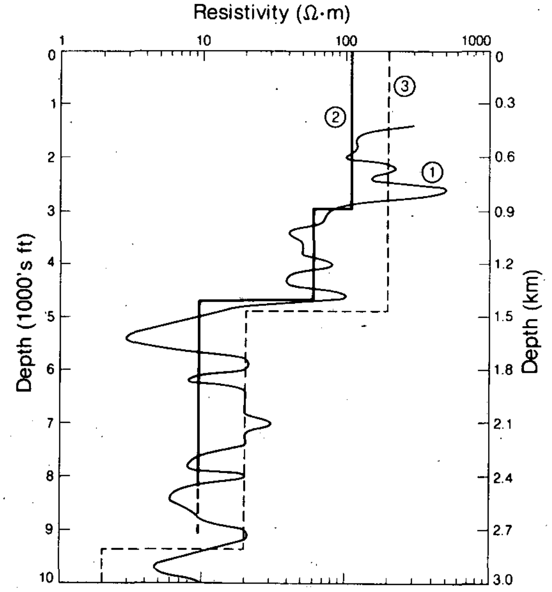

Figure 4. Comparison of a smoothed geophysical resistivity log (curve 1) and the average layered model based on four soundings near the well (curve 2). Curve 3 is a 1-D inversion of a TDEM sounding made at the Santa Rosa dam site on the Yakima River, Washington (Keller et al., 1984). [XBL 8312-6948A]

will be done to evaluate this source of error in the 1-D inversions.

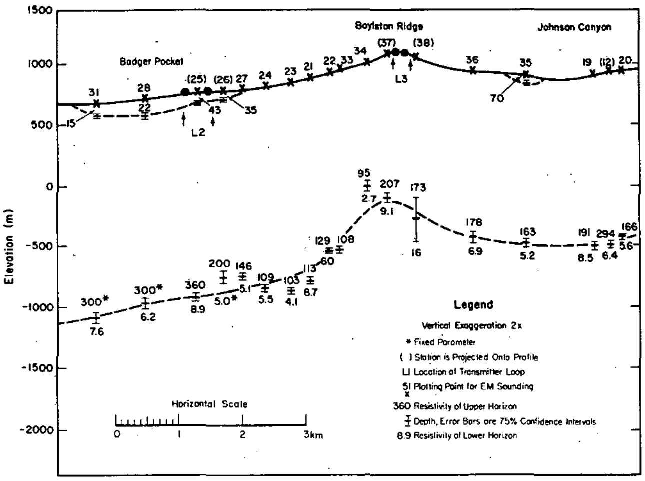

Figure 5. A segment of a resistivity section over the Columbia River basalt near Yakima, Washington, obtained from 1-D inversions of the CSEM soundings. [XBL 8411-6151]

REFERENCES

Keller, G.V., Pritchard, J.I., Jacobson, J.J., and Harthill, N., 1984. Megasource time-domain electromagnetic sounding methods. Geophysics, v. 49, p. 993–1009.

Lee, K.H., and Morrison, H.F., 1985. A numerical solution for the electromagnetic scattering by a two-dimensional inhomogeneity. Geophysics, v. 50, no. 3, p. 466–472.

Morrison, H.F., Lee, K.H., and Brzeski, J., 1985. Electromagnetic sounding: Mapping of sedimentary sections beneath basalt flows. In preparation.

Wilt, M., Goldstein, N.E., Stark, M., Haught, J.R., and Morrison, H.F., 1983. Experience with the EM-60 electromagnetic system for geothermal exploration in Nevada. Geophysics, v. 48, p. 1090–1101.

Magnetometer Array Studies of Natural Electromagnetic Fields (10^{-4}–1.0 Hz)

H.F. Morrison, J. Clarke, and E. Nichols*

Measurements of the surface impedance of the earth (magnetotellurics) and of the vertical component of the natural electromagnetic field are interpreted on the assumption that the incident fields are uniform plane waves. It has become apparent that these measurements are biased by fields that do not satisfy this homogeneous plane-wave assumption.

Dramatic evidence of this was presented by Gamble et al. (1979) and Clarke et al. (1983) when they introduced a method of impedance measurement using a remote reference magnetometer. In this experiment, it was assumed that only fields that were coherent over an appreciable horizontal distance were needed for the impedance calculation and that the noises that bias the result were uncorrelated over these same distances. In the calculations of the impedance, the magnetic field cross-powers between the base and the remote stations are used in place of autopowers at the base station alone. This technique was spectacularly successful in reducing errors in impedance measurements and is now the standard measurement technique in magnetotelluric (MT) surveys.

The results of remote reference MT measurements clearly showed that noise, uncorrelated over horizontal separations as small as 200 m, indeed causes bias errors in standard MT processing (Goubau et al., 1984). Apart from determining the spectra of this noise, the remote reference studies did not address the nature or source of the noise itself.

Five sources of noise could bias these measurements.

1. Sensor noise (magnetic detectors, electrodes, or instrumental noise). This obvious source was one of the reasons for introducing the low-noise superconducting quantum interference device (SQUID) magnetometers, but they have made no discernible improvement on the resulting impedance accuracy.
2. Local, near-field electric or magnetic sources (electrical equipment, machinery, etc.).
3. Movement or tilt of the magnetic sensors in the earth's main magnetic field.

---

*Materials and Molecular Research Division, Lawrence Berkeley Laboratory.

4. Quasi-static magnetic field fluctuations caused by time variations in the vertical static electric field.

5. Source effects—the presence of inhomogeneous plane waves of short horizontal wavelength in the source field itself.

In fact, many of the noise sources may exist simultaneously, and this may have led to widely different conclusions as to the appropriate sensor separation for successful noise removal. Near-field effects of a cultural nature would be expected to have much shorter correlation lengths than magnetospheric source effects. Instrument noise would be removed using two sensors side by side [this has been put to good advantage by Morrison et al. (1984) in a cross-power field technique for measuring sensor noise].

Apart from the scientific interest in determining the source of these noise fields, there are several practical applications that have led us to undertake some detailed studies using arrays of three-component SQUID magnetometers. Listed below are the experiments in which the differences in magnetic field at two or more stations are of interest.

1. Cancellation or reduction of the natural electromagnetic field at a receiver in a controlled-source electromagnetic sounding experiment. Direct cancellation of the natural field—the noise in this experiment—brings about a direct improvement in signal-to-noise ratio that can otherwise be achieved only by increasing the power of the source or by increasing the time of signal averaging. In either case, the total signal energy required increases as the square of the desired improvement in signal-to-noise ratio (if the noise is Gaussian). The increased energy is even greater if the noise is nonstationary.

2. Detection of level changes or transient changes in the magnetic field in the vicinity of a magnetometer. In one such experiment we attempted to map the change that occurs in the magnetic field when a magnetic proppant is injected into a hydraulic fracture. Very small changes in static magnetic field must be mapped by a surface array of magnetometers if the form of the resulting anomaly is to be related to the distribution of proppant in the fracture. Another important application of this field differencing is the use of magnetometer arrays for detecting stress-related changes in the magnetization of crustal rocks and for detecting the passage of submarines. Differencing to cancel the time variations of the magnetic field is a first step in improving the sensitivity of a search sensor, either fixed or airborne.

3. Measurement of gradients of the magnetic field for the purpose of studying the electromagnetic response of conductivity inhomogeneities, studying source effects, or making geomagnetic depth soundings.

ARRAY STUDIES: GRASS VALLEY, NEVADA, OCTOBER 1984

We have obtained, through support from the Gas Research Institute, seven SQUID magnetometers (manufactured by SHE Corporation), each equipped with internal biaxial horizontal tiltmeters. The cryogenic tiltmeters are mounted with the SQUID sensors in the dewar. They have a resolution of 30 nanoradians of tilt, which corresponds to a change in the measured vertical field of 1 mγ (assuming a 50,000-γ field with an inclination of 45°). With theoretical sensitivities of SQUID sensors better than 0.1 mγ, it is clear that very small tilt motions could easily set the noise floor of SQUIDs at 1.0 mγ or higher in field applications. Such small movements may be caused by thermal strains in the dewar-sensor-liquid helium system or simply by ground deformation due to tidal strain and seismic waves.

Four SQUID magnetometers were deployed to cover the array shown in Fig. 1. Each measurement site consisted of a 4-ft-deep fiber-glass-lined vault containing the magnetometer and the external tiltmeter mounted on a granite slab, a microbaragraph, orthogonal *E*-field lines 200 m in length, and a temperature sensor. All the outputs from these trans-

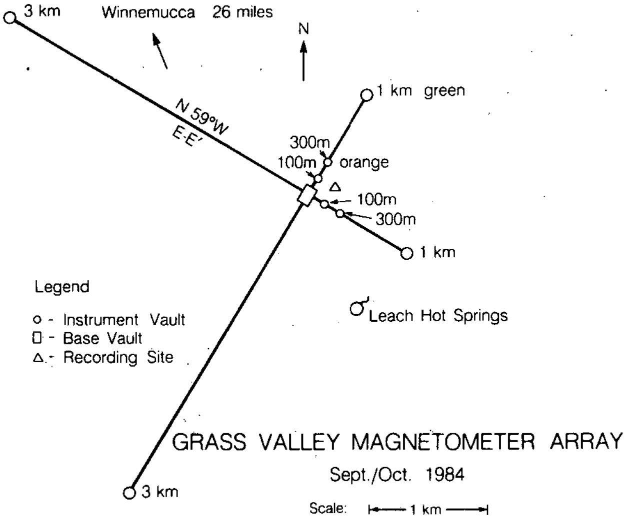

Figure 1. Layout of the magnetometer array used in the Grass Valley, Nevada, noise experiment. Two magnetometers were located at the base vault; the other two were moved to the various vaults shown by circles at distances of 1, 100, 300, 1000, and 3000 m from the base vault. [XBL 851-10241]

ducers were amplified, low-pass filtered at 0.5 Hz, and sent to the acquisition system through a line-driver amplifier. At the base station two magnetometers were mounted on a single rectangular granite slab. The two other magnetometers and associated sensors were set up in the various vaults along two orthogonal lines (Fig. 1). Relative to the base station, magnetometer separations of 1 m, 100 m, 300 m, 1 km, and 3.0 km were obtained. Between 36 and 48 hours of data was recorded for each setup. The field level was high during the experiment, with considerable P_c and P_i activity recorded at each setup.

The orthogonal electric field dipoles at the base station and at each of the remote sites consisted of standard copper/copper sulfate electrodes. The voltage differences were amplified and filtered at the midpoint of the array and then transmitted through optical isolators to line drivers and thence to the data acquisition system.

The data acquisition system consisted of 80 channels of 0.3-Hz four-pole Butterworth low-pass (anti-alias) filters leading into a Hewlett Packard (3495A) multiplexer and followed by a Hewlett Packard (3456A) 5-1/2-digit voltmeter. The voltmeter was then connected by HP-IB bus to a Hewlett Packard Model 9020 computer. Data were stored on a 132-Mbyte disk (7914) driven by the 9020. The sampling rate on each of the 80 channels was 2 Hz. The anti-aliasing filters produced over 100 dB of attenuation at this frequency. The disk filled after approximately 48 hours of data acquisition, at which point data on the disk were dumped to tape and stored. The multitasking features of the HP 9020 allowed us to process and display results during the data acquisition. For example, a graphics program permitted a data display of the time series, and a processing program computed spectra and other parameters of the fields.

DATA PROCESSING

Noise reduction by differencing the output of two separated magnetometers involves a sequence of operations, the success of which is ultimately measured by a least-squares criterion applied to the resulting differences. These operations are listed below in a rough priority order.

1. Calibration errors. The coefficient relating output voltage to field at the sensor must be accurately determined if the differences are to be accurate.
2. Orientation errors. Like components of separated sensors must be parallel (similarly, the three components of the SQUID sensor must be orthogonal) or the magnetic field differences will be in error. Because it is virtually impossible to align the sensors with a high degree of precision, misorientation must be corrected for in the processing.
3. Sensor tilt is a form of orientation error that varies in time. Tilt corrections are more easily made in the time domain, since tilt results in a multiplicative change in the output of a given sensor (component) and correction would require a convolution operation if applied to the spectra.
4. Differences due to magnetic field gradients caused by local conductivity inhomogeneities in the ground can be measured by obtaining a conventional transfer function between components after accounting for items (1), (2), and (3) above.
5. The remaining differences are due to the other noise sources mentioned earlier. This is the noise background in which signals produced by controlled sources or by changes in magnetic field level must be detected.

In processing the Nevada data, we first adopted a straightforward regression analysis of the magnetic

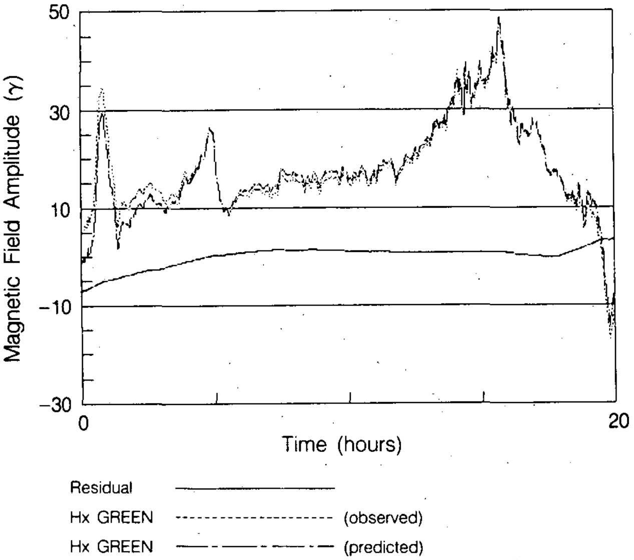

```
                 LEAST SQUARES SOLUTION
Parameter #   Channel #                    Coefficient
 1 (mean)                                    -.03839
 2           49 (Hx ORANGE)                  1.07541
Sum of residuals∧2: 4.22785E+03         Standard deviation: 2.02995E+00
Range of predicted: -1.74348E+01   TO   4.79072E+01
Range of residual: -7.00203E+00    TO   3.46706E+00
Number of points: 1028                  Data File: GV-INLINE
```

Figure 2. Example of least-squares analysis applied to the H_x components of two magnetometers 700 m apart. The residual curve is the difference in the H_x observed at station Green and the H_x predicted from a least-squares regression analysis using H_x observed at station Orange. [XBL 851-10242]

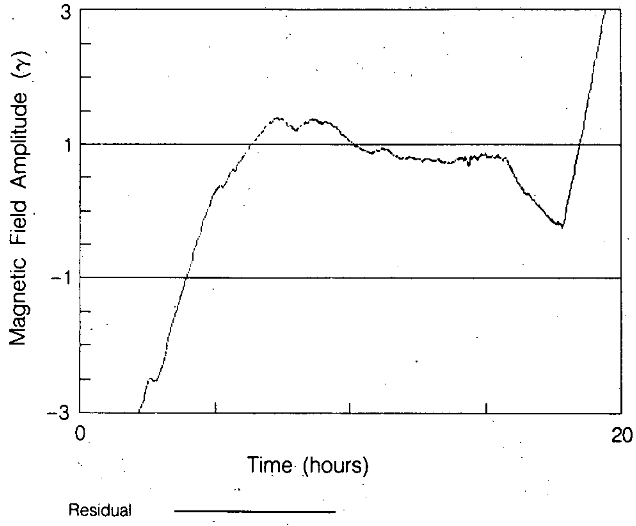

```
                    LEAST SQUARES SOLUTION
Parameter #   Channel #                  Coefficient
 1 (mean)                                 -.03839
 2          49 (Hx ORANGE)                1.07541
Sum of residuals∧2: 4.22785E+03           Standard deviation: 2.02995E+00
Range of predicted: -1.74348E+01    TO    4.79072E+01
Range of residual: -7.00203E+00     TO    3.46706E+00
Number of points: 1028                    Data File: GV-INLINE
Start time: 18:04:46 14 Oct 1984          Printed: 09:20:42 31 Oct 1984
```

Figure 3. An expanded view of the residual curve in Fig. 2. [XBL 851-10243]

field components at one site against those at another. Thus we performed a least-squares fit of the form

$$H_{x1} = a + bH_{x2} + cH_{y2} + dH_{z2} \qquad (1)$$

to determine the coefficients a, b, c, and d. The letter subscripts refer to the components, and the numerical subscripts refer to the site. This process finds, experimentally, the ratio of the calibration coefficients and the static misorientation error.

We next included the tilt, T, in the regression; i.e., we included terms $\alpha T_x + \beta T_y$ in Eq. (1). This process determines a new set of coefficients that accounts for differential tilt of the magnetometers relative to each other and the earth's magnetic field. The coefficients so determined should be independent of time unless the instrument transfer functions are time dependent or the relative orientation of the magnetometers changes in time.

Figures 2 through 5 show an example of noise reduction by means of the least-squares analysis applied to the H_x component of one magnetometer (Green) 700 m away from a reference magnetometer (Orange). Figure 2 shows the residual magnetic field (noise) when only the first two terms in Eq. (1) are used:

$$H_{x1} = a + bH_{x2},$$

where the residual is defined as

$$R_x \equiv H_{x1}(\text{observed}) - (a + bH_{x2}).$$

The residual magnetic field is shown in an expanded scale in Fig. 3. The residual field variations are only slightly reduced when they are included in all three components of the reference magnetometer least-squares corrections (Fig. 4). However, the noise reduction is enormously improved when two components of tilt at both sites are also included in the regression analysis (Fig. 5). In this example, direct linear differencing reduced the peak-to-peak residuals by 37 dB. Improvements of up to 60 dB have been obtained in the signal-to-noise ratio. This example shows the importance of tilt correction; the residuals are reduced by an order of magnitude when the tilt parameters are included in the regression.

We have not yet advanced to the next step of determining the frequency-domain transfer functions between the corrected data of each site. This operation will presumably reduce the residuals even further, especially for the larger station spacing.

Another very interesting approach to this problem has been to determine coefficients for a time-

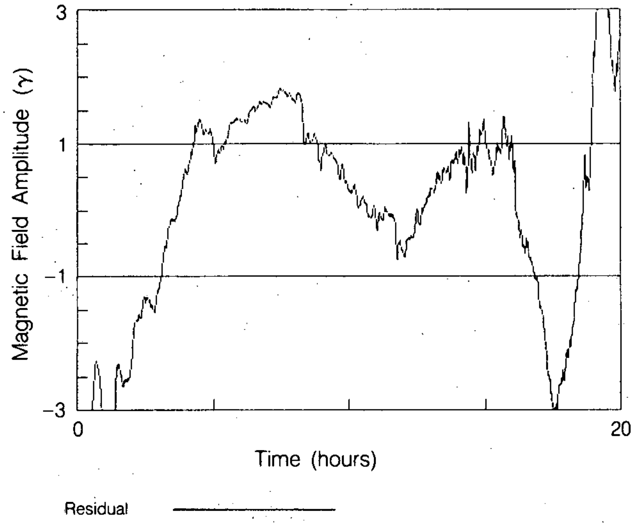

```
                    LEAST SQUARES SOLUTION
Parameter #   Channel #                  Coefficient
 1 (mean)                                 -.62625
 2          49 (Hx ORANGE)                1.04943
 3          50 (Hy ORANGE)                .08674
 4          51 (Hz ORANGE)                .34971
Sum of residuals∧2: 2.96321E+03           Standard deviation: 1.70110E+00
Range of predicted: -1.60281E+01    TO    4.73084E+01
Range of residual: -6.27222E+00     TO    3.89558E+00
Number of points: 1028                    Data File: GV-INLINE
Start time: 18:04:46 14 Oct 1984          Printed: 09:22:49 31 Oct 1984
```

Figure 4. The residual after H_x at station Green is predicted from a least-squares regression analysis using H_x, H_y, and H_z at station Orange. [XBL 851-10244]

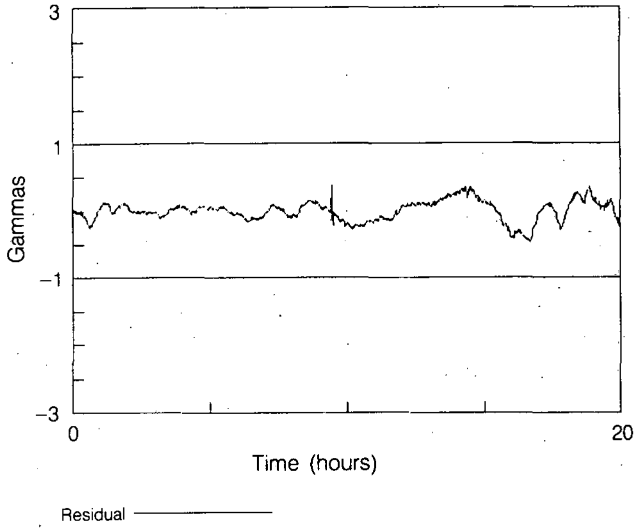

```
                    LEAST SQUARES SOLUTION
Parameter #   Channel #                    Coefficient
 1  (mean)                                  7.05359
 2        49 (Hx ORANGE)                    1.09162
 3        50 (Hy ORANGE)                    -.01360
 4        51 (Hz ORANGE)                    -.04704
 5        37 (Txi GREEN)                   19.43422
 6        38 (Tyi GREEN)                     .96449
 7        53 (Txi ORANGE)                 -29.85207
 8        54 (Tyi ORANGE)                  34.95585
Sum of residuals∧2: 2.36985E+01        Standard deviation: 1.52426E+01
Range of predicted: -1.42195E+01   TO  4.89513E+01
Range of residual:  -4.69608E+01   TO  3.88368E+01
Number of points: 1028                 Data File: GV-INLINE
```

Figure 5. An example of noise improvement that can be achieved using least-squares regression when two components of tilt at each station are included in the analysis. [XBL 851-10245]

domain autoregressive (AR) filter for relating one sensor to another. In this approach one utilizes the strong AR correlations that have been observed to exist in successive time periods at one given site. For example, in the case of the H_x component at site 1, the AR processes are of the form

$$H_{x1}(t) = (1 + \theta_x)\, H_{x1}(t - 1) - \theta_x\, H_{x1}(t - 2) + n(t),$$

where $n(t)$ is a random noise term.

Estimation of the autoregressive and noise parameters have been made using Bayesian filtering techniques that have been developed by R.M. Oliver and his graduate students in the Operations Research Center and are available to us in the form of interactive computer software on the campus IBM 3081.

FUTURE WORK

This magnetometer array and in-field data-acquisition and processing system has now seen over 2 months' field service and has already acquired over 2Gbytes of high-quality multistation EM field data plus tilt, barometric pressure, electric field, and temperature. Much work remains to be done to study the noise spectra of the magnetic and electric fields and their relation to tilt, pressure gradients (as possible cause of ground tilt), and site separation. The system is now fully debugged; after the processing of the magnetic-hydrofracture-proppant-mapping experiment it will be available for further array studies.

A natural extension of the present work would be to increase the array dimensions to determine field properties over distances of tens or hundreds of kilometers. Such studies are critical for determining the fundamental limits of magnetic airborne detection.

The problem of determining whether an anomalous magnetic field is present at a particular observation point x_1, y_1, z_1 depends on:

1. Knowledge of the earth's static magnetic field at x_1, y_1, z_1.
2. Knowledge of the time-varying field at x_1, y_1, z_1. This can be determined to first order by knowing the time-varying field at some other point x_0, y_0, z_0. This transfer function could be obtained experimentally, or it could be predicted from prior knowledge of the conductivity distribution.
3. Corrections based on spatial variations of the incident field-source effects.

The last two points are the unknowns in large array schemes for detecting magnetic anomalies. It is not known how well an array can characterize the incident field and, in turn, how well the transfer function can be determined.

Only after these points are addressed can further sources of noise, such as internal waves in marine operations, be evaluated.

REFERENCES

Clarke, J., Gamble, T.D., Goubau, W.M., Koch, R.H., and Miracky, R.F., 1983. Remote reference magnetotellurics. Equipment and procedures. Geophys. Prospect., v. 31, p. 149–170.

Gamble, T.D., Goubau, W.M., and Clarke, J., 1979. Magnetotellurics with a remote reference. Geophysics, v. 44, p. 53–68.

Goubau, W.M., Maxton, P.M., Koch, R.H., and Clarke, J., 1984. Noise correlation lengths in remote reference magnetotellurics. Geophysics, v. 49, p. 433–438.

Morrison, H.F., Conti, U., Labson, V.F., Nichols, E., and Goldstein, N.E., 1984. Field tests of noise in SQUID and induction coil magnetometers. Lawrence Berkeley Laboratory Report LBID-901.

Design and Noise Tests of New Induction Coil Magnetometers

H.F. Morrison, U. Conti, V.F. Labson,*
E. Nichols, and N.E. Goldstein

Research in magnetotellurics (MT) began at Lawrence Berkeley Laboratory in 1974, and studies at that time involved use of early superconducting quantum interference device (SQUID) magnetometers (Morrison et al., 1979). Their low intrinsic noise levels offered the hope that SQUIDs might be very useful in reducing magnetic noise observed in the field, especially in the 0.1–5 Hz band, which has low signal strength yet is often critically important for interpreting MT sounding data. In fact, however, the low intrinsic noise of the sensors did little to improve impedance estimates, and the main advantage of SQUIDs was their small size and compactness compared to the very heavy and cumbersome induction coils used for low-frequency data acquisition before they were introduced. On the other hand, the main disadvantages of SQUID magnetometers have been found to be the expense and difficulty in providing liquid helium at remote field sites and maintaining their electronics.

A major influence on the way geophysicists collect and analyze magnetic data came from Gamble et al. (1979), who made a breakthrough in reducing the errors in impedance estimates by calculating the estimates from cross-powers using signals from a remote reference magnetometer. This technique revealed that large bias errors in impedance estimates were due either to unexpectedly large noise in the magnetic field or to some other noise source not predicted from the SQUID sensor noise determinations carried out under shielded laboratory conditions. With the remote reference technique, estimates of the noise itself can be obtained by use of the auto- and cross-powers of two sensor outputs. Actual SQUID noise levels determined this way in the field turned out to be much higher than laboratory results had indicated (Goubau et al., 1983).

At the same time that remote reference magnetotelluric measurements and noise studies were demonstrating that SQUID magnetometers were not as necessary as initially believed, developments in the design of sensitive, low-noise induction coil magnetometers were indicating that they could be a practical, low-cost alternative to SQUID magnetometers. On the basis of electronic design by Stanley and Tinkler (1982) and Clerc and Gilbert (1964), we developed small, low-noise induction coils that, because of their feedback design, provide a flat response for magnetic field, *B*, from 1.0 Hz to > 10 kHz (Labson et al., 1984). These coils performed so well that we decided to develop a low-frequency version to replace our aging and troublesome SQUID magnetometers that we had been using for several years for MT and controlled-source EM soundings.

COIL DESIGN

Design criteria centered on building a coil 4 ft in length less than 15 lb in weight with a matching amplifier providing a flat response to magnetic field from 1 to 500 Hz and with a noise level over the 0.001- to 500-Hz bandwidth at least as good as values obtained with SQUIDs in the field. Because of the restriction of state-of-the-art electronics, the amplifier had to be designed first.

The requirement that this coil magnetometer must have low noise at low frequency led to the choice of a chopper-stabilized amplifier. Stanley and Tinkler (1982) described an amplifier for induction coils that has very good low-frequency noise characteristics. In their application, the coil is tuned with a capacitor to a frequency of 14 Hz, and the coil-amplifier combination has a maximum operational frequency of 10 Hz. Moreover, the high sensitivity of the system around 14 Hz gives it the tendency to oscillate from bursts of signal energy in the band around resonance (14 Hz).

For this reason and because our requirements called for a sensor with a frequency band from 0.001 to 500 Hz, it was necessary to modify the amplifier circuit and to adopt a feedback technique that eliminates the natural resonances of the coil and makes the response to *B* flat over a wide frequency range. A schematic diagram of the amplifier developed for the coil magnetometer is shown in Fig. 1, and a typical coil response is shown in Fig. 2.

Given the design of the amplifier, the coil design is then tailored to the noise characteristics of the amplifier and to the requirements of size and weight. The most important parameter is the coil length, because the ability of the μ-metal core to concentrate the magnetic field inside the coil winding depends largely on the length-to-diameter ratio of the core. Fifty-two inches was finally chosen as a practical upper limit to facilitate handling the coils in the field.

---

* Visiting researcher.

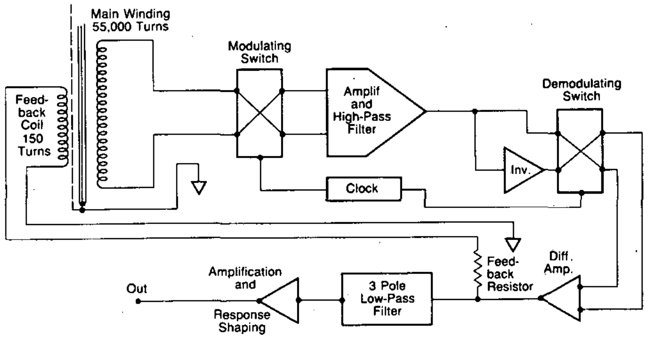

Figure 1. Schematic diagram of detector and amplifier for the low-frequency induction coil magnetometer. [XBL 843-10297]

At this point of the design the weight of the coil is approximately fixed, since large variations in weight will produce only small variations in noise characteristics or sensitivity. The final design produced a coil of about 15 lb in weight. Table 1 shows the principal characteristics of the coil system.

To minimize the distance between the windings and the amplifier, a multilayer structure of small, round, printed circuit boards was made to fit into one end of the fiber-glass coil casing. A single cable connects to the coil assembly to bring power to the circuitry and take the output signal to the recording equipment.

NOISE ANALYSIS

The noise spectra of the magnetic field sensors were measured with and without a μ-metal magnetic shield in the field. In both cases, the noise spectra were determined by digital Fourier analysis of the sensors' output. The in-field measurements provided reliable noise estimates, and the method developed is summarized here.

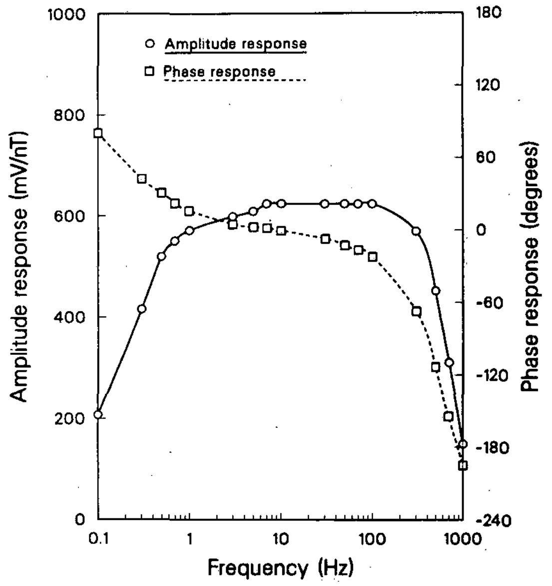

Figure 2. Coil response functions. [XCG 845-13077]

Table 1. Coil magnetometer specifications.

Parameters	Specifications
Length	52 in.
Diameter	2-1/4 in.
Weight	15 lb
Response: upper 3 dB point	500 Hz
lower 3 dB point	0.1 Hz
Sensitivity (flat band)	500 mV/γ
Main winding: number of turns	55,000
wire size	#30
Feedback winding: number of turns	150
wire size	#30
Inductance	1250 H
Natural coil resonance	140 Hz

For cases in which precise and accurate coil-amplifier calibrations are lacking, it becomes more difficult to determine the noise component in the magnetic field spectrum. A technique that we have developed to get around this problem uses the coherence function, γ^2, defined as

$$\gamma^2 \equiv \frac{|\overline{BA^*}|^2}{(\overline{AA^*})\,(\overline{BB^*})}, \tag{1}$$

where A and B are the simultaneous magnetic field spectra from two similar instruments, * denotes a complex conjugate, and $\overline{BB^*} \equiv$ the time average of BB^* over many time records. If the signal in A and B are equal and designated as S, then

$$\gamma^2 = \frac{|(1+\epsilon_A^*)(1+\epsilon_B)\overline{SS^*}\,|^2}{[1+\epsilon_A|^2(\overline{SS^*}+\overline{n_A n_A^*})]\,[1+\epsilon_B|^2(\overline{SS^*}+\overline{n_B n_B^*})]}, \tag{2}$$

where ϵ_A,ϵ_B are the unknown calibration errors in A and B and n_A, n_B are the apparent sensor noises in A and B. From Eq. (2) we can derive a simple relationship between noise and coherence by assuming that n_A and n_B are independent but equal in magnitude. Morrison et al. (1984) show that the ratio of noise power to total output power from sensor A, written as X, is

$$X = 1 - \gamma \tag{3}$$

and that

$$\overline{nn^*} = (1 - \gamma)\,|1 + \epsilon_A|^2\,\overline{AA^*}. \tag{4}$$

Notice that ϵ still appears in Eq. (4), but it can be seen that small calibration errors produce little error in $\overline{nn^*}$.

FIELD RESULTS AND CONCLUSIONS

Field tests were conducted using two separated SQUID magnetometers (manufactured by the SHE Corporation and loaned to us for the test by Z-Axis Inc.) and two pairs of the prototype induction coils described above.

The coils were buried in vertical sleeves, completely below the surface. The SQUIDs were placed in holes with the sensor electronics above the ground surface and covered by a solid windshield. SQUIDs and coil pairs were separated by about 10 m.

Figures 3, 4, and 5 compare the results between the vertical component of a SQUID magnetometer and the corresponding component of an induction coil magnetometer. The straight autopowers (natural field signal plus noise) are shown first in Fig. 3. The coherences between separated SQUID and coil pairs are shown in Fig. 4, and the noises calculated using the coherence method described above are presented in Fig. 5. Note that in Fig. 5 we represent noise in terms of an equivalent magnetic field strength.

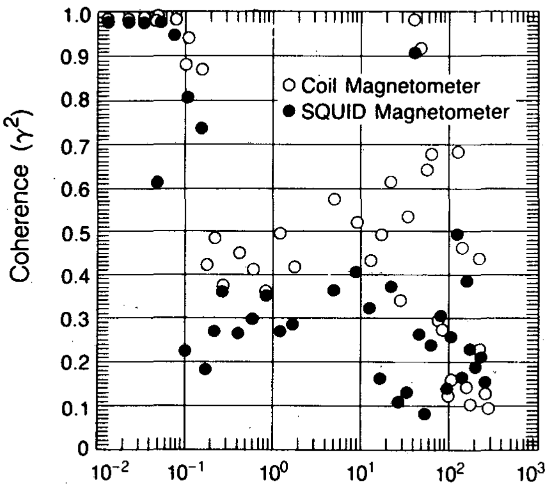

Figure 4. Comparison of coherences (γ^2) of SQUID and induction coil magnetometer components. [XBL 843-10296]

With relatively little averaging there is some scatter in the noise data, but is is quite clear that sensor noise from the coils is considerably less than from the SQUIDs above 0.3 Hz. The coils give a remarkably low noise level of 40 × $10^{-6} nT/\sqrt{Hz}$ at 100 Hz. Below 0.1 Hz the coil noise is virtually identical to the SQUID noise. Further tests and

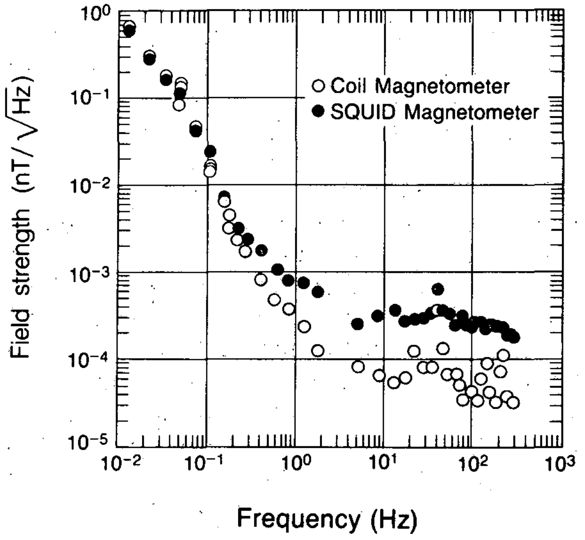

Figure 3. Comparison of the vertical field strengths measured by means of a SQUID magnetometer and a coil magnetometer 10 m away. Field strength is calculated from the square root of the autopower and contains natural geomagnetic signal plus noise. [XBL 843-10298]

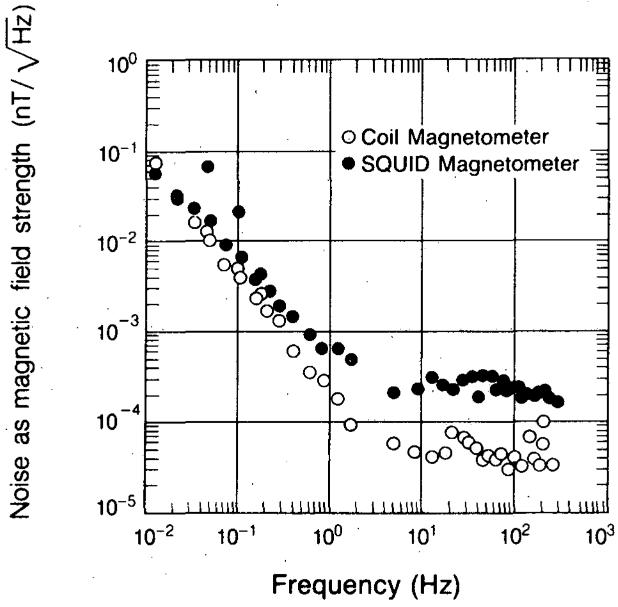

Figure 5. Comparison of noise represented as equivalent magnetic field strength for SQUID and coil magnetometer. Noise strength is calculated from the square root of the noise power given in Eq. (4). [XBL 843-10295]

design modifications are in progress to determine whether additional reduction in coil noise is possible.

The fact that both SQUID and coils see the same noise for low frequencies (which is above the noise theoretically predicted for either of them) suggests a local external source, which is *uncorrelated over a distance of 10 m.* There is no proven explanation for this phenomenon, but it may be due to wind-induced vibrations. As a practical matter for the measurement of natural field impedance or fields from controlled sources, the noise is at or below the natural field level, and SQUIDs of the type tested are used routinely to get excellent data with reference sensors. This experiment has shown that lightweight coils can be built to achieve field performance identical to that of commercially available SQUIDs.

REFERENCES

Clerc, G., and Gilbert, D., 1964. La contre-réaction de flux appliquée aux bobines a noyau magnétique utilisées pour l'enregistrement des variations rapides du champ magnétique. Ann. Geophys., v. 20, no. 4, p. 499–502.

Gamble, T.D., Goubau, W.M., and Clarke, J., 1979. Magnetotellurics with a remote reference. Geophysics, v. 44, p. 53–68.

Goubau, W.M., Maxton, P.M., Koch, R.H., and Clarke, J., 1984. Noise correlation lengths in remote reference magnetotellurics. Geophysics, v. 49, no. 4, p. 433–438.

Labson, V.F., Becker, A., Morrison, H.F., and Conti, U., 1985. Geophysical exploration with audiofrequency natural magnetic fields. Geophysics, v. 50, no. 4, p. 656–664.

Morrison, H.F., Lee, K.H., Oppliger, G., and Dey, A., 1979. Magnetotelluric studies in Grass Valley, Nevada. Lawrence Berkeley Laboratory Report LBL-8646, 160 p.

Morrison, H.F., Conti, U., Labson, V.F., Nichols, E., and Goldstein, N.E., 1984. Field tests of noise in SQUID and induction coil magnetometers. Lawrence Berkeley Laboratory Report LBID-901, 15 p.

Stanley, W.D., and Tinkler, R.D., 1982. A practical, low-noise coil system for magnetotellurics. Denver, Colorado, U.S. Geol. Surv. Open-File Report, 33 p.

Low-Frequency Electromagnetic Surface-to-Borehole Logging

K.H. Lee, H.F. Morrison, and D. Kennedy

Controlled-source electromagnetic sounding (CSEM) is becoming a valuable tool for resolving certain geologic features in problem areas where seismic reflection methods are unsatisfactory. Examples of such situations are the detection of electrically conductive sediments beneath volcanic flows or overthrust sections of older rock. Typically, the transmitters and receivers are located on the surface, and the observed EM responses, as functions of array geometry in either the time or the frequency domain, are used to infer the conductivity distribution at depth. Examples of such surveys using a horizontal loop source developed by Lawrence Berkeley Laboratory and the Engineering Geoscience group at U.C. Berkeley are given by Wilt et al. (1983). Examples of data taken with a grounded wire source are given by Keller et al. (1983). To date, most of the published studies deal with mineral and geothermal exploration.

Another type of sounding can be made if a drill hole is available in the area. In this case, the transmitter is located on the surface and the receiver lowered down the hole. The advantage of surface-to-borehole sounding is that the method is inherently more sensitive to subsurface layering or inhomogeneities than surface-only measurements.

Surface-to-borehole electromagnetic measurements have not yet been reported for petroleum exploration, although vertical seismic profiling (VSP) is an example of a seismic surface-to-borehole technique that is frequently used. A surface-to-borehole EM technique for petroleum exploration would also have inherent advantages over surface measurement and conventional well logs for determining subsurface conditions away from or below the well. In particular, it may also be possible to determine regional conductivity distributions in the presence of the casing.

DISCUSSION OF THE TECHNIQUE

To illustrate the technique we assume that a drill hole penetrates an arbitrarily layered earth to some

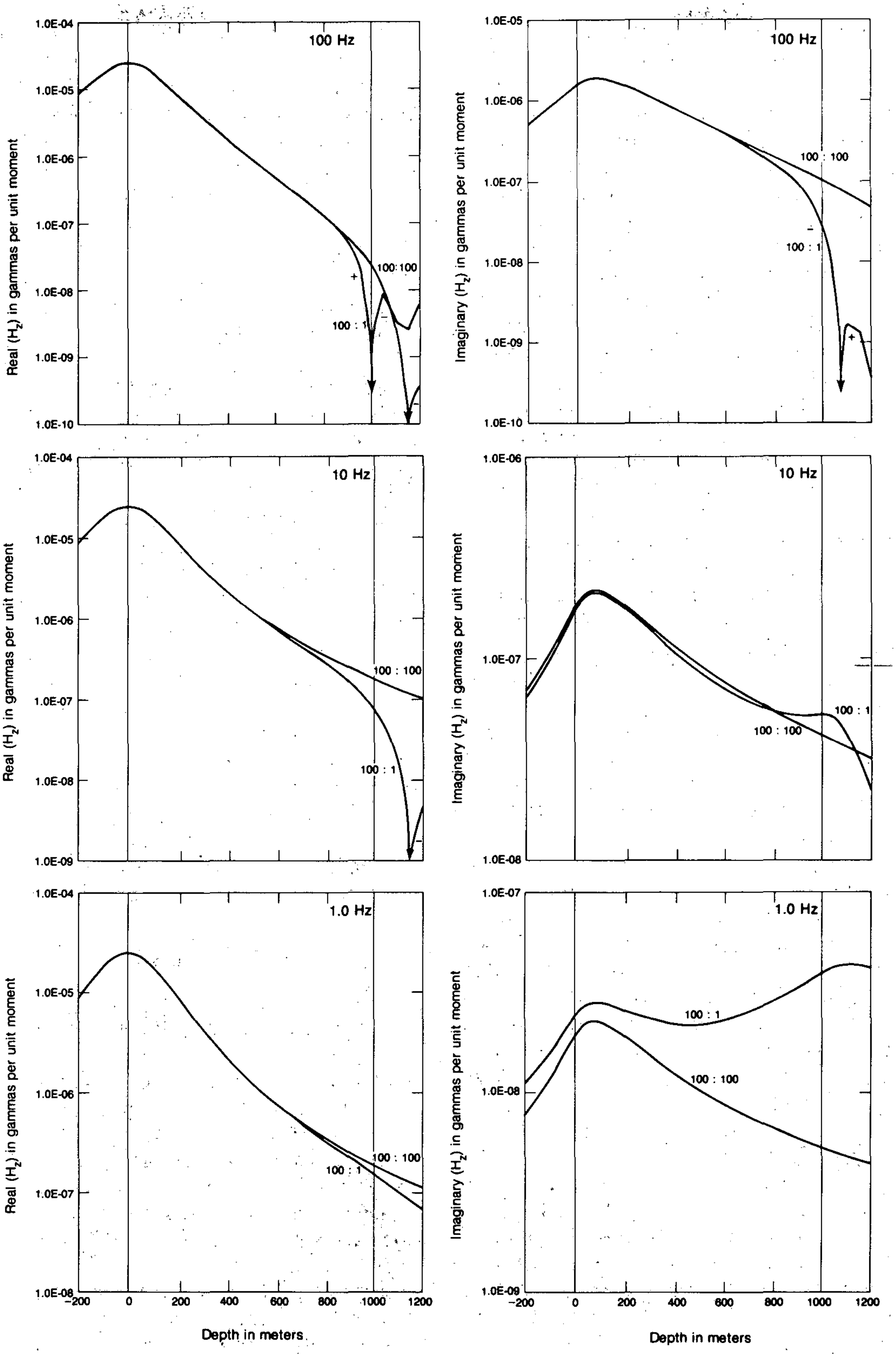

Figure 1. Real and quadrature parts of H as a function of position in the drill hole for the half-space model (ρ_1:ρ_2 = 100:100) and the two-layer model (ρ_1:ρ_2 = 100:1). [XBL 8411-6160]

depth. A horizontal EM transmitter loop, coaxial with the hole, energizes the earth by means of a broadband EM signal. A suitable magnetic field detector measures the resultant field within the well. Despite the potential usefulness of this arrangement for increasing the resolution of layered model parameters or for increasing the sensitivity of soundings to structure or layering below the drill hole, we do not yet have a numerical solution for the general case of an *n*-layered earth. However, to illustrate the methodology and its advantages, we have rewritten and executed a program that calculates the vertical fields in a two-layer earth along the axis of a borehole concentric with the loop. This program could be generalized to give the magnetic and electric response in any layer of a multilayer model and at any radial distance from the axis of the loop.

Calculations were made to show that the in-hole fields are indeed sensitive to boundaries between layers of different conductivity when the receiver passes through them. This property relates to how well conductivity could be measured as a function of depth and thus to the question of resistivity logging in cased wells. Preliminary calculations suggest that the conductivity may be measured through the casing at low frequencies.

In the test models described here, a two-layer earth is energized by a horizontal loop with a 200-m radius. The dipole moment, M, is thus equal to $4\pi I \times 10^4$, where I is the current. The field strengths have been calculated in the frequency domain in the borehole and along the surface. They are expressed in units of gammas (10^{-5} oersteds) for a transmitter moment of unity. Practical values are obtained merely by multiplying the calculated results by the actual transmitter moment. The fields are calculated first for an infinite half-space model whose resistivity, ρ, is that of the upper layer (ρ_1 = 100 ohm·m) and then for the two-layer model with a conductive basement, ρ_2, of 1 ohm·m at 1.0 km. The response curves for each are identified in Fig. 1 by the ρ_1:ρ_2 values. The fields have not been normalized by the primary free-space field.

In general, the resolution of layer parameters depends on how a particular magnetic field component changes in response to a change in parameters. Thus the best quantity to use for detecting a basement conductor is the field component that undergoes the largest change in value when the conductor is brought into the half-space. This same criterion is used to choose the best transmitter-receiver geometry. The actual field values and their differences, rather than ratios, would be employed in this evaluation, since there are practical noise limits in the actual measurements. For example, the half-space and two-layer models might produce a field ratio that is huge at some low frequency, but the low signal strength that might occur in practice could be below the detection level of the sensor.

Figure 1 shows the in-phase (real) and quadrature (imaginary) parts of the vertical magnetic field, H_z, as a function of depth and for excitation frequencies of 100, 10, and 1 Hz. Real H_z is dominated by the primary field from the transmitter, and the only significant differences between the two models occur very close to the interface. At 100 Hz the skin depth is 500 m in the first layer, hence the conductor is difficult to detect until one is virtually on top of it. There would be little difficulty in accurately locating the interface, however, if the borehole were to penetrate it. The quadrature field falls off much more slowly but still shows the conductor as the detector penetrates the interface. At 10 Hz the real component again sharply defines the interface, but the cross-over point is almost 200 m below the interface. On the other hand, the quadrature field is in a transition stage, having values ranging from less than to much greater than the half-space response. At 1.0 Hz the real component is weakly affected by the interface, and it would be difficult to estimate the depth of the interface from this piece of information alone. There is a dramatic difference between the two models in the quadrature component, and the difference increases with depth. The conductor is well detected anywhere in the hole, but the position of the interface, given as the receiver moves through it, might be less precise because of the lower resolving power of the low-frequency EM wave.

THE EFFECT OF CASING

One of the problems associated with borehole sounding is to identify the effects of steel casing on the measurement. To study this we formulated the problem of a circular loop of radius 100 m coaxial with a cylindrical shell (casing) in a conducting whole-space (Fig. 2). The conductivity and the relative permeability of the casing material used are 10^6 mho/m and 10^3 units, respectively. The fields are calculated on the axis of the casing as a function of the ac current frequency in the loop. The model is idealized, since in practice the loop would lie on the surface of the half-space. However, for receivers distant from the loop it is unlikely that the results are significantly affected by this whole-space representation.

Figure 2 shows the computed results plotted in a standard Argand diagram. The in-phase and quadrature secondary fields are those that would be measured at a point 500 m below the loop transmitter.

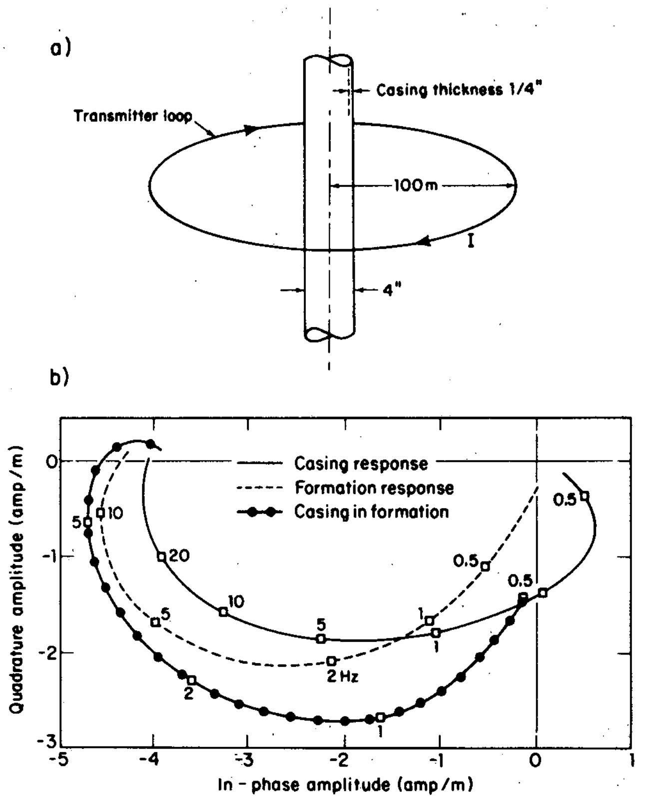

Figure 2. Argand plot of the responses of a receiver in the casing in free space, in the formation, and with casing in the formation. Casing and transmitter are in the whole-space. [XBL 8410-8858]

The response inside the casing alone (in free space), the response in an uncased hole in a formation of 1 ohm·m resistivity, and the response in a cased hole in the same formation are all shown on the same plot. From this plot it is evident that the formation response is of the same order as the casing response in a frequency window from 0.5 to 20 Hz. The change in response for a change in formation resistivity at a constant frequency is a measure of the sensitivity of the technique for determining formation resistivity. Our preliminary study indicates that for the range 1.0–10.0 ohm·m, the important range for sedimentary rock studies, the sensitivity is very good.

CONCLUSION

In summary, the high-frequency data (⩾ 100 Hz) serve to locate the interface accurately, and presumably to measure the conductivity contrast, if the sensor passes through the interface. To infer the depth of the interface from a position in the hole above it, low-frequency values of the quadrature component at any point are satisfactory. The difference between the two models increases with depth, showing that the closer the receiver approaches the conductor, the better it is resolved.

An important question at this point is whether measurements made on the surface at various distances from the transmitter could resolve the conductor just as well as measurements made in the hole. To illustrate this situation we have calculated fields on the surface with different offsets from the transmitter as a function of frequency. These fields are then compared with those computed in the borehole for their amplitudes and amplitude differences. As one might expect, there are strong patterns in the response curve at different offsets, indicating that the layering could indeed be well resolved with the surface data, but in every case the in-hole data for field strength are greater, and the maximum difference between models is often an order of magnitude greater for the in-hole data.

From these preliminary analyses we conclude that there are no surface data that could resolve the layering as well as in the in-hole quadrature data. Further, it should be noted that no surface data even approach the resolution provided by high-frequency field measurements taken across the interface at depth.

REFERENCES

Keller, G.V., and Jacobson, J.J., 1983. Deep electromagnetic soundings northeast of The Geysers steam fields. Geothermal Resour. Counc., Trans., v. 7, p. 497–503.

Wilt, M., Goldstein, N.E., Stark, M., Haught, J.R., and Morrison, H.F., 1983. Experience with the EM-60 electromagnetic system for geothermal exploration in Nevada. Geophysics, v. 48, p. 1090–1101.

Comparison of Time- and Frequency-Domain Responses from Two Line Sources and a Rectangular Loop

M. Mackiewicz and H.F. Morrison

We have been trying to develop a model that would allow us to interpret electromagnetic (EM) sounding data from a complex EM (i.e., 3-D) source by approximating it with a simpler source that leads to an earth response more easily interpreted by means of currently available inversion routines. One obvious substitute for a long rectangular loop is a pair of line sources arranged in parallel; we had shown earlier (Mackiewicz and Morrison (1984) that in the frequency domain this approximation is not very good. Additional study has shown that this approximation is even worse for time-domain excitation.

MODEL

In this study we have calculated the frequency- and time-domain responses due to two similar sources: (1) a rectangular loop 1100 × 500 m and (2) two parallel lines of opposite polarity, 500 m apart. For simplicity we chose an earth model consisting of a resistive half-space (1000 ohm·m) and a conductive half-space (1 ohm·m). Fields were calculated at distances of 500 and 2500 m from the center of the sources, but only data for the 500-m position will be presented here.

The time domain response was obtained for a square wave with a period of 33 ms and a pulse duration of 8.25 ms. Frequency-domain results are plotted as a function of conductivity-frequency product to accommodate low- and high-resistivity half-spaces on the same graph. It is not possible to incorporate spatial dependence in the induction number because it is different for each source. Time-domain results are plotted as a function of time. Because the ratio of time over conductivity cannot be used with the transmitter current waveform that was chosen, time-domain curves are plotted separately for each case.

RESULTS

Figure 1 presents the frequency-domain H_z amplitude response for parallel-line and square-loop sources at a point 500 m from the center of the transmitter. Note that throughout the frequency spectrum, the shape of the response remains similar for both sources. In logarithmic space the response differs by a constant; at high frequencies the curves are parallel to each other. This characteristic suggests that a rectangular loop response can be adjusted by a constant in logarithmic space to obtain values

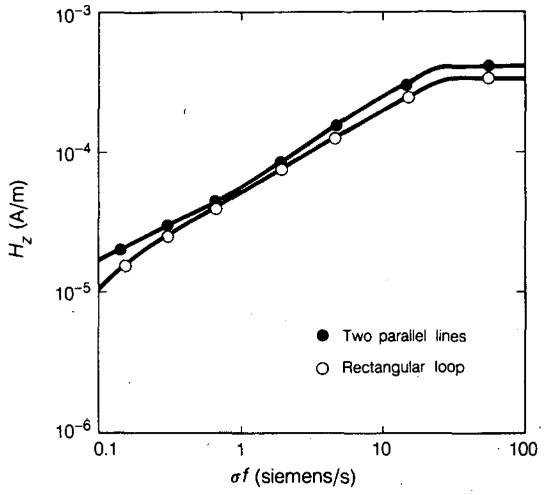

Figure 1. A frequency-domain comparison of the vertical magnetic field (H_z) amplitude responses for a 1100 × 500 m rectangular loop and two parallel lines over a half-space. The point of measurement is 500 m from the center of the sources. [XBL 854-0459]

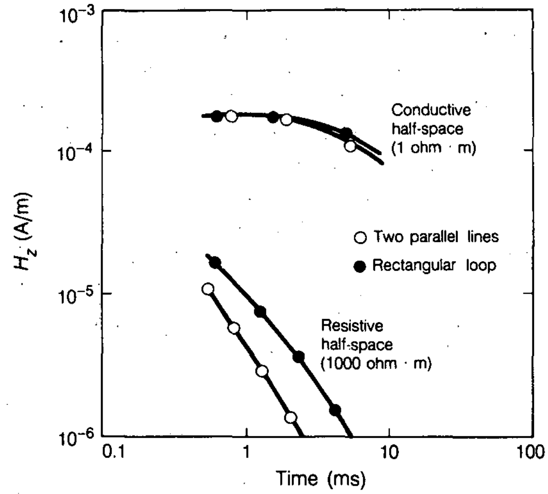

Figure 2. A time-domain comparison of the vertical magnetic field (H_z) response for a 1100 × 500 m rectangular loop and two parallel lines for resistive (1000 ohm·m) and conductive (1 ohm·m) half-spaces. The current in the transmitter was a square wave with a period of 33 ms and a pulse duration of 8.25 ms. [XBL 854-0459]

observed with parallel-line sources. Similar results hold for the horizontal field amplitude, H_x, and for receiver positions far from the transmitter. The separation between the curves increases with distances from the transmitter loop.

In the time domain the situation is different. Figure 2 shows that although the response matches fairly well at early times, it rapidly deteriorates at late times, particularly over the resistive half-space. The lack of agreement at late times confirms the results presented recently by Nabighian and Oristaglio (1984), who have shown that asymptotic expansions for finite and infinite sources differ at late times, making any corrections impossible even in a simple case like a half-space.

CONCLUSIONS

It appears that in frequency-domain EM analysis, there exists a possibility of using the lower-dimensional source to approximate the more complicated geometry of a rectangular loop. However, in the time domain the differences between rectangular-loop and parallel-line sources are impossible to quantify, making the adjustment between these two sources impossible.

REFERENCES

Mackiewicz, M., and Morrison, H.F., 1984. The accuracy of two line sources for approximating the fields of a large rectangular loop: Frequency domain. *In* Earth Sciences Division Annual Report 1983. Lawrence Berkeley Laboratory Report LBL-16920, p. 155–156.

Nabighian, N.M., and Oristaglio, M.L., 1984. On the approximation of finite loop sources by two-dimensional line sources. Geophysics, v. 49, p. 1027–1029.

Time-Domain Scale Modeling for the Interpretation of EM Sounding Data

M.J. Wilt and A. Becker

The interpretation of controlled-source electromagnetic (CSEM) sounding data is typically accomplished by finding a layered-earth fit to the decay curve of the secondary fields (in time-domain soundings) or the amplitude-phase spectra (in frequency-domain soundings). Iterative least-squares inversion techniques are available that provide a 1-D fit to the data. If a good set of observed data is acquired, this method can produce reliable interpretations for many geologic environments. However, where an abrupt lateral change in resistivity occurs, such as near a vertical fault boundary, the 1-D inversions will be in error. The 2-D and 3-D structures distort the secondary EM field, thereby causing 1-D inversions to be in substantial error near a discontinuity. This is particularly true where vertical contacts occur at or near the surface.

Although numerical models are available for 2-D and simple 3-D inhomogeneities in a layered earth (Lee, 1978), there do not yet exist reliable solutions for cases in which the inhomogeneities are at or near the surface. This class of problems is of major importance in EM sounding and may be addressed only through the use of physical or scale models. This article describes the design and initial results of a scale model EM system constructed to assess the effects of vertical contacts on EM sounding data.

EXPERIMENT DESIGN

We are examining two basic scale models with the measurements shown in Figs. 1 and 2: (1) a 2-D discontinuous surface layer in a resistive host rock (air) and (2) a 3-D surface inhomogeneity in a less conductive medium. Neither of these models has been successfully implemented numerically, but each has great practical importance. They are particularly useful in assessing the effects of lateral discontinuities on the determination of the thickness and conductivity of a surface conductive layer and the underlying layers. The models will be made at a scale of 1:10,000 (10 cm = 1 km). This scale is large enough so that detailed measurements can be made but small enough so that materials are of a manageable size and weight.

Model 1a consists of a slab of lead 1 m × 1 m × 2.5 cm (Fig. 1). This represents a semi-infinite 10-ohm·m layer 500 m thick. The material

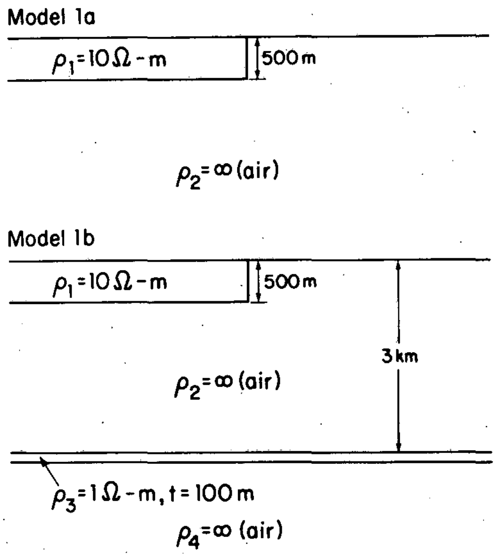

Figure 1. Model 1a: discontinuous conductive surface layer to be studied with scale-model system. Model 1b: discontinuous surface layer with deep conductive layer. [XBL 8410-8862]

weighs approximately 600 lb and requires special supports. Model 1b has a deeper conductive layer at a depth of 3 km. This is represented by an aluminum sheet 1 m × 1 m × 0.5 cm.

The host material of model 2a is a graphite disk 0.7 m in radius and 20 cm thick (Fig. 2a). This material represents a 200-ohm·m horizontal layer 3 km thick. Cut into the surface of this material is a cavity 2 cm deep, 15 cm wide, and 20 cm long that is filled with mercury. This inhomogeneity represents a 3 × 4 km block 400 m thick with a resistivity of 20 ohm·m. In model 2b the deep conductive layer is represented by a sheet of aluminum 1 m × 1 m × 0.5 cm.

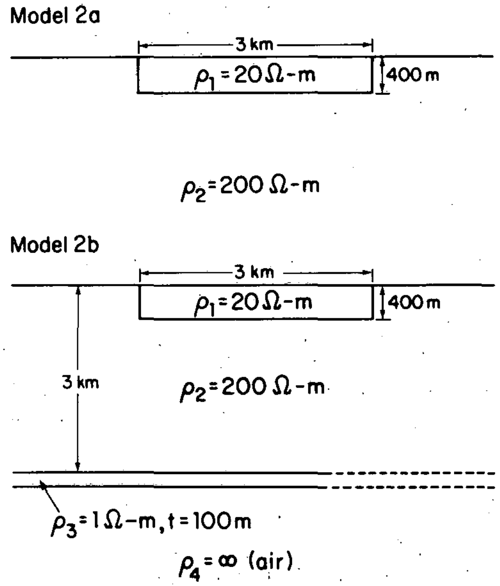

Figure 2. Model 2a: conductive inhomogeneity embedded in a less conductive medium. Model 2b: conductive inhomogeneity with a deep conductive layer. [XBL 8410-8863]

MEASUREMENT SYSTEM AND EXPERIMENTAL PLAN

The measurement system shown schematically in Fig. 3 consists of a computer-controlled receiver section and a function generator to produce transmitter waveforms. The transmitter current has a triangular waveform with a frequency of 6–20 Hz, dependent on the model type. A 4-cm^2 horizontal coil is used as the transmitter. The signal from this source is adequate for receivers located up to 0.5 m from the source.

The multichannel receiver section consists of 1–4 small, circular receiver coils (r = 1 cm) connected to a multiplexer that mixes data into data lines for input to a two-channel Nicolet storage oscilloscope. The maximum number of channels is determined by the highest frequency of the modeling measurements, since the oscilloscope can sample no faster than 100 kHz. Signals are automatically averaged and stored in the oscilloscope before processing by the computer.

The HP9835 desktop computer is the controller and data processor for the system. The computer initiates a time stack by triggering the oscilloscope and collects data directly from the scope memory. The computer stacks the results, performs the calibration corrections and error calculations, and prints and plots the results. Frequency-domain results will

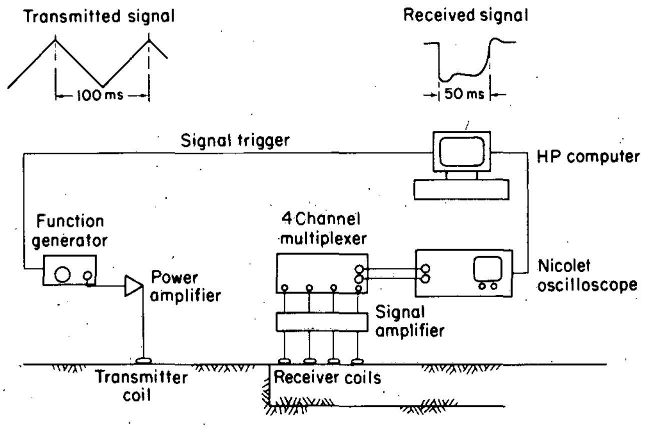

Figure 3. Schematic diagram of scale-modeling system. [XBL 8410-8861]

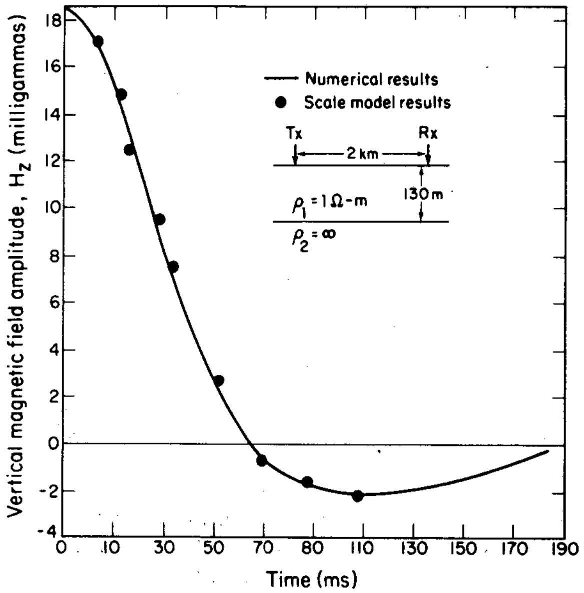

Figure 4. Comparison of numerical and scale-model results for the model of a layer over a resistive half-space. [XBL 8410-8860]

be obtained by utilizing a spectrum analyzer available from another project.

Physically, measurements are made on a thin plastic sheet that overlies the model and on which grid lines have been drawn. Transmitter and receivers are moved manually from point to point. For each model the total magnetic field is measured from a number of transmitter positions. Transmitter-receiver separations range from 0 (coincident loop) to 25 cm (5 km). Selected model data will be fitted to 1-D (layered) models using a least-squares inversion routine. This will be done to assess the error involved in using a layered-model interpretation for data taken over different sections of the model.

PRELIMINARY RESULTS

Initial measurements consisted of obtaining a time-domain response over a 0.65-cm-thick, flat-lying aluminum sheet in air. This model represents a 1-ohm·m, 130-m-thick layer over an infinitely resistive half-space. Figure 4 compares scale-model fields at selected times with the numerical solution for the layered model; the numerical and scale-model data are in close agreement for the case considered.

REFERENCE

Lee, K.H., 1978. Electromagnetic scattering by a two-dimensional inhomogeneity due to an oscillating magnetic dipole (Ph.D. thesis). University of California, Berkeley.

Time-Domain Scale Modeling for the Detection of Fractures and Cavities

S. Dallal and A. Becker

The application of controlled-source electromagnetic soundings for the detection of subsurface cavities and fractures is a relatively new problem in applied geophysics. With the exception of limited general studies by Faldus et al. (1963) and Kaspar and Pecen (1975), no published information appears to be available on the subject of electromagnetic scattering of a void or a planar fracture in a conductive half-space. To determine whether commercial instrumentation can be used for this purpose, we have constructed scale models that simulate the electromagnetic field scattering by such features. We measure the secondary anomalous fields in the time domain and interpret them in terms of the current distribution around the target anomaly. Upon completing our study we hope our analysis will provide the field geophysicist with a full set of criteria that relates the scattered electromagnetic field's morphology to the target's geometrical parameters. This paper describes the design and initial results of a scale-modeling experiment using metal models.

THE SCALE MODEL

The controlled-source, time-domain method consists of inducing current in the earth by means of a magnetic dipole source and then observing the decay of the magnetic field (the secondary field) that results after the inducing field is abruptly turned off. For our scale-model experiments we use a pair of coils: a transmitter-receiver pair mounted in a 3-inch-high coil apparatus as shown in Fig. 1. The coils are mounted on a fiber-glass base that can be manually moved over the metal model.

The coil configuration used in this experiment is called "minimum-coupled" because the horizontal receiver coil will detect no primary magnetic field from the transmitter and will detect a secondary magnetic field only when the coils approach an inhomogeneity such as a void or fracture. Large lead sheets measuring 4 ft × 4 ft are being used to simulate the earth.

A scale of 1:1000 (1 cm = 10 m) is used to model the effects of cavities and fractures located within a homogeneous 100-ohm·m surface layer. Cavities are represented by cutting holes into the lead, and fractures are represented by placing two lead sheets side by side. The cavities and fractures are buried by placing them below another lead sheet. Different structures are modeled by changing either the lead thickness or the cavity and fracture size.

The primary field is created by a signal generator and amplifier that provides a square-wave current pulse of 2A in the transmitter coil. Signals detected by the receiver coil are fed to a Nicolet digital oscilloscope for digitization and stacking to improve the signal-to-noise ratio. After a sufficient number of stacks, the stored waveform is transferred to an HP9835 desktop computer for analysis. The computer makes the calibration corrections, calculates the errors, and prints and plots the results.

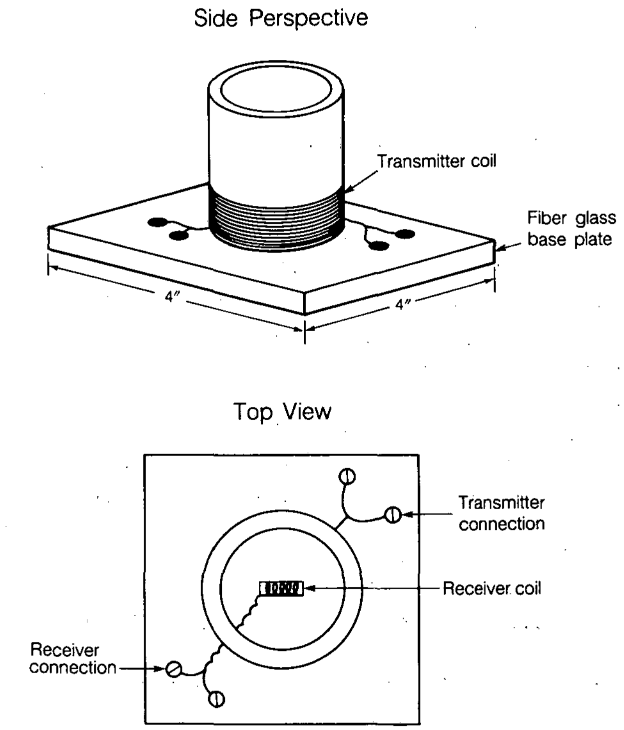

Figure 1. The transmitter-receiver coil apparatus. [XBL 8411-6166]

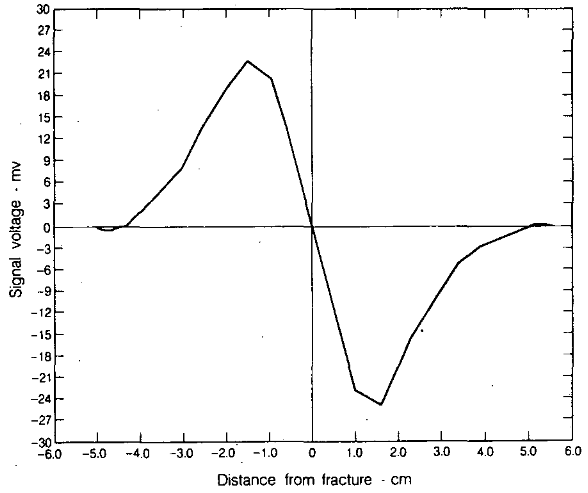

Figure 2. The time-domain EM anomaly over a narrow, vertical fracture in a 50-m-thick, 100-ohm·m layer. The anomaly is expressed here in terms of the receiver coil voltage 30 μs after the transmitter current is turned off. The fracture width would be ≤ 1 cm. [XBL 8411-6165]

PRELIMINARY RESULTS

At this time, we have just completed constructing and testing our first scale model, which represents a resistive fracture zone in the earth. Figure 2 shows the horizontal field anomaly due to two 1-mm-thick lead sheets positioned side by side. By virtue of the electromagnetic scaling laws, this model is equivalent to a narrow, linear fracture in a 50-m-thick, 100-ohm·m layer. The observed fracture anomaly shows a distinctive crossover directly above the fracture, which is characteristic of conducting edges.

ACKNOWLEDGEMENT

This modeling work was supported mainly by the Electronics Engineering Department of Lawrence Livermore National Laboratory.

REFERENCES

Faldus, K., Vaclav, P., Praus, O., and Tobyasora, M., 1963. A study of the electromagnetic field of a magnetic vertical dipole on the model of a homogeneous half-space with a spherical cavity. Studia Geophys. Geod., v. 7, p. 372–396

Kaspar, M., and Pecen, J., 1975. Finding the caves in a Karst formation by means of electromagnetic waves. Geophys. Prospect., v. 23, no. 4, p. 611–621.

Subsurface Resistivity Changes at the Cerro Prieto Geothermal Field

*M.J. Wilt, N.E. Goldstein, and Y. Sasaki**

In 1978 Lawrence Berkeley Laboratory (LBL), in cooperation with the Comisión Federal de Electricidad (CFE), began making dipole-dipole resistivity measurements over the Cerro Prieto geothermal field. When production began in 1973, the plant had a capacity of 75 MW. The resistivity survey objectives were (1) to delineate subsurface resistivity variations that might relate to reservoir boundaries and hydrogeology, and (2) to determine by means of repeated measurements whether changes due to fluid extraction were occurring. Initial measurements were made along two long lines (D–D′ and E–E′ in Fig. 1) oriented approximately at right angles to the structural grain of the region. Permanent current electrodes consisting of aluminum sheets were buried at 1-km intervals. After the first year it was decided to repeat measurements on line E–E′ only because it passed directly over the production area whereas D–D′ did not cross an area of interest.

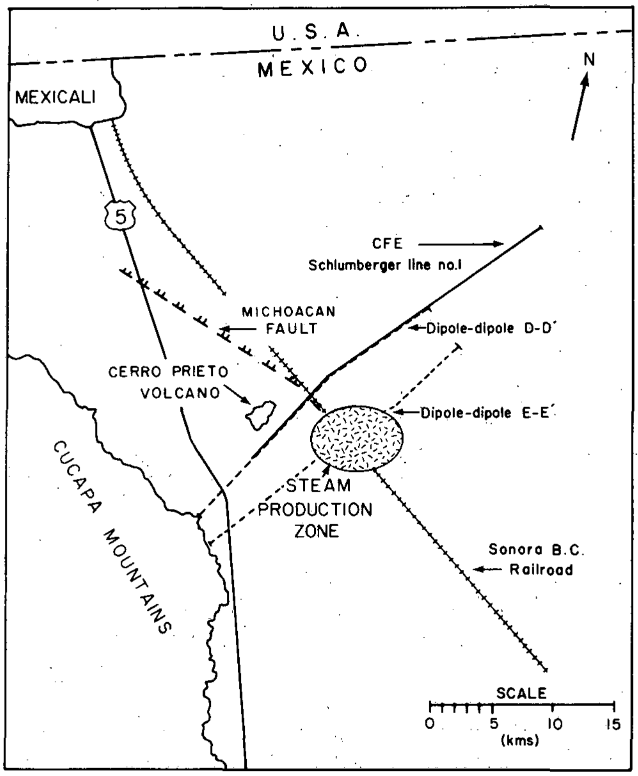

Figure 1. Location map of the Cerro Prieto geothermal field and dipole-dipole lines D–D′ and E–E′. [XBL 788-1632]

DATA ACQUISITION

A schematic diagram of the field system is shown in Fig. 2. The 25-kW generator is capable of providing square-wave currents of up to 80 A peak to peak into the ground at up to 1200 V for periods from 1 to 100 s. This power source is easy to move yet powerful enough to provide adequate signals at distant stations. For the Cerro Prieto surveys, current with a 40-s period was used to minimize inductive coupling effects due to the low-resistivity ground.

Signals are measured simultaneously across four colinear dipoles spaced at integer multiples *(n)* of 1 to 7 times the 1-km transmitter dipole length. The signals are detected with porous copper/copper sulfate electrodes and then low-pass filtered to remove 60-Hz and telluric noise. After amplification the signals are digitized, stacked, and decomposed into Fourier components using a multichannel digital signal processor (Morrison et al., 1978). This system is very effective for obtaining high-quality data. Cerro Prieto survey errors due to telluric and man-made noise have varied between 0.1 and 5%, the errors increasing with increasing dipole separation.

APPARENT RESISTIVITY CHANGES

Because the data obtained in 1978 were later judged to have unacceptably high errors, we use the results from the 1979 survey as our baseline data set (Wilt and Goldstein, 1981). Apparent resistivity changes at 1, 1.5, 2.5, and 4 years after 1979 are plotted on dipole-dipole pseudosections (Fig. 3). Each successive pseudosection shows the cumulative per-

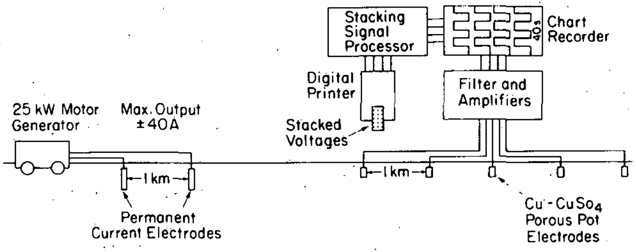

Figure 2. Schematic diagram of the resistivity data acquisition system. [XBL 816-3203]

---

*Faculty of Engineering, Kyushu University, Kyushu, Japan.

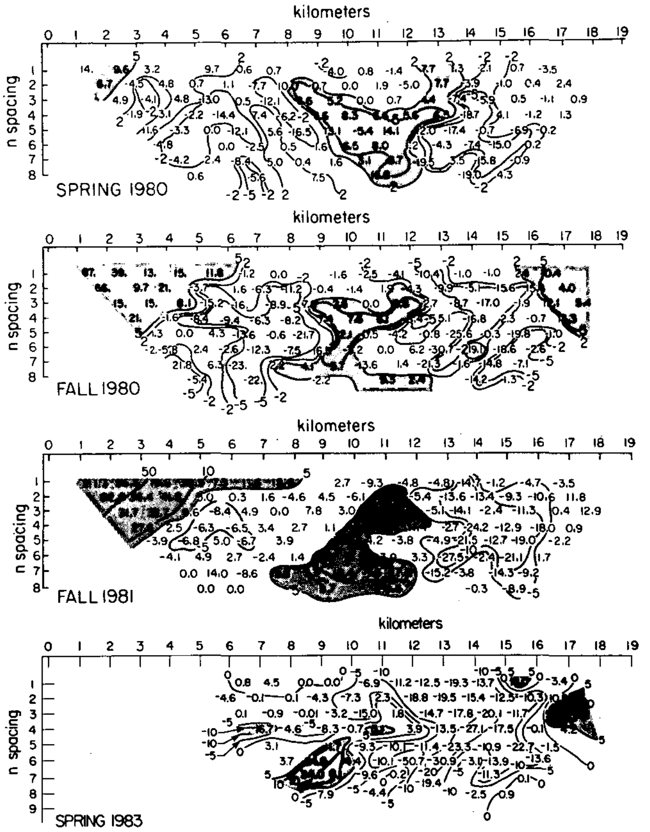

Figure 3. Apparent resistivity changes along line E–E′, plotted in pseudosection form, relative to the 1979 data set. From top to bottom these pseudosections show the percent change in apparent resistivity 1, 1.5, 2.5, and 4 years after the 1979 baseline data were acquired. Areas of dark stipple show resistivity increases greater than 5%. Areas of light stipple show resistivity decreases greater than 5%. [XBL 825-10150A]

centage change from 1979. During the time span covered by these measurements, virtually all of the extracted fluid was derived from the α reservoir, located approximately between stations 10 and 12 at a depth of 1.0 to 1.4 km. Only a small amount of brine was reinjected into a single well during the time span. Little change is observed for small *n*-spacings over that part of the line that crosses the production zone, but the western end of the line, adjacent to the Cupapá Mountains, shows large changes at small *n*-spacings due to the irrigation of new farming plots.

Over that part of the profile approximately corresponding to the production zone, the apparent resistivities have increased at an average annual rate of about 5%. This is attributed to an influx of fresh water into the α reservoir in response to the drop in pressure caused by fluid production during the 1979–1982 period (Wilt and Goldstein, 1984). In support of this belief, it has been noted that chloride concentrations in the water produced by many of the Cerro Prieto wells have decreased over this time period (Grant et al., 1984; Truesdell et al., 1984). Geochemical data suggest that fresh water enters the system from the sides and from above through a leaky caprock (Grant et al., 1984). The resistivity data do not clearly indicate pathways for fluid flow, as measurements are heavily volume averaged and data limited to one profile.

The zone of decreasing resistivity east of the production zone, between stations 12 and 16, is a major feature in Fig. 3, but its cause is not definitely known. Such a pronounced decrease in the subsurface resistivity must be caused by major adjustments in groundwater temperature and/or salinity. Some of the change can be explained by the cessation of farming and irrigation in 1981, which has allowed the shallow groundwater to become more saline and warmer. This predominately affects the small *n*-spacings of the pseudosections (n = 1 and 2) in Fig. 3, but the decrease in resistivity in the deeper parts of the section suggests that changes in the temperature or salinity are occurring at depth. If the percent-change pseudosections are examined in sequence from spring 1980 to fall 1982, the area of apparent resistivity decrease appears to intensify and change shape. The −10% contour appears to move upward and westward with time, suggesting a pulse of hot water ascending into the reservoir region through a sandy gap in the shaly caprock, as proposed by Halfman et al. (1984). At about the time of the baseline measurements, fluid production doubled to 150 MW, hence this pulse may represent a groundwater response to the pressure change due to the increased production. Using some simple reservoir engineering calculations, we estimate that such a pulse would require less than 5 years to move the 2.5 km from east of the reservoir into the production zone (G.S. Bodvarsson, personal communication, 1984).

Figure 4 displays the apparent resistivity changes over the 18-month period from fall 1981 to spring 1983. The recent pattern of change is significantly different from those shown in the cumulative-change pseudosections. It suggests that even though the resistivity decline is continuing between stations 13 and 16, a reversal in resistivity change has occurred between stations 9 and 13; i.e., resistivities now seem to be declining within the region of the α reservoir. This reversal is difficult to explain because the continued decline in chloride content of the brines indicates that the reservoir is being recharged by cool, fresh water, and this should produce a resistivity increase. One possible explanation, consistent with

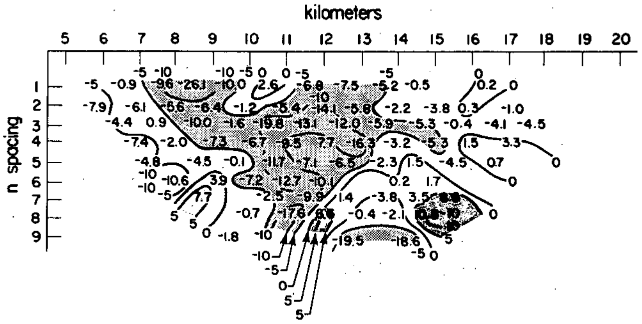

Figure 4. Apparent resistivity changes along E–E′, plotted in pseudosection form for the period from fall 1981 to spring 1983. [XBL 843-10290]

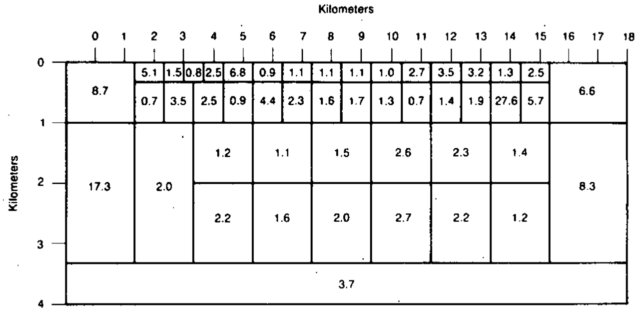

Figure 5. A two-dimensional subsurface resistivity model produced by means of a finite-element, automatic, least-squares, interactive technique for the 1979 data set. [XBL 844-9441]

changes in the silica content of the produced brines, is that (1) the boiling zones in the α reservoir have decreased in size as the reservoir temperature has dropped below the boiling point for that depth (A.H. Truesdell, personal communication, 1984), and (2) the increase in liquid saturation has had a significant effect on apparent resistivities.

QUANTITATIVE ESTIMATES OF SUBSURFACE RESISTIVITY CHANGE

The pseudosection representation is merely a convention for plotting data and does not depict the true resistivity distribution. To get a better quantitative interpretation of the percent-change pseudosections, we made preliminary trials with an automatic, 2-D, least-squares inversion code (Sasaki, 1982; Wilt et al., 1984). This algorithm finds, in an iterative fashion, a subsurface distribution of resistivity that yields a pseudosection matching the observed pseudosection. The starting model in the inversion is the 2-D model found from a labor-intensive interpretation of the 1979 baseline data (Wilt et al., 1980).

The 2-D, finite-element optimization code used a different mesh design than we originally used in obtaining the Cerro Prieto resistivity model, hence the model sections appear somewhat different, although they are electrically equivalent. The 2-D resistivity model obtained from the optimization procedure for the 1979 data is given in Fig. 5. It is very similar to our original 2-D model, although there are differences between the two, particularly in the shallow part of the section. Figure 6 is a resistivity model obtained by inverting the fall 1980 data set. Comparison of Figs. 5 and 6 reveals several areas of significant differences. Between stations 13 and 16 at depths between 1 and 3 km, the resistivity has decreased by more than 40%. This suggests that profound changes in fluid temperature and salinity are occurring in this region. Since this area corresponds to an area of hot water recharge, as proposed by Elders et al. (1981), Grant et al. (1984), and Halfman et al. (1984), it is possible that the changes are the result of increased temperatures and water salinity due to additional hot water recharge. Between stations 11 and 13 a 20% increase in resistivity is observed at depths between 1 and 3 km. This area corresponds to the present production zone, and the magnitude of the change is consistent with changes in fluid chemistry (Grant et al., 1984; Truesdell et al., 1984). Between stations 1 and 2 the shallow resistivity has changed dramatically, mainly because large amounts of fresh water have been used here for irrigation of new farming plots.

ONGOING WORK

In 1983 baseline measurements were made on a new northwest-southeast line (F–F′) that crosses E–E′ at an angle of 60°. By having two monitoring lines crossing over the field, we will be in a better position to track large-scale movements of subsur-

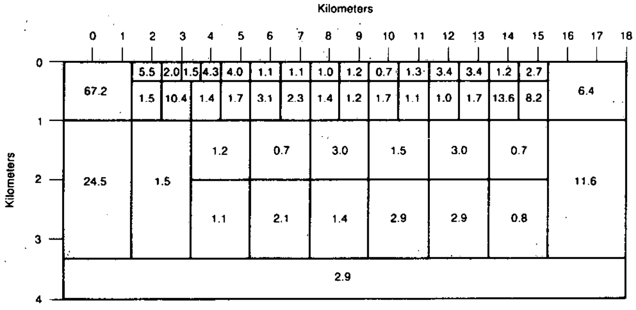

Figure 6. A two-dimensional subsurface resistivity model for the 1980 data set. Compare block resistivities to those in Fig. 5 for a sense of the change in subsurface resistivities during the period 1979–1980. [XBL 844-9440]

face fluids. In addition, line F–F′ crosses an area of wells that supply steam to a new electrical generating plant (Cerro Prieto II), which was commissioned in late 1984. The new power will more than double installed capacity to a total of 400 MW. Future measurements on this line may indicate how the reservoir is responding to massive changes in fluid withdrawal and recharge.

The finite-element optimization code (Sasaki, 1982) is being merged with the finite-difference, 2-D forward model (Dey, 1976; Dey and Morrison, 1976) so that the analyses of all the data sets can be made relative to a common 2-D mesh.

REFERENCES

Dey, A., 1976. Resistivity modeling for arbitrary shaped two-dimensional structures. Part II, User's guide to the FORTRAN algorithm RESIS2D. Lawrence Berkeley Laboratory Report LBL-5283, 56 p.

Dey, A., and Morrison, H.F., 1976. Resistivity modeling for arbitrary two-dimensional structures. Part I, Theoretical formulation. Lawrence Berkeley Laboratory Report LBL-5233, 18 p.

Elders, W.A., Williams, A.E., and Hoagland, J.R., 1981. An integrated model for the natural flow regime in the Cerro Prieto geothermal field based upon petrological and isotope geochemical criteria. *In* Proceedings, Third Symposium on the Cerro Prieto Geothermal Field, Baja California, Mexico, March 24–26, 1981. Lawrence Berkeley Laboratory Report LBL-11967, p. 102–110.

Grant, M.A., Truesdell, A.H., and Mañón, A., 1984. Production induced boiling and cold water entry in the Cerro Prieto geothermal reservoir indicated by chemical and physical measurements. Geothermics, v. 13, no. 1/2, p. 117–140.

Halfman, S.E., Lippmann, M.J., Zelwer, R., and Howard, J.H., 1984. Geologic interpretation of geothermal fluid movement in Cerro Prieto Field, Baja California, Mexico. Am. Assoc. Petrol. Geol. Bull., v. 68, p. 18–30.

Morrison, H.F., Goldstein, N.E., Hoversten, M., Oppliger, G., and Riveros, C., 1978. Description, field and data analysis of a controlled-source EM system (EM-60). Lawrence Berkeley Laboratory Report LBL-7088, 150 p.

Sasaki, Y., 1982, Automatic interpretation of induced polarization data over two-dimensional structures. Mem. Fac. Eng., Kyushu Univ., Japan, v. 42, no. 1, p. 59–70.

Truesdell, A.H., Nehring, N.L., Thompson, J.M., Janik, C.J., and Coplen, T.B., 1984. A review of progress in understanding the fluid geochemistry of the Cerro Prieto geothermal system. Geothermics, v. 13, no. 1/2, p. 65–74.

Wilt, M.J., and Goldstein, N.E., 1981. Resistivity monitoring at Cerro Prieto. Geothermics, v. 10, no. 3/4, p. 183–194.

Wilt, M.J., and Goldstein, N.E., 1984. Interpretation of dipole-dipole resistivity monitoring data at Cerro Prieto. Geothermics, v. 13, no. 1/2, p. 13–26.

Wilt, M.J., Goldstein, N.E., and Razo, M., 1980. LBL resistivity studies at Cerro Prieto. Geothermics, v. 9, no. 1/2, p. 15–26.

Wilt, M., Goldstein, N.E., and Sasaki, Y., 1984. Long-term dipole-dipole resistivity monitoring at the Cerro Prieto geothermal field. Trans., Geothermal Resour. Counc., v. 8, p. 235–240.

Results of Repetitive Gravity Studies at Heber Geothermal Field, Imperial County, California

R.B. Grannell and D. Curtis*[†]

A precise gravity network was established at the Heber geothermal field in early 1981 to monitor possible variations in mass and elevation that could occur as a result of tectonic activity or geothermal production. The network was partially reoccupied in early 1982 and again in early 1983; the entire gravity network was reoccupied in early 1984. The initial 1981 gravity survey and the 1984 reoccupation were conducted coincidentally with second-order leveling of the field (carried out by Chevron); consequently,

---

*Department of Geological Sciences, California State University, Long Beach.

[†] Division of Oil and Gas, California Department of Conservation, Long Beach.

approximately 80% of the Heber gravity stations are located on leveling monuments, including several first-order monuments also occupied by Imperial County.

Two 50-MW power plants are under construction in the Heber area and are expected to be on line by fall 1985. Because all of the produced brine will be reinjected, we may not detect gravity changes resulting from the exploitation activities.

REGIONAL SETTING

The Heber area is located just north of the U.S.-Mexican border in the Salton-Mexicali structural trough (Fig. 1). Heat flow values are elevated throughout the region but are particularly high over postulated pull-apart basins associated with a sea-floor spreading regime. Tectonic activity is widening and deepening the trough, although uplift has occurred locally (Gilmore and Castle, 1983). Substantial subsidence has accompanied major earthquakes, such as the 50-cm elevation change reported near Brawley after the 1979 Mexicali ($M = 6+$) earthquake, but subsidence occurs aseismically as well (Lofgren, 1979). Natural subsidence can be a major cause of positive gravity increases.

The Salton trough contains up to 20,000 ft of Colorado River deposits, marine sediments, and alluvial fan material from the mountainous areas that bound the trough. Geothermal production at shallow levels is from permeable sandy facies; at deeper levels, where thermal metamorphism has caused densification and loss of permeability, production is from fractures.

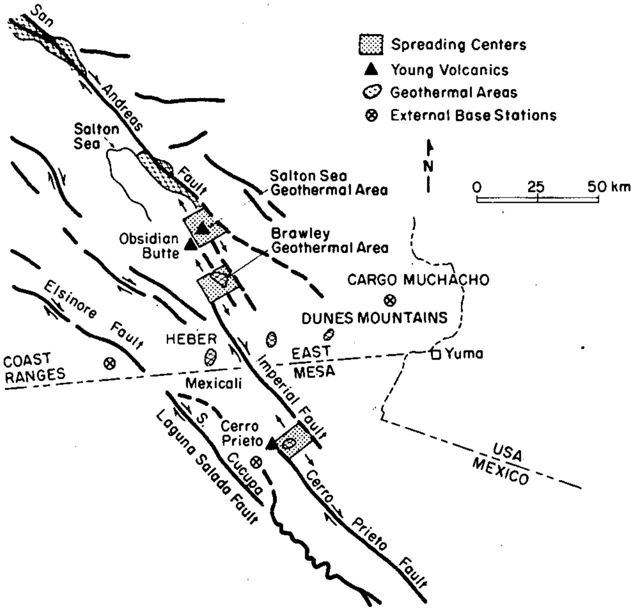

Figure 1. Index map, Salton trough area, showing Cerro Prieto and Heber geothermal fields. [XBL 825-2230]

COLLECTION AND REDUCTION OF GRAVITY VALUES

The procedures used to collect and reduce the gravity observations in the Heber geothermal field have been described in detail by Grannell (1982) and will only be summarized here.

The 1981 data set was collected with two LaCoste and Romberg G gravity meters. The later occupations were made primarily with a LaCoste and Romberg D meter. All three meters were calibrated on a line located in the Santa Ana Mountains of southern California, where the gravity range is the same as in the Heber field. Calibration problems probably account for no more than 15 microgals (μGal) of error in 100 milligals (mGal) of range. The gravity survey in the Heber area shows about 14 mGal of variation within the geothermal field itself but is tied to an external base (see next paragraph) that has an observed gravity value some 108 mGal lower.

The Heber gravity network (Fig. 2) originally consisted of 65 stations tied to three base stations within the geothermal field. Problems with water fluctuations in canal catchment ponds, and subsequent gravity variations of about 24 μGal, caused the abandonment of one of these base stations, and the 1984 survey utilized only two base stations. The addition of 31 stations in 1984, and our failure to recover four previous stations, changed the total number of gravity stations in the Heber network to 92. Since the tectonic activity within the trough suggests that any station within the field may be unstable, the internal bases were tied to two external bases located on first-order leveling monuments at bedrock sites; one is in the Coast Ranges to the west and the other in the Cargo Muchacho Mountains to the east.

Each station was usually tied to one of the internal bases at least four times. A variation of the Canadian tie method (Dragert et al., 1981; Grannell, 1982) was used in the first three surveys, and the looping technique (Grannell, 1982) was used in the 1984 survey. The bases were tied to each other a minimum of 12 times. Meter readings were reduced to observed gravity values by multiplication with a calibration constant, application of a tidal correction, and removal of tares as appropriate (Grannell, 1982; Schwartz, 1984). The resulting gravity values were then subtracted from the base value and the differences averaged for each station. If calculated station standard errors did not yield a precision value of less

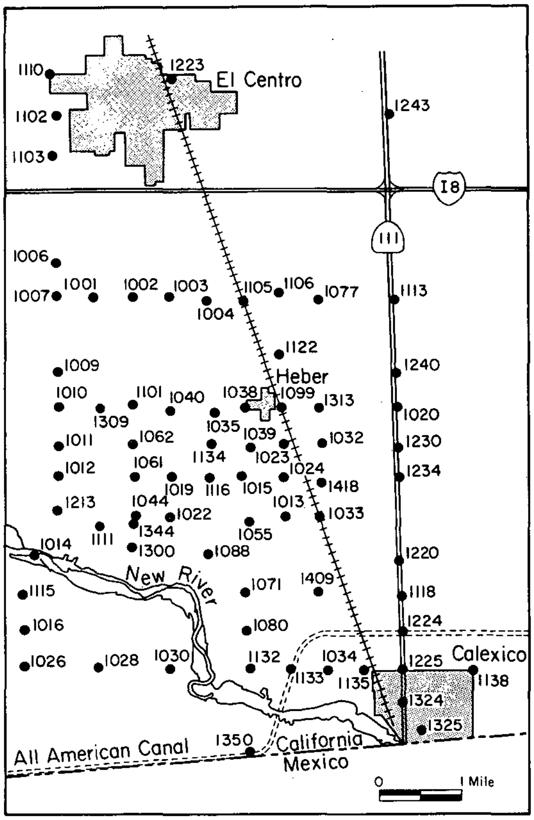

Figure 2. Location map of gravity stations in the Heber area. Most of the stations are situated at roadway intersections. [XBL 855-10425]

than 10 μGal, additional values were measured. The final reduction steps were to refer all the gravity mean differences to a single base station and to calculate pooled standard deviation values for the entire gravity survey each year. The final data set for each year thus consists of (1) a mean gravity difference for each station relative to one of the bases (Y1224, a first-order leveling monument located in Calexico), (2) the standard error calculated at the 95% confidence level for each station difference, and (3) a pooled standard deviation value for the entire survey.

INTERPRETATION OF GRAVITY RESULTS

The pooled standard deviation values average 8 μGal for all four surveys at Heber. Consequently, on an overall basis, gravity changes of 12 μGal (the combined errors from both values involved in calculating the change) should be significant. On a station-by-station basis, with the standard error values applied, the mathematical definition of "significant change" may vary. On this basis, most changes larger than 15 μGal should be significant.

The longest time span covered by the gravity occupations is the 3-year interval from early 1981 to early 1984. During that interval, changes averaging -20 μGal were seen throughout most of the geothermal field, and few systematic patterns were observed. This variation is probably due to a change in the average water level in the All American Canal, located near a prime base station (Y1224). Verification for this supposition could come either from the leveling data or from records kept by the Imperial County Irrigation District. The leveling data will also be affected by mass variations (Whitcomb, 1976), but our modeling, based on the formula for the potential field of a right rectangular prism (derived by Zhou, 1984), suggests that the effect is minimal for small gravity variations, a fraction of a millimeter for a 10-μGal change. Thus the 20-μGal change observed should produce less than 1 mm variation in the relative station elevations if the gravity variations are indeed due to mass variations. Similarly, if the overall average water level for the canal changed between 1981 and 1984, the records should show this variation.

The only significant observed changes likely to be due to noncultural sources are two large (30–40 μGal) positive changes seen in El Centro, at the northern limits of the thermal anomaly. Positive temporal gravity variations are consistent with subsidence, and these variations may be due to aseismic deepening of the Salton trough by 15–20 cm. If these changes are real and permanent, they should be clearly indicated when the first-order leveling is repeated in the fall of 1986, as planned by the Imperial County Department of Public Works (Bob Estes, personal communication, 1984).

Substantial changes of up to 50 μGal were noted between 1981 and 1982. These were of local distribution but were noted at several clustered stations. These changes disappeared again from 1982 to 1983. Such ephemeral changes could be associated with a combination of high groundwater levels in some years or canal level variations. Canal level variations can cause gravity changes as large as 24 μGal (Grannell, 1982), and rainfall, though always sparse in this arid environment, was triple the normal level at 20 cm in the 1982–1983 season.

SUGGESTIONS FOR FURTHER WORK

Because the base station must be in an area not undergoing mass changes, the continued use of Y1224 as a base depends on whether we can be adequately correct for the effects of water level variations. If such corrections are impossible, another site will be chosen. The major reason for the initial selection of this location was its status as a first-order benchmark in the area least likely to undergo subsidence in the Heber area. Other such benchmarks in Calexico, where Y1224 is located, also are situated close to canals, occupy areas subjected to heavy traffic across the border, or are located on abandoned buildings that could be razed. From the standpoint of continuity, the correction process is the more desirable alternative and should be attempted prior to relocation of this primary base.

The problem of fluctuating water levels in canals is the most serious one affecting the high-precision, repetitive gravity surveys in the area. For small canals the effect can be minimized by being randomized; that is, measurements taken at different times (except when water levels are reduced to zero during the annual cleaning) should provide a representative value. For moderate and large-sized canals, some alternate stations on permanent locations should be chosen near the canal stations. It is perhaps unfortunate that all the benchmarks in this region were placed on canal structures close to the water. So far, however, few fluctuations in gravity values have been observed except on the larger canals.

Corrections should be made for water fluctuations in the best way possible for all stations where gravity variations may be caused by fluctuations in water levels. Some correlations should be attempted between rainfall episodes and local gravity fluctuations.

ACKNOWLEDGEMENTS

The gravity work by R.B. Grannell at Heber was partially supported by the Department of Energy through the Lawrence Berkeley Laboratory. D. Curtis was supported in the field by released time from his employment with the Division of Oil and Gas, California Department of Conservation.

REFERENCES

Dragert, H., Lambert, A., and Liard, J., 1981. Repeated precise gravity measurements on Vancouver Island, British Columbia. J. Geophys. Res., v. 86, no. B7, p. 6097–6106.

Gilmore, T., and Castle, R., 1983. Tectonic preservation of the divide between the Salton basin and the Gulf of California. Geology, v. 11, no. 8, p. 474–477.

Grannell, R., 1982. Repetitive precision gravity studies at the Cerro Prieto and Heber geothermal fields. Lawrence Berkeley Laboratory Report LBL-15073, p. 95.

Lofgren, B., 1979. Measured crustal deformation in the Imperial Valley, California. *In* Proceedings, First Symposium on the Cerro Prieto Geothermal Field, Baja California, Mexico, September 20–22, 1978. Lawrence Berkeley Laboratory Report LBL-7098, p. 141–147.

Schwartz, M., 1984. Computer comparison of dedrifting versus tare removal in precision gravity studies (M.S. thesis). California State University at Long Beach.

Whitcomb, J., 1976. New vertical geodesy. J. Geophys. Res., v. 81, no. 26, p. 4937–4944.

Zhou, H., 1984. Prismatic method in solving the gravitational potential (M.S. thesis). California State University at Long Beach.

APPENDIXES

APPENDIX A: ABSTRACTS OF JOURNAL ARTICLES

Bakun, W.H., and McEvilly, T.V., 1984
Recurrence models and Parkfield, California, earthquakes
J. Geophys. Res., v. 89, no. B5, p. 3051 – 3058

Main shocks of the earthquake sequences that occurred on the Parkfield section of the San Andreas fault in central California in 1922, 1934, and 1966 are characterized by southeast rupture expansion over the same 20- to 30-km-long section of the fault. Whereas the seismic moments for the 1922 and 1934 events are identical to within a precision of 10%, the seismic moment for 1966 is 20% greater than for the earlier events to within a precision of 20%. The Parkfield area seismicity, in general, seems well described by a recurring moderate size characteristic earthquake, repeating the same epicenter, magnitude, seismic moment, rupture area, and southeast direction of rupture expansion. An unexplained 10 year advance of the 1934 event is the only discrepancy in the hypothesis that the Parkfield earthquakes in 1857, 1881, 1901, 1922, 1934, and 1966 represent a strictly periodic process. Assuming the strictly periodic model and the absence since 1966 of the perturbations hypothesized for the 1922 to 1934 period, the next characteristic Parkfield earthquake should occur between 1983 and 1993.

Bodvarsson, G.S., Benson, S.M., Sigurdsson, O., and Stefansson, V., 1984
The Krafla geothermal field, Iceland. 1. Analysis of well test data
Water Resour. Res., v. 20, no. 11, p. 1515 – 1530 (LBL-16203)

Extensive modeling studies of the Krafla geothermal field in Iceland are presented in a series of four papers. This first paper describes the geological settings of the field and the analysis of well test data.

The geothermal system at Krafla is very complex, with a single-phase liquid reservoir overlying a two-phase reservoir. The reservoir rocks are volcanic with sequences of basalt flows, hyloclastics, and intrusions. The fluid flow in the reservoir is fracture-dominated.

Considerable pressure transient data from injection tests have been gathered from the Krafla wells. These data are analyzed to yield the transmissivity distribution in the reservoir system. As the data are complicated by various factors (wellbore effects, nonisothermal effects, two-phase flow, and fractured rocks) the applicability of conventional well test analysis methods is questionable. We have developed a methodology to analyze injection tests for such systems. The results obtained show that the transmissivity of the Krafla reservoir is low, averaging 2 Darcy-meters (Dm). The average transmissivity of most commercially successful geothermal fields is an order of magnitude higher.

Bodvarsson, G.S., Pruess, K., Stefansson, V., and Eliasson, E.T., 1984
The Krafla geothermal field, Iceland. 2. The natural state of the system
Water Resour. Res., v. 20, no. 11, p. 1531 – 1544 (LBL-16204)

A model of the natural state of the Krafla reservoir system in Iceland has been developed. The model consists of a vertical cross section which includes reservoirs in both old and new well fields. The physical processes considered include mass transport, conductive and convective heat transfer and boiling, and condensation. Natural heat losses to surface manifestations (springs) are also included. The model matches very well all relevant data from the Krafla field. The natural flow of hot fluids through the reservoirs is estimated as approximately 20 kg/s. Steam escaping to surface springs constitutes the bulk of the heat losses in the area modeled. Conductive heat losses through the cap rock are approximately 1 W/m^2, and heat recharge from below is about 2 W/m^2.

Bodvarsson, G.S., Pruess, K., Stefansson, V., and Eliasson, E.T., 1984
The Krafla geothermal field, Iceland. 3. The generating capacity of the field
Water Resour. Res., v. 20, no. 11, p. 1545 – 1561 (LBL-16205)

This paper presents analytical and numerical studies of the generating capacity of the Krafla field. A general lumped-parameter model is developed, which can be used to obtain rough estimates of the generating capacity of a geothermal field based on the size of the wellfield, the average formation porosity, and the amount of recharge to the system. The model is applied to the old wellfield at Krafla. More sophisticated calculations of the generating capacity of the Krafla field are also performed using distributed-parameter models. Two-dimensional areal models of the various reservoir regions at Krafla are developed and their generating capacities (MW_e) evaluated. The results obtained indicate that the old wellfield can sustain steam production of 30 MW_e for 30 years. The estimated power potential of the new wellfield is 20 MW_e for 30 years. To obtain the required steam production several additional wells may be drilled in the old and new wellfields.

Bodvarsson, G.S., Pruess, K., and O'Sullivan, M.J., 1985
Injection and energy recovery in fractured geothermal reservoirs
Soc. Petrol. Eng. J., in press (LBL-15344)

Numerical studies of the effects of injection on the behavior of production wells completed in fractured two-phase geothermal reservoirs are presented. In these studies the multiple-interacting-continua (MINC) method is employed for the modeling of idealized fractured reservoirs. Simulations are carried out for a five-spot well pattern with various well spacings, fracture spacings, and injection fractions. The production rates from the wells are calculated using a deliverability model. The results of the studies show that injection into two-phase fractured reservoirs increases flow rates and decreases enthalpies of producing wells. These two effects offset each other so that injection tends to have small effects on the usable energy output of production wells in the short term. However, if a sufficiently large fraction of the produced fluids is injected, the fracture system may become liquid-filled and an increased steam rate is obtained. Our studies show that injection greatly increases the long-term energy output from wells, as it helps extract heat from the reservoir rocks. If a high fraction of the produced fluids is injected, the ultimate energy recovery will increase manyfold.

Brittain, H.G., Perry, D.L., and Tsao, L., 1984
Luminescence studies of thorium hydrolysis products
J. Lumin., v. 28, p. 257 – 265 (LBL-15974)

Raising the pH of an aqueous solution of thorium salts results in the precipitation of a hydrated thorium oxide, rather than in the generation of a hydroxide species. At room temperature, this material does not exhibit any emissive properties, but upon cooling to 77°K a strong green luminescence can be observed. The emission spectrum is fairly broad and is characterized by an emission lifetime of 125 μsec. Emission from a thorium hydrolysis product has not hitherto been reported in the literature. Calcination of this material at 800°C for three hours produces thorium dioxide after dehydration of the hydrolysis product, and this material does not exhibit any luminescence properties at any temperature. These materials (hydrolysis products) are important in the documentation of models related to chemical species formed under high pH geologic conditions.

Brittain, H.G., Perry, D.L., and Tsao, L., 1984
Photophysical studies of uranyl complexes. 4. X-ray photoelectron and luminescence studies of hydrolyzed uranyl salts
Inorg. Chem., v. 23, p. 1232–1237 (LBL-16975)

The solid state hydrolysis products of the uranyl ion, UO_2^{2+}, have been studied using x-ray photoelectron spectroscopy (XPS) and luminescence spectroscopy. The hydrolysis products consisted of uranium oxides and various forms of uranyl hydroxides, two of the most important classes of uranium species involved in the geologic transport of uranium. Evidence for carbon dioxide chemisorption by the complexes from the atmosphere, leading to mixed oxide/hydroxide/carbonate complexes, is discussed.

Brittain, H.G., Perry, D.L., and Tsao, L., 1984
Photophysical studies of uranyl complexes. 5. Luminescence spectrum of $K_4UO_2(CO_3)_3$
J. Lumin., v. 29, p. 285–294 (LBL-17516)

The photoluminescence spectrum of the potassium salt of the $UO_2(CO_3)_3^{4-}$ ion, one of the most important chemical species of uranium in geologic and oceanographic environments, has been studied under conditions of high resolution at cryogenic temperatures. The bonding parameters of this compound are important, since they control the chemical reactions of the species involved in geologic migration. Additionally, they are responsible for the close association of uranium with coal and peat deposits.

Brittain, H.G., Perry, D.L., and Tsao, L., 1984
Photophysical studies of uranyl complexes. 6. Luminescence spectra of bis(imidazolium)tetrachlorodioxouranate(VI) and bis(2-methylimidazolium)tetrachlorodioxouranate(VI)
Spectrochim. Acta, v. 40A, no. 7, p. 651–655 (LBL-17573)

Detailed luminescence spectral studies of the title compounds have been conducted at 4.2 K in an effort to better understand the chemistry of the imidazolium/uranium interaction. This interaction is extremely important, since the imidazolium cation has been shown to be the only species known to stabilize the quite air-sensitive $(UO_2)_2(OH)_2^{2+}$ dimer that is known to play a role in the chemistry of uranium under elevated pH conditions observed in geologic environments.

Carnahan, C.L., and Remer, J.S., 1984
Nonequilibrium and equilibrium sorption with a linear sorption isotherm during mass transport through an infinite porous medium: Some analytical solutions
J. Hydrol., v. 73, p. 227-258 (LBL-19256).

Analytical solutions have been developed for the three-dimensional axisymmetric problem of solute transport in a steady field of groundwater flow with nonequilibrium mass transfer of a radioactive species between fluid and solid phases, and with unequal longitudinal and lateral hydrodynamic dispersion. Interphase mass transfer is described by a first-order rate expression. Solutions are presented also for the case of equilibrium distribution of solute between fluid and solid phases. Three types of release from a point source were considered: instantaneous release of a finite mass of solute, continuous release at an exponentially decaying rate, and release for a finite period of time. Computational results for point-source solutions show the expected variation of sorptive retardation effects progressing from the case of no sorption, through cases of nonequilibrium sorption, to the case of equilibrium sorption. The point-source solutions can be integrated over finite regions of space to provide analytical solutions for regions of solute release having finite spatial extents and various geometrical shapes, thus considerably extending the utility of the point-source solutions.

Chun, K.-Y., 1984
Crustal shear velocity and attenuation structures in vicinity of the Nevada Test Site
Bull. Seismol. Soc. Am., in press (LBL-17858)

Pure path group velocities of Rayleigh and Love waves in the period range 3 to 50 seconds have been measured to determine a model of the fine crustal shear velocity structure within approximately a 400 kilometer radius of the Nevada Test Site (NTS). The source events consist of 22 underground nuclear explosions and 10 associated collapses at the NTS. The receivers are 4 broadband seismographs of the University of California Lawrence Livermore National Laboratory (LLNL) network, calibrated and adjusted prior to each explosion event in order to attain maximum amplitude without clipping. The seismographic stations are evenly distributed azimuthally and located at epicentral distances varying from 188 to 413 kilometers. The measured group velocities, determined using the phase-matched filter (PMF) method to eliminate multipathing, represent the lowest observed within the Basin and Range, of which the study area is a part; the same can be said about the quality factor Q_r of the fundamental mode Rayleigh waves. Comparisons between the current and previous studies and among previous studies suggest that both group and phase velocities of the fundamental mode Rayleigh waves increase sharply immediately beyond the boundary of the study region.

The main features of the models derived from the observed dispersion data, which include fundamental mode Love and Rayleigh waves (3–51 sec), plus first higher mode Rayleigh waves in the period range 1.8 to 4.7 seconds, are:

(1) an average crustal thickness of approximately 28 kilometers;

(2) a low average crustal shear velocity of around 3.55 km/sec;

(3) a shallow crustal low velocity zone (LVZ) in the depth range 7.3 to 13.8 kilometers, the minimum shear velocity in the LVZ being 3.3 km/sec;

(4) a bottom crustal layer 7 to 10 kilometers thick with a shear velocity of 3.70 to 3.90 km/sec; and

(5) a low shear velocity of 4.36 km/sec in the upper mantle.

In detail, the derived models are path-dependent. The most prominent LVZ is found along the paths NTS–Landers and NTS–Mina, where the average crustal velocities are noticeably low; the least well-developed LVZ is found along the path NTS–Elko, where the average crustal velocity is noticeably higher. The velocity structure differences are found to correlate with the distribution of heat flow subprovinces within the Basin and Range province. Specifically, in areas where heat flow is relatively low, the average crustal velocity is high and the LVZ is poorly developed, and vice versa.

The main features of the regional shear wave attenuation structure, determined from the inversion of the Q_r data, are:

(1) an average shear wave quality factor Q_s of about 207 in the topmost 7.3 km; and

(2) an underlying, broad zone with an anomalously low Q_s of 37.

Note that the top of the low Q_s zone coincides with that of the LVZ. Uncertainties in the Q_s estimate are, however, quite large.

A single, horizontally layered earth model is found somewhat inadequate to explain simultaneously the observed Rayleigh and Love wave dispersion data along any propagation paths, except for those from the NTS to Landers. This discrepancy is probably attributable to the regional crustal thickness variations, both gradual and abrupt in nature, found in previous refraction studies.

Endo, H.K., Long, J.C.S., Wilson, C.R., and Witherspoon, P.A., 1984
A model for investigating mechanical transport in fracture networks
Water Resour. Res., v. 20, no. 10, p. 1390–1400 (LBL-17475)

A technique is presented to determine when anisotropic fracture systems can be modeled as equivalent porous media (continua) for transport. In order to use the continuum approach, one must demonstrate that the fracture system has the same transport behavior as an equivalent porous medium. Hydraulic effective porosity is calculated as the product of specific discharge and mean travel time, divided by linear length of travel. Specific discharge and hydraulic effective porosity are measured in different directions of flow in regions of varying size with constant hydraulic gradients. If the fracture system behaves like an equivalent porous medium, directional flow has the following properties: (1) specific discharge can be predicted from a permeability tensor and (2) hydraulic effective porosity is independent of direction of flow. A numerical model has been developed to simulate mechanical transport under steady flow in a discrete fracture network. The model is used to determine the distribution of travel times from inlet to outlet for fluid traveling in stream tubes. We have examined only systems with parallel fracture sets in which all fractures are long compared to the region under study. These systems satisfy criterion 1 in that flux can be calculated using a porous medium equivalent. However, these systems do not satisfy criterion 2 because hydraulic effective porosity is shown to be directionally dependent. Thus, even though flux can be accurately predicted using porous medium assumptions for some fracture systems, it may not be possible to accurately predict mechanical transport using these same assumptions.

Fyfe, W.F., Babuska, V., Price, N.J., Schmid, E., Tsang, C.F., Uyeda, S., and Velde, B., 1984
The geology of nuclear waste disposal
Nature, v. 310, no. 16, p. 537–540

An ICSU committee on the geological disposal of high-level radioactive wastes has concluded that century-long interim storage is essential and that disposal in subduction trenches and ocean sediments deserves more attention. For energy planners to reach the best possible compromises between energy production and environmental deterioration, clear demonstrations that nuclear wastes can be safely stored are necessary. But nuclear wastes may be dangerous for at least thousands of years, so all demonstrations must rely on indirect scientific arguments and predictions. This is why geologists must be involved for they, more than others, can demonstrate that sensitive materials are preserved in certain rocks and not in others.

If there have been problems and time delays in providing the necessary answers, it must be remembered that scientists have never before been asked to answer disposal problems on this time scale. Further, the problems are not unique to the disposal of nuclear wastes, for there are others (mercury, cadmium, lead, etc.) which have infinite lifetimes. Only in the recent decades has man become capable of modifying the surface environment of our planet to such an extent that such problems have reached critical importance.

The basic questions that arose were these: (1) Is secure storage possible for periods of thousands of years? (2) What is the optimum period of interim surface storage? (3) Where and in what rock types is the optimum site for disposal? (4) Is present geotechnology adequate, or must new technology be developed for disposal engineering?

A major radwaste (radioactive waste) repository might involve a cavity of the order of 10^7 m^3 (0.01 km^3). Do we have evidence that comparable volumes of sensitive (soluble) natural materials have been preserved intact for periods of millions of years? The clear demonstration of integrity in natural systems must be one of the most important aspects of discussions on site selection.

Goldstein, N.E., Wilt, M.J., and Corrigan, D.J., 1984
Analysis of the Nuevo León magnetic anomaly and its possible relation to the Cerro Prieto magmatic-hydrothermal system
Geothermics, v. 13, no. 1/2, p. 3–11 (LBL-14900)

The broad dipolar magnetic anomaly whose positive peak is centered near Ejido Nuevo León, some 5 km east of the Cerro Prieto I power plant, has long been suspected to have a genetic relationship to the thermal source of the Cerro Prieto geothermal system. This suspicion was reinforced after several deep geothermal wells, drilled to depths of 3–3.5 km over the anomaly, intersected an apparent dike-sill complex consisting mainly of diabase but with minor rhyodacite. A detailed fit of the observed magnetic field to a computer model indicates that the source may be approximated by a tabular block 4 × 6 km in area, 3.7 km in depth, 2.3 km thick, and dipping slightly to the north. Mafic dike chips from one well, NL-1, were analyzed by means of electron microprobe analyses which showed them to contain a titanomagnetite that is paramagnetic at in situ temperature conditions. As the dike mineralogy does not account for the magnetic anomaly, the magnetic source is believed to be a deeper, magnetite-rich assemblage of peridotite-gabbro plutons. The suite of igneous rocks was probably emplaced at a shallow depth in response to crustal extension and thinning brought on by en echelon strike-slip faulting. The bottom of the magnetic source body, at an estimated depth of 6 km, is presumed to be at or near that of the Curie isotherm (575°C) for magnetite, the principal ferromagnetic mineral in peridotitic-gabbroic rocks.

The geological model derived from the magnetic study is generally supported by other geophysical data. In particular, earthquake data suggest dike injection is occurring at depths of 6–11 km in an area beneath the magnetic source. Thus, it is possible that heat for the geothermal field is being maintained by continuing crustal and magnetic activity.

Goodman, R.E., Amadei, B., and Sitar, N., 1984
Uplift pressure in crack below dam
J. Energy Eng., v. 109, no. 4, p. 207–221

A specific analytical solution for flow through a horizontal crack of finite length drained by a series of vertical drains is presented. The solution is used to derive diagrams of uplift pressure on the base of a dam and to demonstrate the influence of drains on the distribution and magnitude of uplift forces. Our solution shows that there should be an almost linear drop in hydraulic head from the entrance to the crack at the heel of the dam to the line of drains, followed by a slight rise in head to the end of the crack. This is consistent with a previously suggested solution for porous media. The results show that drain holes are effective in substantially reducing uplift pressures in a crack and have the greatest influence when located between approximately one half and one fifth of the length of the crack from its upstream end.

Halfman, S.E., Lippmann, M.J., Zelwer, R., and Howard, J.H., 1984
Geologic interpretation of geothermal fluid movement in Cerro Prieto field, Baja California, Mexico
Am. Assoc. Petrol. Geol. Bull., v. 68, no. 1, p. 18–30 (LBL-15201)

A geologic model of the liquid-dominated Cerro Prieto geothermal field was developed on the basis of geophysical and lithologic well logs. The direction of subsurface geothermal fluid flow before exploitation and the geologic features controlling this movement were determined by integrating well completion and downhole temperature data with the geologic model.

The data show that fluid (possibly heated by intrusive dikes found in wells drilled in the eastern area of the field) enters the system from the east at depths > 10,000 ft (>3,050 m). The fluid moves westward through sandstone beds and rises to shallow depths through fault zones and permeable sandy gaps in the overlying shale layers. The shale layers provide local cap rocks. Some of the hot fluid reaches the surface west of the field, in an area characterized by numerous geothermal manifestations. The rest of the fluid mixes with colder ground waters west of the geothermal resource.

Halfman, S.E., Lippmann, M.J., and Gilreath, J.A., 1985
Cerro Prieto case history: Use of wireline logs to characterize a geothermal reservoir
Soc. Petrol. Eng. J., in press (LBL-17374)

The Cerro Prieto geothermal field, Baja California, Mexico, is located in the Salton Trough, a rift basin filled mainly with Colorado River sediments. As part of a multidisciplinary study of this geothermal system, a comprehensive wireline log analysis was undertaken. It established the physical properties of the various sedimentary units; their depositional environment; their hydrothermal alteration; the location, attitude, and displacement of faults; and the subsurface circulation of the geothermal fluids.

The methodology used and the application of the results to further exploration and development of this high-temperature geothermal resource are presented.

King, M.S., 1984
Elastic-wave velocities in quartz monzonite at different levels of water saturation
Int. J. Rock Mech. Min. Sci. Geomech. Abstr., v. 21, no. 1, p. 35–38 (LBL-16665)

During a comprehensive rock mechanics and geophysics research programme associated with large-scale heater tests at a subsurface depth of 340 m in an abandoned iron-ore mine in central Sweden, it became evident that the interpretation of cross-hole acoustic surveys required a knowledge of compressional (V_p) and shear-wave (V_s) velocities in the granitic rock under different conditions of stress and water saturation. A number of workers have reported significant increases in V_p at low stress levels when dry rocks containing porosity predominantly in the form of cracks were saturated with water. However, they also reported little change in V_s for rocks of this type with changes in water saturation.

Reported here are the results of laboratory ultrasonic velocity measurements made on quartz monzonite core specimens recovered from two of the vertical boreholes surrounding one of the heaters referred to above. The specimens were tested first in their fully water-saturated state and then oven-dried. The dry specimens were then stored in an atmosphere of 100% relative humidity and tested periodically over a period of 3-1/2 months, by which time they had reached almost full saturation.

It is concluded that rocks containing porosity predominately in the form of cracks and maintained in an environment of 100% relative humidity for periods of time of the order of months can become more than 90% water saturated. Small increases in moisture content of dry rocks containing appreciable crack porosity result in substantial increases in V_p and V_s. The Kuster and Toksöz model provides a convenient framework within which to study the variation of elastic wave velocities in partly and fully water-saturated low porosity rocks.

King, M.S., 1984
The influence of clay-sized particles on seismic velocity for Canadian permafrost
Can. J. Earth Sci., v. 21, p. 19–24 (LBL-16174)

Seismic wave velocities have been measured on 37 unconsolidated permafrost samples as a function of temperature in the range −16° to +5°C. The samples, taken from a number of locations in the Canadian Arctic Islands, the Beaufort Sea, and the Mackenzie River, were tightly sealed immediately upon recovery in several layers of polyethylene film and maintained in their frozen state during storage, specimen preparation, and until they were tested under controlled-environmental conditions. During testing, the specimens were subjected to a constant hydrostatic confining stress of 0.35 MPa (50 psi) under drained conditions. At no stage was a deviatoric stress applied to the permafrost specimens. The fraction of clay-sized particles in the test specimens varied from almost zero to approximately 65%. At temperatures above 0°C the compressional-wave velocity was observed to be a function only of porosity, with virtually no dependence upon the fraction of clay-sized particles. Calculation of the fractional ice content of the permafrost pore space from the Kuster and Toksöz theory showed that for a given fraction of clay-sized particles the ice content increases with an increase in porosity. It is concluded that the compressional-wave velocity for unconsolidated permafrost from the Canadian Arctic is a function of the water-filled porosity, irrespective of the original porosity, clay content, or temperature.

Lee, K.H., and Morrison, H.F., 1985
A numerical solution for the electromagnetic scattering by a two-dimensional inhomogeneity
Geophysics, v. 50, no. 3, in press (LBL-17856)

A numerical solution for electromagnetic scattering from a two-dimensional earth model of arbitrary conductivity distribution has been developed and compared with analog model results. A frequency domain variational integral is fourier transformed in the strike direction, and a solution is obtained using finite elements for each of a finite number of harmonics or wave numbers in transform space. The solution is obtained in terms of the secondary electric fields. The secondary magnetic field is computed numerically by integrating over the scattering currents in harmonic space and then finally inverse fourier transforming.

Lee, K.H., and Morrison, H.F., 1985
A solution for TM-mode plane waves incident on a two-dimensional inhomogeneity
Geophysics, v. 50, no. 7, in press (LBL-17857)

A solution for the electromagnetic fields scattered from a two-dimensional inhomogeneity in a conducting half-space has been obtained for an incident TM-mode plane wave; the magnetic field is polarized parallel to the strike of the inhomogeneity. The approach has been to determine the scattering currents within the inhomogeneity using an integral equation for the electric fields. This solution is similar in concept to earlier studies of TE-mode scattering from two-dimensional inhomogeneities, and it completes the analysis of the scattering of arbitrary plane waves using the integral equation approach. For simple bodies in the earth, integral equation solution offers significant computation advantages over alternate finite element or finite difference methods of solution.

Lee, R.C., and Johnson, L.R., 1984
Extremal bounds on the seismic velocities in the earth's mantle
Geophys. J. Roy. Astr. Soc., v. 77, p. 667–681 (LBL-19258)

Based on global travel-time constraints of the function $\tau(p)$ (Lee and Johnson), the confidence region for the lower mantle *P* and *S* velocity profiles have been determined. An exact method (Bessonova *et al.*) is used to compute the extremal bounds on velocity. Bounds on the lower mantle *P* velocity have an average resolution of 70 km in the depth range of ~800–2900 km. The average bound width is ~0.14 km s^{-1} at the 97 per cent confidence level. Bounds on the lower mantle *S* velocity have an average resolution of 85 km in the depth range ~850–2900 km and an average width of 0.13 km s^{-1}. These results indicate that significant differences exist among the published velocity models and that the bounds can be used to discriminate among them.

The confidence regions are computed with an assumed upper mantle velocity model and are therefore subject to small baseline adjustments in velocity. The introduction of approximate bounds on the upper mantle $\tau(p)$ increases the lower mantle bound width by 30 per cent (for the *P* velocity). In this case, one obtains constraints on the absolute velocity function.

Lee, R.C., and Johnson, L.R., 1984
Tau estimates for mantle P- and S-waves from global travel-time observations
Geophys. J. Roy. Astr. Soc., v. 77, p. 655–666 (LBL-19259)

Travel-time data from the *ISC Bulletin* were used to determine a $\tau(p)$ confidence region for mantle *P*– and *S*-waves. One year of *P* data, amounting to approximately 108 000 travel times, and four years of *S* data, amounting to approximately 75 000 travel times, were used. Geometrical path corrections were applied to place all sources and receivers at a common radius of 6338 km. A preliminary test was devised and applied to the travel-time data to determine if they were suitable for the estimation of $\tau(p)$. This criterion precluded construction of complete tau functions for the mantle, particularly the upper mantle. Thirty-five confidence intervals for the mean $\tau(p)$ were computed at the 99.9 per cent confidence level from the *P* data, and 23 were computed from the *S* data. Most confidence interval widths were less than 0.2 s for *P*-waves, and less than 0.8 s for *S*-waves. Comparison with computed $\tau(p)$ for several published velocity models indicates significant differences among the models in the $\tau(p)$ domain.

Lippmann, M.J., Goldstein, N.E., Halfman, S.E., and Witherspoon, P.A., 1984
Exploration and development of the Cerro Prieto geothermal field
J. Petrol. Technol., v. 36, no. 10, p. 1579–1591 (LBL-15594)

A multidisciplinary effort to locate, delineate, and characterize the geothermal system at Cerro Prieto field, Baja California, Mexico, began in the late 1950's. It led to the identification of an important high-temperature, liquid-dominated geothermal system which went into production in 1973. This paper summarizes and discusses the exploration and monitoring studies related to this field.

Lippmann, M.J., and Bodvarsson, G.S., 1985
The Heber geothermal field, California: Natural state and exploitation modeling studies
J. Geophys. Res., v. 90, no. B1, p. 745–758 (LBL-17572)

Using numerical simulation techniques and an axisymmetric model of the Heber geothermal field, the natural (preexploitation) state of the system and its response to fluid production are analyzed. The results of the study indicate that the Heber geothermal anomaly is sustained by the upflow of hot water through a central zone of relatively high permeability. The best model suggests that in its natural state the system is recharged at depth by a 15-MW_t (megawatts thermal) (reference temperature 0°C) convective heat source. The existence of an axisymmetric convection pattern, whose axis coincides with the center of the Heber anomaly, is also suggested. At the lower part of the ascending hot water plume the deep recharge water mixes with colder water moving laterally toward the axis of the system. In the upper part the rising plume spreads radially outward after reaching the bottom of the cap rock, at about 550 m depth. The model results suggest that the so-called cap rock is quite permeable (5×10^{-15} m^2) with convection controlling its temperature distribution. The results also show reduced permeability (10×10^{-15} m^2) of the upper zones in the outer region of the system that may be due to mineral precipitation. In modeling the exploitation of the field the generation rate is allowed to build up over a period of 10 years; after that, 30 years of constant power production is assumed. Full (100%) injection of the spent brines is considered; the fluids being injected 2250 m ("near injection") or 4250 m ("far injection") from the center of the system. The study shows that a maximum of 6000 kg/s (equivalent to approximately 300 MW_e (megawatts electric)) of fluids may be produced for the near injection case but only 3000 kg/s (equivalent to approximately 150 MW_e) for the far injection case. The results indicate that the possible extraction rates (generating capacity) are generally limited by the pressure drop in the reservoir. The average temperature of the produced fluids will decline 10°–18°C over the 40-year period.

Long, J.C.S., and Witherspoon, P.A., 1985
The relationship of the degree of interconnection to permeability in fracture networks
J. Geophys. Res., in press (LBL-18446)

The problem of determining the permeability of a rock mass containing a system of finite fractures is highly dependent on both the degree of interconnection between fractures and the heterogeneity of individual fracture characteristics. This paper examines how degree of interconnection affects both magnitude and nature of the fracture permeability. The interconnection between given fracture sets is a complex function of: (a) fracture density, i.e. the number of fractures per unit volume, and (b) the fracture extent or size. Unfortunately, neither the density nor the extent of fractures is easily determined from borehole data. However, fracture frequency can be directly measured in a borehole because it is simply the number of fractures intersected per unit length of the borehole. The frequency is a measure of the product of fracture density and size because the probability of a fracture intersecting a borehole is proportional to this product. The effect of the degree of interconnection was investigated by numerically simulating flow in fracture networks where fracture size and density varied inversely while the product of these two parameters was held fixed. Directional permeabilities of a number of such networks were determined, and the hydraulic behavior of each fracture system was compared to that of an ideal porous medium. The permeability of the rock matrix between the fractures was assumed to be low enough to be negligible. The results show that as fracture length increases, the degree of interconnection increases. Thus, for a given fracture frequency as measured in a borehole, the permeability of the system increases as fracture length is increased and density is proportionally decreased. Also, fracture systems with shorter, but more dense fractures, behave less like porous media than do systems with longer but less dense fractures. Knowledge of fracture frequency and orientation alone is inadequate when determining permeability or deciding the important question of whether a given system behaves like a porous medium. For many cases where these parameters can be measured in the borehole, it is critical to know fracture length in order to predict the degree of fracture network interconnection. However, for certain cases where fractures are larger than some critical size, it may not be necessary to know fracture lengths exactly.

Majer, E.L., and McEvilly, T.V., 1985
Acoustic emission and wave propagation monitoring at the spent fuel test—Climax
Int. J. Rock Mech. Min. Sci. Geomech. Abstr., in press (LBL-17546)

For more than 3-1/2 years, transient acoustic emission events along with *P*- and *S*-wave velocities and amplitudes were monitored by a 15-station 1–10 kHz bandwidth seismographic network in a heated underground test repository. Automated seismic processing analyzed the transient events for location and source properties, while daily pulsing of a piezoelectric reference source provided precise measurement of changes in velocity and amplitude. The site was a spent fuel repository test facility 420 m below ground in the Climax Stock quartz monzonite in Nevada, where spent fuel assemblies and heaters simulated repository conditions. Temperatures in the rock reached only 80°C, but produced abundant acoustic emission events and large changes in *S*-wave amplitudes. *P*-wave velocities and amplitudes were not affected by the heating or cool-down process. The effects seen are postulated to be due to crack closure and dewatering of the rock mass.

Murdoch, J.B., Stebbins, J.F., and Carmichael, I.S.E., 1985
High-resolution ^{29}Si NMR study of silicate and aluminosilicate glasses. The effect of network-modifying cations
Am. Mineral., in press (LBL-17537)

The effect of network-modifying alkali and alkaline-earth cations on the degree of polymerization in silicate glasses is investigated using ^{29}Si magic-angle spinning NMR. The NMR line width is found to increase (reflecting a broader range of silicate environments) as the polarizing power of the cation increases. A similar effect occurs in three-dimensional framework aluminosilicate glasses: smaller, more highly charged cations create greater variety in the distribution of silicate and aluminate tetrahedra. Line widths as a function of the silicon-to-aluminum ratio suggest, however, that Loewenstein's aluminum avoidance principle is largely obeyed. Spectra of three natural silicic glasses are analyzed in terms of the Si/Al ratio and the concentration of paramagnetic species.

Narasimhan, T.N., Kanehiro, B.Y., and Witherspoon, P.A., 1984
Interpretation of earth tide response of three deep, confined aquifers
J. Geophys. Res., v. 89, no. B3, p. 1913–1924 (LBL-12093)

The response of a confined, areally infinite aquifer to external loads imposed by earth tides is examined. Because the gravitational influence of celestial objects occurs over large areas of the earth, the confined aquifer is assumed to respond in an undrained fashion. Since undrained response is controlled by water compressibility, earth tide response can be directly used only to evaluate porous medium compressibility if porosity is known. Moreover, since specific storage S_s quantifies a drained behavior of the porous medium, one cannot directly estimate S_s from earth tide response. Except for the fact that barometric changes act both on the water surface in the well and on the aquifer as a whole while stress changes associated with earth tides act only in the aquifer, the two phenomena influence the confined aquifer in much the same way. In other words, barometric response contains only as much information on the elastic properties of the aquifer as the earth tide response does. Factors such as well bore storage, aquifer transmissivity, and storage coefficient contribute to time lag and damping of the aquifer response as observed in the well. Analysis shows that the observation of fluid pressure changes alone, without concurrent measurement of external stress changes, is insufficient to interpret uniquely earth tide response. In the present work, change in external stress is estimated from dilatation by assuming a reasonable value for bulk modulus. Earth tide response of geothermal aquifers from Marysville, Montana; East Mesa, California; and Raft River Valley, Idaho, were analyzed, and the ratio of S_s to porosity was estimated. Comparison of these estimates with independent pumping tests shows reasonable agreement.

Noorishad, J., Tsang, C.F., and Witherspoon, P.A., 1984
Coupled thermal-hydraulic-mechanical phenomena in saturated fractured porous rocks: Numerical approach
J. Geophys. Res., v. 89, no. B12, p. 10,365–10,373 (LBL-16513)

The fundamentals of the theory of consolidation and thermoelasticity are recast into the formulation of a phenomenon called thermohydroelasticity. Subsequently, a variational principle and Galerkin formulation are combined with the finite element method to develop a new technique to investigate coupled thermal-hydraulic-mechanical behavior of liquid-saturated, fractured porous rocks. A code-to-code verification of the method is performed. Finally, the environment of a heater emplaced in hard rock is simulated. The effects of the coupled thermal stresses in the fractured rock are evident from the dramatic reduction of permeability due to the deformation of the fractures. These results can improve the understanding of observations and displacement measurements made in the in situ experiments at the Stripa mine in Sweden.

O'Sullivan, M.J., Bodvarsson, G.S., Pruess, K., and Blakeley, M.R., 1985
Fluid and heat flow in gas-rich geothermal reservoirs
Soc. Petrol. Eng. J., in press (LBL-16329)

Numerical simulation techniques are used to study the effects of noncondensible gases (CO_2) on geothermal reservoir behavior in the natural state and during exploitation. It is shown that the presence of CO_2 has large effects on the thermodynamic conditions of a reservoir in the natural state, especially on temperature distributions and phase compositions. The gas will expand two-phase zones and increase gas saturations to enable flow of CO_2 through the system. During exploitation, the early pressure drop is primarily due to "degassing" of the system. This process can cause a very rapid initial pressure drop, on the order of tens of bars, depending upon the initial partial pressure of CO_2. The flowing gas content from wells can provide information on in-place gas saturations and relative permeability curves that apply at a given geothermal resource. Site-specific studies are made for the gas-rich two-phase reservoir at the Ohaaki geothermal field in New Zealand. A simple lumped-parameter model and a vertical column model are applied to the field data. The results obtained agree well with the natural thermodynamic state of the Ohaaki field (pressure and temperature profiles) and a partial pressure of 15–25 bars is calculated in the primary reservoirs. The models also agree reasonably well with field data obtained during exploitation of the field. The treatment of thermophysical properties of H_2O–CO_2 mixtures for different phase compositions is summarized.

Paulsson, B.N.P., Cook, N.G.W., and McEvilly, T.V., 1985
Elastic-wave velocities and attenuation in an underground granite repository for nuclear waste
Geophysics, in press (LBL-19263)

The behavior of a quartz monzonite rock mass subjected to a thermal load from emplaced canisters with electric heaters simulating high level nuclear waste was monitored by a crosshole seismic technique in a drift 340 m below the surface in the Stripa mine facility in Sweden. Travel-times and amplitudes of 20–60 kHz ultrasonic compressional (*P*) and shear (*S*) waves were measured over the experiment duration of 750 days, on 2–4 meter paths between four diamond-drilled boreholes around a heater. The signals were transmitted between the boreholes in six different directions and at different depths. Path-averaged *P*- and *S*-wave velocities were obtained from the times of flight of pulses of acoustic waves between separate *P*- and *S*-wave piezoelectric transmitter and receiver crystals. The attenuation, Q^{-1}, was obtained by a spectral ratio technique. When the heater was turned on, the *P*- and *S*-wave velocities increased up to 4% and 10% respectively and stabilized at the elevated values. The *P*-wave velocities along a particular profile were found to increase linearly with the mean temperatures in the profiles sampled. These mean temperatures increased 25–55°C during the course of the experiment. When the heater was turned off after 398 days of heating, the velocities decreased with temperature and finally reached levels in most cases below those observed prior to the heating of the rock. The highest thermal stress close to the heater has been estimated at 55 MPa. Q_α values increased throughout the heating interval, reaching changes of up to 60% shortly after heater turn-off. The Q values reveal no direct correlation with temperature or the closely associated thermal stress, although these phenomena clearly are driving the variation in Q. There is strong evidence relating attenuation properties to fracture closure and pore pressure changes associated with the draining of the rock mass.

Perry, D.L., Tsao, L., and Brittain, H.G., 1984
X-ray photoelectron and infrared spectroscopic studies of the decarboxylation/oxidation of cerium(III) carbonate octahydrate
J. Mater. Sci. Lett., v. 3, p. 1017–1019 (LBL-17651)

X-ray photoelectron and infrared spectroscopic investigations were conducted on both oxidation decarboxylation processes that occur during the thermal treatment of cerium(III) carbonate octahydrate. The cerium(III)–cerium(IV) transition can be viewed as an analogue of actinide(III)–actinide(IV) transitions, transitions that are important from a modeling standpoint of nuclear waste repository chemistry. Additionally, the initial compound represents a hydrated carbonate species, a species that is thought to be an important ligand combination in such models.

Pitzer, K.S., and Li, Y.-g., 1984
Critical phenomena and thermodynamics of dilute aqueous sodium chloride to 823 K
Proc. Nat. Acad. Sci. USA, v. 81, p. 1268–1271 (LBL-16831)

Semiempirical equations are developed that represent the behavior of dilute solutions of NaCl in water (steam) in the range 723–823 K where ion pairing is extensive. This supplements the equations given earlier for more concentrated solutions. In this temperature range the system NaCl/H_2O shows critical behavior with two phases below the critical pressure. The equations for the dilute solutions yield critical behavior. Though the equations for concentrated solutions do not yield critical behavior at the critical pressure, only a very small interpolation function is required to connect smoothly the two equations. The ion-pairing equilibrium constants are reported as well as the Gibbs energies of hydration for both ions and ion pairs.

Pitzer, K.S., and Simonson, J.M., 1984
Ion pairing in a system continuously miscible from the fused salt to dilute solution
J. Am. Chem. Soc., v. 106, p. 1973–1977 (LBL-16315)

Electrostatic ion pairing is well known for highly charged ionic systems in water or for 1–1 electrolytes in solvents of low dielectric constant. Davies first presented equations for the conductance of such systems in which the solute fraction of ion pairs reached a maximum and then decreased with further increase in concentration. This apparent "redissociation" phenomenon is investigated by experimental measurements, theory, and model calculations. The solvent activity is measured at 373 K for the system tetra-*n*-butylammonium picrate in 1-butanol for which the conductance and viscosity are known. Over the measured range from solute mole fraction 0.08 to 0.94 the activity data can be fitted without ion pairing by using a simple equation including a Debye–Hückel term and a van Laar term. But conductance data demonstrate ion pairing in more dilute solutions, and both sets of data can be fitted with a model including ion pairing. The ion distribution implied by this model is calculated. In the "redissociation" range the fraction of defined "ion pairs" does diminish, but the total probability of finding unlike ions near one another steadily increases with increasing concentration. Thus there is redissociation only in a formal sense in terms of a particular model.

Pitzer, K.S., Olsen, J., Simonson, J.M., Roy, R.N., Gibbons, J.J., and Rowe, L., 1985
Thermodynamics of aqueous magnesium and calcium bicarbonates and mixtures with chloride
J. Chem. Eng. Data, in press (LBL-17571)

The potential for the cell $Pt,H_2,CO_2/M(HCO_3)_2$, $MCl_2,CO_2(aq)/AgCl,Ag$ with M = Mg and Ca was measured over a wide range of molalities at 298.15 K. The data were interpreted by the mixed-electrolyte equations of Pitzer and Kim to yield the ion-interaction parameters for MG^{++}, HCO_3^-, and for Ca^{++}, HCO_3^-. The trace activity coefficients of $M(HCO_3)_2$ in MCl_2 and in NaCl are calculated.

Pitzer, K.S., Peiper, J.C., and Busey, R.H., 1984
Thermodynamic properties of aqueous sodium chloride solutions
Phys. Chem. Ref. Data, v. 13, p. 1–102 (LBL-15512)

Experimental measurements of the osmotic and activity coefficients, the enthalpy, and the heat capacity were used to derive a semiempirical equation for the thermodynamic properties of NaCl(aq) at constant pressure. This equation may be combined with results contained in the previous paper on the volumetric properties to yield a complete equation of state valid in the region 273 K$\leqslant$T$\leqslant$ 573 K, saturation pressure $\leqslant P \leqslant$ 1 kbar, $0 \leqslant m \leqslant 6.0$ mol kg^{-1}. It is shown that this equation may be extrapolated to higher solute molalities at lower pressures. An estimation of uncertainties in various quantities is given. Tables of values for various thermodynamic properties are presented in the appendix.

Pruess, K., and Bodvarsson, G.S., 1984
Thermal effects of reinjection in geothermal reservoirs with major vertical fractures
J. Petrol. Technol., v. 36, no. 10, p. 1567–1578, (LBL-16269)

In many geothermal fields there is evidence of rapid migration of injected fluids along "preferential flow paths," presumably along fractures. The potential for unacceptable fluid temperature decline at production wells as a consequence of large-scale injection is of obvious concern to geothermal developers, and methods are needed for evaluating the thermal response of these "fast paths" to injection. One difficulty encountered in analyzing test data is that the geometry of the flow path(s) may be speculative and ambiguous, leading to unreliable predictions of thermal interference. Fast pathways often may be provided by major vertical or nearly vertical fractures and faults with approximately linear flow geometry.

This paper discusses possibilities for characterizing the thermal properties of fast paths by means of different types of tests (tracers, pressure transients, nonisothermal injection). Thermal breakthrough in vertical fractures is examined in some detail by using an idealized model for which an analytical solution is available. The model shows that rapid tracer returns are not necessarily indicative of rapid thermal interference. Thermal breakthrough predictions can be made from tracer data only if both fluid residence time and tracer dispersion are taken into account. However, because of the geometric simplifications necessary in analyzing the tracer data, thermal interference estimates on this basis appear questionable. Pressure transient tests can provide additional parameters for thermal interference predictions, but they cannot resolve the problem of nonuniqueness. A more reliable determination of thermal characteristics of fast paths appears possible from nonisothermal injection tests, combined with numerical simulation. We employ a mixed numerical/semianalytical approach to model the three-dimensional (3D) fluid and heat flow in injection-production systems in vertical fractures, with heat transfer to and from the adjacent rock matrix. Illustrative calculations of thermal recovery after different injection periods suggest that shutting-in an injection well can prevent unacceptable temperature declines at production wells.

Pruess, K., and Narasimhan, T.N., 1984
A practical method for modeling fluid and heat flow in fractured porous media
Soc. Petrol. Eng. J., in press (LBL-13487)

A "Multiple Interacting Continua" method (MINC) is presented which is applicable for numerical simulation of heat and multiphase fluid flow in multidimensional, fractured porous media. This method is a generalization of the double-porosity concept. The partitioning of the flow domain into computational volume elements is based on the criterion of approximate thermodynamic equilibrium at all times within each element. The thermodynamic conditions in the rock matrix are assumed to be primarily controlled by the distance from the fractures, which leads to the use of nested grid blocks. The MINC concept is implemented through the Integral Finite Difference (IFD) method. No analytical approximations are made for the coupling between the fracture and matrix continua. Instead, the transient flow of fluid and heat between matrix and fractures is treated by a numerical method. The geometric parameters needed in a simulation are preprocessed from a specification of fracture spacings and apertures and the geometry of the matrix blocks.

The MINC method is verified by comparison with the analytical solution of Warren and Root. Illustrative applications are given for several geothermal reservoir engineering problems.

Pruess, K., Bodvarsson, G.S., Stefansson, V., and Eliasson, E.T., 1984
The Krafla geothermal field, Iceland 4. History match and prediction of individual well performance
Water Resour. Res., v. 20, no. 11, p. 1561 – 1584 (LBL-16206)

A detailed distributed parameter model, in which all wells are represented individually, is reported for the Krafla geothermal system. The model is based on a synthesis of geological, geophysical, geochemical, and reservoir engineering data from the field. Numerical simulations achieve an approximate match for production rates and flowing enthalpies for 10 wells during the period 1976–1982. Predictions of future field performance on a well-by-well basis are presented for alternative field development plans, including additional production wells and reinjection of waste fluids.

Rezowalli, J.J., King, M.S., and Myer, L.R., 1984
Cross-hole acoustic surveying in basalt
Int. J. Rock Mech. Min. Sci. Geomech. Abstr., v. 21, p. 213 – 216 (LBL-17314)

The *in situ* assessment of geomechanical characteristics of rock masses is an essential prerequisite to the design and analysis of structures, both on the surface and underground. A particular *in situ* investigative technique that continues to show promise for this purpose is the cross-hole higher-frequency acoustic method.

The purpose of this technical note is to present preliminary results of a series of cross-hole acoustic measurement performed in a tunnel situated in a basaltic rock mass. The tunnel, at a subsurface depth of 46 m, was excavated by conventional drill-and-blast techniques. Located well above the water table, the rock mass is characterized as dense basalt with a jointing structure of 0.15 to 0.36 m thick vertical columns cut by low-angle cross joints.

The objectives of the test program were: first, to evaluate *in situ* dynamic elastic properties and to assess their spatial variation around the opening; second, to evaluate the extent of blast damage around the opening; and third, to assess the spatial variation of jointing and fracturing around the opening. Analysis of the data included an evaluation of the velocities and frequency spectra of compressional and shear waves transmitted through the rock.

It is concluded that the acoustic velocity and attenuation data are clearly indicative of an anisotropic, jointed rock mass, with a greater intensity of jointing in the horizontal than the vertical direction. Low acoustic velocities are indicative of blast damage and of zones of intense jointing or fractures. The same trend is seen also in the values of dynamic elastic modulus. The dynamic Poisson's ratio, however, appears to be relatively insensitive to the degree of jointing or fracturing.

Roy, R.N., Gibbons, J.J., Williams, R., Godwin, L., Baker, G., Simonson, J.M., and Pitzer, K.S., 1984
The thermodynamics of aqueous carbonate solutions. II. Mixtures of potassium carbonate, bicarbonate, and chloride
J. Chem. Thermodyn., v. 16, p. 303-315 (LBL-19260)

Potentials for the cell without liquid junction: $\mathrm{Pt}|\mathrm{H}_2|\mathrm{K}_2\mathrm{CO}_3(m_1)$, $\mathrm{KHCO}_3(m_2)$, $\mathrm{KCl}(m_3)|\mathrm{AgCl}|\mathrm{Ag}$ have been obtained over a broad range of solute molalities at 278.15, 298.15, 310.15, and 381.15 K. These results have been used in conjunction with previously available electrochemical-cell and isopiestic quantities to calculate activity and osmotic coefficients of aqueous K_2CO_3 and $KHCO_3$ using the ion-interaction equations of Pitzer for mixed-electrolyte systems.

Schmidt, D.P., Soo, H., and Radke, C.J., 1984
Linear oil displacement by the emulsion entrapment process
Soc. Petrol. Eng. J., June 1984, p. 351 – 360 (LBL-14926)

Lack of mobility control is a major impediment to successful EOR, especially for high-viscosity oils. This paper presents experimental and theoretical results for continuous, linear, secondary oil displacement using dilute, stable suspensions of oil drops. The major hypothesis is that the oil/water (O/W) emulsion provides microscopic mobility control through entrapment or local permeability reduction, not through viscosity-ratio improvement. To describe the displacement process, previous emulsion filtration theory is extended to longer cores and to two-phase flow. Agreement between theory and experiment is satisfactory for continuous secondary oil displacement with 1- to 2-μm [1- to 2-micron] diameter drops of volume concentrations up to 5% in unconsolidated sandpacks with permeabilities ranging from 1 to 3 μm^2 [1 to 3 darcies].

Dilute suspensions of stable oil drops in water also are successful in diverting flow in parallel-coreflooding to the lower-permeability core; therefore, they provide macroscopic mobility control.

Secor, R.B., and Radke, C.J., 1985
Spill-over of the diffuse double layer on montmorillonite particles
J. Colloid Interface Sci., in press (LBL-19261)

The Poisson-Boltzmann equation is solved exactly for a thin, cylindrical disk with a positive edge charge and a negative face charge. Surface charge densities and particle dimensions are representative of montmorillonite clay. For low indifferent electrolyte concentrations the negative electrostatic field emanating from the particle face spills over into the edge region. Accordingly, the positively charged edge exhibits a negative electrostatic field. This results in a repulsive electrostatic potential for interparticle edge-face interactions and for solution anion-particle edge interactions.

Shi, G.H., and Goodman, R.E., 1984
Two-dimensional discontinuous deformation analysis
Int. J. Numer. Anal. Methods Geomech., in press (LBL-19262)

This paper explains a novel "back-analysis" scheme to determine rock mass behavior modes from an array of deformational measurements. The *input* will be the locations of data points and the set of measured displacements, as well as description of the locations and orientations of planes of discontinuity, and the blocks they determine. The *output*, drawn by the computer, will be the set of block displacements, rotations, and strains that determine the behavioral mode of the mass.

Soo, H., and Radke, C.J., 1984
The flow mechanism of dilute, stable emulsions in porous media
Ind. Eng. Chem. Fundamen., v. 23, no. 3, p. 342 – 347 (LBL-17474)

This work establishes the flow mechanism of dilute, stable emulsions in fine grained porous media. Oil-in-water emulsions of mean drop sizes ranging from 1 to 10 μm are studied in sandpacks of 0.57 and 1.15 μm^2 permeability at a superficial velocity of 0.07 mm/s. Low viscosity oil drops cause permeability reductions of up to 80%, with 4 to 5 μm size drops being the most effective. By examining drop sizes and pores sizes, as well as transient effluent emulsion concentration and transient pressure data, we find that permeability reductions during emulsion flow are caused by droplet capture mechanisms similar to those found for solid particle deep-bed filtration. The proposed filtration mechanism is verified by a micromodel study.

Soo, H., and Radke, C.J., 1984
Velocity effects in emulsion flow through porous media
J. Colloid Interface Sci., v. 102, no. 2, p. 462–476 (LBL-19264)

Velocity plays an important role in the flow behavior of dispersed drops in underground media. Its magnitude designates whether a drop is captured, breaks up, or percolates through the medium. A quantitative description of these effects is lacking. This work investigates the possible roles of velocity in the transport of dilute, stable oil-in-water emulsions through underground porous media from the viewpoint of deep-bed filtration. A wide range of capillary number is considered. Theoretical analyses are presented for droplets having sizes corresponding to the two capture regimes of straining and interception. For the straining capture regime, the effect of velocity is important when capillary number is on the order of 10^{-4} or above. For the interception capture regime, velocity effects are important when capture is in the secondary-minimum energy well and the velocity is close to a critical re-entrainment value. In both capture regimes drop breakup occurs only when the capillary number is about unity. The theoretical findings are verified by new experimental studies on the flow of oil-in-water emulsions at velocities of 0.005 to 0.08 cm/s in sandpacks with permeabilities of 0.7 and 2 μm^2.

Soo, H., and Radke, C.J., 1985
A filtration model for the flow of dilute, stable emulsions in porous media. Part I: Theoretical
Chem. Eng. Sci., in press (LBL-19266)

Flow of dilute, stable emulsions in porous media is important in several oil recovery processes. Because underground media have relatively low permeabilities, the emulsion drop sizes may overlap the pore sizes. Hence, strong interaction occurs between the emulsion droplets and pore constrictions, and local flow redistribution occurs within the porous medium. To predict quantitatively how emulsions are transported in underground media, a theoretical model is required which correctly accounts for the interactions between the flowing droplets and the pore walls.

In part I of this work, we present a simplified filtration model describing the flow of stable, dilute emulsions in unconsolidated porous media. In the model, emulsion drops are captured in pores by straining and interception and, thus, reduce the overall permeability. Transient flow behavior is characterized by three parameters: a filter coefficient, a flow-redistribution parameter, and a flow-restriction parameter. The filter coefficient controls the sharpness of the emulsion front, the flow-redistribution parameter dictates the steady-state retention, as well as the flow redistribution phenomenon, and the flow-restriction parameter describes the effectiveness of retained drops in reducing permeability.

Critical comparison is made between the new filtration theory and the current continuum-viscous and retardation models for emulsion flow in porous media. Only the filtration picture is able to explain all the experimental observations. Quantitative comparison between the filtration flow theory and experiment is presented in part II.

Soo, H., and Radke, C.J., 1985
A filtration model for the flow of dilute, stable emulsions in porous media. Part II: Parameter evaluation and estimation
Chem. Eng. Sci., in press (LBL-19265)

Part I of this work outlined a new theory, based on deep-bed filtration concepts, to describe the flow of dilute, stable emulsions in underground porous media. Here, in part II, we quantitatively test the proposed theory against experimental data and we indicate how the filtration model parameters can be estimated from first principles.

Comparison is made between the theory and data on transient permeability and effluent concentration for dilute, oil-in-water emulsions of mean drop-size diameters ranging from 1 to 10 μm and volume concentrations of 0.5 to 2.5 percent flowing in quartz sandpacks of 0.57 to 2.0 μm^2 permeability. The pH of the continuous aqueous phase is kept constant at 10. Filtration theory successfully represents the data, permitting unambiguous evaluation of the theoretical parameters.

Procedures are described for a priori calculation of the filtration parameters from knowledge of the drop size and the pore-size and grain-size distributions of the porous medium. Good agreement is achieved between the experimentally determined parameters and their estimated values. Thus, the proposed filtration model provides a reliable tool for predicting emulsion flow behavior in porous media.

Soo, H., and Radke, C.J., 1985
Contrasts between the flow of dilute, stable liquid and solid dispersions in underground porous media
Am. Inst. Chem. Eng. J., in press (LBL-18447)

Transport of fines is important in many underground processes such as in enhanced oil recovery. With water-sensitive reservoirs, abrupt decreases in salinity can lead to solid particle entrainment with subsequent plugging and loss of fluid injection rates (Mungan, 1965; Muecke, 1979; Gruesbeck and Collins, 1982; Khilar and Fogler, 1983). Likewise, oil-in-water emulsions may form inadvertently in steam (Doscher, 1967) or chemical (Willhite et al., 1980) flooding, or they may be injected to improve sweep efficiency (Jennings et al., 1974; Schmidt et al., 1984). These applications call for an improved understanding of the flow of both liquid and solid aqueous dispersions in porous media where the pore and particle sizes may be comparable.

This work investigates the flow behavior of stabilized dispersions of liquid and solid particles in porous media under conditions where the two types of suspension have, as closely as possible, the identical physical and chemical characteristics. That is, liquid droplets and solid particles of the same particle size and shape, same bulk density, and about the same surface charge density are suspended in aqueous solution at identical volume concentrations and injected into a porous medium of known pore-size distribution. We find that both the solid and liquid suspensions follow deep-bed filtration principles (Herzig et al., 1970) but they flow in distinctly different fashions.

Stebbins, J.F., and Carmichael, I.S.E., 1984
The heat of fusion of fayalite
Am. Mineral., v. 69, p. 292−297 (LBL-16237)

The relative enthalpies ($H_T - H_{300K}$) of crystalline fayalite (Fe_2SiO_4) and of the liquids resulting from the melting of fayalite in platinum and iron-plated capsules have been measured from 985 to 1705 K by drop calorimetry. Analyses of the samples quenched from the liquid show that because of incongruent melting and disproportionation of FeO during cooling, a mixture of phases was produced, possibly including the mineral laihunite ($\sim Fe_3(SiO_4)_2$). Measured enthalpies have been corrected for these effects, resulting in an enthalpy of equilibrium, incongruent melting at 1490 K of 88.4 ± 1.1 kJ mol^{-1} and an enthalpy of hypothetical congruent melting of 89.3 ± 1.1 kJ mol^{-1}.

Stebbins, J.F., Carmichael, I.S.E., and Moret, L.K., 1984
Heat capacities and entropies of silicate liquids and glasses
Contrib. Mineral. Petrol., v. 86, p. 131−148 (LBL-17312)

The heat capacities of several dozen silicate glasses and liquids composed of SiO_2, TiO_2, Al_2O_3, Fe_2O_3, FeO, MgO, CaO, BaO, Li_2O, Na_2O, K_2O, and Rb_2O have been measured by differential scanning and drop calorimetry. These results have been combined with data from the literature to fit C_p as a function of composition. A model assuming ideal mixing (linear combination) of partial molar heat capacities of oxide components (each of which is independent of composition), reproduces the glass data within error. The assumption of constancy of $\bar{C}_{p,i}$ is less accurate for the liquids, but data are not sufficient to adequately constrain a more complex model. For liquids containing alkali metal and alkaline earth oxides, heat capacities are systematically greater in liquids with high "field strength" network modifying cations. Entropies of fusion (per g-atom) and changes of configurational entropy with temperature are similarly affected by composition. Both smaller cation size and greater charge are therefore inferred to lead to greater development of new structural configurations with increasing temperature in silicate liquids.

Stebbins, J.F., Murdoch, J.B., Schneider, E., Carmichael, I.S.E., and Pines, A., 1985
A high temperature nuclear magnetic resonance study of ^{23}Na, ^{27}Al, and ^{29}Si in molten silicates
Nature, in press (LBL-18515)

To directly study the dynamics of molecular motion and structural rearrangement in molten silicates, and to compare liquid and glass structure, we have developed a novel, high-temperature, high-resolution NMR apparatus. We report here the first data on ^{23}Na, ^{27}Al, and ^{29}Si in liquids in the system Na_2O–Al_2O_3–SiO_2, at temperatures to about 1300°C. As has been observed in glasses and crystals, chemical shift values (δ) of ^{29}Si in melts become more negative (greater chemical shielding) with increased polymerization. Similarly, $\delta(^{23}Na)$ decreases with increases in the ratio O/Na. Relaxation times T_2 for ^{23}Na and ^{29}Si dramatically decrease with falling temperature until liquid-like spectra become solid-like. ^{27}Al spectra are very broad at all temperatures due to strong quadrupole coupling.

Stump, B.W., and Johnson, L.R., 1984
Near-field source characterization of contained nuclear explosions in tuff
Bull. Geol. Soc. Am., v. 74, no. 1, p. 1–26

The seismic sources of three contained nuclear explosions in tuff at Pahute Mesa are characterized by applying the moment tensor source representation to near-field accelerometer recordings of the events. Propagation path effects are accounted for in the study by generalized ray calculations for several plane-layered models. Synthetic seismograms generated from the estimated sources model well the distance and azimuthal variations in the data. The moment tensors are dominated by the isotropic component with the absolute ratio of isotropic to deviatoric component varying between 2 and 20, depending on the particular Green's function. The isotropic sources indicate the procedure is a good measure of relative yield while the absolute yield is dependent upon the exact Green's function. Source time functions indicate the possibility of a double-pulse source separated by 1.0 to 1.5 sec. This interpretation is limited by the fact that phase information is the least well-resolved portion of the study. In contrast, the stability of the spectral characteristics, such as corner frequency, high-frequency roll-off, and peak value, shows the value of the moment tensor in the frequency domain for yield and discrimination studies.

Taylor, J.A., and Perry, D.L., 1984
An x-ray photoelectron (XPS) and electron energy loss study of the oxidation of lead
J. Vac. Sci. Technol., v. 2, p. 771−774 (LBL-17515)

Lead-oxygen compounds and the exposures of clean polycrystalline Pb^0 to O_2, H_2O, and air at various temperatures have been studied with x-ray photoelectron (XPS) and electron energy loss (EELS) spectroscopies. Results indicate that the shape of the Auger O *KVV* lines and EELS are sufficiently different to distinguish PbO, PbO_2, Pb_3O_4, and carbonate-hydroxide. Differences in the EELS spectra indicate that orthorhombic PbO is formed on clean Pb^0 exposed to dry O_2 at temperatures below the melting point of Pb^0, and tetragonal PbO is formed at or above its melting point.

Tsang, C.F., Mangold, D.C., Doughty, C., and Lippmann, M.J., 1984
Prediction of reinjection effects in the Cerro Prieto geothermal system
Geothermics, v. 13, no. 1/2, p. 141−162 (LBL-14895)

The response of the Cerro Prieto geothermal field to different reinjection schemes is predicted using a two-dimensional vertical reservoir model with single- or two-phase flow. The advance of cold fronts and pressure changes in the system associated with the injection operations are computed, taking into consideration the geologic characteristics of the field. The effects of well location, depth and rates of injection are analyzed. Results indicate that significant pressure maintenance effects may be realized in a carefully designed reinjection operation.

Tsang, Y.W., 1984
The effect of tortuosity on fluid flow through a single fracture
Water Resour. Res., v. 20, no. 9, p. 1209−1215 (LBL-16044)

Calculations to investigate the effect of path tortuosity and connectivity on fluid flow rate through a single rough fracture were carried out. The flow paths are represented by electrical resistors placed on a two-dimensional grid, and the resistances vary as the inverse of the fracture aperture cubed. The electric current through the circuit bears a one-to-one correspondence to the fluid flow rate. Both fracture apertures derived from measurements and from hypothetical analytic functions were used in a parameter study to investigate the dependence of tortuosity on fracture roughness characteristics. It was found that the more small apertures there are in the aperture distribution, the larger is the effect of tortuosity. When the fraction of contact area between the fracture surfaces rises above 30%, the aperture distributions are invariably large at small apertures, and the effect of fracture roughness and flow path tortuosity depresses flow rate from the value predicted by the parallel plate representation of a fracture by three or more orders of magnitude. The impact of these results on the calculations and measurements in fracture hydrology is discussed.

Vasco, D.W., and Johnson, L.R., 1985
Extremal inversion of static earth displacements due to volume sources
Geophys. J. Roy. Astr. Soc., v. 80, in press (LBL-19268)

The inverse problem of using static displacements observed at the surface to infer volume changes within the Earth is considered. This problem can be put in a form such that the method of ideal bodies and the method of positivity constraints may both be applied. Thus all of the techniques previously developed for the gravity inverse problem can be extended to the static displacement problem. Given bounds on the depth, the greatest lower bound on the fractional volume change can be estimated, or, given bounds on the fractional volume change, the least upper bound on the depth can be estimated. Methods of placing bounds on generalized moments of the perturbing body are also developed, and techniques of handling errors in the data are discussed.

Examples are given for both two- and three-dimensional problems. The ideal method is suited for both 2- and 3-D problems when only two data points are considered, but is unwieldy for more data points. The method of positivity constraints is more versatile and can be used when there are many data points in the case of 2-D problems, but it may lead to an excessive amount of computation in 3-D problems.

Weres, O., 1984
Numerical evaluation of surface condensers for geothermal power plants
Geothermics, v. 13, no. 4, p. 293−304 (LBL-15047)

The transport and partitioning of gases in four surface condensers for geothermal power plants has been modeled numerically. A vent condenser between the main condenser and the first stage gas ejectors improves hydrogen sulphide partitioning, particularly if the condensate from it, and from the inter- and aftercondensers, is recirculated to the main condenser tube bundles. Regardless of steam composition, hydrogen sulphide emissions may be largely eliminated by a Stretford Unit combined with a suitable surface condenser. However, if the steam contains ammonia it may be necessary to add sulphur dioxide to neutralize part of the ammonia. In no case is hydrogen peroxide needed to largely eliminate hydrogen sulphide air pollution.

Weres, O., 1984
Numerical evaluation of contact and hybrid condensers for geothermal power plants
Geothermics, in press (LBL-15048)

The transport and partitioning of gases in two contact condensers in use at The Geysers has been modeled numerically. Improvements on these designs have been investigated. Adding a surface type vent condenser between the main condenser and the first stage gas ejectors improves hydrogen sulphide partitioning dramatically. This "hybrid condenser" can match the performance of a surface condenser. Adding a contact type gas cooler allows 90% partitioning to be attained with steam that contains little ammonia. (This has been demonstrated in practice by Glover and Hart.)

Weres, O., Tsao, L., and Chhatre, R.M., 1985
Catalytic oxidation of aqueous hydrogen sulfide in the presence of sulfite
Corrosion, in press (LBL-15482).

Nickel sulfate catalyzes the reaction of hydrogen sulfide with oxygen in aqueous solution. This reaction was studied. An empirical rate expression and reaction mechanism were deduced. The rate of oxidation is independent of oxygen concentration and pH over the range investigated. The reaction rate is one-half order in nickel, and changes from second to first order in sulfide with increasing concentration. The oxidation reaction is an autocatalytic, free radical chain reaction. Nickel catalyzes the chain initiation step, and polysulfido radical-ions propagate the chains. Colloidal sulfur is a major, frequently undesirable reaction product. Sodium sulfite suppresses formation of colloidal sulfur by converting it to thiosulfate.

Cobalt is an equally potent catalyst, but a colloidal dispersion of cobalt oxysulfide is produced. Iron compounds are much weaker catalysts; iron citrate and iron HEDTA (N-hydroxyethylenediaminetriacetic acid) were the best among those tested.

White, A.F., 1984
Weathering characteristics of natural glass and influences on associated water chemistry
J. Non-Cryst. Solids, v. 67, p. 225−244 (LBL-16391)

Weathering rates and mechanisms of volcanic glasses at ambient temperature are investigated both experimentally and in the natural environment. As documented previously for man-made glasses, natural silicate glasses weather by a two step process involving surface corrosion and cation interdiffusion. Diffusion rates display a strong valence state-dependence with monovalent species less pH-dependent than bivalent species. Rates of release also decrease with increasing aqueous concentrations and glass-surface to solution-volume ratios. Numerical solutions to Fick's second law of diffusion are presented for surface-concentration dependent diffusion and diffusion coupled with surface corrosion. Calculated diffusion coefficients of 1×20^{-19} cm^2 $\times$ 5^{-1} and activation energies of 95 kJ mol^{-1} are in agreement with data for man-made glasses.

Geochemical data are presented for short and long term natural weathering of glassy rocks. XPS data for glass phases in the 1980 Mount St. Helens ash fall indicate rapid loss of readily exchangeable surface cations followed by longer term diffusion release. Incongruent leaching of Tertiary-age vitric tuffs in Nevada is found to control associated groundwater chemistry.

White, A.F., and Yee, A., 1984
Surface oxidation-reduction kinetics associated with experimental basalt/water reactions at 25°C
Chem. Geol., in press (LBL-17578)

Distributions of Fe(II) and Fe(III) during basalt/water interaction were experimentally investigated under open and closed system O_2 conditions at 25°C. XPS analyses showed oxidized iron on the surface of basalt, the concentration of which decreased as a function of reaction pH. Concurrent increases in Fe(II) and decreases in Fe(III) in solutions at pHs less than 5 indicated continued surface oxidization by the reaction

$$(\mathrm{Fe(II)}) \cdot 1/ZM^{z}_{\mathrm{Basalt}} + \mathrm{Fe(III)}_{\mathrm{Solution}}$$

$$+ \mathrm{Fe(III)}_{\mathrm{Basalt}} + \mathrm{Fe(II)}_{\mathrm{Solution}} + 1/ZM^{z}_{\mathrm{Solution}}$$

where the electrical charge in solution is balanced by dissolution of a cation from the basalt.

At neutral to basic pH, Fe(I) is oxidizated to Fe(III) and precipitated as ferric oxyhydroxide in the presence of O_2. Fe(II) is also strongly sorbed on the basalt surface resulting in low aqueous concentrations even under anoxic conditions. The rate of O_2 uptake increased with decreasing pHs. Diffusion coefficients of the order 10^{-4}cm^{2}s^{-1} were calculated using a one-dimensional diffusion model and suggest grain boundary diffusion in iron oxides.

White, A.F., and Yee, A., 1985
Aqueous oxidation-reduction kinetics associated with coupled electron-cation transfer from iron silicates at 25°C
Geochim. Cosmochim. Acta, in press (LBL-19269)

Mechanisms and kinetics of aqueous Fe^{+2}/Fe^{+3} oxidation-reduction and dissolved O_2 interaction in the presence of augite, biotite and hornblende were studied in oxic and anoxic solutions at pH 1–9 at 25°C. Oxidation of surface iron on the minerals coincided with both surface release of Fe^{+2} and reduction of Fe^{+3} in solution. Reaction with iron silicates consumed dissolved oxygen at a rate that increased with decreasing pH.

Both Fe^{+3} and O_2 consumption were shown to be controlled by coupled electron-cation transfer reactions of the form

$$[\mathrm{Fe}^{+2}, 1/zM^{+z}]_{\mathrm{silicate}} + \mathrm{Fe}^{+3} \rightarrow [\mathrm{Fe}^{+3}]_{\mathrm{silicate}} + \mathrm{Fe}^{+2} + 1/zM^{+z}$$

and

$$[\mathrm{Fe}^{+2}, 1/zM^{+z}]_{\mathrm{silicate}} + \mathrm{H}^{+} + 1/4\mathrm{O}_2 \rightarrow [\mathrm{Fe}^{+3}]_{\mathrm{silicate}}$$

$$+ 1/zM^{+z} + 1/2\mathrm{H}_2\mathrm{O}$$

where M is a cation of charge $+z$. The spontaneous reduction of aqueous Fe^{+3} in the presence of precipitated $Fe(OH)_3$ bracketed the surface oxidation standard half-cell between +0.33 and +0.52 volts. Concurrent hydrolysis reactions involving cation release from the iron silicates were suppressed by the above reactions. Calculated oxidation depths in the minerals varied between 12 and 80 Å and were apparently controlled by rates of solid-state cation diffusion.

White, A.F., Delany, J.M., Narasimhan, T.N., and Smith, A., 1984
Groundwater contamination from an inactive uranium mill tailings pile. 1. Application of a chemical mixing model
Water Resour. Res., v. 20, no. 11, p. 1743–1752 (LBL-17812)

Low-*p*H process waters contained in a number of inactive and abandoned uranium mill tailings in the United States represent potential sources of radionuclide and trace metal contamination of groundwater. Detailed investigations at a typical site at Riverton, Wyoming, indicate that chemical transport occurs from initial dewatering of the tailings, downward infiltration due to precipitation, and groundwater intrusion into the base of the tailings pile. Except for elevated uranium and molybdenum concentrations, current radionuclide and trace metal transport is limited by the near-neutral *p*H conditions of the groundwater. Significant reactions include the dissolution of calcite, production of CO_2, and precipitation of gypsum and the hydroxides of iron and aluminum. A geochemical mixing model employing the PHREEQE computer code is used to estimate current rates of the groundwater contamination by tailings water. A maximum mixing of 1.7% of pore water is a factor of 2 less than steady state estimates based on hydraulic parameters.

Wilt, M.J., and Goldstein, N.E., 1984
Interpretation of dipole-dipole resistivity monitoring data at Cerro Prieto
Geothermics, v. 13, no. 1/2, p. 13–25 (LBL-14499)

Repetitive dipole-dipole resistivity data have been taken on a yearly basis by LBL at Cerro Prieto since 1978. Stations along a single profile line extending from the Cucapa Mountains to the center of the Mexicali Valley and passing over the present production zone have been remeasured with sufficient accuracy to detect subsurface changes in resistivity, some of which are probably related to fluid production. The precision of the most recent measurements (November, 1981) averages about 1%. Results from 2.5 years of monitoring indicate a 5% annual increase in apparent resistivity over the present production area and decreases in apparent resistivity of the same magnitude in the regions immediately eastward and westward from the production zone. The increase in resistivity in the production zone is most likely due to dilution of reservoir fluids with fresher water, as evidenced by a drop in chloride content of produced waters. An attempt was made to determine whether specific lithologic zones in wellbores show resistivity changes with time by comparing well logs from newly drilled wells with logs from older nearby wells. Results show that lateral resistivity variations within stratigraphic units between closely spaced wells are sufficient to obscure possible temporal changes. The area of decreasing resistivity in the eastern part of the field is associated with a steeply dipping conductive body, a zone of higher thermal gradients and an increase in shale thickness in the section. Well log analysis shows that the low resistivity is mostly due to higher temperatures. Decreasing resistivity in this area may be caused by an influx of hotter and more saline brines from depth. Recent measurements also show dramatic increase in near-surface resistivity at the western end of the monitored line. This is most likely due to recent changes in local irrigation practices which resulted in a general improvement in groundwater quality. To investigate the phenomenon of resistivity changes caused by groundwater movement and chemical reactions, we propose the establishment of an additional resistivity line crossing both the new eastern production zone and the present survey line at an angle of 60°. This line would permit the acquisition of baseline data over the future production zone (Cerro Prieto II and III areas), in conjunction with the present line, and would establish a grid of stations which could be used to map subsurface groundwater fronts.

Wollenberg, H.A., Smith, A.R., Mosier, D.F., Flexser, S., and Clark, M., 1984
Radon-222 in groundwater of the Long Valley caldera, California
Pure Appl. Geophys., v. 122, in press (LBL-17636)

In the long Valley caldera, where seismicity has continued essentially uninterrupted since mid-1980 and uplift is documented, samples of water from hot, warm, and cold springs have been collected since September, 1982, and their ^{222}Rn concentrations analyzed. Concurrently, rocks encompassing the hydrologic systems feeding the springs were analyzed for their radioelement contents, because their uranium is the ultimate source of the ^{222}Rn in the water.

The ^{222}Rn concentration in the springs varies inversely with their temperature and specific conductance. High concentrations (1500 to 2500 picocuries per liter) occur in dilute cold springs on the margins of the caldera, while low contents (12 to 25 pCi/l) occur in hot to boiling springs. Spring-water radon concentrations also correlate slightly with the uranium content of the encompassing rocks.

A continuous monitoring system was installed in August, 1983, at a spring issuing from basalt, to provide hourly records of radon concentration. A gamma detector is submerged in a natural pool, and we have observed that the radioactivity measured in this manner is due almost entirely to the ^{222}Rn concentration of the water. Initial operation shows diurnal and semidiurnal variations in the ^{222}Rn concentration of the springwater that are ascribed to earth tides, suggesting that those variations are responding to small changes in stress in the rocks encompassing the hydrologic system.

Zimmerman, R.W., 1984
Elastic moduli of a solid with spherical pores: New self-consistent method
Int. J. Rock Mech. Min. Sci. Geomech. Abstr. v. 21, p. 339–343

Various analytical approaches have been taken in attacking the general problem of predicting the elastic moduli of a solid containing pores or inclusions. For even the simplest case, that of an isotropic material randomly permeated with spherical inclusions, the results obtained do not always agree with each other beyond the terms which are first-order in inclusion concentration. The earliest attempt to solve this particular problem was by analyzing the effects of inclusions as if each one were unaffected by the presence of its neighbors. The self-consistent scheme was then developed to account for the elastic interaction of inclusions or pores. However, it was later suggested that the self-consistent method overestimates the effect of pores in lowering the elastic moduli, in that it implicitly takes interactions between pairs of pores into account twice. A modification of the self-consistent method, which avoids this double interaction error, is applied here to the case of spherical pores or inclusions. The results have been compared with those obtained using several other theoretical approaches. The modified self-consistent method has been demonstrated to predict accurately the experimentally measured elastic moduli of solids containing spherical pores and inclusions that have been reported in the literature.

Zimmerman, R.W., 1985
Compressibility of an isolated spheroidal cavity in an isotropic elastic medium
ASME J. Appl. Mech., in press

A spheroidal cavity in an infinite, isotropic, elastic medium provides a useful model for voids, which are often present in rocks, ceramics, and porous metals. In its limiting forms, the spheroid can represent a sphere, an infinitely long cylinder, or a flat "penny-shaped" crack. Although the problem of the elastic field around a spheroidal cavity has been examined in the past, the focus of these studies has usually been on stress concentrations. Consequently, there are certain features applicable to pore compressibility that appear to have escaped notice. It is shown here that the pore compressibility of a prolate spheroid, whose shape can range from a sphere to a cylinder, is essentially a function only of the shear modulus and is nearly independent of the compressibility of the matrix material. It is also shown that the asymptotic expression for the pore compressibility of an oblate spheroid of vanishingly small aspect ratio (the usual model for the penny-shaped crack) is actually highly accurate over nearly the entire range of oblate spheroid aspect ratios.

APPENDIX B: LBL REPORTS, BOOKS, CONFERENCES, PROCEEDINGS

LBL REPORTS

LBL-11865 (SAC-48)
Gale, J.E., and Raven, K.G., 1980. Effects of sample size on the stress-permeability relationships for natural fractures.

LBL-13071 (SAC-42)
Rouleau, A., Gale, J.E., and Baleshta, J., 1981. Fracture mapping in the ventilation drift at Stripa: Procedures and Results.

LBL-13101 (SAC-46)
Gale, J.E., 1981. Fracture and hydrology data from field studies at Stripa, Sweden.

LBL-13327 (SAC-53)
Lingle, R., Nelson, P.H., DuBois, A.O., and Seliden, H., 1984. Performance of borehole deformation gauges and vibrating wire stressmeters at Stripa, Sweden.

LBL-13392 (SAC-47)
Galbraith, R.M., Wilson, C.R., DuBois, A.O., Lundgren, S.A., McPherson, M.J., and West, G.W., 1981. Equipment design, installation, and operation for the macropermeability experiment at Stripa, Sweden.

LBL-13531 (SAC-50)
DuBois, A.O., Hood, M., Binnall, E.P., and Andersson, L., 1981. Extensometer performance during heater experiments at Stripa.

LBL-14878 (SAC-49)
Gale, J.E., Rouleau, A., and Wilson, C.R., 1982. Progress in the hydrogeological characterization of the Stripa site.

LBL-15009 (SAC-44)
Doe, T.W., Ingevald, K., Strindell, L., Leijon, B., Hustrulid, W., Majer, E., and Carlsson, H., 1983. In situ stress measurements at the Stripa mine, Sweden.

LBL-15050
Javandel, I., 1983. Field determination of the hydrologic properties and parameters that control the vertical component of groundwater movement.

LBL-16346 (SAC-51)
Paulsson, B.N.P., 1983. Seismic velocities and attenuation in a heated undergound granitic repository (Vol.I).

LBL-16346 (SAC-51)
Paulsson, B.N.P., 1983. Seismic velocities and attenuation in a heated underground granitic repository (Vol. II).

LBL-16518
Weres, O., Michel, M., Harnden, W., and Newton, A., 1984. Downhole sampling of geopressured gas wells: Final report for 1982–1984.

LBL-16563
Feng, R., and McEvilly, T.V., 1983. Interpretation of seismic reflection profiling data for the structure of the San Andreas fault zone.

LBL-16883
Fox, D.J., 1984. Hydrothermal alteration in well Baca 22, Baca geothermal area, Valles Caldera, New Mexico.

LBL-16920
Earth Sciences Division, 1984. Earth Sciences Division Annual Report 1983.

LBL-17084
Goldstein, N.E., and Tsang, C.F., 1983. A review of lessons learned from the DOE/Union Baca geothermal project and their application to CSDP drilling in the Valles Caldera, New Mexico.

LBL-17133
Carnahan, C.L., Miller, C.W., and Remer, J.S., 1984. Verification and improvement of predictive algorithms for radionuclide migration.

LBL-17417
Wilt, M., and Vonder Haar, S., 1984. Geological and geophysical appraisal of the Baca geothermal field, Valles Caldera, New Mexico.

LBL-17491
Endo, H.K., 1984. Mechanical transport in two-dimensional networks of fractures (Ph.D. thesis).

LBL-17635
Doe, T.W., and McClain, W.C., 1984. Rock mechanics issues and research needs in the disposal of wastes in hydraulic fractures.

LBL-17675
Spencer, R.K., and Tsang, C.-F., 1984. Listing of scientific data on the Baca geothermal field.

LBL-17745
Apps, J.A., 1983. Geochemistry research planning for the underground storage of high-level nuclear waste.

LBL-17814
Narasimhan, T.N., 1984. Geometry-imbedded Darcy's law and transient subsurface flow.

LBL-18102
Weres, O., Harnden, W., Biocca, A., and Solbau, R., 1984. Operating instructions for LBL/GRI downhole sampler and sample extraction system.

LBL-18473
Wang, J.S.Y., and Narasimhan, T.N., 1984. Hydrologic mechanisms governing fluid flow in partially saturated, fractured, porous tuff at Yucca Mountain.

LBL-18564
Williams, C.F., Narasimhan, T.N., Anderson, R.N., Zoback, M.D., and Becker, K., 1984. Convection in oceanic crust: Numerical simulation of observations from DSDP hole 504B, Costa Rica rift.

BOOKS

Goodman, R.E., and Shi, G.-H., 1984. Block Theory and Its Application to Rock Engineering. Englewood Cliffs, New Jersey, Prentice-Hall.

Javandel, I., Doughty, C., and Tsang, C.F., 1984. Groundwater Transport: Handbook of Mathematical Models. Water Resources Monograph Series (Vol. 10). Washington, D.C., American Geophysical Union, 228 p.

Narasimhan, T.N., and Goyal, K.P., 1984. Subsidence due to geothermal fluid withdrawal. *In* Reviews in Engineering Geology (Vol. VI). Boulder, Geological Society of America, p. 35–66.

White, A.F., Benson, L.V., and Yee, A., 1985. Weathering of the May 1980 Mt. St. Helens ash fall and its effect on the Iron Creek watershed, Washington. *In* S. Coleman and D. Rethier (eds.), Chemical Weathering Rates of Rocks and Minerals. New York, Academic Press, in press.

White, A.F., Delany, J.M., Truesdell, A., Janik, K., Goff, F., and Crecraft, H., 1984. Fluid chemistry of the Baca geothermal field, Valles Caldera, New Mexico. *In* New Mexico Geological Society Guidebook, 35th Field Conference. Socorro, New Mexico Geological Society, p. 257–263.

CONFERENCES AND PROCEEDINGS

Benson, S.M., 1983. Interpretation of interference data from the Klamath Falls, Oregon, geothermal resource. Presented at the Stanford Ninth Annual Workshop on Geothermal Reservoir Engineering, Stanford, California, December 13–15, 1983 (LBL-16671).

Blakeslee, S., 1984. Seismic discrimination of a geothermal field, Cerro Prieto. Presented at the Geothermal Resources Council 1984 Annual Meeting, Reno, Nevada, August 26–29, 1984 (LBL-17859).

Bodvarsson, G.S., 1984. Numerical studies of enthalpy and CO_2 transients in two-phase wells. Presented at the Geothermal Resources Council 1984 Annual Meeting, Reno, Nevada, August 26–29, 1984 (LBL-17694).

Bodvarsson, G.S., and Pruess, K., 1983. Modeling studies of geothermal systems with a free water surface. Presented at the Stanford Ninth Annual Workshop on Geothermal Reservoir Engineering, Stanford, California, December 13–15, 1983 (LBL-17146).

Boyce, G.M., Doe, T.W., and Majer, E., 1984. Laboratory hydraulic fracturing stress measurements in salt. To be presented at the 25th U.S. Rock Mechanics Symposium, Northeastern University, Evanston, Illinois, June 21–23, 1984 (LBL-17520).

Brookins, D.G., Murphy, M.T., and Wollenberg, H.A., 1983. Geochemical studies of Columbia River basalts. Presented at the Materials Research Society 1983 Annual Meeting, Boston, Massachusetts, November 14–17, 1983 (LBL-17151).

Brookins, D.G., Murphy, M.T., and Wollenberg, H.A., 1983. Strontium isotopic study of fracture filling materials in the Grande Ronde Basalt, Washington. Presented at the Materials Research Society 1983 Annual Meeting, Boston, Massachusetts, November 14–17, 1983 (LBL-17159).

Chambré, P.L., Lung, H., and Pigford, T.H., 1984. Time-dependent mass transfer through backfill. Submitted to the 1984 Annual Meeting of the American Nuclear Society, New Orleans, Louisiana, June 3-7, 1984 (LBL-18444).

Chambré, P.L., Williams, W.J., Kim, C.L., Zavoshy, S., and Pigford, T.H., 1984. Time-temperature dissolution and radionuclide transport. Submitted to the 1984 Annual Meeting of the American Nuclear Society, New Orleans, Louisiana, June 3-7, 1984 (LBL-18445).

Dominguez, B., and Lippmann, M.J., 1983. Some comments on the La Primavera geothermal field, Mexico. Presented at the Stanford Ninth Annual Workshop on Geothermal Reservoir Engineering, Stanford, California, December 13–15, 1983 (LBL-16706).

Earth Sciences Division, 1984. Panel Report on Coupled Thermal–Mechanical–Hydro–Chemical Processes Associated with a Nuclear Waste Repository, Panel Meeting, Lawrence Berkeley Laboratory, January 25–27, 1984 (LBL-18250).

Earth Sciences Division, 1984. Proceedings of the Workshop on Geophysical Modeling of the Long Valley Caldera, Lawrence Berkeley Laboratory, February 8–9, 1984 (LBL-18106).

Earth Sciences Division, 1984. Proposed scientific activities for the Salton Sea Scientific Drilling Project. Presented at the Ogle Meeting on Geothermal Systems, Stanford, California, May 16–17, 1984 (LBL-17716).

Earth Sciences Division, 1984. Workshop on CSDP data needs for the Baca geothermal field: A summary, Lawrence Berkeley Laboratory, December 2, 1983 (LBL-17695).

Kim, C.L., Zavoshy, S.J., Chambré, P.L., and Pigford, T.H., 1984. Near-field and far-field mass transfer in a geologic repository. Submitted to the 1984 Winter Meeting of the American Nuclear Society, Washington, D.C., November 11-16, 1984 (LBL-18077).

Lippmann, M.J., and Bodvarsson, G.S., 1983. The generating capacity of the Heber geothermal field, California. Presented at the Stanford Ninth Annual Workshop on Geothermal Reservoir Engineering, Stanford, California, December 13–15, 1983 (LBL-16677).

Morrison, H.F., Lee, K.H., and Kennedy, D., 1984. Low frequency electromagnetic logging. Presented at the 54th Annual International SEG Meeting, Atlanta, Georgia, December 2–6, 1984.

Paulsson, B.N.P., and King, M.S., 1984. Seismic velocities and attenuation in an underground granitic waste repository subjected to heating. Presented at the ISRM: Symposium on Design and Performance of Underground Excavations, Cambridge, England, September 3–6, 1984 (LBL-17402).

Perry, D.L., Tsao, L., and Taylor, J.A., 1984. Surface studies of the interaction of copper ions with metal sulfide minerals. Presented at the 165th National Meeting of the Electrochemical Society, Symposium on the Electrochemistry in Mineral and Metal Processing, Cincinnati, Ohio, May 6–11, 1984 (LBL-17912).

Pigford, T.H., 1984. Assessing the performance of geologic repositories for nuclear waste. Presented at the ASCE Conference, Energy '84, Pasadena, California, August 19–22, 1984 (LBL-18270).

Pitzer, K.S., 1984. Thermodynamic properties of aqueous NaCl from 273 to 283 K with estimates for higher temperatures. Presented at the International Conference on the Properties of Steam, Moscow, Russia, September 3—7, 1984 (LBL-18183).

Pitzer, K.S., and Simonson, J.M., 1984. Thermodynamics of multicomponent, miscible ionic systems: Theory and equations. Presented at the 1984 International Chemical Congress of Pacific Basin Societies, Honolulu, Hawaii, December 16—21, 1984 (LBL-17839).

Pruess, K., Bodvarsson, G.S., and Stefansson, V., 1983. Analysis of production data from the Krafla geothermal field, Iceland. Presented at the Stanford Ninth Annual Workshop on Geothermal Reservoir Engineering, Stanford, California, December 13—15, 1983 (LBL-17145).

Pruess, K., and Wang, J.S.Y., 1983. TOUGH—A numerical model for nonisothermal unsaturated flow to study waste canister heating effects. Presented at the Materials Research Society 1983 Annual Meeting, Boston, Massachusetts, November 14—17, 1983 (LBL-16946).

Shi, G.-H., and Goodman, R.E., 1984. Discontinuous deformation analysis. Proceedings, 25th Symposium on Rock Mechanics, Evanston, Illinois, June 24-27, 1984 (LBL-17696).

Solbau, R.D., Benson, S.M., and Goranson, C.B., 1983. The development and use of a high temperature downhole flowmeter for geothermal well logging. Presented at the Stanford Ninth Annual Workshop on Geothermal Reservoir Engineering, Stanford, California, December 13—15, 1983 (LBL-16672).

Verma, A.K., Pruess, K., Bodvarsson, G.S., Tsang, C.F., and Witherspoon, P.A., 1983. Design and development of a test facility to study two-phase steam/water flow in porous media. Presented at the Stanford Ninth Annual Workshop on Geothermal Reservoir Engineering, Stanford, California, December 13—15, 1983 (LBL-17172).

Vonder Haar, S.P., 1984. Porosity of coastal deltaic sandstones, Cerro Prieto geothermal field, Baja California, Mexico. Presented at the Geothermal Resources Council 1984 Annual Meeting, Reno, Nevada, August 26—29, 1984 (LBL-17650).

Wilt, M., Goldstein, N.E., and Sasaki, Y., 1984. Long-term dipole-dipole resistivity monitoring at the Cerro Prieto geothermal field. Presented at the Geothermal Resources Council 1984 Annual Meeting, Reno, Nevada, August 26—29, 1984 (LBL-17644).

Yang, H.-J.P., and Bogy, D.B., 1984. Elastodynamic stress intensity factors of an interface finite-width crack. Presented at the Review of Progress in Quantitative Nondestructive Evaluation Conference, San Diego, California, July 9—13, 1984 (LBL-18051).

Zavoshy, S.J., Chambré, P.L., and Pigford, T.H., 1984. Waste package mass transfer rates in a geologic repository. Submitted to the 1984 Winter Meeting of the American Nuclear Society, Washington, D.C., November 11-16, 1984 (LBL-18079).

APPENDIX C. HOSTED MEETINGS

WORKSHOP ON CSDP DATA NEEDS: BACA GEOTHERMAL FIELD

December 2, 1983

The purpose of the meeting was to discuss the scientific data needs of the Continental Scientific Drilling Program (CSDP) community and to introduce the researchers involved in the CSDP program to the available geologic, geophysical, geochemical, and reservoir engineering data on the Baca geothermal field at Valles Caldera, New Mexico. The information is from the Baca cooperative geothermal project, jointly sponsored by the U.S. Department of Energy, Union Oil Company, and Public Service Company of New Mexico. The data have been collected in the Baca Data Base, available from the Earth Sciences Division of Lawrence Berkeley Laboratory (LBL), and are cataloged in Lawrence Berkeley Laboratory Report LBL-17675.

Workshop participants included over 40 researchers involved in CSDP activities. A workshop Executive Summary is available as LBL-17695, which also briefly reviews the data needs for CSDP.

COUPLED THERMAL-MECHANICAL-HYDRO-CHEMICAL PROCESSES ASSOCIATED WITH A NUCLEAR WASTE REPOSITORY

January 25–27, 1984

A key issue in the long-term performance of a nuclear waste repository is the estimation of travel time and rate of transport of radioactive elements from the repository to the accessible environment. This estimation must be based on an understanding of the combined effects of thermal (T), hydraulic (H), geomechanical (M), and geochemical (C) phenomena that may affect such transport. A summary of the relevant key issues is contained in one of the articles in the Reservoir Engineering and Hydrogeology section of this report. The meeting was organized in recognition of the need to have a multidisciplinary investigation of the coupled physical and chemical interactions in geologic systems, with the aim of increasing our understanding of the important processes affecting the long-term performance of a nuclear waste repository. Some 15 experts representing the disciplines of groundwater hydrology, rock mechanics, and geochemistry were invited from academic, commercial, and governmental institutions as well as LBL. The discussions and preliminary findings from this meeting are summarized in Lawrence Berkeley Laboratory Report LBL-18250.

WORKSHOP ON GEOPHYSICAL MODELING OF THE LONG VALLEY CALDERA

February 8–9, 1984

The meeting was convened to review and to integrate the results of geophysical investigations made in the Long Valley area since 1980 and to attempt to reach a consensus on the key elements of a geophysical model for the caldera, including present uncertainties and outstanding issues. The workshop also addressed the significance of results with respect to questions of Sierran Front tectonics, caldera evolution and structure, past and current hydrothermal processes, and recent magma movement.

The Long Valley caldera is one of the most intensively studied geologic features in the United States. Scientific studies of the hot springs and of the caldera's volcanic history began about 40 years ago. Recent increases in seismic activity and caldera deformation have significantly increased the pace of detailed geologic, hydrologic, geophysical, and geochemical investigation. The Long Valley caldera is one of several sites selected in 1979 by the Thermal Regimes panel of the Continental Scientific Drilling Committee for review in preparation for proposed drilling into an active hydrothermal-magmatic system for scientific purposes. Workshop participation was limited to about 15 scientists—from national laboratories, the U.S. Geological Survey, and universities—who have been directly involved in data acquisition and interpretation. The workshop's mission was to define points of agreement and disagreement as to the various geophysical data sets and their interpretation and to point the way to resolution of important outstanding questions. The workshop proceedings are available in Lawrence Berkeley Laboratory Report LBL-18106.

LAWRENCE BERKELEY LABORATORY
TECHNICAL INFORMATION DEPARTMENT
UNIVERSITY OF CALIFORNIA
BERKELEY, CALIFORNIA 94720